GOVP1199814488

국제공동연구사업
최종보고서

결정성장에 있어서 회전유동 대류현상의 해석

Convection in rotating flows in crystal growth

주관연구기관
한국과학기술원

과학기술부

제 출 문

과학기술부 장관 귀하

본 보고서를 " 결정성장에 있어서 회전유동 대류현상의 해석"과제의 보고서로 제출합니다.

1998. 11.

주관연구기관명 : 한국과학기술원

주관연구책임자 : 현 재 민

연 구 원 : 성 형 진

" : 김 문 언

" : 박 승 오

" : 임 태 규

" : 황 권 상

" : 전 경 빈

" : 백 진 욱

" : 정 용 만

" : 이 인 원

" : 김 원 년

" : 심 영 민

" : 이 창 호

" : 정 광 효

" : 김 기 빈

" : 배 준 호

요 약 문

Ⅰ. 제 목

결정성장에 있어서 회전유동 대류현상의 해석

Ⅱ. 공동연구개발 목적 및 상대국과의 공동연구 역할분담 체계

자연대류현상의 유체유동및 열전달과 회전유체유동에 대한 KAIST와 일본 Kyushu Univ.연구팀과의 국제공동연구를 수행한다. KAIST와 Ozoe 연구팀의 상호이익증진과 협력연구를 수행함으로서 실험및 계산능력의 중대가 기대된다. 또한 연구개발의 잠재력이 강화될 것이다. 첨단기계전자산업에서 자주발생하는 결정성장문제에 관계된 유동및 열전달 특성에대한 풍부한 연구자료를 제공할 것이다. 계산 소프트웨어의 제공, 개발과, 또한 실제회전기계의 성능향상방법과 기법을 제시한다.

KAIST측에서는 본 연구 주제에 대하여 주로 이론적 전개와 소형모형실험을 수행하였다. KAIST에서는 박사학생 10여명이 논문연구를 수행한다. 수치적분 방법론, 실험기법의 개발, 회전계의 유동, 비정상유동등이 주된 연구대상이다. 일본측 연구팀은 '결정성장에 있어서 이중확산 자연대류'라는 연구과제에 대한 연구를 수행하였다. 일본측에서는 회전하는 원통용기내의 회전유동의 심도있는 실험및 수치계산을 행한다.

Ⅲ. 공동연구기관 및 연구책임자의 연구 수행 능력

본 연구의 공동연구기관은 일본 Kyushu Univ.의 Inst. of Advanced Material study이며, 상대방 연구책임자는 H. Ozoe로서 Kyushu Univ. 의 교수이다. Kyushu Univ.의 Ozeo 연구팀은 본 연구와 관련된 분야에서 진보된 연구성과와 연구능력을 보유하고 있다. Ozoe교수의 연구팀에서는 초대형계산기와 첨단전자장비

를 사용하여, 회전기계 내부의 열유동해석에 대한 연구를 진행해 오고 있으며, 세계적으로 가장 선두의 연구능력을 보유하고 있다. 회전LDV등의 실험장치를 보유하고 있으며 10여명의 석사급 이상의 연구생과 연구원을 보유하고 있다. 1년 평균 30여편의 논문을 일본국내와 국제학술회의에 발표하고 있다. 또한, Kyushu대학의 연구팀은 오래동안 일본정부로부터 연구비지원을 받아옴으로써, 연구능력을 인정 받아오고 있다.

본 연구의 연구책임자는 한국과학기술원 기계공학과에 재직중인 현재민 교수이다. 현재민 교수는 한국과학기술원에서 지난 10여년간 회전유체유동 및 성층유체유동에 대한 폭넓은 학술연구를 수행하여 오고 있으며, 그 연구결과를 세계유명학술지에 다수 발표함으로써 세계적인 석학으로 인정받고 있다. 그리고, 여러 가지 유체 유동과 열전달에 관련된 연구과제를 성공적으로 수행하여왔다. 또한, 이 분야에 대한 다수의 연구인력을 양성함으로써, 세계적으로 유명한 연구팀을 형성하였다. 따라서, 본 연구과제의 성공에 충분한 연구능력을 가지고 있다고 할 수 있다.

IV. 공동연구개발의 내용 및 범위

1. Spin-up of a double-diffusive fluid in a cylinder (회전하는 원통용기내부 이중확산 유체의 스핀업)

2. Numerical solution for the spin-up from rest with a free surface (자유표면을 가진 유체의 정지상태에서의 스핀-업에 관한 수치적 연구)

3. Convective heat transfer in a cylinder with a rotating lid under stable stratification (회전하는 덮개를 가지는 안정성층화된 실린더 내의 대류열전달)

4. Transient confiend natural convection with internal heat generation (내부열원을 가지는 용기내의 과도자연대류)

5. Flow driven by a torsionally-oscillating shrouded endwall disk (비틀림

적으로 요동하는 덮개판에 의한 유동)

6. Natural convection in an enclosure having a vertical sidewall with time-varying temperature (측벽에 시간에 따른 온도변화를 가한 용기내의 자연대류)

7. Mass transfer characteristics for a rotating cup-like cylinder (회전하는 컵 모양의 실린더에 대한 물질전달현상)

8. Flow and mass transfer measurements for a flat plate of finite thickness in pulsating flow (요동하는 유동에 놓여진 유한한 두께의 평판에 대한 유동 및 물질전달 측정)

9. Transient natural convection in a cavity with walls of finite thickness (유한한 두께의 벽을 가지는 용기 내의 과도 자연대류)

10. Resonant enhancement of natural convection heat transfer in a square enclosure (사각용기내의 자연대류열전달의 공진적 증가)

11. Augmentation of convective heat transfer by a torsionally-oscillating shrouded underlay disk (비틀림적으로 요동하는 덮개판에 의한 대류열전달의 조정)

12. Axisymmetric inertial oscillation in a rotating cylindrical container (회전하는 원통 용기내에서의 축대칭 관성진동)

13. Effect of aspect ratio on mass transfer from a rotating cup (회전하는 컵으로부터의 물질전달에 관한 세장비의 효과)

V. 공동연구개발 결과

자연대류현상의 유체유동 및 열전달과 회전유체유동에 대한 KAIST와 일본 Kyushu Univ.연구팀과의 국제공동연구를 효과적으로 수행하였다. KAIST와 Ozoe 연구팀의 상호협력연구를 수행함으로서 실험및 계산능력이 향상되었다. 또한, 연구원들의 훈련을 통한 연구개발의 잠재력이 강화되었다. 첨단기계전자산업에서 자주발생하는 결정성장문제에 관계된 유동및 열전달 특성에 대한 풍부한 연구자료를 제공하였다. 수치해석에 필요한 계산소프트웨어를 개발 하였고, 실제 회전기계의 성능향상방법과 기법을 제시하였다. 본 연구과제와 관련된 많은 연구 결과를 해외 유명 학술지에 게재하였다.

VI. 공동연구개발 결과의 활용 계획

회전하는 원통용기내의 유동장은 회전결정성장장치의 간단한 모형을 제시하며, 이에 대한 수치적, 모형실험적 자료들을 회전결정성장장치의 설계 및 운전에 기술적 정보로 활용한다.

본 연구수행을 통하여 개발된 PTV(Particle Tracking Velocimetry)은 유동의 전 영역에 대하여 동시에 속도측정을 가능하게 하여 유체역학분야의 실험효율의 증대를 가져온다.

SUMMARY
(영문요약문)

The crystal growth technique used for the semi-conductor wafer is a kernel for semi-conductor chip production. The understandings of the fluid flow and heat/mass transfer in ratating flow in the crystal growth technique are essential for the high-quality crystal. This project was designed for these phenomena with the title, 'Convection in rotating flows in crystal growth'. The main target of this research was to gain a physical insight into the nature of the fluid flow and heat transfer generated by the natural convection and the rotating flow.

For this purpose, an international cooperative research project between KAIST and Kyushu Univ.(Japan) has been carried out. The Kyushu Univ. team has been building up research results and capabilities for this field.

The KAIST team directed endeavors to theoretical approach and numerical simulation. The governing fluid dynamics equations were solved numerically and the accumulated technical know-how of the KAIST team was fully utilized.

The Kyushu Univ. team has performed the project named 'Double diffusive natural convection in crystal growth'. The Japanese team conducted detailed experiments and numerical simulations for the buoyant flow in a rotating cylindrical container.

From the cooperative research, mutual benefits have been extensive and the developements in the experimental and numerical simulation techniques were realized. In this report, highlights of research results on the fluid flow and heat transfer related to the crystal growth are given. And, these results were published in international science journals. Finally, the present results from the cooperative research could be applied to the design and operation of the crystal growth techniques.

CONTENTS
(영문목차)

목 차

제1장. 서론

제1절. 연구개발의 필요성

물질가공의 설계와 운전에 있어서 회전유체유동및 열전달에 대한 지식이 요구된다. 반도체칩의 생산에 핵심적인 부분인 반도체웨이퍼의 결정성장과정상에서 발생하는 유동, 열전달 그리고 밀도전달에 대한 회전유체유동과 열전달의 지식이 고순도의 결정을 생산하는대 요구되고 있는 실정이다.

이와 같이 열전달및 밀도전달을 수반한 회전유체유동은 폭넓은 열유체기계분야에서 그 응용성이 높다. 결정성장문제, 원심분리기, 터보기계등에서 효율 및 운전능력의 향상을 위해서는 유체유동 및 열전달특성을 파악하는 것이 중요하다. 본 KAIST에서는 지난 몇 년간 이에 대한 학술적 연구를 실험 및 수치계산에 의해 수행하여 왔다. 이와같은 연구성과는 본 과제의 성공적인 연구에 초석이 되고있다. KAIST연구팀의 장점은 석사급이상의 전산유체역학 및 실험유체역학 분야에서 훈련된 풍부한 연구인력이 있다는 것이다. 위에서 제기된 분야의 문제점을 잘 인지하고있는 KAIST팀은 국내에서 이루어진 다른 연구성과와 더불어 이러한 과제들에 대한 기초적인 토대를 구축하고 있다. 또한, 이와 관련된 문제를 해결하기 위한 실험기법 및 수치계산의 성숙된 기술적 측면은 국외 유명학술지를 통해 국내외적으로 인정받고 있다. 또한 KAIST에서는 대학원 과정의 회전유동의 정규 강좌가 설치, 운영 되고 있다.

회전유체기계의 효율 및 운전능력의 향상을 위하여 유동 및 열전달에 대한 기초적인 지식의 확보가 필수적이다. 미국과 일본을 중심으로 이에 대한 연구가 활발히 진행되고 있다. 또한 최근에 국내에서도 그 관심이 고조되고 있다. 열전달을 수반한는 고순도 결정성장문제, 원심분리기 문제, 복잡한 형상을 갖는 터보기계의 내부 유동장 문제에 대한 연구는 CRAY-2 수퍼 컴퓨터의 도움으로 전산유체역학의 괄목할만한 성장을 가져왔으며 또한 실험유체분야에서도 첨단전자장비의 도움으로 인하여 질적으로 성장된 연구 분위기가 이루어 지고 있다.

본 연구는 일본, Kyushu Univ.(Inst. of Advanced Material study)와의 공동연구를 통하여 진보된 연구성과의 도입과 연구의 질적향상을 이루고자 한다. 이 분야에 대한 Kyushu Univ.의 Ozeo 연구팀의 성과를 살펴보면 다음과 같다. 회전유

동, 대류 유동특성에 대한 연구를 수치계산과 고도의 실험을 수행하였다. 대류 유동장을 슈퍼컴퓨터를 이용하여 진보된 수치기법의 적용을 통하여 괄목할 만한 연구성과를 이루였으며 또한 회전LDV를 이용 회전을 수반한 자연대류유동 내부의 정량적인 유동장 정보를 제시하였다. 이와 같이 수치적 실험적 연구방법에 상당한 노하우를 보유하고 있다.

요약하면 고순도 결정성장문제에서 대류유체유동 및 열전달에 대한 실험적 수치적 예측에 대한 연구는 효율향상과 운전능력의 배양에 필수요소를 제공할 것이다. 본 연구의 성공적인 수행을 위하여 이 분야에 진보된 기술 및 인력을 보유하고 있는 일본과의 공동연구가 절실히 요구된다. 이와 같은 국제공동연구를 통하여 일본측의 진보된 연구성과의 도입과 연구인력의 상호교환을 통하여 이분야에 대한 국내의 성숙된 연구분위기를 형성할 수 있다. 또한 급격히 발달되고 있는 회전대류유동의 정량적인 가시화(PTV,PIV), 수치적 모사방법등이 크게 주목을 끌고 있다. 본 연구에서는 실제 산업체의 기술개발능력의 향상, 제품품질의 개량등의 고도기술의 선도와 개발에 관련이 있다. 이와 동시에 기초적 공학문로서의 영역의 확보와 더불어 학술적 연구, 고등공학자의 교육을 통하여 국내 학술 연구 노력의 자극과 위상을 높이게 된다.

본 연구는 한일 과학기술공동위원회에서 협의된 사항이며, 연구기관사이의 협력 각서가 교환되어 있다. 또한 양쪽 협력기관이 공동으로 연구비를 지원할 계획을 가지고 있다. 연구원의 단기 방문외에도, 박사후 과정의 연구원을 장기간 교환, 체재연구하는 구체적인 방안을 고려하고 있다. Kyushu대학의 연구팀은 오래동안 일본정부로부터 연구비지원을 받아왔으며, 공동연구의 활발한 성과가 기대된다.

제2절. 연구개발의 목표

1. 연구개발의 최종목표

자연대류현상의 유체유동및 열전달과 회전유체유동에 대한 KAIST와 일본 Kyushu Univ. 연구팀과의 국제공동연구를 수행한다.

KAIST와 Ozoe 연구팀의 상호이익증진과 협력연구를 수행함으로서 실험및 계산

능력의 증대가 기대된다. 또한 연구개발의 잠재력이 강화될 것이다. 첨단기계전자산업에서 자주발생하는 결정성장문제에 관계된 유동및 열전달 특성에대한 풍부한 연구자료를 제공할 것이다. 계산 소프트웨어의 제공, 개발과, 또한 실제회전기계의 성능향상방법과 기법을 제시 한다.

2. 년차별 연구개발 목표

1차연도 (95/10 - 96/9)

회전대류 내부의 유동특성 조사

- 정량적인 image processing 기법적용, 속도장 조사
- 수치계산 병행으로 상세한 유동장 제시
- 회전기계 내부유동의 모델정립

2차연도 (96/10 - 97/9)

회전기계 내부의 열전달조사

- 열전달의 증가 현상 조사
- 열전달 management 조사

회전유체기계 내부의 비정상유동 연구

- 유동의 활성화 조사

3차연도 (97/10 - 98/9)

Unsteady high speed rotating flow and heat transport

- 성층화된 유체의 복합적인 resonance 조사

Non-axisymmetric high speed rotating flow and heat transfer

- 3차원 수치계산기법 개발
- LDV와 PIV에 의한 속도장 측정

제3절. 연구개발 추진전략 및 추진체계

1. 연구개발 추진전략

본 연구에서는 고속회전하는 원통용기 내부의 유체유동을 수치적분과 모형실험에 의해 수행할 것이다. 특히 유체역학 방정식(Navier-Stokes equation)을 풀기 위한 수치격자망과 수치적 해석방법을 만드는데 각별한 관심이 있다. 또한 계산결과를 가시적형태로 나타내는 실제적인 방법에도 같은 비중의 중요성이 주어질 것이다. 컴퓨터 도표화와 주변장치에 대해서도 상세히 검토될 것이다. 수치적인 방법에 의한 물리적인 통찰력은 모형실험의 효과적인 연구에 기여하며 수치계산 결과의 검증을 보여준다. 실험방법은 전체유동장의 정량적인 가시화를 시도하여 속도장을 보여준다. 또한 LDV를 통한 정밀한 속도를 측정한다.

일본측 INOUE연구팀과의 공동 연구를 통하여 회전유체기계 내부의 대류확산 유동 및 열전달 현상을 규명한다.

2. 연구개발 추진체계

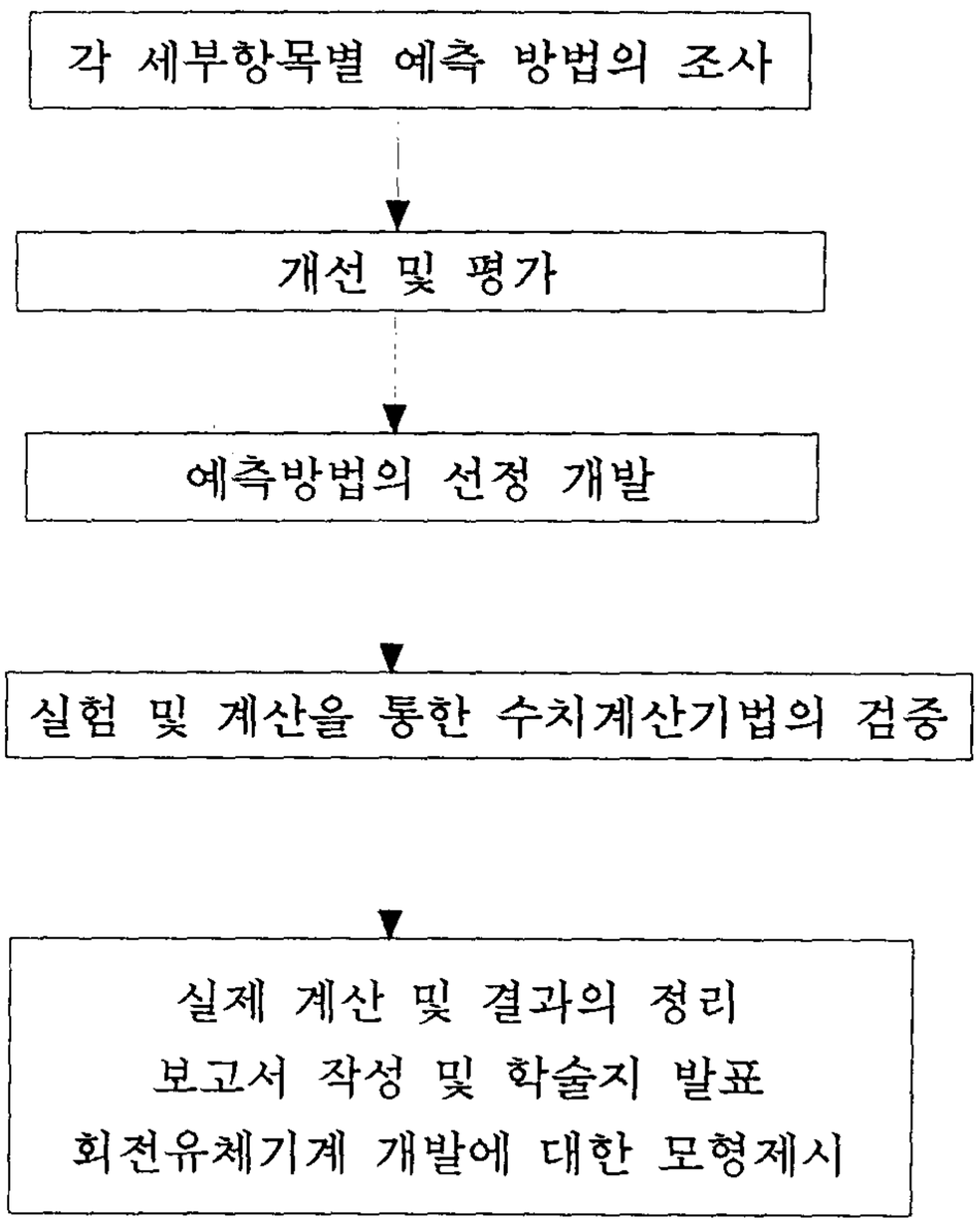

제2장. 국내외 기술개발 현황

제1절. 연구사례의 조사

1. 외국의 경우

회전유체기계내의 열, 유체유동 및 물질전달에 대한 풍부한 연구사례가 국외 유명 학술지에 발표되었다. 시험기법 및 수치계산에 대한 상당한 노하우를 보유하고 있다. 대표적인 것으로 결정성장을 들 수 있다.

이에 대한 구체적인 외국의 연구 사례들을 살펴보면 불순물 즉, 결정의 줄무늬 성장은 많은 이론적 연구들을 통해서 광범위하게 다루어 졌다. Witt와 Gatos는 InSb에서 불순물줄무늬의 성질에 대해서 연구한 결과 용해된 물질내에서 온도변동의 주기는 결정 시편의 줄무늬와 관련이 있다는 것을 밝혔다. Chedzey와 Hurle는 온도변동의 파형과 용해된 줄무늬의 간격과의 관계를 찾아내었다. Whiffin등은 용해된 실리콘 산화물의 표면에서의 회전유동형태를 관찰하고, 회전율의 변화에 따른 유동의 변화에 관해서 보고하였고, Jones는 초크랄스키 용해금속 모델의 온도진동에 관한 상세한 연구를 시도하였다. Ostrach는 온도변동에 있어서 열모세관작용의 역할에 대해 지적하였다.

최근에는, Munakata와 Tanasawa가 초크랄스키 모형에서의 진동하는 유동의 발생에 대한 프란틀수와 레일리히수의 영향에 관해 연구하였다. Munakata와 Tanasawa는 진동하는 유동은 초크랄스키 대류계의 특성이고, 그것이 줄무늬의 원인일 것이라고 밝혔다. Ozoe연구진은 실리콘 기름을 이용하여 초크랄스키 버크유동에 대한 유동가시화와 온도변동측정을 수행하였다. 원래의 결정성장과정동안 유동장 및 온도장의 해석은 매우 어려우므로 기존의 연구들은 상경계면을 평면으로 가정하고 계면곡률의 영향을 무시하고 해석하였지만, 계면형상이 결정품질에 절대적으로 중요한 영향을 미친다는 사실이 인정되면서 계면의 거동을 예측할 수 있는 모델을 연구하기 시작하였다. Kopetsch는 소규모 노에 대한 비정상해석을 통하여, 도가니 온도가 증가함에 따라 계면이 볼록한 상태에서 오목한 상태로 변하는 결과를 제시하였지만 결정 및 도가니의 회전을 고려하지 않았다. Derby와 Xiao는 비교적 큰 도가니에서 성장하는 산화결정의 경우 결정의 회전속도가 커질수록 계면이 오목해지는 결과를 제시하였다. Derby와 Brown은 계면 및 meniscus

형상, 결정봉직경 등을 일괄적으로 결정하는 thermal-capillary모델을 개발하여 비회전 결정성장과정에서 인출속도에 따른 계면형태와 결정봉직경을 구하였다. Kinney와 Brown은 층류모델과 k-ε난류모델을 각각 사용하여 예측된 회전각속도에 따른 계면형상의 변화는 다루지 않았다. Virzi는 전도만을 고려한 모델을 사용하였고, Kinney등은 시스템에 대한 계산결과와 실험결과를 비교하였다. Berkowski등은 여러 매개변수들에 대하여 물과 글리세롤 용액을 이용하여 모사실험을 행하였다. Hirata등도 모사실험을 통해서 평면상경계가 이루어지는 조건을 구해냈다. Trauth등은 lithium niobate단결정 성장실험을 통해 결정봉의 회전속도가 임계값이상일 때 계면형상이 반전됨을 밝혔다.

주어진 운전조건하에서 결정봉의 인출속도에 대한 연구들도 많이 이루어져왔다. Rea는 결정봉크기와 각종시스템 매개변수의 함수로서 최대 인출속도를 구하였다. Johansen은 시간변수 대신 성장방향길이를 독립변수로 채택하였다. 그 외에도 수많은 연구들이 활발히 이루어지고 있다.

2. 국내의 경우

국내에서도 turbine cascade주위의 유동과 결정성장 현상에 대해서 많은 연구사례가 있다. 그러나, 회전계 내부의 전체적이고 포괄적인 열유동해석은 극히 소수의 연구진에 의해 이루어지고 있는 실정이다. 그러나 KAIST에서는 지난 몇 년동안 국내의 부진한 연구영역인 회전유체계 내의 열유동해석에 대한 선두적인 연구를 수행하여 왔다.

3. 조사연구개발사례에 대한 평가

국외의 풍부한 연구에 비해 국내의 연구는 미진한 상태이며 활발한 연구가 요구되고 있는 실정이다.

제2절. 세부기술사항 및 검토분석

1. 기술적인 평가 : 결정성장문제

초크랄스키방법

결정과 도가니상의 회전력 차이에 의한 결정성장방법의 이종이며 결정이 형성되는 경계면에서의 온도상태가 중요하다. 회전조건에 따라서 순수결정의 정도가 결정될 뿐만 아니라 주기적인 유동이 형성된다. 결국 대류에 의한 열전달의 효과의 증대와 불순물의 분리가 요구되고 있는 실정이다.

ACRT(Accelerated Crucible Rotation Technique)

결정의 형성에서 강제대류에 의한 열전달 및 물질의 혼합은 중요한 문제이다. 외부적인 물질의 유입에 의한 대류의 생성은 불가능하다. 결국 용기의 회전에 변화를 가함으로써 에크만 경계층에 의한 대류의 효과를 줄 수 있다. 이러한 회전의 주기적인 교반에 대한 연구가 요구되고 있는 실정이다.

2. 경제적인 평가

본 연구의 성공적인 수행은 장기적으로 첨단전자 산업에서 국외의 기술에 대한 로열티의 감소가 기대된다. 결과의 응용을 통한 시제품의 생산은 수출의 효과가 기대된다.

3. 산업기술에 미치는 파급효과 분석

장기적으로 기술도입의 비용을 줄일 수 있으며 또한 기술의 역수출이 기대된다.

제3절. 산업계 현황

1.제품의 발전주기 (Product life cycle)로 볼 때

(1) 생산하려는 제품이 세계시장에서 현재 어느 상태에 있으며
(2) 생산 또는 수출을 시작할 때에 제품이 선진국에서는 어느 상태에 있을 것인지 각각 아래의 커브위에 (1), (2)로 표기함

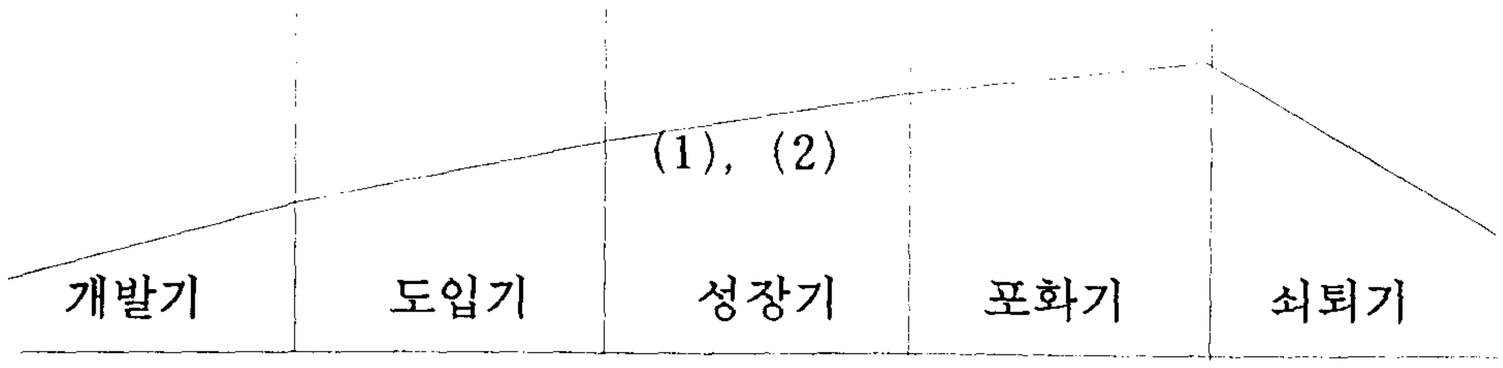

2. 시장규모

0 주시장(국가 또는 지역) : 일본, 동남아지역, 미주 구라파지역

0 시장규모

구 분	현재의 시장규모
세계시장규모	100 억$
한국시장규모	100 억원

3. 세계시장의 성격 (해당안에 모두 표시)

■안정성이 큼 ■영속성이 있음

■성장성이 있음 ■독점성(또는 과점성)이 있음

4. 본 기술을 보유하고 있는 외국회사는 ?

회사 : Rolls-Royce Ltd(영국) 외 5개사 이상

제3장. 상대국과의 공동연구 역할분담 체계

제1절. 국제 공동 개발 추진계획

1. 추진배경

회전유체기계는 최근 첨단 기계전자산업의 핵심적 요소를 이루고 있으며 내부의 열 유동의 정확한 이해는 고효율, 고정밀도의 제품설계및 운전에 극히 중요하다. 문제의 복잡성을 고려하여, 수치계산과 모형실험이 일본등에서 활발히 이루어 지고 있다. 일본의 연구현황은 Super-computer와 첨단전자기기의 활용으로 가장 발달된 위치를 가지고있다. 그러나 국내에서는 연구의 활성화 단계에 있으며 국제공동연구를 통하여 이러한 연구분야의 개척과 큰 활성화가 긴요한 과제이다.

2. 성공가능성

Ozoe교수의 연구팀에서는 70년대 말 부터 초대형계산기와 첨단전자장비를 사용하여, 회전기계 내부의 열유동해석에 대한 연구가 진행되어 왔다. 이러한 노력은 80년도 말에 더욱 가속화 되어 세계적으로 가장 선두의 연구능력을 보유하고 있다. 또한 KAIST연구팀은 이에 대한 기초적 학술연구를 통하여 모형실험과 수치적분에 대한 경험을 축적하였다. 두 연구팀의 상호협력에 의한 연구는 학문적 기술적 연구의 큰 결실이 기대된다.

3. 상대측 실적

상대방 연구책임자는 H. Ozoe이며, Kyushu Univ. 의 교수이다. 회전LDV등의 실험장치를 보유하고 있으며 10여명의 석사급 이상의 연구생과 연구원을 보유하고 있다. 1년 평균 30여편의 논문을 일본국내와 국제학술회의에 발표하고 있다.

4. 연구인원 이용

KAIST측에서는 주로 이론적 전개와 소형모형실험을 수행할것이며 일본측은 대형계산과 고정밀의 모형실험에 주력할 것이다.

5. 추진체제 일정

KAIST에서는 박사학생 10여명이 논문연구를 수행한다. 수치적분 방법론, 실험기법의 개발, 회전계의 유동, 비정상유동등이 주된 연구대상이다. 일본측에서는 회전하는 원통용기내의 회전유동의 심도있는 실험및 수치계산을 행한다.

양측 연구책임자는 약 2회이상의 상호방문을 하여 세미나, 학술토론을 한다. 그리고 양측 연구자들은 국제학술회의에 공동참가, 연구자료의 상호교환을 적절한 시기에 행한다. 박사후 과정 (Post-dotoral Program)의 상호교류, 장기체재를 통하여 연구의 심도 있는 발전을 도모하게 된다. 또한 한국정부, 일본정부의 공동연구비 지원 협력체계를 구성할 계획이다.

제2절. 역할분담 체계

KAIST측에서는 본 연구 주제에 대하여 주로 이론적 전개와 소형모형실험을 수행하였다.(연구목표 및 내용 참조)

일본측 연구팀은 '결정성장에 있어서 이중확산 자연대류'라는 연구과제에 대한 연구를 수행하였다. 뒷 페이지에 일본측 연구개발내용 및 상호협력관계를 첨부하였다.

様式2

科学研究費補助金（国際学術研究）交付申請書			
研究代表者	所属部局	職（専攻）	ふりがな 氏名
	機能物質科学研究所	教授 （熱工学）	おぞえ　ひろゆき 尾添　紘之
研究課題	（和文）結晶成長における二重拡散自然対流現象とミクロ構造		
	（英文）Double Diffusive Natural Convection in Crystal Growth		

調査研究の目的

集積回路基板に多用される単結晶は融液の固化によって作られるがその際ドーパントや不純物はその偏析係数が通常1より小さく、融液中に蓄積され逆拡散していく。その際、重力場では濃度差対流を引き起こす可能性が指摘されており温度差対流と共存し、二重拡散自然対流が生じていると考えられる。また融液流速の変動によって結晶中の不純物や組成に成長方向にむらが生じ、歩留りの低下を引き起こしている。この場合、温度、濃度、速度の三種の境界層の厚さが時間的に変動し、結晶成長界面では複雑な局所的流動の発生や消滅が起こっていると予想されるが、このような過渡特性に関する詳細な情報、解析はほとんど知られていない。本研究計画はこれらの解明を目指す。

本年度の調査研究実施計画

1．8月、9月の2ヶ月にわたり、鎌倉助教授がデルフト工科大学（オランダ）において、気相系における二重拡散自然対流のモデル化ならびに数値解析について研究調査にあたる。これはCVDによる結晶成長とも関連するもので、新しい局面を開くことが期待できる。同学、Hoogendorn教授は斯界の権威である。なお、現地より後述リガへの調査に同行する。
2．8月後半、尾添はリガ（ラトビア）における高名なラトビア科学研究所を訪問し、液体金属における二重拡散自然対流と磁場効果に関する研究調査を行う。これは液体金属の結晶成長に関連するもので、我々の成果も発表し、討論を予定している。
3．同時期、平野はマサチューセッツ工科大学（米国）において、乱流対流数値計算法の調査研究と二重拡散への応用に関する調査を行う、またその後、共同研究者のKamotani教授をケースウエスタンリザーブ大学（米国）に訪問し、その後の宇宙実験結果と中間研究打ち合わせを行う。
4．11月中旬、共同研究者のKamotani教授が来日し、表面張力二重拡散自然対流に関する研究のまとめの打ち合わせを行う。
5．12月中旬、尾添は韓国にHyun教授を訪問し、回転系二重拡散自然対流に関する研究の検討を予定している。
6．12月末に、韓国より、Hyun教授が来日し、回転系二重拡散対流に関する研究とりまとめを行う。
7．平成8年1月に、韓国よりSung教授が来日し、結晶成長に関する研究とりまとめを行う。

研究区分	共同研究	研究機関名	九州大学	課題番号	06044171

	氏　　名	研究機関・部局・職	役割分担（本年度の調査研究実施計画に対する分担事項を記入すること。）
研究組織 研究代表者及び研究分担者	（研究代表者） 尾添　紘之	九州大学・ 機能物質科学研究所・教授	総括、結晶成長過程に関連する二重拡散自然対流の解明
	（研究分担者） Yasuhiro Kamotani	ケースウエスタンリザーブ大学・ 工学部・教授	表面張力流による二重拡散対流の解明
	Jae Min Hyun	韓国科学技術院・ 工学部・教授	回転流動場における二重拡散対流の解明
	鎌倉　勝善	富山工業高等専門学校・ 助教授	結晶成長過程に関連する二重拡散自然対流の実験ならびに数値解析
	平野　博之	九州大学・ 機能物質科学研究所・助手	結晶成長過程に関連する二重拡散自然対流の実験ならびに数値解析
	Euung Jin Sung	韓国科学技術院・ 工学部・教授	結晶成長過程における二重拡散対流の数値解析
	計　6　名 うち国外　3　名		

調査研究計画日程

調査研究実施国　　日本、オランダ、ラトビア、米国、韓国

年月日	旅行日程 出発地（　）	旅行日程 到着地（　）	旅行日程 滞在地（　）	研究者氏名	調査研究事項
7. 8. 1	富山（日本）	デルフト（オランダ）	デルフト（オランダ）	鎌倉勝善	気相系における二重拡散自然対流のモデル化に関する研究
8.20	デルフト（オランダ）	リガ（ラトビア）	リガ（ラトビア）		液体金属の二重拡散自然対流に関する研究調査
8.27	リガ（ラトビア）	デルフト（オランダ）	デルフト（オランダ）		
9.29	デルフト（オランダ）				
9.30		富山（日本）			
7. 8.20	福岡（日本）	リガ（ラトビア）	リガ（ラトビア）	尾添紘之	液体金属における二重拡散自然対流と磁場効果に関する研究調査
27	リガ（ラトビア）				
28		福岡（日本）			
7. 8.20	福岡（日本）	ボストン（米国）	ボストン（米国）	平野博之	乱流対流数値計算法の調査研究と二重拡散への応用に関する研究のため
26	ボストン（米国）	クリーブランド（米国）	クリーブランド（米国）		
29	クリーブランド（米国）				
30		福岡（日本）			
7. 11. 5	クリーブランド（米国）			Yasuhiro Kamotani	界面張力二重拡散自然対流に関する討論と講演
6		福岡（日本）	福岡（日本）		
11.18	福岡（日本）	クリーブランド（米国）			
7. 12.12	福岡（日本）	ソウル（韓国）	ソウル（韓国）	尾添紘之	回転系における二重拡散自然対流に関する討論と講演
12.17	ソウル（韓国）	福岡（日本）			
7. 12.21	ソウル（韓国）	福岡（日本）	福岡（日本）	J.M.Hyun	回転系における二重拡散自然対流の数値解析結果のとりまとめならびに講演
27	福岡（日本）	ソウル（韓国）			
7. 12.21	ソウル（韓国）	福岡（日本）	福岡（日本）	H.J.Sung	結晶成長における二重拡散自然対流の数値解析結果のとりまとめならびに講演
27	福岡（日本）	ソウル（韓国）			

合計					
	派遣　（延べ人数）	4人			
	招へい　（延べ人数）	3人	課題番号	06044171	
研究区分	共同研究	研究機関名	九州大学	研究代表者名	尾添　紘之

平成６年度国際学術研究―共同研究計画調書（新規）

（Monbusho International Scientific Research Program: Joint Research）

1. コード番号	機関番号（研究機関において記入）		2. 審査希望分野（右の系のそれぞれ1つを○で囲むこと）	系 1. 人文科学系 2. 社会科学系 3. 理学系 ④ 工学系 5. 農学・動・植物系 6. 医学系	部 （文学ー社会学を除く） （法学、経済学、農業経済学、社会学） （生物学を除く） （工学） （農学ー農業経済学を除く、生物学） （医学）
	整理番号（研究機関において記入）				
	主な研究領域コード	4 1 5			

3. 研究代表者	所属研究機関・部局・職名・氏名印	九州大学・機能物質科学研究所　教授　尾添　紘之（ふりがな：おぞえ ひろゆき）　印
4. 相手側対応研究グループ（代表者氏名・所属機関名・職名・所在国）		Jae Min HYUN, KAIST, Professor, Korea; Yasuhiro Kamotani, Case Western Reserve Univ., Professor, U.S.A.
5. 共同研究計画名	和文	結晶成長における二重拡散自然対流現象とミクロ構造
	英文（タイプ打）	Double diffusive natural convection in crystal growth
6. 研究期間		自 平成６年度 ～ 至 平成８年度

7. 研究組織

氏名（年齢）	所属機関・部局・職名	専門領域	学位	役割分担（本年度計画の分担事項）
○研究代表者 おぞえ ひろゆき 尾添　紘之　(51)	九州大学・機能物質科学研究所・教授	熱工学	Ph.D.（ペンシルベニア大学） 工博（京大）	総括、結晶成長相変化過程および二重拡散自然対流の解明
○研究分担者 やすひろ かもたに Yasuhiro Kamotani　(53)	ケースウエスタンリザーブ大学・工学部・教授	伝熱工学	Ph.D.（ケースウエスタンリザーブ大学）	表面張力流による二重拡散対流の解明
ぜえ みん ひゃん Jae Min Hyun　(46)	韓国科学技術院・工学部・教授	流体工学	Ph.D.（ラトガース大学）	回転流動場における二重拡散対流の解明
かまくら かつよし 鎌倉　勝善　(49)	富山工業高等専門学校・助教授	物質工学	工博（九州大学）	電極を用いた二重拡散対流のミクロ構造の研究
合計 4 名 （うち国外 2 名）				

＊国外の研究分担者については、個々の研究者ごとにプロフィール（別紙様式による）を作成し計画調書の最終頁に綴付けすること。

8. 研究計画の目的

集積回路基板に多用される単結晶は融液の固化によって作られるがその際ドーパントや不純物はその偏析係数が通常1より小さく、融液中に蓄積され逆拡散していくが、重力場では濃度差対流を引き起こす可能性が指摘されており温度差対流と共存し、二重拡散自然対流が生じていると考えられる。また融液流速の変動によって結晶中の不純物や組成に成長方向にむらが生じ、歩留りの低下を引き起こしている。この場合、温度、濃度、速度の三種の境界層の厚さが時間的に変動し、結晶成長界面では再融解や組成変動に基づく局所的過冷却域（constitutional super cooling）の発生や消滅が起こっていると予想されるが、このような過渡特性に関する詳細な情報、解析はほとんど知られていない。本研究計画はこれらの解明を目指す。

9. 関連する国際共同研究名

10. 年度	平成６年度	平成７年度	平成８年度
＊年度別申請額（千円未満切り捨て）	4,701 千円	3,305 千円	3,770 千円
年度別派遣計画（延べ人数）	3 人	2 人	2 人
年度別招へい計画（延べ人数）	3 人	2 人	2 人

11. 研究計画の必要性及び期待できる成果

金属半導体や各種光学機器に使用されている化合物半導体は現在の情報化社会、可視化情報社会をハード面から支える最も重要な素材の一つであることは異論のないところであろう。これら半導体材料はそのほとんどが融液の固化という方法によって作製されており、必然的に融液の流動状態に依存している。融液は振動流や乱流状態を呈し、固化単結晶の組成や結晶構造に周期的変動や格子欠陥を発生させていると考えられ、単結晶棒から作った薄膜を基板として集積電子回路を構築していく過程で相当の歩留りの低下を招き製造コストを押し上げ、効率の低下をきたしている。この液固相変化過程において不純物や添加ドーパントの液相側への蓄積と二重対流拡散また固相の部分的再融解や再固化による不純物のとり込み等の機構や現象の詳細（特に過渡的特性）が不明であり、これらを明らかにすることができれば、液相流動状態を適切に制御し、均質な組成を持つ素材の作製と歩留りの飛躍的向上が期待でき、現在の高価な集積回路の価格を適正なものとでき、各種電算情報機器の低価格化も期待される。

12. 共同研究を始めるに至った経緯及び準備状況（相手側グループとの連絡書簡等があればその写しを本頁下に綴付けすること。）

米国側代表者カモタニ教授は二重拡散自然対流の電位勾配の場における研究や、振動流、無重力場における結晶成長の問題等を行ってきた。1991年4月米国リノ市のJSME/ASME合同会議ならびに1992年10月北京でのISTP国際会議で会う機会があり、二重拡散自然対流の問題が結晶成長において重要であり、振動流とも複合的に関連し、共同して研究したらどうかという提案を行ったところ前向きに考えていただける由であった。一方、韓国科学技術院（KAIST）のHyun教授は国内外の学会で多数回会うと共に既に相互訪問を行っている間柄であるが、結晶成長と二重拡散自然対流の問題に最近研究を集中しており、本年1月来学時に、是非共同研究をやりたいとの申し出もあり、今回、カモタニ教授との3者共同研究を企画したものである。

鎌倉氏と尾添はこの6年間二重拡散自然対流について共同研究を行ってきており、その成果は5件の国際学会誌等へ発表し、今後も多くの発表を予定している。なお本グループの一つの特徴は本テーマに三者長年たずさわっているだけでなく、カモタニ、Hyun氏共、NASAの研究員の経歴を持ち、日本語も理解できるという共通因子を共有する組み合わせで、成果の進捗も大いに期待できる。

13. 相手側の役割分担（研究内容及び研究経費の分担について記載のこと。また、相手側が何らかの研究助成を受ける予定の場合はその具体的制度名を．さらに日本側が相手側の経費を負担する場合はその理由を記入すること。）

ケースウエスタンリザーブ大学のカモタニ教授
現在NASAからの研究費で表面張力流及び二重拡散自然対流の研究をしているのでそれを継続すると共に二つのテーマをまとめた表面張力流による二重拡散対流の実験と解析を行なう。研究費は引き続きNASAから支給される。現在回転容器内での二重拡散流の実験を行なっているが流れの研究が終り次第電極表面でのミクロの解析を行なう。今無重力での二重拡散自然対流の実験の計画をしているがそれを具体的に進める。

韓国科学技術院のHyun教授
回転系における二重拡散対流の定常ならびに非定常特性について、重要な無次元数の特定、関連する熱・物質移動特性の解明等を行なう。これは数値解析ならびに流動系の可視化実験によって行なう。またコリオリ力や電磁力場の検討も考えている。さらに非定常流の特性振動数の同定等も試み、結晶成長技術の向上に資する。

14. 研究計画全体の概要

アメリカ側、ケースウエスタンリザーブ大学のKamotani教授、韓国側、韓国科学技術院Hyun教授と日本側、尾添・鎌倉の三者からなる国際共同研究組織により、結晶成長における二重拡散自然対流現象とミクロ構造を明らかにしようとするものである。すなわち、初年度においては、二重拡散自然対流の移動量測定のための実験装置の開発、回転場における二重拡散対流の解析コードの開発、無重力下における表面張力流による二重拡散対流の実験装置計画、解析コードの開発を三者それぞれに実施すると共に、相互訪問により、研究打ち合わせ、研究協力等を実施する。第2年度においては、相変化界面近傍における二重拡散対流の解析とミクロ構造の検討、無重力下における実験をSpace Shaulleで実施し、表面張力流のデータ収集、任意傾斜下の回転円筒内の二重拡散対流の解析実施。相互訪問による研究協力。
第3年度においては、ミクロスケール対流と固化樹枝状結晶との関連の検討、それにおよぼす回転強制流の効果の検討。また表面張力流の解析結果と無重力実験データとの比較検討、スペクトル法による三次元解析コードの開発と有効無次元数の同定ならびに三者打ち合せ会議による最終レポートのまとめを行なう。

15. 年度別の具体的研究内容（箇条書きで連続した年度計画を記入のこと）

（平成6年度） 尾添・鎌倉 1. 鉛直加熱・冷却面を有する矩形容器の下方に高濃度液、上方に溶媒液を持つ最も基本的な場合でも、濃度分布が変化するので、二重拡散自然対流の強さも変化する。加熱面上、冷却面上の温度、濃度境界層の構造の過渡的変化を数値解析により明らかにする。 2. 無重力場における表面張力駆動対流のある場合の二重拡散自然対流の数値解析ならびに対応する実験装置の設計を試みる。 3. 鉛直加熱・冷却壁から溶質が溶解、析出する場合には、濃度、速度、温度の境界層が複雑に影響し合うと共に過渡的にも変化する。そこで加熱・冷却壁を電極とし、界面近くのミクロ構造の解析法の開発に着手する。	Kamotani 1. 回転容器内での二重拡散対流の実験による熱・物質移動速度の測定。 2. 無重力下における二重拡散対流の実験計画立案 3. 来日時また、こちらからの訪米時、電極利用による二重拡散対流の実験装置開発指針。 Hyun 1. 回転円筒容器内の二重拡散対流の円筒回転後の過渡特性の解析的研究。 2. 円筒壁のステップ加熱後の過渡特性時間と、ステップ回転加速後の特性時間が二重拡散自然対流に与える影響に関する比較検討。これらは共に軸対称流を仮定して行なう。
（平成7年度） 尾添・鎌倉 1. ブリッジマン法による結晶成長の場合、冷却面上で固化が発生するが、二重拡散対流によってミクロな流動形態も変化する。相変化界面近傍の二重拡散、振動流れ、過冷却等の効果について、理論的解析を試みる。 2. 無重力場における浮遊帯域法結晶成長現象において、表面張力の強さが周方向に必ずしも一様でないため、周期的振動流が生じることが知られているが、このような三次元場振動対流の数値解析法の開発に進む。 3. 電場の存在する場合における相変化プロセスの実験装置の開発ならびに数値解析プログラムの開発を試みる。	Kamotani 1. 回転円筒電極表面近傍の境界層のミクロ構造の解析と前年度の実験結果による検証。 2. 無重力下における表面張力流による二重拡散対流の実験をNASAのSpace Shuttleで実施し、データ収集。 Hyun 1. 水平あるいは傾斜した回転円筒密閉容器内の二重拡散対流の強い回転力場も含めた解析コードの開発。 2. 上記系の重要な無次元パラメータの多数の組み合わせについての数値解析の実施。
（平成8年度） 尾添・鎌倉 1. 二重拡散自然対流を伴う相変化プロセスにおいてはマクロな対流に加えて樹枝状固化面近くのミクロスケールの対流も生じていると予想され、それがまたデンドライトの構造にも変化を与えていると考えられるが、複雑な形状の固相、液相のため従来研究が不充分でそのような場合の解析をめざす。 2. 回転場における結晶成長融液の流れには例えば液面近くには三次元的流れがこれに重畳して発生していることが操業現場では知られているが、このような複雑な流れ場の解析をさらに進めていく。	Kamotani 1. 表面張力流による二重拡散対流の実験の継続ならびに解析研究の実施。 2. 前年度から収集しているSpace Shattle(NASA)での実験データの分析と理論解析との比較検討。 Hyun 1. 回転系における完全な三次元非定常解析コードをスペクトル法によって作製する。これにより円筒周方向や、水平面上の非一様境界条件というチョクラルスキー結晶成長法の現実のものをより適切に模擬できるようになる。 2. 種々の実際的な条件を入れた三次元数値解析の実施に進み、二重拡散対流の特性をより明らかにする。

16. 平成6年度派遣・招へい計画（研究協力者については備考欄にその旨記載）

氏　　名	日　　程	用　務　先（国名）	共 同 研 究 事 項	備　　考
カモタニ　ヤスヒロ	平成6.5.15～ 6.6.14	九州大学機能研（日本）ならびに富山工業高等専門学校（日本）	二重拡散自然対流の電気化学実験装置による移動量測定に関する研究	研究実施の三者打合わせと実験装置の開発のため招へいを要する。
Jae Min Hyun	平成6.5.20～ 6.5.27	九州大学機能研（日本）	研究実施についての打合せと回転場効果（コリオリ力）取り扱い法開発のため	研究実施の三者打合わせとプログラム開発のため招へいを要する。
鎌倉　勝善	平成6.7.15～ 6.8.30	ケースウエスタンリザーブ大学（米国）	無重力下における表面張力流による二重拡散自然対流の実験ならびに数値解析に関する研究	
尾添　紘之	平成6.10.15～ 6.10.22	韓国科学技術院（韓国）	回転場による二重拡散自然対流境界層の厚さに関する解析法開発	
尾添　紘之	平成6.12.1～ 6.12.20	ケースウエスタンリザーブ大学（米国）	二重拡散自然対流境界層内のミクロ構造に関する研究	
Jae Min Hyun	平成7.2.1～ 7.2.20	九州大学機能研（日本）ならびに富山工業高等専門学校（日本）	回転場における二重拡散自然対流の数値解析法の開発ならびに可視化処理開発のため	計算結果の可視化装置法開発のため招へいを要する。

제4장. 공동연구기관 및 연구책임자의 연구수행능력

제1절. 공동연구기관의 연구수행능력

본 연구의 공동연구기관은 일본 Kyushu Univ.의 Inst. of Advanced Material study이며, 상대방 연구책임자는 H. Ozoe로서 Kyushu Univ. 의 교수이다. Kyushu Univ.의 Ozeo 연구팀은 본 연구와 관련된 분야에서 진보된 연구성과와 연구능력을 보유하고 있다. Ozoe교수의 연구팀에서는 70년대 말 부터 초대형계산기와 첨단전자장비를 사용하여, 회전기계 내부의 열유동해석에 대한 연구가 진행되어 왔다. 이러한 노력은 80년도 말에 더욱 가속화 되어 세계적으로 가장 선두의 연구능력을 보유하고 있다. 회전LDV등의 실험장치를 보유하고 있으며 10여명의 석사급 이상의 연구생과 연구원을 보유하고 있다. 1년 평균 30여편의 논문을 일본국내와 국제학술회의에 발표하고 있다.

구체적인 연구성과를 살펴보면 다음과 같다. 회전유동, 대류 유동특성에 대한 연구를 수치계산과 고도의 실험을 통하여 수행하였다. 대류 유동장을 슈퍼컴퓨터를 이용하여 진보된 수치기법의 적용을 통하여 괄목할 만한 연구성과를 이루었으며, 회전LDV를 이용 회전을 수반한 자연대류유동 내부의 정량적인 유동장 정보를 제시하였다. 그리고, 이와 같은 수치적 실험적 연구방법에 상당한 노하우를 보유하고 있다.

또한, Kyushu대학의 연구팀은 오래동안 일본정부로부터 연구비지원을 받아옴으로써, 연구능력을 인정 받아오고 있다. 따라서, 본 연구와 관련해서 훌륭한 국제공동연구를 수행할 수 있다고 할 수 있다.

제2절. 연구책임자의 연구수행능력

1. 연구책임자

본 연구의 연구책임자는 한국과학기술원 기계공학과에 재직중인 현재민 교수이다. 현재민 교수는 한국과학기술원에서 지난 10여년간 회전유체유동 및 성층

유체유동에 대한 폭넓은 학술연구를 수행하여 오고 있으며, 그 연구결과를 세계 유명학술지에 다수 발표함으로써 세계적인 석학으로 인정받고 있다. 그리고, 여러 가지 유체 유동과 열전달에 관련된 연구과제를 성공적으로 수행하여왔다. 또한, 이 분야에 대한 다수의 연구인력을 양성함으로써, 세계적으로 유명한 연구팀을 형성하였다. 따라서, 본 연구과제의 성공에 충분한 연구능력을 가지고 있다고 할 수 있다.

2. 연구책임자 인적사항

성 명	한글	현 재 민	한자	玄 在 民	영문	Jae Min HYUN
주민등록번호	460903-1068327					
현 주 소 (자 택)	우:135-110, Tel : 02-544-7369, FAX : 02-545-8606 서울특별시 강남구 압구정동 한양아파트 42동 502호					
재 직 기 관	학교명 및 소속학과	한국과학기술원 기계공학과				
	직 급	교 수	담당보직명			
	주 소	우:305-701, Tel : 042-869-3012, FAX : 042-869-3210 대전광역시 유성구 구성동 373-1 한국과학기술원 기계공학과				
전공분야	대분야	공학	중분야	기계공학	세분야	열 및 유체공학

3. 연구책임자 학력

구 분	기 간	학 교 명	전 공	취득국가(주명)
학 사	1964-1968	서울대학교 공과대학 기계공학과	기계공학	한국(서울)
석 사	1969-1971	Princeton University Aero. Mech. Sci.	기계공학 (유체공학)	USA(New Jersey)
박 사	1971-1973	Rutgers University Mechanical Engineering	기계공학 (유체공학)	USA(New Jersey)
(최종학위논문명) Medium & large scale disturbances of a deep baroclinic fluid			(지도교수) Richard Peskin	
최종학위취득일자	1973	귀국 일자	1985	

4. 연구책임자 주요경력

기 간	근 무 기 관 명	직급 및 직위
85.9 - 현재	한국과학기술원 기계공학과	교수
90.8 - 90.12	Inst. Computational Fluid Dynamics (ICFD, Japan)	Visitor
90.4 - 90.8	Inst. of Space & Astronautical Science (ISAS, Japan)	Visiting Research Scientist
82.1 - 85.8	Department of Mechanical Engineering (Clarkson University U. S. A.)	Associate Professor
79. - 81.	National Research Council (NRC) NASA Marshall Space Flight Center (Alabama, U. S. A.)	Senior Research Associate
79. - 81.	University of Alabama, Department of Mechanical Engineering	Lecturer
77. - 78.	Drexel University Department of Physics (U. S. A.)	Assistant Professor
74.8 - 75.	University of Michigan, College of Engineering (Michigan, U. S. A.)	Visitor
73. - 76.	Korea Inst. of Science & Technology (Seoul, Korea)	Research Scientist
74. - 76.	Seoul National University (Korea)	Lecturer

5. 연구책임자 주요연구업적 (최근 5년간)

연구제목	주용내용	연구기간	발표서적 또는 학술지명	연구 수행 기관	역할	연구비 지급기관
첨단 전자장비의 열·유동특성의 수치적 계산과 모형실험	전자장비에서의 열전달	1991.6~ 1994.10	ASME	KAIST	연구 책임자	과학기술처 (국제공동)
회전하고 있는 용기내의 점성유체의 유동과 열전달	회전상태에서의 유동 및 열전달	1992.8~ 1994.7	ASME J. Fluids Engineering	KAIST	연구 책임자	과학재단 (국제공동)
초고압 연료분사계내에서 유체의 유동특성 해석	고압 유체 유동 특성 및 열전달 해석	1995.8~ 1996.8	Int. J. Heat Mass Transfer	KAIST	연구 책임자	두원정공 (주)
VM사이클 열펌프용 재생기의 특성해석 및 실험적 연구	열펌프 재생기 내부의 유동특성	1994.8~ 1996.8	Int. J. Heat Mass Transfer	KAIST	연구 책임자	한국과학 기술연구원

6. 연구책임자 인력양성실적

구 분	현지도인원	총배출인원
석 사	2 명	27 명
박 사	5 명	15 명

7. 연구책임자 학술연구실적

가. BOOK EDITED

J. H. Kim, J. M. Hyun & C. O. Lee, 1991: Fluids Engineering: Korea-U.S. Progress. Hemisphere Publishing Co., New York, pp. 623.

나. JOURNAL PUBLICATIONS [Last Five Years, 1993~]

R. Iwatsu, J. M. Hyun & K. Kuwahara, 1993: Mixed convection in a driven-cavity with stable vertical temperature gradient. Int. j. Heat Mass Transfer, Vol 36, pp. 1601 - 1608

T. Fusegi, J. M. Hyun & K. Kuwahara, 1993: Three - dimensional natural convection in a cube with walls of finite conductance. Int. j. Heat Mass Transfer, Vol 36, pp. 1993 - 1997

T. G. Lim, S. Choi & J. M. Hyun, 1993: Transient interface shape of a two - layer liquid in an abruptly rotating cylinder. ASME J. Fluids Engineering, Vol 115, pp 324-329

H. J. Sung, W. K. Cho & J. M. Hyun, 1993: Double - diffusive convection in a rotating annulus with horizontal temperature and salinity gradients. Int. j. Heat Mass Transfer, Vol 36, pp. 3773 - 3782.

S. Y. Kim, B. H. Kang & J. M. Hyun, 1993: Heat transfer in the thermally-developing region of a pulsating channel flow. Int. j. Heat Mass Transfer, Vol 36, pp. 4257 - 4266.

R. Iwatsu, J. M. Hyun & K. Kuwahara, 1993: Numerical simulations of three - dimensional flows in a cavity with an oscillating wall ASME J. Fluids Engineering, Vol 115, pp 680 - 686

J. H. Chung & J. M. Hyun, 1994: Heat transfer from a fully-developed pulsating flow in a curved pipe. Int. J. Heat Mass Transfer, Vol. 37, pp.43-52.

J. S. Park & J. M. Hyun, 1994: Dynamical structure of compressible-fluid flows in an abruptly-rotating cylinder. J. Phy. Soc., Vol. 63, pp.528-535.

J. S. Lee, J. H. Kim & J. M. Hyun, 1994: Temperature measurements during heat-up af a contained homogeneous fluid. Int. J. Heat Fluid Flow, Vol. 15, pp.111-115.

D. I. Shin & J. M. Hyun, 1994: Flow in a cylinder driven by rotating split-disk endwalls.
Fluid Dynamics Research, Vol. 13, pp.317-327.

S. Y. Kim, B. H. Kang & J. M. Hyun, 1994: Heat transfer from pulsating flow in a channel filled with porous media. Int. J. Heat Mass Transfer, Vol. 37, pp. 2025-2033.

K. S. Hwang, H. J. Sung & J. M. Hyun, 1994: Experimental study of mass transfer from a cylinder in pulsating flow. Int. J. Heat Mass Transfer, Vol. 37, pp. 2203-2210.

Y. N. Kim, H. J. Sung & J. M. Hyun, 1994: Discrete vortex simulation of pulsating flow behind a normal plate. ASME J. Fluids Engineering, Vol 116, pp. 862-869.

K. Y. Kim & J. M. Hyun, 1994: Spin-up from rest of a two-layer liquid in a cylinder. ASME J. Fluids Engineering, Vol. 116, pp. 808-814.

J. W. Kim & J. M. Hyun, 1995: Propagation of the velocity shear front in spin-up from rest in a cut-cone. ASME J. Fluids Engineering, Vol. 117, pp. 58-61.

H. J. Sung, C. K. Chun & J. M. Hyun, 1995: Experimental study of uniform-shear flow past a rotating cylinder. ASME J. Fluids Engineering, Vol. 117, pp. 62-67.

W. N. Kim & J. M. Hyun, 1995: Mass transfer characteristics for a rotating cup-like cylinder. Int. J. Heat Mass Transfer, Vol. 38, pp. 2959-2967.

R. Iwatsu & J. M. Hyun, 1995: Three-dimensional driven-cavity flow with a vertical temperature gradient. Int. J. Heat Mass Transfer, Vol. 38, no. 18, pp. 3319-3328.

H. J. Sung, S. Y. Kim & J. M. Hyun, 1995: Forced convection from an

isolated heat source in a chennel with porous medium. Int. J. Heat Fluid Flow, Vol. 16, pp. 527-535.

W.N.Kim, J.M.Hyun & H. Ozoe, 1996 : Effect of aspect ratio on mass transfer from a rotating cup. Int. J. Heat Mass Transfer, Vol. 39, pp. 2375-2377.

K.S.Hwang, H.J.Sung & J.M.Hyun, 1996: Mass transfer measurement from a blunt-faced flat plate in a uniform stream. Int. J. Heat Fluid Flow, Vol. 17, pp. 179-182.

K.Y.Kim & J.M.Hyun, 1996 : Solution for spin-up from rest of liquid with a free surface. AIAA Journal, Vol. 34, pp. 1441-1446.

H.S.Kwak & J.M.Hyun, 1996 : Natural convection in an cavity with a vertical sidewall having time-varing temperature. J. Fluid Mechanics, Vol. 329, pp. 65-88.

J.S.Park & J.M.Hyun, 1997 : transient Stewartson layers of a rotating compressible fluid. Fluid Dynamics Research, Vol. 19, pp. 303-325.

T.G.Lim & J.M.Hyun, 1997: Flow driven by a torsionally oscillating shrouded endwall disk. ASME J. Fluids Engineering, vol. 119 ,pp. 115-121.

K.Fujimura, H.Koyama & J.M.Hyun, 1997: Time-dependent vortex breakdown in a cylinder with a rotating endwall disk. ASME J. Fluids Engineering, vol. 119, pp.450-453

J.W.Kim & J.M.Hyun, 1997: Axisymmetrical inertial oscillations in transient rotating flows in a cylinder. ASME J. Fluids Engineering, vol.119, pp.390-396.

Z.Guo, H.J.Sung & J.M.Hyun, 1997: Pulsating flow and heat transfer in an annulus partially filled with porous media. Numerical Heat Transfer, Part A, Vol. 31, pp.517-527

Y.M.Shim & J.M.Hyun, 1997: Transient confined natural convection with

internal heat generation. Int. J. Heat Fluid Flow, vol.18, pp.328-333.

W.N.Kim & J.M.Hyun, 1997: Convective heat transfer in a cylinder with rotating lid under stable stratification. Int. J. Heat Fluid Flow, vol.18, pp.384-388.

C.H.Lee & J.M.Hyun, 1997: Spin-up of a double-diffusive fluid in a cylinder. Int. J. Heat Fluid Flow , vo.18, pp. 507-517

J. Wojtkowiak, W.N.Kim & J.M.Hyun, 1997: Numerical simulations of a piston-type flowmeter of high linearity. Flow Measurement & Instrumentation, vol.7, pp.69-75.

J. Wojtkowiak, W.N.Kim & J.M.Hyun, 1997: Computations of the flow characteristics of a rotating-piston-type flowmeter,. Flow Measurement & Instrumentation, vol. 8, pp.17-25.

K.H.Chung & J.M.Hyun, 1997: Transient natural convection in a cavity with walls of finite thickness. Numerical Heat Transfer, Part A, vol. 32, pp.749-767.

S.Y.Kim, B.H.Kang & J.M.Hyun,1998: Forced convective heat transfer from two heated blocks in pulsating channel flow. Int. J. Heat Mass Transfer, vol.41, pp.625-634.

H.S.Kwak, K.Kuwahara & J.M.Hyun, 1998: Symmertic flow in a modified Hadley cell model with a free surface. Geophys. Astrophys. Fluid Dyn. vol.87, pp.215-230

H.S.Kwak, K. Kuwahara & J.M.Hyun, 1998:Convective cool-down of a contained fluid through its maximum density temperature. Int. J. Heat Mass Transfer.vol.41, pp.323-333

H. S. Kwak , K. Kuwahara & J. M. Hyun, 1998: Resonant enhancement of natural convective heat transfer with a time - periodic forcing. Int. j. Heat Mass Transfer. vol.41, pp.2837-2846

J. S. PARK & J. M. Hyun, 1998: Transient sidewall shear layers of a rapidly - rotating compressible fluid. Fluid Dynamic Research, vol.22, pp.215-230

H.S.Kwak, K.Kuwahara & J.M.Hyun, 1998: Prediction of resonant frequency in time varying natural convection in a cavity. Int. J. Heat Mass Transfer.vol.41, pp.3157-3160

J.S.Park & J.M.Hyun, 1998: Transient behavior of buoyancy layer in a stratified fluid. Int. J. Heat Mass Transfer(in press)

K.S.Hwang, H.J.Sung & J.M.Hyun, 1998: Flow and mass transfer characteristics for a blunt-faced plate in pulsating flow. Int. J. Heat Mass Transfer. vol.41, pp.2827-2836

T.G.Lim & J.M.Hyun, 1998: Augmentation of convective heat transfer by a torsionally oscillating disk,inder. Int. J. Heat Mass Transfer. Vol.41, pp.1267-1277

J. Wojtkowiak & J. M. Hyun, 1998: Flow and heat transfer in a pipe containg a coaxially - rotating disk. Revision Submitted to Applied Scientific Research.

G. B. Kim & J. M. Hyun, 1998: Buoyant convection in a non-rectangular cavity with non-vertical insulating sidewalls. Int. J. Heat Mass Transfer(in press)

A. Bethancourt, M. Hashiguchi, K. Kuwahara & J. M. Hyun, 1998: Natural convection of a two - layered fluid in a side - heated cavity. Revision Submitted to Int. J. Heat Mass Transfer.

C. H. Lee & J. M. Hyun, 1998: Flow of a stratified fluid in a cylinder with a rotating lid. Int. J. Heat Mass Transfer.(in press)

J. W. Paek, B. H. Kang & J. M. Hyun, 1998: Transient cool-down characteristics of a porous medium in pulsating flow. Submitted to Int. J. Heat Mass Transfer.

J. W. Paek, B. H. Kang & J. M. Hyun, 1998: Experimental studies of transient cool-down of a heterogeneous porous body in throughflow. Submitted to Int. J. Heat Fluid Flow.

B. H. Kang & J. M. Hyun, 1998: Measurement of thermal conductivity and permeability of aluminum foam metal. Submitted to Int. J. Thermophysical Properties..

다. REVIEW PAPERS

J. M. Hyun, 1994: "Unsteady buoyant convection in an enclosure," in "Advances in Heat Transfer", ed. by J. Hartnett & T. Irvine, Vol. 24, Academic Press, New York, pp. 277-320.

T. Fusegi & J. M. Hyun, 1994: Laminar and transitional natural convection in an enclosure with complex and realistic conditions. Int. J. Heat Fluid Flow, Vol. 15, pp. 258-268.

J. M. Hyun, 1995: A survey of thermal engineering research activity in Korea. J. Heat Transfer Soc. Japan, Vol. 34, No. 134, pp. 11-18.

H. Koyama, K. Fujimura & J. M. Hyun 1995: Vortex breakdown in spin-up and spin-down of a disk in a closed cylinder. (in Japanese). NAGARE, Vol. 14, pp. 171-172.

H. S. Kwak & J. M. Hyun, 1998: Unsteady natural convection in an enclosure. Keynote Lecture Paper, Proc. of the 11th IHTC (Int'l Heat Transfer Conf.), Vol. 1, pp. 341-356

제5장. 공동연구개발 수행 내용 및 결과

제 1 장

Spin-up of a double-diffusive fluid in a cylinder

(회전하는 원통용기내부 이중확산 유체의 스핀업)

요 약 문

종횡비가 1인 원통용기 내부의 이중확산유체의 스핀-엎 현상에 대한 수치해석이 수행되었다. 온도와 농도 경계조건은 전체적인 밀도장이 중력에 대하여 안정한 분포를 가지도록 주어졌다. 방사대칭, 비정상 Navier-Stokes 방정식에 대하여 수치해를 구하였으며, Boussinesq 가정이 사용되었다. 주요한 무차원수들이 인지되었다. Ekman 수가 매우 작고, Pr 수가 O(1)인 경우에 넓은 범위의 성층화수 St, 부력비 R_ρ, 그리고 Le 수에 대하여 수치해석을 수행하였다. 원주방향 속도의 변화가 묘사되었고, 자오면 상의 유동형태가 분석되었다. 이중확산유체에 대하여 전체적인 스핀-엎 과정은 단일확산 유체에 비하여 느리게 나타났고, 이러한 경향은 부력비 R_ρ가 커질수록 두드러졌다. 위치에 따른 스핀-엎 속도의 차이는 St와 R_ρ가 증가함에 따라 커진다. 밀도, 온도, 농도 교란의 크기에 대한 이중확산의 효과가 조사되었고, 스핀엎에 대한 Le 수의 영향이 조사되었다.

Keywords : 스핀엎, 이중확산, 성층유동

Abstract

A numerical study is made of the linearized spin-up process of a double-diffusive fluid in a vertically-mounted cylindrical vessel of aspect ratio O(1). Both the temperature and concentration conditions render gravitationally-stable contributions to the overall density profile. Numerical solutions are acquired to the time-dependent axisymmetric Navier-Stokes equations, using the standard Boussinesq-fluid approximations. The major nondimensional parameters are identified. Results are compiled for small Ekman number, the Prandtl number ~O(1), and broad ranges of the stratification number St, buoyancy ratio Rρ and Lewis number Le, are dealt with. The evolution of the azimuthal velocities is described, and the attendant meridional flows are depicted. The global spin-up process is retarded for a double-diffusive fluid, and this trend is more pronounced as R_ρ increases. The spatial non-uniformity of the rate of spin-up is enhanced as St and R_ρ increase. The effects of double-diffusion on the fields of perturbation density, temperature and concentration are plotted. The impact of Le on spin-up is illustrated, and the plots of the perturbation physical variables of interest are presented.

Keywords : spin-up, double-diffusive fluid, stratified flow.

Notation

Ar	aspect ratio
E	Ekman number
H	height of cylinder
Le	Lewis number
N	frequency
p	dimensionless reduced pressure
Pr	Prandtl number
R	radius of cylinder
R_ρ	buoyancy ratio
St	overall stratification parameter
S	dimensionless concentration
S_i	initial concentration
S'	perturbation concentration
T	dimensionless temperature
T_i	initial temperature
T'	perturbation temperature
u	dimensionless radial velocity
v	dimensionless azimuthal velocity
w	dimensionless vertical velocity
r,θ,z	cylindrical coordinates

GREEK SYMBOLS

α_T	thermal expansion coefficient
α_S	solutal expansion coefficient
β_S	solutal Rossby number
β_T	thermal Rossby number
ΔT	temperature difference between top and bottom endwall disks

ΔS	concentration difference between top and bottom endwall disks
$\Delta\Omega$	angular velocity difference
κ_T	thermal diffusivity
κ_S	solutal diffusivity
ν	kinematic viscosity
ρ	dimensionless density
ρ_o	reference density
ρ_i	initial density
ρ'	perturbation density
τ	dimensionless spin-up time scale(=E-1/2)
Ω_f	final angular velocity
Ω_i	initial angular velocity

1. Introduction

Spin-up refers to the transient adjustment process of a fluid from one state of rigid-body rotation to another of different rotation rate. This classical flow model has occupied the center stage in the research of transient rotating fluid dynamics and associated transport phenomena. Applications can be found in a diverse array of geophysical fluid systems as well as in rotating machinery.

For definiteness, the model-building efforts have been directed to the case of an incompressible fluid, which completely fills a vertically-mounted closed cylindrical container of aspect ratio O(1). A major nondimensional parameter is the Ekman number $E \equiv \nu/\Omega_i H^2$, in which ν denotes the kinematic viscosity of the fluid, Ω_i the rotation rate of the initial state, and H the characteristic dimension of the container. For most relevant applications, E<<1. This implies that the principal effects of viscosity are confined to thin boundary layers on the solid boundary walls. When the change in the rotation rate of the container between the initial state (Ω_i) and the final state ($\Omega_i + \Delta\Omega$) is small, i.e., the Rossby number $\epsilon \equiv \Delta\Omega/\Omega_i << 1$, Greenspan and Howard(1963) presented a linearized analysis for a homogeneous fluid. It was clearly demonstrated that the Ekman boundary layers form on the endwall disks, which, in turn, generate meridional circulation. In the interior, the radially-inward meridional motions bring forth an increase of angular velocity by virtue of angular momentum conservation. It is significant to note that the adjustment process in the bulk of interior is substantially accomplished over the so-called spin-up time scale $\tau_s \sim O(E^{-1/2}\Omega_i^{-1})$, rather than the usual diffusive time scale $\tau_d \sim O(E^{-1}\Omega_i^{-1})$. The fundamental notions of this model have since been verified by numerical and experimental endeavors [e.g., Warn-Varnas et al.(1978)].

Studies on spin-up of a stably-stratified fluid disclosed that the Ekman layer-induced meridional circulation is still the most prominent dynamical element [Walin(1969), Sakurai(1969)]. However, due to the suppression of vertical motions by stratification, the meridional flows do not fill the entire interior of the container.

Consequently, the spin-up process in the interior proceeds in a spatially non-uniform manner. The fluids in the areas near the endwall disks approach the final-state rotation faster than in the areas near the mid-height of the cylinder. In the above investigations, the variation of the fluid density is caused by either a temperature or a concentration difference which is imposed between the two horizontal endwall disks of the cylinder [Buzyna & Veronis(1971), Saunders & Beardsley(1975)]. Detailed descriptions of the flow and temperature fields were given in the numerical solutions by Hyun et al.(1982).

As pointed out earlier, the preceding studies on spin-up dealt with the situations in which the variation of the fluid density stems from the non-uniformity of a single diffusing agent, i.e., temperature(heat) or concentration. The simultaneous presence of two(or possibly more) diffusing agents, e.g., temperature and concentration, has been generally known to lead to complex flow patterns and transport properties in the fluid system[e.g., see the review article by Turner (1974)]. Numerous accounts have been given in the literature to depict these double-diffusive convective flows in a non-rotating framework under pertinent boundary conditions[e.g. Lee & Hyun(1991a,1991b), Hyun & Lee(1990), Ostrach et al.(1987)]. The importance of this subject matter in a rotating environment is recognized in recent industrial applications such as the Czochralski technique in growing single crystals[e.g. Kobayashi(1980), Brown(1988), Sung et al.(1993,1995)]. In this case, the melt is in a rotating container, and the density of the melt is determined by the combined fields of temperature and concentration. The findings of the present study may not be of direct quantitative relevance to actual crystal growth applications, since the pertinent parameters are not precisely matched to those in the applications., However, it suffices to state that the overall qualitative trends can be captured by the present endeavors.

In the context of spin-up, the transient flow and transport characteristics of a double-diffusive fluid warrant an in-depth examination. In the present work, numerical solutions are acquired for the fundamental flow model of the linearized spin-up for small Ekman number. The principal nondimensional parameters are identified, and the time-dependent velocity, temperature and concentration fields are described for varying dimensionless parameters. A key ingredient of the solution is to demonstrate the degrees

of advancement of spin-up for large Lewis numbers, which are typical of realistic crystal growth situations.

It is recalled that the principal focus of the present study is directed to linearized flow regimes in which . In many applications, however, a significant problem is the spin-up process from the initial state of rest, which is characterized by strong nonlinearities. An elegant nonlinear flow model for a homogeneous fluid was brought forth by Wedemeyer(1964), and it was subsequently refined for a single-diffusive stratified fluid [e. g., Greenspan, 1980; Hyun, 1983]. A study of the spin-up from rest of a double-diffusive stratified fluid is underway, and the results will be reported in a later account.

2. Formulation

Consider a vertically-mounted right circular cylindrical container [height H, radius R], which is completely filled with an incompressible fluid. The cylindrical coordinates (r, ϑ, z) are defined as shown in Fig.1.

At the initial state, the fluid and the container are in rigid-body rotation with angular velocity Ω_i. The temperature and concentration are, respectively, T_H and S_L at the top horizontal endwall disk (z=H/2), and TL and SH at the bottom horizontal endwall disk (z=-H/2). Notice that, in the present problem setup, both temperature and concentration make stabilizing contributions to the overall density stratification, i.e., $\Delta T(\equiv T_H - T_L) > 0$ and $\Delta S(\equiv S_H - S_L) > 0$. The cylindrical sidewall (r=R) is thermally-insulated and impervious to concentration flux. Furthermore, it is assumed that $\Omega_i^2 H/g << 1$ so that the Sweet-Eddington flow can be neglected [Buzyna & Veronis(1971)], and at the initial state no relative internal flow is allowed. At the initial instant t=0, the rotation rate of the container is abruptly increased to $\Omega_i + \Delta\Omega$, and the resulting time-dependent flow of the interior fluid is to be examined. As an extension of the prior works, the Rossby number $\varepsilon[\equiv \Delta\Omega/\Omega_i] \ll 1$, which permits a linearized analysis of the problem.

The Boussinesq approximation is invoked to express the variation of density ρ:

$$\rho = \rho_o[1 - \alpha_{T(T-T_o)} + \alpha_s(S - S_o)] \tag{1}$$

In the above, subscript o denotes the reference values, and aT and aS refer, respectively, to the coefficients of volumetric expansion with respect to temperature T and concentration S. In accordance with the Boussinesq-fluid assumption, all the physical properties are taken to be constant. It is advantageous to introduce the nondimensionalized quantities (starred), which are related to their dimensional counterparts (unstarred) in the following fashion :

$$t^* = t\Omega_i; \quad (u^*, v^*, w^*) = (u, v, w)/R\Omega_i; \quad (r^*, z^*) = (r, z)/H;$$

$$S^* = \frac{S - S_o}{\Delta S}; \quad T^* = \frac{T - T_o}{\Delta T}$$

The governing, properly-nondimensionalized, time-dependent, full, axisymmetric Navier-Stokes equations, written in a cylindrical frame rotating at Ω_i with the corresponding velocity components (u*,v*,w*), are (after dropping asterisk) :

$$\frac{1}{r}\frac{\partial(ru)}{\partial r}+\frac{\partial w}{\partial z}=0 \tag{2}$$

$$\frac{\partial u}{\partial t}+u\frac{\partial u}{\partial r}+w\frac{\partial u}{\partial z}-\left(2+\frac{v}{r}\right)v=-\frac{\partial p}{\partial r}+E\left(\nabla^2 u-\frac{u}{r^2}\right) \tag{3}$$

$$\frac{\partial v}{\partial t}+u\frac{\partial v}{\partial r}+w\frac{\partial v}{\partial z}+\left(2+\frac{v}{r}\right)u=E\left(\nabla^2 v-\frac{v}{r^2}\right) \tag{4}$$

$$\frac{\partial w}{\partial t}+u\frac{\partial w}{\partial r}+w\frac{\partial w}{\partial z}=-\frac{\partial p}{\partial z}+\beta_T T-\beta_S S+E\nabla^2 w \tag{5}$$

$$\frac{\partial T}{\partial t}+u\frac{\partial T}{\partial r}+w\frac{\partial T}{\partial z}=\frac{E}{Pr}(\nabla^2 T) \tag{6}$$

$$\frac{\partial S}{\partial t}+u\frac{\partial S}{\partial r}+w\frac{\partial S}{\partial z}=\frac{E}{PrLe}(\nabla^2 S)$$

As stated earlier, in the initial state, the fluid is motionless with vertically-linear distributions of temperature and concentration :

$$\frac{\partial T}{\partial z}=1,\ \frac{\partial S}{\partial z}=-1,\ u=v=w=0 \text{ at } t=0 \tag{8}$$

The boundary conditions, which reflect the instantaneous increase of the rotation rate of the container, are expressed as

$$T=0,\ S=0,\ \frac{\partial u}{\partial z}=\frac{\partial v}{\partial z}=w=0 \qquad \text{at } z=0 \tag{9a}$$

$$T=0,\ S=0,\ u=w=0,\ v=r\varepsilon \qquad \text{at } z=-0.5 \tag{9b}$$

$$\frac{\partial T}{\partial r}=\frac{\partial S}{\partial r}=0,\ u=w=0,\ v=\left(\frac{R}{H}\right)\varepsilon \qquad \text{at } r=R/H \tag{9c}$$

$$\frac{\partial T}{\partial r}=\frac{\partial S}{\partial r}=0,\ u=\frac{\partial(v/r)}{\partial r}=\frac{\partial w}{\partial r}=0 \quad \text{at } r=r_i \tag{9d}$$

Notice that the problem formulation is anti-symmetric with respect to the cylinder mid-height z=0. Therefore, only the bottom half of the cylinder is considered [see

9(a)-9(c)]. Also, in order to meet the numerical stability requirements at the central axis r=0, the axis conditions are applied at a small, but finite, value $r=r_i$. This kind of treatment of the axis conditions, which perhaps is not a completely settled issue, has been widely used in practice and discussed at length [e. g., Warn-Varnas et al.(1978), Hyun et al.(1982), Hyun&Kwak(1989), Lang et al.(1994)]. In the present work, in several exemplary calculations, the computed results at a typical interior point, e. g., the mid-radius and quarter-height point, differed less than 0.1% as r_i changed from 0.001 to 0.01. In most runs, r_i was set 0.005.

The pertinent dimensionless parameters that emerge in the equations are

$E=\frac{\nu}{\Omega_i H^2}$, Ekman number ;

$\varepsilon=\frac{\Delta\Omega}{\Omega_i}$, Rossby number ;

$\mathrm{Pr}=\frac{\nu}{\kappa}$, Prandtl number ;

$Le=\frac{\kappa_T}{\kappa_S}$, Lewis number ;

$R_\rho=\frac{\alpha_S \Delta S}{\alpha_T \Delta T}$, buoyancy ratio ;

$St=\left(\frac{N}{\Omega_i}\right)^2$, stratification number ;

where the frequency is defined.

$N=[(\alpha_T g\Delta T+\alpha_S g\Delta S)/H]^{\frac{1}{2}}$;

$\beta_T=\alpha_T g\Delta/H\Omega_i^2$, thermal Rossby number ;

$\beta_S=\alpha_S g\Delta/H\Omega_i^2$, solutal Rossby number.

In the above, κ_T and κ_S refer respectively to the thermal and concentration diffusivities. The Lewis number Le indicates their ratio, and in many double-diffusive

situations of practical interest, Le is much larger than unity. This implies that heat is diffused at a much higher rate than concentration. The buoyancy ratio Rr denotes the contribution of solutal stratification, relative to that of thermal stratification, in the make-up of the total density stratification. The effect of overall fluid stratification, in comparison to the effect of rotation, is measured by St.

In passing, if the T and S variations make opposing contributions to the overall density stratification, the global flow pattern is anticipated to be strongly characterized by the value of Le. This flow configuration will be examined in the forthcoming research endeavors.

Numerical solutions to the above system of equations were obtained by adopting the well-established SIMPLER algorithm [Patankar(1980)]. The specifics of this numerical procedure have been documented extensively, and computations were straightforward. Staggered and stretched mesh networks were deployed, and the grid points used were typically in the axial plane. The time interval Δt was 3.8510-4τ_S. The grid-stretching was implemented such that typically eight grid points are placed within the Ekman boundary layer. Grid-convergence tests were conducted by repeating calculations for several sample runs by using grids (40x40) and (80x80). The corresponding changes in the results at the cylinder mid-radius, quarter-height were less than 0.1%. Also, time step-convergence tests were performed by deploying Δt at $3.85x10^{-4}\tau_S$, and $3.85x10^{-5}\tau_S$. Again, the variations in the results were smaller than 0.1%. Furthermore, some of the well-known higher-order differencing schemes [e.g. Hayase et al.(1992), Patankar(1980)] were employed, and the results of these exercises were highly mutually-consistent for the parameter values of present concern.

3. Results and discussion

Time-marching solutions were secured for broad ranges of principal nondimensional parameters. In view of the presence of a large number of parameters, attention was focused to the qualitative changes in flow characteristics as St, R_ρ, Le and E are altered. In order to facilitate direct comparisons with the previous accounts on single-diffusive spin-up, it was set Ar=1.0, Pr=1.0, and ε=0.05 to simulate linearized problems.

First, Figs. 2 and 3 display the progress of spin-up, as exhibited by the evolution of the azimuthal velocity, (v/rε), at different radial and axial locations. The Ekman number was set E=1.4110-3, and, in order to simulate realistic double-diffusive convection problems, Le=100. Time is normalized by using the spin-up time scale $\tau \equiv E^{-\frac{1}{2}}$, which was ascertained in the classical analysis by Greenspan and Howard(1963). Plot (a) illustrates the case of non-stratified(homogeneous) fluid spin-up, i.e., St=0. Plots (b), (c) and (d) exemplify the results of a stratified fluid by setting St=10.0, but with different values of the buoyancy ratio R_ρ. The case of R_ρ=0, shown in plot (b), corresponds to the spin-up of a single-diffusive fluid, i.e., the only diffusing agent is temperature. As is clear in Fig.2 for z=0, the region in the vicinity of the sidewall is heavily influenced by viscous effects. Spin-up in this area proceeds at a fast rate. In the interior region, i.e., at small and moderate radii, the dominant mechanism for spin-up for a homogeneous fluid is inviscid in nature. As expounded by Greenspan & Howard(1963), the Ekman layer suctions at both endwall disks produce radially-inward meridional motions in the interior. Angular momentum is conserved in the inviscid interior, therefore, the angular velocity at a given location increases with time as the radius of the fluid element decreases. As is clearly seen in plot (a) of Fig.2, the rate of increase of the scaled angular velocity v/rε is fairly uniform in the bulk of the interior. In the region close to the sidewall, the fluid adjustment process is heavily influenced by viscous effects, which yields a relatively rapid and smooth evolution. This feature is reproduced well in the present numerical computations.

For a stratified fluid, a different picture emerges. The rate of spin-up is not spatially uniform in the interior. In general, at mid-height, spin-up proceeds at a slower rate for a stratified fluid than for a homogeneous fluid. This feature is explained by noting that, for a stratified fluid, the meridional circulation tends to be restricted in the regions close to the endwall disks. In other words, due to the inhibition of vertical velocities by stable stratification, the meridional flows can not penetrate up to the mid-height of the cylinder. Consequently, as will be seen in Fig.3, spin-up is enhanced(retarded) in the region close to the endwall(mid-height) of the cylinder. This flow character was pointed out by Sakurai(1969) and Hyun et al.(1982, 1983) for the spin-up of a single-diffusive stratified fluid. The calculated data in Figs. 2 & 3 are supportive of these earlier findings. Furthermore, under the same overall stratification, the rate of spin-up decreases as the buoyancy ratio R_ρ increases.

It is interesting to note the presence of high-frequency oscillations in the interior. For a homogeneous fluid, these oscillations are identified to be the inertial mode of frequency $2\Omega_i$ [see Warn-Varnas et al.(1978)]. For a stratified fluid, the oscillations reflect the existence of modified inertial-internal gravity modes with higher frequencies than that of the inertial mode [Hyun et al. (1982)]. As asserted earlier, the relative effects of viscosity increase for a stratified fluid; therefore, these high-frequency oscillations are damped out faster as the strength of stratification increases.

Fig.3 illustrates the above-mentioned axial variations of $v/r\varepsilon$. Obviously, very close to the endwall, a viscously-controlled Ekman layer is seen. For a homogeneous fluid, the rate of spin-up is substantially uniform in the interior [see plot (a)]. However, axial variations of $v/r\varepsilon$ are appreciable for a stratified fluid, and this trend is more pronounced for a double-diffusive fluid with large R_ρ. The retardation of spin-up near the mid-height is discernible in these plots.

The computational results are re-arranged to display the systematic influences of the relevant parameters. Fig.4 exhibits the explicit effect of St on the spin-up at the mid-height, mid-radius of the cylinder [z=0, r=0.5]. The slowing-down of spin-up with increasing stratification is in evidence. The impact of Rr is shown in Fig.5, which underscores the retardation of spin-up as R_ρ increases. These features are in line with

the physical explanations which were put forth earlier.

The patterns of the meridional flows of a double-diffusive fluid are illustrated in Fig. 6. The meridional stream function y(dimensional) is defined such that $u^* = \frac{1}{r^*}\frac{\partial \Psi^*}{\partial z^*}$, $w^* = -\frac{1}{r^*}\frac{\partial \Psi^*}{\partial r^*}$. The present problem formulation is anti-symmetric with respect to the cylinder mid-height(z=0), therefore, only the bottom half of the cylinder is shown. For a non-stratified fluid (see Fig.6(a) for St=0), the counter-clockwise meridional circulation fills the entire cavity, as stressed earlier [Warn-Varnas et al(1978)]. As illustrated in Fig.6(b), the fluid stratification suppresses vertical motions, therefore, the extent of meridional circulation is restricted closer to the endwall disks. This trend becomes more pronounced as the fluid is double-diffusively stratified. As depicted in Figs. 6(c) and (d), the meridional flow weakens in strength and shrinks in size. It is important to observe that for the same value of St, as R_ρ increases, the meridional flows weaken and the extent of the counter-clockwise cell is confined to a region close to the endwall. In summary, the depiction of the meridional flows indicates that an increase of R_ρ, under the same overall stratification, is equivalent to an increase of St for a single-diffusive fluid.

In an effort to delineate the specific impacts of the parameters of a double-diffusive fluid, the fields of perturbation quantities in the axial plane are depicted. For this purpose, the perturbation density ρ' is defined as [Saunders & Beardsley(1975)] :

$$\rho' = \frac{g}{\Omega^2 H \varepsilon}[\rho - \rho_i(z)]$$

in which ρ and $\rho_i(z)$ denote the instantaneous density and the initial-state density, respectively. Similarly, the perturbation temperature T' and the perturbation concentration S' are introduced :

$$T' = \frac{\beta_T}{\varepsilon}[T - T_i(z)],$$

$$S' = \frac{\beta_S}{\varepsilon}[S - S_i(z)]$$

Fig.7 is an exemplary plot of ρ' in the bottom half of the cylinder. In general, as a result of spin-up flows, the density at small and moderate radii is smaller than the initial value, i.e., ρ'<0 ; and at large radii, ρ'>0. This can be explained by noting the existence of a counter-clockwise meridional cell, as displayed in Fig.6. At large radii, the counter-clockwise motion brings the fluid of high density from below, which, therefore, causes positive perturbation densities. At small and moderate radii, the axial flows are toward the endwall, which carry the fluid of low density from above; negative perturbation densities are observed in these regions. The magnitudes of perturbation densities tend to be augmented in the vicinity of the endwall, as R_ρ increases. This is expected in view of the clustering of meridional flows in the neighborhood of the endwall, as R_ρ increases.

The perturbation temperatures are plotted in Fig.8. Because of the action of meridional flows, fluids of low temperature, originating from the bottom endwall region, move to the large-radii region. At small and moderate radii, fluids of high temperature, originating from the mid-height region, move downward by the counter-clockwise meridional circulation. The magnitudes of perturbation temperature are substantial for the case of a single-diffusive fluid[see Fig.8(a)]. For a double-diffusive fluid, the global patterns of perturbation temperature field remain qualitatively unchanged. However, as is apparent in Figs.8(b) and 8(c), the perturbation temperatures are very small in magnitude as Rr increases [note the difference in scales for the contour values of ΔT' in Fig.8]. It is important to recognize that, for a substantially stratified fluid, the temperature field in the course of spin-up is only slightly altered from the initial state linear profile when R_ρ is large. As can be inferred from Figs.7 and 8, for a double-diffusive fluid with large R_ρ , the perturbation density is contributed predominantly by the perturbation concentration, which is illustrated in Fig.9. For a strongly-stratified fluid, as R_ρ increases, the magnitudes of S' increase and the iso-S' lines tend to cluster near the endwall.

Finally, the specific effect of the Lewis number Le is examined. Fig.10 shows that the rate of spin-up is generally retarded as Le increases. Combining the above computational results for the evolution of azimuthal velocity, a table has been made to show the nondimensional time to reach some arbitrarily-defined value approaching the final state. In Table 1, these are tabulated for an exemplary interior location [near the mid-radius, quarter-height point] to reach . The weakening of the associated meridional circulation, as Le increases, is discernible in Fig.11. As can be seen in Fig.12, the perturbation density increases in magnitude as Le increases. This is attributable to the increase in perturbation concentration for large Le, as exhibited in Fig.13. When Le is large, thermal diffusion proceeds much faster than concentration diffusion. Therefore, the corresponding changes in perturbation temperature for large Le are meager.

In summary, for a double-diffusive fluid of a given St, the case of large Le is equivalent to an increase in the effective overall fluid stratification, which leads to a slow-down in the spin-up process. No published accounts have been reported on experimental measurements/observations of spin-up flows of a double-diffusive fluid. The numerical results of the present endeavor should be subject to experimental verifications.

4. Conclusion

For a double-diffusive fluid, the global spin-up process, as expressed by the evolution of the angular velocity field, is retarded. The attendant counter-clockwise meridional circulation weakens in magnitude and shrinks in size toward the endwall. This retardation is more pronounced for large R_ρ .

The rate of spin-up in the interior is spatially non-uniform for a stratified fluid. This spatial non-uniformity becomes notable for a double-diffusive fluid, as R_ρ increases.

The perturbation densities are negative(positive) in central(peripheral) areas of the meridonal plane. The magnitudes of perturbation densities increase as R_ρ increases. For large R_ρ, the perturbation temperatures are very small in magnitude, but the magnitudes of perturbation concentration are appreciable.

Spin-up is retarded as Le increases. For large Le, the perturbation densities are caused mainly by the perturbation concentrations. As R_ρ increases and as Le increases, the situation is equivalent to increasing the general strength of effective global fluid stratification in the container.

Acknowledgement

The authors are grateful to the referees whose constructive comments led to improvements in the revised manuscript. This work was supported in part by a grant from the ministry of Science and Technology, Korea, under the International Cooperative Research Scheme, in collaboration with Prof. H. Ozoe of Kyushu Univ., Japan.

Reference

Brown, R. A. 1988. Theory of transport processes in single crystal growth from the melt. AIChE J., 34, 881-911.

Buzyna, G. and Veronis, G. 1971. Spin-up of a stratified fluid: theory and experiment. J. Fluid Mech. 50, 579-608.

Greenspan, H. P. & Howard, L. N. 1963. On a time-dependent motion of a rotating fluid. J. Fluid Mech. 17,385-404.

Greenspan, H. P. 1980. A note on the spin-up from rest of a stratified fluid. Geophys. Astrophys. Fluid Dyn. 15, 1-5.

Hayase, T., Humphrey, J. A. C. and Greif, R. 1992. A consistently formulated QUICK scheme for fast and stable convergence using finite-volume iterative calculation procedures. J. comp. Phys. 98, 108-118

Hyun, J. M. 1983. Axisymmetric flows in spin-up from rest of a stratified fluid in a cylinder. Geophysical Fluid Dyn. 23, 127-141.

Hyun, J. M., Fowlis, W. W. and Warn-Varnas, A. 1982. Numerical solutions for the spin-up of a stratified fluid. J. Fluid Mech. 117,71.

Hyun, J. M. and Kwak, H. S. 1989, Flow of a double-diffusive stratified fluid in a differentially-rotating cylinder. Geophys. Astrophys. Fluid Dynamics. 46, 203-219.

Hyun, J. M. and Lee, J. W. 1990. Double-diffusive convection in a rectangle with cooperating horizontal gradients of temperature and concentration. Int. J. Heat Mass Transfer. 33, 1605-1617.

Kobayashi, N. 1980. Computer simulation of heat, mass and fluid flows in melt during Czochralski crystal growth. Comp. Meth. Appl. Mech. Eng., 23, 21-33.

Lang, E., Sridhar, k. and Wilson, N. W. Computational study of disk driven rotating flow in a cylindrical enclosure. J. Fluids Eng., 116, 815-820.

Lee, J. W. and Hyun, J. M. 1991. Double diffusive convection in a cavity under a vertical solutal gradient and a horizontal temperature gradient. Int. J. Heat Mass Transfer, 34, 2423-2427.

Lee, J. W. and Hyun, J. M. 1991. Time-dependent double diffusion in a stably stratified

fluid under lateral heating. Int. J. Heat Mass Transfer, 34, 2409-2421.

Ostarach, S., Jiang, D. and Kamotani, Y. 1987. Thermosolutal convection in shallow enclosures. Proc. ASME-JSME Thermal Engr. Joint Conf., 2, 159-168.

Patankar, S. V. 1980. Numerical Heat Transfer and Fluid Flow. McGraw-Hill, New York

Sakurai, T. 1969. Spin down problem of rotating stratified fluid in thermally insulated circular cylinders. J. Fluid Mech. 36, 689-699.

Saunders, K.D. and Beardsley, R.C. 1975. An experimental study of the spin-up of a thermally stratified rotating fluid. Geophysical Fluid Dyn. 7, 1-27.

Sung, H. J., Cho, W. K. and Hyun, J. M. 1993. Double-diffusive convection in a rotating annulus with horizontal temperature and vertical solutal gradients. Int. J. Heat Mass Transfer, 36, 3773-3782.

Sung, H. J., Jung, Y. J. and Ozoe, H. 1995. Prediction of transient oscillatory flow in czochralski convection. Int. J. Heat Transfer, 38(9), 1627-1636.

Turner, J. S. 1974. Double diffusive phenomena. Ann. Rev. Fluid Mech. 6, 37-56.

Walin, G. 1969. Some aspects of time-dependent motion of a stratified rotating fluid. J. Fluid Mech. 36, 289-307.

Warn-Varnas, A., Fowlis, W. W., Piacsek, S. and Lee, S. M. 1978. Numerical solution and laser-doppler measurements of spin-up. J. Fluid Mech. 85, 609-639.

Wedemeyer, E., H. 1964. The unsteady flow within a spinning cylinder. J. Fluid Mech. 20, 383-399.

Table captions

Table 1.Nondimensional times (t/τ) to reach at a location near the mid-radius, quarter-height point (r=0.5, z=-0.21).

Figure captions

Fig.1. Flow configuration and coordinate system.

Fig.2. Evolution of normalized azimuthal velocity, $v/r\varepsilon$, at mid-height z=0, $E=1.41\times10^{-3}$. Conditions are
(a) homogeneous fluid(St=0);
(b) single-diffusive fluid (St=10.0, R_ρ=0);
(c) double-diffusive fluid (St=10.0, R_ρ=1.0);
(d) double-diffusive fluid (St=10.0, R_ρ=10.0).
The radial positions r are :
r=0.25, _____ ; 0.51, __ __ __ ; 0.75, __ . __ ; 0.95, __...__ ; 0.98, ...

Fig.3. Same as in Fig.2, but at mid-radius r=0.5. The axial positions z are :
z=0.00, _____ ; -0.21, __ __ __ ; -0.40, __ . __ ; -0.45, __...__ ; -0.49, ...

Fig.4. The effect of St on v/re at mid-radius, mid-height [r=0.5, z=0]. R_ρ=1.0.
St=0, _____ ; St=10, __ __ __ ; St=30, __ . __ ; St=100, ...

Fig.5. The effect of R_ρ on $v/r\varepsilon$ at mid-radius, mid-height[r=0.5, z=0]. St=10.0.
R_ρ=0, _____ ; R_ρ=1, __ __ __ ; R_ρ=10, __ . __ .

Fig.6. Plot of meridional stream function, Ψ, in the bottom half of the cylinder. Conditions are Le=100.0, t/τ=0.282. The contour increment is $\Delta\Psi=1.5\times10^{-4}$.
(a) homogeneous fluid (St=0). $\Psi_{max}=2.25\times10^{-4}$;
(b) single-diffusive fluid(St=10.0,R_ρ=0). $\Psi_{max}=8.70\times10^{-5}$;
(c) double-diffusive fluid(St=10.0,R_ρ=1). $\Psi_{max}=5.47\times10^{-5}$;
(d) double-diffusive fluid(St=10.0,R_ρ=10). $\Psi_{max}=3.62\times10^{-5}$.

Fig.7. Plot of perturbation density ρ' in the bottom half of the cylinder. Conditions are St=10.0, Le=100.0, t/τ=0.282. The contour increment $\Delta\rho'$=0.12.
(a) single-diffusive fluid(R_ρ=0). ρ'_{max}=0.650, ρ'_{min}=-0.794;
(b) double-diffusive fluid(R_ρ=1.0). ρ'_{max}=0.963, ρ'_{min}=-1.01;
(c) double-diffusive fluid(R_ρ=10.0). ρ'_{max}=1.18, ρ'_{min}=-1.26.

Fig.8. Plot of perturbation temperature T' in the bottom half of the cylinder. Conditions are St=10.0, Le=100.0, t/τ=0.282. The contour increment $\Delta T'=5.6\times10^{-2}$ for (a)&(b), and $\Delta T'=1.6\times10^{-2}$ for (c).
(a) single-diffusive fluid(R_ρ=0). T'_{max}=0.794, T'_{min}=-0.650;
(b) double-diffusive fluid(R_ρ=1.0). T'_{max}=0.375, T'_{min}=-0.251;
(c) double-diffusive fluid(R_ρ=10.0). T'_{max}=0.065, T'_{min}=-0.039.

Fig.9. Plot of perturbation temperature S' in the bottom half of the cylinder. Conditions are St=10.0, Le=100.0, t/τ=0.282. The contour increment $\Delta S'$=0.13.
(a) R_ρ=1.0. S'_{max}=0.776, S'_{min}=-0.680;
(b) R_ρ=10.0. S'_{max}=1.15, S'_{min}=-1.20.

Fig.10. The effect of Le on $v/r\varepsilon$ at mid-depth z=0. Conditions are St=10.0, R_ρ=1.0
(a) r=0.25, (b) r=0.50.
Le=2, _____ ; 10, __ . __ ; 300, ...

Fig.11. The effect of Le on y, shown for the bottom half of the cylinder . Conditions are St=10.0, R_ρ=1.0, t/τ=0.282. The contour increment $\Delta\Psi$=6.6x10-6.
(a) Le=2.0. $\Psi_{max}=7.55\times10^{-5}$;
(b) Le=10.0. $\Psi_{max}=5.97\times10^{-5}$;
(c) Le=300.0. $\Psi_{max}=5.43\times10^{-5}$.

Fig.12. The effect of Le on ρ', shown for the bottom half of the cylinder . Conditions are St=10.0, R_ρ=1.0, t/τ=0.282. The contour increment $\Delta\rho'$=0.14.
(a) Le=2.0. ρ'_{max}=0.719, ρ'_{min}=-0.865;
(b) Le=10.0. ρ'_{max}=0.854, ρ'_{min}=-0.967;
(c) Le=300.0. ρ'_{max}=0.987, ρ'_{min}=-1.01.

Fig.13. The effect of Le on S', shown for the bottom half of the cylinder . Conditions are St=10.0, R_ρ=1.0, t/τ=0.282. The contour increment $\Delta S'$=0.11.
(a) Le=2.0. S'_{max}=0.429, S'_{min}=-0.482;
(b) Le=10.0. S'_{max}=0.631, S'_{min}=-0.619;
(c) Le=300.0. S'_{max}=0.802, S'_{min}=-0.685.

Case	t/τ
Homogeneous	0.56
Single-diffusion ($R_\rho = 0$)	1.12
$R_\rho = 1.0$, Le = 100	1.64
$R_\rho = 10.0$, Le = 100	1.80
Le = 2.0, $R_\rho = 1.0$	1.23
Le = 10.0, $R_\rho = 1.0$	1.48

Table 1

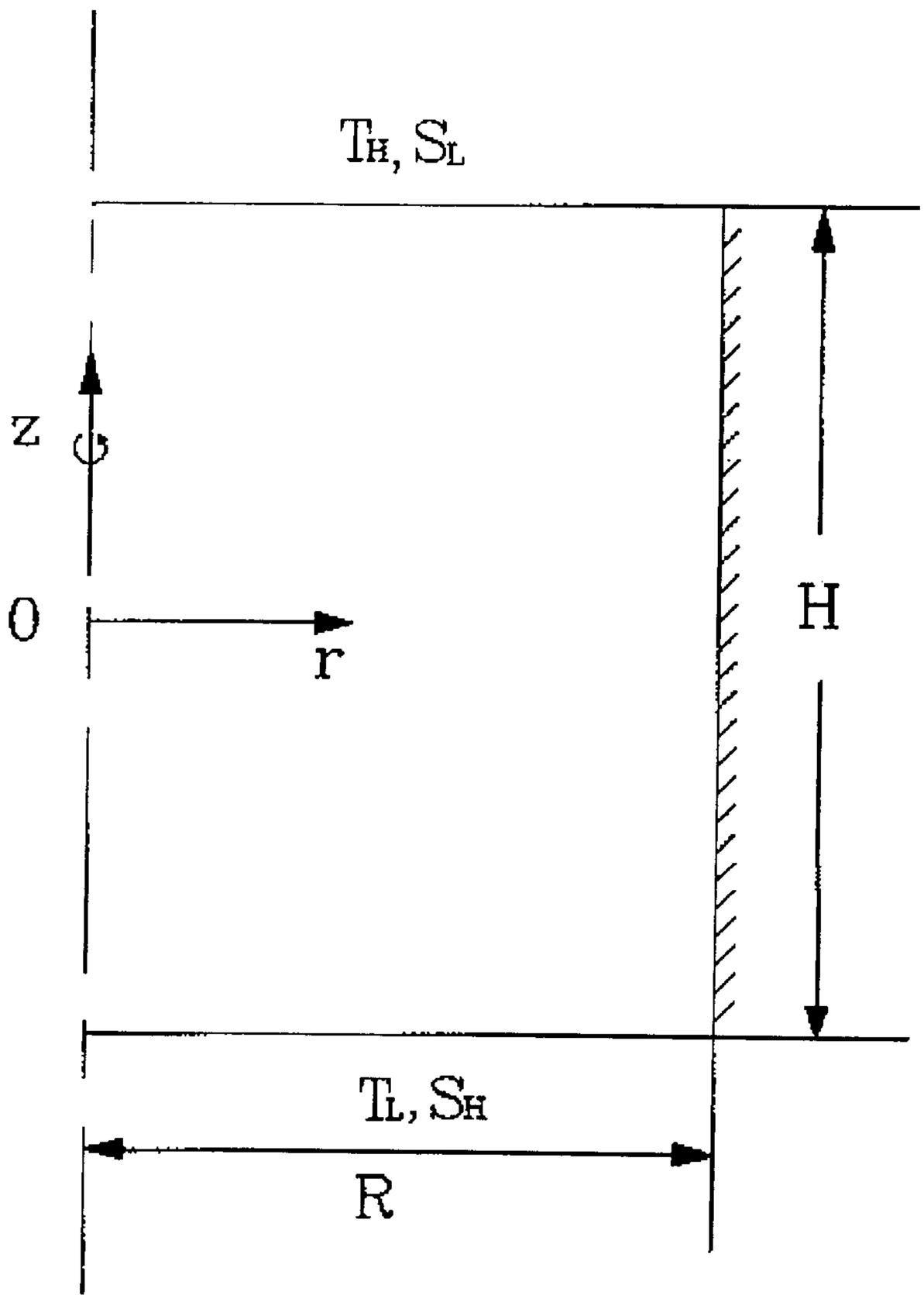

Fig.1

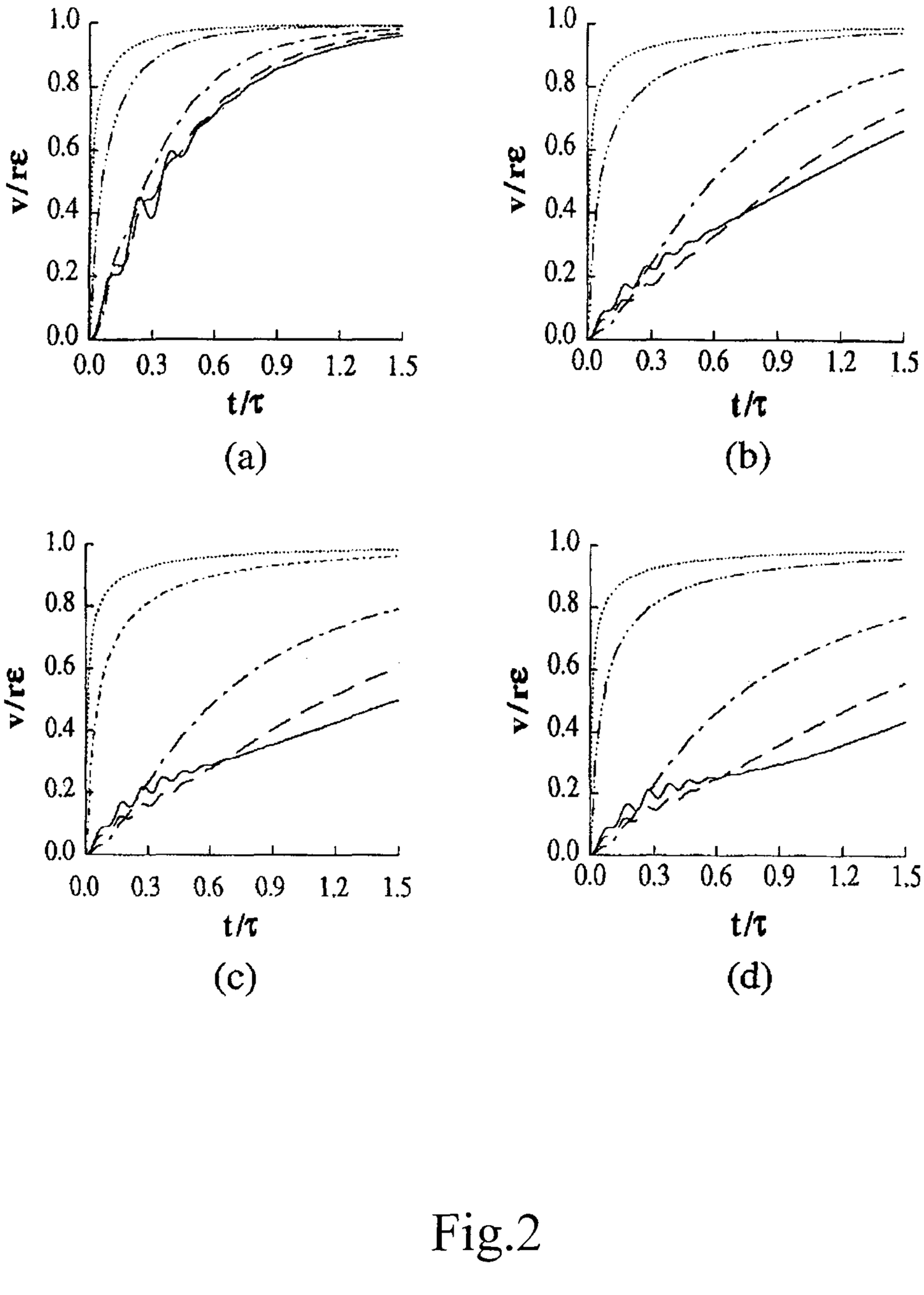

Fig.2

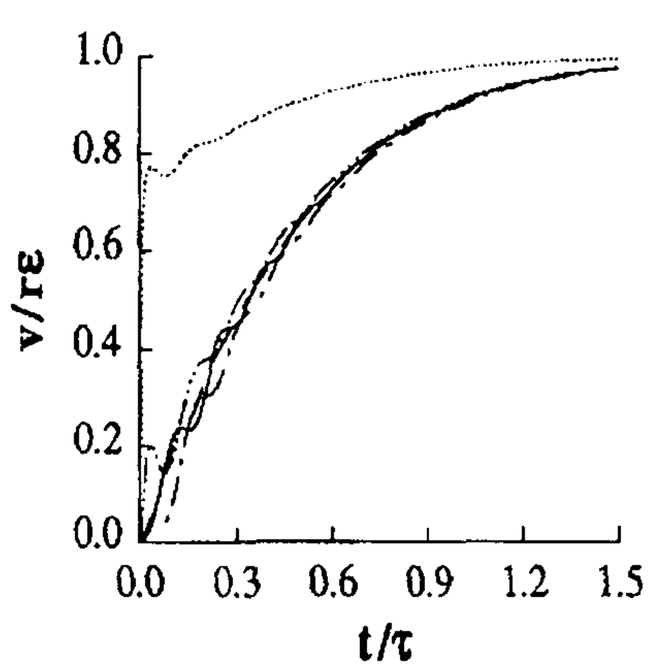
1.0
0.8
0.6
0.4
0.2
0.0
v/rε
0.0 0.3 0.6 0.9 1.2 1.5
t/τ

(a)

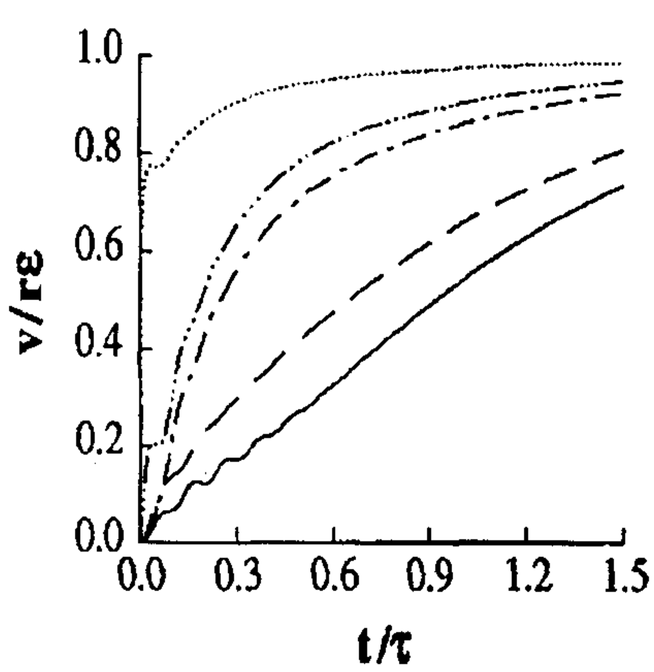
1.0
0.8
0.6
0.4
0.2
0.0
v/rε
0.0 0.3 0.6 0.9 1.2 1.5
t/τ

(b)

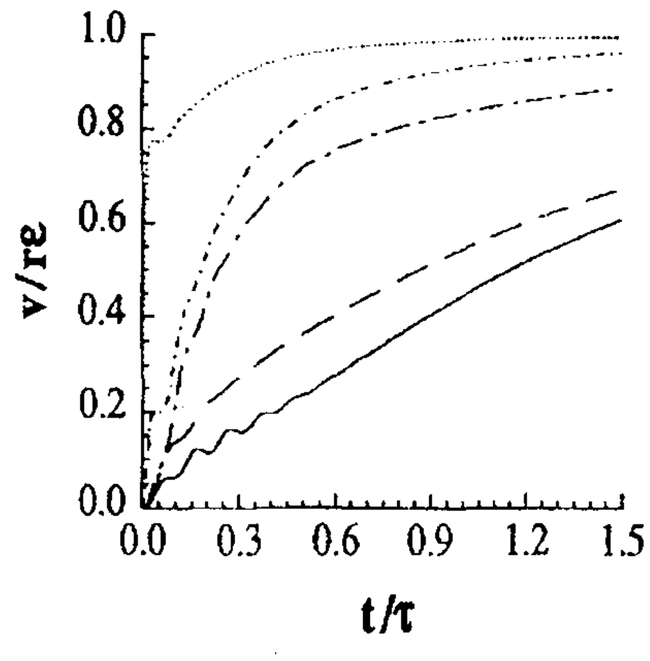
1.0
0.8
0.6
0.4
0.2
0.0
v/rε
0.0 0.3 0.6 0.9 1.2 1.5
t/τ

(c)

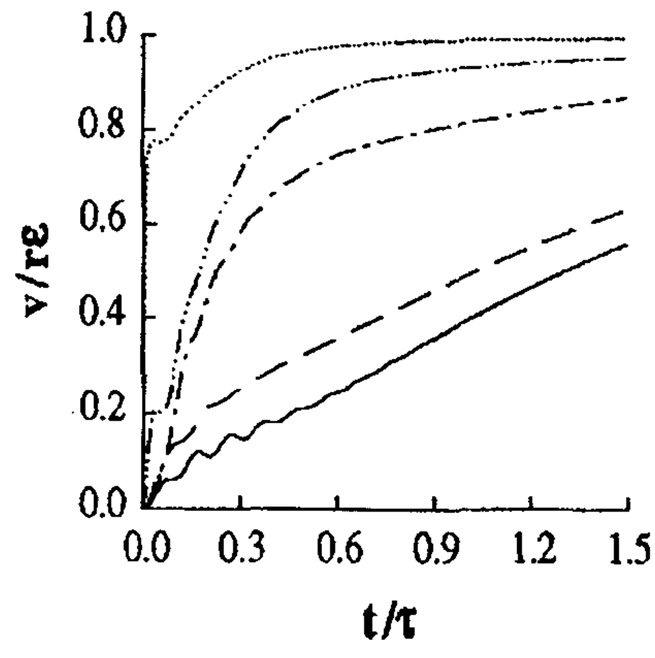
1.0
0.8
0.6
0.4
0.2
0.0
v/rε
0.0 0.3 0.6 0.9 1.2 1.5
t/τ

(d)

Fig.3

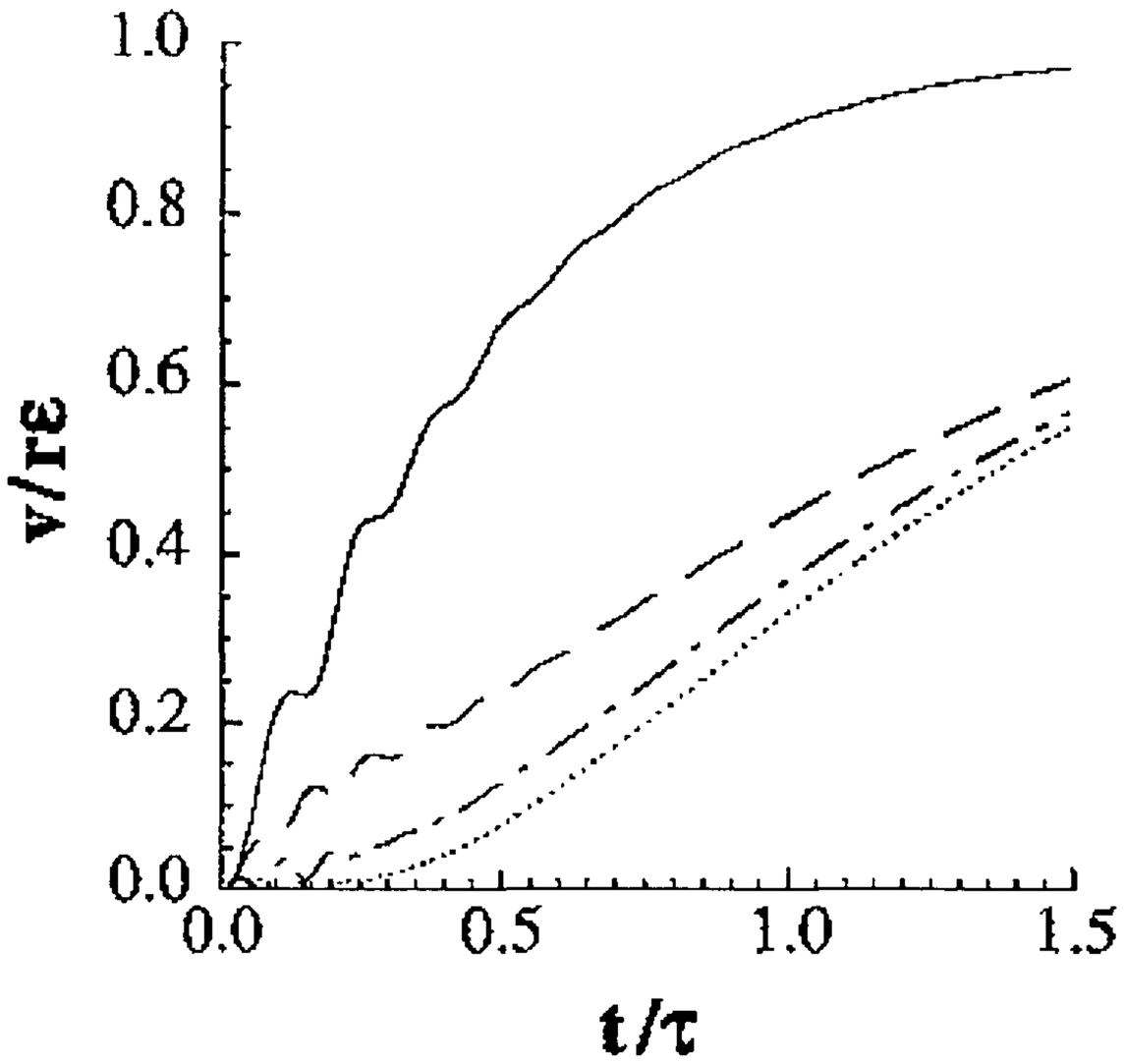
1.0
0.8
0.6
0.4
0.2
0.0
v/rε
0.0
0.5
1.0
1.5
t/τ

Fig.4

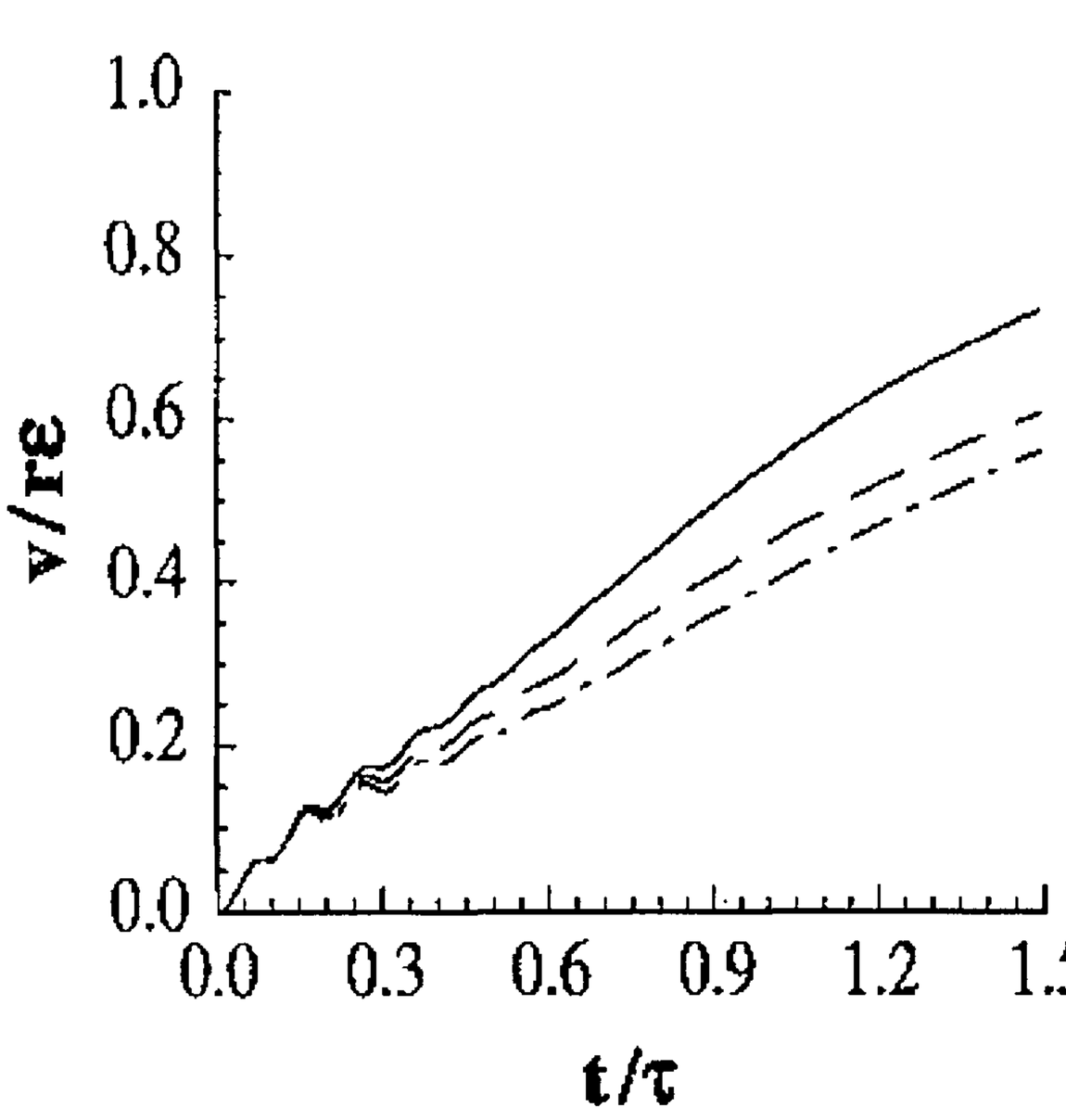
1.0
0.8
0.6
0.4
0.2
0.0
v/rε
0.0
0.3
0.6
0.9
1.2
1.5
t/τ

Fig.5

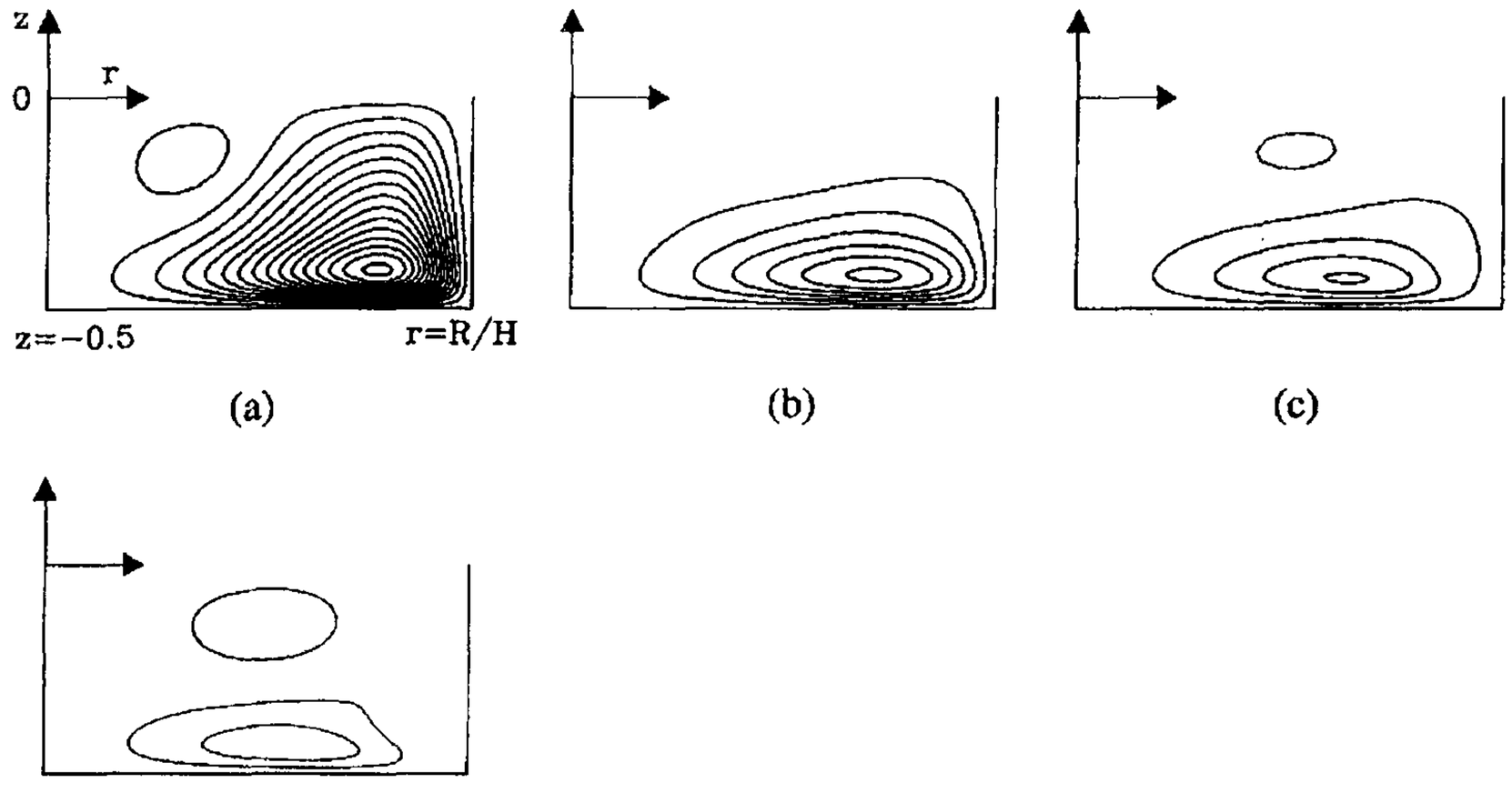

(a) (b) (c)

(d)

Fig.6

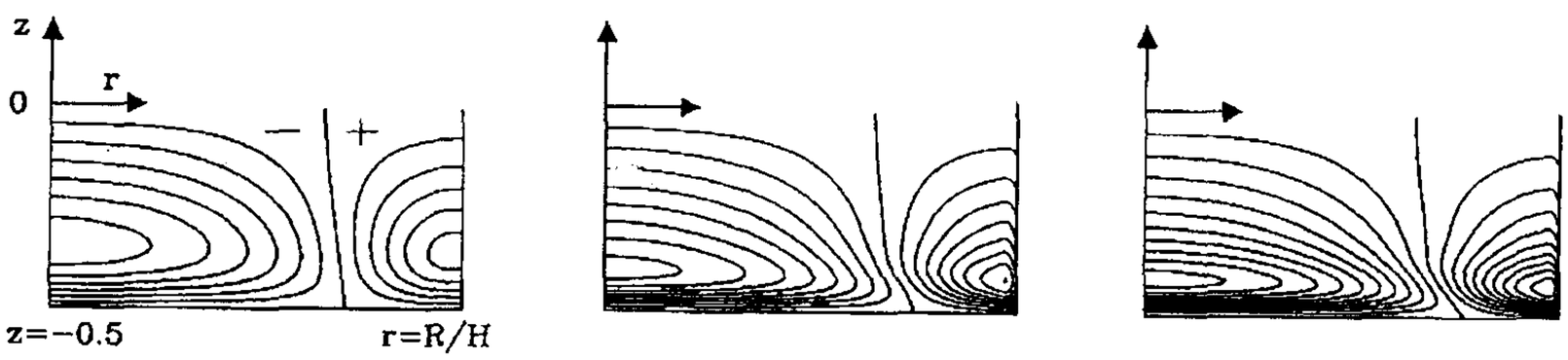

(a) (b) (c)

Fig.7

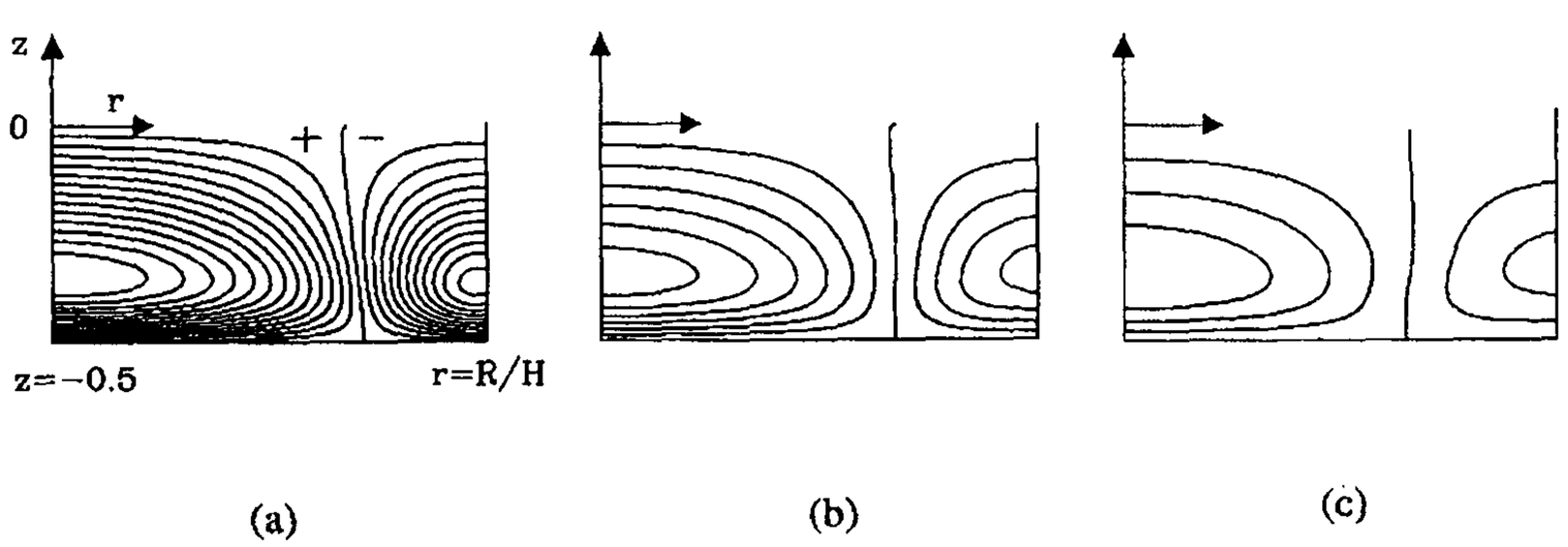

(a) (b) (c)

Fig.8

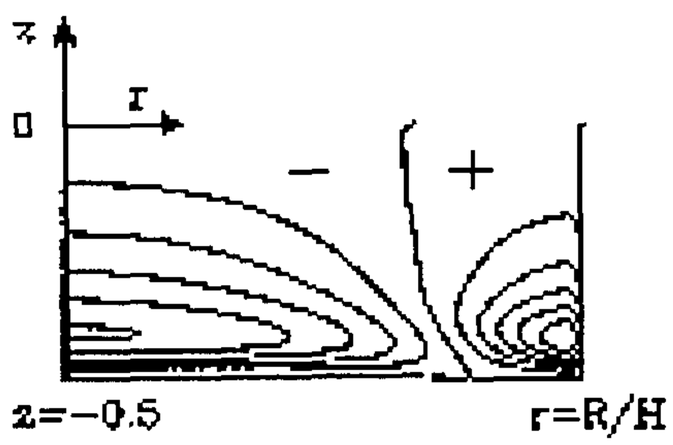

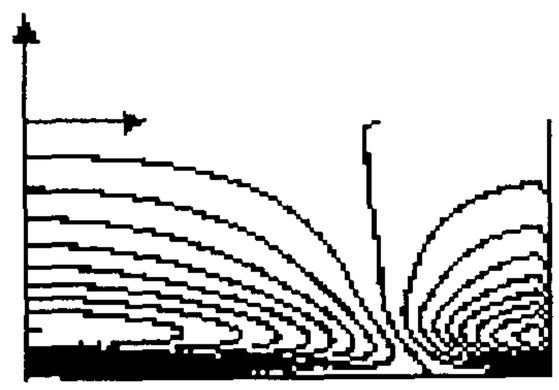

(a) (b)

Fig.9

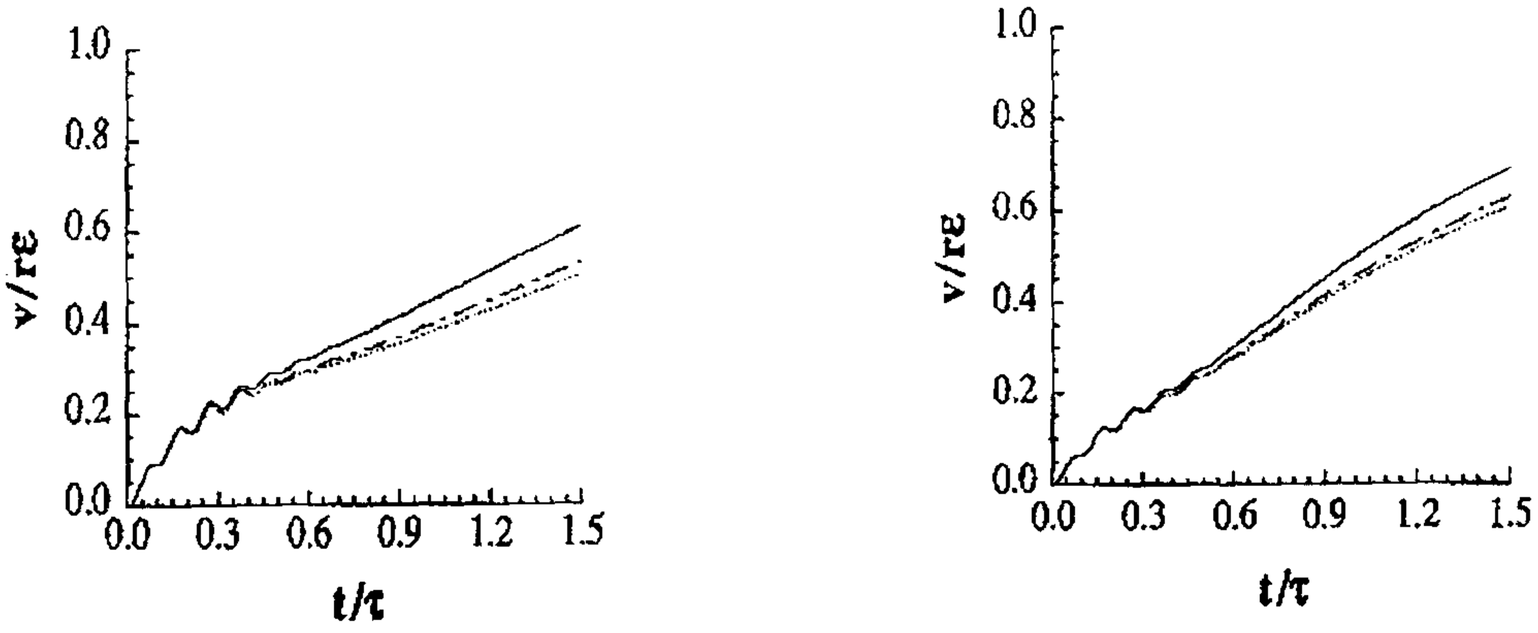
1.0
0.8
0.6
0.4
0.2
0.0
v/rε
0.0 0.3 0.6 0.9 1.2 1.5
t/τ
(a)
1.0
0.8
0.6
0.4
0.2
0.0
v/rε
0.0 0.3 0.6 0.9 1.2 1.5
t/τ
(b)

Fig.10

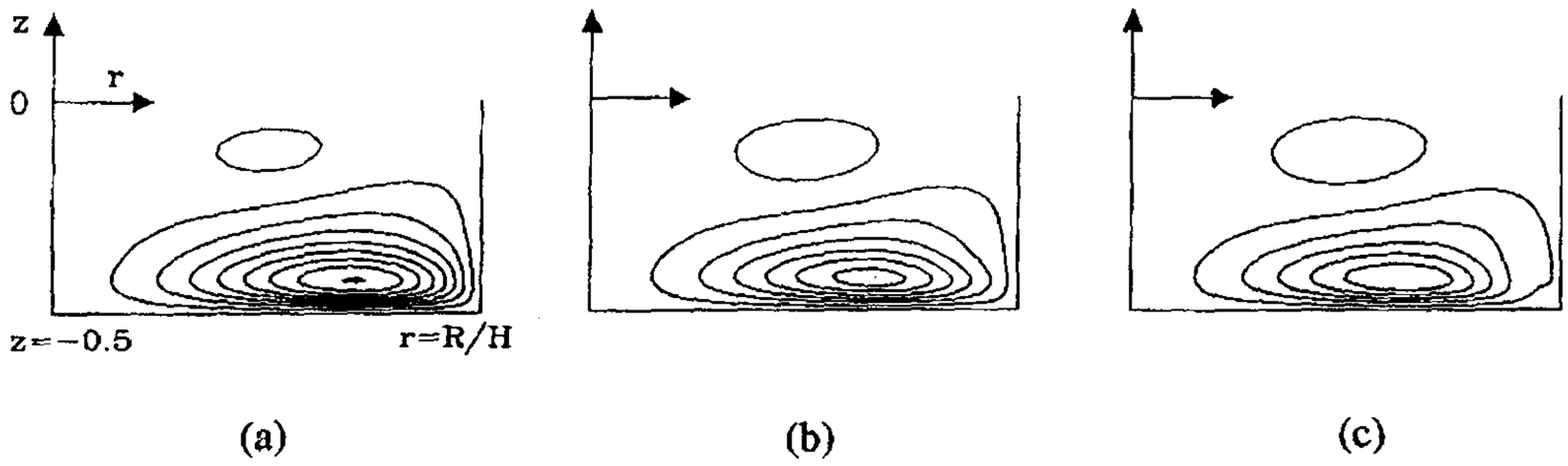
z
r
0
z=−0.5
r=R/H
(a)
(b)
(c)

Fig.11

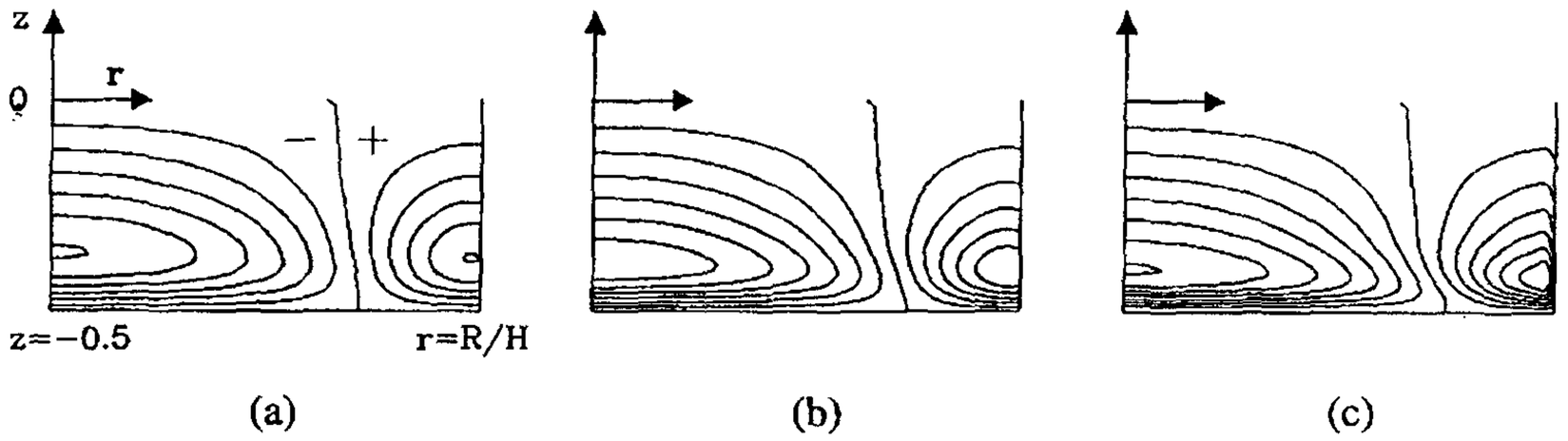

(a) (b) (c)

Fig.12

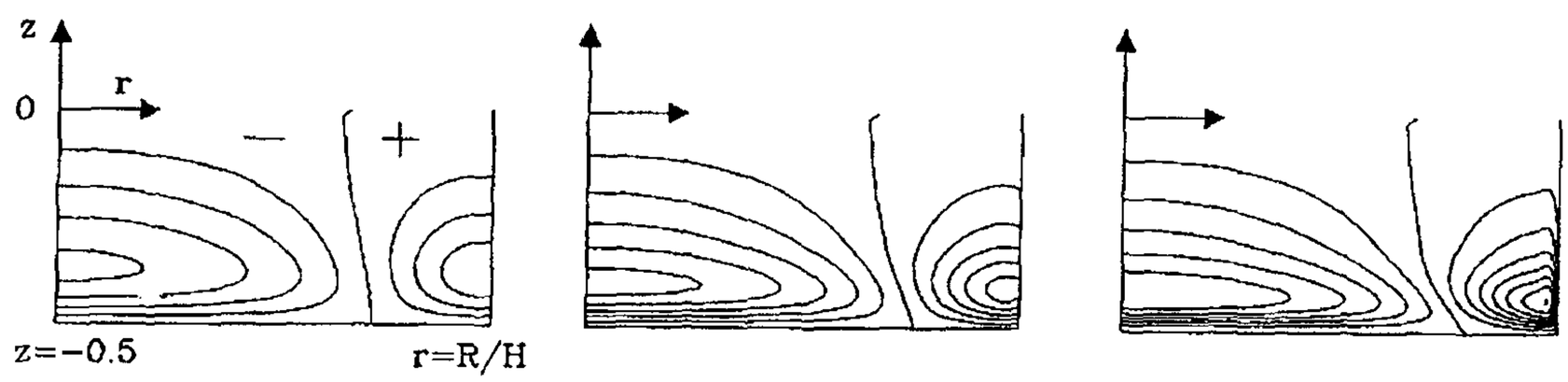

(a) (b) (c)

Fig.13

제 2 장

Numerical Solution for the Spin-Up from Rest with a Free Surface

(자유표면을 가진 유체의 정지상태에서의 스핀-엎에 관한 수치적 연구)

여 백

요약문

일부가 차있는 원통용기 내부유체의 정지상태로 부터의 스핀-엎에 대한 연구를 수행하였다. 시스템의 Ekman 수, $E=\nu/\Omega R^2$는 1보다 매우 작은 수이다. Navier-Stokes 방정식에 대해서 수치해석이 수행되었다. 수치해는 비정상 상태의 (u,v,w) 속도장과 변화하는 자유표면의 형태에 대한 상세한 정보를 제공한다. 이전의 해석적인 모델들과의 정량적인 비교에 특히 주안점을 두었다. 4개의 원형적인 유동형태가 조사되었다. 4개의 경우 모두에 대해서 자유표면 모양과 원주방향속도가 해석적인 예측과 거의 일치하였다. 수치해를 사용하여 비정상 상태의 자오면 상의 유동형태가 묘사되었고, 이러한 유동형태는 해석해의 기본적인 경향과 일치하였다.

Abstract

The problem of spin-up from rest of a liquid in a partially-filled circular cylinder is considered. The Ekman number of the system, $E = \nu/\Omega R^2$, is much smaller than unity. Numerical solutions to the governing Navier-Stokes equations have been secured. The numerical results provide descriptions of the evolving free surface shape as well as the time-dependent three-component (u,v,w) velocity field. Particular attention is given to the task of verifying the capabilities of the analytical model due to Homicz and Gerber (H&G). Numerical results for four prototypical flow configurations are examined. For all of the four cases, close agreement is noted in the free surface contour and azimuthal velocity field between the present numerical results and the predictions of H&G model. Utilizing the numerical data, time-dependent meridional flow fields are depicted. These are consistent with the fundamental notions embedded in the H&G model. The present numerical study is supportive of the basic contentions of the H&G model.

1. Introduction

Transient motions of a viscous fluid in response to a change in rotation rate of the container from Ω_i to Ω_f are termed spin-up. In order to understand the intrinsic dynamics of the flow, geometrically simple axisymmetric cylindrical containers are usually selected for a fundamental analysis. For most technological applications, the representative Ekman number of the system is small, $E \equiv \nu/\Omega R^2 \ll 1$, in which ν denotes the fluid kinematic viscosity, Ω the characteristic rotation rate of the container, and R the characteristic dimension of the container. Studies of spin-up have occupied the centerstage of classical subjects of unsteady rotating fluid dynamics.

The pioneering treatise of Greenspan and Howard(1963) dealt with the situations when the initial state was in a pre-existing rigid-body rotation at Ω_i in a circular cylinder. They further confined attention to linearized problems, in which the step change in rotation rate was small, i.e., $\Delta\Omega[\equiv\Omega_f - \Omega_i] \ll \Omega_f$. It was succinctly shown that the transient process in the bulk of the container interior is accomplished by radial advection of angular momentum, which is driven essentially by the Ekman layer suction mechanism. Accordingly, the global adjustment is substantially attained over the spin-up time scale $E^{-\frac{1}{2}}\Omega_f^{-1}$, rather than the much longer diffusive time scale $E^{-1}\Omega_f^{-1}$.

The extension of the above theoretical contention to the strongly nonlinear flow in a cylinder, starting from the initial state of rest ($\Omega_i \equiv 0, \Delta\Omega = \Omega_f$), was carried out by Wedemeyer(1964). Several heuristic arguments and physical insights were incorporated in the course of constructing an analytical model. The crux of this model is that the interior core region is divided into a nonrotating zone and a rotating zone, which are separated by a radially-propagating cylindrical velocity shear front. The qualitative correctness of this model has since been established by a number of ,numerical and experimental investigations [e.g., Watkins & Hussey, 1977, Weidman, 1976, Kitchens, 1980, Hyun et al., 1983].

The aforesaid classical spin-up models are concerned with the cases when the fluid

completely fills the closed container. As a variation of the above basic configuration, the problem of spin-up from rest of a liquid with a free surface has been studied for some time. The flow properties are of interest from the standpoint of fundamental rotating fluid dynamics research. Also, in practical engineering applications, there are situations in which the liquid fills only a part of the rotating vessel. Knowledge on the transient behavior of a partially-filled fluid in a rotating container is useful for the design and operation of chemical mixers, fluid machinery, centrifuges, etc.

Goller and Ranov(1968) proposed an approximate analytical model, principally based on Wedemeyer's formalism, which would depict the free surface profile during spin-up from rest. Several plausibility arguments, enriched by physical observations, were built into the model. The predictions of this model for the evolving free surface shape were shown to be consistent with the laboratory measurements. However, the model of Goller and Ranov considered only the cases when the deformed free surface did not intersect either of the endwall disks of the cylindrical container. Clearly, the free surface may touch and intersect one or both of the endwall disks, depending on the rotation rate of the container, the liquid fill ratio and the cylinder aspect ratio.

Further refinements of the model were implemented by Homicz & Gerber(1987, hereafter referred to as H&G), extending the methodologies of the Goller and Ranov model. This model is designed to tackle general flow configurations, including the situations when the free surface intersects the endwall disk(s). A number of simplifying assumptions were invoked in the course of the model construction. These efforts led to straightforward schemes to calculate the gross characteristics in the interior core and the resulting deformation of the free surface. The reliability of this model was tested by checking the analytical predictions against the laboratory measurements of transient free surface contour by Choi et al.[1989, 1991]. These comparisons demonstrated satisfactory consistency between the two sets of data. Good agreement was also obtained in the cases when the free surface intersected one or both of the endwall disks. However, as noted by H&G as well as by Choi et al.(1989, 1991), experimental data on comprehensive flow details in the entire cylinder interior have not been available in the published literature. It should be pointed out that, in spin-up flows with $E \ll 1$, the

meridional velocities are $O(E^{1/2})$ of the primary azimuthal velocity. Consequently, direct experimental measurements of the meridional flows are formidable undertakings, although the meridional flows are essential ingredients in the evolution of global flow field. In view of this practical difficulty, one alternative is to seek numerical solutions to the governing equations, and the present paper reports the results of such numerical endeavors. The numerical results of time-dependent azimuthal velocity will be compared with the predictions based upon the Homicz & Gerber model. These exercises will give credence to the validity of the present numerical results. Utilizing these verified numerical solutions, features of transient meridional circulations will be explored. As indicated earlier, an explicit portrayal of meridional flows has not been given by previous analytical and experimental efforts.

One mission of this work is to make a critical assessment of the capabilities of the H&G model by utilizing the numerical solutions of the unapproximated governing equations. Particular emphasis is placed on the model predictions of free surface displacement, including the cases when the free surface intersects the endwall disk(s). Another purpose is to portray the principal structure of both azimuthal and meridional velocities throughout the entire flow domain. Plots describing the flow evolution are illustrated. These depictions were made possible by using the flow data acquired by numerical simulations. In summary, the present numerical solutions are complementary to the preceding analytical model of H&G, and the present results reinforce the qualitative characterizations of the flow structure which have been put forth by formulations of the prior authors.

2. The formulation.

Consider a vertically-mounted closed cylindrical container (radius R, height H), which is partially-filled by a liquid (density ρ, kinematic viscosity ν). At the initial state of rest, the liquid level is L. At t=0, the system abruptly begins to rotate at angular frequency Ω about the central longitudinal axis z [see Fig. 1]. The task is to describe the ensuing motion of liquid. As remarked by H&G and Choi et al.(1989, 1991), the global flow field may be classified into four different patterns, depending on the shape of the final-state free surface. Fig. 2 sketches these four patterns, which were previously presented by Gerber(1975). Clearly, in the final state, the free surface touches only the sidewall (stage 1), or one of the two endwall disks (stage 2a and stage 2b), or both of the endwall disk (stage 3).

Adopting a cylindrical frame (r,θ,z), with corresponding velocity components (u,v,w), the governing time-dependent, axisymmetric, Navier-Stokes equations, in dimensionless form, are

$$\frac{1}{r}\frac{\partial(ru)}{\partial r}+\frac{\partial w}{\partial z}=0$$

$$\frac{\partial u}{\partial t}+u\frac{\partial u}{\partial r}+w\frac{\partial u}{\partial z}-\frac{v^2}{r}=-\frac{\partial p}{\partial r}+E\left(\nabla^2 u-\frac{u}{r^2}\right)$$

$$\frac{\partial v}{\partial t}+u\frac{\partial v}{\partial r}+w\frac{\partial v}{\partial z}+\frac{uv}{r}=E\left(\nabla^2 v-\frac{v}{r^2}\right) \qquad (1)$$

$$\frac{\partial w}{\partial t}+u\frac{\partial w}{\partial r}+w\frac{\partial w}{\partial z}=-\frac{\partial p}{\partial z}+E(\nabla^2 w)-\frac{1}{Ar\cdot Fr}$$

$$\nabla^2\equiv\frac{1}{r}\frac{\partial}{\partial r}\left(r\frac{\partial}{\partial r}\right)+\frac{\partial^2}{\partial z^2}$$

In the above, nondimensionalization has been made by using R, RΩ, Ω^{-1} as reference values for length, velocity, and time, respectively. In (1), the Froude number $Fr\equiv\Omega^2R^2/(gH)$, the Ekman number $E\equiv\nu/R\Omega^2$, and the Reynolds number is defined as $Re\equiv E^{-1}$.

The initial conditions, at t=0, are

$$u=v=w=0 \qquad 0\le r\le 1, 0\le z\le L/R \tag{2}$$

After the cylinder is set in rotation, the non-dimensional height of the deforming free surface is denoted by h(r,t). Disregarding the surface tension effect, the boundary conditions for t>0 may be stated as

$$u=v=0,\quad \frac{\partial w}{\partial r}=0 \qquad \text{at } r=r_i,\ 0\le z\le h(r_i,t), \tag{3a}$$

$$u=w=0,\ v=1 \qquad \text{at } r=1,\ 0\le z\le h(1,t), \tag{3b}$$

$$u=w=0,\ v=r \qquad \text{at } \begin{pmatrix} r\ge r_{TI}, z=H/R, \\ r> r_{BI}, z=0, \end{pmatrix} \tag{3c}$$

$$p=0,\quad \frac{\partial h}{\partial t}+u\frac{\partial h}{\partial r}-w=0 \text{ on } z=h(r,t). \tag{3d}$$

The symmetry condition at the central axis is enforced at $r=r_i$, a small but non-zero radius, as in (3a). This is a customary numerical practice to avoid the singularity at the axis [e.g., Warn-Varnas et al., 1978]. The nonslip conditions at the solid walls are applied only at the wetted zones. Obviously, if the free surface intersects only the cylindrical sidewall (r=1), (3c) is applied at z=0, z=H/R, and $0<r\le 1$. However, if the free surface intersects one or both of the endwall disks [$r_{BI}(t)$ and $r_{TI}(t)$ are the intersecting radius on the bottom and top endwall disk, respectively], (3c) is applicable only to the regions between these intersecting radii and the side wall [refer to Fig. 2].[See H&G].

The system of equations is subject to finite-difference numerical integration. The grid was stretched to cluster more mesh points near the solid walls and the deforming free surface. The advective terms were represented by using the power law advocated by Patankar(1981). The computation of free surface profile was performed by employing the VOF technique of Hirt et al.(1981). Time-marching was done using the explicit scheme, and very small time steps were employed in order to be in line with the VOF

technique. The projection method of Peyret & Tayer(1983) was utilized to solve the Poisson equation for pressure; this has the advantage of handling complex boundary conditions. For typical calculations, the grid network was (50x100) in the (r-z) meridional plane. Several grid-and time step- convergence tests were performed, and the outcome of these tests was mutually consistent. The output of the present numerical procedure was checked against the existing experimental spin-up data for a two-layer liquid [Lim et al., 1993] as well as the laboratory measurements of free surface deformation [Choi et al., 1989,1991]. These model validation efforts turned out to be affirmative, and these established the reliability and accuracy of the present numerical solution methodologies. Calculations were run on the CRAY-2S Supercomputer, and it took approximately one hour of CPU time for each run.

3. Results and discussion

Illustration and discussion of the numerical solutions will be centered on four prototypical runs, which respectively fall into the four characteristic configurations displayed in Fig.2.

Run 1 : $E=0.9\times10^{-4}$, Fr=2.50, L/H=0.5;

Run 2a: $E=0.9\times10^{-4}$, Fr=2.50, L/H=0.75;

Run 2b: $E=0.9\times10^{-4}$, Fr=2.50, L/H=0.25;

Run 3 : $E=0.9\times10^{-4}$, Fr=3.69, L/H=0.5.

Parallel calculations were also made to acquire the analytical model predictions of H&G. It should be recalled that the analytical predictions are obtainable mainly for the dominant azimuthal velocity v(r,t) in the interior core and for the free surface contour h(r,t). The model constants used were K2=1.0, g2=1.01, and strict adherence to the computing calculation procedures stipulated by H&G was made.

The time-evolution of the free surface shape shown in Fig. 3(a) for Run 1 is representative of the case when the final-state free surface intersects only the cylindrical

side wall [sketched in Fig. 2]. As displayed in Fig. 3(a), good agreement is seen between the present numerical results and the model predictions of H&G. The radial profiles of the azimuthal velocity v, along $z'[\equiv z(R/H)]=0.25$, are exhibited in Fig.3(b). Overall consistency between the two sets of data is apparent. A further inspection reveals that the H&G model tends to underpredict slightly the development of the v-field in comparison to the numerical results. The underprediction of v by the Wedemeyer model was discussed previously by Watkins & Hussey (1977) and Hyun et al.(1983) for a completely-filled cylinder, and the present results are in accord with this reasoning.

Fig.4 demonstrates sequential plots showing meridional flows as well as the free surface displacement. The stream function y is defined such that $u=\frac{1}{r}\frac{\partial \Psi}{\partial z}$, $w=-\frac{1}{r}\frac{\partial \Psi}{\partial r}$. The meridional flow induced by the bottom Ekman layer is intense at small times. As time elapses, the fluid in the interior bulk is spun up, and the meridional flow, in general, weakens accordingly. The impact of the free surface deformation on meridional circulation is noticeable mostly in localized areas close to the free surface and in the zones where the free surface curvature is pronounced. The radially inward motion is seen to be aided by the deformation of free surface. These influences, although small in overall magnitude, are discernible in Figs.(4a) and (4b) in the areas adjacent to the free surface with large curvature.

Fig.5 illustrates sequential displays of azimuthal velocity. At small and moderate times, Figs.5(a) and 5(b) clearly demonstrate the existence of a non-rotating zone and a rotating zone, which are separated by a propagating front. The axial uniformity of v in the interior is in evidence. It is noted that, in small localized areas adjacent to strongly curved free surface, the axial uniformity of v is slightly perturbed. In the bulk of the interior, however, the v-field is substantially uniform in the axial direction, and the present numerical results are compatible with the observations of Choi at al.(1989,1991)

In an effort to scrutinize further details, illustrative plots of radial profiles of u and w, at z'=0.25 for Run 1 are presented in Figs. 6&7. The magnitudes of u and w scale with $O(E^{1/2}v)$, as shown in these figures. The location of $|u|_{max}$, which is directed

radially-inward, is seen at large radii at small times, but this location moves to smaller radii as spin-up progresses. For Run 1, at large times, say $t \geq 130.0$, the free surface deformation is such that, at smaller radii, the liquid height is lower than the horizontal cut z'=0.25 exemplified in Fig 5,6 & 7. As asserted in the analytical model development, vertical flows are predominantly downward at small and moderate radii, which are driven by the Ekman pumping. The vertically-upward return circuit is noticeable at large radii close to the sidewall. A close inspection of meridional flow structure is made in Figs. 8-10. Note that, in Fig. 8, the free surface has deformed considerably, and, at this time instant, the free surface intersects the horizontal cut z'=0.5 at $r \leq 0.8$. No liquid exists for r0.8 at this vertical level (z'=0.5). As demonstrated in Fig. 8, the radial velocities are mostly radially-inward (u negative) in much of the liquid interior. However, at vertical level z'=0.5 due to the pronounced influence of deforming free surface, liquid motions are intense and these are directed toward the sidewall. Only in a region very close to the sidewall, weak radially-inward flows are observed. As depicted in Fig. 9, vertical velocity w in the bulk of flow field are downward at moderate and small radii. However, at high elevations (see, e.g., the curve for z'=0.5), because of the dominant effect of deforming free surface, the liquid between the free surface and the sidewall is squeezed upward, which generates positive values of w. Fig.10(a) illustrates evolving vertical profiles of u along the cut r=0.5. Clearly, radial flows, in general, are very weak in the interior. The initial development and subsequent decay of the Ekman layer are discernible in Fig.10(a). The vertical profiles of w at various radial cuts are displayed in Fig.10(b). For comparison purposes, the interior solutions based on the prediction of H&G are shown by broken lines. As is well-known, the Wedemeyer and H&G model predicts that w is linear in z in the interior. Needless-to-say, the vertically-linear profiles of w are applicable only to the interior region, not in the Ekman layers.

The numerical results for Run 2a and Run 2b are similarly arranged in Figs.11-14. Comparisons of the free surface deformation as well as the azimuthal velocity between the numerical results and the predictions of H&G model are satisfactory, as evidenced in Figs. 11 and 13. Furthermore, the meridional flows, as portrayed by the numerical

results in Fig. 12&14, are consistent with the basic conceptual picture envisioned in the H&G model. The plots of meridional stream functions are illustrative of the role of time-dependent Ekman layer and of the meridional flows induced by the deformation of free surface. In a similar fashion, the numerical results for Run 3 are displayed in Figs. 15 and 16. These plots are demonstrative of the good agreement between the present numerical results and the predictions of the H&G model.

4. Conclusion

High-resolution numerical solutions to the governing Navier-Stokes equations have been secured. Comprehensive results for four prototypical flow configurations are presented for detailed examination.

The shape of the evolving free surface has been captured numerically. For all the four exemplary runs, the numerical results are in close agreement with the predictions of the H&G model. The transient azimuthal velocity field is also described, and the two sets of results are mutually consistent.

Taking advantage of the wealth of numerical data, scrutiny is made of the detailed profiles of meridional velocity components. The initial development and subsequent weakening of the Ekman layer are captured well by the numerical solutions. The transient meridional flow field, as constructed by the numerical solutions, is consistent with the fundamental conceptual picture incorporated in the H&G model.

The present numerical study is in support of the basic contentions as well as the prediction capabilities of the H&G model.

References

Choi, S., Kim, J. W., Hyun, J. M., "Experimental Investigation of the Flow with a Free Surface in an Impulsively Rotating Cylinder," ASME Journal of Fluids Engineering, Vol. 111, 1989, pp.439-442.

Choi, S., Kim, J. W., Hyun, J. M., "Transient Free Surface Shape in an Abruptly Rotating, Partially Filled Cylinder," ASME Journal of Fluids Engineering, Vol. 113, 1991, pp. 245-249.

Gerber, N.,1975, "Properties of Rigidly Rotating Liquids in Closed Partially Filled Cylinder", Journal of Applied Mechanics, Trans. of the ASME, pp. 734-735.

Goller, H., and Ranov, T., 1968, "Unsteady Rotating Flow in a Cylinder with a Free Surface," ASME Journal of Basic Engineering, Vol. 90, No. 4, pp. 445-454.

Greenspan, H. P., and Howard, L. N., 1963, " On a Time Dependent Motion of a Rotating Fluid," Journal of Fluid Mechanics, Vol. 17, Part 3, pp. 385-404.

Hirt, C. W., and Nichols, B. D., 1981, "Volume of Fluid (VOF) Method for the Dynamics of Free Boundaries" Journal of Computational Physics, Vol. 39, pp. 201-225.

Homicz, H., and Gerber, N., 1987, "Numerical Model for Fluid Spin-Up from Rest in a Partially Filled Cylinder," ASME Journal of Fluid Engineering, Vol. 109, pp. 195-197.

Hyun, J. M., Leslie, F., Fowlis, W. W., and Warn-Varnas, A., 1983, "Numerical Solutions for Spin-Up from Rest in a Cylinder," Journal of Fluid Mechanics, Vol. 127, pp. 263-281.

Kitchens, C. W. Jr., 1980, "Navier-Stokes Solutions for Spin-Up in a Filled Cylinder," AIAA Journal, Vol. 18, No. 8, pp. 929-934.

Lim, T. G., Choi S. M., and Hyun J. M., 1993, "Transient Interface Shape of a Two-Layer Liquid in an Abruptly Rotating Cylinder," ASME Journal of Fluids Engineering, Vol. 115, pp. 324-329.

Patankar, S.V., 1980, "Numerical Heat Transfer and Fluid Flow," McGraw-Hill, New York.

Peyret, R. & Tayler, T. D., 1983, "Computational methods for fluid flow," Springer-Verlag, New York.

Warn-Varnas, A., Fowlis, W. W., Piacsek, S., and Lee, S. M., 1978, "Numerical Solutions and Laser-Doppler Measurements of Spin-Up," Journal of Fluid Mechanics, Vol. 85, pp. 609-639.

Watkins, W. B. & Hussey, R. G., 1977, " Spin-up from Rest in a Cylinder," Physics of Fluids, Vol. 20, pp. 1596-1604.

Wedemeyer, E. H., 1964, "The Unsteady Flow within a Spinning Cylinder," Journal of Fluid Mechanics, Vol. 20, Part 3, pp. 383-399.

Weidman, P. D., 1976, "On the Spin-Up and Spin-Down of a Rotating Fluid. Part 1: Extending the Wedemeyer Model. Part II: Measurements and Stability," Journal of Fluid Mechanics, Vol. 77, Part 4, pp. 685-735.

Figure Captions

Fig.1 Schema of flow configuration.

Fig.2 Four representative final-state configurations, as described by Gerber(1975).

Fig.3 (a) Time-dependent free-surface contours for Run 1. ____, the present results; ------, the prediction of H&G. The time interval for the curves is $\Delta t=20.0$. The ordinate $z' \equiv z(R/H)$.

(b) Time-dependent azimuthal velocity v.

Fig.4 Sequential plots of meridional stream function y for Run 1.

(a) $t=20.0$, $\Psi_{max}=5.93\times10^{-3}$;

(b) $t=60.0$, $\Psi_{max}=2.33\times10^{-3}$;

(c) $t=140.0$, $\Psi_{max}=8.64\times10^{-4}$.

Fig.5 Plots of the v-field for Run 1. (a) t=20.0, (b) t=60.0, (c) t=140.0.

Fig.6 Radial profiles of u along z'=0.25 for Run 1.

Fig.7 Radial profiles of w along z'=0.25 for Run 1.

Fig.8 Radial profiles of u for Run 1. Time t=40.0.

Fig.9 Radial profiles of w for Run 1. Time t=40.0.

Fig.10 (a) Axial profiles of u for Run 1 along r=0.5.

(b) Axial profiles of w for Run 1 at t=20.0. _____, the present results; ------,

interior solutions of the H&G model.

Fig.11 (a) Free-surface contours for Run 2a.

(b) Azimuthal velocity v for Run 2a.

Fig.12 Meridional stream function y for Run 2a

(a) t=20.0, $\Psi_{max}=5.76x10^{-3}$;

(b) t=60.0, $\Psi_{max}=2.63x10^{-3}$;

(c) t=140.0, $\Psi_{max}=8.05x10^{-4}$.

Fig.13 (a) Free-surface contours for Run 2b.

(b) Azimuthal velocity v for Run 2b.

Fig.14 Meridional stream function y for Run 2b

(a) t=20.0, $\Psi_{max}=4.75x10^{-3}$;

(b) t=60.0, $\Psi_{max}=1.75x10^{-3}$;

(c) t=140.0, $\Psi_{max}=8.18x10^{-4}$.

Fig.15 (a) Free-surface contours for Run 3.

(b) Azimuthal velocity v for Run 3.

Fig.16 Meridional stream function Ψ for Run 3.

(a) t=20.0, $\Psi_{max}=4.50x10^{-3}$;

(b) t=60.0, $\Psi_{max}=1.65x10^{-3}$;

(c) t=140.0, $\Psi_{max}=7.85x10^{-4}$.

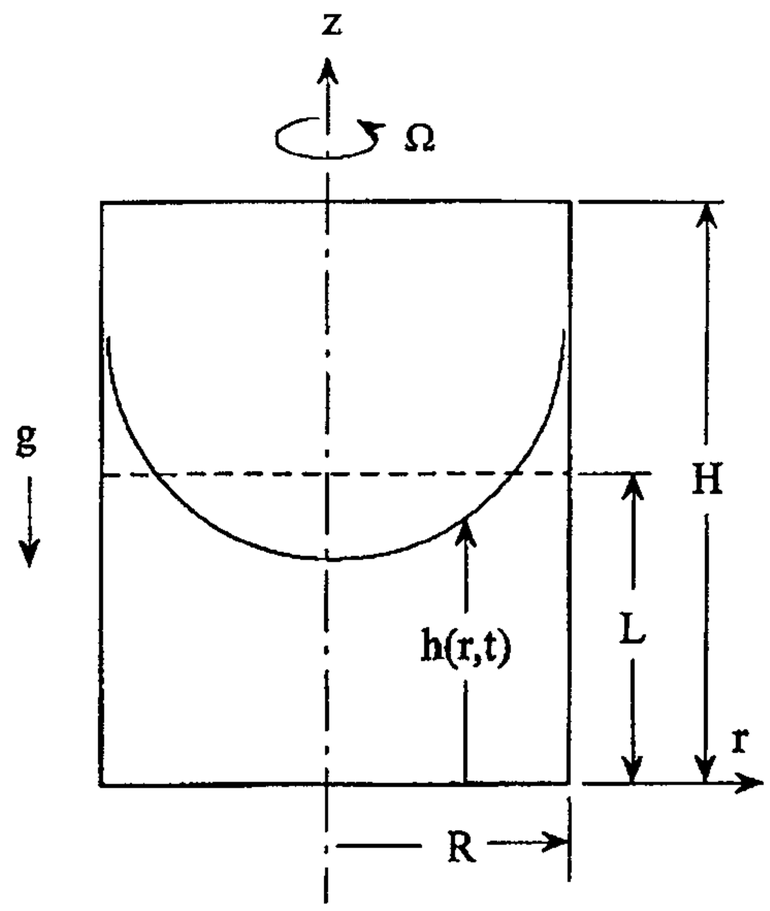

Fig.1

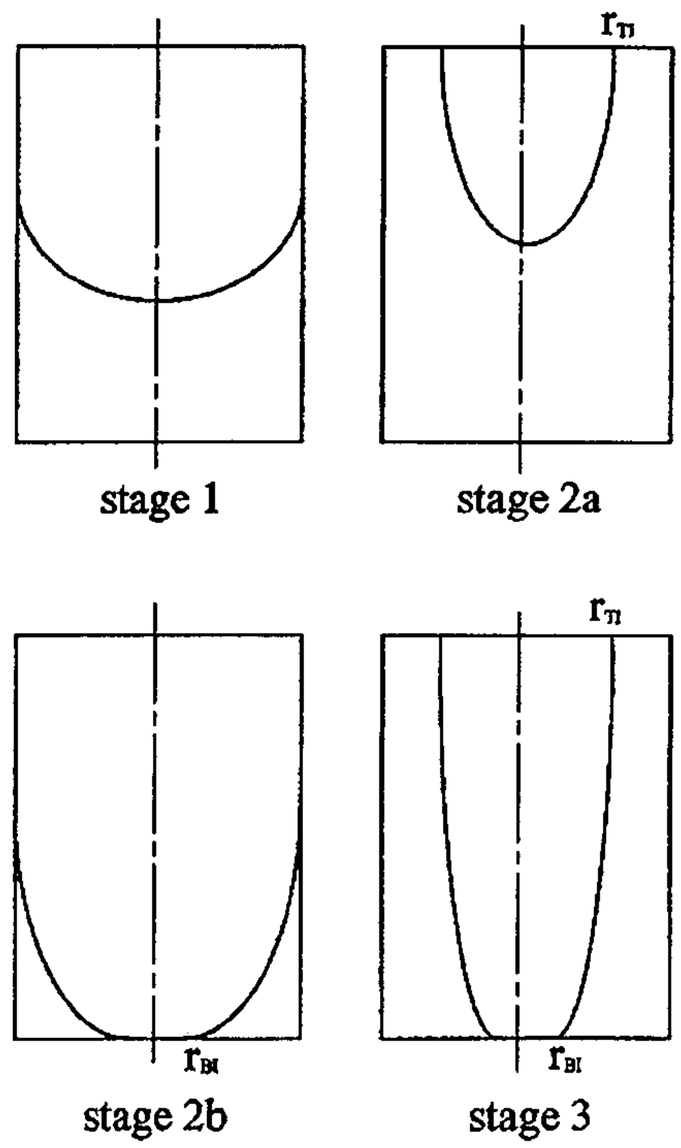

Fig.2

여 백

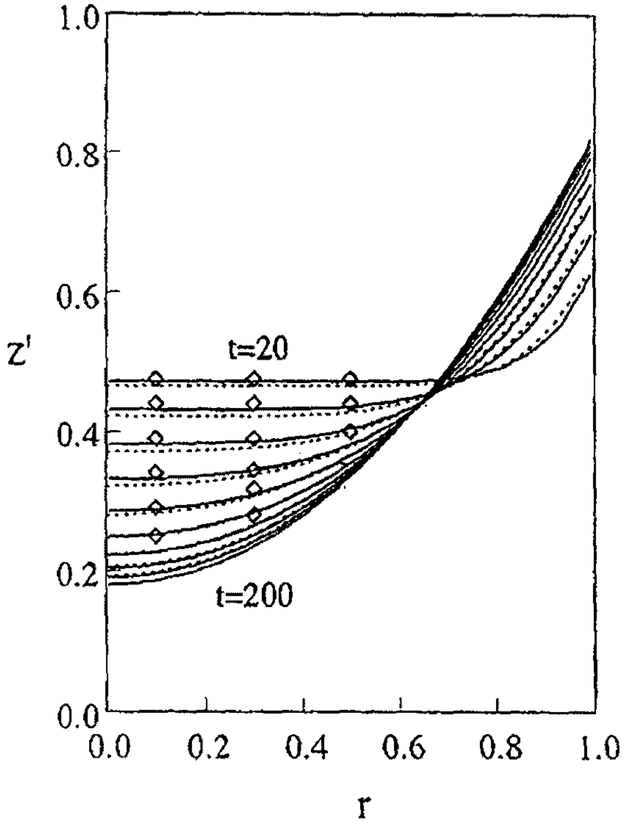
1.0
0.8
0.6
0.4
0.2
0.0
Z'
t=20
t=200
0.0
0.2
0.4
0.6
0.8
1.0
r

Fig.3(a)

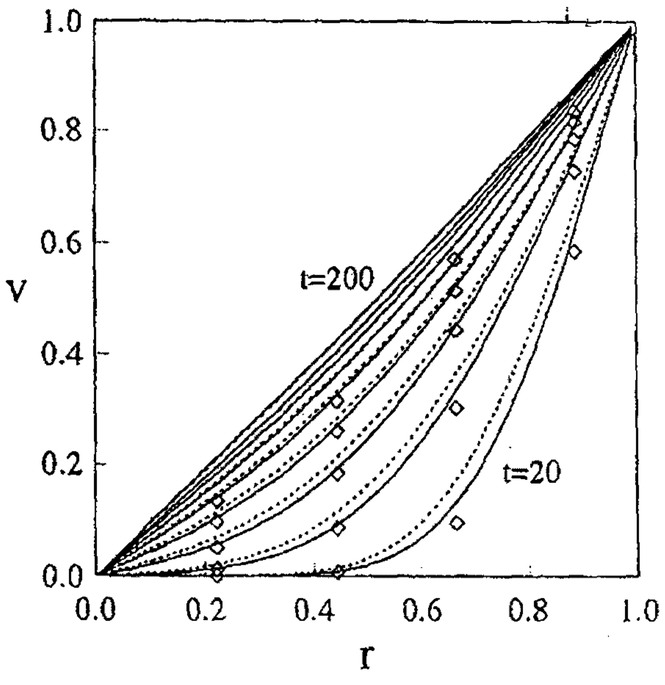
1.0
0.8
0.6
0.4
0.2
0.0
V
t=200
t=20
0.0
0.2
0.4
0.6
0.8
1.0
r

Fig.3(b)

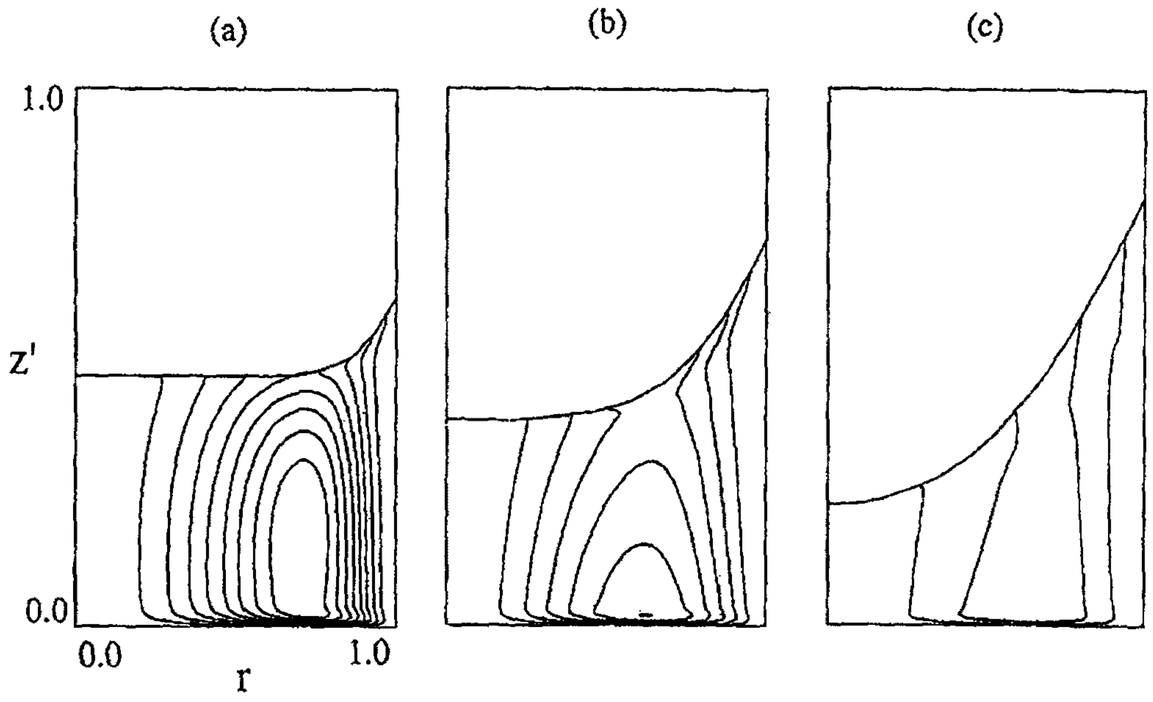

Fig.4

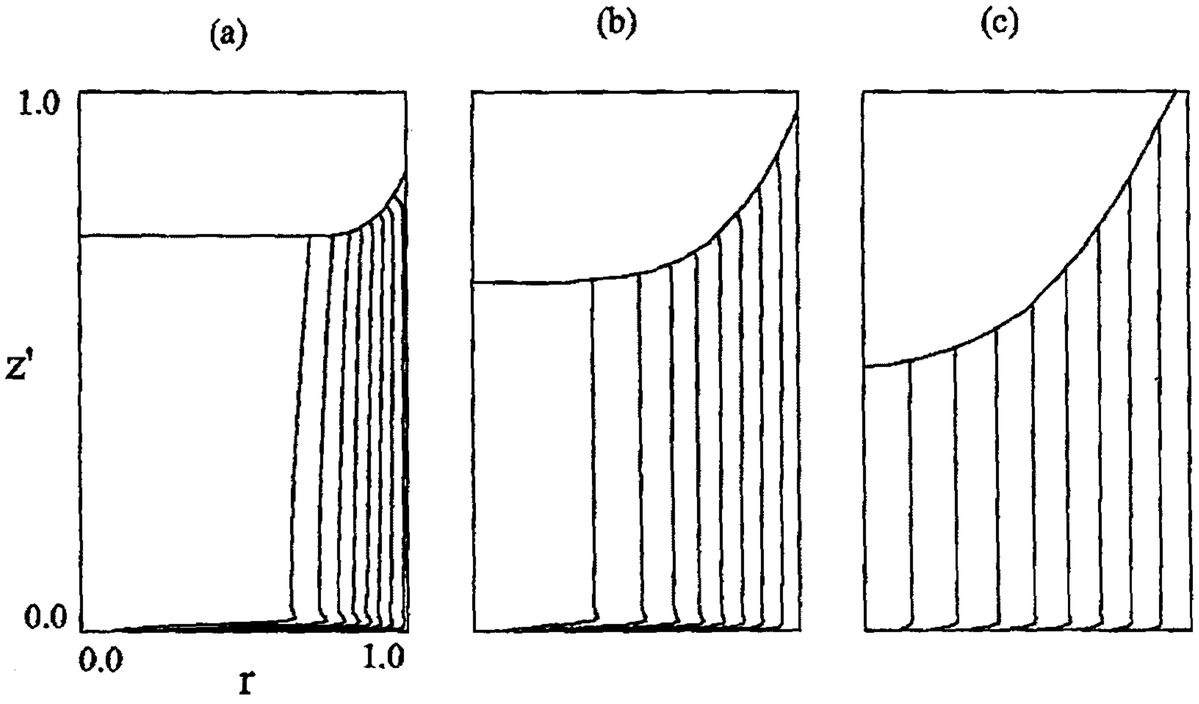

Fig.5

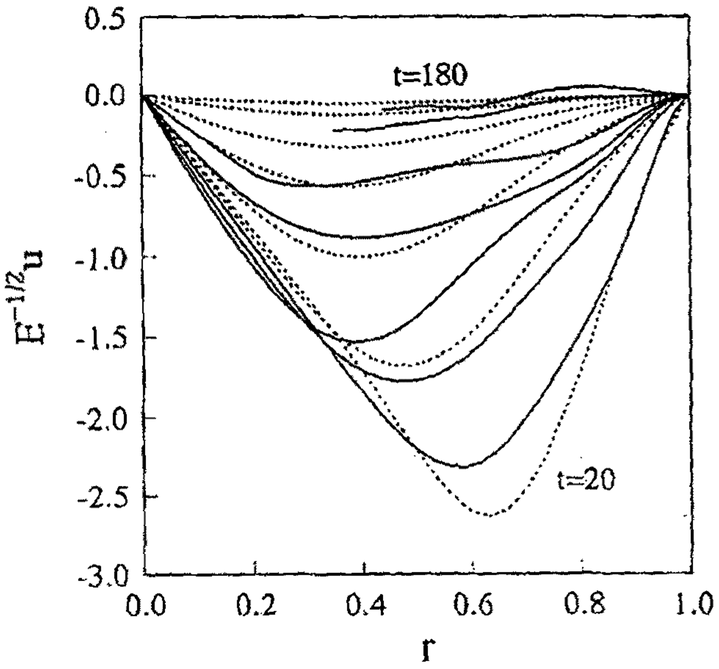
0.5
0.0
-0.5
-1.0
-1.5
-2.0
-2.5
-3.0
$E^{-1/2}u$
t=180
t=20
0.0
0.2
0.4
0.6
0.8
1.0
r

Fig.6

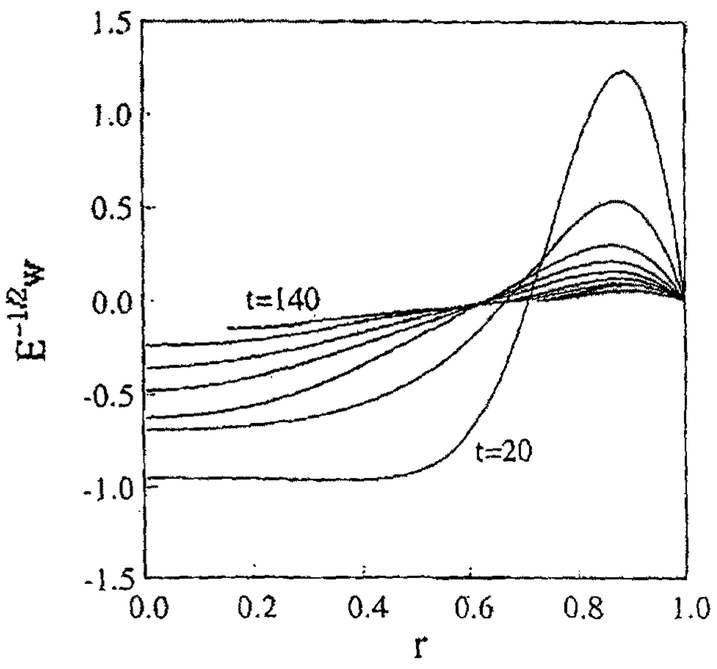
1.5
1.0
0.5
0.0
-0.5
-1.0
-1.5
$E^{-1/2}w$
t=140
t=20
0.0
0.2
0.4
0.6
0.8
1.0
r

Fig.7

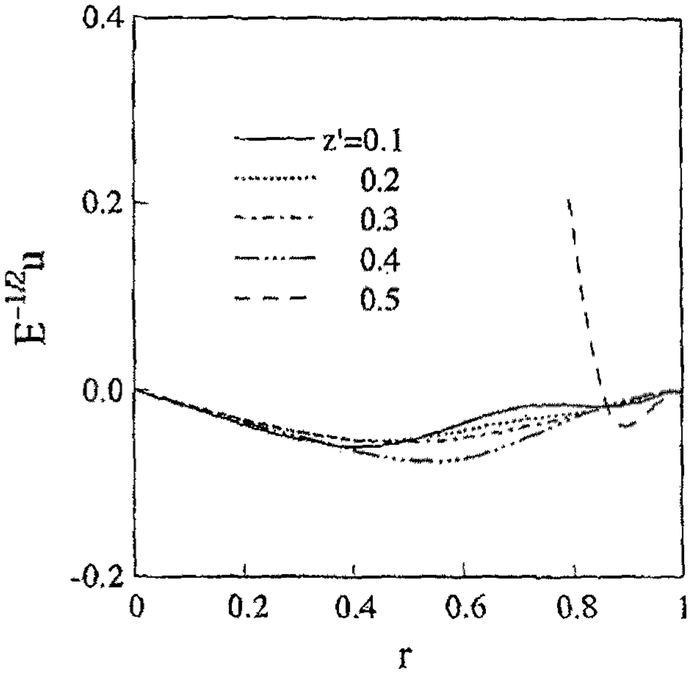
0.4
0.2
0.0
-0.2
0
0.2
0.4
0.6
0.8
1
r
$E^{-1/2}u$
z'=0.1
0.2
0.3
0.4
0.5

Fig.8

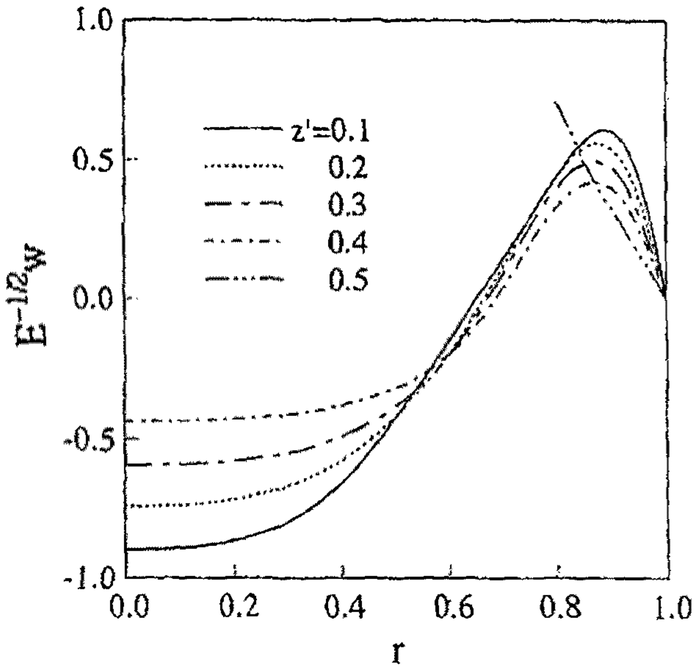
1.0
0.5
0.0
-0.5
-1.0
0.0
0.2
0.4
0.6
0.8
1.0
r
$E^{-1/2}w$
z'=0.1
0.2
0.3
0.4
0.5

Fig.9

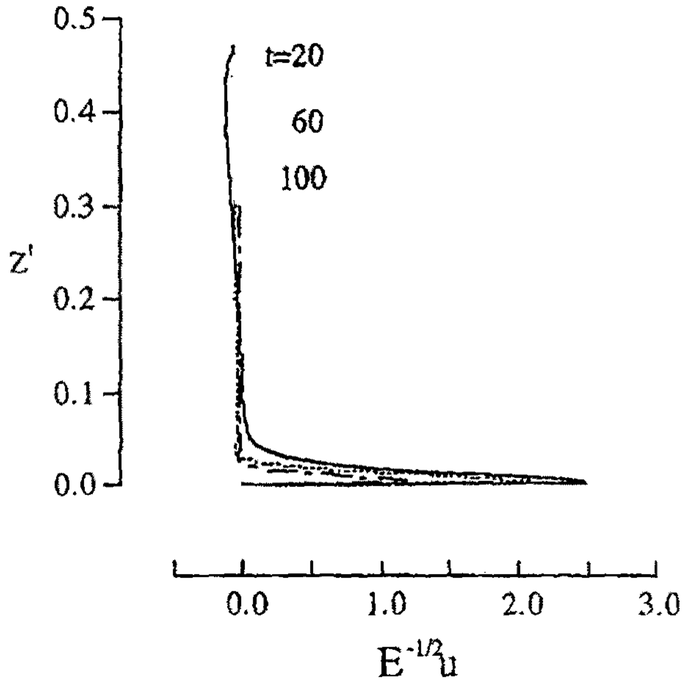

Fig.10(a)

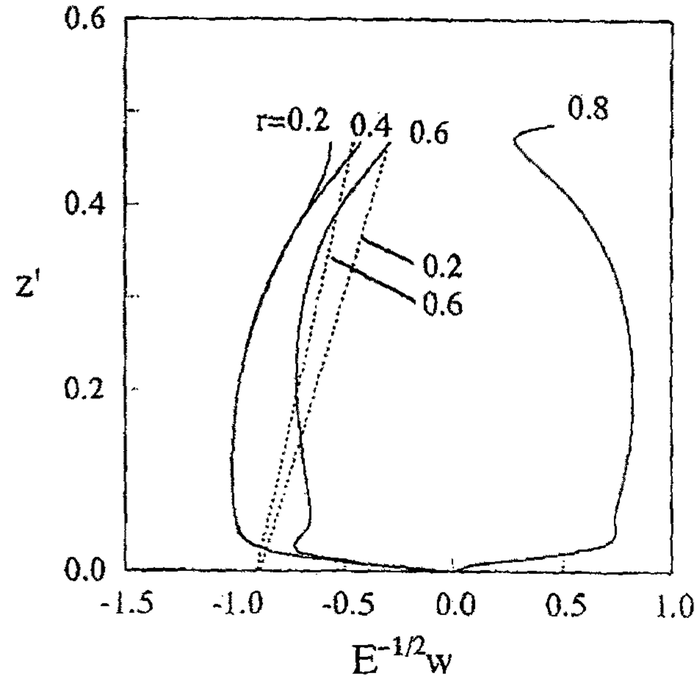

Fig.10(b)

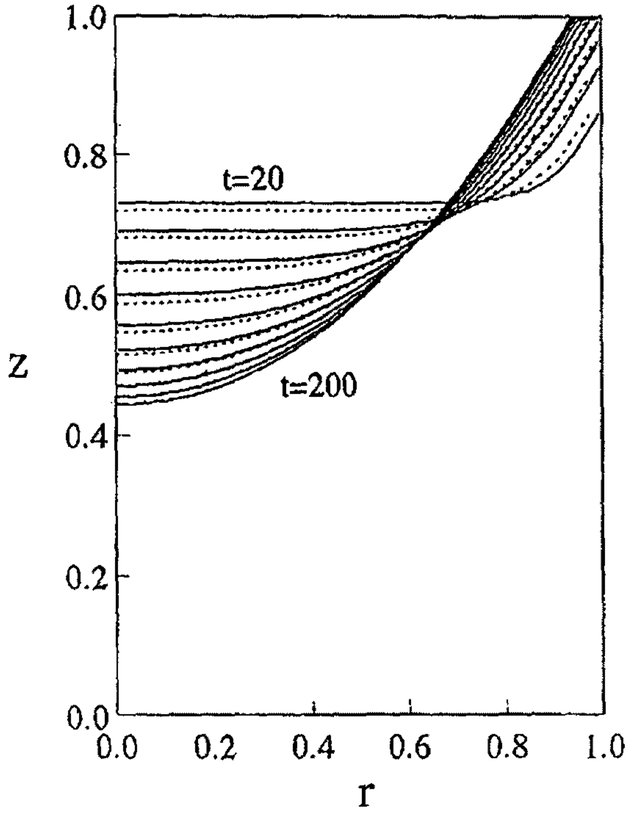

Fig.11(a)

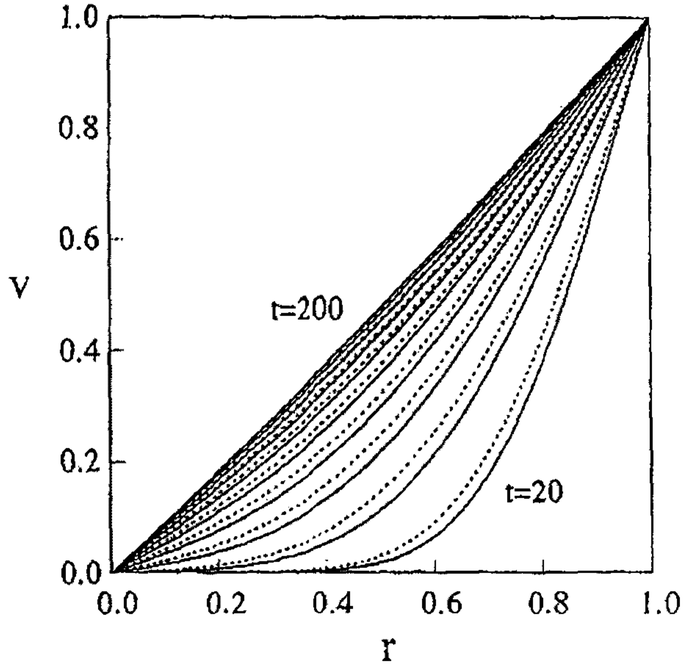

Fig.11(b)

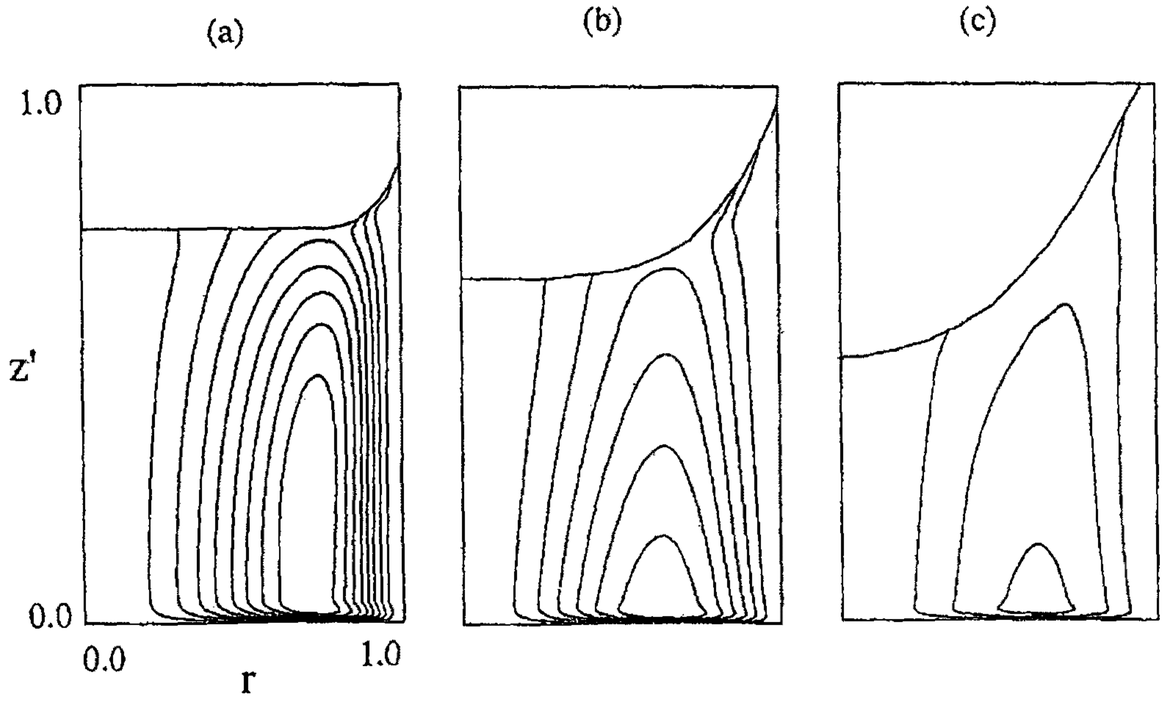

Fig.12

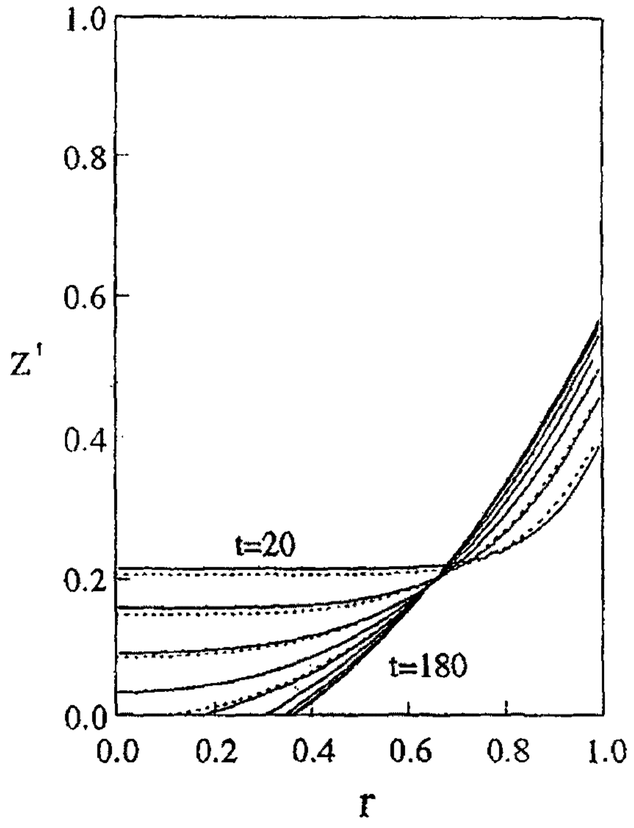

Fig.13(a)

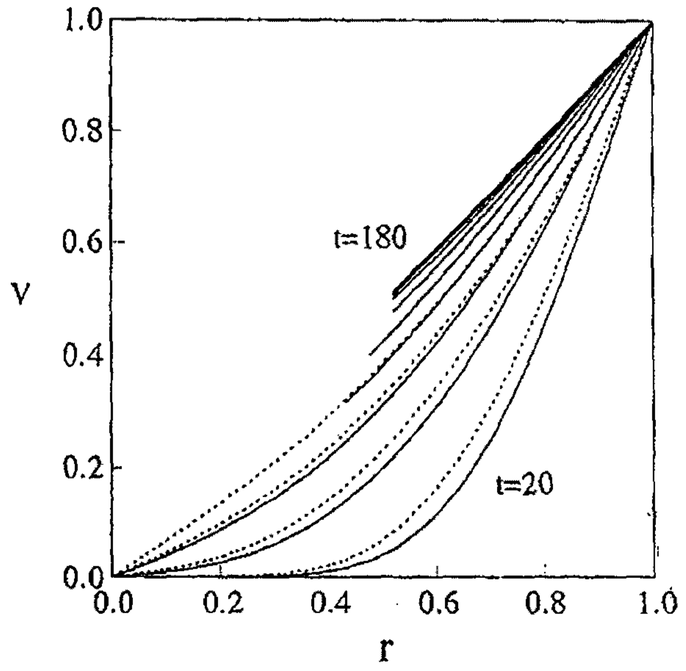

Fig.13(b)

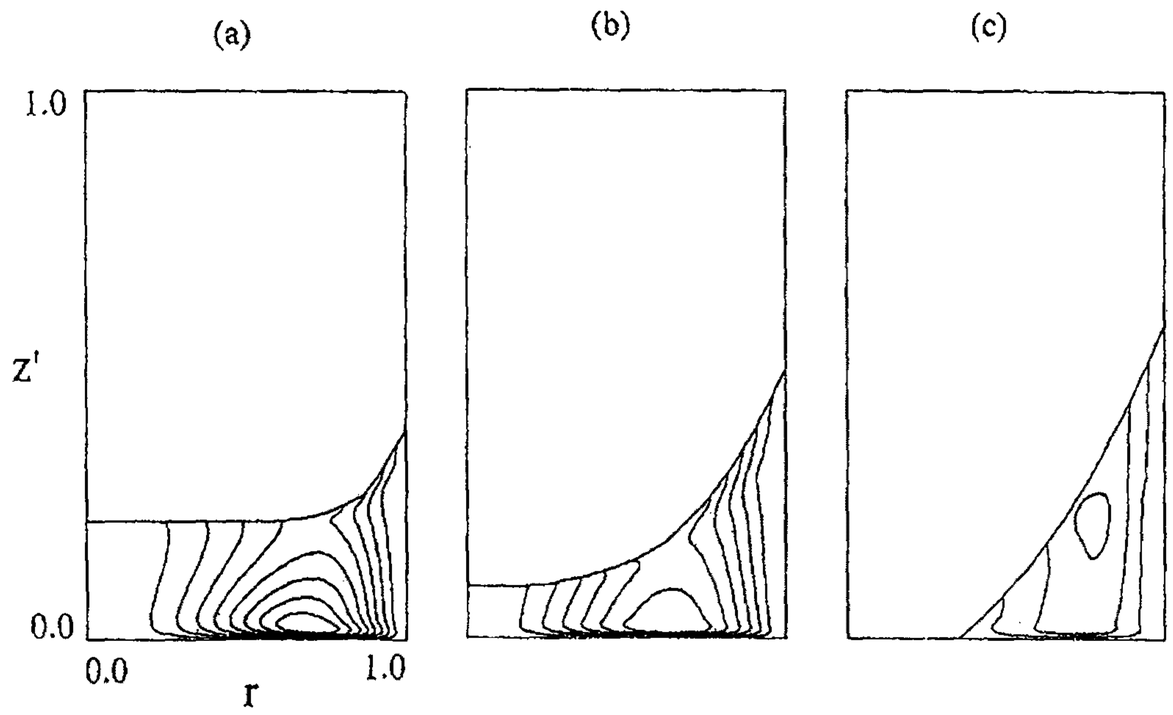

Fig.14

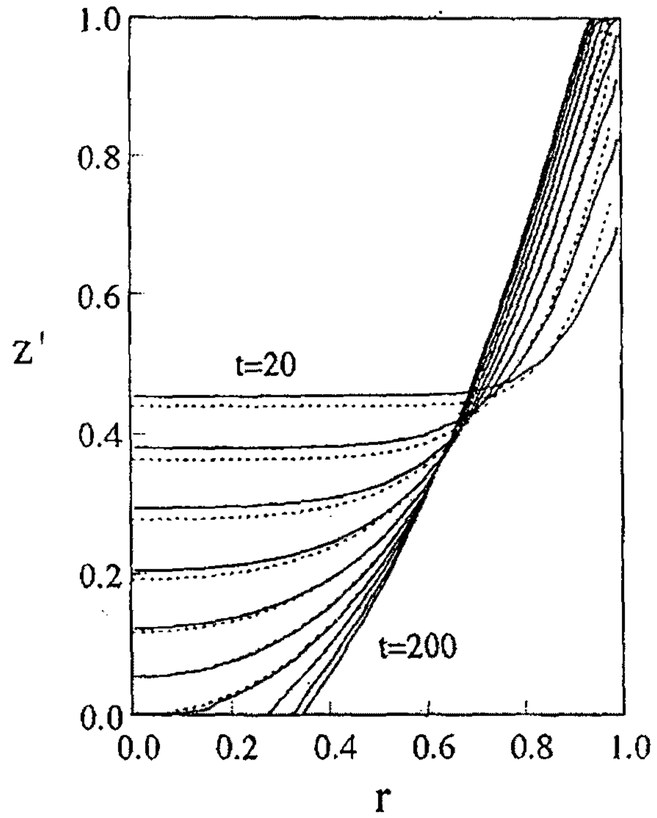

Fig.15(a)

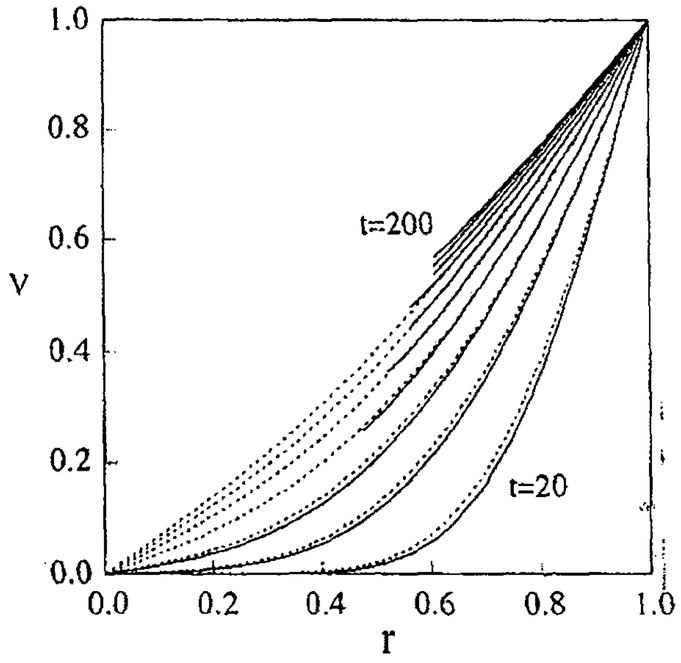

Fig.15(b)

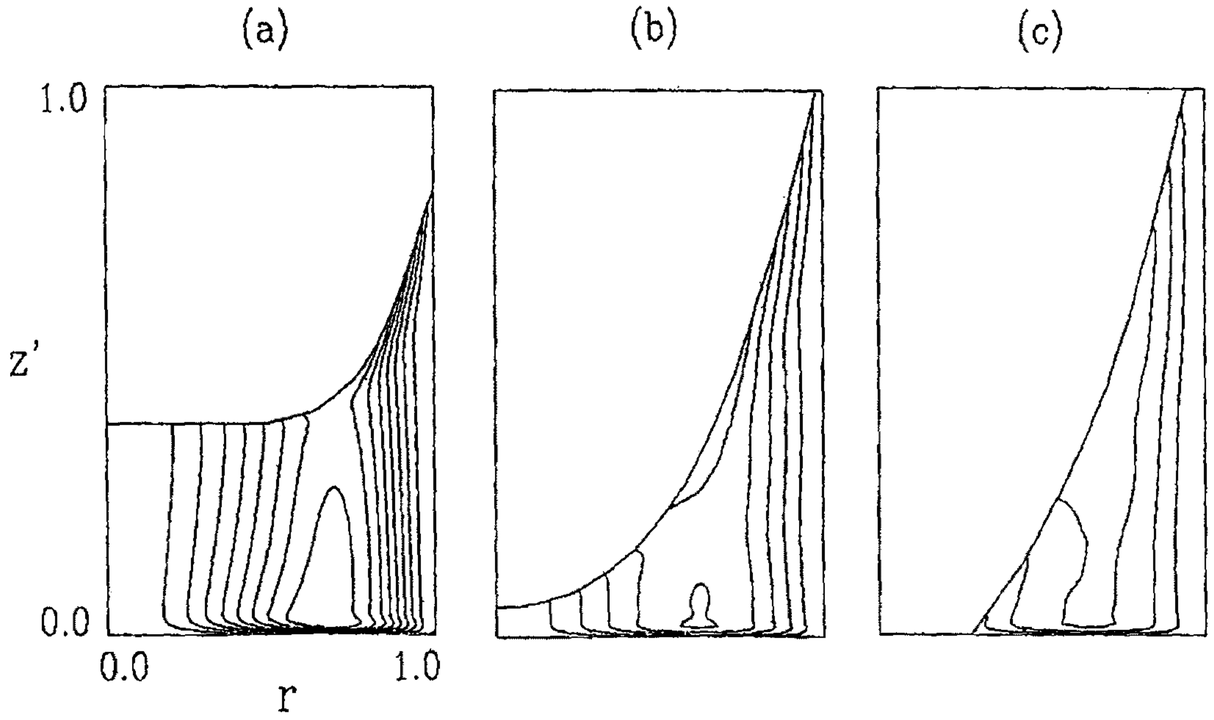

Fig.16

제 3 장

Convective heat transfer in a cylinder with a rotating lid under stable stratification

(회전하는 덮개를 가지는 안정성층화된 실린더 내의 대류열전달)

요 약 문

Boussinesq유체가 가득찬 회전하는 원통용기내에서의 온도장과 유동장이 해석되었다. 원통용기의 윗판은 일정속도로 회전하며, 나머지 고체면은 정지되어 있다. 윗판의 온도 T_T가 아랫판의 온도 T_L보다 큰 경우 즉, $\Delta T(\equiv T_T - T_L) > 0$인 경우를 해석하였다. 지배방정식인 축대칭 Navier-Stokes식의 수치해를 얻었다. Reynolds수 Re가 작을 때, 자오면 순환은 용기의 윗부분에 존재하게 되며, 열전달은 전도에 의해서 지배된다. Re가 크고, Richardson수 Ri가 매우 작을 때, 주 자오면 순환은 원통용기의 내부에서 발생하며, 와류붕괴의 특징인 재순환 방울은 중심축상에 생성된다. 대류활동은 활발하며, 등온선은 내부영역대부분에서 수직으로 생성된다. 그러나, $Ri \gtrsim O(1)$일 때, 재순환 방울은 사라지며, 안정한 성층화에 의해서 전도 열전달이 지배적이 된다. 윗판과 아랫판에서의 지역적 Nusselt수가 도시되었다. Re가 매우 크고 Ri가 작을 때, 중심부근에서 윗판에서의 Nusselt수는 크며, 벽면쪽으로 접근할수록 급격히 감소한다. 이러한 유동 및 열전달 특성은 부력의 동역학적 역할과 일치한다.

Abstract

An analysis is made for flow and temperature fields of a Boussine which completely fills a vertically-mounted, closed, cylindrical vessel. The lid rotates steadily, and the rest of the solid boundaries are stationary. T of the top lid T_T is higher than that of the bottom endwall T_L, i.e., $\Delta T(\equiv T_T - T_L)$ > 0. Numerical solutions are obtained for the governing axisymmetric Navi equations. When the rotational Reynolds number Re is small, the meridional c is located in the upper portion of the cylinder and heat transfer is conducti is very large and the Richardson number Ri very small, the main meridional ci occupies the bulk of the cylinder interior, and a recirculation bubble characteristic of vortex breakdown, can form on the axis. Convective act vigorous, and the isotherms are aligned vertically in much of the interior cor when $Ri \gtrsim O(1)$, the recirculation bubbles disappear, and, due to the stratification, conductive heat transport prevails. Local Nusselt numbers on bottom endwalls are plotted. When Re is very large and Ri small, the Nusselt at the top disk N_T is large at small and moderate radii, and N_T decays rapi the sidewall. These features of flow and heat transfer are consistent with th role of buoyancy.

1. Introduction

We shall consider a finite closed cylindrical container (of radius R H), which is filled completely with a homogeneous incompressible fluid of viscosity ν. Flow is generated by the top endwall disk of the cylinder, whi steadily with constant rotation rate Ω, and the other solid boundaries ar Numerical (e. g., Bertela and Gori, 1982) as well as experimental (Escudi investigations have been performed to examine the properties of this interna overall flow behavior is characterized by two principal nondimensional parame the Reynolds number $Re \equiv R^2\Omega/\nu$, and the cylinder aspect ratio $Ar \equiv H/R$ crucial element of the flow is the presence of meridional motion u, w, in a the dominant azimuthal velocity v. The meridional flow, although small in mag essential to provide necessary interplays between the inertia, viscous, gradient effects on the flow field.

Contrary to the abundance of studies on the foregoing flow, relatively has been reported on the convective transport properties associated with ro boundaries (Sparrow & Chaboki, 1982; Kim & Hyun, 1995; Kim, Hyun & Ozoe, 1996) Lugt and Abboud(1987), in a numerical endeavor, illustrated the flow and te fields in a vertically-mounted cylinder with its top lid rotating steadily. the temperature of the rotating top lid T_T was maintained to be lower than t stationary bottom endwall T_L ; i.e., $\Delta T \equiv T_T - T_L < 0$. The vertical c sidewall was thermally insulated. In this problem formulation, the prevail temperature difference gives rise to a gravitationally unstable configurati solutions were secured by Lugt and Abboud for several illustrative parameter s displayed the qualitative changes in global flow patterns as the buoyancy e included in the analysis. In particular, the occurrence of bubble(s) on the under certain external conditions, commonly interpreted as vortex breakdown (1984; Lugt & Haussling, 1982), was carefully examined. It was asserted that heat transfer from the rotating disk depends on complex dynamics, which invo

Rayleigh number Ra, the Prandtl number $\mathrm{Pr}(\equiv \nu/\kappa)$, in addition to the afore-described Re and Ar.

In the present note, descriptions are made for the flow and heat characteristics in a closed cylinder with its top endwall disk steadily rotat distinction of the present configuration is that the temperature of the top than that of the lower disk, i. e., $\Delta T \equiv T_T - T_L < 0$, thus creating a gra stable stratification. In the absence of the rotation of the top lid, the en rest with a vertically-linear temperature profile. Because of the rotation o three-component velocity fields are generated, which gives rise to augmentat transfer. The present paper discusses the intensification of the internal resulting increase in convectively-controlled heat transport in the fluid. Of behavior of the vortex breakdown bubble, and the attendant heat transfer influence of stable stratification will be scrutinized.

It should be mentioned that the present flow configuration represent setup in geophysical fluid dynamics research. The flow of a stably strat generated by the rotating upper surface, simulates the global motions of atmo oceanic fluids. The relevance of the framework of the present flow arrangeme modeling of large-scale motions of geophysical fluid systems has been empha classical treatises (e. g., Barcilon & Pedlosky, 1967a, b; Linden, 1977; Soward, 1978).

2. The model

Consider a Boussinesq-fluid, for which the relation $\rho = \rho_L(1 - \beta(T - T_L))$ is applicable, where ρ and T refer to density and temperature; respectivel the coefficient of volumetric expansion. The subscript L indicates the refere the bottom endwall. The relevant physical properties are dynamic $\mu(\equiv \rho_L \nu)$; specific heat C_p; thermal conductivity k. These are taken to be

As stated earlier, the fluid is in full contact with the rotating top lid, and no free surface exists.

The governing axisymmetric Navier-Stokes equations in nondimensiona ,written in cylindrical coordinates $(r,\phi,z)$with velocity components (u,v,w) documented (e. g., Lugt & Abboud, 1987). Nondimensionalization has been imple by using $R, R\Omega$, $\rho_L(R\Omega)^2$ and , for scales of length, velocity and respectively. The nondimensional temperature is defined as $\theta \equiv (T - T_L)/(T_T - T_L)$ g denotes the gravity, and the Richardson number is given $Ri = g\beta(T_T - T_L)/R\Omega^2$.

The numerical methodology adopted was based on the well-docume SIMPLER algorithm (Patankar, 1980), together with the QUICK scheme (Hayase e 1994). Staggered and stretched grids were deployed, and extensive grid-conver were conducted. The computations were straightforward, and sample calculati repeated, and the results were consistent with the previously-published numer several rotating and stratified fluid-flow problems (e. g., Lugt & Abboud, 198

3. Results and discussion

The explicit effects of Re and Ri on the meridional flow patte apparent. Fig. 1 shows, in the axial plane, the plots of meridional stream which is defined so that $u = 1/r\partial\Psi/\partial z$, and $w = -1/r\partial\Psi/\partial r$. In order to fa comparisons with the existing studies, the aspect ratio $Ar = 2.0$ and th number Pr =0.7.

Clearly, the cases of Ri=0, i. e., $\Delta T(\equiv T_T - T_L) = 0$, corresp non-stratified(constant-density) fluid motions, and observations are made of first (see the frames in column (1)). In general, the rotation of the top li radially-outward flow in the immediate vicinity of the top disk. The fluid downward near the cylindrical sidewall, and, at small and intermediate radii, directed toward the top disk. This produces a clockwise circulation cell in m

interior region of the cylinder. As is evident in Fig. 1(a), when is low, the impact of the forced convection, arising from the rotation of the top lid, is weak, and, therefore, the main meridional circulation cell is seen to occupy the upper part of the cylinder. However, as increases (see Figs. 1(b), 1(c), 1(d)), the boundary layer-type character near the top lid is manifested, and the meridional circulation stretches out to cover most of the cylinder interior. It is notable that, when exceeds a certain critical value (see Fig. 1(c)), stagnation points, with closed stream surfaces, appear on the axis, forming stagnation bubble(s). This celebrated phenomenon, often referred to as vortex breakdown, has been an issue of central concern in the fluid dynamics literature (e. g. Brown & Lopez, 1990; Berger & Erlebacher, 1995), and detailed discussions on the fundamental physics are beyond the scope of the present paper.

The qualitative changes in the meridional flows, as the temperature $\Delta T(\equiv T_T - T_L) > 0$, is applied, are now scrutinized. The relative impact stabilizing buoyancy effect is characterized by the Richardson number Ri (that, in the present notation, the study of Lugt & Abboud (1987), in which th was cold and the bottom disk was hot, dealt with the situations of $Ri < 0$.

As illustrated in Fig. 1, the principal changes brought forth by imp are that the extent of the main circulation is reduced. Especially when Re i meridional circulation contains a thin, well-defined boundary layer adjacen lid. When is appreciable (see frame (5) of Fig. 1(d) for Ri=10.0), the main tends to be confined to a narrow strip near the top lid at large radii. intensity of the meridional flows (u, w) weakens substantially as Ri inc $Ri \gtrsim O(1)$. Also noticeable is that the separation bubble on the axis is sup increases to $Ri \gtrsim O(1)$. In other words, under the prevailing stable strati vortex breakdown is prevented (or lessened). These features are indicati inhibition of meridional flows, particularly the vertical velocity, in t stabilizing influences of buoyancy $\Delta T > 0$. It is recalled that, in the case

buoyancy ($\Delta T < 0$) as treated by Lugt & Abboud (1987), the bubble becomes larger with the increase of the absolute value of $Ri(<0)$. In that case, the fluid of greater density is formed near the top lid, and this fluid sinks along the sidewall, which gives rise to intensified undulations in the central axis region. The physical interpretations of the meridional flow patterns of Fig. 1 for $\Delta T > 0$ are consistent with the above-stated arguments on the role of buoyancy.

The temperature field is demonstrated in Fig. 2. Obviously, when i conduction is the principal heat transport mode, and the isotherms are mostly (see Fig. 2(a)). For large (see Figs. 2(c), 2(d)) with small , convection do the isotherms in the middle core region tend to be vertically oriented. The field also exhibits a boundary layer-character near the top and bottom However, when $Ri \gtrsim O(1)$, buoyancy inhibits convective motions, and, as displ frame (5) of Fig. 2(d), conduction prevails, and the isotherms are aligned in horizontal direction in the bulk of the cylinder. Expectedly, these chara $\Delta T > 0$ are opposite to the trend detectable in the exemplary calculations Lugt & Abboud for $\Delta T < 0$

Computations are made of the local Nusselt numbers at the top lid and endwall, which are defined as $Nu_T = \partial \theta / \partial z|_{z=A_r}$ and $Nu_L = \partial \theta / \partial z|_{z=0}$.

Fig. 3 shows the radial profiles of Nu_T . For small Re (see Fi convective heat transfer is generally meager, therefore, the values of Nu Locally, Nu_T is large in the central area, and Nu_T decreases as r increases sidewall. Clearly, the rotation of the top lid induces upward flows at small contributes to increased heat transports in these regions. The fluid at lar downward along the sidewall, which causes decreasing Nu_T in these are $Ri \gtrsim O(1)$, the stabilizing buoyancy further reduces convective activities, to lower values of Nu_T .

For large Re (see Fig. 3(d)), owing to vigorous convective activities values of Nu_T increase (note the difference in scales for Nu_T in Figs. 3(a

The value of Nu_T is large at small and moderate radii, and in a relatively narrow zone close to the sidewall, Nu_T decreases rapidly. Also, the suppression of Nu_T due to the stable stratification is more pronounced for large Re .

Fig. 4 illustrates Nu_L . Again, when Re is small (see Fig. 4(a)), the activity can not reach the bottom endwall, and, therefore, heat transfer nea portion of the cylinder is overwhelmingly conductive. For large Re (see Fig. shows strong dependence on Ri . When the buoyancy effect is minimal (see the for Ri=0.01), convection is vigorous near the bottom. It is seen that Nu_T with $r$increasing at small and moderate radii until $r \cong 0.7$. At larger radii, the weakening meridional motions, Nu_L decreases. When the buoyancy eff substantial (see the curve for Ri = 10.0), as explained earlier, fluid moti bottom endwall are greatly suppressed, and conductive heat transport preva bottom region. It is recalled that the radius, not the height, of the cylinde the nondimensionalization. Accordingly, in the limit of conductive hea $Nu = 1/Ar(=0.5)$ =1, as displayed in Fig. 4.

Here, it is worth noting that the area-integrated Nusselt numbers are for both the top and bottom disks, as expected. The contribution of the loc number increases are r^2 , therefore, the behavior of the Nu_T near the sidew dominant contributions to the total heat transfer rate.

4. Conclusion

When Re is small, the effect of the rotating top lid is confined to portion of the cylinder. Heat transfer is predominantly conductive. With the Re, the main meridional clockwise circulation occupies most of the cylind when $Ri = 0$. When Re is very large, a separation bubble, which is characte vortex breakdown, forms on the axis. However, when $Ri \gtrsim O(1)$, vertical ve

are suppressed, and the separation bubble disappears; under strong stabili convective activities weaken and conduction prevails in much of the cylinder. These features are consistent with the overall role of the buoyancy in the dynamical balance.

Local variations of Nu_T and Nu_L are computed. When Re is large, Nu_T is large at small and moderate radii, and Nu_T decays rapidly near the sidewall. However, Nu_T is substantially reduced when $Ri \gtrsim O(1)$. In accordance with the meridional flow pattern, Nu_L for large Re increases with radial distance until $r \cong 0.7$ after which Nu_L decreases slightly with r.

The results of the present numerical solutions are subject to ex verification. A preliminary account was given on experimental flow visualizat 1995), and further developments will be dealt with in subsequent reports.

References

1. Barcilon, V. and Pedlosky, J. 1967. Linear theory of rotating stratified f J. Fluid Mech, 29, 1-16

2. Barcilon, V. and Pedlosky, J. 1967. On the steady motions produced by a stratification in a rapidly rotating fluid. J. Fluid Mech, 29, 673-690

Berger, S. A. and Erlebacher, G. 1995. Vortex breakdown incipience: The considerations. Phys. Fluids, 7, 972-982

3. Bertela, M and Gori, F. 1982. Laminar flow in cylindrical container with cover. Trans. ASME J. Fluids Engng, 104, 31-39

4. Brown, G. L. and Lopez, J. M. 1990. Axisymmetric vortex breakdown Par Physical mechanisms. J. Fluid Mech, 221, 553-576.

5. Escudier, M. P. 1984. Observations of the flow produced in a cylindrical v a rotating endwall. Exp. Fluids, 2, 189-196

6. Hayase, T., Humphrey, J. A. C., and Grief, R. 1994. A consistently fo

QUICK scheme for fast and stable convergence using finite-volume iterative c procedures. J. Comput. Phy, 98, 108-118

7.Hyun, J. M. 1995. Flow driven by a shrouded rotating disk with time-de angular frequency. Proc. Int. Seminar on Manufacturing of Advanced Materials., Kyushu Univ., Kyusu, Japan, Nov. 6-7

8.Kim, W. N. and Hyun, J. M. 1995. Mass transfer characteristics for a rotating cup-like cylinder. Int. J. Heat Mass Transfer, 38, 2959-2967

9.Kim, W. N., Hyun, J. M., and Ozoe. 1996. Effect of aspect ratio on mass from a rotating cup. Int. J. Heat Mass Transfer, 39, 2375-2377

Leibovich. 1984. Vortex stability and breakdown : survey and extension. AIA 1192-1206

10.Linden, P. F. 1977. The flow of a stratified fluid in a rotating annulu Mech, 79, 435-447

11.Lugt, H. J. and Abboud, M. 1987. Axisymmetric vortex breakdown with and wi temperature effects in a container with a rotating lid. J. Fluid Mech, 179, 17

12.Lugt, H. J. and Haussling, H. J. 1982. Axisymmetric vortex breakdown in fluid within a container. Trans. ASME J. Appl. Mech, 49, 921-923

Patankar, S. V. 1980. Numerical Heat Transfer and Fluid Flow. McGraw-Hill,New

13.Roberts, P. H. and Soward, A. M. 1978. Rotating Fluids in Geophysics. Ac Press, London

14.Sparrow, E. M. and Chaboki, A. 1982. Heat transfer coefficients for a cup-l rotating about its own axis. Int. J. Heat Mass Transfer, 25, 1333-1341

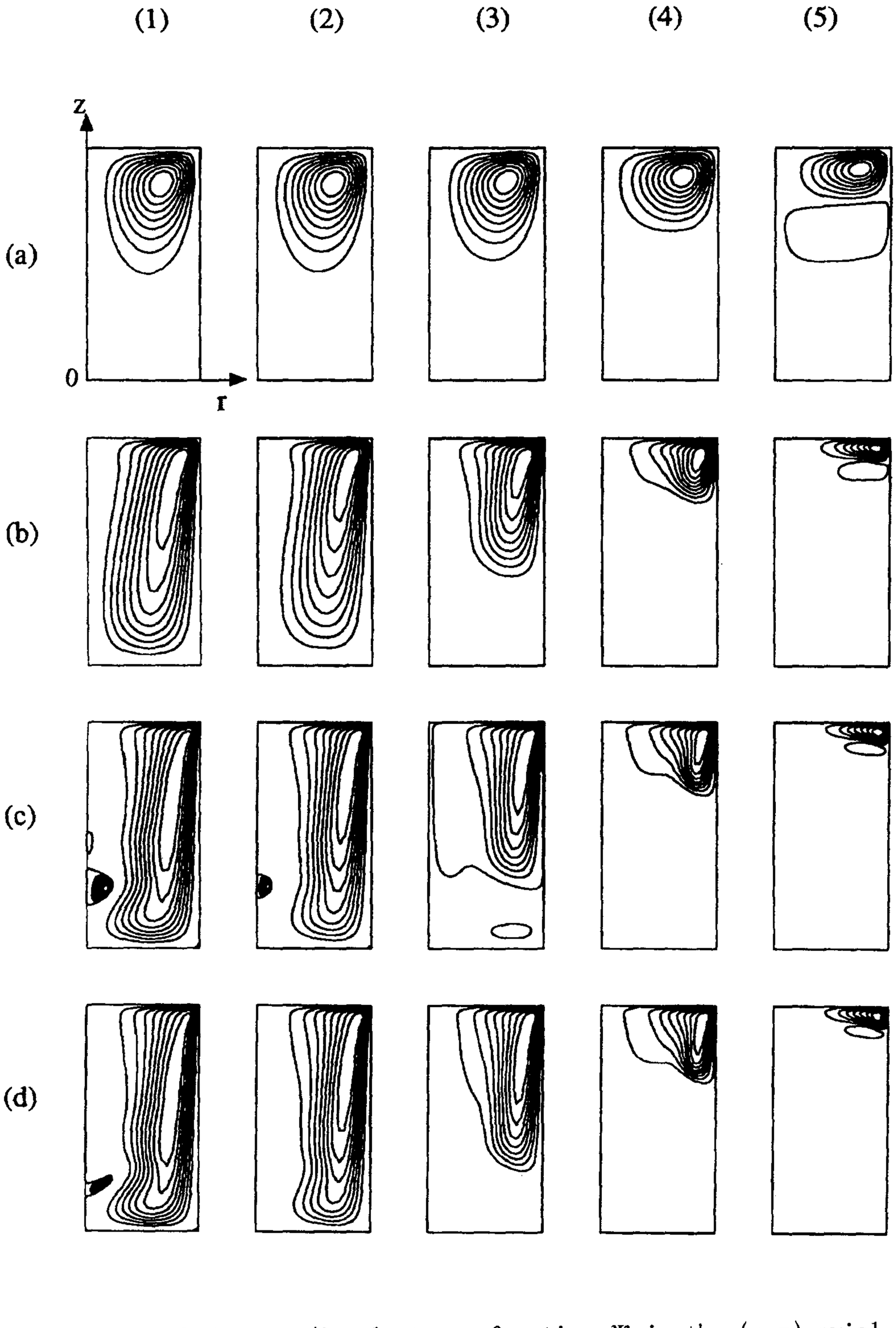

Fig. 1. Plots of the meridional stream function Ψ in the (r-z) axial plane

Values of Re are : (a) 100, (b) 1000, (c) 2000, (d) 2500.

Values of Ri are : (1) 0.0, (2) 0.01, (3) 0.1, (4) 1.0, (5) 10.0.

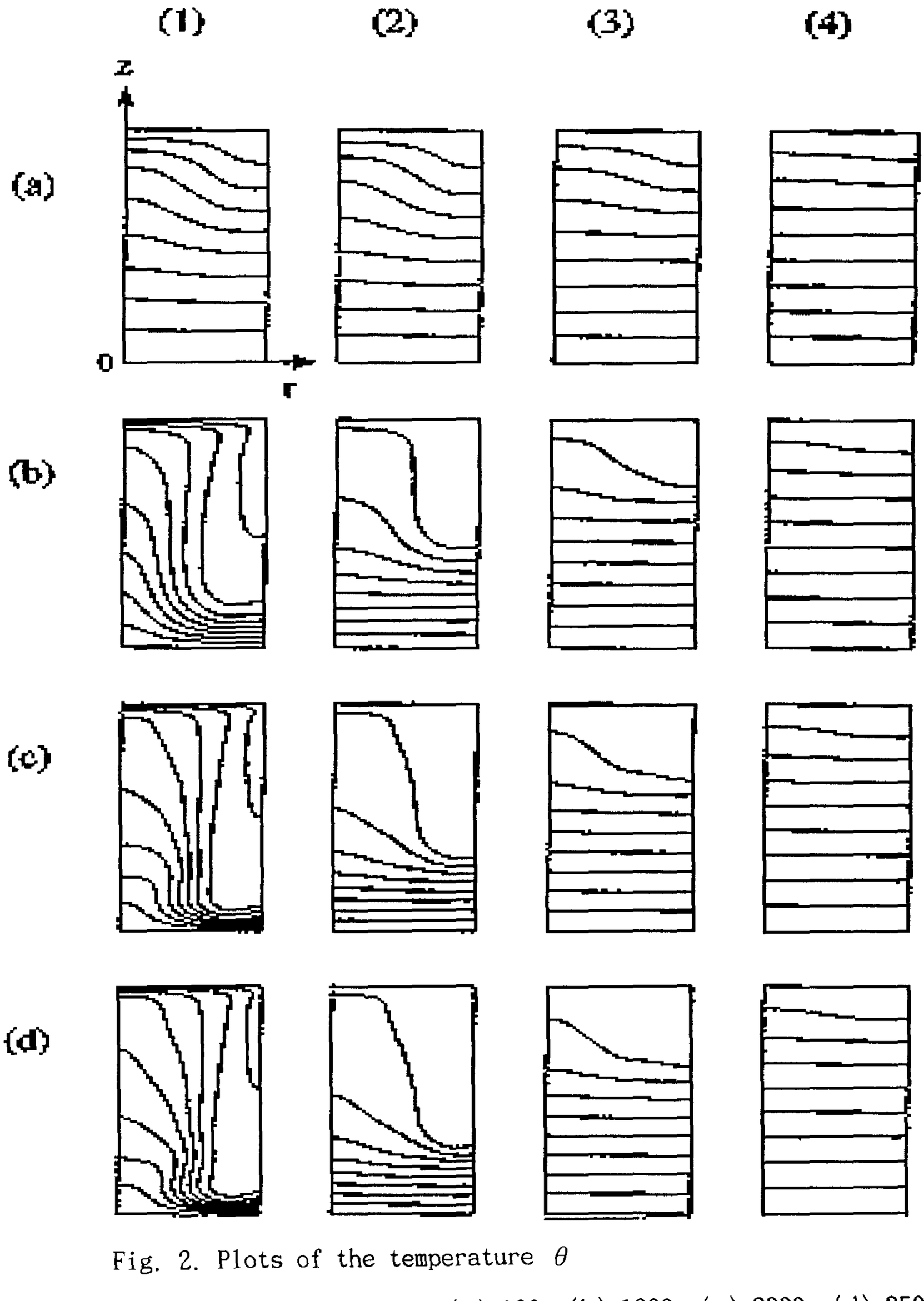

Fig. 2. Plots of the temperature θ

Values of Re are : (a) 100, (b) 1000, (c) 2000, (d) 2500

Values of Ri are : (1) 0.01, (2) 0.1, (3) 1.0, (4) 10.0.

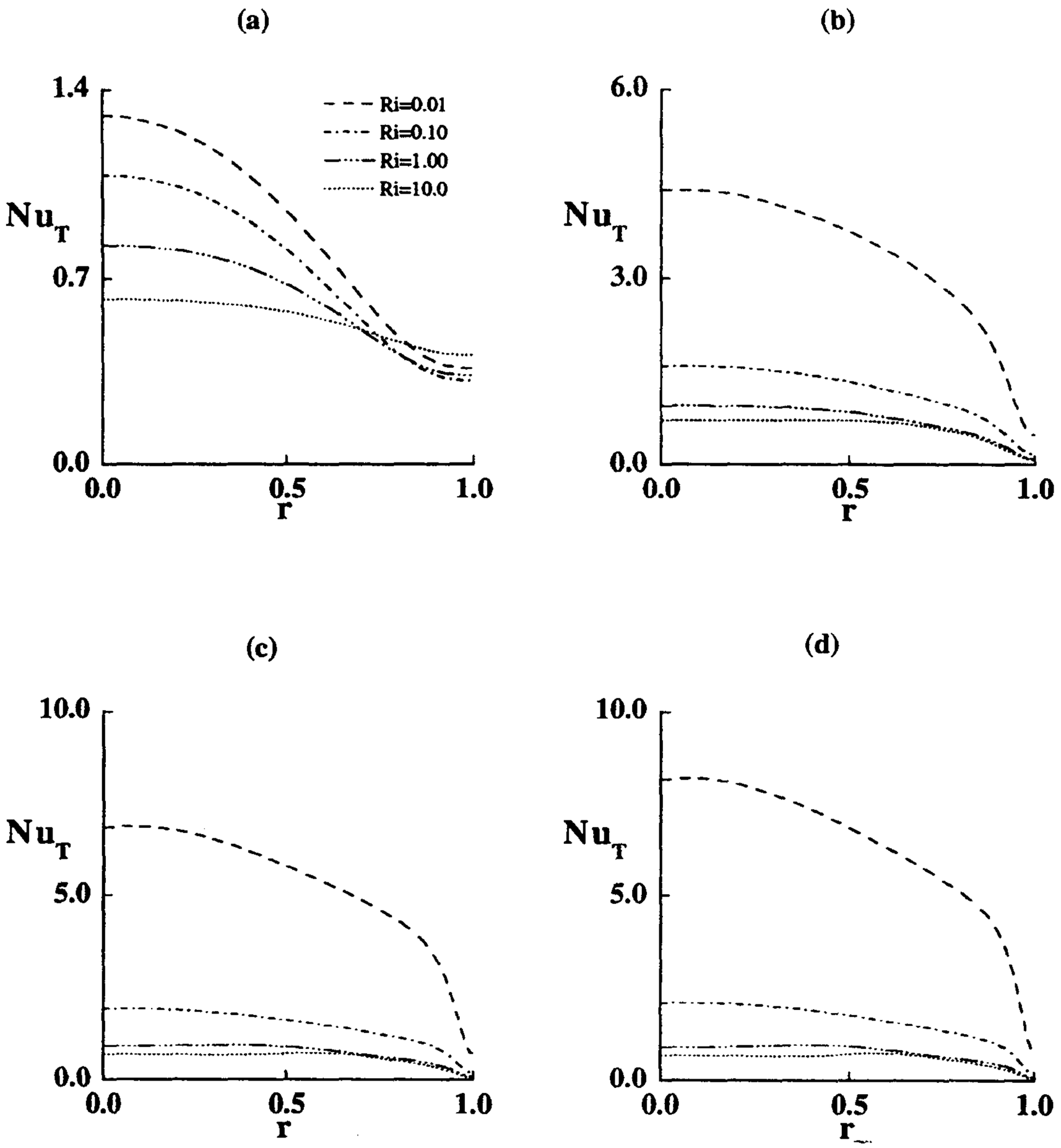

Fig. 3. Radial profiles of N_T.

(a) Re =100, (b) Re=1000, (c) Re=2000, (d) Re=2500.

;Values of Ri are : _ _ _, Ri = 0.01; _ . _ ., Ri=0.10

; _ .. _, Ri=1.00; . . . ., Ri =10.0.

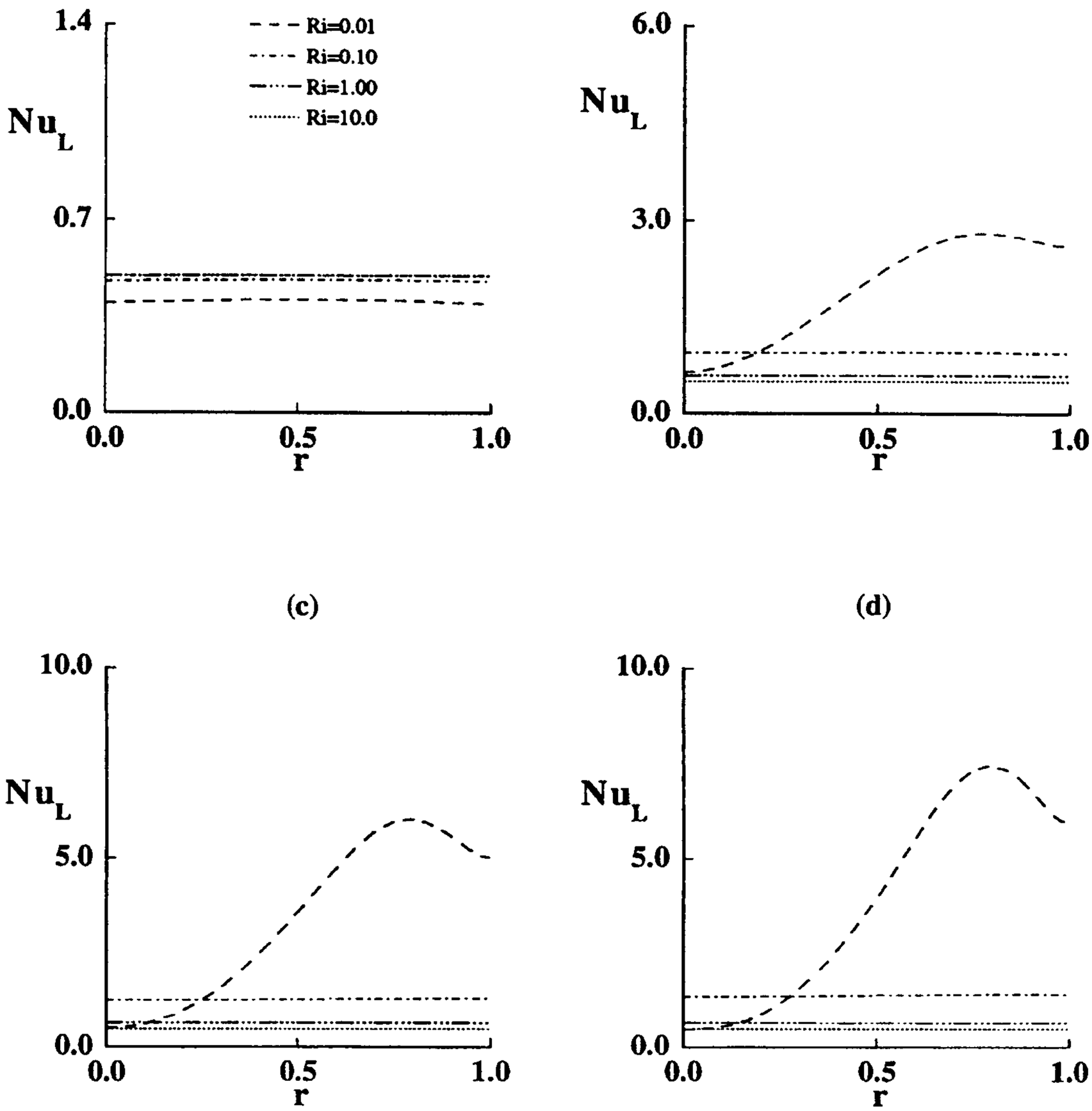

Fig. 4. Same as in Fig. 3, except for Nu_L

제 4 절

Transient confiend natural convection with internal heat generation
(내부열원을 가지는 용기내의 과도자연대류)

요 약 문

사각용기내에서의 자연대류의 시간에 따른 변하를 묘사하기 위한 수치적 연구를 수행하였따. 두 수직벽을 외부레일리수(Ra_E)로 표현되는 서로다른 온도로 유지한 정상상태 유동장이 수립되었다. 내부레일리수(Ra_I)로 적절히 정의된 균일한 내부열생성이 시간이 0에서 갑자기 주어졌다. 이에따라 나타나는 최종상태까지의 과정을 큰 Ra_E와 Ra_I 그리고 Pr~O(1)에 대하여 지배방정식을 수치적으로 풀어서 묘사하였다. 내부 가열이 작은 경우외부 가열에 의해 구동되는 주요 순환셀(circulation cell)은 거의 영향을 받지 않았고, 이런 유형을 단계1로 이름붙였다. Ra_E/Ra_I가 비교적 클 때 가열된 측벽의 윗쪽 코너부근에 반대방향의 순환셀이 추가적으로 나타나며, 단계2로 명기되었다. Ra_E/Ra_I가 아주 클 때는 세가지 단계를 포함한다. 처음 두 단계의 정성적인 유동은 이전에 묘사된 것에 대응한다. 단계3에서는 전 용기가 두 개의 반대방향의 순환셀로 채워진다. 최종상태의 특징은 내부가열이 지배적인 유동에 대한 이전의 실험적 가시화 결과와 일치한다. 벽에서의 평균너셀수의 시간에 따른 변화를 분석하였고, 전체적인 안정화를 특징지을 수 있는 시간척도는 $Ra_I^{-1/4}$로 표현되어진다.

ELSEVIER

Transient confined natural convection with internal heat generation

Young Min Shim and Jae Min Hyun
Department of Mechanical Engineering, Korea Advanced Institute of Science and Technology, Taegon, South Korea

Numerical studies are conducted to describe the time-dependent adjustment of natural convection in a square cavity. A steady flow field had been established by maintaining different temperatures at the two vertical sidewalls, and this effect is represented by the external Rayleigh number Ra_E. A uniform internal heat generation, which is measured by a properly defined internal Rayleigh number Ra_I, is switched on impulsively at $t=0$. The ensuing process of settlement to final state, for large Ra_E and Ra_I, and $Pr \sim O(1)$, is depicted by solving the governing equations numerically. When the effect of internal heating is small, the major circulation cell, which has been driven by external heating, remains little affected, and this pattern is termed stage I. When Ra_I/Ra_E is moderately large, an additional oppositely directed circulation cell appears in the upper corner region of the heated sidewall, which is denoted stage II. When Ra_I/Ra_E is very large, three stages are encompassed. The qualitative flows of the first two stages correspond to those described earlier. In stage III, the whole cavity is occupied by two oppositely directed circulation cells. The final-state features are consistent with the preceding experimental visualizations for the flow dominated by internal heating effects. Time histories of the average Nusselt number on the wall are analyzed, and the overall time characterizing the global adjustment is shown to scale with $Ra_I^{-1/4}$

Keywords: natural convection; internal heat generation, transient processes

Introduction

Natural convection in a closed square cavity, with the two vertical sidewalls maintained at different temperatures, has posed a classical configuration for benchmark testing (e.g., Davis 1983). The flow and attendant heat transfer are characterized by the externally controllable Rayleigh number $Ra_E(\equiv \beta g \Delta T L^3/\nu\kappa)$ and the Prandtl number $Pr(\equiv \nu/\kappa)$. Here, ΔT denotes the imposed temperature difference between the two sidewalls ($\Delta T \equiv T_H - T_C$), β the coefficient of volumetric expansion for a Boussinesq fluid, g the gravity, L the height of the cavity, ν and κ the kinematic viscosity and thermal diffusivity of the fluid, respectively. It has been demonstrated that for large Ra_E and $Pr \sim O(1)$, which pertain to many practical systems, the global flow is of boundary layer type. Prominent features of the convection in this side-heated square cavity have been documented extensively (e.g., Ostrach 1988; Hyun 1994).

Studies have been made of the responses of the enclosed fluid system when a differential sidewall heating and an internal heat generation are present concurrently. These efforts (Acharya and Goldstein 1985; Lee and Goldstein 1988; Kawara et al. 1994; Fusegi et al. 1992) were concerned with such technological applications as in nuclear reactors and geothermal heat extractions. The introduction of internal heat generation is represented by the internal Rayleigh number $Ra_I(\equiv g\beta QL^5/\nu\kappa k)$, in which Q denotes the rate of uniform internal heat generation, and k is the coefficient of thermal conductivity of the fluid. One significant finding of the above investigations is that, when Ra_I is substantially larger than Ra_E, the overall flow is directed downward on both the heated and cooled vertical sidewalls. Recent experimental visualizations of Kawara et al. (1994), by passing electric current through a liquid solution, classified the qualitative flow patterns in the Ra_E–Ra_I regimen diagram. For several limited cases, detailed measurements of local temperature field and heat flux were obtained, and these corroborated the depictions of the global flow character of Kawara et al.

It is notable that all of the prior works dealt with the steady-state situations in which the externally specified conditions were enforced in a time-invariant manner. Here, we probe into the transient features of confined convection when the thermal forcings are applied abruptly. Specifically, attention is directed to a sidewall-heated square cavity, in which uniform internal heat generation is started impulsively. The ensuing time-dependent process of adjustment is examined. This setup constitutes a self-standing dynamical problem from a theoretical standpoint. On the practical side, the transient approach to the final state is of relevance to the start-up (or shut-off) phase of industrial devices with internal heat generation. In this paper, numerical solutions are acquired that display the sequences of flow and thermal fields, in response to an instantaneously started internal heat generation, for large Ra_E and Ra_I with $Pr \sim O(1)$.

Address reprint requests to Prof. J. M. Hyun, Department of Mechanical Engineering, Korea Advanced Institute of Science and Technology, 373-1 Kusong-Dong, Yusong-Gu, Taejon 305-701, South Korea.

Received 27 January 1996; accepted 7 September 1996

Int. J. Heat and Fluid Flow 18: 328–333, 1997

0142-727X/97/$17.00
PII S0142-727X(97)00027-1

In particular, we endeavor to characterize the time scale over which the global flow substantially settles to the final state by analyzing the numerical data.

Formulation

The governing Navier–Stokes equations, for a Boussinesq fluid, written in nondimensional form, are (e.g., Davis 1983):

$$\frac{\partial U}{\partial X} + \frac{\partial V}{\partial Y} = 0 \tag{1}$$

$$\frac{\partial U}{\partial t} + U\frac{\partial U}{\partial X} + V\frac{\partial U}{\partial Y} = -\frac{\partial P}{\partial X} + \frac{\partial^2 U}{\partial X^2} + \frac{\partial^2 U}{\partial Y^2} \tag{2}$$

$$\frac{\partial V}{\partial t} + U\frac{\partial V}{\partial X} + V\frac{\partial V}{\partial Y} = -\frac{\partial P}{\partial Y} + \frac{\partial^2 V}{\partial X^2} + \frac{\partial^2 V}{\partial Y^2} + \frac{\mathrm{Ra}_E}{\mathrm{Pr}}\theta \tag{3}$$

$$\frac{\partial \theta}{\partial t} + U\frac{\partial \theta}{\partial X} + V\frac{\partial \theta}{\partial Y} = \frac{1}{\mathrm{Pr}}\left[\frac{\partial^2 \theta}{\partial X^2} + \frac{\partial^2 \theta}{\partial Y^2}\right] + \frac{\mathrm{Ra}_I}{\mathrm{Ra}_E \mathrm{Pr}} \tag{4}$$

in which (U,V) stand for the velocity components, t time, P pressure, θ temperature.

In the above, nondimensionalizations were made so that $(X,Y) \equiv (x^*, y^*/L)$, $(U,V) \equiv [u^*, v^*/(\nu/L)]$, $P \equiv p^*/[\rho(\nu/L)^2]$, $\theta \equiv [T-(T_H+T_C)/2]/(T_H-T_C)$, $t \equiv t^*/(L^2/\nu)$, where dimensional quantities are denoted by an asterisk. The principal dimensionless parameters explicitly appearing in the equations are the previously defined $\mathrm{Ra}_E, \mathrm{Ra}_I, \mathrm{Pr}$.

In accordance with the problem statement, the boundary conditions are (see Figure 1).

on $X = 0, 1$ and $Y = 0, 1$:

$$U = V = 0$$

on $X = 0$:

$$\theta = 0.5$$

on $X = 1$:

$$\theta = -0.5$$

on $Y = 0, 1$:

$$\frac{\partial \theta}{\partial Y} = 0$$

The steady state, which had previously been established by the differential sidewall heating, with no internal heat generation ($Q = 0$), was taken to be the initial state. At $t = 0$, Q is suddenly switched on to this pre-established, sidewall-heated square cavity, and the subsequent flows are depicted.

Numerical solutions were procured by using the well-known computational procedures SIMPLER (Patankar 1980). A staggered and stretched mesh was selected, with the grid points clustered near the solid boundaries. Specifics of the numerical calculations have been elaborated in the literature. For the majority of runs, the grid network adopted was 40×40, and the time increment Δt was 10^{-5}. Extensive tests were carried out to ascertain the grid- and time interval-convergence by deploying grids 80×80 and 60×60. The variations in the computed results were shown to be smaller than 1%. Calculations were also repeated to check the present results against the published data of steady-state problems. Specific comparisons can be made between the present results depicted in Figures 2a, 3a, and 4a and the corresponding steady solutions of Davis (1983) tor the sidewall-heated cavity. Also, in the limit $\mathrm{Ra}_I = 0$ and $\mathrm{Ra}_E \leq 10^3$, the heat transfer is predominantly conductive. These explicit comparisons were previously shown in Hyun and Lee (1989). Similar endeavors are made by comparing the present results illustrated in Figures 3d and 4f and the corresponding steady solutions of Acharya and Goldstein (1985), which include internal heat generation. The outcome of such comparisons was demonstrated in Fusegi et al. (1992). These efforts provided credence to the accuracies of the present numerical model output.

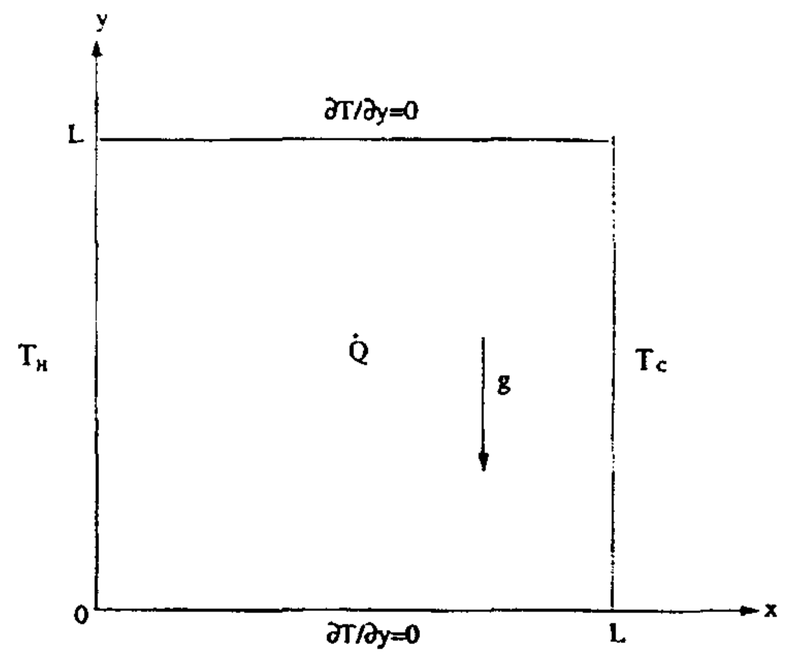

Figure 1 Schematic of the flow configuration

Results and discussion

Systematically organized computational runs were made for $\mathrm{Pr} = 0.7$, covering two major parameter sets; i.e., set 1: $\mathrm{Ra}_E = 10^5$, $10^5 \leq \mathrm{Ra}_I \leq 10^8$; and set 2: $10^5 \leq \mathrm{Ra}_E \leq 10^7$, $\mathrm{Ra}_I = 2 \times 10^7$.

The selection of the above parameter sets was made to encompass the ranges of (Ra_E–Ra_I) combinations corresponding to the three distinctive final-state flow patterns, as disclosed in the regime diagram of Kawara et al. (1994). Also, the parameter sets for air $\mathrm{Pr} = 0.7$ correspond closely to the steady-state results

Notation

g	gravity
Nu	local Nusselt number
Pr	Prandtl number
Q	rate of internal heat generation
Ra_E	external Rayleigh number
Ra_I	internal Rayleigh number
ΔT	temperature difference
U,V	velocity components
x, y	rectangular coordinates

of Acharya and Goldstein (1985). As asserted in Fusegi et al. (1992), the global patterns of flow and temperature fields are qualitatively similar as Pr covers the range $O(1) \leq Pr \leq 10$.

First, Figure 2 shows the evolution of flow and thermal fields when the relative impact of internal heat generation is minor. The entire adjustment process, starting from the sidewall-heated established state, is dominated by the external heating. Therefore, the qualitative transient flow character is virtually unaffected. Only minor quantitative weakenings of flow at small times attributable to the introduction of Q, and their subsequent slight recoveries to the finale-state, are discernible. The flow field is characterized by the presence of a single clockwise circulation cell, which occupies much of the cavity interior. Throughout the entire curse of evolution, the temperature field deviates little from the initial-state features of the sidewall heated cavity. For the run of Figure 2, because the values of Ra_E and Ra_I are rather high, concentration of flow in thin boundary layers is evident. The flow displayed in Figure 2 was classified as Pattern I in the steady-state experiment of Kawara et al. (1994).

Next, considerations are given to the cases when the effects of external heating and internal heat generation are comparable. Figure 3 is illustrative of the sequences of flow and thermal fields for such cases. Immediately after the switch on of Q, the flow field is still mostly governed by the pre-existing external heating. Throughout the cavity interior, a single clockwise circulation cell is visible. The cavity interior region, apart from the sidewall boundary layers, is substantially stratified, with a near-liner vertical temperature distribution. As time elapses, the impact of internal heat generation provides an aiding (opposing) buoyancy effect to the fluid in the vicinity of the cold (heat) sidewall. The sinking (rising) motion in the boundary layer on the cold (hot) sidewall is, therefore, enhanced (hindered). In the bulk of the interior, generally rising motions are induced because of the presence of internal heat generation. At moderate times (see Figure 3b), caused by this differential buoyancy effect, flows are intensified near the bottom part of the cold sidewall. In the upper corner region of the hot sidewall, the additional negative buoyancy arising from Q begins to produce a vertically downward motion. As time progresses toward the final state, a small counterclockwise circulation cell in this corner is evident. As can be noted by inspecting the value of Ψ_{max}, local intensifications of flows are seen as the final state is approached. The large-time flow behavior (see Figure 3d) is characteristic of Pattern II, which was portrayed by Kawara et al. (1994). The evolution of the isotherms is of interest. At small times, because of the dominance of external heating, the isotherms are diagonally symmetric with respect to the cavity center. At moderate times, this point symmetry is destroyed as a consequence of the accumulated effect of Q. At large times, isotherms are nearly vertical and clustered in the vicinity of the cold wall, in particular, in the upper corner region. Near the hot sidewall, the isotherm of T_H divides the isotherms into two groups, one attached to the top and the other attached to the bottom horizontal wall, respectively. The cumulative effect of Q brings forth an increase of the overall thermal energy in the cavity. As shown in Figure 3d, at large times, the maximum temperature in the cavity is appreciably higher than T_H.

The evolution of flow, when the effect of internal heat generation is dominant, is depicted in Figure 4. At very early times, the flow is still under the influence of external heating and, as expected, a single clockwise circulating cell occupies much of the cavity. In the intermediate stage, the impact of Q begins to be felt, and an additional differential buoyancy is produced. As is evident in Figure 4c and d, a small-sized, counterclockwise circulation emerges in the upper corner of the heated sidewall. This is similar to the previously mentioned Pattern II of Kawara et al. (1994). As time passes, the relative effect of internal heat generation outweighs that of external heating. In the central portion of the cavity interior, generally rising motions prevail. Near the hot wall, the sinking motion arising from the negative buoyancy attributable to Q is appreciable. In the vicinity of the cold wall, the sinking motion is augmented. In the last stage settling into the final state, the whole cavity is occupied by two circulating cells; i.e., a counterclockwise (clockwise) cell near the hot (cold) wall side, respectively. This is characteristic of Pattern III, as visualized in the experiment of Kawara et al. In summary, when

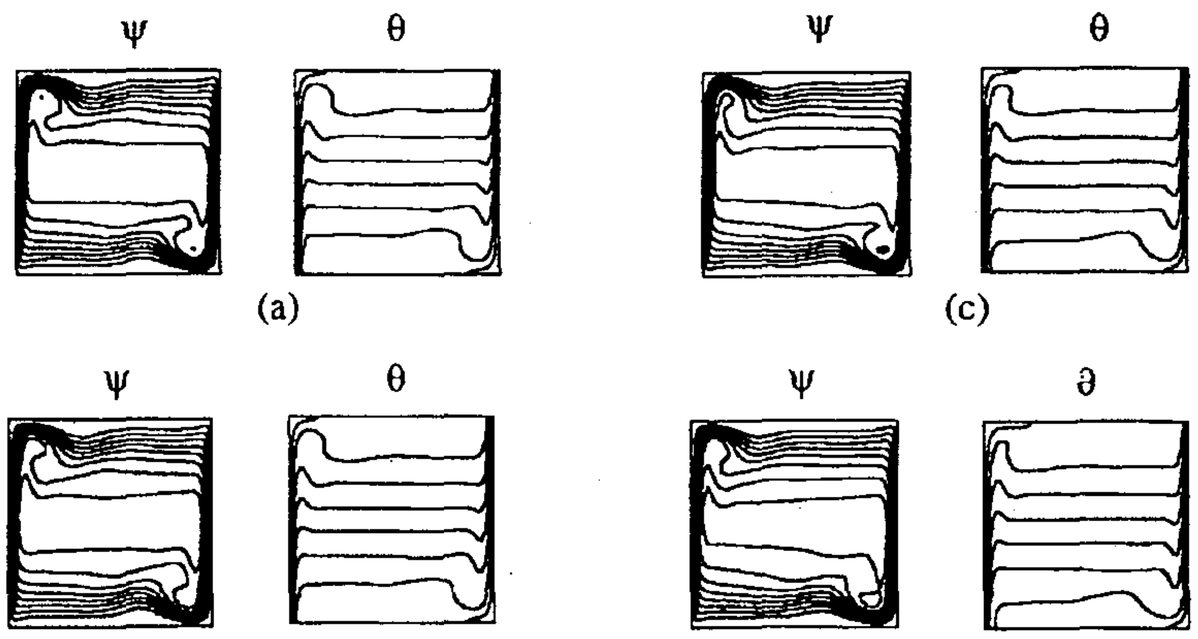

Figure 2 Sequential plots of stream function (ψ) and isotherms (θ); $Ra_E = 10^7$, $Ra_I = 2 \times 10^7$; (a) $t=0$, $\psi_{max} = 2.23 \times 10^{-4}$, $\psi_{min} = -43.3$, $\theta_{max} = 0.50$; (b) $t=0.0001$, $\psi_{max} = 3.08 \times 10^{-2}$, $\psi_{min} = -41.8$, $\theta_{max} = 0.50$; (c) $t=0.01$, $\psi_{max} = 4.33 \times 10^{-4}$, $\psi_{min} = -42.7$, $\theta_{max} = 0.50$; (d) $t=0.1$, $\psi_{max} = 1.54 \times 10^{-5}$, $\psi_{min} = -43.3$, $\theta_{max} = 0.50$

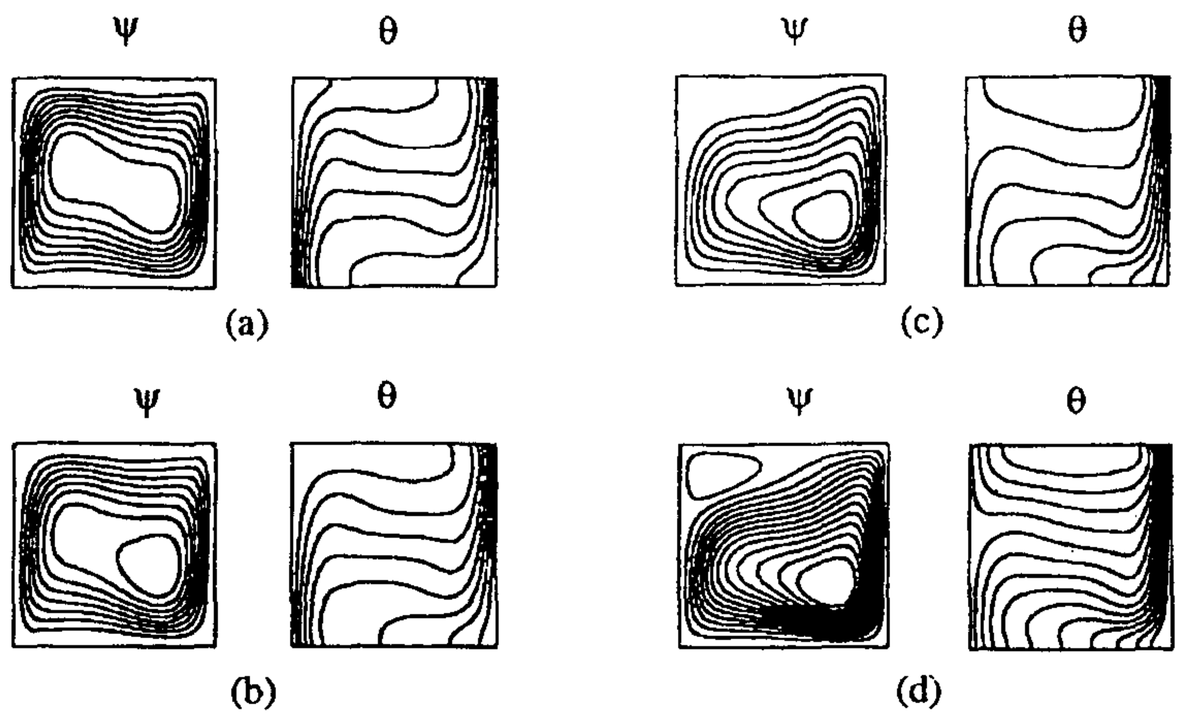

Figure 3 Sequential plots of stream function (ψ) and isotherms (θ); $Ra_\varepsilon = 10^5$, $Ra_t = 10^6$; (a) $t=0$, $\psi_{max} = 6.18 \times 10^{-7}$, $\psi_{min} = -13.7$, $\theta_{max} = 0.50$; (b) $t=0.01$, $\psi_{max} = 3.85 \times 10^{-4}$, $\psi_{min} = -14.8$, $\theta_{max} = 0.51$; (c) $t=0.05$, $\psi_{max} = 4.34 \times 10^{-1}$, $\psi_{min} = -16.8$, $\theta_{max} = 0.75$; (d) $t=0.1$, $\psi_{max} = 1.56$, $\psi_{min} = -17.0$, $\theta_{max} = 0.87$

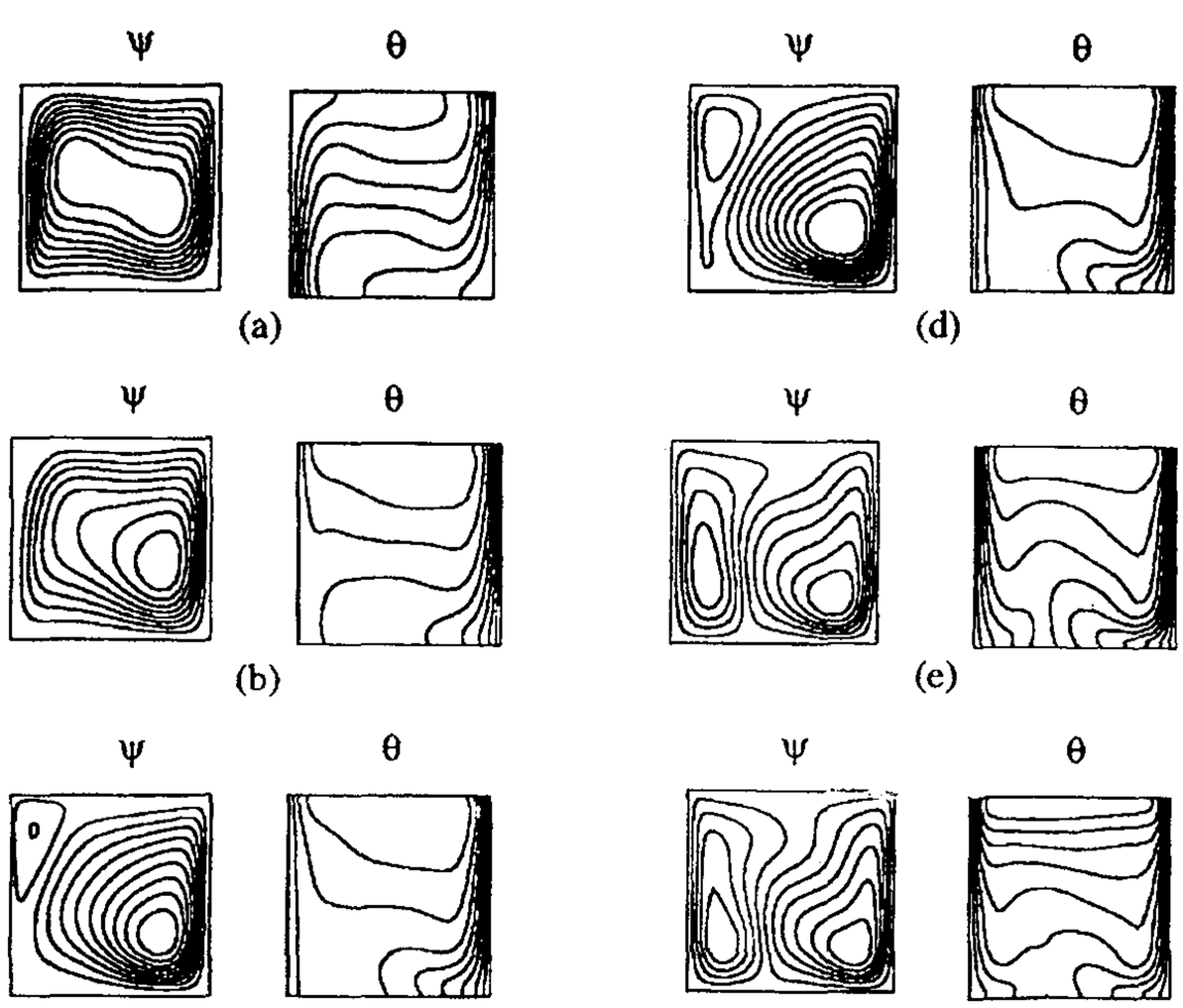

Figure 4 Sequential plots of stream function (ψ) and isotherms (θ); $Ra_\varepsilon = 10^5$, $Ra_t = 10^7$; (a) $t=0.0001$, $\psi_{max} = 4.11 \times 10^{-5}$, $\psi_{min} = -13.7$, $\theta_{max} = 0.50$; (b) $t=0.005$, $\psi_{max} = 4.73 \times 10^{-1}$, $\psi_{min} = -17.1$, $\theta_{max} = 1.05$; (c) $t=0.008$, $\psi_{max} = 2.69$, $\psi_{min} = -22.0$, $\theta_{max} = 1.44$; (d) $t=0.01$, $\psi_{max} = 5.96$, $\psi_{min} = -24.0$, $\theta_{max} = 1.71$; (e) $t=0.02$, $\psi_{max} = 16.4$, $\psi_{min} = -24.5$, $\theta_{max} = 2.95$; (f) $t=0.1$, $\psi_{max} = 17.2$, $\psi_{min} = -24.1$, $\theta_{max} = 5.54$

the effect of internal heat generation is dominant, the flow undergoes the three stages, passing through Patterns I, II, and III of Kawara et al. The evolution of the associated thermal fields, as exhibited in Figure 4, is also revealing. In the first stage, the temperature distribution, shown in Figure 4a, is typical of the conventional sidewall-heated cavity. With the introduction of Q, the crowding (thinning out) of the isotherms in the vicinity of the cold (hot) sidewall is apparent, as in Figure 4b. In the completion of the second stage (see Figure 4d), the near-linear temperature profiles in the cavity interior are broken. In the upper part of the cavity interior, temperature distributions tend to become horizontally uniform and vertically linear. However, in the bottom part of the cavity interior, in line with the emergence of two circulation cells of comparable magnitude, the isotherms are divided into two groups. In the last phase of the adjustment process (Figure 4f), the velocity and temperature fields display features that are characteristic of the cavity flow under dominant influence of internal heat generation. The total thermal energy in the cavity is on the increase during the adjustment process. This is reflected in the values of maximum temperature in the system, as time progresses. As the final state is approached, T_{max} is substantially larger than T_H.

It is of interest to gauge the time over which the overall adjustment is substantially accomplished. For this purpose, it is useful to plot the time histories of the average Nusselt number on the hot sidewall, which is defined as

$$\overline{\mathrm{Nu}} = \int_0^1 \left(\frac{\partial \theta}{\partial X}\right)_{X=0} \mathrm{d}Y$$

The objective here is to characterize the principal time scale for the flows to settle from the impulsive start to the final state. Based on the numerical data, the computed $\overline{\mathrm{Nu}}$ traces are exhibited in Figure 5. The four frames illustrated in Figure 5 encompass the situations whose final states lead to the three specific patterns describes earlier. When the effect of Q is relatively minor (see Figure 5a), the overall values of $\overline{\mathrm{Nu}}$ are moderate, and the decay of $\overline{\mathrm{Nu}}$ with time is mild. Obviously, because the flow is little affected by Q, the temporal variation of $\overline{\mathrm{Nu}}$ is expectedly small. In Figure 5b, the relative importance of Q is comparable to that of external heating, and the total heat transfer on the hot wall shows a steeper decay with time. When the flow is dominated by Q, as seen in Figure 5c and d, the total heat transfer on the hot wall is directed go the environment (note that $\overline{\mathrm{Nu}}$ is negative), and the heat transfer rate increases substantially as $\mathrm{Ra}_I/\mathrm{Ra}_E$ becomes large. Inspecting these time traces of $\overline{\mathrm{Nu}}$, a curve fitting is attempted in the exponential decay form; i.e., $\overline{\mathrm{Nu}} \sim A_0 + A_1[1 - \exp(-t/t_c)]$. The time constant t_c implies that the adjustment to the final state is approximately 63% completed. After considerable numerical effort, it is found that t_c is closely scaled with $\mathrm{Ra}_I^{-1/4}$. This may be explained in physical terms. When the impact of Q is weak, such as in Figure 5a, the numerical values of Ra_E and Ra_I are of the same order of magnitude. In this case, the flow adjustment is controlled by the external heating, and the relevant time scale for the global process has been established to be $O(\mathrm{Ra}_E^{-1/4})$, which is comparable to $O(\mathrm{Ra}_I^{-1/4})$. When the influence of Q is appreciable or overwhelming, the time-dependent motions arise principally because of the switch on of the internal heat generation, as demonstrated in Figures 3 and 4. For these cases, the evolution of flow is largely controlled by the accumulated effect of internal heating. The establishment of the boundary layers, which is dominated by internal heat generation, is crucial to drive the counter-

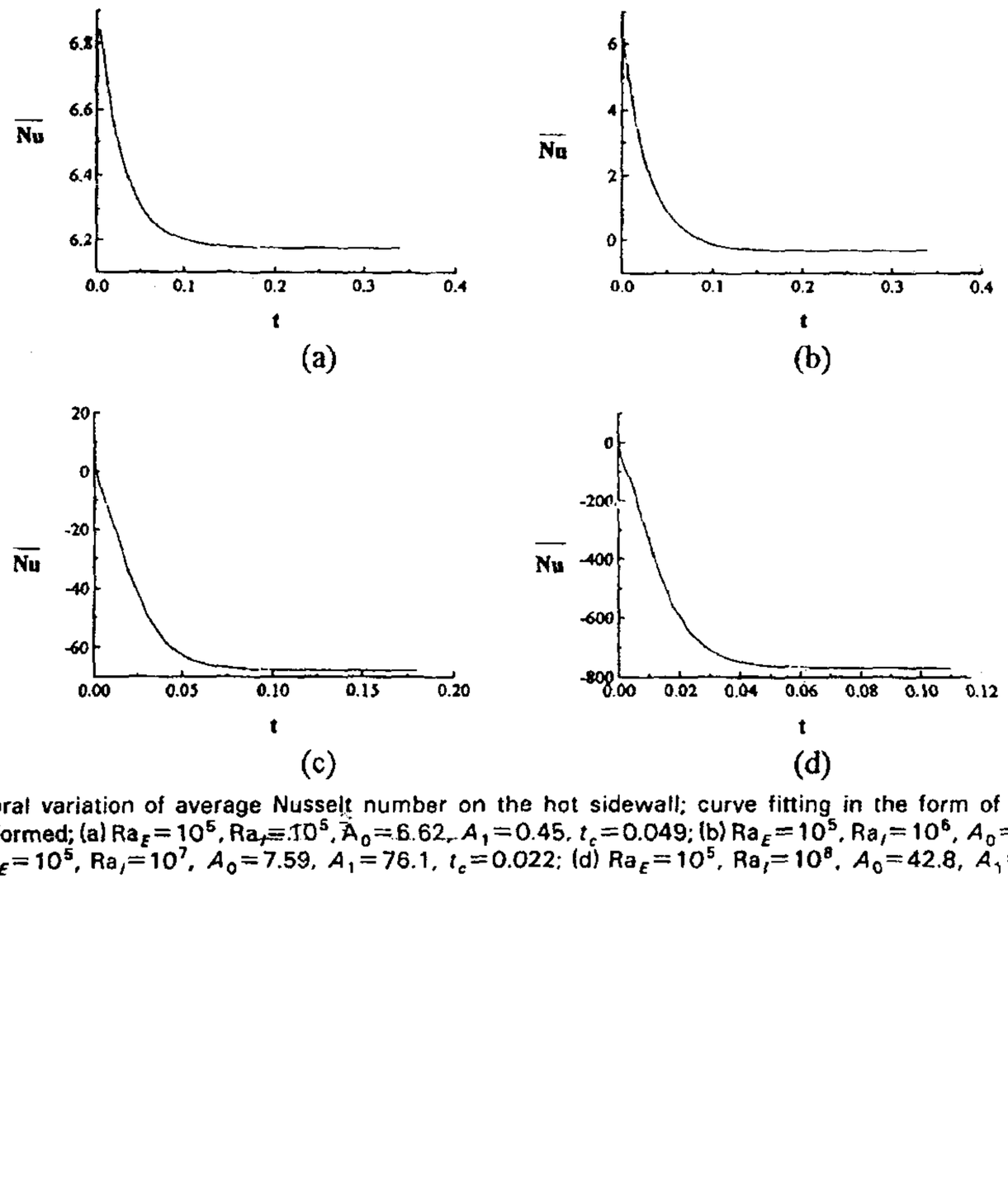

Figure 5 Temporal variation of average Nusselt number on the hot sidewall; curve fitting in the form of $\overline{\mathrm{Nu}} = A_0 - A_1[1 - \exp(-t/t_c)]$ is performed; (a) $\mathrm{Ra}_E = 10^5$, $\mathrm{Ra}_I = 10^5$, $A_0 = 6.62$, $A_1 = 0.45$, $t_c = 0.049$; (b) $\mathrm{Ra}_E = 10^5$, $\mathrm{Ra}_I = 10^6$, $A_0 = 7.44$, $A_1 = 1.00$, $t_c = 0.025$; (c) $\mathrm{Ra}_E = 10^5$, $\mathrm{Ra}_I = 10^7$, $A_0 = 7.59$, $A_1 = 76.1$, $t_c = 0.022$; (d) $\mathrm{Ra}_E = 10^5$, $\mathrm{Ra}_I = 10^8$, $A_0 = 42.8$, $A_1 = 820$, $t_c = 0.013$

clockwise circulation cell. In the final state, the thickness of boundary layer is given as $Ra_I^{-1/4}$. Therefore, in order to grow to this thickness, the time needed would be $Ra_I^{-1/4}$, using the present nondimensionalization schemes. The numerical fittings, which point to the time scale $O(Ra_I^{-1/4})$, are consistent with the above qualitative physical reasoning.

Conclusion

Numerical results indicate that when Ra_I/Ra_E is substantially large, the evolution encompasses the three stages. The first stage is typified by a single cell. In the second stage, an additional small oppositely directed cell appears in the upper corner region of the hot sidewall. In the last stage settling to the final state, the whole cavity is occupied by two circulation cells. The large-time behavior is consistent with Pattern III of the steady-state visualization of Kawara et al. (1994). In conjunction with the flow development, the temperature field undergoes an evolutionary process leading to the final state.

Numerical data for the evolution of the average Nusselt number of the hot sidewall are analyzed. When the impact of internal heat generation is dominant, the global flow adjustment is substantially achieved over the time that is scaled with $O(Ra_I^{-1/4})$.

References

Acharya, S. and Goldstein, R. J. 1985. Natural convection in an externally heated vertical or inclined square box containing internal energy sources. *J. Heat Transfer*, **107**, 855–866

deVahl Davis, G. 1983. Natural convection of air in a square cavity: A benchmark numerical solution. *Int. J. Num. Meth. Fluids*, **3**, 249–264

Fusegi, T., Hyun, J. M. and Kuwahara, K. 1992. Natural convection in a differentially heated square cavity with internal heat generation. *Num. Heat Transfer*, **21** 215–229

Hyun, J. M. 1994. Unsteady buoyant convection in an enclosure. *Adv. Heat Transfer*, **24**, 277–230

Hyun, J. M. and Lee, J. W. 1989. Numerical solution for transient natural convection in a square cavity with different sidewall temperatures. *Int. J. Heat Fluid Flow*, **10**, 146–151

Kawara, Z. Takahashi, O. Serizawa, A. and Michiyoshi, I. 1994. Natural convection in a confined regime with internal heating. *Proc. 1st Symposium on Heat Mass Transfer*, (Kansai Branch of the Heat Transfer Soc. Japan, Nov. 28–29), 153–158

Lee, J. H. and Goldstein, R. J. 1988. Experimental study on natural convection heat transfer in an inclined square enclosure containing internal energy sources. *J. Heat Transfer*, **110**, 345–349

Ostrach, S. 1988. Natural convection in enclosures. *J. Heat Transfer* **110**, 1175–1190

Patankar, S. V. 1980. *Numerical Heat Transfer and Fluid Flow*. Hemisphere, Bristol, PA

제 5 절

Flow driven by a torsionally-oscillating shrouded endwall disk

(비틀림적으로 요동하는 덮개판에 의한 유동)

요 약 문

유한한 용기형상에서 요동하는 덮개판에 의해 구동되는 시간에 따른 점성유체의 유동에 대한 연구를 수행하였다. 위 벽의 속도가 비틀림방향으로 Ωcosλt와 같이 요동하는 실린더형 용기내의 유동에 대한 Navier-Stokes식에 대한 수치해가 구해졌다. 높은 레일리수에서 세방향 속도를 자세히 조사하였다. 무차원 요동진폭의 값 ε (=Ω/λ)은 $\varepsilon \gtrsim O(1)$의 범위를 다루었다. ε<<1에 대한 방위각방향 유동에 대한 수치적 결과는 그전의 해석적인 모델에 의한 예측과 일치한다. 방위각방향 유동은 스톡스층 두께(Stokes layer thickness)에 주로 한정되어 나타난다. 자오면유동에 대한 직접적인 확장법을 이용한 해석적인 예측은 수치적인 결과와 오차를 나타낸다. 유한한 ε값에서 정상상태 자오면유동이 표현되었다. 자오면 정상상태 유동의 정량적인 형태는 실험적인 유동가시화로 증명되었다. 전체적인 유동 특성에 대한 레이놀즈수의 실질적인 영향이 면밀히 조사되었다. 요동하는 판에서의 토크계수의 변화를 수치 데이터를 처리하여 얻었다.

Abstract

A study is made of time-dependent flow of a viscous fluid driven by an oscillating shrouded disk in finite geometry. Numerical solutions to the Navier-Stokes equations are obtained for the flow in a cylindrical cavity with its upper endwall disk executing torsional oscillation at a velocity $\Omega\cos\lambda t$. Details of the three-component velocity field are examined at high Reynolds number. The value of the nondimensional amplitude of disk oscillation, $\varepsilon=\Omega/\lambda$, encompasses a range up to $\varepsilon \gtrsim O(1)$. The numerical results for the azimuthal flow for $\varepsilon<<1$ are consistent with the predictions of the earlier analytical model. The azimuthal flow is largely confined to the Stokes layer thickness. The analytical predictions of the meridional flow, based on a straightforward expansion technique, display discrepancies from the numerical results. The steady meridional streaming at finite values of ε is exhibited. The qualitative patterns of meridional steady streaming are verified by laboratory flow visualizations. The explicit effect of Re on the overall flow character is scrutinized. The numerical data are processed to describe the behavior of the torque coefficient at the oscillating disk.

NOMENCLATURE

A = aspect ratio of the cylinder [$\equiv \frac{H}{R}$]

A( ) = amplitude of the fluctuating component

C_{ke}=kinetic energy coefficient

C_T = torque coefficient

C_p= pressure coefficient

E = Ekman number [$\equiv \frac{\nu}{H^2 \Omega}$]

H = cylindrical container height

J = Bessel function

N= Brunt-Vaisala frequency [$\equiv \left(\frac{\alpha g \triangle T}{H} \right)^{\frac{1}{2}}$]

Nu = Nusselt number

Pr=Prandtl number [$\equiv \frac{\mu / \rho_B}{k/(\rho_B c_p)}$]

R = cylindrical container radius

Re = rotational Reynolds number [$\equiv \frac{R^2 \Omega}{\nu}$]

S = Stokes layer thickness [$\equiv \left(\frac{2\nu}{\lambda} \right)^{\frac{1}{2}}$]

St_A = stratification number

T = torque on the disk (in Chp.2) or temperature (in Chp.3)

T_B = temperature at the bottom disk

T_T = temperature at the top disk

c_p = specific heat

k = thermal conductivity

(r, ϕ, z) = cylindrical coordinates

(u, v, w) = velocity components

(u_f, w_f) = unsteady fluctuating parts of meridional flows

(u_s, w_s) = steady parts of meridional flows

GREEK SYMBOLS

Ω = mean rotation speed

$e\varepsilon$ = non-dimensional amplitude of oscillation

δ_s = non-dimensional Stokes layer thickness [$\equiv (2\nu/\lambda)^{1/2}/H$]

δ_E = non-dimensional Ekman layer thickness [$\equiv (2\nu/\Omega)^{1/2}/H$]

η_S = axial coordinate scaled by the Stokes layer thickness [$\equiv (H-z)/\ (2\nu/\lambda)^{1/2}$]

η_E = axial coordinate scaled by the Ekman layer thickness [$\equiv (H-z)/\ (2\nu/\Omega)^{1/2}$]

λ = torsional-oscillating frequency

μ = viscosity coefficient

ν = kinematic viscosity

θ = nondimensional temperature [$\equiv \frac{T-T_B}{\triangle T}$]

ρ = density

σ_{mn} = eigen-frequency

τ_i = spin-up time [$\equiv E^{-\frac{1}{2}}\ \Omega^{-1}$ for $\varepsilon > O(1)$, ($\equiv E^{-\frac{1}{2}}\ \Omega^{-1}\ \varepsilon^{-1}$ for $\varepsilon < O(1)$)]

Ψ = meridional streamfunction

ξ_{mn} = zeros of the first order Bessel function $J_1(\xi)$

SUBSCRIPTS

s = cycle-averaged component

f = unsteady fluctuating component

m = the number of waves or cells in the radial direction

n = the number of waves or cells in the axial direction

INTRODUCTION

Flow of a viscous fluid induced by a rotating disk constitutes a classical problem. The rudimentary configuration is flow in an infinite expanse of fluid, maintained by a steadily rotating infinite disk. The fluid at infinity is assumed to be at rest. The description of the three-component velocity field (u,v,w), under the assumption of axisymmetric, was given by von Karman [see e.g., Schlichting, 1968], in which similarity considerations were adopted. Depictions of several other fundamental flow configurations involving a rotating infinite disk have been documented in the textbooks. Subsequent authors considered the case of one (or more) rotating disk(s) of finite size. This represents an effort to move closer to realism. For many realistic systems, the rotating disk(s) is shrouded by a cylindrical sidewall, and the domain of flow is restricted to finite geometry. Numerical and experimental attempts have been reported, which illustrate the behavior of viscous fluid flow driven by rotating disk(s) at constant angular frequency in a confined apparatus [e.g., see Pao, 1971; Tomlan & Hudson, 1971; Alonso, 1975; Lang et al., 1994].

A perusal of the recent literature reveals that the majority of prior studies have been concerned with time-invariant flows, which are established by a steadily rotating disk. The problem of viscous flows caused by a disk executing a time-dependent rotation has received relatively little attention. The canonical setup in this case is when the disk performs torsional oscillations. The determination of the fluid flow is of direct relevance to practical techniques of measuring the coefficient of viscosity. Also, this presents a significant self-standing problem in fluid dynamics research. The knowledge gained from this elemental flow configuration offers baseline information. This is vital to a proper understanding of the flows about a disk, which undergoes a more complex unsteady rotational motion.

Early studies on torsional oscillations of a disk in a viscous fluid were undertaken by Rosenblat [1959]. In this model, the otherwise motionless fluid domain is assumed to be unbounded in space, and flows arise due to a small-amplitude torsional oscillation of an infinite plane disk. A systematic expansion of the velocity components in powers

of nondimensional oscillation amplitude was made, which resulted in a series of linear partial differential equations. One important achievement of this analysis is the identification of a second-order meridional flow, which consists of a steady term and a term of frequency twice that of the disk. An insightful interpretation of the primary (azimuthal) as well as secondary (meridional) velocity components was presented, and the inner structure of radial flow was scrutinized. Benney [1961], by means of an extended analytical methodology, discussed the applicability of higher approximations and of different geometrical conditions. The outcome of these theoretical endeavors of Benney [1961] was shown to be consistent with the essential results of Rosenblat [1959]. No other comparable independent studies appear to have been reported in the literature [Singh at al., 1988].

It is noted that these previous analytical models were formulated with several restrictive assumptions. In order to yield a tractable mathematical system, the analyses were inherently limited to the cases when the dimensionless amplitude of the disk oscillation was small. Another key assumption of the analysis was that the disk was infinite in size, and that an infinite expanse of fluid was considered. It is emphasized that the issues of a finite shrouded disk executing a finite-amplitude torsional oscillation have yet to be addressed. The present paper aims to tackle these technical points. The engineering relevance of flows driven by an oscillating disk has been noted in recent technological developments. Larrousse [1987] demonstrated potential applications of a continuous process of spin-up and spin-down, which can be simulated by an oscillating disk, in growing crystals. Also, the oscillating-disk flow serves as a rudimentary model in the important topic of fluid mixing [Ottino, 1990].

In this work, numerical studies and laboratory flow visualizations have been made of more practically relevant flows of a viscous fluid in a cylinder, which are driven by a finite, shrouded, torsionally-oscillating endwall disk.

Numerical solutions to the unapproximated Navier-Stokes equations are secured for the flow in a closed cylindrical container of radius R. For definiteness, the angular velocity of the upper endwall disk at z=H is $\Omega\cos\lambda t$, and the rest of the cylindrical surface walls are at rest. In accordance with the original problem statement, the

rotational Reynolds number, $Re=R^2 \Omega/\nu$, where ν denotes the kinematic viscosity, emerges to be the major parameter. In the present paper, concern is directed to the situations in which Re>>1; this is of direct relevance to industrial applications. The nondimensional amplitude of the disk oscillation, $\varepsilon \equiv \Omega/\lambda$, is permitted to encompass a broad range up to $\varepsilon > O(1)$. This relaxes the restriction, $\varepsilon << 1$, of the preceding theoretical analysis. The time-dependent numerical solutions are processed to exhibit principal features of three-dimensional flow fields. The primary interest is focused on the flow characteristics in the central portions of the cylinder interior, where the sidewall effects are minimal. The structure of the azimuthal flow, both time-averaged and fluctuating parts, is scrutinized. The presence of significant meridional flows is discussed; and, in particular, the quasi-steady periodic behavior of meridional flows is examined. In the interior region far away from the sidewall, the gross features of azimuthal flow are shown to be in accord with the analytical predictions when e is small. Laboratory flow visualization experiments have been conducted to verify the qualitative patterns of the meridional streaming. The numerically-constructed flow fields are shown to be consistent with the visualizations.

The numerical flow data have been processed to evaluate the time-dependent torque experienced by the oscillating disk. The explicit effects of Re and e are delineated, which will be of interest to practical techniques of measuring viscosity.

The numerical model

As shown in Fig. 2.1, an incompressible fluid of density r fills completely a cylindrical container. The aspect ratio A(=H/R) is, for most computations, O(1). The fluid is in contact with the upper endwall disk (z=H), and no free surface exists. Denoting the velocity components (u,v,w) for cylindrical coordinates (r, ϕ,z), the fluid motion is governed by the axisymmetric, time-dependent, Navier-Stokes equations :

$$\frac{\partial u}{\partial t} = -\frac{1}{r}\frac{\partial}{\partial r}(ruu) - \frac{\partial}{\partial z}(uw) + \frac{v^2}{r} - \frac{1}{\rho}\frac{\partial p}{\partial r} + \nu\left[\frac{\partial}{\partial r}\frac{1}{r}\frac{\partial}{\partial r}(ru) + \frac{\partial^2 u}{\partial z^2}\right] \tag{2.1}$$

$$\frac{\partial v}{\partial t} = -\frac{1}{r}\frac{\partial}{\partial r}(ruv) - \frac{\partial}{\partial z}(vw) + \frac{uv}{r} + \nu\left[\frac{\partial}{\partial r}\frac{1}{r}\frac{\partial}{\partial r}(rv) + \frac{\partial^2 v}{\partial z^2}\right] \tag{2.2}$$

$$\frac{\partial w}{\partial t} = -\frac{1}{r}\frac{\partial}{\partial r}(ruw) - \frac{\partial}{\partial z}(uw) - \frac{1}{\rho}\frac{\partial p}{\partial z} + \nu\left[\frac{1}{r}\frac{\partial}{\partial r}\left(r\frac{\partial w}{\partial r}\right) + \frac{\partial^2 w}{\partial z^2}\right] \tag{2.3}$$

$$\frac{1}{r}\frac{\partial}{\partial r}(ru) + \frac{\partial w}{\partial z} = 0 \tag{2.4}$$

At the initial state, the fluid is at rest

$$u=v=w=0 \text{ at } t=0. \tag{2.5}$$

All computations were started from an initially motionless state, and at time zero a rotational speed is imposed on the top disk. The thrust of the present effort lies in the large-time, quasi-steady, periodic behavior. In accordance with the problem statement, the boundary conditions are

$$u=v=w=0 \qquad \text{at } r=R \tag{2.6}$$

$$u=v=w=0 \qquad \text{at } z=0 \tag{2.7}$$

$$u=w=0,\ v=r\Omega\cos\lambda t \qquad \text{at } z=H. \tag{2.8}$$

where $\Omega=\varepsilon\lambda$. To satisfy numerical stability requirements, the boundary conditions at

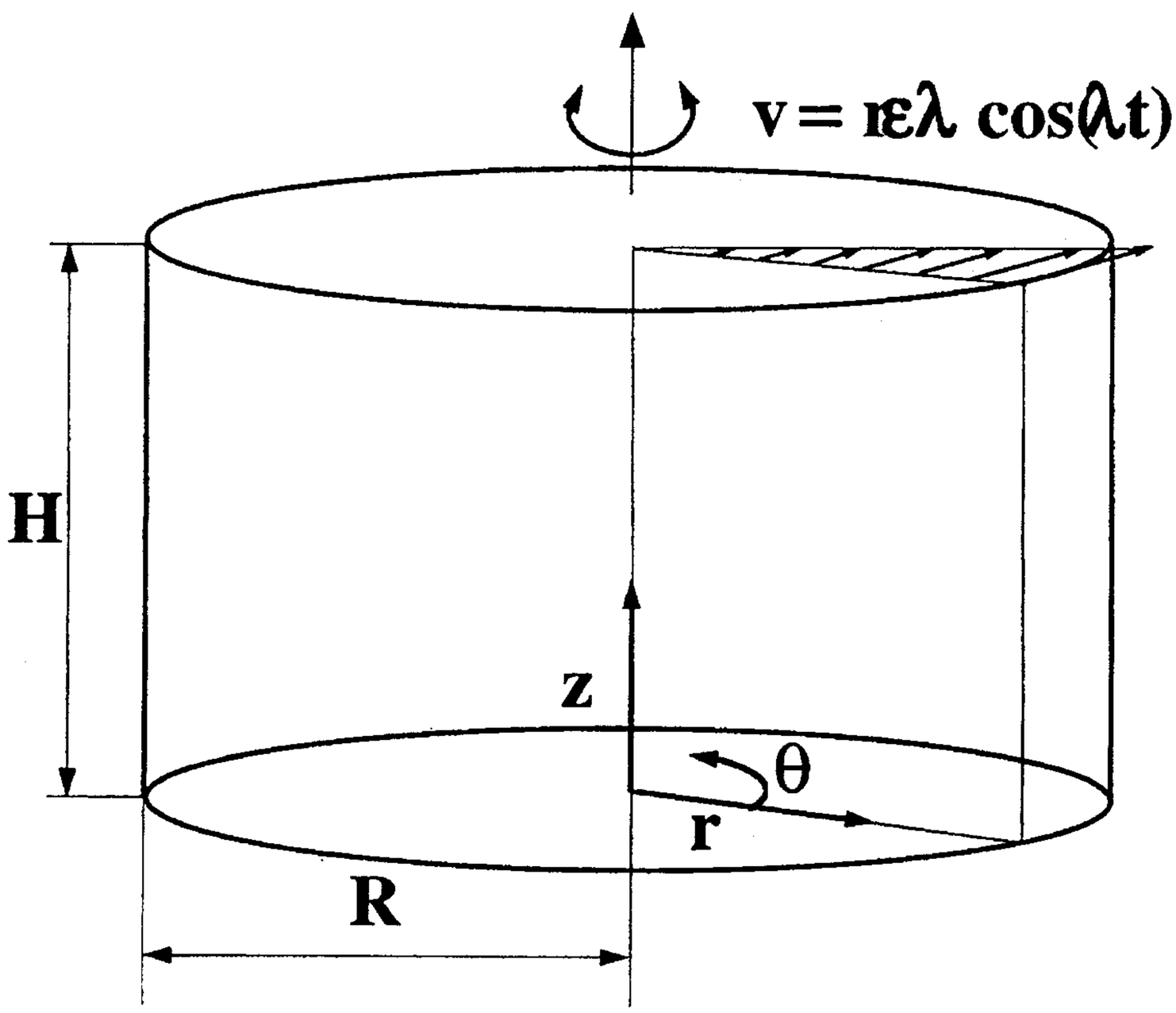

Figure 2.1 Flow geometry and coordinate system.

the central axis are applied at a small, but finite, radius ($r=r_i$) [see Warn-Varnas et al., 1978]:

$$u=0, \quad \frac{\partial(v/r)}{\partial r}=0, \quad \frac{\partial w}{\partial r}=0 \qquad \text{at } r=r_i$$

The above system of equations is solved by using a well-established finite-difference numerical procedure. The numerical model selected is essentially a mark-and-cell scheme, and it has been validated in a number of rotating flow simulations [e.g., Warn-Varnas et al.,1978; Hyun et al., 1983]. The specifics of the numerical schemes and algorithms have been documented [Williams, 1969; Warn-Varnas et al., 1978], and they are not reproduced here. The highlights of this numerical model are that the Poisson equation is solved by an ADI iterative approach and the differencing performed on a staggered mesh. Grid points were clustered near the solid boundaries, particularly near the oscillating upper endwall disk. Restrictions on the time step are subject to the Courant-Friedrichs-Lewy condition $\Delta t \leq \Delta s/u_{max}$, where Δs is the smallest grid spacing and u_{max} is the largest velocity. Convergence was declared when the relative difference between two successive iterations fell below 10^{-5}. The time step Δt was taken to be sufficiently small to insure both numerical stability and resolution of the results. To determine the number of grid points necessary to obtain grid-independent solutions, a series of calculations with different space discretization have been conducted. Exemplary results of this test are shown in Fig. 2.2, which demonstrate the grid-convergence based on such comprehensive studies. For most computations, the mesh network was typically (52X62) in the (r-z) axial plane, and Δt was chosen such that one oscillating cycle consisted of 2048($=2^{11}$) time steps. In the case of a steady rotating disk, numerical results were in excellent agreement with the experimental data obtained by using the LDA technique [Sorensen & Loc, 1989].

Time-dependent solutions were produced by executing a time-marching integration of the governing equations. Guided by the preceding studies on spin-up [Greenspan & Howard, 1963; Wedemeyer, 1964], the transitory time τ_t to reach the quasi-steady

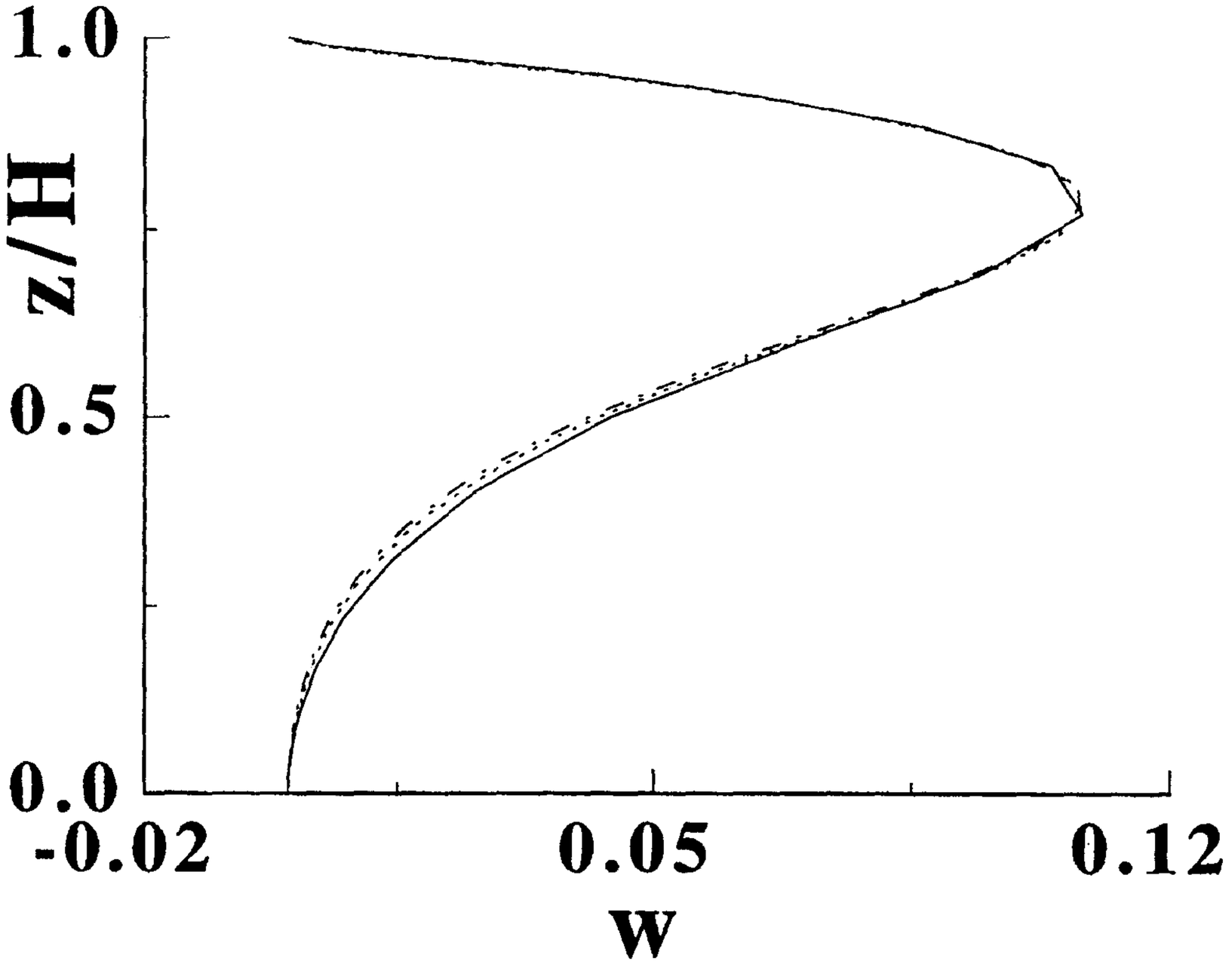

Figure 2.2 Exemplary results of grid-convergence tests. Re=500, A=1.0, ε=1.0, and at r/R=0.5. Grid points are: , 22X22; ..... ,52X52; . , 82X82.

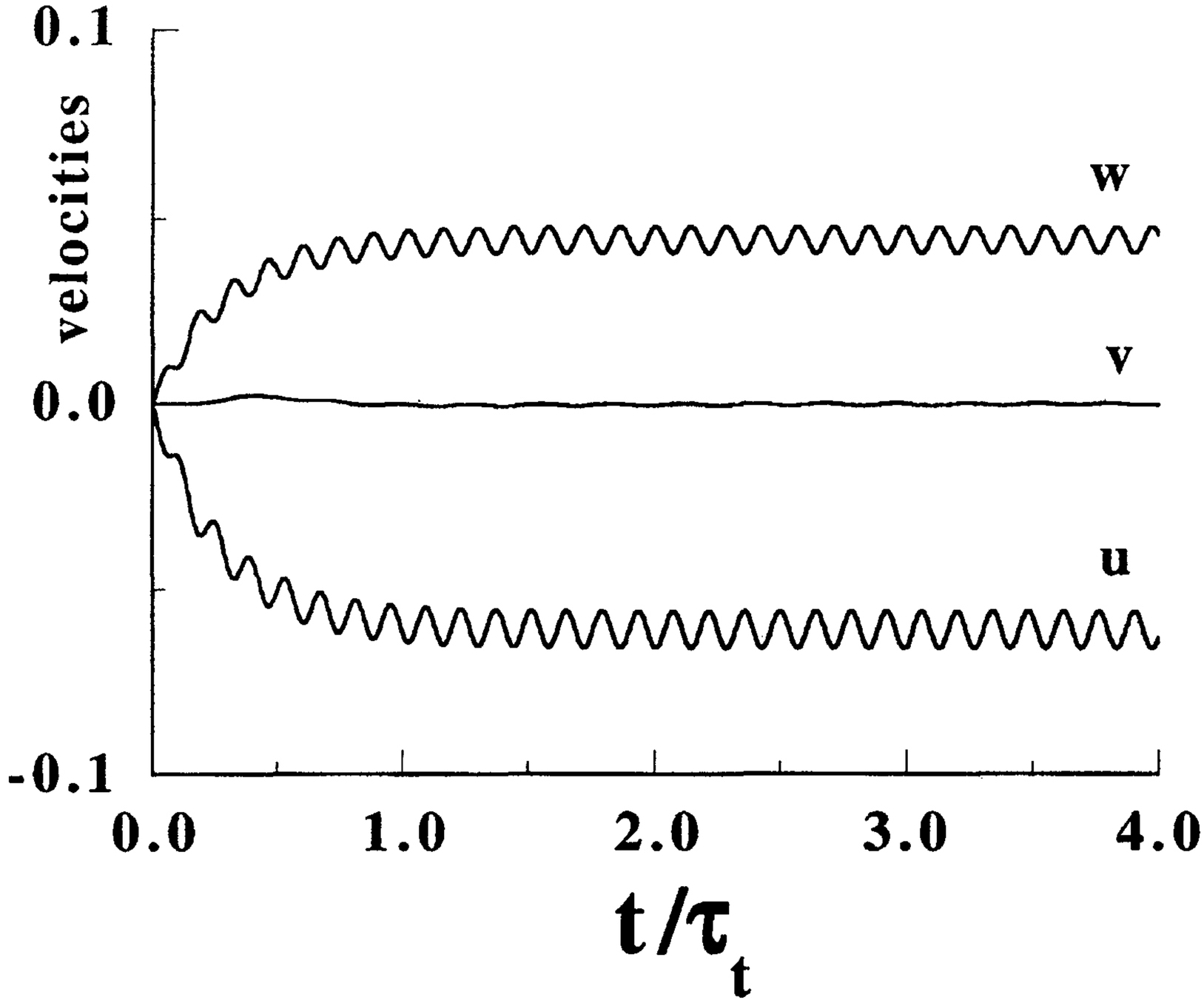

Figure 2.3 Examplary plots of velocity evolutions. Re=500, A=1.0, and ε=1.0. Position is at r/R=0.5, z/H=0.5.

periodic state is estimated as

$$\tau_t \sim E^{-1/2}\ \Omega^{-1} \qquad \varepsilon > O(1) \qquad (2.9)$$

$$\tau_t \sim E^{-1/2}\ \Omega^{-1}\ \varepsilon^{-1} \qquad \varepsilon < O(1)$$

in which E($\equiv \frac{\nu}{\Omega H^2}$) is the Ekman number. The estimate of τ_t for $\varepsilon < O(1)$ is also consistent with the prediction by the theoretical analysis of Rosenblat [1959] In the present study, calculations continued up to a time level of nearly $2\tau_t$, at which the quasi-steady state was shown to have been established. Details of temporal evolutions of the numerical data are exemplified in Fig. 2.3. Typically, the transitory stage from t=0 to the quasi-steady state encompasses less than ten cycles. In the present study, the quasi-steady state was thought to have been established when the nondimensional values of the flow variables differ less than 10^{-5} over the interval of one cycle.

Quantitative assessments of the numerical accuracy of the present calculations have been made. The azimuthal velocity at mid-radius and at z/H=0.98 of the cylinder, obtained by using the (52X62) mesh, for values of e smaller than 0.1, was in agreement with the analytical result of Rosenblat [1959] within 1%. Also, for several sample cases, comparisons were made between the present results and the results acquired by employing the numerical code based on the SIMPLE algorithm [Patankar, 1980]. These two sets of data were mutually consistent to a high degree of accuracy.

Results and discussion

The numerical results for an aspect ratio A=1.0 are to be scrutinized. No noticeable qualitative changes are observed as Re varies, from Re=100 to 2000, thus in the ensuing discussions, the results at Re=500 are exemplified. Also, as stated earlier, the flow structure in the central interior region is of interest. This is the region in which the direct effects of the sidewall are minimized, and, therefore, cross-comparisons of the numerical results with the theoretical predictions are meaningful in this central interior

region.

First, the azimuthal velocity structure is examined. The analysis of Rosenblat gave a closed-form expression for v as

$$v=\varepsilon\lambda r\{\ G_0+\ \varepsilon^{2}\ G_2\}, \tag{2.10}$$

in which

$$G_0=\ e^{-\eta}\cos(\lambda t-\eta), \tag{2.11}$$

and $\eta\equiv z/\ (2\nu/\lambda)^{1/2}$ denotes the axial coordinate scaled by the Stokes shear layer thickness $S\equiv\ (2\nu/\lambda)^{1/2}$. The first term in (10) indicates the classical Stokes shear-wave solution for an infinite flat plate executing a rectilinear torsional oscillation in its own plane in a fluid otherwise at rest [see, e.g., Schlichting, 1968]. The G_2 term represents the second-order correction to v, and G_2 contains higher harmonics up to 3λ. The detailed expression for G_2 is very lengthy and complicated, and the reader is referred to equations (44a)-(44b) of the original paper by Rosenblat. Notice again that the validity of the analytical approach of Rosenblat is restricted by the requirement that ε be small.

Fig. 2.4 illustrates the axial profile of v in the central area (r/R=0.5). Clearly, when ε is small, almost perfect agreement is seen between the numerical results and the analytical predictions. Much of the azimuthal velocities are confined to the Stokes layer, and v decays rapidly outside of the Stokes layer. As ε increases, the axial extent of non-vanishing v increases. The comprehensive data on v demonstrate that, when ε is small, the dominant behavior of v in the interior core is describable by the Stokes shear-wave solution at the primary harmonic. As seen in Fig. 2.4, as ε becomes finite, the contributions of higher harmonics are not negligible, and the v-profiles exhibit more complex patterns over a broader region into the fluid. It is important to observe that, even when ε is appreciable, the dominant parts of non-vanishing v-profiles are still concentrated to the Stokes layer thickness. In the figures, the nondimensional axial coordinate scaled by the Stokes shear layer thickness S is indicated in the parenthesis. Note the difference in scales used in the ordinates of Fig. 2.4.

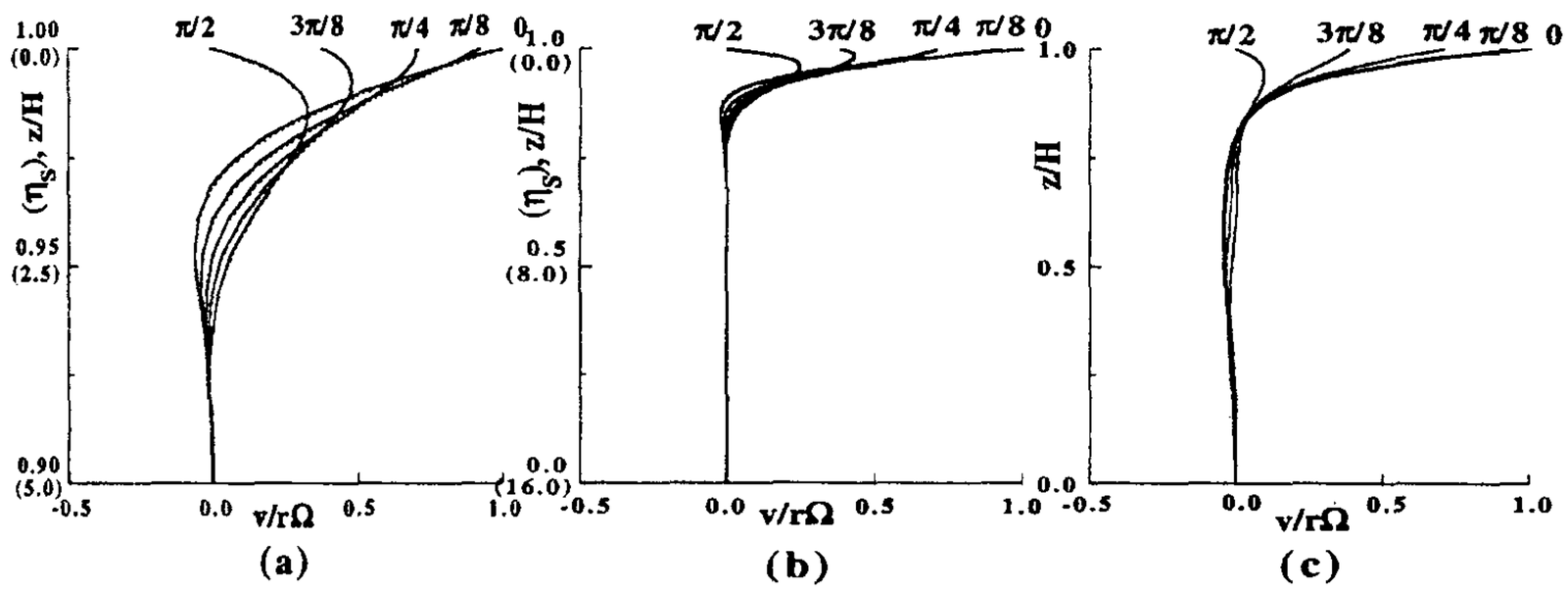

Figure 2.4 Azimuthal velocity profile, $\frac{v}{r\varepsilon\lambda}$ versus z/H . In (a), ——— , numerical results; ..... , analytical solutions. No analytical solutions are given in plots (b) and (c). Times for the curves are λt=0, λt=π/8, λt=π/4, λt=3π/8, λt=π/2. (a) ε=0.1, (b) ε=1.0, (c) ε=5.0.

One prominent distinction between the case of a rectilinearly oscillating flat plate and the case of a circularly oscillating disk lies in the meridional flow. It is well-known that, for the classical Stokes problem involving a rectilinearly oscillating infinite flat plate, meridional flows are identically zero. However, for the problem of a circularly oscillating disk, the presence of meridional flows (u,w) is a crucial element in the overall dynamics.

In conformity with the customary treatment, the meridional flows (u,w) are decomposed into time-averaged steady parts (u_s,w_s) and unsteady fluctuating parts (u_f,w_f), respectively. Rosenblat, by assuming $\varepsilon \ll 1$, carried out regular expansion procedures up to the first order in ε. These manipulations produced closed-form solutions for (u_s,w_s) as well as (u_f,w_f), as stipulated in equations (31)-(34) of Rosenblat [1959]. For the sake of completeness, these analytical solutions are reproduced here :

$$u_f = \frac{r\varepsilon^2\lambda}{4}\left\{e^{-\sqrt{2}\eta}\sin\left(2\tau-\sqrt{2}\eta\right)-e^{-2\eta}\sin\left(2\tau-2\eta\right)\right\} \tag{2.12}$$

$$w_f = \frac{\varepsilon^2\lambda}{8}\sqrt{\frac{2\nu}{\lambda}}\left\{\begin{array}{l}\left(2-\sqrt{2}\right)\cos\left(2\tau+\frac{1}{4}\pi\right)\\ -2e^{-\sqrt{2}\eta}\cos\left(2\tau-\sqrt{2}\eta+\frac{1}{4}\pi\right)+\sqrt{2}e^{-2\eta}\cos\left(2\tau-2\eta+\frac{1}{4}\pi\right)\end{array}\right\} \tag{2.13}$$

$$u_s = \frac{r\varepsilon^2\lambda}{4}\left\{1-e^{-2\eta}\right\} \tag{2.14}$$

$$w_s = \frac{\varepsilon^2\lambda}{4}\sqrt{\frac{2\nu}{\lambda}}\left\{1-2\eta-e^{-2\eta}\right\} \tag{2.15}$$

However, in a later development in the same paper, Rosenblat asserted the inadequacy of such a straightforward expansion technique which led to eqns.(2.12)-(2.15). This deficiency turned up in an unacceptable behavior of u_s and w_s at far fields from the disk. In an effort to rectify this shortcoming of the regular expansion approach, Rosenblat proposed an approximate Pohlhausen-type integral method to obtain an estimate of the axial extent of the region of non-vanishing steady radial flow. The particulars of this methodology are long and they are elaborated in eqns. (58)-(62) of Rosenblat [1959], to which the interested reader is referred.

Fig. 2.5 displays the axial profiles of u_f. Again, when ε is very small, nearly

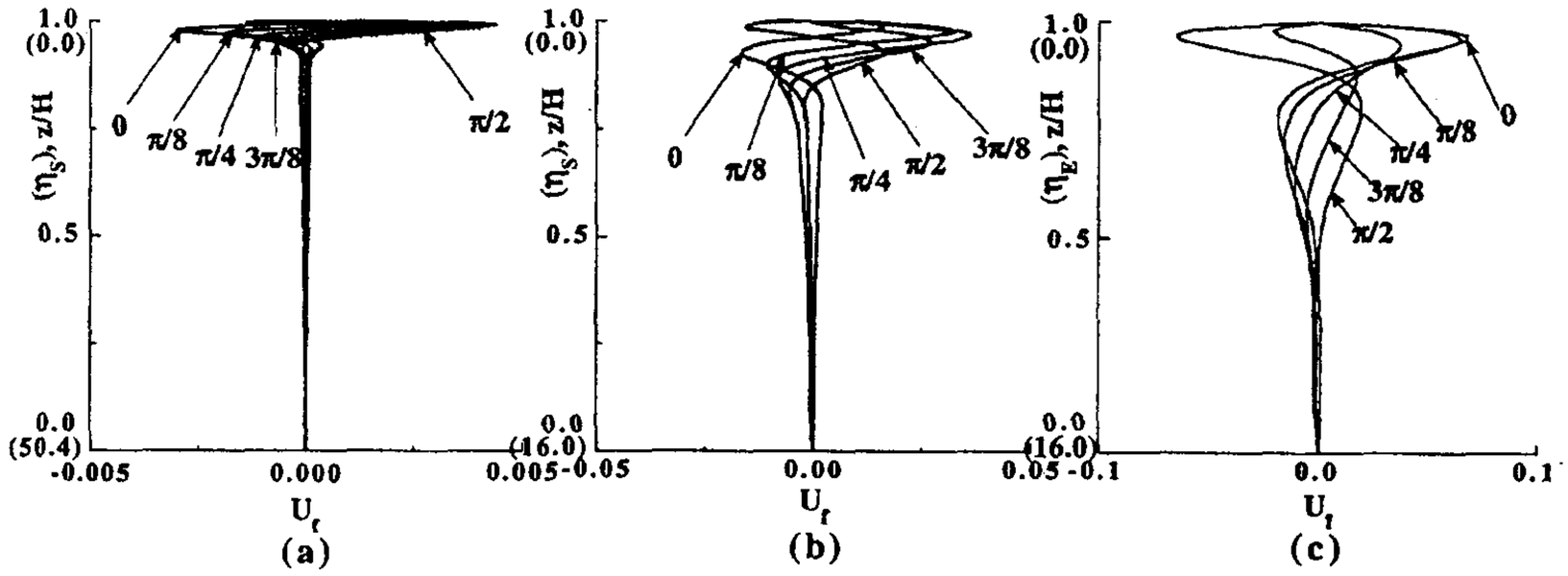

Figure 2.5 Profile of the fluctuating part of radial velocity, $U_f[\equiv \frac{u_f}{r\varepsilon\lambda}]$ versus z/H. ——— , numerical results ; ..... , analytical solutions [eqn.(2.12)]. Times for the curves are $\lambda t=0$, $\lambda t=\pi/8$, $\lambda t=\pi/4$, $\lambda t=3\pi/8$, $\lambda t=\pi/2$.

(a) $\varepsilon=0.1$, (b) $\varepsilon=1.0$, (c) $\varepsilon=5.0$.

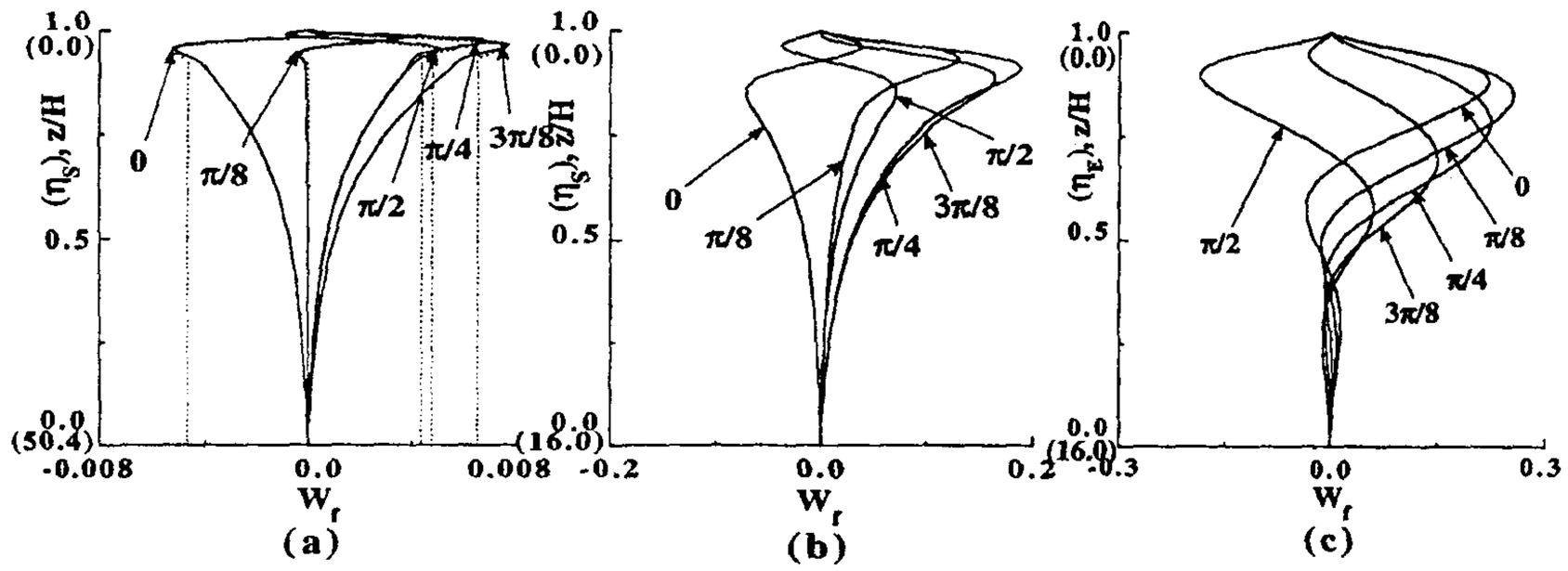

Figure 2.6 Profile of the fluctuating part of axial velocity, $W_f[\equiv \frac{w_f\, Re^{1/2}}{R\varepsilon\lambda}]$ versus z/H: ——————, numerical results; ..... , analytical solutions [eqn.(2.13)]. Times for the curves are $\lambda t=0$, $\lambda t=\pi/8$, $\lambda t=\pi/4$, $\lambda t=3\pi/8$, $\lambda t=\pi/2$.

(a) $\varepsilon=0.1$, (b) $\varepsilon=1.0$, (c) $\varepsilon=5.0$.

complete agreement is discernible between the numerical results and the analytical solutions [eqn (2.12)]. The non-vanishing u_f is concentrated to the Stokes layer thickness $S\sim (2\nu/\lambda)^{1/2}$, and u_f is practically zero outside the Stokes layer. This implies that, in the interior region outside the Stokes layer thickness, the fluctuating

part of radial velocity is negligibly small. When ε is appreciable, the dominant parts of non-vanishing u_f-profiles are still concentrated to the Stokes layer thickness. Note that, even when ε is finite, the principal parts of non-vanishing u_f are still largely confined to the Stokes layer thickness. In Fig. 2.5, for the sake of comparisons, the coordinates z based on the Stokes layer thickness, $\delta_S = (2\nu/\lambda)^{1/2}/H$, and the Ekman layer thickness, $\delta_E = (2\nu/\varepsilon\lambda)^{1/2}/H$, are indicated in the parentheses.

The pattern of w_f is also revealing, as shown in Fig.2.6. As portrayed in Eqn. (2.13), the first term of w_f is not a function of z, and only the second and third terms decay exponentially outside the Stokes layer. Also, note that the overall magnitude of w_f is O(S/r) of u_f. At moderate radii [e.g., see the curves at r/R=0.5 in Fig. 2.6], the Stokes layer thickness S is much smaller than the radial distance r. Therefore, it is important to recognize that w_f is indeed orders of magnitude smaller than u_f for the parameter values of present concern. The profiles of w_f illustrate considerable discrepancies between the numerical results and the predictions. It is noteworthy that the infinite-disk linearized analytical model of Rosenblat gives almost axially-uniform w_f outside of the Stokes layer. This is in contrast to the numerical results, which exhibit an appreciable z-dependence of w_f throughout much of the interior region. This is believed to be attributable to the general inadequacy of the straightforward regular series expansion technique adopted in Rosenblat.

A significant feature of the present investigation is the behavior of steady parts of meridional flows, i.e., (u_s,w_s). As stressed earlier, eqns.(2.14) and (2.15) were acquired by Rosenblat in a series-expansion formalism. Of particular interest are the far-field patterns of (u_s,w_s) at large distances away from the oscillating disk. First, u_s-profiles are exemplified in Fig. 2.7. The numerical results show that, near the oscillating disk, a positive u_s is discernible, implying the existence of steady radially-outward flow. This has to be balanced by a negative u_s (radially-inward flow) at mid-height axial locations.

In the bottom region of the cylinder, u_s approaches zero to satisfy the no-slip condition at the lower stationary disk. It is evident in Fig. 2.7 that eqn.(2.14), termed the potential-flow solution by Rosenblat, yields an inappropriate picture for u_s in much of the axial extent. As is apparent in Fig. 2.7, this potential-flow solution (shown by dots) gives a constant, finite value of u_s at the far fields, which begins at a small axial distance from the disk. In conjunction with this constant-u_s in the bulk of the interior, w_s of eqn.(2.15) [as shown by dots in Fig.2.8] diverges almost linearly as z moves away from the disk. These far-field solutions of u_s and w_s, of eqns.(2.14) and (2.15), which are the results of a straightforward series-expansion technique, are clearly unacceptable. This anomalous behavior was pointed out by Rosenblat himself, and he proposed an amended calculation procedure based on an approximate Pohlhausen-type method. The crux of this improved representation of u_s is that the convective inertia terms have to be properly included in the determination of flow character at large distances from the disk. The dashed lines of Figs.2.7&2.8 are the results computed following the modified version of Rosenblat's analytical prediction. As illuminated in Fig.2.7, the qualitative trends of this improved solution are consistent with the numerical results, although quantitative discrepancies are apparent. As is evident in eqns.(2.14) and (15), the overall magnitude of w_s is O(S/r) of u_s. This points to the overall smallness of w_s in comparison to u_s in realistic situations. The axial profiles of w_s, exhibited in Fig.8, clearly demonstrate that a non-vanishing positive w_s is discernible up to moderate axial distances from the upper oscillating disk. This asserts that, in the bulk of the central interior region of the cylinder, a steady axial streaming toward the oscillating disk exists. As ε increases, the impact of this steady pumping effect is felt in a broader axial extent and its strength becomes more pronounced in the region father away from the oscillating disk.

Utilizing the numerical solutions, depictions are made in Fig. 2.9 of the global pattern of clockwise-circulatory steady meridional streaming. In Fig. 2.9, plots of the meridional streamfunction Ψ for u_s and w_s are given. Here, Ψ is defined such that $u_s = \frac{1}{r}\frac{\partial \Psi}{\partial z}$, $w_s = -\frac{1}{r}\frac{\partial \Psi}{\partial r}$. The oscillation of the disk generates steady axial motions

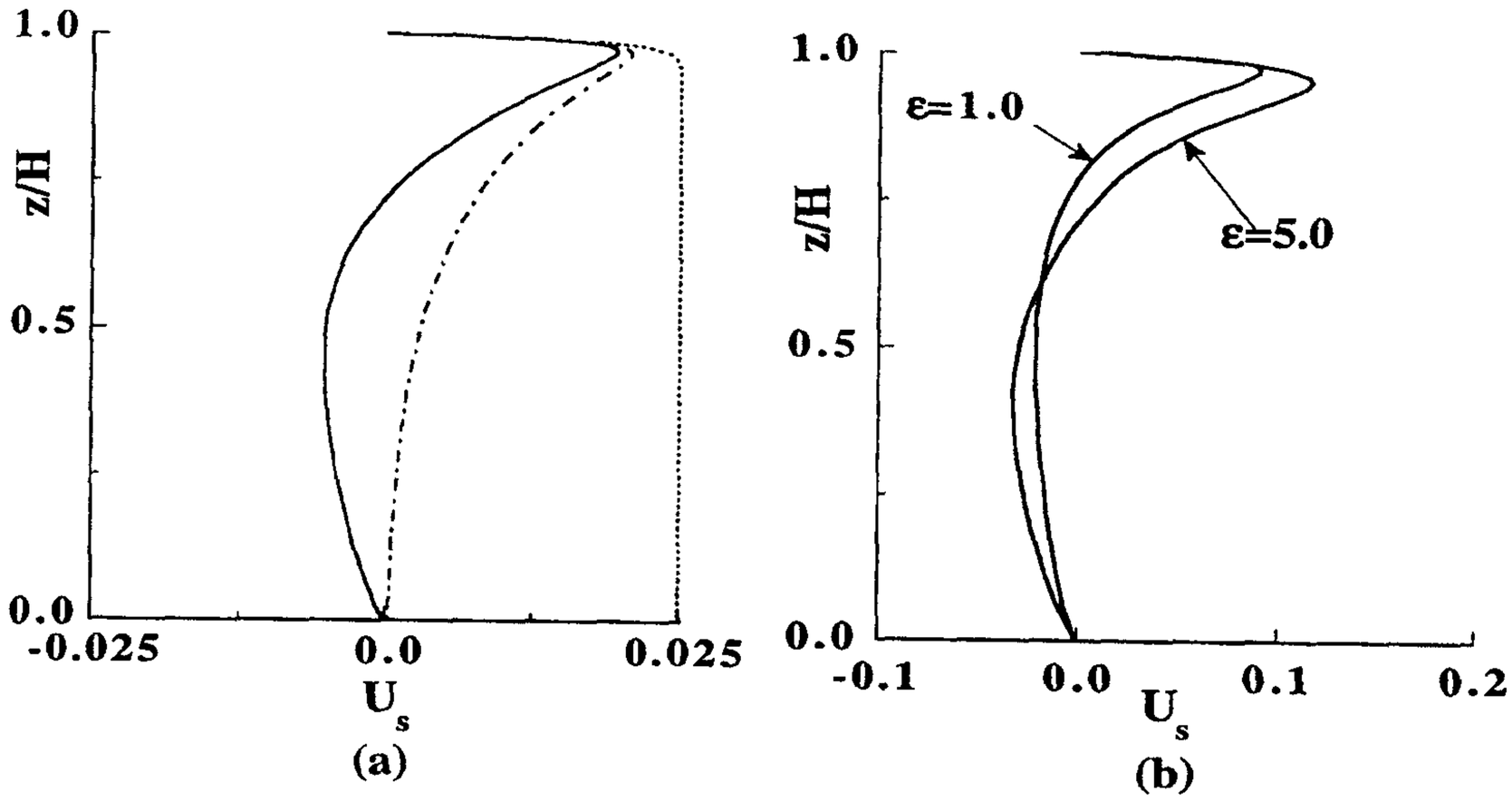

Figure 2.7 Profile of the steady part of radial velocity, $U_s[\equiv \frac{u_s}{r\epsilon\lambda}]$ versus z/H : ——— ——— ——— , numerical results ; ——— . , improved analytical solution [eqn. (59) of Rosenblat]; ..... , analytical solution [eqn.(2.14)].

(a) ε=0.1, (b) ε=1.0 & 5.0.

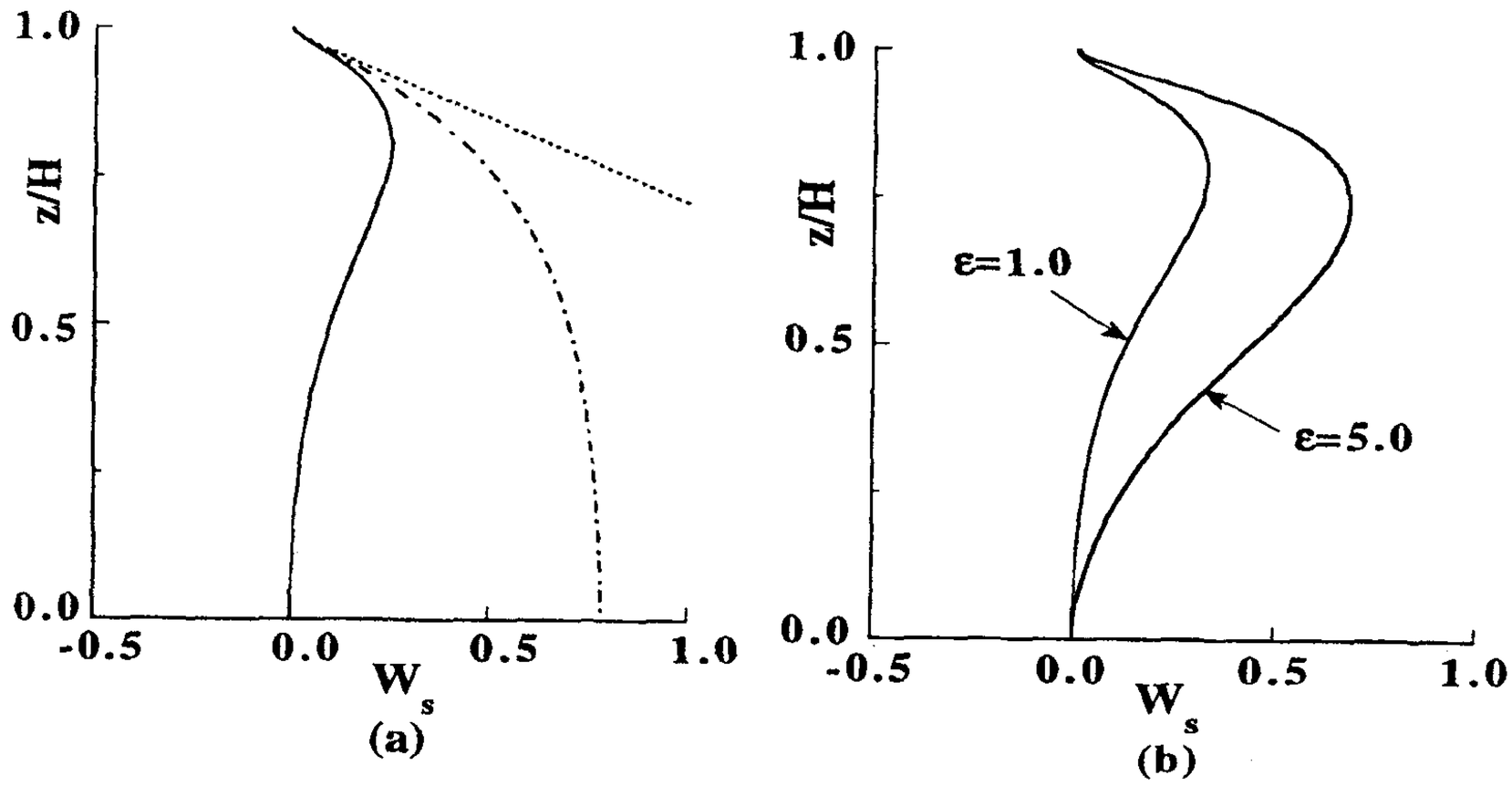

Figure 2.8 Profile of the steady part of axial velocity, $W_s[\equiv \frac{w_s\, Re^{1/2}}{R\varepsilon\lambda}]$ versus z/H : ..... , numerical results ; .... , improved analytical solution [eqn. (59) of Rosenblat]; ..... , analytical solution [eqn. (2.15)]. (a) ε=0.1, (b) ε=1.0 & 5.0.

toward the oscillating disk at small and moderate radii. In the vicinity of the oscillating disk, the fluid is propelled radially outward. At large radii near the cylindrical sidewall, constrained by the finite geometry of the cylinder, the steady streaming turns away from the upper disk along the sidewall. This completes the overall circulatory path. The qualitative pattern of circulation remains largely unchanged as ε increases to a finite value; however, as anticipated, the flow intensifies as ε increases, as reflected in the maximum Ψ-values in Fig. 2.9. In summary, the present numerical solutions clearly demonstrate the existence of a small, but non-vanishing, steady meridional streaming, which is maintained by the disk oscillation. In the region near the hub, the meridional steady streaming is very weak, as demonstrated in Fig. 2.9.

Companion laboratory flow visualizations were performed to portray the qualitative patterns of the meridional streaming. The experimental apparatus consisted of a closed cylindrical cavity (R=5.4 cm, H=5.4 cm) fabricated with plexiglass, together with an AC servo-motor unit which was controlled by a function generator, a slitbeam generator and photographic image-recording devices interfaced with a computer [see Choi et al., 1989,1991; Lim et al., 1993]. The time interval between successive photographic frames was chosen to be larger then the period of the oscillating disk. Typically, six consecutive frames were overlapped to produce images of steady streaming; an example is displayed in Fig.2.10 [for Re=496, A=1.0, ε=1.1]. The working fluid was a water-glycerine mixture. A number of such flow visualizations were made for varying values of Re, ε, and they show qualitative agreement with the numerically-constructed meridional steady streamings.

The azimuthal flow data near the oscillating disk were processed to determine the torque T experienced by the disk:

$$T = 2\pi\rho\nu \int_0^R \left(\frac{\partial v(r, z=H, t}{\partial z} \right) r^2 dr, \tag{2.16}$$

from which the torque coefficient C_T is computed as

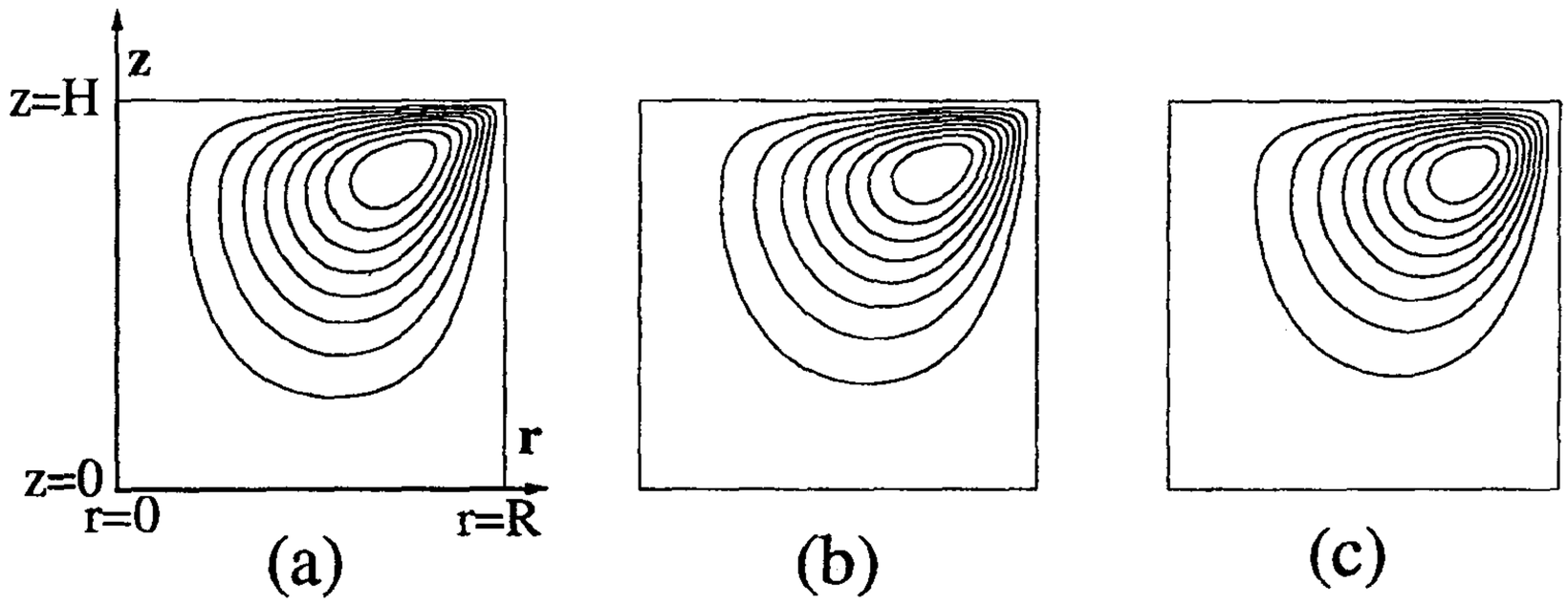

Figure 2.9 Plots of meridional stream function Ψ for steady meridional flows (u_s,w_s), nondimensionalized by $\varepsilon\lambda R^3 Re^{-1/2}$. $|\Psi|_{max}$ denotes the maximum value of Ψ, and $\Delta\Psi$ the contour increment.

(a) ε=0.1, $|\Psi|_{max}$ = 0.0689, $\Delta\Psi$ =0.00689;

(b) ε=1.0, $|\Psi|_{max}$ = 0.137, $\Delta\Psi$ =0.0137;

(c) ε=5.0, $|\Psi|_{max}$ = 0.162, $\Delta\Psi$ = 0.0162.

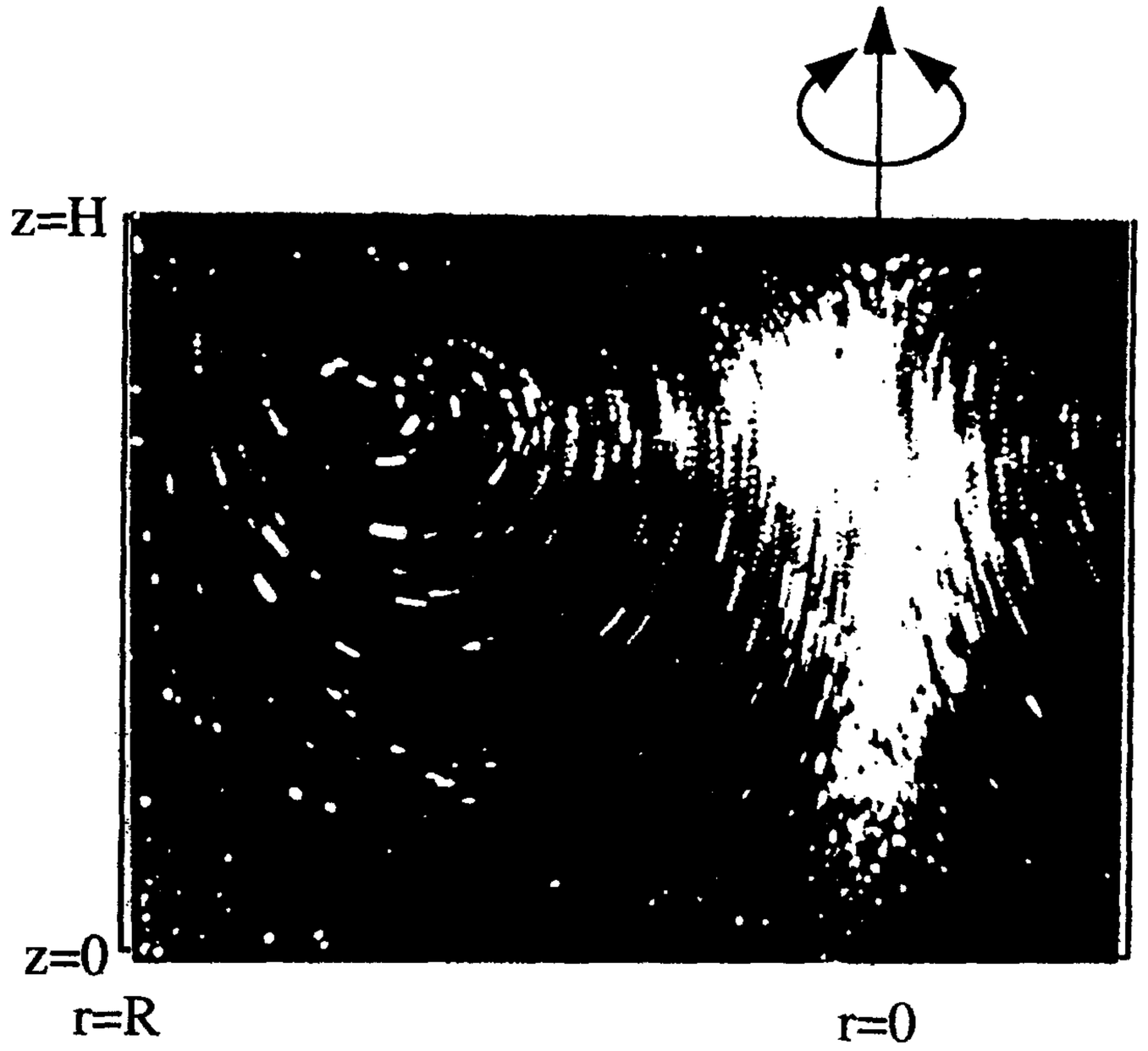

Figure 2.10 Exemplary flow visualization of meridional steady streaming. Conditions are: Re=496, ε=1.1, and A=1.0. The uncertainty in measuring the location is estimated to be 8 percent.

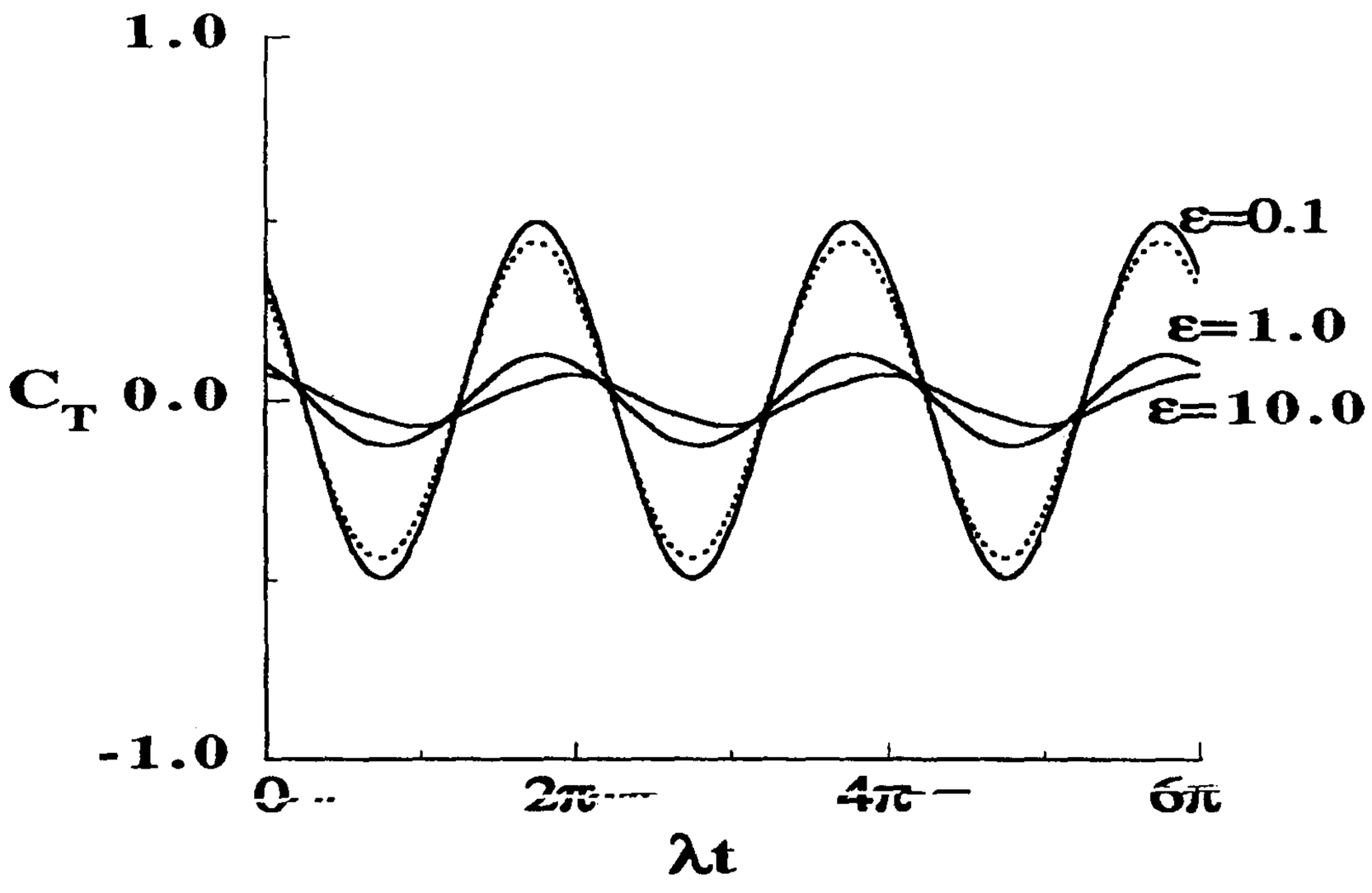

Figure 2.11 Time history of torque coefficient, C_T ———— , numerical results for ε=0.1, 1.0, and 10.0; - - - - , Rosenblat's solution for ε=0.1.

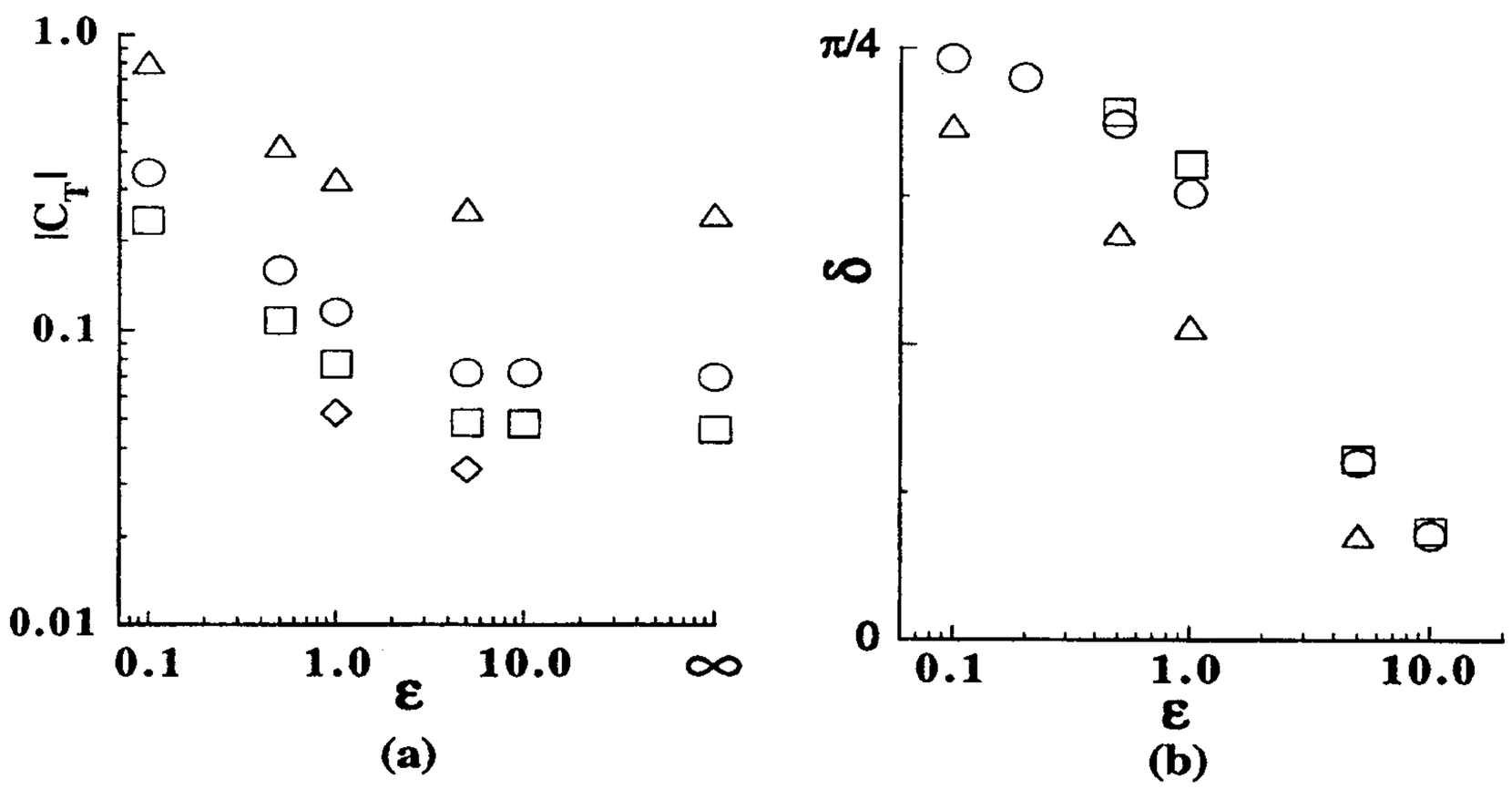

Figure 2.12 Behavior of $|C_T|$ and δ with ε and Re. △,Re=100; ○,Re=500; □, Re=1000; ◇, Re=2000. (a) $|C_T|$, (b) δ.

$$C_T = \frac{2T}{\rho R^5 \Omega^2}. \quad (2.17)$$

Typical time histories of C_T are displayed in Fig.2.11. The application of the fast Fourier transform indicates that C_T. is dominated by the base harmonic for $\varepsilon < O(1)$, and the magnitudes of the higher-harmonic terms are typically less then 1% of the base-harmonic term. In the case of ε=5.0, the magnitude of the third-harmonic(3λ) is about 5% of that of the base harmonic. Consequently, for the parameter values of present interest, C_T can be approximated as

$$C_T \cong |C_T| \cos(\lambda t + \delta). \quad (2.18)$$

The variations of $|C_T|$ and δ with ε and Re are shown in Fig.2.12. As anticipated, when ε is very small, the phase of C_T is π/4 ahead of the disk oscillation. These findings on $|C_T|$ and δ for ε<<1 are in line with the theoretical prediction. The present results show that, as e increases, δ decreases, implying that the phase lead is reduced. The amplitude $|C_T|$ decreases substantially as ε or Re increases.

Conclusion

Much of the azimuthal velocities are confined to the Stokes layer. When ε is small, the analytical predictions of v are in excellent agreement with the numerical results. As ε increases, the effects of the higher harmonics are felt, and the v-profiles display more complex patterns in a broader axial extent.

The unsteady fluctuating part of the radial velocity, u_f , is largely confined to the Stokes layer thickness. The fluctuating part of the axial velocity, w_f , is much smaller than u_f for the parameter values of present concern. The analytical predictions for w_f , based on the straightforward regular expansion technique, show substantial variances with the numerical solutions.

The behavior of (u_s, w_s), the steady part of the meridional velocity, is analyzed in detail. Near the oscillating disk, a steady radially-outward flow is seen. At mid-height axial locations, a radially-inward flow is present. In the region near the stationary disk, u_s approaches zero. A non-vanishing w_s is discernible up to moderate axial distances from the oscillating disk. In the bulk of the central interior region, a steady axial streaming toward the oscillating disk exists. As ε increases, the steady streaming becomes more pronounced in a broader axial extent.

The torque coefficient is dominated by the base harmonic. The phase advance of $|C_T|$ over the disk oscillation decreases as ε increases or Re decreases. Also, $|C_T|$ is reduced substantially as e increases to a value of O(1) or Re increases. In the region of $\varepsilon > O(1)$, as ε increases, $|C_T|$ converges to the values of the steady rotating disk.

제 6 장

Natural convection in an enclosure having a vertical sidewall with time-varying temperature

(측벽에 시간에 따른 온도변화를 가한 용기내의 자연대류)

요 약 문

측벽의 온도가 시간에 따라 변하고 내부에 비압축성, 부시네스크 유체가 가득 채워진 밀폐용기 내에서의 자연대류현상에 대한 연구가 수치적으로 행해졌다. 차가운 옆벽면은 일정온도 T_C로 유지되고 마주보는 벽면은 온도가 $T_H = \overline{T_H} + \Delta T' \sin ft$ 로 시간에 따라 변하는 가열벽면이다. 비정상 Navier-Stokes 방정식에 대한 포괄적인 수치해가 얻어졌다. 내부에서의 열전달 요동이 급증하는 것으로 특징 지워지는 공진현상의 존재와 특성이 이러한 수치계산 결과로부터 심도 있게 규명되었다. 열전달 요동의 증감의 무차원가진주파수 ω에 따른 의존성을 보여주는 결과가 제시되었다. 이 결과는 이전의 Kazmierczak와 Chinoda(1992)의 연구에서, 그들이 공진현상의 존재를 밝히진 못한 이유를 설명해 주고 있다. 또한 본 연구의 결과는 열전달에 있어서의 공진현상은 큰 Ra와 Pr~O(1)일 때 더욱더 뚜렷해짐을 밝혔다. 이러한 공진현상의 물리적 메커니즘을 철저히 규명하기 위해 유동과 열전달에 관계된 변수들의 요동성분의 시간에 따른 변화양상을 깊이 있게 관찰하여 그 결과를 체계 있게 정리하였다. 아울러 본 연구의 타당성과 응용성을 밝히기 위해 기존의 연구들과의 비교도 이루어 졌다.

Abstract

A numerical study is performed for time-varying natural convection of an incompressible Boussinesq fluid in a sidewall-heated square cavity. The temperature at the cold sidewall T_C is constant, but at the hot sidewall a time-varying temperature condition is prescribed, $T_H = \overline{T_H} + \Delta T' \sin ft$. Comprehensive numerical solutions are secured to the time-dependent Navier-Stokes equations. The numerical results are analyzed in detail to elucidate the existence of resonance, which is characterized by maximal amplification of the fluctuations of heat transfer in the interior. Plots describing the dependence of the amplification of heat transfer fluctuations on the nondimensional forcing frequency ω are presented. The failure of Kazmierczak and Chinoda (1992) to identify resonance is shown to be attributable to the scarcity and limitation of the parameter values adopted in that study. The present results illustrate that resonance becomes more distinctive for large *Ra* and *Pr*~*O*(1). The physical mechanism of resonance is delineated by examining the evolutions of oscillating components of flow and temperature fields. Specific comparisons are conducted for the resonance frequency ω_r between the present results and several other previous predictions based on the scaling arguments.

1. Introduction

Natural convection in a closed cavity with different temperatures imposed on the two facing vertical sidewalls has been extensively studied in recent years (e.g., Ostrach 1982; Hyun 1994). For a geometrically simple rectangular enclosure, the major nondimensional parameters are the Rayleigh number $Ra \equiv \alpha g \Delta T H^3 / \nu\kappa$, the cavity aspect ratio $Ar \equiv H / L$, and the Prandtl number $Pr \equiv \nu / \kappa$. In the above, g denotes the gravity, a the coefficient of thermometric expansion, DT the temperature difference between the two vertical walls, n the kinematic viscosity, k the thermal diffusivity, and H and L the height and width of the enclosure, respectively. Interest is often focused in the convection-dominant regime Ra>>1. For a standard configuration Ar=1, benchmark solutions were published to describe the flow and thermal fields (de Vahl Davies & Jones 1983).

The bulk of the studies on natural convection in an enclosure has dealt with the situations when the boundary conditions are enforced in a time-invariant manner (Ostrach 1982). Convection in a confined space, driven by time-dependent boundary conditions, constitutes a separate class of problems. A classical flow configuration was proposed by Patterson & Imberger (1980). In this model, the fluid and the rectangular container surfaces are motionless and in thermal equilibrium at uniform temperature TO at the initial state. At time t=0, the temperatures at the two vertical surfaces are abruptly changed to $To + \Delta T / 2 \quad To - \Delta T / 2$, respectively. The horizontal surfaces are insulated. The subsequent evolution of flow and thermal fields inside the enclosure, in response to this step change in the boundary conditions, was depicted. Various essential transient characteristics pertinent to this basic model have been explored by numerous investigators (e.g., Yewell et al. 1982; Ivey 1984; Paolucci & Chenoweth 1989; Patterson & Armfield 1990; Le Quere 1990; Paolucci 1990; Bark et al. 1992).

As observed by Lage & Bejan (1993) and Hyun (1994), accounts on unsteady natural convection in an enclosure, in which the thermal boundary conditions undergo continuous temporal variations, are scarce. Vasseur & Robillard (1982) considered

convective cooling of a fluid in a cavity with a sidewall of temporally-decreasing temperature. Schladow et al. (1989) treated natural convection in a cavity, in which the temperatures of the wall increased linearly with time. The primary intention of these works was to verify certain numerical techniques or to explain the discrepancies between numerical simulations and experimental results. The rudimentary physics was basically similar to the unsteady convection due to a step change in thermal conditions in the sidewall-heated cavity.

A significantly new approach was taken by Lage & Bejan (1993). Instead of the usual step change in thermal boundary conditions, they considered the cases when the thermal boundary conditions were continuously changing with time. Specifically, concern was directed to a rectangular cavity with a constant-temperature cold sidewall. At the other vertical sidewall, a time-dependent heat flux was prescribed. The heat flux fluctuated in a square-wave fashion about the mean value. The fundamental question was the way in which the periodicity of the sidewall heating affected the time-dependent flow and attendant heat transfer in the enclosure. The crux of the argument is focused on the possibility of resonance of the fluid system with the oscillation of the externally-supplied heat input at the vertical sidewall.

Physically, resonance describes the phenomenon that the eigenmodes of a system are excited and amplified if this system is exposed to an external excitation with the correct natural frequency. This problem statement has serious ramifications from the standpoint of fundamental dynamics of natural convection. In practical applications, the problem models, for example, natural convection in a room which is heated periodically on a daily basis. Even more appealing is the convection in a confined space in many of the electronic devices, where time-dependent flows are induced due to the periodic energizing of the on and off modes.

Numerical studies of Lage & Bejan (1993), at high Rayleigh numbers, clearly established the existence of resonance to the periodic heating at the sidewall. The resonance was identified by the occurrence of maximal fluctuations of the local velocity and the Nusselt numbers. Also, the resonance frequency f_r as well as the amplification of the Nusselt number Nu is shown to be dependent on Pr. Subsequent scale analyses

by Lage & Bejan showed a fair qualitative agreement between the predicted values and the numerical results for f_r. In summary, the study of Lage & Bejan underscores a serious undertaking to uncover the existence of resonance phenomenon in natural convection when a continuously-changing thermal boundary condition is adopted.

The presence of resonant convection in an enclosure was also noted in the context of mixed convection. Iwatsu et al. (1992) examined convective motions of an incompressible fluid in a cavity with an externally-imposed temperature difference between the top torsionally-oscillating hot lid and the bottom stationary cold endwall. The aim was to explore enhancement of heat transfer in the vertical direction by means of a mechanically-driven oscillation of the top lid. Clearly, if no mechanical oscillation is given, the heat transfer will be entirely conductive in a stably-stratified motionless fluid. The results of extensive numerical computations revealed the existence of resonance to particular frequencies of the lid oscillation. When resonance occurs, heat transfers as well as velocity fluctuations are augmented, which suggest potentially useful applications in technological systems.

In a related problem setup, Kazmierczak & Chinoda (1992) conducted numerical studies of natural convection in a square cavity with one vertical sidewall at a constant temperature T_C. The temperature at the other vertical sidewall varied sinusoidally in time about the mean value $T_H (> T_C)$.The numerical simulations produced periodic solutions for one Rayleigh number ($Ra = 1.4 \times 10^5$) and one Prandtl number (Pr=7) and for three different frequencies of the sidewall temperature oscillations. The solutions demonstrated that the interior flow fluctuations changed monotonically with the frequency of wall temperature oscillations. In essence, no resonance was detected between the temporal variations of the sidewall temperature and the resulting flow oscillations. As to resonance, the numerical account of Kazmierczak & Chinoda (1992) is at variance with the qualitative conclusions of Lage & Bejan (1993) and of Iwatsu et al. (1992), although the precise problem formulations may be slightly different.

Flow oscillations in a sidewall-heated cavity have been discussed extensively. Patterson & Imberger (1980) reported the presence of internal gravity oscillation modes

in the transient approach to steady-state. Ivey (1984) explained the experimentally-observed oscillatory transient behavior based on the concept of internal hydraulic jump. Chenoweth & Paolucci (1986) found that the hydraulic jumps were responsible for the first transition to the time-dependent flow for low aspect ratios. Le Quere & Alziary (1986) and Le Quere (1990) observed the flow oscillations due to the sidewall boundary layer waves. Paolucci & Chenoweth (1989) examined the onset and the frequencies of the oscillatory instabilities. More recently, Xia et al. (1995) investigated the stability of natural convection in a square cavity by using the same problem setup of Kazmierczak & Chinoda (1992). Attention was given to illustrate the effect of imposed wall temperature oscillations on the onset of oscillatory instability and flow transitions. Only one particular value of the imposed external frequency was considered in their calculations.

Comprehensive and far-ranging numerical computations are performed in the present work for the same problem formulation as was used by Kazmierczak & Chinoda (1992). The purpose is to obtain detailed numerical solutions over a much broader range of the frequency of the hot wall temperature oscillation. The scopes of relevant parameter values have been considerably extended. By undertaking full-scale numerical calculations and systematic post-processing analyses, a definite assertion will be made as to the existence of resonance of fluid flows to certain frequencies of the wall temperature oscillations. Furthermore, it will be shown that the previous computational results of Kazmierczak & Chinoda (1992) for three different values of frequency represent only a narrow portion of the whole spectrum of solutions. Due to the limited frequency resolution achieved by Kazmierczak & Chinoda (1992), a distinct evidence of resonance between the flow fluctuation and the frequency of wall temperature oscillation was not seen. However, the present numerical results illustrate that the fluctuations of flow and heat transfer responses display peak values at certain frequencies, if computations span much extended ranges of the frequency with considerably finer resolution. These efforts place the apparent disagreements among the previous works in proper perspective.

In the present paper, an overview of the time-dependent interior flow and

associated heat transfer, in response to the oscillating sidewall temperature condition, is given. The details of fluctuating flow and temperature fields over a cycle will be thoroughly analyzed. Emphasis will be placed on obtaining a physical interpretation of the nature of convective resonance phenomenon. In particular, inspection of the fluctuations of flow and temperature structures, both in the core and in the boundary layers, leads to the identification of the resonance frequency of the system. The numerically obtained resonance frequency is compared with the predictions of the previous models based on scaling arguments. The extensive numerical undertakings of the present study shed light on the fundamental physical mechanism inherent to the confined natural convection with time-varying forcings at the boundary.

2. The mathematical formulation

Consider a square cavity (height/width=H/L=1.0), which is filled with an incompressible Boussinesq fluid. All the physical properties are taken to be constant. The top and bottom horizontal walls are thermally insulated.The leftside vertical wall (x=0) is maintained at a constant temperature T_C. The temperature at the right vertical wall (x=L), T_H, varies sinusoidally with time as $T_H = T_H + \Delta T' \sin ft$, where the mean-value $T_H \equiv T_C + \Delta T$, ΔT>0; $\Delta T'$ and f respectively denote the amplitude and frequency of oscillation. Figure 1 shows a schema of the flow configuration and coordinate system, and figure 2 depicts the time-varying thermal boundary condition at the hot vertical wall.

The flow is governed by the time-dependent Navier-Stokes equations, which, in nondimensional form, are

$$\frac{\partial U}{\partial \tau} + \frac{\partial}{\partial X}\left(U^2\right) + \frac{\partial}{\partial Y}\left(VU\right) = -\frac{\partial P}{\partial X} + \left(\frac{\mathrm{Pr}}{Ra}\right)^{1/2} \nabla^2 U \,, \qquad (1)$$

$$\frac{\partial V}{\partial \tau} + \frac{\partial}{\partial X}\left(UV\right) + \frac{\partial}{\partial Y}\left(V^2\right) = -\frac{\partial P}{\partial Y} + \theta + \left(\frac{\mathrm{Pr}}{Ra}\right)^{1/2} \nabla^2 V \,, \qquad (2)$$

$$\frac{\partial\theta}{\partial\tau} + \frac{\partial}{\partial X}(U\theta) + \frac{\partial}{\partial Y}(V\theta) = \left(\frac{1}{Ra\ \mathrm{Pr}}\right)^{1/2} \nabla^2\theta \,, \tag{3}$$

$$\frac{\partial U}{\partial X} + \frac{\partial V}{\partial Y} = 0 \,, \tag{4}$$

where $\nabla^2 = \frac{\partial^2}{\partial X^2} + \frac{\partial^2}{\partial Y^2}$.

In line with the problem description, the boundary conditions are

$$U = V = \frac{\partial\theta}{\partial Y} = 0, \text{ at } Y = 0,\ 1; \tag{5a}$$

$$U = V = \theta = 0, \text{ at } X = 0; \tag{5b}$$

$$U = V = 0,\ \theta = 1 + \varepsilon\, sin(\omega\tau) \text{ at } X = 1 \tag{5c}$$

In the above, nondimensionalization has been made in a similar fashion to Lage & Bejan (1991, 1993) :

$$\tau = t\ (RaPr)^{1/2} \frac{\alpha}{H^2} \,, \tag{6a}$$

$$(X,\ Y) = \frac{(x,\ y)}{H} \,, \tag{6b}$$

$$(U,\ V) = (u,\ v)\ (RaPr)^{-1/2} \frac{H}{\alpha} \,, \tag{6c}$$

$$\theta = \frac{T - T_C}{T_H - T_C} \,, \tag{6d}$$

$$P = \frac{(p + \rho g y)\ H^2}{\rho\ \alpha^2 RaPr} \,. \tag{6e}$$

It should be pointed out that time is made dimensionless, as shown in (6a), by referring to the reciprocal of the system Brunt-Vaisala frequency N, i.e.,

$$N = [\alpha g(T_H - T_C)/H]^{1/2} = (RaPr)^{1/2} \frac{\alpha}{H^2} \,. \tag{7}$$

The relevant parameters, in addition to the already-defined *Ra* and *Pr*, are

$$\varepsilon \equiv \Delta T' / (\overline{T_H} - T_C), \tag{8a}$$

$$\omega \equiv f / N, \tag{8b}$$

which are the nondimensional amplitude and frequency of the wall temperature oscillation, respectively.

3. Numerical computations

The system of equations (1)-(5) was solved numerically by employing a finite-volume procedure based on the SIMPLER algorithm (Patankar 1980). The governing equations were discretized on a staggered grid. Spatial differencing schemes of the second-order accuracy were adopted for the equation terms. A central differencing was used for the diffusion terms, and a recently-modified version of the QUICK scheme was utilized for calculating the nonlinear convective terms (Hayase et al. 1992). All of the boundary conditions were also treated by using second-order differencings to maintain the same accuracy in the whole computational domain.

The time integration was performed by using an iterative Eulerian implicit method of accuracy $O(\mathrm{D}t)$. The convergence of the solutions was declared at each time step when the maximum relative change between two consecutive iteration levels falls below 10^{-4} for U, V and θ. A parallel checking was performed to ensure that mass continuity in every computational control volume should be satisfied within a relative error 10^{-8}.

For all the calculations discussed in this paper, a grid with (62x52) mesh points in the (X,Y) domain was selected. To resolve thin boundary layers adjacent to the solid walls, grid stretching was implemented such that at least 5 grid points were located in a boundary layer. A more severe grid clustering was adopted for the horizontal grid than for the vertical one. The present grid resolution was adequate to

delineate the boundary-layer structure, although it may not be sufficient to identify the boundary layer waves (Le Quere 1990). However, for the present parameter ranges of Ra and Pr, the boundary layer waves are not of major concern (see, e.g., Paolucci & Chenoweth 1989). Extensive grid sensitivity tests were carried out, and the outcome showed that the reliability and accuracy of the present methodologies were sufficient to capture the principal features, both in the boundary layers and in the core. A very small time step $\Delta\tau = 2\pi / 1024\,\omega$, i.e., 1024 time steps per period, was used.

Verification of the present numerical model was achieved by repeating calculations for the classical model of Patterson & Imberger (1980). For several values of *Ra* and *Pr*, the transient behavior of flow and heat transfer of the present results was in close agreement with the prior works (e.g., Patterson & Imberger 1980; Patterson & Armfield 1990).

Full-dress numerical computations were acquired for Ra=10^5, 10^6, and 10^7; Pr=0.07, 0.7, and 7.0, and $0.01 \le \omega \le 10.0$, and for the aspect ratio 1.0. The nondimensional amplitude e of the wall temperature oscillation was set ε=0.1; this choice was made such that the oscillating part of the wall temperature would not seriously alter the characteristic regime of the basic flow (Kazmierczak & Chinoda 1992). For each set of (*Ra,Pr*) pair, more than 20 cases of computations, by using different values of ω, were executed.

Here, it is helpful to have an overview of the physical significance of the parameters selected in this work. The preceding studies provided order-of-magnitude estimates of the scales of the relevant physical variables pertinent to the canonical models of time-dependent convection in a sidewall-heated cavity (e.g., Patterson & Imberger 1980; Lage & Bejan 1991). These scales are summarized in table 1. Obviously, for all the combinations of (Ra,Pr), the flow regime of present concern is of the boundary-layer type. A major feature of this flow regime is the inseparable coupling between the interior core and the boundary layers on the solid walls (e.g., Jischke & Doty 1975). The time-dependent buoyant motion, in response to the changes in the sidewall thermal conditions, is characterized by three timescales (e.g., Sakurai & Matsuda 1972; Jischke & Doty 1975; Hyun 1994). The shortest timescale, τ_B, is for

the formation of the boundary layers on the vertical sidewalls, and in the present nondimensionalization scheme, $\tau_B \sim O(1)$. The longest timescale, τ_D, represents the diffusion time, and $\tau_D \sim O(Ra^{1/2})$. The intermediate one is the convective timescale, $\tau_F \sim O(Ra^{1/4})$, over which much of the fluid in the cavity passes through the vertical boundary layers. The dominant time-dependent motion, including the process of thermal adjustment in the interior by convective core filling, is substantially accomplished over τ_F.

In view of the parameter ranges selected in the $p0.01 \le \omega \le 10.0$, the above-mentioned timescales are included, in a comprehensive way, in the analysis.resent work,

The numerical data are processed to obtain the instantaneous Nusselt number *Nu*, averaged over a vertical plane at $X=a$:

$$Nu_{X=a} = \frac{L}{H}\int_0^A [U\theta(RaPr)^{1/2} - \frac{\partial\theta}{\partial X}]_{X=a}\, dY \quad . \tag{9}$$

Here, it is advantageous to introduce several operators. In order to assess the impact of the oscillation relative to the corresponding non-oscillating value, a definition is made

$$\phi^* = \frac{\phi - \phi_{ss}}{\phi_{ss}}, \tag{10}$$

where ϕ represents any time-dependent property, and the subscript ss denotes the corresponding value in the case of non-oscillating wall temperature ($\varepsilon=0$). The amplitude A(f) and the mean-value $\bar{\phi}$ of an oscillating property over a cycle may be written as

$$A(\phi) = \frac{Max\{\phi(\tau)\} - Min\{\phi(\tau)\}}{2}, \quad \text{for } \tau^o \le \tau \le \tau^o + \frac{2\pi}{\omega}, \tag{11a}$$

$$\overline{\phi} = \int_{\tau_0}^{\tau_0 + 2\pi/\omega} \phi(\tau)\, d\tau \;\Big/\; (2\pi/\omega) \,. \qquad (11b)$$

In the course of actual computations, a steady-state solution was first procured for a given pair of (Ra,Pr) by setting $\varepsilon = 0$. This is referred to as the basic state, which is summarized in table 2. The streamfunction y is defined in a usual way, i.e., ($U = \partial\psi/\partial Y, V = -\partial\psi/\partial X$). Subsequently, this basic state was used as the initial condition to compute for the time-varying wall temperature conditions $\varepsilon \neq 0$. This approach, which was put forth by Lage & Bejan (1993), saves a considerable amount of numerical efforts, in particular, for high frequencies. Figure 3 recapitulates the well-established features of the basic-state flow for Ra=10^6 and Pr=0.7 (see e.g., de Vahl Davies & Jones 1983). Clearly, the global flow field can be divided into the well-stratified interior core and the boundary layers on the solid walls. The majority of fluid transport is accomplished via the boundary layers, and the interior core is characterized by a stable stratification.

4. Results and discussion

4.1 Quasi-periodic natural convection responding to the oscillatory thermal boundary condition

Figure 4 portrays the temporal behavior of Nu*, as defined in (10) at three locations, i.e., the cold sidewall (Nu_C^*), the vertical mid-plane X=0.5 (Nu_M^*), and the hot sidewall (Nu_H^*).

Figure 4(a) typifies the case of small ω (ω=0.01). It is immediately clear that, only after about one cycle, the values of Nu* settle down to a form very close to a sinusoidal oscillation. It is also important to notice that the Nu*-values throughout the entire cavity vary with time almost in unison, i.e., with roughly the same amplitude and in phase. This reflects the fact that the period of the wall temperature oscillation,

$\tau_P \equiv 2\pi/\omega$, is much larger than the characteristic time for dominant adjustment of the interior fluid. Alternatively speaking, since the temporal change in the wall thermal condition is very slow, the flow in the entire cavity at every instant behaves like a time-invariant system. The small phase lags discernible in figure 4(a) indicate the time delays for the thermal disturbances originated at the hot wall to reach the position under consideration.

Figure 4(b), for a high frequency (ω=10.0), displays the quasi-steady periodic states. In this case, the shortest time scale τ_B needed for a temperature disturbance to propagate through a distance δ_T, which is the thickness of thermal boundary layer, by conduction is greater than τ_P. Consequently, over τ_P, the effect of the hot wall temperature oscillation can not penetrate even across the vertical boundary layer thickness. The fluctuations of Nu_C and of Nu_M are negligible in magnitude, whereas Nu_H oscillates with an amplitude comparable to the basic-state Nusselt number. The impacts of the oscillating temperature wall condition are confined to a narrow region adjacent to the hot wall. This physical picture can be inferred from the well-established Stokes second problem (e.g., Schlichting 1968).

Figure 4(c), at an intermediate value of ω, is paradigmatic of a resonant case. The Nusselt numbers everywhere in the cavity show oscillations, although the amplitudes vary spatially. The quasi-steady periodic state is achieved after a few cycles. It is important to notice in figure 4(c) that the amplitude of Nu_M is larger than that of Nu_H. Put it differently, the fluctuation in heat transfer is more vigorous in the interior core than near the hot wall at which the temperature oscillation is applied. It is recalled that ε=0.1; however, the gain in resulting heat transfer at the mid-plane reaches nearly 35% of the corresponding basic state, i.e., $A(Nu_M^*)$=0.345.

Figure 5 exhibits the behavior of the interior velocity, by plotting ψ_{max}*. The response of the flow field is in line with that of heat transfer. The impact of the wall temperature oscillation is moderate for low frequency (see figure 5(a) for ω=0.01), but is negligibly small for high frequency (see figure 5(b) for ω=10.0). Very close to the resonance condition, the velocity fluctuations are amplified (see figure 5(c)). Note the

difference in the scales of the ordinates in figures 5(a), 5(b) and 5(c).temporal variations of maximum streamfunction

It is also worth pointing out that the shape of the Ψ_{max}*-curves in figure 5 suggests the presence of the primary mode, which corresponds to ω, plus the subsidiary modes. For low ω, the dominance of the primary mode is discernible. However, at high ω, the influence of subsidiary modes is more conspicuous. As seen in figure 5(b), a quasi-steady mono-periodic state has not been attained even after nearly 40 cycles, and Ψ_{max} vacillates with a multitude of frequencies

Figure 6 (for Ra=10^6, Pr=0.7) illustrates the effect of ω on the global flow and heat transfer characteristics in the quasi-steady periodic state. Figures 6(a), 6(b) and 6(c) plot the amplitude of Nu* at three locations. A useful approach proposed by Lage & Bejan (1993) was adopted in that resonance in the present natural convection problem is characterized by a maximum fluctuation in the total heat transfer rate through the vertical mid-plane of the cavity. This is also coupled to the occurrence of maximum fluctuations in local velocity and temperature of the enclosed fluid. Iwatsu et al. (1992) followed a conceptually similar path. Here, the resonance frequency, ω_r, is identified to be the frequency at which the amplitude of Nu_M fluctuation shows a peak value. These are listed in table 2.

The presence of resonance is corroborated in figure 6(b), with the resonance frequency $\omega_r \cong 0.68$. At low frequencies, $A(Nu_M^*)$ remains nearly constant. In a narrow band surroundingω_r, $A(Nu_M^*)$ is substantially amplified, with a peak value at ω_r. As ω increases beyond ω_r, $A(Nu_M^*)$ decreases rapidly to approach zero.

The dependence of the fluctuations of Nu_H and Nu_C on ω is displayed in figures 6(a) and 6(c), respectively. For $\omega < \omega_r$, the fluctuation of Nu_H (Nu_C) generally increases (decreases) with frequency. Note the difference in scales of the ordinates between figure 6(a) and figure 6(c). As increases beyond ω_r, $A(Nu_H^*)$ increases steeply, whereas $A(Nu_C^*)$ becomes very small. A less distinctive peak is visible in the plot of $A(Nu_C^*)$ at $\omega \cong \omega_r$. Figure 6(d) exhibits the dependence of velocity fluctuations

on ω. Resonance, as exemplified by a peak value of $A(\Psi_{max}{}^*)$, is in evidence. Clearly, the value of the time-dependent $_{\Psi_{max}}$ (for ε=0) is enhanced about 31% above the basic-state $_{\Psi_{max}}$ (for ε=0.1).

The effect of ω on the cycle-averaged values of $\overline{\Psi_{max}{}^*}$ and $\overline{Nu^*}$ is depicted in figures 6(e) and 6(f). In general, the influence of the wall temperature oscillation on $\overline{\Psi_{max}{}^*}$ is meager, in comparison to that on $A(\Psi_{max}{}^*)$. Note the difference between the scales of the ordinates of figures 6(d), 6(e) and 6(f). It is difficult to draw any definitive conclusion at this moment, but it is conjectured that such a relatively small impact on the averaged quantities may stem from the fact that ε=0.1 in the present computations. The amplitude of the wall temperature oscillation ε=0.1 is not sufficient to seriously disturb or alter the structures of the time-averaged flow and temperature fields.

The effects of *Ra* and *Pr* are scrutinized in figure 7, by executing calculations for the entire sets of (Ra,Pr) listed in table 2. Although the results display quantitative differences, as anticipated, the overall qualitative features remain substantially unchanged. For all the cases computed, the existence of distinctive resonance is reconfirmed, and this trend becomes more pronounced as Ra increases. When Ra is relatively small (see the curves for $Ra=10^5$), resonance is less clear-cut. Also, $A(Nu_M^*)$ is nearly independent of Ra at low frequencies, and $A(Nu_M^*)$ becomes vanishingly small at high frequencies. The influence of Ra is mainly felt only in a narrow frequency band surrounding ω_r, which is termed the resonance band. Within this frequency band, the fluctuation of Nu_M^* is notably amplified as *Ra* increases.

The effect of *Pr* is also manifested in figure 7. The general qualitative patterns of the $A(Nu_M^*)$ vs. ω curves are similar. For a very small value of Pr, as shown in figure 7(b) for Pr=0.07 and $Ra=10^6$, the secondary and third peaks are visible. These subsidiary peaks are thought to be the harmonics of the fundamental frequency ω_r. Another important observation is that, for the same *Ra*, $A(Nu_M^*)$ for *Pr*=0.7 is much greater than that for *Pr*=0.07 or for *Pr*=7.0. A plausible explanation may be given based on the physical grounds. The ultimate source of the resonance in the natural

convection is the thermal disturbances excited by the hot wall temperature oscillation. These disturbances are then transported via convective currents. A departure from Pr=1 implies unequal dampings by viscosity and thermal diffusion effects. For $Pr>O(1)$, viscous diffusion is the major damping mechanism for the propagation of the disturbances, whereas $Pr<O(1)$, thermal diffusion weakens the thermal disturbances. Consequently, for a fluid of $Pr\sim O(1)$, resonance is expected to generate most dramatic consequences. This can also be ascertained from the results of Lage & Bejan (1993), which showed that for a fixed Ra, the fluctuation of Nu was most amplified for $Pr\sim O(1)$.

It is now of interest, in light of the present comprehensive numerical results to recast the earlier study of Kazmierczak & Chinoda (1992) on the same problem setup. As remarked previously, they used larger values of ε, i.e., ε=0.2, 0.4, and 0.8. However, their numerical solutions reported a monotonic dependency of the fluctuations in flow and heat transfer on w, and no explicit resonance was seen. It can be shown that their failure to capture resonance was attributable to the extreme limitations of the parameter values of their computations and to the poor resolution of frequency bands. The only pair of (Ra,Pr) chosen in their study was $Ra=1.5\times10^5$, Pr=7.0. Unfortunately, for their choice of (Ra,Pr), the consequence of resonant convection is generally feeble (see the present results for $Ra=10^5$, Pr=7.0 in figure 7(c)). On top of this, their computations encompassed only three different values of frequency. If these are translated under the present nondimensionalization, their runs No. 1, 4 and 5 correspond to ω=0.6132, 1.1226 and 0.3066, respectively, in the present study (these results are indicated in figure 7(c) as black circles). As can be easily understood in figure 7(c), the above three points of Kazmierczak and Chinoda are too coarse to capture any sign of a peak around $\omega_r \cong 0.56$. In fact, a closer perusal of figures 6 and 13 of Kazmierczak and Chinoda (1992) suggests that the fluctuation of Nu_M at ω=0.6132 is slightly more intensified than the other two cases. This observation is consistent with the present results demonstrated in figure 7(c).

4.2 *Identification of the resonance frequency*

Lage & Bejan (1993), by devising a concept of the rotation of a fluid wheel, stated that resonance is expected if the period of oscillation of the external boundary condition coincides with the time duration over which the effect of cyclic heating rotates through the full cavity. The period t_W of one rotation of a fluid wheel was scaled as

$$t_W \sim 4H / V_O, \tag{12}$$

in which the fluid rotates like a wheel of diameter H with velocity V_O. These baseline physical considerations are similar to the case of a driven pendulum; t_W is associated with the natural frequency of the pendulum.

In subsequent developments, Lage & Bejan adopted the longitudinal velocity in the vertical boundary layer to estimate V_O in equation (12). This scaling emphasizes the significance of the boundary layer structure of the basic state, under the belief that the bulk of the fluid transport in the basic state is achieved through the boundary layers. Therefore, in this model, the impacts of the oscillating thermal boundary condition travel by way of the circulations of the basic state through the boundary layers. Cementing these arguments, the nondimensional resonance frequency may be expressed as

$$\omega_r = \begin{cases} \pi/2, & \text{for } Pr < 1, \\ \dfrac{\pi}{2}\mathrm{Pr}^{-1/2}, & \text{for } Pr \geq 1. \end{cases} \tag{13}$$

A small modification to (13) may now be obtained. If cognizance can be taken of both the transverse velocity in the horizontal boundary layer and the longitudinal velocity in the vertical boundary layer, (13) can be rewritten in a slightly amended form:

$$\omega_r = \begin{cases} \dfrac{\pi}{1+(RaPr)^{1/6}}, & \text{for } Pr < 1, \\ \dfrac{\pi}{Pr^{1/2}(1+Ra^{1/6})}, & \text{for } Pr \geq 1. \end{cases} \tag{14}$$

The heuristic scale analysis approach of Lage & Bejan (1993) will now be slightly modified and expanded to incorporate the numerical results of the present computations. It was found, as shown in figure 7, that both the resonance frequency ω_r and the width of the resonance band are little affected by Ra and Pr. Only the case of Pr=0.07 shows a slight variance with Ra. The effects of Pr on ω_r are also weak. Recalling that time was made dimensionless by using $1/N$, these findings are suggestive of the fact that resonance is closely linked to internal gravity wave oscillations.

As stated earlier, it is essential to identify the eigenmodes of oscillations of the system. In a sidewall-heated cavity, several oscillatory modes of natural convection have been discussed (Patterson & Imberger 1980; Ivey 1984; Le Quere & Alziary 1986; Paolucci & Chenoweth 1989; Le Quere 1990; Xia et al. 1995). Paolucci & Chenoweth (1989) calculated the frequencies of the internal wave oscillation and boundary-layer wave oscillations. The frequency of internal wave oscillation suggested by Paolucci & Chenoweth (1989) is, in dimensional form,

$$f^I = C_i \frac{N}{[Ar + (n/q)^2 / Ar]^{1/2}}, \tag{15}$$

where C_i is a parameter indicating the strength of stratification, and q and n are the wavenumbers in the horizontal and vertical directions, respectively. For the fundamental mode, Ar=1.0, n/q=1 (Paolucci & Chenoweth 1989) and in the present dimensionless form,

$$\omega^I = \frac{C_i}{\sqrt{2}}. \tag{16}$$

Paolucci & Chenoweth (1989) found that C_i was approximately constant and slightly less than unity for Pr=0.71. In the present study, following Paolucci (1990), the stratification factor, Ci, of the basic-state was calculated by using a linear fitting to the vertical temperature distribution at the horizontal mid-width plane of the cavity (X=0.5). This is listed in table 2. The estimated values of C_i for Pr=0.7 are shown to be in good agreement with those obtained by Paolucci & Chenoweth (1989) for Pr=0.71. The order-of-magnitude strength of the overall core stratification remains largely unchanged as Ra and Pr vary. Based on this argument, equation (16) indicates that the frequency of internal gravity mode, if scaled by using the Brunt-Vaisala frequency, is nearly constant. This is corroborative of the foregoing statement that, at resonance, the internal wave oscillations are excited.

The numerically-determined values for the resonance frequency ω_r are compiled in figure 8 for all the computational runs of the present study. Also shown in figure 8 are the predictions by equations (13) and (14). Quantitative discrepancies are seen between the present numerical results and the prediction based on the scaling of Lage & Bejan (1993). It appears that, in line with the statement of Lage & Bejan, the prediction by scale analysis tends to underpredict ω_r for Pr>O(1) and overpredict ω_r for Pr<O(1). It is immediately clear in figure 8 that the present numerical data for ω_r cluster around the frequency ω' of equation (16) with C_i=1. Figure 8 also shows the frequency of internal wave oscillations, based on the value C_i in table 2. These illustrate close agreement with the numerical data for ω_r for $Pr \geq O(1)$.

It is pointed out that, for all the sets of (Ra, Pr) in the present study with ε =0, no oscillatory motions are seen in the steady state. This is consistent with the results of Paolucci & Chenoweth (ε=0); in the range of Ra examined in this paper, the amplitudes of internal wave oscillations are decaying eventually. However, in the present problem with the periodic thermal boundary condition at the sidewall, a continuous energy source with a frequency close to that of the internal waves is provided, and the internal wave oscillations are maintained due to resonance.

4.3 *Flow response at resonance*

The discussion will now be centered on describing the detailed time-dependent flow and temperature structures at resonance. In order to gain a physical insight into the mechanism of resonance, it is necessary to scrutinize the details of the oscillating components of flow. These exercises carry added significance in light of the fact that the oscillatory characteristics are masked by the dominant basic-state features. A thorough and complete analysis will be made of $\psi'(\equiv \psi - \psi_{ss})$ and $\theta'(\equiv \theta - \theta_{ss})$, where the subscript *ss* refers to the basic state (ε=0).

The history of the relative influence of the hot wall thermal boundary condition is portrayed in figure 9. A cycle is divided into four phases. The first (last) half of a cycle, $\tau_a \le \tau < \tau_e$ ($\tau_e \le \tau < \tau_{a'}$) can be interpreted as a heating (cooling) mode relative to the basic-state, since $\theta_H \ge \overline{\theta}_H (\theta_H \le \overline{\theta}_H)$. Also, phases I and IV (phases II and III) are characterized by a positive (negative) rate of change of θ_H. An analogy between the present problem and the driven pendulum can be drawn as shown in figure 9(b).

Figure 10 displays time-dependent profiles of θ' along the mid-depth plane (Y=0.5) under the resonant condition ($\omega=\omega_r$) for Ra=10^6, Pr=0.7. The global features of the temperature field, including the structures of thermal boundary layers and core stratification, display little changes with time. However, figure 10 discloses the periodic tilting of the interior isotherms. Due to this oscillatory tilting of the isotherms, the fluid in the interior core experiences a situation as if the gravity vector changes its direction in an oscillatory manner with time. It is stressed that this periodic tilting of the interior isotherms is most pronounced when $\omega \approx \omega_r$. This is supportive of the earlier assertion that the flow resonates to the internal wave oscillations.

Figure 11 (for *Ra*=10^6, *Pr*=0.7) exhibits sequential plots ψ' and θ' for the resonance case. At time $\tau = \tau_a$, the full domain of fluid is occupied by a clockwise (CW) circulating cell, which was developed by the relative cooling in the previous cycle. As θ_H' increases in phase I (see frames a, b, c), a new CCW circulation forms near the hot vertical sidewall and this grows to push the CW circulation to the

cold-wall side. At $\tau = \tau_c$, the CCW cell occupying the half-cavity is characterized by two centers of circulation (see frame c): one is located in the upper right corner and the other is in the central region of the cavity. In phase II (see frames c, d, e), the CCW cell fills much of the whole cavity, and the two centers of circulation merge into one which moves to the cold-wall side. Around $\tau \approx \tau_e$, the strength of this CCW circulation is maximized. During the relative cooling period($\tau_e \leq \tau \leq \tau_{a'}$) a reverse process takes place. In the above-described fashion, in a cycle, the CW and CCW circulating cells are developed and subsequently disappear.

A close inspection of the evolution of θ' provides an insightful understanding of the resonance. In figure 11(a), the appearance of cool spots, which are characterized by negative values of θ', is visible in the upper right corner region. These represent the horizontal intrusion of cold disturbances which were generated under the relative cooling mode of the previous cycle and were transported by buoyant currents in the hot-wall boundary layer. As can be readily observed in figures 11(b) and 11(c), these cold disturbances do not travel through the upper boundary layer with the convective currents of the basic state; rather, these disturbances move across the interior region of the cavity. By the time when the hot disturbances, which are generated subsequently at the hot wall, begin to occupy the central region of the cavity, the cold disturbances are divided into two parts. The cold disturbances in the upper zone are isolated and they die out by the succeeding hot fluids; however, those in the lower zone turn around at the cold sidewall and move toward the hot sidewall in the circuit made through the lower region of the cavity. This movement of the cold spot through the lower region, which was generated by the relative cooling of the previous cycle, provides an essential clue for the resonant convection.

Following up the above discussion, the effects of relative heating are traced. In figure 11(a), around $\tau = \tau_a$, hot disturbances due to the increase in θ_H grow in the hot-wall boundary layer. Notice, in this frame, that another zone of positive θ' (hot spots) is evident in the lower right quarter of the cavity. The appearance of this region is attributable to the above-described returning of the relative heating effects of the

previous cycle. Figure 11(b) exhibits the presence of two modes of propagation of the hot disturbances: one is in the upper right corner (denoted by region A in figure 11), and the other starts directly from the middle heights of the hot-wall boundary layer (denoted by region B in figure 11). The former represents the intrusion of the fluid parcels which were heated in the present cycle and are transported by the basic-state upwelling buoyant currents in the hot-wall boundary layer. The latter stands for the interaction of heating effects of the present cycle with the returning of heating effects of the previous cycle. Around $\tau = \tau_c$, these two hot spots propagate into the interior region and they merge into a single zone. This merging intensifies the hot disturbances in the interior core; this pushes to the cold-wall side the cold disturbances which occupy the central portion of the cavity. Afterwards, these hot disturbances travel directly across the bulk of the interior. In a similar manner, cold disturbances are newly created under the relative cooling mode, and these strongly interact with the returning of the cooling effects of the previous cycle. These processes are repeated in every cycle.

Descriptions of the above pictures of the behavior of oscillating components is analogous to the resonance of a driven pendulum shown in figure 9(b). If an external excitation is applied to the pendulum which is initially motionless, the pendulum starts oscillation with its natural frequency, ω_r. If there is no damping, the pendulum continues to oscillate permanently. Suppose that an external forcing is continuously applied to the pendulum at every time instant when the pendulum passes the original position ($\tau=\tau_a$), i.e., the frequency ω of the external forcing is $\omega=\omega_r$. The pendulum gains additional angular momentum, which produces resonance so that the oscillation is amplified. For an ideal system with no damping, the amplitude grows unbounded. In the present fluid system, viscous and diffusive dampings restrict the amplification to an appropriate level. Fluctuations of flow and associated convective heat transfer are intensified most when the effects of the oscillating temperature boundary condition by the previous cycle and by the current cycle are synchronized. If this temporal matching is achieved, maximal impacts of the time-varying hot-wall conditions are imparted to the fluid, and this constitutes the ground for resonance.

Evolutions of ψ' and θ' at off-resonance frequencies are displayed in figure

12 (at ω=0.5) and figure 13 (at ω=1.0).

When $\omega < \omega_r$, the period of the hot-wall temperature oscillation is larger than the time required for the thermal effects to span the full fluid domain. This is corroborated in figure 12(a); at time $\tau = \tau_a$, the presence of the CCW circulation is felt in much of the lower half of the cavity. This is in contrast with the picture at $\tau = \tau_a$ of the resonance case (see figure 11(a)), in which the CW circulation fills the majority of the cavity interior. The CW circulation, in the case of $\omega < \omega_r$, can not fill the full cavity domain due to the remaining effects of the relative heating of the previous cycle (the relative heating of the new cycle has not been in effect). As readily recognized in figures 12(b) and 12(c), the interaction between two hot spots of different temporal origins is much weaker than for the resonance case.

Figure 13 (at ω=1.0) illustrates the results for $\omega > \omega_r$. The period of the change of the wall boundary condition is shorter than the time for the thermal effects to span the entire cavity. The ψ'- frame of figure 13(a) displays that a pair of counter-rotating circulation cells are arranged more or less in the horizontal direction. The CW (CCW) circulation in the left (right) half of the cavity represents the residual impacts of the relative cooling (heating) of the previous cycle. The θ'-frames portray similar patterns. At $\tau = \tau_a$, a good part of the left-half of the cavity is occupied by hot disturbances (positive θ'), whereas the right-half mostly by cold disturbances (negative θ'). At this instant, the temperature condition at the hot wall has been switched to a relative heating mode; however, the effect of relative heating of the previous cycle has not yet completed its travel across the cavity. Accordingly, the resonant interaction between the relative heating effects of the current and the previous cycles is not in evidence. Rather, as seen in figure 13(c), the horizontally-arranged structure of the alternating regions of positive and negative θ' inhibits the propagation of the effect of the hot-wall temperature oscillation. Owing to the blocking role of this structure, the impacts of the oscillating hot-wall temperature condition of the past cycles can not return to the hot-wall side. The rapid decline in the fluctuation of Nu_M with ω when. $\omega > \omega_r$ (see figure 6 and figure 7) can be explained by the above-cited physical

picture.

5. Concluding remarks

Far-ranging numerical computations have been conducted to study natural convection in a sidewall-heated square cavity with the time-varying temperature boundary condition at the hot sidewall, $\theta_H = 1 + \varepsilon \sin(\omega\tau)$. The numerical calculations clearly established resonance at certain selected frequency(ω_r) by monitoring the maximization of fluctuations in the heat transfer rate in the interior region. For $\omega < \omega_r$, the fluid response to the hot-wall temperature oscillation is qualitatively similar to the case of an impulsive step change given to the boundary wall. For $\omega > \omega_r$, the influence of the boundary condition is confined to a narrow region adjacent to the hot sidewall.

The resonance phenomenon is more distinct and the amplification of Nu_M is more pronounced, as Ra increases for Pr~O(1). However, the resonance frequency ω_r, nondimensionalized by using the system Brunt-Vaisala frequency, is nearly independent of Ra and Pr. In the resonant case, the impacts of the hot-wall temperature oscillation are conspicuous in the interior core and the temperature field in the interior core displays a periodic tilting of isotherms. These suggest that the flow under present investigation resonates to the internal wave oscillations. The estimations of ω_r, based on the internal wave modes, lead to a qualitative agreement with the present numerical results.

The underlying mechanism of resonance is scrutinized by examining the details of oscillating components of flow and temperature fields. Analogous to the driven pendulum problem, resonance is due to strong interactions between the effects of oscillatory thermal boundary conditions generated by the previous and by the current cycles. The influence of the sinusoidally-varying thermal wall condition synchronizes with the returning impact of the wall condition produced in the previous cycle. For a resonant case, the CCW and CW circulations in the oscillatory flow field undergo a full growth and a subsequent disappearance over a cycle. The thermal disturbances from the

hot sidewall move through much of the interior core and return to the original position over a period.

It is worth noting that the major impetus of the present study was to search for resonance of natural in the sidewall-heated cavity. The ranges of relatively small Rayleigh numbers were covered so that the time-invariant steady state exists when $\varepsilon=0$. As reported by Paolucci & Chenoweth (1989), for a higher value of *Ra*, internal wave oscillations are present even in the steady state. In this situation, it is expected that resonance results in a more dramatic amplification of oscillations. If the value of *Ra* is much higher, boundary layer waves may also be activated (Paolucci & Chenoweth 1989; Le Quere 1990). These are not of major interest in the present study.

References

BARK, F. H., ALAVYOON, F. & DAHLKILD, A. A. 1992 On steady free convection in vertical slots due to prescribed fluxes of heat or mass at the vertical walls. *J. Fluid Mech.* **235**, 665-689.

CHENOWETH, D. R. & PAOLUCCI, S. 1986 Natural convection in an enclosed vertical air layer with large horizontal temperature differences. *J. Fluid Mech.* **169**, 173-210.

DE VAHL DAVIS G. & JONES, I. P. 1983 Natural convection in a square cavity - a comparison exercise. *Int. J. Num. Methods Fluids* **3**, 227-248.

HAYASE, T., HUMPHERY, J. A. C. & GRIEF, R. 1992 A consistently formulated QUICK scheme for fast and stable convergence using finite-volume iterative calculation procedures. *J. Comp. Phys.* **98**, 108-118.

HYUN, J. M. 1994 Unsteady buoyant convection in an enclosure, *Advances in Heat Transfer* **34**, 277-320.

IVEY, G. N. 1984 Experiments on transient natural convection in a cavity. *J. Fluid Mech.* **144**, 389-401.

IWATSU, R., HYUN, J. M. & KUWAHARA, K. 1992 Convection in a differentially-heated square cavity with a torsionally-oscillating lid. *Int. J. Heat Mass Transfer* **35**, 1069-1076.

JISCHKE, M. C. & DOTY, R. T. 1975 Linearlized buoyant motion in a closed container. *J. Fluid Mech.* **71**, 729-754.

KAZMIERCZAK, M. & CHINODA, Z. 1992 Buoyancy-driven flow in an enclosure with time-periodic conditions. *Int. J. Heat Mass Transfer* **35**, 1507-1518.

LAGE, J. L. & BEJAN, A. 1991 The Ra-Pr domain of laminar natural convection in an enclosure heated from the side. *Numerical Heat Transfer Part A* **19**, 21-41.

LAGE, J. L. & BEJAN, A. 1993 The resonance of natural convection in an enclosure heated periodically from the side. *Int. J. Heat Mass Transfer* **36**, 2027-2038.

LE QUERE, P. & ALZIARY DE ROQUETFORT, T. 1986 Transition to unsteady

natural convection of air in differentially heated vertical cavities. *Proc. ASME Winter Annual Meeting, ASME HTD*, vol. 60, pp. 29-36. Anaheim, California.

LE QUERE, P. 1990 Transition to unsteady natural convection in a tall water-filled cavity. *Phys. Fluids A* **2**, 503-514.

OSTRACH, S. 1982 Natural convection heat transfer in cavities and cells. *Proc. 7th Int. Heat Transfer Conf.*, Munich, Vol. **6**, 365-379.

PAOLUCCI, S. & CHENOWETH, D. R. 1989 Transition to chaos in a differentially heated vertical cavity. *J. Fluid Mech.* **201**, 379-410.

PAOLUCCI, S. 1990 Direct numerical simulation of two-dimensional turbulent natural convection in an enclosed cavity. *J. Fluid Mech.* **215**, 229-262.

PATANKAR, S. V. 1980 *Numerical Heat Transfer and Fluid Flow*. McGraw-Hill, New York.

PATTERSON, J. & ARMFIELD, S. W. 1990 Transient features of natural convection in a cavity. *J. Fluid Mech.* **219**, 469-497.

PATTERSON, J. & IMBERGER, J. 1980 Unsteady natural convection in a rectangular cavity. *J. Fluid Mech.* **100**, 65-86.

SAKURAI, T. & MATSUDA, T. 1972 A temperature adjustment process in a Boussinesq fluid via a buoyancy-induced meridional circulation. *J. Fluid Mech.* **54**, 417-421.

SCHLADOW, S. G., PATTERSON, J. & STREET, R. L. 1989 Transient flow in a side-heated cavity at high Rayleigh number: a numerical study. *J. Fluid Mech.* **200**, 121-148.

SCHLICHTING, H. 1968 *Boundary Layer Theory*. McGraw-Hill, New York.

VASSEUR, P. & ROBILLARD, L. 1982 Natural convection in a rectangular cavity with wall temperature decreasing at a uniform rate. *Warme-u. Stoffubertr.* **16**, 199-207.

XIA, Q, YANG, K. T. & MUKUTMONI, D. 1995 Effect of imposed wall temerature oscillations on the stability of natural convection in a square enclosure. *ASME J Heat Transfer* **117**, 113-120.

YEWELL, R., POULIKAKOS, D. & BEJAN, A. 1982 Transient natural convection experiments in shallow enclosures. *ASME J Heat Transfer* **104**, 533-538.

Table Captions

Table 1 The relevant scales in the unsteady natural convection in a sidewall-heated cavity. The quantities in [ ] denote dimensionless values by using the nondimensionalization schemes of equation (6).

Table 2 Summary of the present numerical simulations. C_i indicates the strength of interior stratification.

Figure Captions

Figure 1 Sketch of the flow configuration.

Figure 2 Time-dependent temperature boundary condition at the vertical sidewalls.

Figure 3 (a) Streamfunctions and (b) isotherms of the basic state (ε=0.0) for Ra=10^6 and Pr=0.7. The increment of contour level $\Delta\psi$ is ψ_{max}/10 and the value of ψ_{max} is listed in table 2. $\Delta\theta$=0.1.

Figure 4 Time-dependent behavior of the overall Nusselt numbers for Ra=10^6 and Pr=0.7: (a) ω=0.01; (b) ω=10.0; and (c) ω=0.68. Symbols ○,□,△ represent the Nusselt numbers at the hot vertical wall (X=0.0), at the vertical mid-plane (X=0.5), and at the cold vertical wall (X=1.0), respectively. Note that * denotes a normalized quantity by using equation (10).

Figure 5 Time-dependent behavior of the normalized maximum streamfunction ψ_{max}* for Ra=10^6, and Pr=0.7 : (a) ω=0.01; (b) ω=10.0; (c) ω=0.68.

Figure 6 Variations of the fluctuations of flow variables with ω. (a) $A(Nu_H^*)$; (b) $A(Nu_M^*)$; (c) $A(Nu_C^*)$; (d) $A(\psi_{max}^*)$; (e) $\overline{\psi_{max}^*}$; and (f) $\overline{Nu^*}$. Ra=10^6, Pr=0.7.

Figure 7 Effects of Ra and Pr on the $A(Nu_M^*)$-ω variations.

Figure 8 Values of the resonance frequency ω_r. Continuous lines are based on the scaling arguments, equations (13), (14) and (16). ●,■,▲ denote the present numerical results for Ra=10^5, 10^6, 10^7, respectively. ○,□,△ represent the values based on equation (16), when C_i is evaluated by using the vertical

temperature distribution of the present numerical results for $\varepsilon=0$ at the mid-width of the cavity.

Figure 9 (a) Characterizations of heating and cooling modes relative to the basic-state at the hot wall. (b) An analogous model of a driven pendulum.

Figure 10 Time-dependent profiles of the oscillating temperature component, θ', in the horizontal mid-plane (Y=0.5). $Ra=10^6$, $Pr=0.7$ and $\omega=0.68$. The time instants are : ○, $\tau=\tau_a$; □, $\tau=\tau_b$; △, $\tau=\tau_c$; ◇, $\tau=\tau_d$; ●, $\tau=\tau_e$; ■, $\tau=\tau_f$; ▲, $\tau=\tau_g$; ◆, $\tau=\tau_h$.

Figure 11 Sequential plots showing the oscillating part of streamfunctions (left column) and of isotherms (right column). $Ra=10^6$, $Pr=0.7$, and $\omega=0.68(\cong \omega_r)$. The time instants are the same as in figure 9 The contour increments are $\Delta\psi'=7.5\times10^{-4}$ and $\Delta\theta'$=0.01. The number, n, in the figures indicates the contour value $n\cdot\Delta\psi'$ or $n\cdot\Delta\theta'$.

Figure 12 Same as in figure 11, except for $Ra=10^6$, $Pr=0.7$, and $\omega=0.5(<\omega_r)$. $\Delta\psi'=5\times10^{-4}$.

Figure 13 Same as in figure 11, except for $Ra=10^6$, $Pr=0.7$, and $\omega=1.0(>\omega_r)$. $\Delta\psi'=5\times10^{-4}$

		$Pr>1$	$Pr<1$
length	vertical viscous boundary layer thickness, δ_V	$Ra^{-1/4}Pr^{1/2}H$	$(RaPr)^{-1/4}H$
	vertical thermal boundary layer thickness, δ_T	$Ra^{-1/4}H$	$Ra^{-1/4}Pr^{1/4}H$
	horizontal viscous boundary layer thickness, δ_H	$Ra^{-3/16}Ar^{-1/4}H$	$(RaPr)^{-3/16}Ar^{-1/4}H$
velocity	longitudinal velocity in the vertical boundary layer, v_V	$Ra^{1/2}\frac{\chi}{H}$	$\frac{\chi}{H}(\mathrm{RaPr})^{1/2}$
	horizontal velocity in the horizontal viscous layer, v_H	$Ra^{7/16}Ar^{1/4}\frac{\chi}{H}$	$\frac{\chi}{H}(\mathrm{RaPr})^{7/16}\mathrm{Ar}^{-1/4}$
time	vertical boundary layer forming time, $t_B[\tau_B]$	$Ra^{-1/2}\frac{H^2}{\chi}[\mathrm{Pr}^{1/2}]$	$(\mathrm{RaPr})^{-1/2}\frac{\cdot H^2}{\chi}[1]$
	convective time, $t_F[\tau_F]$	$Ra^{-1/4}Ar^{-1}\frac{H^2}{\chi}$ $[Ar^{-1}Ra^{1/4}Pr^{1/2}]$	$\frac{H^2}{\chi}\mathrm{Ra}^{-1/4}\mathrm{Pr}^{-3/4}\mathrm{Ar}^{-1}$ $[Ar^{-1}Ra^{1/4}\ Pr^{-1/2}]$
	diffusion time, $t_D[\tau_D]$	$Ar^{-2}\frac{H^2}{\chi}$ $[Ar^{-2}\ Ra^{1/2}\ Pr^{1/2}]$	$\frac{H^2}{\chi}\mathrm{Ar}^{-2}$ $[Ar^{-2}Ra^{1/2}Pr^{1/2}]$

				results of the basic state (ε=0.0)		
Pr	*Ra*	ymax	*Nu*	C_i evaluated at X=0.5		resonance frequency ω_r
0.07	105	9.2395	10-2	3.8103	0.8349	0.80
0.07	106	4.7024 ×	10-2	7.0342	0.8674	0.70
0.7	105	3.6223 ×	10-2	4.5154	0.9560	0.68
0.7	106	2.0011 ×	10-2	8.8107	0.9810	0.68
0.7	107	1.1347 ×	10-2	16.495	0.9597	0.67
7.0	105	1.3188 ×	10-2	4.7190	0.8635	0.55
7.0	106	7.4000 ×	10-3	9.2153	0.8006	0.57
7.0	107	4.1044 ×	10-3	17.304	0.7738	0.56

Table 2. Summary of the present numerical simulations.
C_i indicates the strength of interior stratification

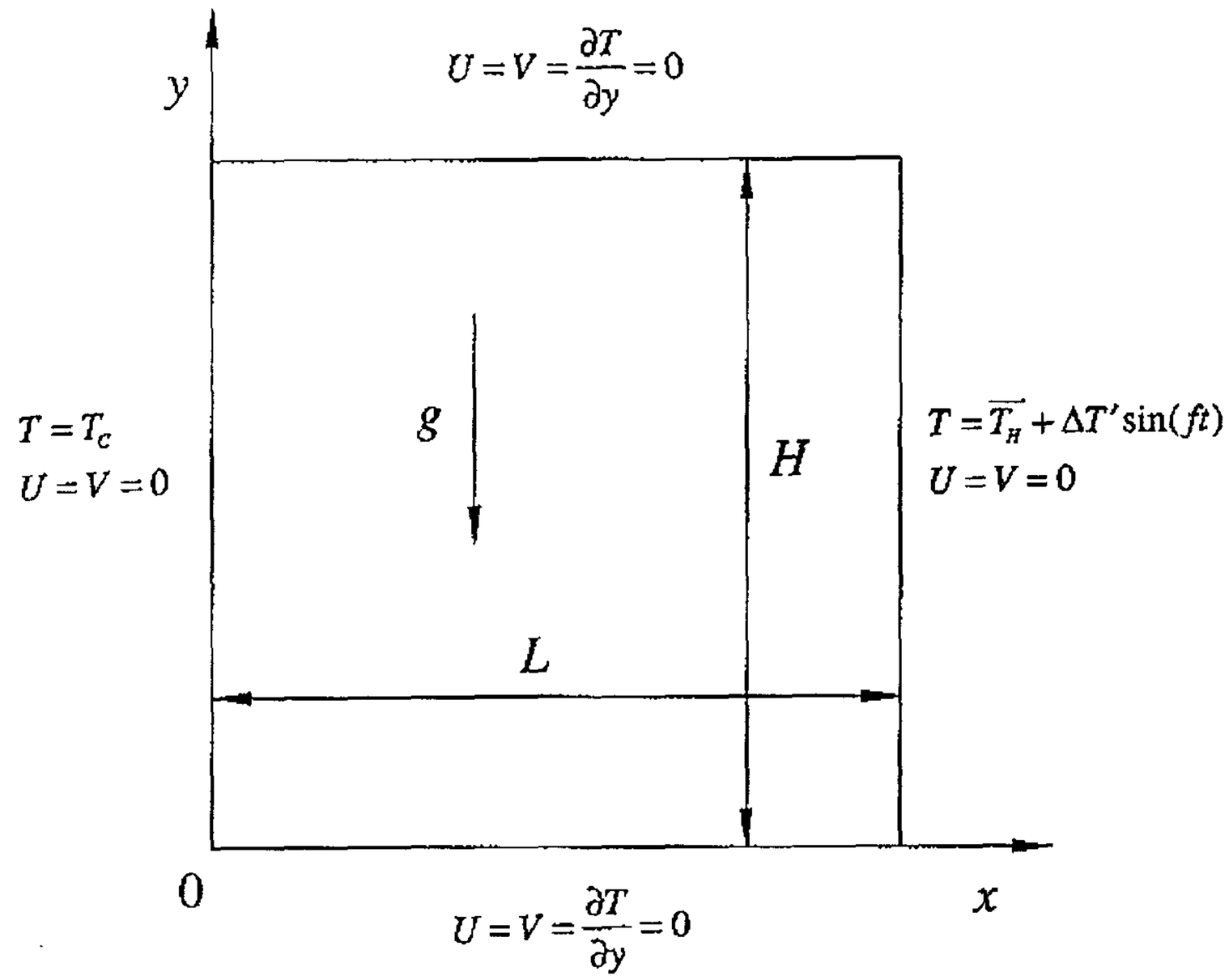

Figure 1 Sketch of the flow configuration.

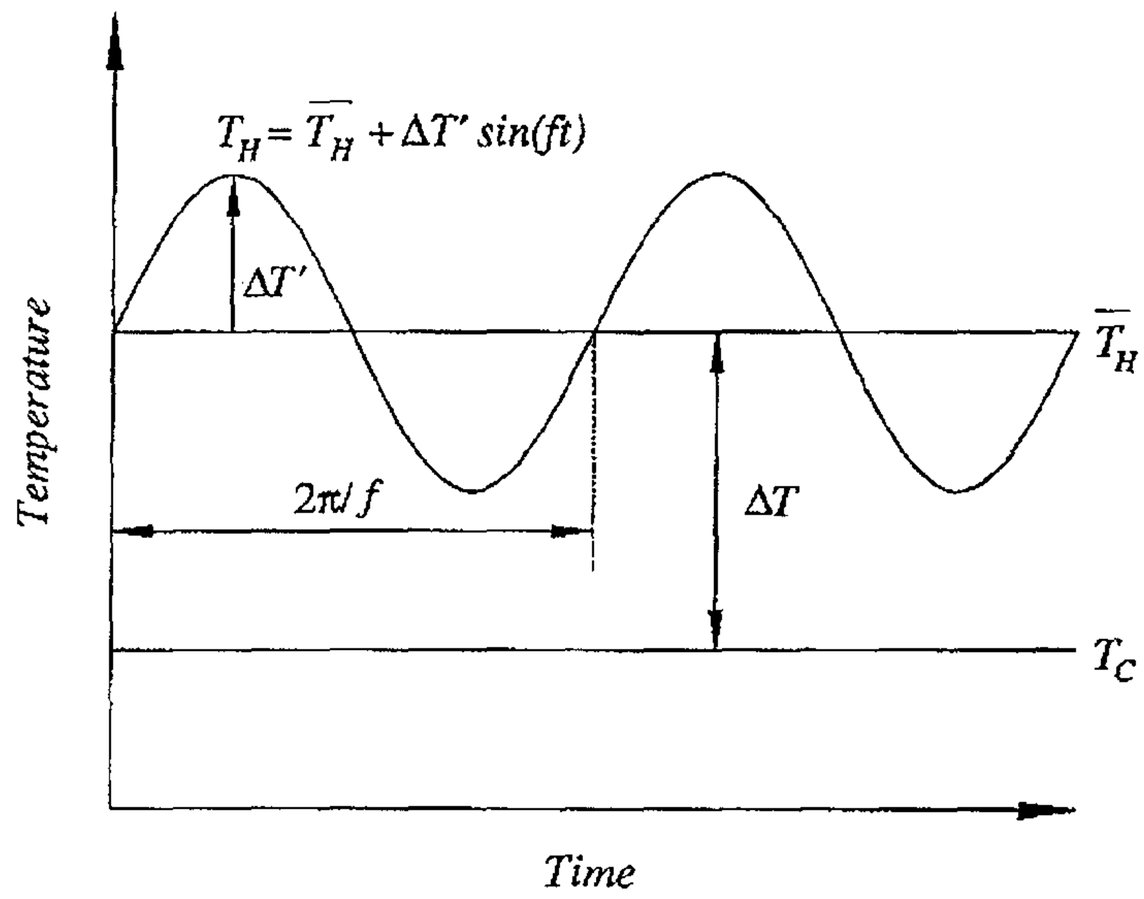

Figure 2 Time-dependent temperature boundary condition at the vertical sidewalls

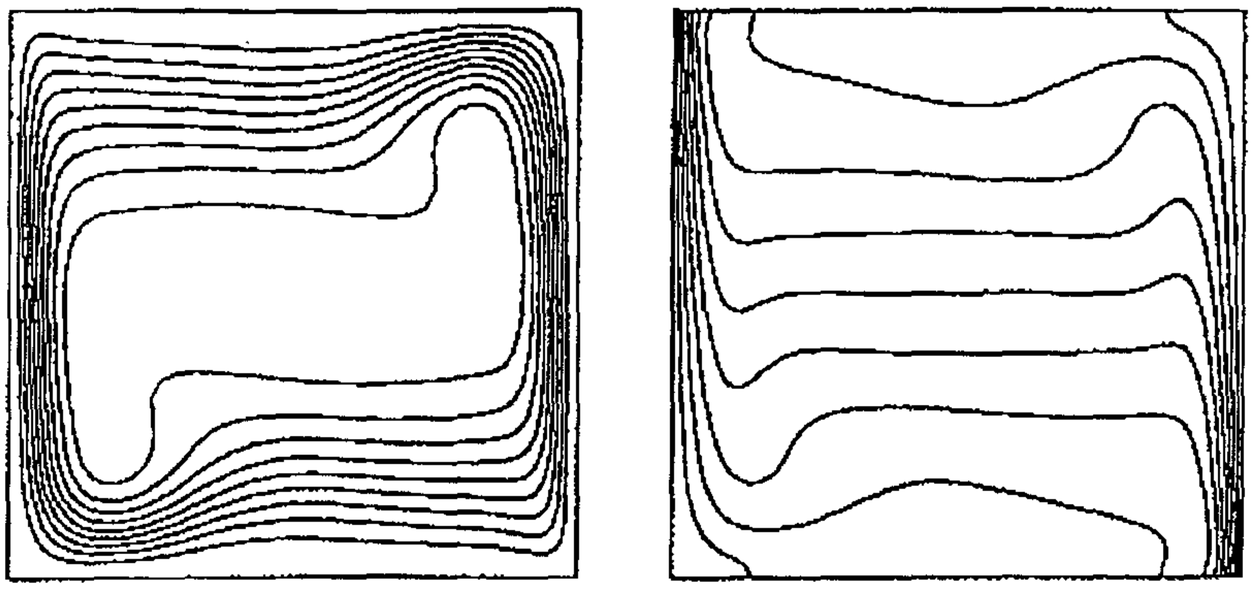

(a) (b)

Figure 3 (a) Streamfunctions and (b) isotherms of the basic state (ε=0.0) for Ra=10^6 and Pr=0.7. The increment of contour level $\Delta\psi$ is ψ_{max}/10 and the value of ψ_{max} is listed in table 2. $\Delta\theta$=0.1.

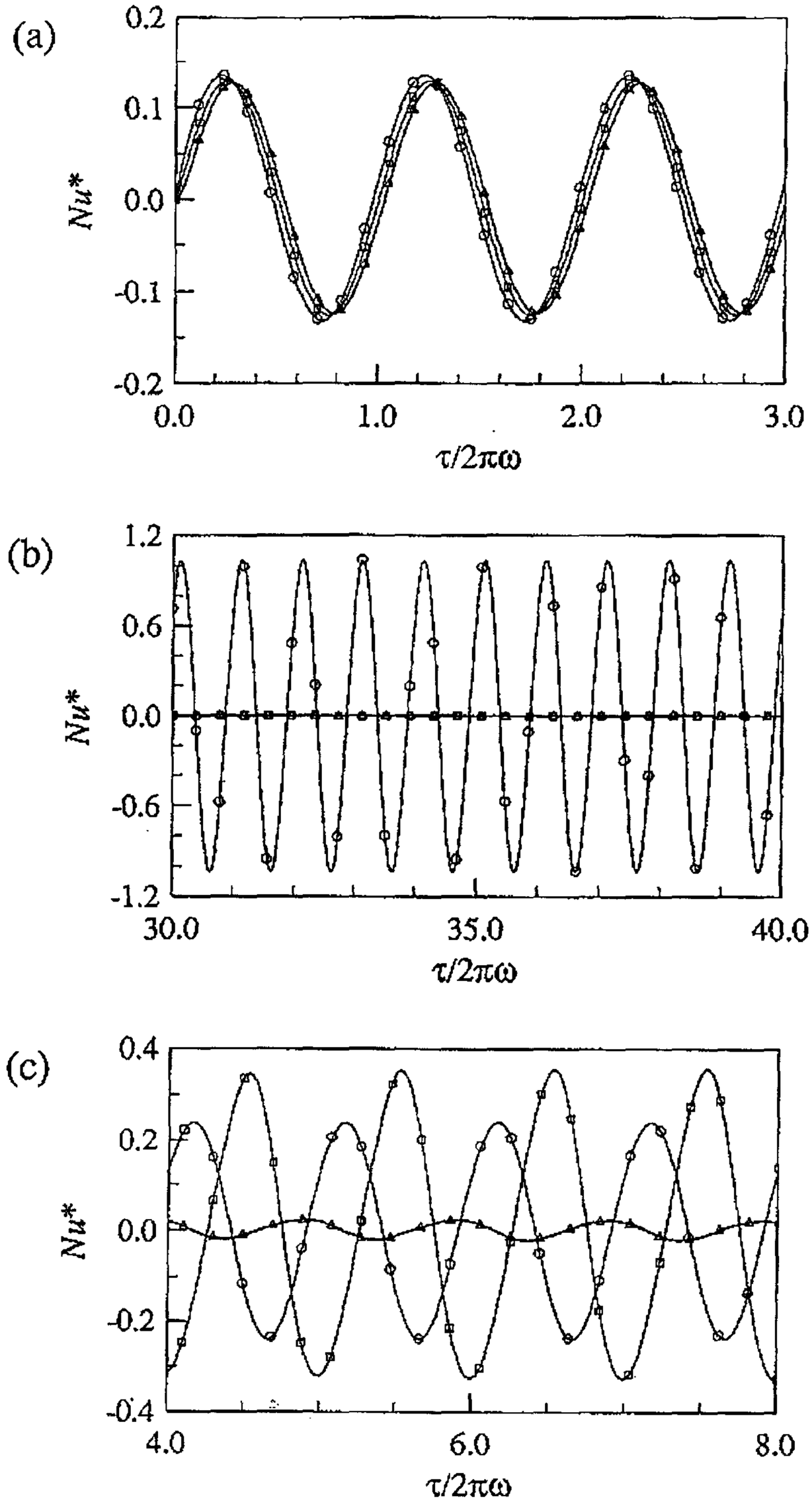

Figure 4 Time-dependent behavior of the overall Nusselt numbers for $Ra=10^6$ and $Pr=0.7$: (a) $\omega=0.01$; (b) $\omega=10.0$; and (c) $\omega=0.68$. Symbols ○,□,△ represent the Nusselt numbers at the hot vertical wall ($X=0.0$), at the vertical mid-plane ($X=0.5$), and at the cold vertical wall ($X=1.0$), respectively. Note that * denotes a normalized quantity by using equation (10).

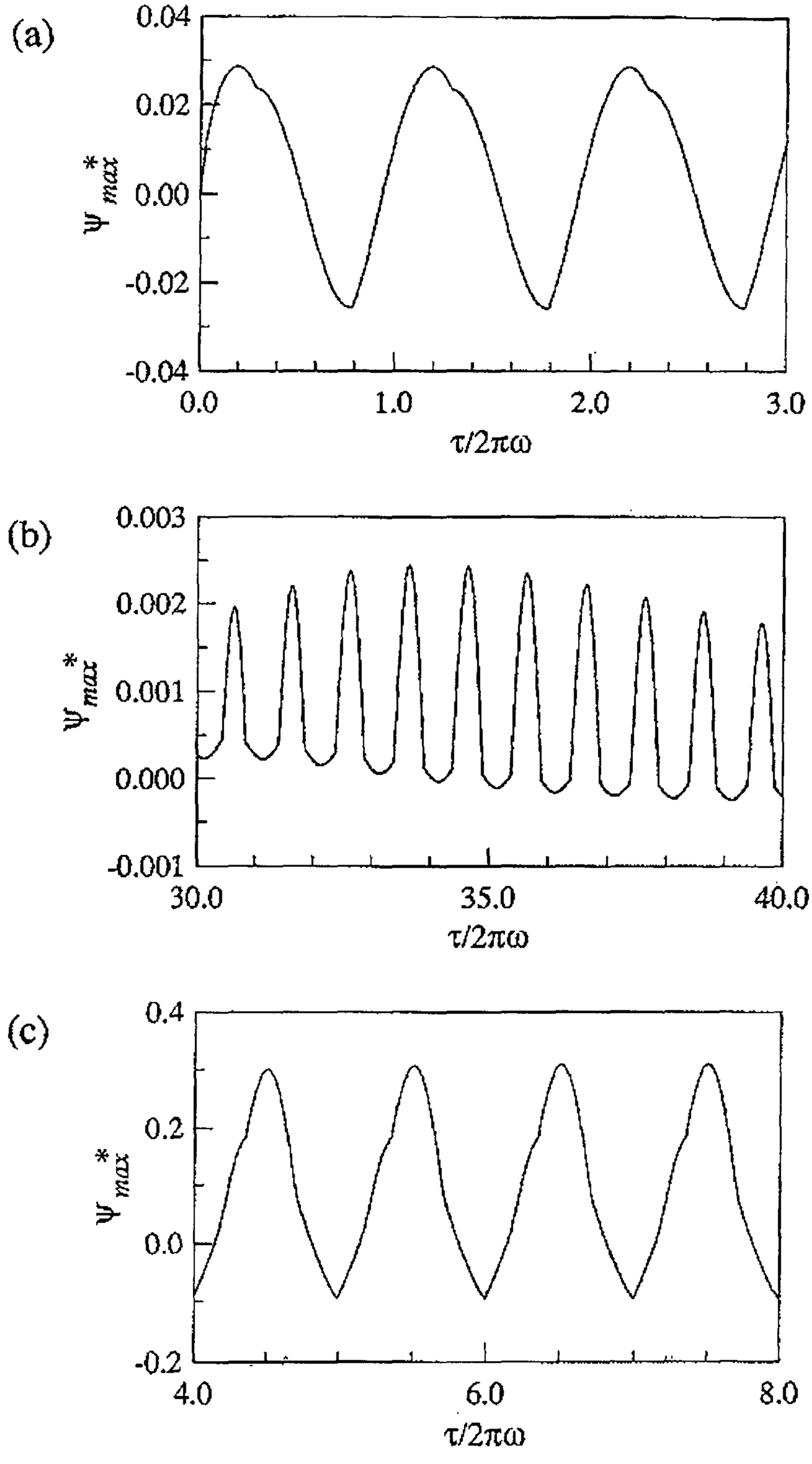

Figure 5 Time-dependent behavior of the normalized maximum streamfunction $\psi_{max}{}^*$ for $Ra=10^6$, and $Pr=0.7$: (a) ω=0.01; (b) ω=10.0; (c) ω=0.68.

(a)

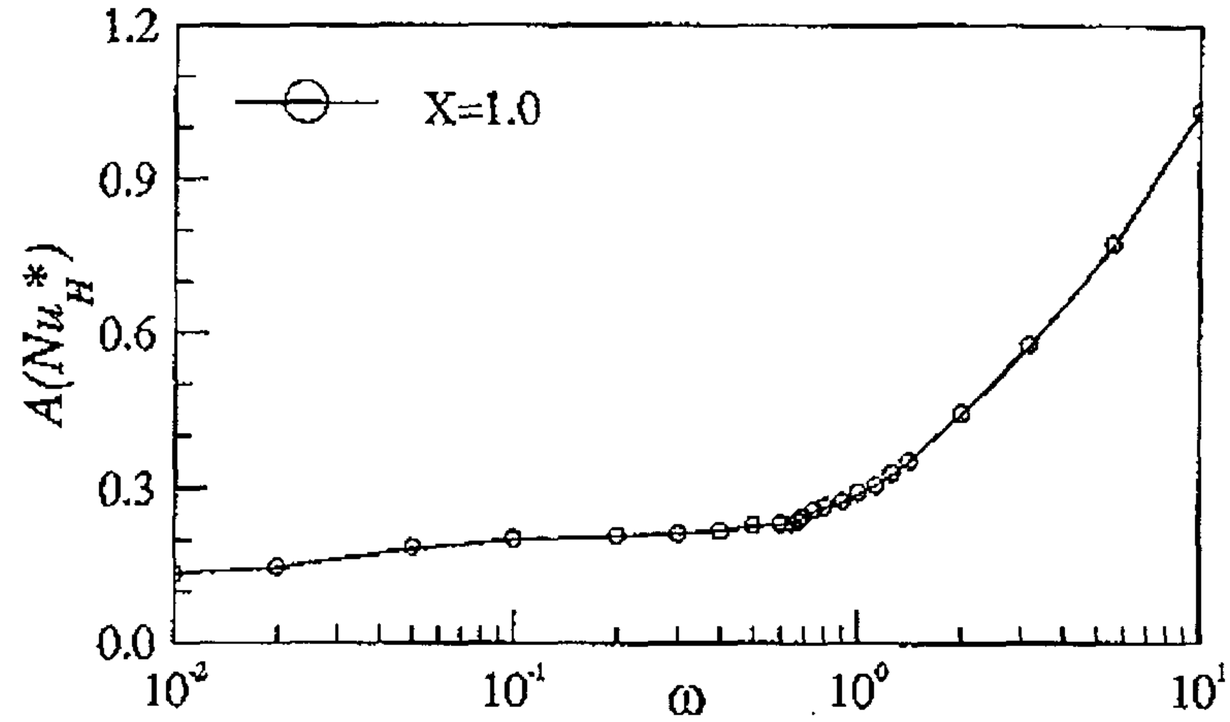
X=1.0
$A(Nu_H^*)$
1.2
0.9
0.6
0.3
0.0
10^{-2}
10^{-1}
10^{0}
10^{1}
ω

(b)

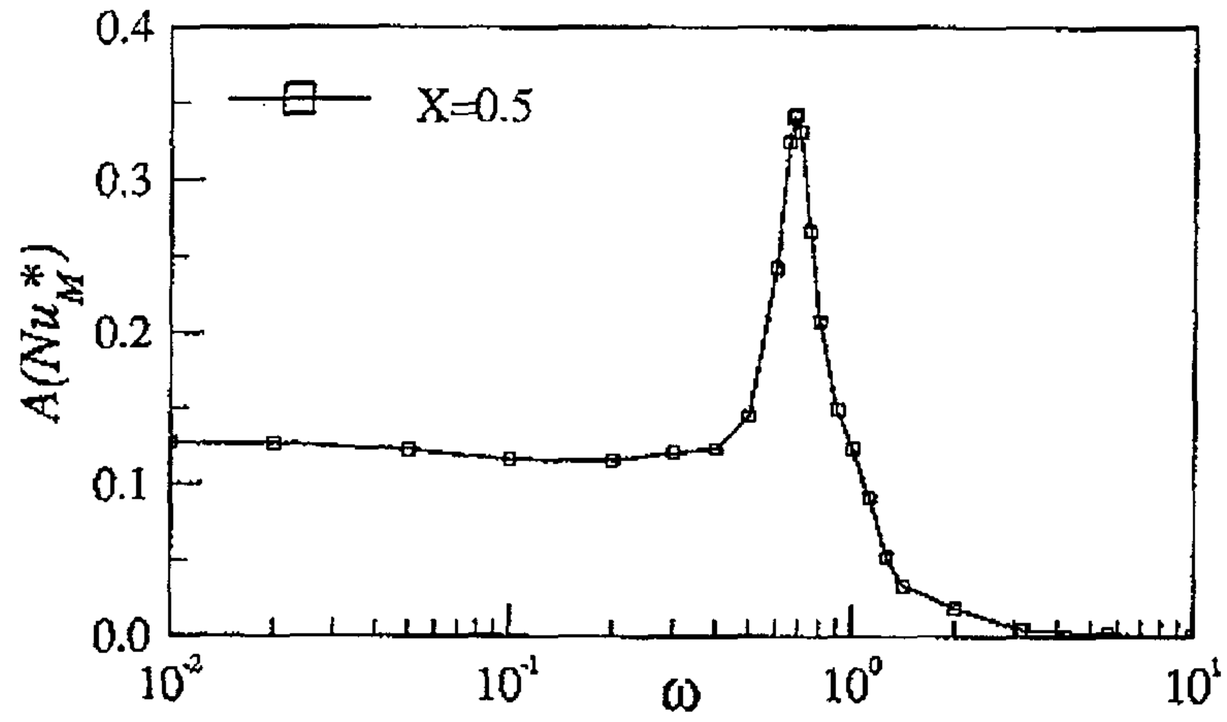
X=0.5
$A(Nu_M^*)$
0.4
0.3
0.2
0.1
0.0
10^{-2}
10^{-1}
10^{0}
10^{1}
ω

(c)

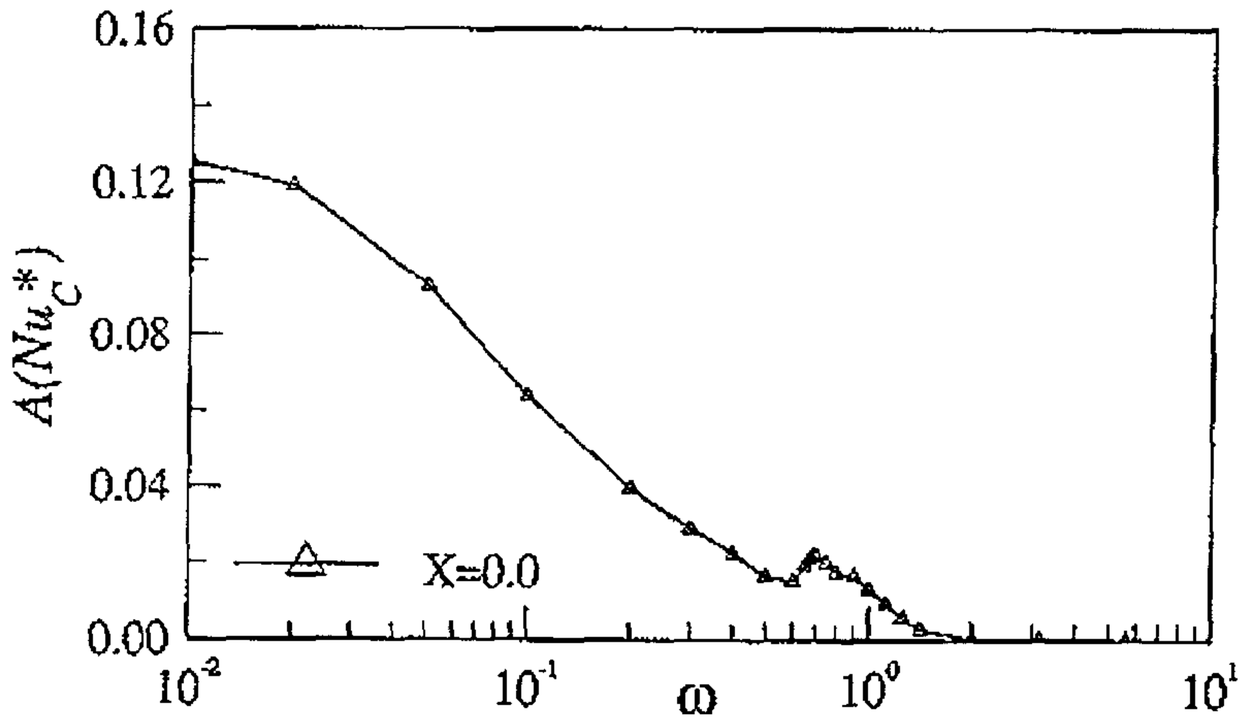
X=0.0
$A(Nu_C^*)$
0.16
0.12
0.08
0.04
0.00
10^{-2}
10^{-1}
10^{0}
10^{1}
ω

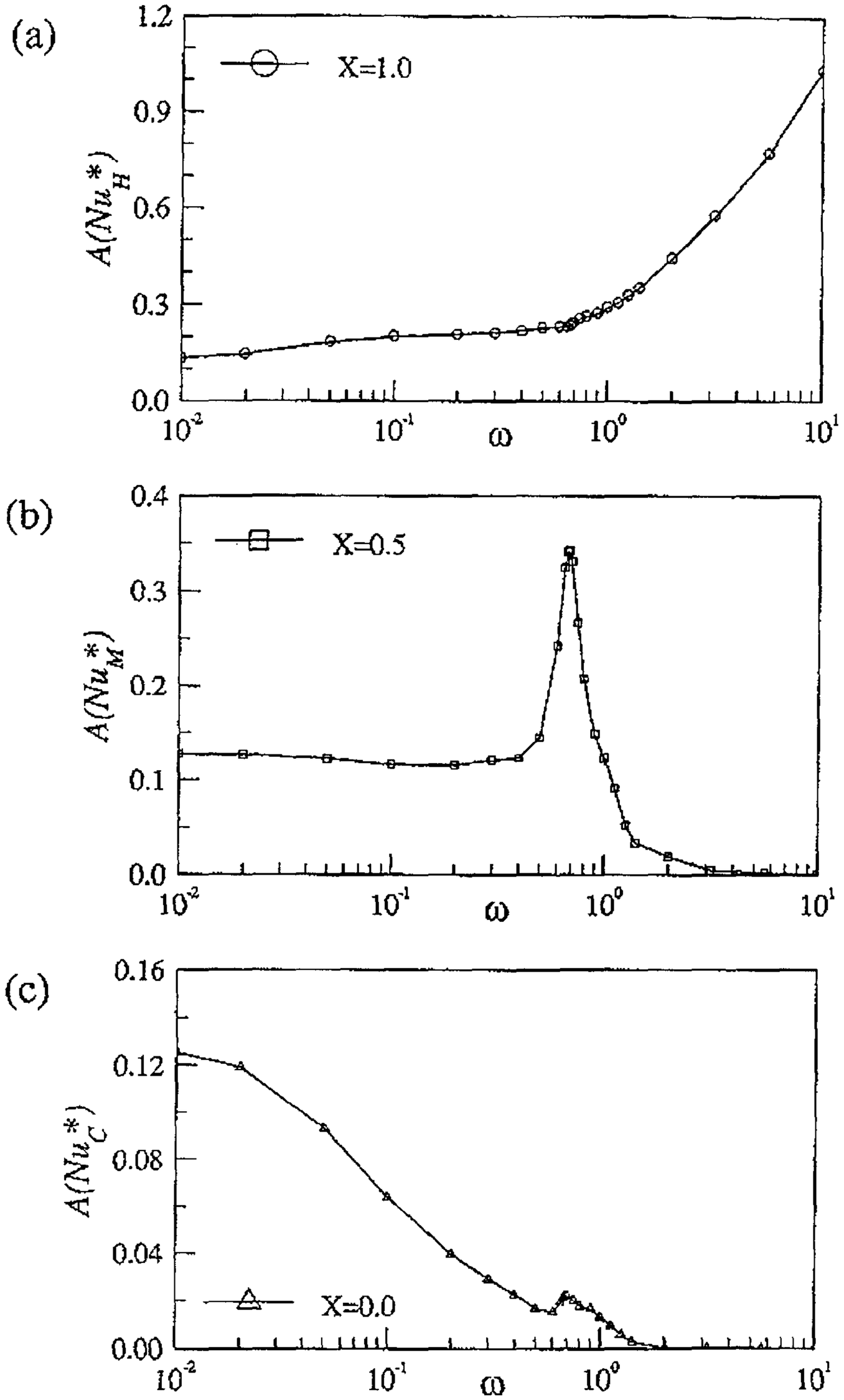

Figure 6 Variations of the fluctuations of flow variables with ω. (a) $A(Nu_H^*)$; (b) $A(Nu_M^*)$; (c) $A(Nu_C^*)$; (d) $A(\psi_{max}^*)$; (e) $\overline{\psi_{max}^*}$; and (f) $\overline{Nu^*}$. $Ra=10^6$, $Pr=0.7$.

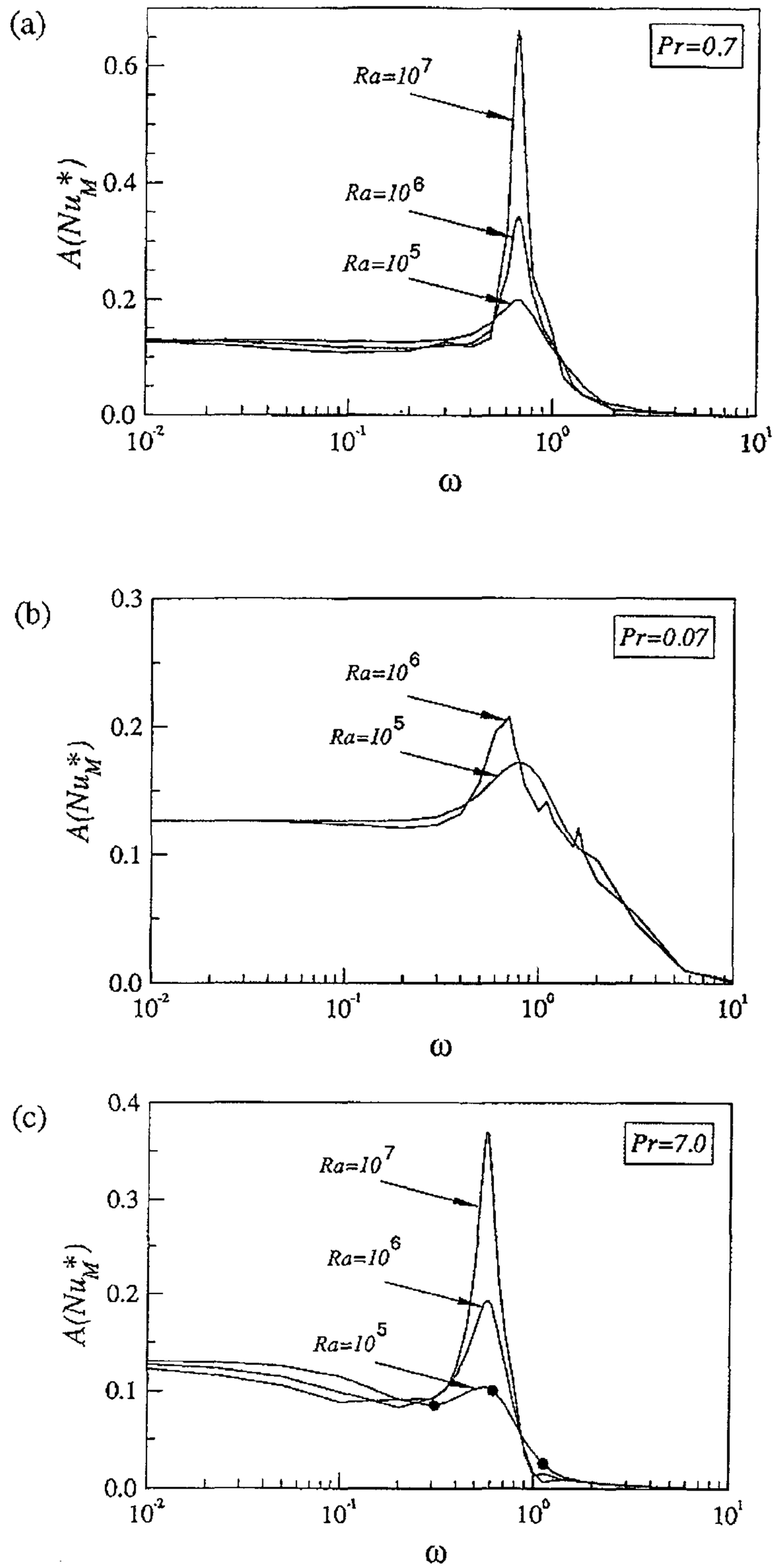

Figure 7 Effects of *Ra* and *Pr* on the $A(Nu_M^*)$-ω variations

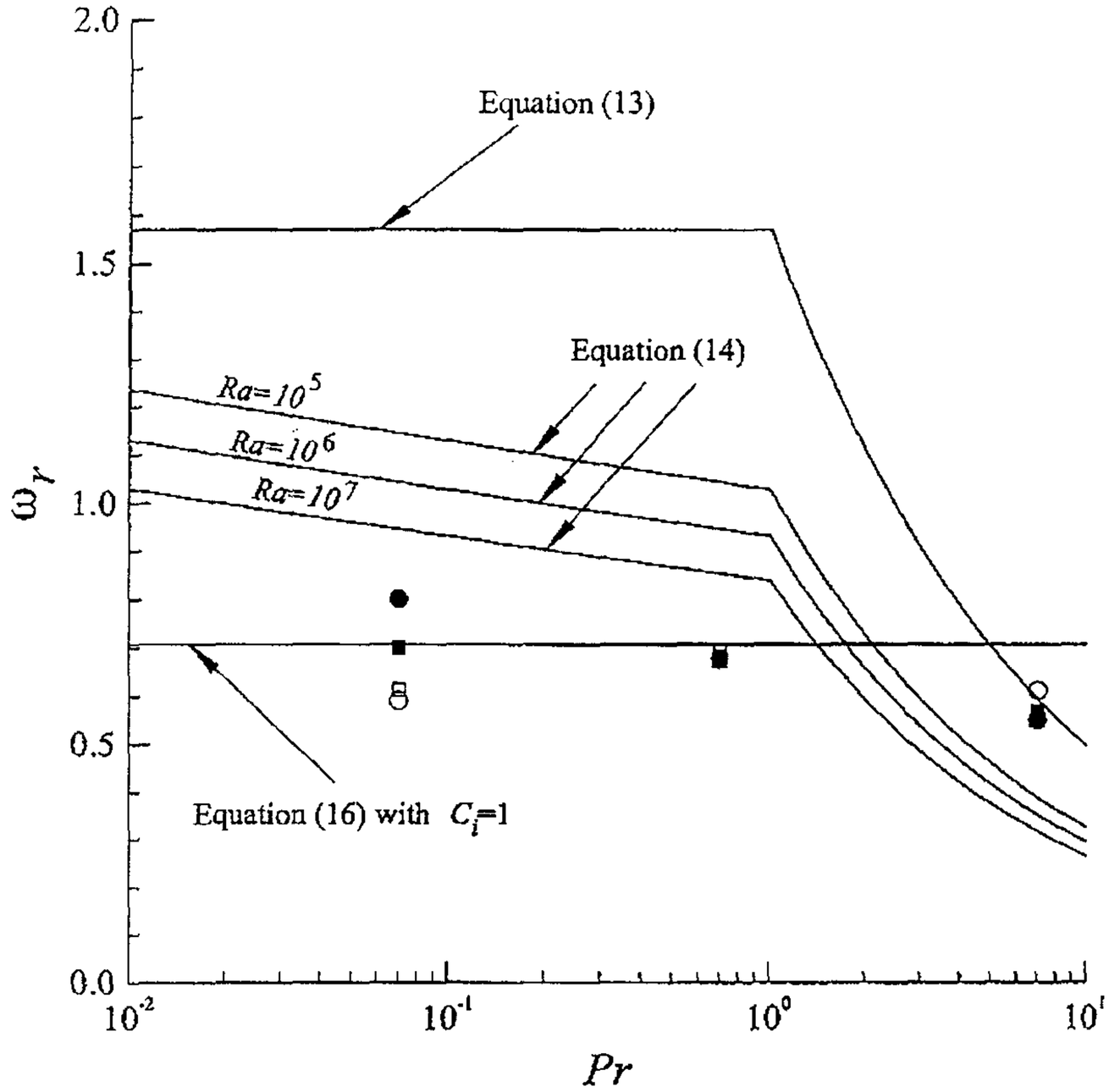

Figure 8 Values of the resonance frequency w*r*. Continuous lines are based on the scaling arguments, equations (13), (14) and (16). ●,■,▲ denote the present numerical results for Ra=10^5, 10^6, 10^7, respectively. ○,□,△ represent the values based on equation (16), when *Ci* is evaluated by using the vertical temperature distribution of the present numerical results for ε=0 at the mid-width of the cavity.

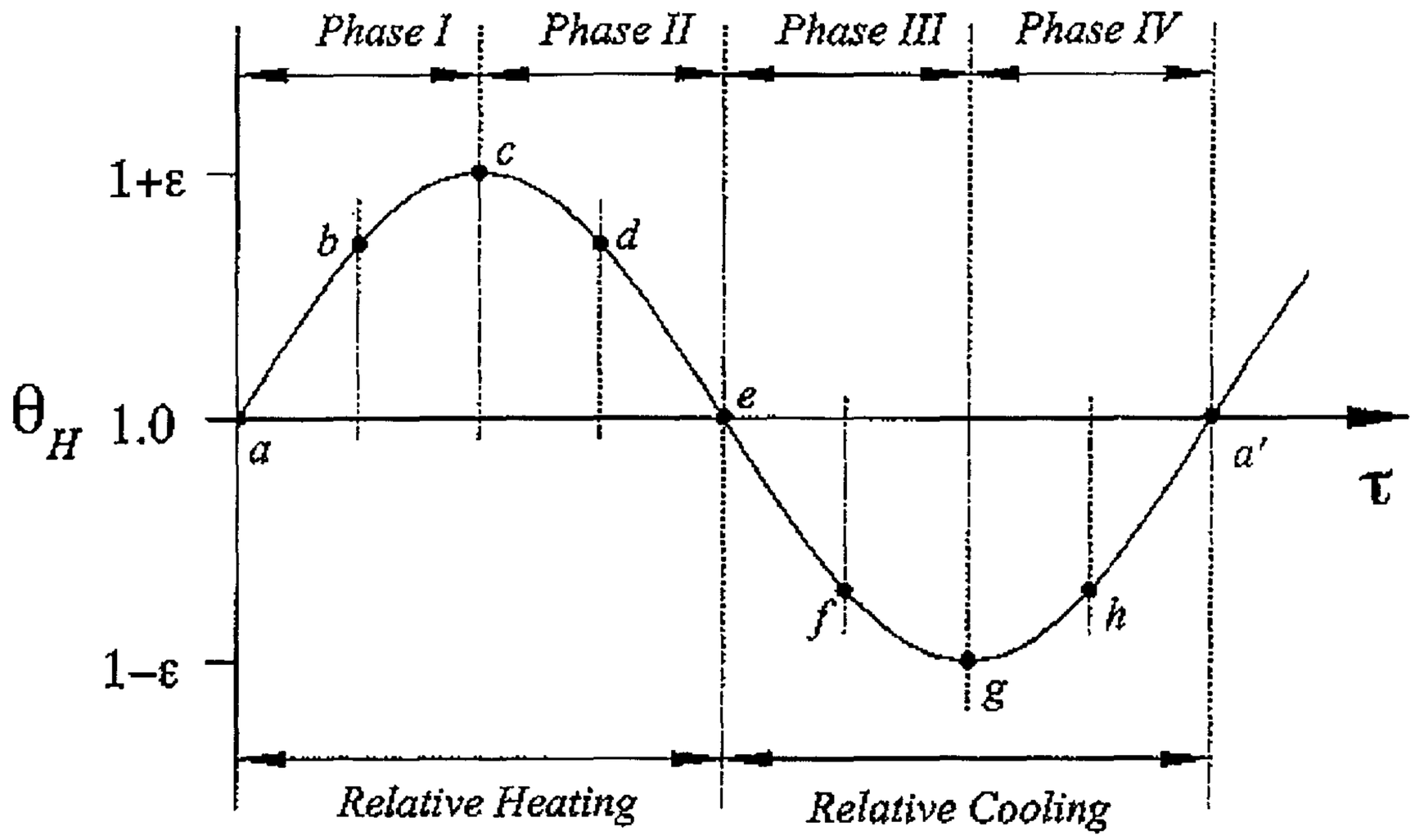

(a)

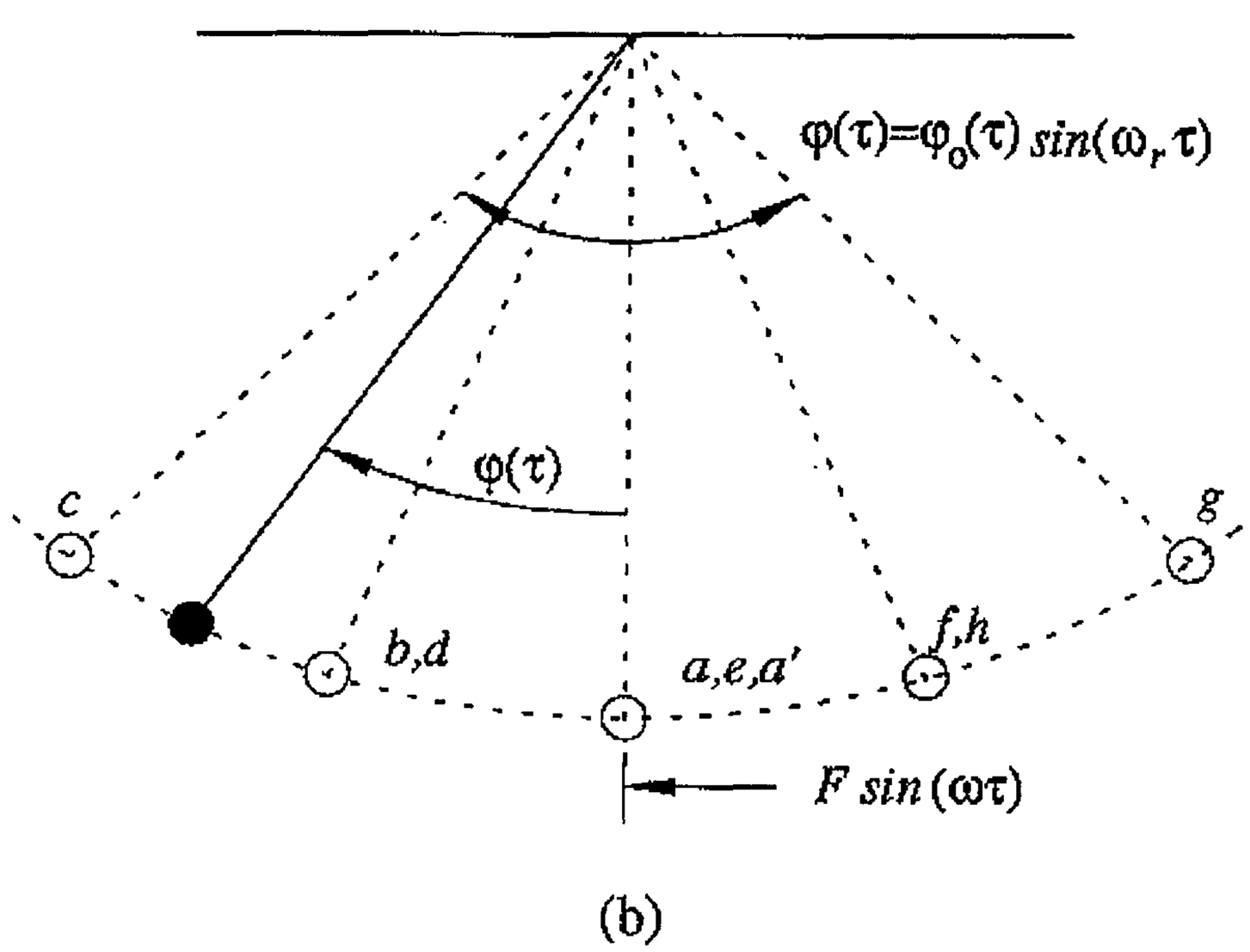

(b)

Figure 9 (a) Characterizations of heating and cooling modes relative to the basic-state at the hot wall. (b) An analogous model of a driven pendulum.

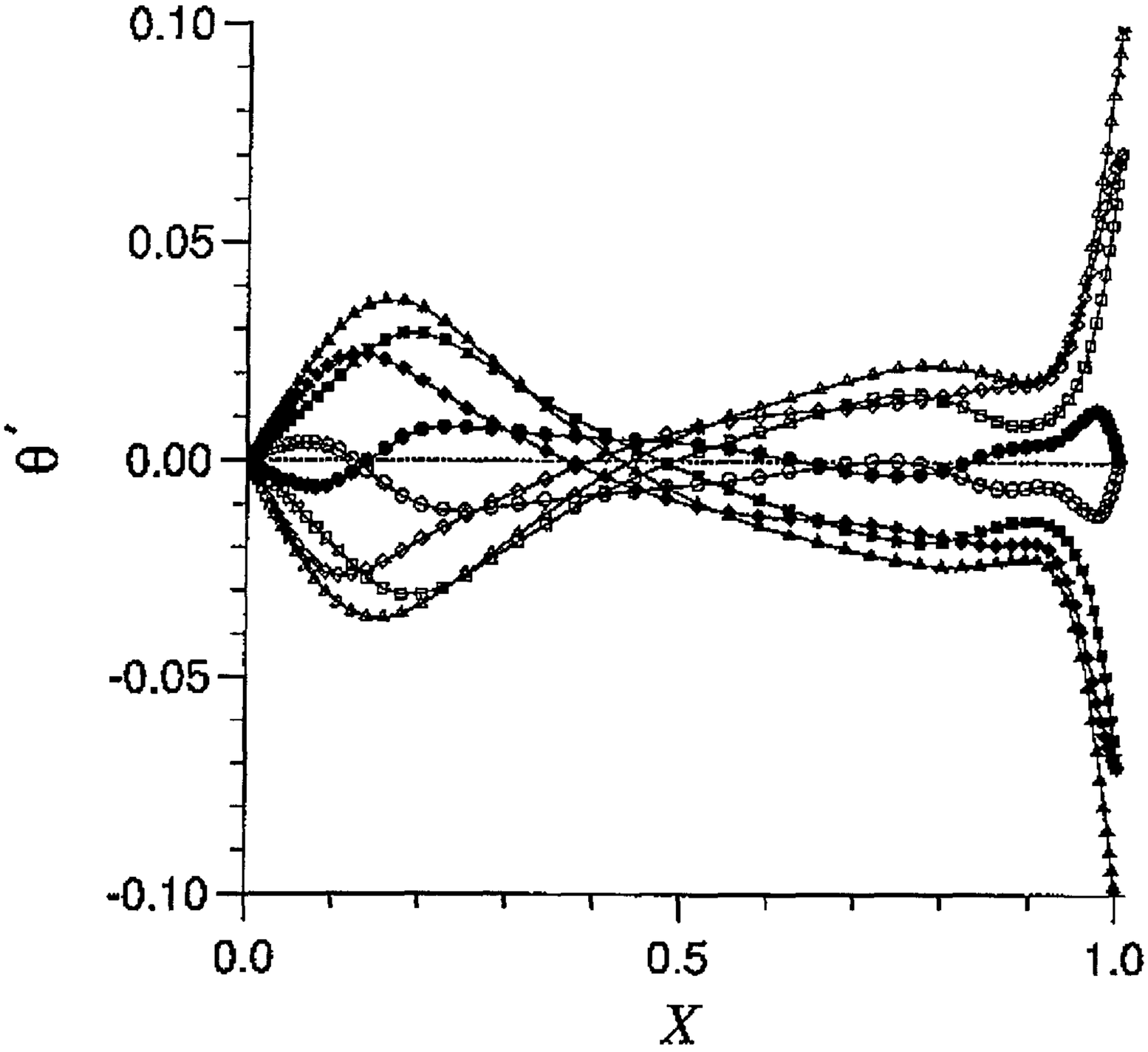

Figure 10 Time-dependent profiles of the oscillating temperature component, θ', in the horizontal mid-plane (Y=0.5). Ra=10^6, Pr=0.7 and ω=0.68. The time instants are : ○, $\tau = \tau_a$; □, $\tau = \tau_b$; △, $\tau = \tau_c$; ◇, $\tau = \tau_d$; ●, $\tau = \tau_e$; ■, $\tau = \tau_f$; ▲, $\tau = \tau_g$; ◆, $\tau = \tau_h$

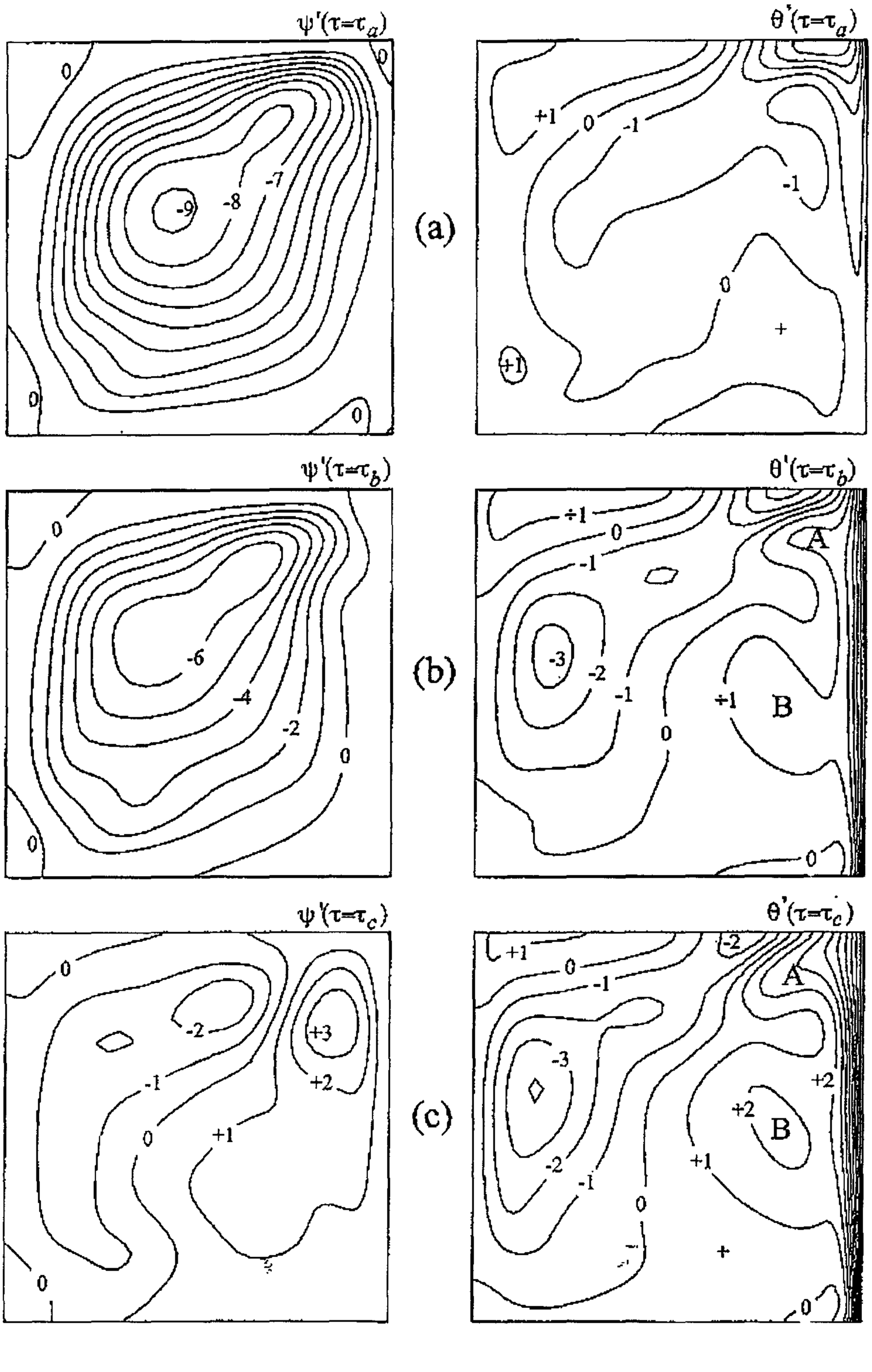
ψ'(τ=τ_a)
θ'(τ=τ_a)
(a)
ψ'(τ=τ_b)
θ'(τ=τ_b)
(b)
ψ'(τ=τ_c)
θ'(τ=τ_c)
(c)
A
B

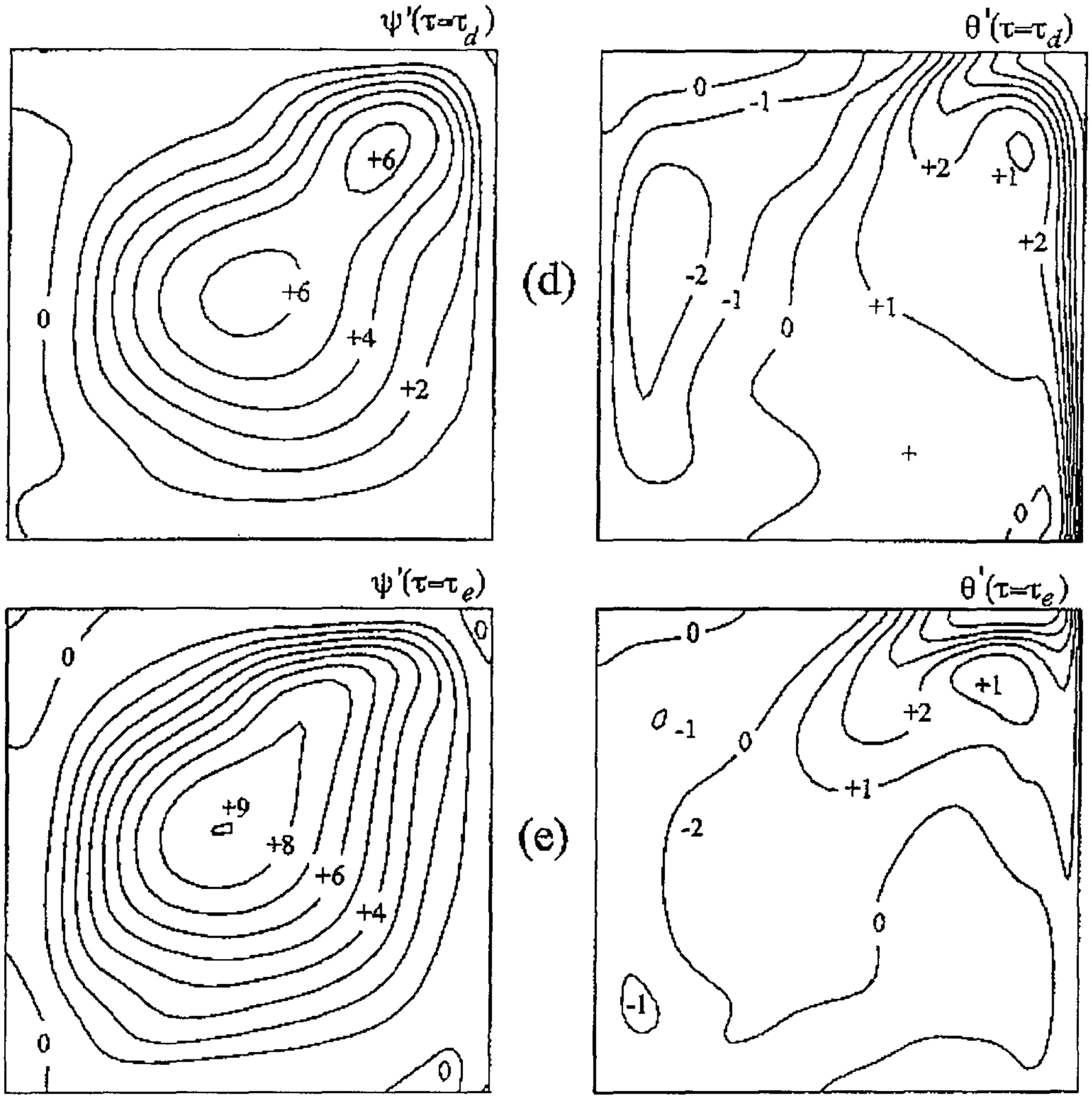

Figure 11 Sequential plots showing the oscillating part of streamfunctions (left column) and of isotherms (right column). Ra=10^6, Pr=0.7, and ω=0.68($\cong \omega_r$). The time instants are the same as in figure 9 The contour increments are $\cdot\Delta\psi' = 7.5\times10^{-4}$ and $\Delta\theta'$=0.01. The number, n, in the figures indicates the contour value $n\cdot\Delta\psi'$ or $n\cdot\Delta\theta'$.

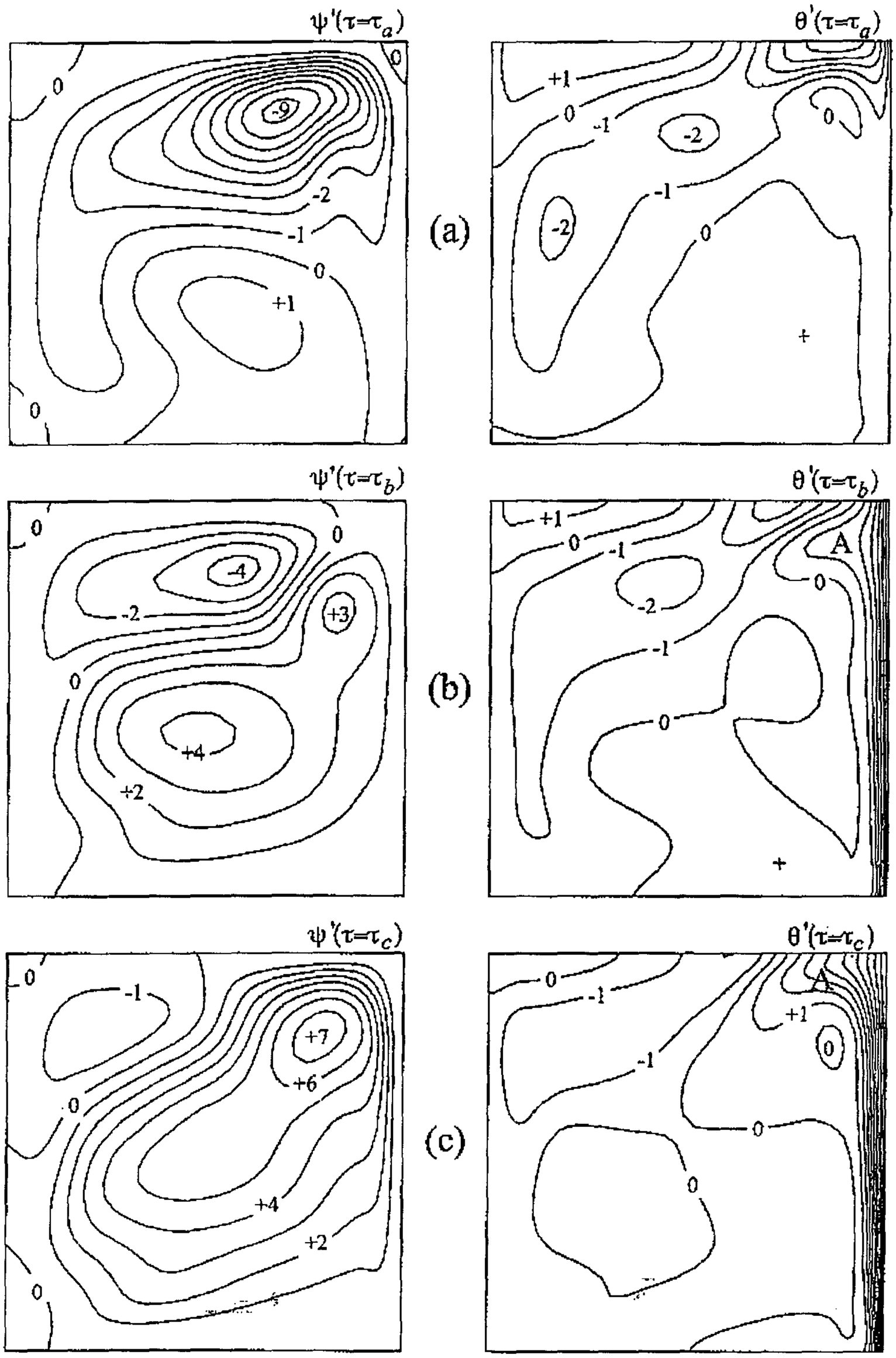

Figure 12 Same as in figure 11, except for $Ra=10^6$, $Pr=0.7$, and $\omega=0.5(<\omega_r)$

$\Delta\psi' = 5\times10^{-4}$.

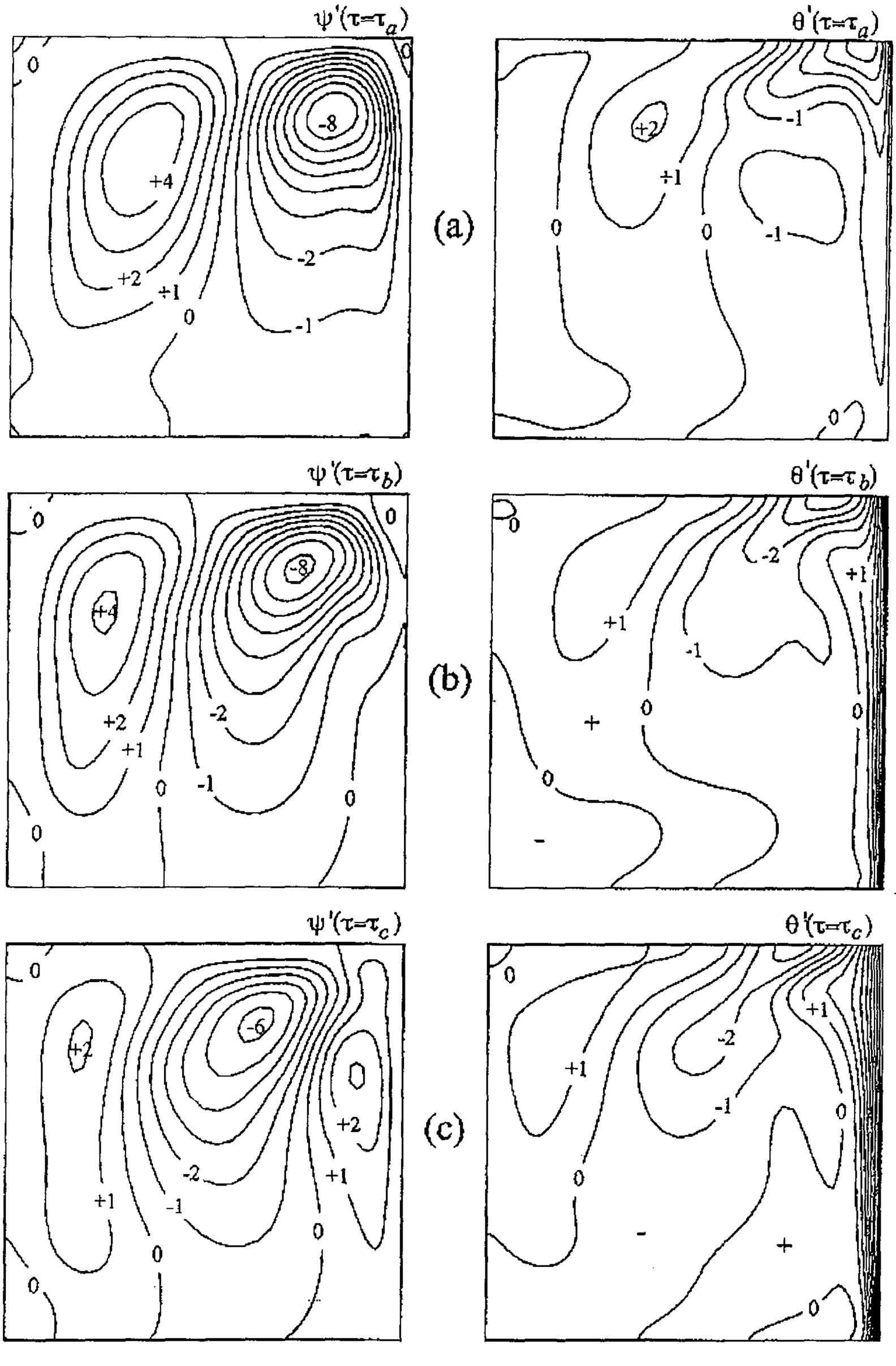

Figure 13 Same as in figure 11, except for Ra=10^6, Pr=0.7, and ω=1.0($>\omega_r$)

$\Delta\psi' = 5\times10^{-4}$.

제 7 장

Mass transfer characteristics for a rotating cup-like cylinder

(회전하는 컵 모양의 실린더에 대한 물질전달현상)

요 약 문

중심축에대하여 일정하게 회전하는 컵모양실린더의 유체유동과 물질전달 특성에 관한 수치연구가 행해졌다. 본 연구는 평균 Sherwood수만을 결과로 제시한 Sparrow와 Chaboki의 물질전달 실험을 모사한 것이다. 넓은 범위의 Reynold수에대하여 식의 포괄적이 수치해를 얻었다. 수치적으로 구축된 유동가시화를 통해서 속도장과 농도장의 구조를 제시한다. 대류전달 현상에 직접적을 영향을 미치는 좌우면 유동의 형태가 분석되었다. 회전방향유동의 분포가 제시되었다. 컵의 안쪽 면에서의 지역적 Sherwood 수를 도시화하였다. 바닥 면에서 물질전달이 발생하는 경우와
발생하지 않는 경우 두 가지에 관한 지역적 물질 전달 특성에 관하여 물리적으로 해석하였다. 수치적으로 구한 Sherwood수는 실험치 와 잘 일치한다.

Abstract

A numerical study is made of flow and mass transfer characteristic cup-like cylinder, which rotates steadily about its own central longitudin study simulates the earlier mass transfer experiment of Sparrow and Chabok provided only the averaged value of Sherwood number. Comprehensive nume solutions have been obtained to the Navier-Stokes equations over an extended Reynolds number. Numerically-constructed flow visualizations exhibit the st three-component velocity and concentration fields. The patterns of meridi which are directly responsible for convective transport, are analyzed. The di azimuthal flow are illustrated. Plots of the local Sherwood number at the in of the cup are given. Physically plausible descriptions are presented of th transfer characteristics for both cases of a transferring base endw non-transferring base endwall. The numerical results of the cavity-average number are consistent with the previous experimental data.

1. Introduction

Fluid flow and transport processes involving a rotating solid body po problem in fluid dynamics research. Convective fluid motions are induced rotating body, and these fluid flows give rise to enhanced transfer coeffici the surface of the body and the fluid. Several geometrically-simple body sh been considered, and associated augmentation of transport properties documented [e.g., [1-7]]. In particular, transport phenomenon in the interior cup-like cylindrical vessel, which rotates about its central axis, is of spec illustrated in Fig.1, owing to the cylinder rotation, there arise complex fl the cup interior as well as in the surroundings of the cup. Because of these activities, transfer coefficients at the inner cylindrical sidewall and at t disk of the cup are significantly increased. Determination of these transfer

important in the design and operation of a multitude of rotating fluid machinery, such as a chemical mixer, centrifuge, etc.

Sparrow and Chaboki [8] conducted a pioneering experimental investig mass transfer coefficients for a rotating cup, as sketched in Fig. 1. experimental methodology was naphthalene sublimation technique, which is k possess higher degrees of accuracy in assessing transport properties. In the two variants of boundary conditions were implemented. In one case, referred t A, the base endwall disk was equipped such that no mass transfer was permitte surface. This is equivalent to an adiabatic disk in heat transfer. Mass allowed only at the cylindrical sidewall surface, at which the naphthalene c was kept constant. In the other case, termed type B, both the cylindrical s the base disk were maintained at uniform concentration of naphthalene. analogous to the constant-temperature wall condition in heat transfer situatio

Extensive laboratory measurements of Sparrow and Chaboki [8] present overall mass transfer coefficients, which were embodied in the average number, over ranges of the rotational Reynolds number (Re) and of the cylind ratio (L/D, where L and D denote the height and diameter of the cylinder, resp Utilizing these data, experimental correlations were suggested for high Reynolds numbers, $Re \gtrsim O(10^3)$. These expressed the overall Sherwood number in the form :

$$\overline{Sh} = a Re^m (L/D)^n \qquad (1)$$

The empirically-fitted eqn. (1) was shown to reproduce adequat measurement data for the afore-stated two types of boundary conditions.

In summary, these laboratory measurements of [8] provided valuable inf on the averaged transfer coefficients for a rotating cup-like container. however, that the convective flow structure inside the cup was not examine experiments, no flow visualizations were conducted, and measurements were n of the field of naphthalene concentration. In [8], only the overall coeffic

transfer for the entire inner surface of cup was reported, and the local variance of mass transfer was not scrutinized. It is worthy of mention that no other published accounts are found in the literature which address the fundamental issues of transport phenomenon for a rotating vessel such as the one treated by Sparrow & Chaboki [8].

In this paper, it is proposed to seek comprehensive numerical soluti governing Navier-Stokes equation. The main advantage of numerical approaches details of flow and concentration fields, both at the solid surfaces and in region of the cup, can be described. The global structures of flow and concen the cup interior and in the surroundings close to the cup opening, are e ascertaining the impact of rotation-induced convection on the augmentation o processes. In the present efforts, numerical solutions are procured in t ranges comparable to the experimental conditions of Sparrow and Chabok numerical results thus obtained are in accord with the measurement data of ov transfer coefficients. These endeavors give credence to the present numeric and, based on these validations, numerical computations will be extended to broader ranges of Re and L/D than those of Sparrow and Chaboki. As stressed descriptions will be rendered of three-component flow and of concentration fi rotating cup. Numerically-constructed flow visualizations will be made, illustrate the convective characteristics of mass transfer. Systematically-organized computations illuminate the parametric dependence of transfer properties on Re and L/D as well as on the type of boundary conditions imposed on the body surfaces. On balance, the present paper represents an expanded and reinforced numerical model counterpart to the preceding experimental program of Sparrow and Chaboki.

2. Formulation and numerical model

In reference to the configuration of Fig. 1, the inner radius and he cup are respectively R and L, and w denotes the rotation rate of the cup. Th

governed by the Navier-Stokes equations of motions. For a cylindrical coordinate frame (r,q,z), with corresponding velocity components (u,v,w), these equations in dimensionless form are written as

$$u\frac{\partial u}{\partial r} + w\frac{\partial u}{\partial z} - \frac{v^2}{r} = -\frac{\partial p}{\partial r} + \frac{1}{Re}\left(\frac{\partial^2 u}{\partial r^2} + \frac{1}{r}\frac{\partial u}{\partial r} + \frac{\partial^2 u}{\partial r^2} - \frac{u}{r^2}\right) \tag{2}$$

$$u\frac{\partial v}{\partial r} + w\frac{\partial v}{\partial z} + \frac{uv}{r} = \frac{1}{Re}\left(\frac{\partial^2 v}{\partial r^2} + \frac{1}{r}\frac{\partial v}{\partial r} + \frac{\partial^2 v}{\partial r^2} - \frac{v}{r^2}\right) \tag{3}$$

$$u\frac{\partial w}{\partial r} + w\frac{\partial w}{\partial z} = -\frac{\partial p}{\partial z} + \frac{1}{Re}\left(\frac{\partial^2 w}{\partial r^2} + \frac{1}{r}\frac{\partial w}{\partial r} + \frac{\partial^2 w}{\partial z^2}\right) \tag{4}$$

$$\frac{1}{r}\frac{\partial (ru)}{\partial r} + \frac{\partial w}{\partial z} = 0 \tag{5}$$

$$u\frac{\partial C}{\partial r} + w\frac{\partial C}{\partial z} = \frac{1}{ReSc}\left(\frac{\partial^2 C}{\partial r^2} + \frac{1}{r}\frac{\partial C}{\partial r} + \frac{\partial^2 C}{\partial r^2}\right) \tag{6}$$

In the above, C denotes the dimensionless concentration, and other not standard. In the nondimensionalization, length is referenced by R, and veloc The dimensionless parameters are Re [$\equiv wR^2/\nu$], the rotating Reynolds num [$\equiv \nu/D$], the Schmidt number, in which n is kinematic viscosity and D diffu concentration. These physical properties are taken to be constant.

In accordance with the problem statement, the fluid far from the cup and at constant concentration C=0. Due to the cylinder rotation, fluid m generated inside and near the cup. The associated boundary conditions are

$$u=w=0,\ v=1 \quad \text{at } r=1,\ 0\leq z\leq L/R,$$
$$u=w=0,\ v=r \quad \text{at } 0\leq r\leq 1\ ,\ z=0. \tag{7}$$

For the concentration, in line with the experiments of Sparrow and Cha type A (a non transferring base):

$$C=1 \quad \text{at } r=1,\ 0\le z\le L/R,$$

and

$$\frac{\partial C}{\partial z}=0 \qquad \text{at } 0 \quad r \quad 1\ ,\ z=0, \tag{8a}$$

and, for type B (the cylindrical sidewall and the base endwall di constant concentration):

$$C=1 \quad \text{at } r=1,\ 0 \quad z \quad L/R,\ \text{at } 0 \quad r \quad 1\ ,\ z=0. \tag{8}$$

In the experiment of [8], the outer surface of the cylindrical si non-transferring, i.e.,

$$u=w=0,\ v=Ro,\ \ ,\ \frac{\partial C}{\partial r}=0 \quad \text{at } r=Ro \quad 0\le z\le L/R \tag{9}$$

where Ro denotes the nondimensional radius of the outer surface of the solid w

The above system of equations is solved by adopting the well-est numerical algorithm SIMPLER [9]. The particulars of the finite-differencing s solution procedures have been widely publicized, and they need not be rec here. As illustrated in Fig. 1, the calculation domain was taken to be suffi to simulate the experimental circumstances. The outer boundary of the computation domain was set rc = 15.0 and zc = 15.0. A systematic check was made to ascertain the sensitivity of the results to the size of domain. For several sets of pertinent external parameters, as rc and zc were varied between 10.0 to 20.0, the corresponding changes in the computed velocity and concentration fields inside the cup were typically less than 1%. The boundary conditions at the outer surface of this domain were specified as

$$\frac{\partial (ru)}{\partial r}=v=w=0,\ C=0 \quad \text{at} \quad r=r_c \tag{10}$$

$$u=v=\frac{\partial (w)}{\partial z}=0,\ C=0 \quad \text{at} \quad z=z_c \tag{11a}$$

$$u=v=w=0, \quad C=0 \quad \text{at} \quad z=0, \quad Ro \leq r \leq r_c \tag{11b}$$

As seen in (11b), the outer boundary condition at z=0 simulates the exp condition of [8]; in the experiment, the rotating cup was placed on a large table. Again, it is pointed out that the flow field in the interior of t concern, and these far-outer conditions are shown to have negligibly small i the interior flows.

At the central axis, symmetry requirements are enforced

$$u=v=\frac{\partial w}{\partial r}=0, \quad \frac{\partial C}{\partial r}=0 \ \text{at} \ r=0 \tag{12}$$

A staggered and stretched mesh was selected, with the grid points near the solid boundaries. Correspondingly fewer grid points were employed radii and heights in the computational domain. The actual thickness of cylindrical sidewall of the experiment was not stated in [8]. In the pre Ro=1.01 was used. It is noted that the conditions at the outer surfac non-transferring cylindrical wall (r=Ro) have minimal impact on the glo development inside the cup. Therefore, the precise value of Ro is of little c Extensive sensitivity tests were conducted of the computed results to grid stretching formula. These exercises confirmed satisfactory grid-convergence of the results. For most calculations, a grid network of 60×70 in the (r-z) plane was adopted.

3. Results and discussion

In conformity with the naphthalene experiment of [8], Sc = 2.5, and

in the computations. The range of Re encompassed $30 \lesssim Re \lesssim 3500$, although the experiment of [8] covered only the high-Re regime $Re \gtrsim 800$. The objective here is to undertake a comprehensive simulation such that eminent flow characteristics for relatively low Re values may also be identified. In the present mass transfer simulations, the velocity field and concentration field are not coupled. It follows that, for both type A and type B, the flow pattern is the same; only the concentration field differs.

The numerical results are now processed to disclose the three-c velocity structure and concentration. Of particular interest is the meridion pattern in the (r-z) axial plane. It is convenient to introduce the meri function Ψ, which is defined such that

$$u = \frac{1}{r} \frac{\partial \Psi}{\partial z}$$

$$w = -\frac{1}{r} \frac{\partial \Psi}{\partial r}$$

The behavior of meridional flow is directly responsible for the enhancement of transport phenomena [[4]-[7]]. In Figs. 2-5, a series of plots y and C, are given for varying values of Re. First, the global flow characterized. In general, the rotation of the endwall disk of the cup induce toward the base from the surroundings. This is a well-documented elementa driven by a rotating disk. For high Re, the Ekman boundary layer is formed disk and the axial flow is scaled with $Re^{-1/2}Rw$ (dimensional). This consequence of the celebrated Ekman layer pumping effect [see, e.g., [10] present problem, since the base of the cup is finite in size and shroud cylindrical wall, the downward axial flow has to move radially outward at mod large radii. At large radii near the cylindrical wall in the interior of the cup, due to the constraint of mass continuity, an upward flow is maintained to exit into the surroundings. The overall circuit of meridional fluid motions may thus be described as a kind of washing process. Namely, fresh fluid is drawn from the surroundings into the cup interior, and while traveling over the surfaces of the base and of the cylindrical wall, the

fluid washes off the naphthalene. This naphthalene-enriched fluid leaves through the cup opening at large radii and enters into the surroundings [[6], [7]].

Fig. 2 exemplifies the results for low Re. In this case, the convect due to the rotation of the cup is comparatively weak, as demonstrated in Fig. 2(a). The general flow structure exhibits the above-described qualitative pattern. For low Re, the concentration field is heavily influenced by conduction. In Fig. 2(c), in the bulk of the cup interior, concentration decreases fairly monotonically from the cylindrical wall toward the axis. Since the base disk is non-transferring, the iso-concentration lines encounter the base perpendicularly. In Fig. 2(d), the base is transferring, and, concentration decreases almost linearly from the solid surfaces toward the central interior region. Considerable influence of conduction is also discernible in Fig. 2(d).

At large Re, it is conspicuous that the boundary-layer-like flow c manifested. The penetration of the fluid into the cup interior is more effec in Fig. 5(b). The boundary layers, both on the disk and the cylindrical wall, and thin. Figs. 5(c) and 5(d) indicate that, at large Re, naphthalene tends to to thin boundary layers adjacent to the solid walls, and in the bulk of the i of the cup, concentration is very weak. A gradual shiftover of the flow char one with a substantial effect of conduction [Fig. 2] to one with an ove influence of convection [Fig. 5], is depicted in Figs. 2-5. It is interestin the qualitative difference in the C-field between type A and type B at lar illustrated in Figs. 5(c) and 5(d). When the base is non-transferring, th reaches the vicinity of the bottom of the cylindrical wall has very low co Therefore, the concentration boundary layer on the cylindrical wall is thin In the case of a transferring base, a concentration boundary layer is present As a result, the fluid that moves upward in the boundary layer on the cylind has already been enriched by the base disk. Consequently, the concentration boundary layer on the cylindrical wall is thicker and comparatively less

distinct than for the case of a non-transferring disk. The flow visualizations and the depiction of the C-fields are consistent with the afore-stated physical portrayals.

The numerical results are analyzed further to permit a quantitative ev the effect of Re. Fig. 6 illustrates the radial profiles of axial velocity. At of the cup interior [Fig. 6(a) for z=0.5L/R], as Re increases, the intensific well as the thinning of the boundary layer at the cylindrical wall, is evident. At the opening of the cup [Fig. 6(b) for z=1.0L/R], a similar trend is visible. However, at this height, the magnitude of the upward motion is greater and the boundary layer is thinner than in the interior regions [note the difference in the scales of the ordinates of Figs. 6(a) and 6(b)].

Representative vertical profiles of the radial velocity at several ra are displayed in Fig. 7. In the central interior region, curves for r=0. demonstrate that the cylindrical sidewall effects are insignificant. At large curve for r=0.8], considerable sidewall effects are discernible. At low value horizontal velocities in the central region are directed radially outward in in the bottom portion of the cavity, and u decreases monotonically with heig increases, it is evident that the boundary layer-type flow character prevails Fig. 7(d), at large Re, in the bulk of the interior, u is practically zero. O and distinctive Ekman layer on the base disk, a paradigmatic variation of u w is seen. The effect of the sidewall on the flow behavior is comparatively s Re takes a large value.

The structure of the azimuthal velocity v is now examined. Fig. 8 vertical profiles of the angular velocity (v/r). Note that, due to the rotat the primary flow of O(1) exists in the azimuthal direction. When Re is low 8(a)], the entire flow field is heavily influenced by viscosity effects. variations appear to be fairly monotonic in much of the interior. As Re inc establishment of boundary layer is evident, and the effect of the no-slip con cylindrical wall is confined to a narrow strip close to the wall. At large Re Fig. 8(d), the bulk of the interior core is nearly non-rotating. The rotating

fluids are concentrated to the Ekman layer on the disk and to the cylindrical wall boundary layer. This is in confirmation of the much-studied behavior of bounded rotating fluid motions at large Re [e.g., [10-12]].

Now, compiling the numerical data, the local Sherwood number Sh, $Sh \equiv \frac{\partial C}{\partial n}$ where n is the coordinate normal to the solid wall surface, has been calcula 9. Fig.9(a) demonstrates the Sh-distribution on the cylindrical wall for type A. For this case, the base is non-transferring[$Sh_b \equiv 0$ at the base]; therefore, the fluid that reaches the bottom region of the cylindrical wall is of very low concentration, since the fluid has not been enriched with naphthalene while traveling over the disk. Because of a large concentration difference between the fluid and the cylindrical wall, mass transfer is vigorous and the resulting Sh_c is high in the bottom portion of the cylindrical wall. As the fluid flows upward along the cylinder wall around intermediate heights, the fluid becomes enriched in naphthalene. This reduces the difference in naphthalene concentration between the fluid and the solid wall; consequently, Sh_c decreases in these regions. Near the opening of the cup, as displayed in Figs. 2-5, the fluid makes a sharp turn radially outward to exit into the surroundings. This generates steep velocity gradients, together with the thinning of the concentration boundary layer, in this localized zone. Therefore, Sh becomes large locally, and the Sh-behavior in Fig. 9(a) is compatible with this physical reasoning. The Sh-distributions for type B, for which both the base and the cylindrical wall are transferring, are displayed in Fig. 9(b) and Fig. 9(c). As portrayed in the flow visualization pictures of Figs. 2-5, fresh fluid is sucked into the cavity interior over much of small and moderate radii. This fluid, with almost zero concentration, penetrates down to the base disk over this radial extent. Consequently, mass transfer from the base (C=1.0) to the fluid is vigorous, which turns up in a large, and radially-uniform, value of Sh_b over much of the disk [see Fig. 9(b)]. When the fluid reaches large radii close to

the corner adjoining the bottom of the cylindrical wall, the fluid has been appreciably enriched with naphthalene. This brings forth a drop in mass transfer rates, which shows up in decreasing Sh at large radii of the disk as well as in the lower zones of the cylindrical wall. At mid-heights of the cylindrical wall, because of intensified convective flows in the vertical boundary layer at the cylindrical wall, Sh_c tends to increase slightly with height. Near the opening of the cup, due to a sharp turn of the flow direction, as the fluid exits into the surroundings, the thickness of concentration boundary layer decreases. This, together with large velocity gradients, gives rise to substantially enhanced transfer processes. Large values of Sh_c in the opening region of the cylindrical wall of the cup, as demonstrated in Fig. 9(c), are indicative of the reasonableness of the above physical interpretations. Note that the average value of Sh_c for type A is generally larger than for type B [note the difference in scales for Sh_c between Figs. 9(a) and 9(c)]. This observation is in accord with the earlier findings of [8].

Finally, the computed data for local Sh are integrated to produce value $\overline{\mathrm{Sh}}$, which was previously reported by the experiment of [8]. Fig. 10 cross-comparisons between the measured value of $\overline{\mathrm{Sh}}$ and the present numerical It should be mentioned that the experimental data of [8] were secured only large-Re regime, i.e. $\mathrm{Re} \gtrsim 800$. For both type A and type B, it is evident tha of data are in close agreement. The present results are in support empirically-fitted correlation of [8]

$$\overline{Sh} = 0.283\, Re^{0.485} \left(L/(2R)\right)^{-0.465}$$

which is plotted in solid line in Fig. 10. It is remarked that, as an overall mass transfer coefficient $\overline{\mathrm{Sh}}$ is larger for the case of a non-trans This finding was stated by [8], and the present numerical results are consist

experimental observations.

4. Conclusion

Fluid inducement into of the cup interior intensifies as Re increase Re, the global flow pattern is convectively-controlled, with distinct and t layers present on the solid walls. The concentration boundary layer at the cylindrical wall is thicker for the case of a transferring base (type B) then for a non-transferring base (type A). At small and intermediate radii, w is negative and fairly uniform in the radial direction. At large radii near the cylindrical wall, large positive values of w are seen.

At large Re, the angular velocity (v/r) is very small in much of interior. Only in the regions adjacent to the solid walls, v/r is appreciable.

Detailed descriptions of the local Sherwood number are given. cylindrical wall, Sh becomes large near the opening of the cup. In the c transferring base, Sh is fairly uniform at small and moderate radii of the d decreases radially at large radii close to the cylindrical wall.

The computed mean Sherwood number $\overline{Sh}$ is in close agreement with available experimental data of [8]. The overall $\overline{value}$ of Sh · is larg non-transferring base than for a transferring base.

Acknowledgment. This work was supported in part by research contracts Tong Yang Magic Co. and from Tong Yang Industrial Machinery Co. of Korea.

5. Reference

REFERENCES

1. E. M. Sparrow and J. L. Gregg, Heat transfer from a rotating disk to any Prandtl number, ASME J. Heat Transfer 81, 249-251 (1959).

2. F. Kreith, Convection heat transfer in rotating systems, Adv. Heat T 129-251 (1968).

3. S. M. Tieng and A. C. Yan, Experimental investigation on convective heat transfer of heated spinning sphere, Int. J. Heat Mass Transfer 36, 599-610 (1993).

4. S. Gilham, P. C. Ivey, J. M. Owen and J. R. Pincombe, Self-induced flo rotating tube, J. Fluid Mech. 230, 505-524 (1991).

5. S. Gilham, P. C. Ivey and J. M. Owen, Self-induced flow and heat tran a rotating tube, Int. J. Heat Fluid Flow 14, 27-36 (1993).

6. R. Shimada, S. Naito, S. Kumagai and T. Takeyama, Enhancement heat tr from a rotating disc using a turbulence prometer (In Japanese), Trans. of 53-487, 984-990 (1988).

7. K. Hirose, T. Yokoyama and M. Ouchi Heat convection on brake disk (In Japanese), Paper number E245, 31st Heat transfer symposium of Japan, Sapporo, May (1994).

8. E. M. Sparrow and A. Chaboki, Heat transfer coefficients for a cup-li rotating about its own axis, Int. J. Heat Mass Transfer 25, 1333-1341 (1982).

9. S. V. Patankar, Numerical Heat Transfer and Fluid Hemisphere/McGraw-Hill, New York (1980).

10. H. P. Greenspan, The Theory of Rotating Fluid. Cambridge University Cambridge (1968).

11. J. M. Hyun, Flow in an open tank with a free surface driven by the s bottom, ASME J. Fluids Engineering 107, 495-499 (1985).

12. T. G. Lim, S. Choi and J. M. Hyun, Transient interface shape of a tw in an abruptly rotating cylinder, ASME J. Fluids Engineering 115, 324-329 (199

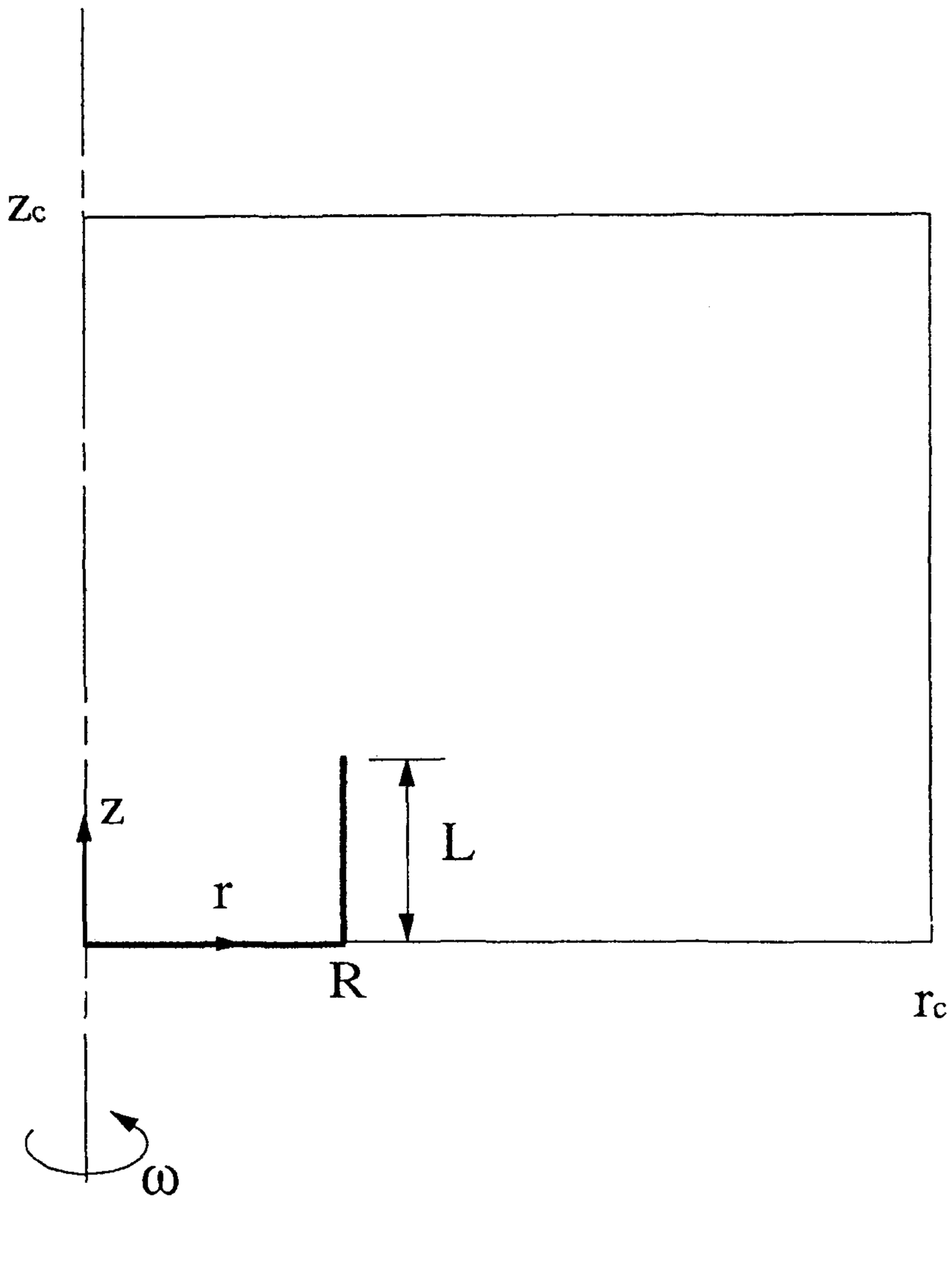

Fig. 1. Problem geometry and computational domain.

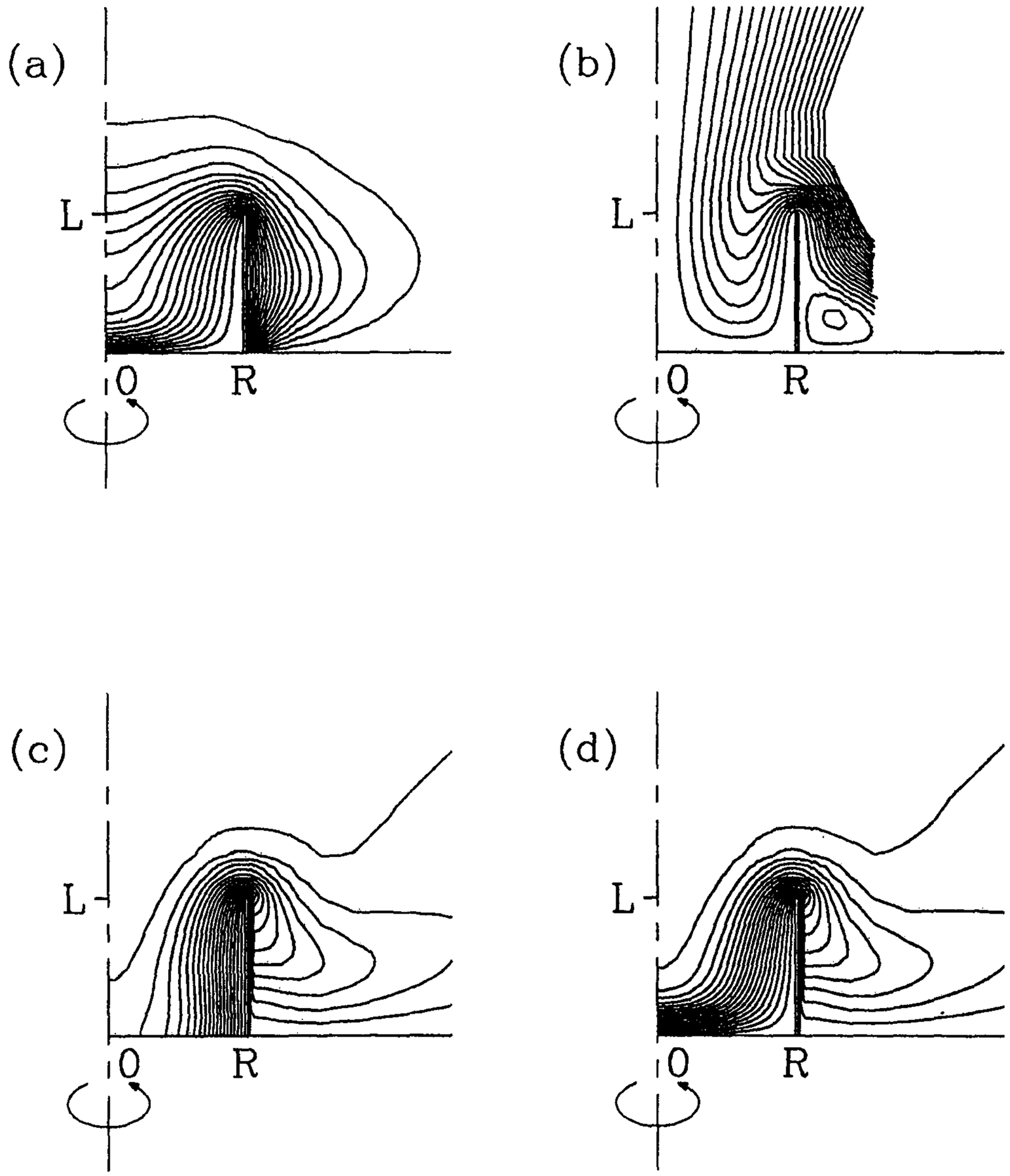

Fig. 2. Re=50. The number of contours is 20.

(a) angular velocity (v/r) field,

(b) plots of meridional stream function Ψ,

(c) concentration (C) field for type A,

(d) concentration (C) field for type B.

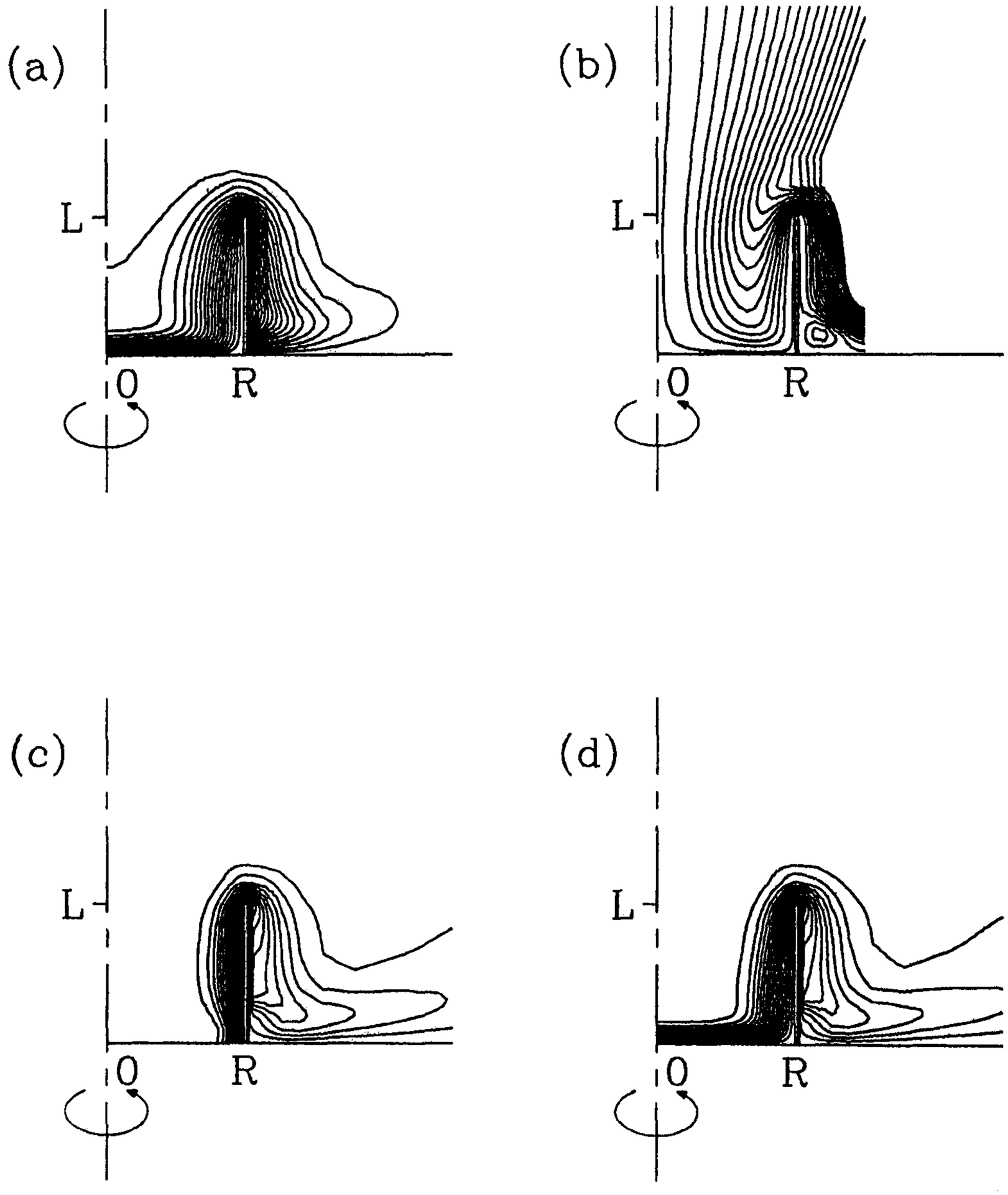

Fig. 3. Same as in Fig. 2, except for Re=200

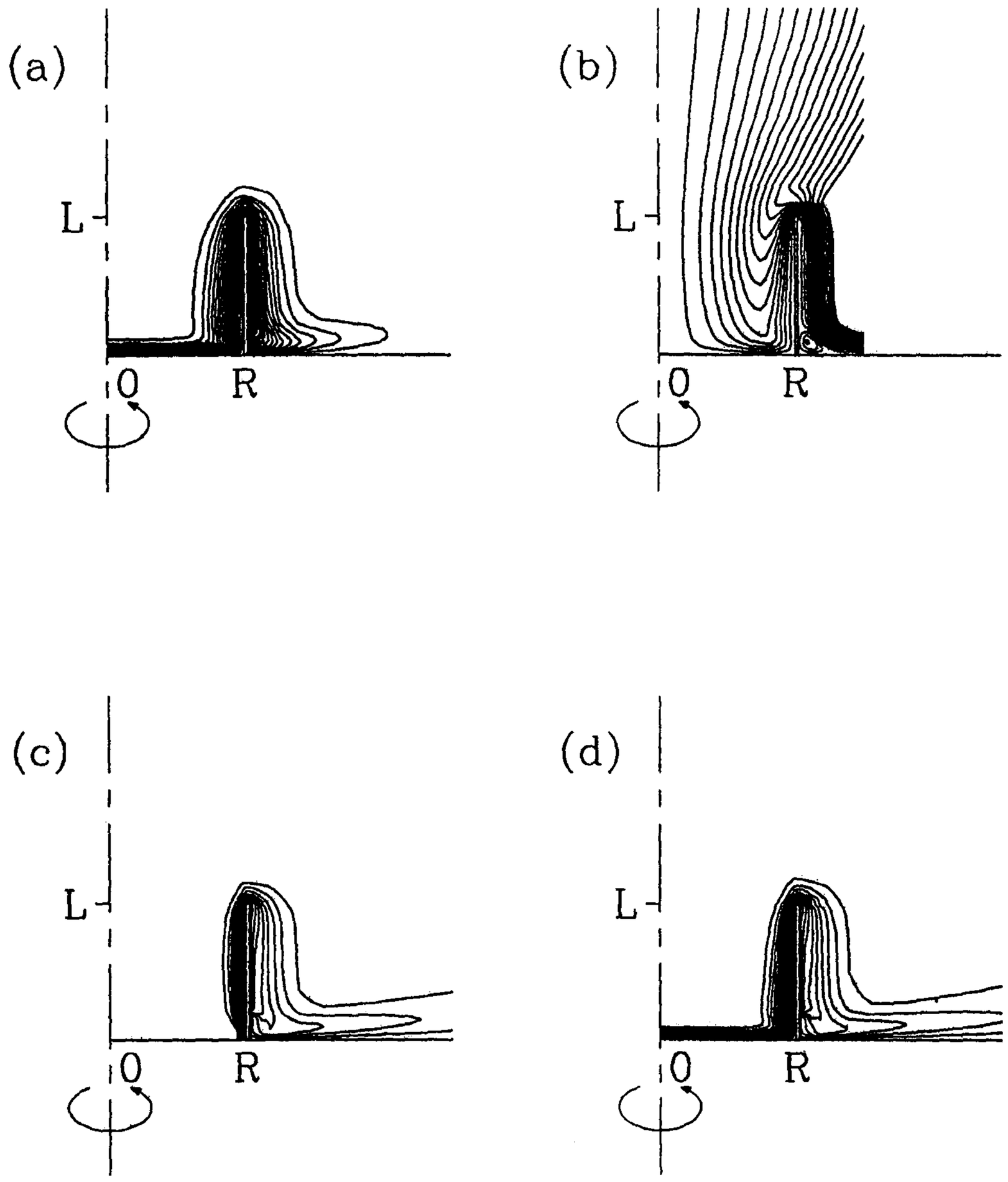

Fig. 4. Same as in Fig. 2, except for Re=800

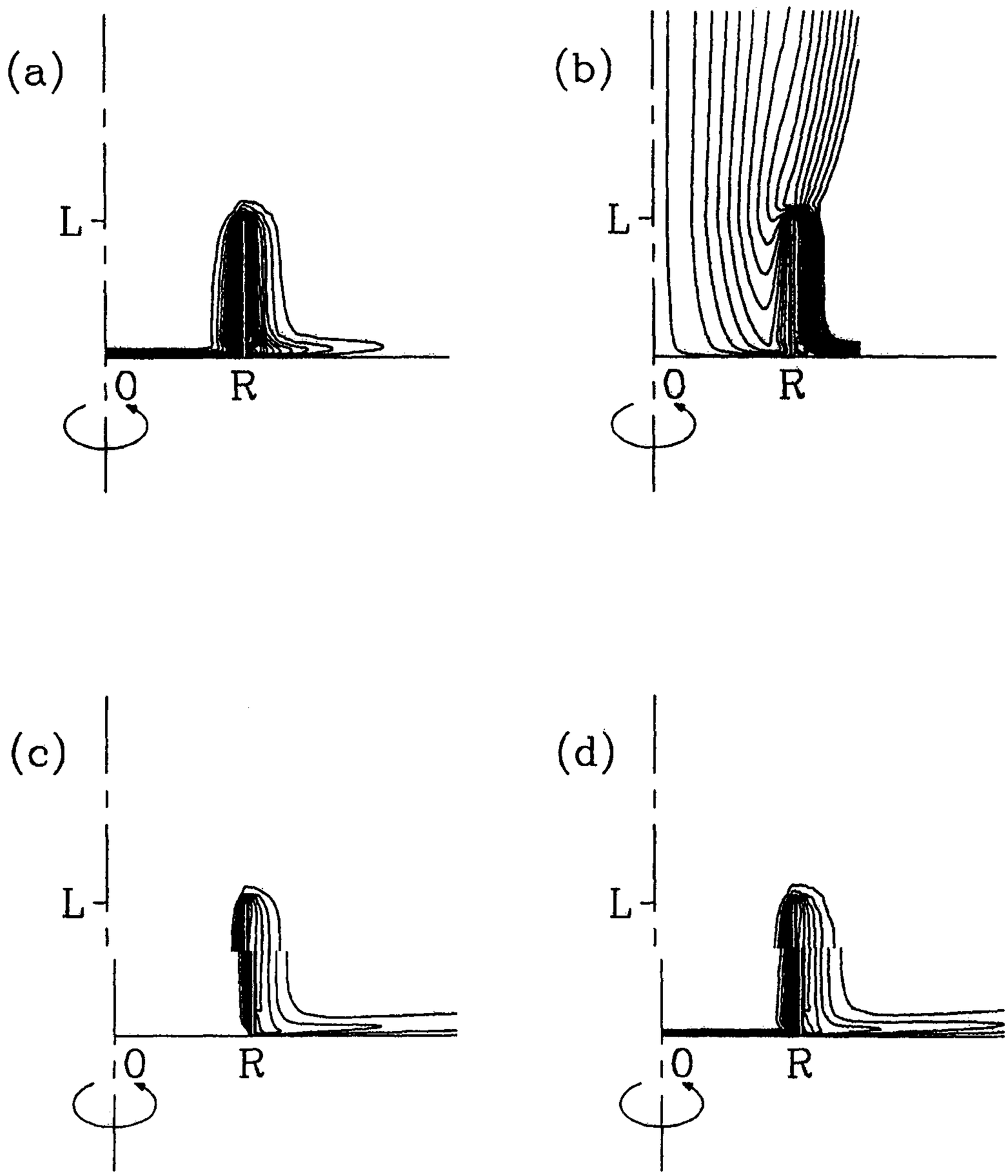

Fig. 5. Same as in Fig. 2, except for Re=3200

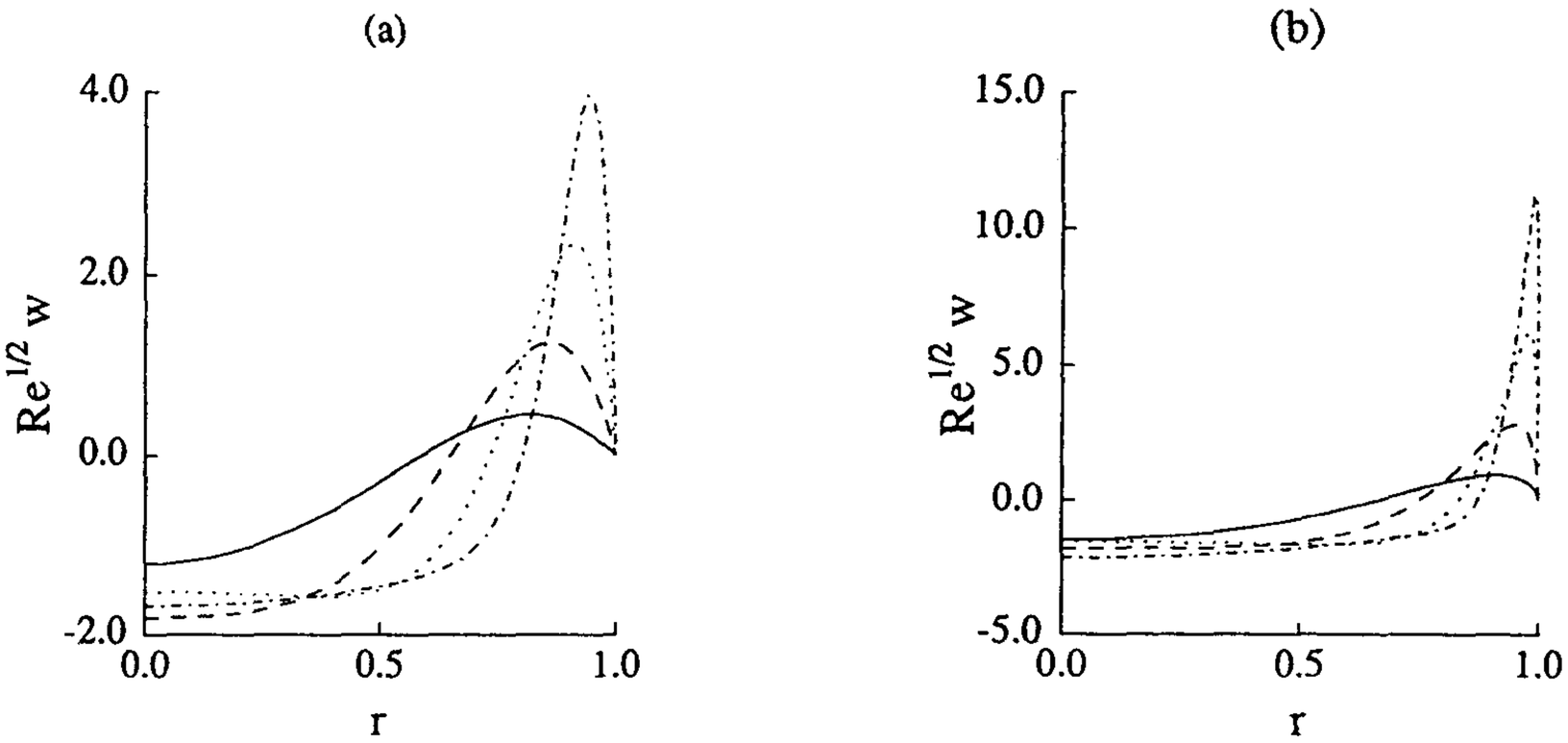

Fig. 6. Radial profiles of axial velocity w.

(a) z(R/L)=0.5,

(b) z(R/L)=1.0; (——)Re=50; (— —)Re=200

(- - - - -)Re=800; (—— —)Re=3200.

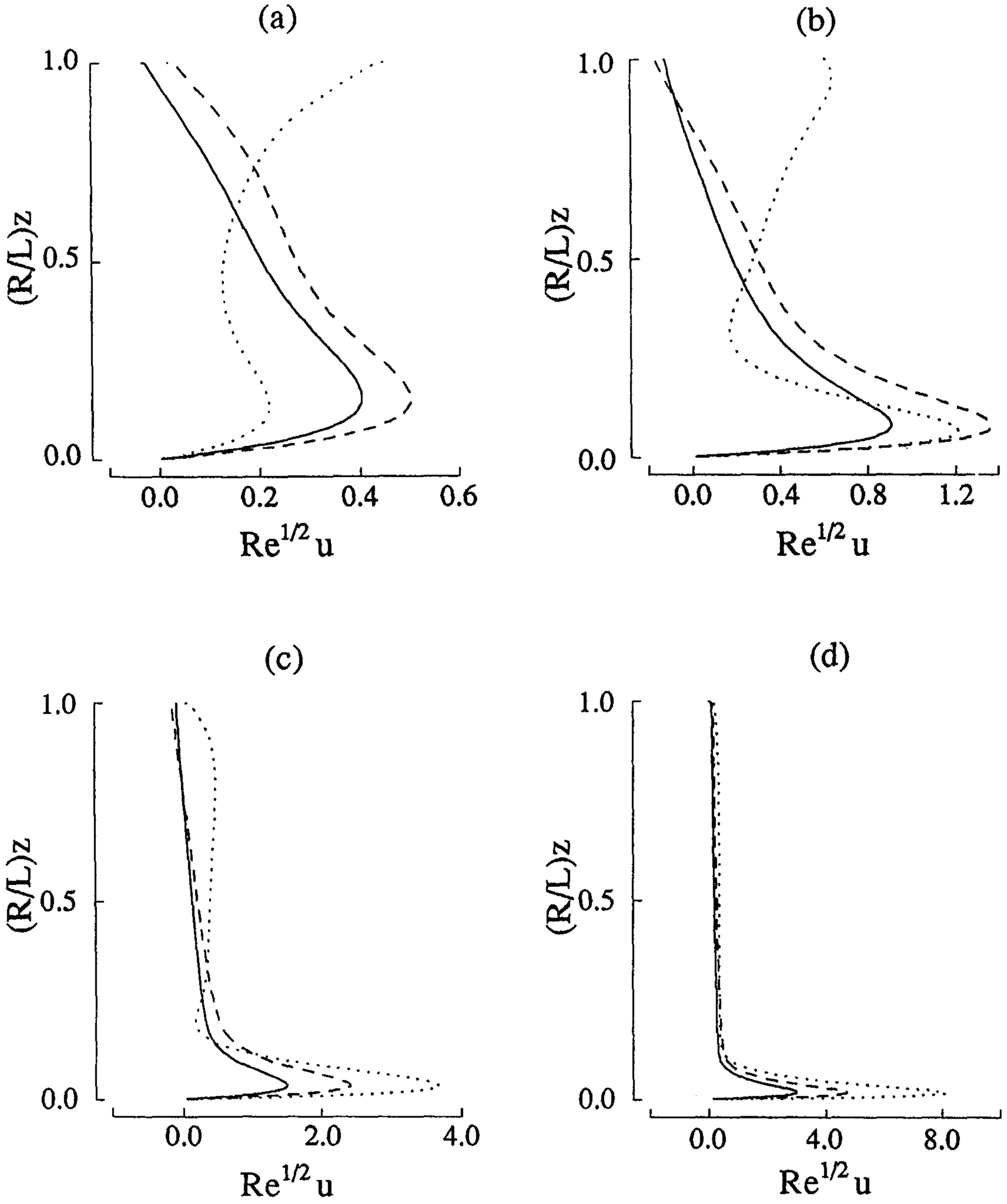

Fig. 7. Axial profiles of radial velocity u.

(a) Re=50, (b) Re=200, (c) Re=800, (d) Re=3200.

(———) r=0.3; (— —), r=0.5; (- - -) r=0.8.

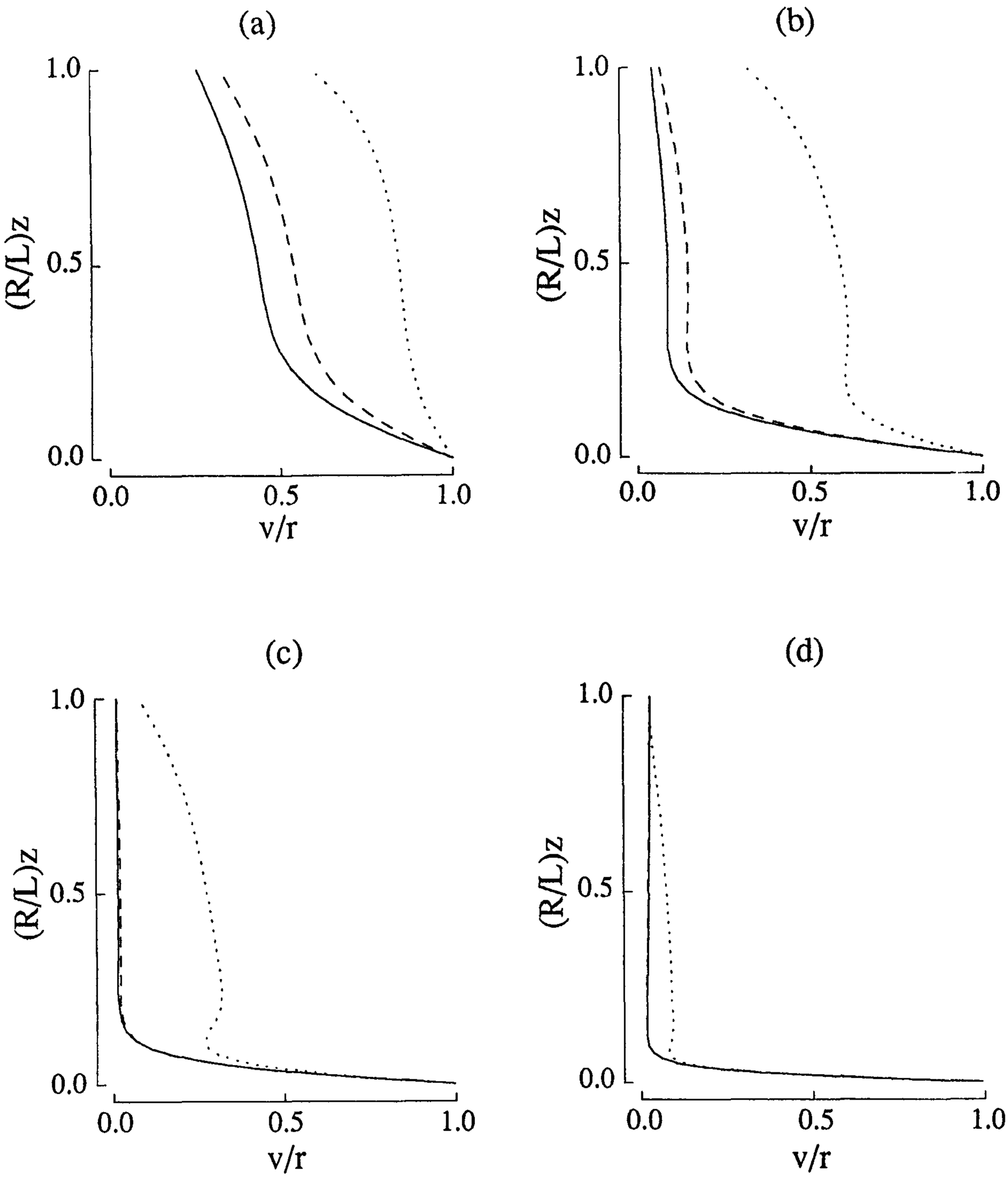

Fig. 8. Angular velocity (v/r) structures.

(a) Re=50, (b) Re=200, (c) Re=800, (d) Re=3200.

(———)r=0.3; (— — —)r=0.5; (- - - -)r=0.8.

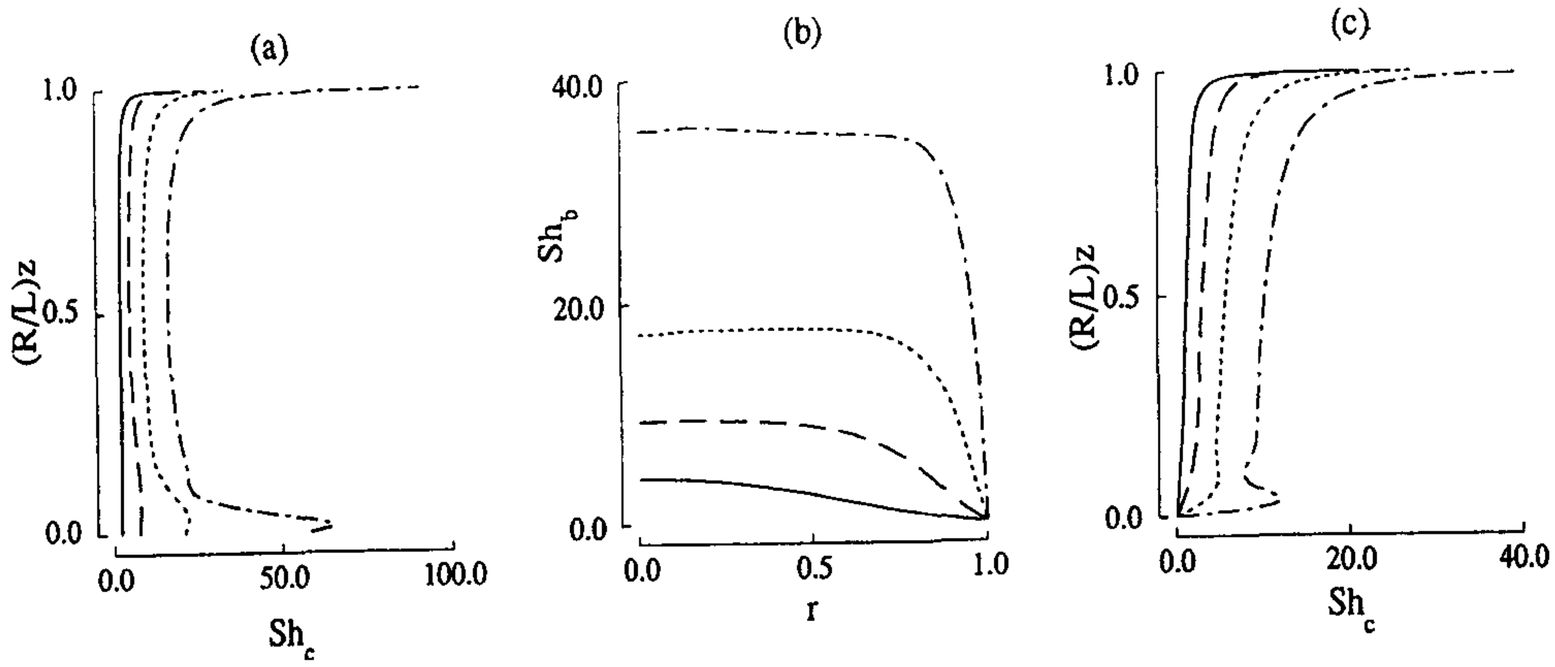

Fig. 9. Distributions of the local Sherwood number.

(a) local Sherwood number Shc at the cylindrical wall. Type A,

(b) local Sherwood number Shb at the base disk. Type B,

(c) local Sherwood number Shc at the cylindrical wall. Type B.

(————)Re=50; (— — —)Re=200;

(------)Re=800; (-—-—) Re=3200.

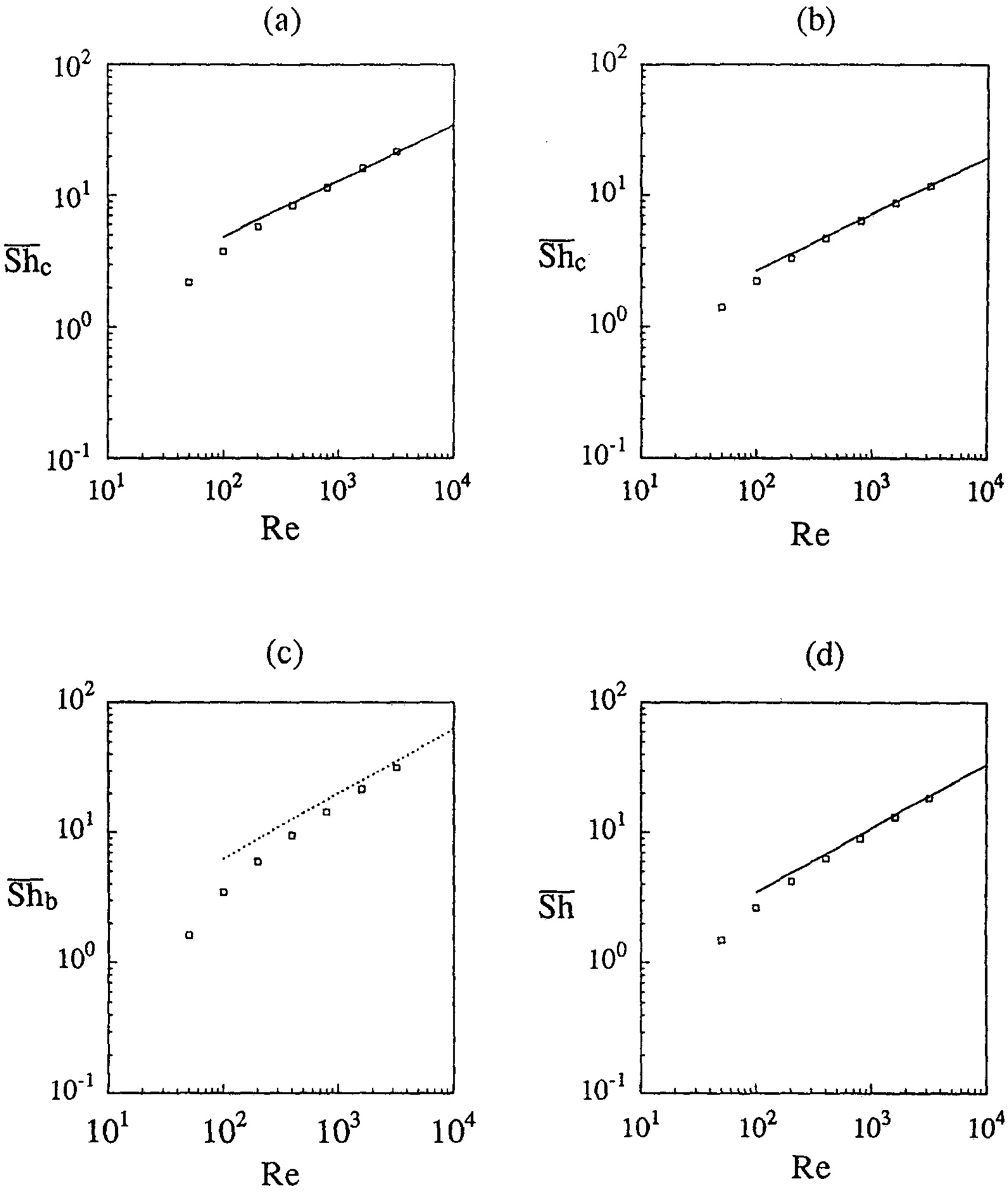

Fig. 10. Averaged Sherwood number $\overline{Sh}$ vs. Re.

(a) $\overline{Shc}$ at the cylindrical wall. Type A,

(b) $\overline{Shc}$ at the cylindrical wall. Type B,

(c) $\overline{Shb}$ at the base disk. Type B,

(d) $\overline{Sh}$ at the entire wall surface. Type B.

(———) experimental results of [8];

(⊞) the present numerical data.

(- - - -) result for rotating disk of [1,8].

제 8 절

Flow and Mass Transfer Measurements for a Flat Plate of Finite Thickness in Pulsating Flow

(요동하는 유동에 놓여진 유한한 두께의 평판에 대한 유동 및 물질전달 측정)

요 약 문

$U_\infty = U_o(1 + A_o\cos 2\pi f_p t)$와 같이 요동하는 자유유동장에 놓여진 유한한 두께의 풍툭한 평판위에서 유동과 물질전달에 대한 실험측정을 하였다. 작고 적당한 레이놀즈수($770 \leq Re_H \leq 8000$)에 대하여 저난류강도 풍동실험을 수행하였다. 요동은 음향스피커에 의해 생성된다. 대부분의 실험은 f_p = 20.0 - 80.0 Hz 와 $A_o \leq 0.15$의 범위에서 수행되었다. 유동의 물성치는 I형과 스플릿필름계기(split-film probes)로 측정하였다. 물질전달은 나프탈렌 승화법으로 측정되었다. 요동하면서 전진하는 유동에 대하여 벽정압(wall static pressure), 길이방향의 평균속도, 난류강도, 셔유드수(Sh, Sherwood number)등을 시작모서리 박리점으로부터 측정된 유동방향거리 x^*에 대한 함수로 나타내었다.

A_o와 f_p가 증가함에 따라 시평균 재부착길이는 현저하게 감소되었다. 이것은 박리기포의 높이와 길이가 동시에 축소되는 것, C_p가 회복되는 위치가 상류로 이동하는 것, 최소 C_p 값이 감소하는 것, 역류가 강화되는 것, 난류에너지의 현저한 변화가 보이는 것 등을 의미한다. 박리기포에서 Sh에 대한 요동의 역할은 현저한다. Sh는 박리점으로 부터 단조적으로 감소하여 2차 박리점 부근에서 최대값을 가진다. 그리고, 2차 박리점을 지난 이후에는 x^*가 증가함에 따라 Sh수는 현저하게 증가하여 재부착점에서 최대치를 가진 후에 감소한다. 2차박리점과 Sh가 최대점을 가지는 지점은 A_o나 f_p가 증가함에 따라 더욱 상류로 이동한다. 큰 Re_H수에서 Sh에 대한 요동의 상대적인 영향이 약해진다.

Abstract

Laboratory measurements were made of flow and mass transfer over a blunt flat plate of finite thickness, which is placed in a pulsating free stream, $U_\infty = U_o(1 + A_o\cos 2\pi f_p t)$. Low turbulence-intensity wind tunnel experiments were conducted for small and moderate Reynolds numbers, $770 \leq Re_H \leq 8000$. Pulsation was generated by means of an acoustic speaker. The majority of experiments were carried out in the ranges of f_p = 20.0 - 80.0 Hz and $A_o \leq 0.15$. Flow properties were measured by I-type and split-film probes. Mass transfer rates were measured by employing the naphthalene sublimation technique. The present results for non-pulsation flows (A_o = 0.0) were shown to be consistent with the published data. For pulsating approach flows, results are provided for the distributions of the wall static pressure, the longitudinal mean velocity and turbulent intensity, and the Sherwood number, Sh, as a function of the stream-wise distance x^* measured from the leading-edge separation point. As A_o or f_p increases, the time-mean reattachment length is reduced significantly. This implies that the height and length of separation bubble shrink simultaneously; the position where C_p is recovered moves upstream, and the minimum value of C_p decreases; the reverse flow is intensified; and a substantial augmentation of turbulent energy is discernible. In the separation bubble, the effect of pulsation on Sh is conspicuous. Sh decreases monotonically from the separation point to the minimum value near the secondary separation point; and Sh increases appreciably with increasing x^*, after passing the secondary separation point to the maximum value at the reattachment point; and afterward, Sh decreases. The secondary separation point and the position where Sh has a maximum move further upstream, as A_o or f_p increases. At large Re_H, the relative influence of pulsation on Sh weakens.

Nomenclature

Roman symbols

A_0 pulsating amplitude

C_P pressure coefficient ($\equiv(p-p_o)/0.5rU_o^2$)

H half thickness of the flat plate, m

f_p pulsating frequency, 1/s

p_o static pressure of free stream , kg/s

Re_H Reynolds number ($Re_H \equiv UH/n$)

Re_{2H} Reynolds number ($Re_{2H} \equiv U2H/n$)

Sh Sherwood number

U_∞ longitudinal local mean velocity, m/s

U_o free stream mean velocity, m/s

U free stream velocity, m/s

u longitudinal fluctuation velocity, m/s

$\overline{u^2}$ longitudinal component of turbulent energy, m^2/s^2

u_{rms} r.m.s. value of fluctuating longitudinal velocity component ($\sqrt{\overline{u^2}}$), m/s

x streamwise distance from the separation leading-edge, m

x^* nondimensional streamwise distance from the leading edge ($\equiv x/H$)

x_R mean reattachment length for pulsating flows, m

x_{R0} mean reattachment length for non-pulsating flows, m

x^*_R nondimensional streamwise distance from the leading edge ($\equiv x/x_R$)

y vertical distance from the surface of the plate, m

y_c the y position where u_{rms} is maximum

y_d time-mean height of the edge of the separated shear layer ($U/U_{max}=1.0$)

z spanwise distance from the centerline, m

Greek symbols

r density of air, kg/m^3

g_p forward-flow time fraction

n kinematic viscosity, m^2/s

1. Introduction

Flow about a blunt-faced body, placed in a uniform stream, has been extensively studied. In particular, as a benchmark configuration, much work has been reported for a two-dimensional, semi-infinite flat plate of finite thickness, which is aligned parallel to a uniform approaching stream [1-17].

The canonical flow structure includes a variety of essential dynamical elements (see Fig. 1). The flow separates at the sharp corner of the blunt face, and this separated flow reattaches at a downstream location on the surface of the plate. This forms the well-known pattern of a separation bubble, which is defined as a re-circulating region bounded by a separated shear layer and a solid surface. The flow is characterized by rolled-up vortices in the shear layer and their interaction with the surface [7]. Farther downstream of the reattachment, the flow undergoes a region of redevelopment, and the overall flow exhibits extremely complex characteristics afterward.

The extent of the recirculating region was described in the experiments by Lane and Loehrke [8], Ota et al. [11] and by Sasaki and Kiya [16] at low and moderate Reynolds numbers. It was found that the steady, laminar separation bubble on the plate grows in size with increasing Reynolds number. The maximum reattachment length was observed at Re_{2H} 325, at which oscillations begin in the separated shear layer. As the Reynolds number increases further, the separated shear layer becomes unsteady and the bubble shrinks in size. For large Reynolds numbers, the flow reattachment occurs at about four or five times the plate thickness downstream from the leading edge, and the phenomenon is largely independent of the Reynolds number [2, 5, 10-11].

Ota and his colleagues [10-13] measured velocity, pressure and turbulence characteristics in the separated, reattached, and redevelopment regions. One major finding was that the mean flow properties approach a nearly fully developed flow at about 20 plate-thicknesses downstream from the leading-edge.

The effect of the free stream turbulence intensity was studied experimentally in Ref. 1. It was shown that the free stream turbulence promotes rolling-up of the separated shear layer. The rolled-up large-scale vortices were shed downstream from the separation bubble with a frequency of approximately 0.65 U_o/x_{R0} [2, 5-7]. The knowledge on

rolled-up vortices is useful in analyzing the turbulence properties, especially in the reattachment region.

Recently, attempts have been made to exert a control on the separated and reattaching flows by introducing localized periodic disturbances immediately behind the separation edge [18-19]. It was learned that, by providing a sinusoidal disturbance at a proper frequency, considerable alterations were achieved in the overall characteristics of the separated and reattaching flows. The particular frequency of disturbance tested was found to be 4-5 times the frequency of shedding of large-scale vortices from the separation bubble. These studies illustrated the significant role played by the large-scale vortices. At the same time, it was demonstrated that the shedding of vortices as well as the global flow features could be controlled to a considerable degree by externally-provided localized excitations.

The present study proposes to investigate the separated flow over a blunt-faced body in a more practical and widely-encountered situation. Instead of the localized periodic forcing in the vicinity of the separation edge [18-19], the present work seeks to control the global flow pattern by utilizing the free stream, which contains a well-defined single-frequency pulsation. The oncoming free stream is expressed as $U_\infty = U_o(1+A_o\cos 2\pi f_p t)$. This type of pulsating free stream is in fact a closer representation of some of practical engineering problems, such as partially-separated cascade wings and structures exposed to winds. In such applications, inevitable oscillatory components in the approaching free stream, to the lowest approximation, are represented in the above-shown pulsating oncoming flow. The purpose of this study is to depict the impact of free stream pulsation on the formation of the leading-edge separation bubble as well as the shedding of large-scale vortices and on the alterations of transport processes.

A comprehensive and systematically-organized experimental program has been executed. Emphasis is placed on documenting the flow and mass transfer features at moderate Reynolds numbers, Re_H = 1000 and 2000. The pulsation amplitude A_o and frequency f_p are allowed to vary over broad ranges. The mission is to portray the mean and fluctuating velocity fields, both in the stream-wise and cross-stream-wise directions, and the transport properties exemplified by the Sherwood number Sh.

In the present experiments, a specially-designed open-circuit blower-type wind tunnel was constructed. The flows were measured by using hot-wires and split-film sensors. The mass transfer measurements were conducted by employing the naphthalene sublimation technique. These methods have been demonstrated to be effective for a variety of related research subjects [4, 20], and they are variable experimental tools for the problem in hand.

2. Experimental apparatus and procedure

The air speed in the test section (250 mm x 250mm), U_o, was in the range of 1.5 to 12.0 m/s, and the turbulent intensity of the free stream was less than 0.3 % [4, 20]. The flat plate, which was fabricated with acrylic resin, was 12.1mm thick, 250 mm wide, and 550 mm long. The plate was sufficiently long to prevent the interaction between the separated shear layers emanating from both edges [5-7]. The blockage of the plate was 4.84 %, which was small so that the main structure of the flow under investigation would not be affected much by the finiteness of the test section [2]. Also, the aspect ratio was 20, which was large enough to render the flow near the centerline approximately two-dimensional [2, 5-7]. The front face of the flat plate was precision-machined to be oriented perpendicular to the oncoming stream. The location of this face was 450mm downstream of the inlet of the test section.

The pulsation of the free stream was achieved by placing a speaker in the settling chamber. The sinusoidal signal was produced by using a function generator. This signal was passed through an audio amplifier, and it then was sent to the speaker. It is believed that the method of producing pulsation by acoustic means, as in the present work, leads to a simple and straightforward experimental design. To assess the quality of the pulsation superimposed on the uniform free stream, the power spectrum of the free stream velocity field data obtained by an I-type hot-wire was analyzed previously [20]. Based on extensive surveys of the free stream velocity fields, the oncoming velocity has been found, to a high degree of accuracy, to have a sinusoidal pulsation, i.e., expressible by $U_\infty = U_o(1+A_o\cos 2\pi f_p t)$. For the wind-tunnel test rig of the present study, the majority of

experiments were carried out in the ranges of f_p = 20.0-80.0 Hz, $A_o \leq 0.15$.

The mean velocity distribution was measured by using a standard pitot tube and a micro-manometer. To measure the wall static pressure, a total of 42 pressure taps at the centerline of the upper surface of the plate were drilled. A scannivalve and a micro-manometer with a resolution of 0.013 mm of water column were attached therein. The pressure signal (sampling frequency of 6 Hz) was sent to an IBM-486 personal computer through an A/D converter. A total of 4096 pressure signals at a given location were time-averaged to obtain the local pressure coefficient.

To measure flow properties, the hot-wire technique was utilized with constant temperature anemometers (TSI-IFA 100). The sensing material of I- and X-type probes was a 5mm, platinum-plated, tungsten wire. A single-wire probe (TSI model 1250) was used to monitor the turbulent intensity as well as the pulsation amplitude and frequency of the free stream. A cross-wire probe (TSI model 1246-T1.5) was deployed to measure the turbulent properties except in the re-circulation region. A split-film probe (TSI model 1288) was utilized to depict the flow characteristics, especially in the re-circulating separation bubble.

To ensure precise measurement positioning, probes were made to move in the x and y directions by a remote-controlled two-dimensional traverse system. The resolution was found to be within 0.025 mm. Accurate positioning of the probe was accomplished by a digital height gauge with a sighting microscope, which had a resolution less than 0.01 mm.

Measurement data of mean velocities, turbulence intensities, and forward-flow time fractions were stored after low-pass filtering at a cut-off frequency of 10 kHz. The frequency response characteristics of the hot-wire probes and the split-film sensors were about 20-30 kHz, and these cut-off frequencies were adequate for the present measurements. The velocity signals were digitized at a rate of 10 kHz by using a digitizer (IFA-200), which was equipped with a 14-bit A/D converter. For each measurement point, 40960 digitized data were compiled in a removable hard disk (Syquest media) of a personal computer (IBM-486).

Care was exercised in implementing the naphthalene sublimation technique, which

formed the core of mass transfer experiments. The naphthalene-cast portion of the plate was finished to ensure that it had the same roughness and thickness as the rest of the steel plate. In order to quantify the sublimated naphthalene, an automated data acquisition system was installed. The components included a depth gauge with a signal conditioner, a digital voltmeter connected to a GPIB interface, a positioning apparatus driven by stepper motors and an IBM-486 personal computer. Prior to each reading, the gauge was allowed a 0.5-s stabilization period. The measurement of the naphthalene surface profile was performed at a constant room-temperature, which would alleviate possible errors caused by natural convection.

The span-wise variations of mass transfer properties were checked, and they were monitored to be within 1.0%. However, to increase accuracy, measurements were taken at nine span-wise locations($z/H = 0.0, \pm 0.5, \pm 1.0, \pm 1.5, \pm 2.0$) and they were averaged out at each stream-wise position.

The derivation of the non-dimensional mass transfer coefficient, Sherwood number (Sh), and the full implications of this method have been thoroughly explained in the preceding publications [4, 20].

3. Results and Discussion

3.1 Flow Characteristics

Figure 2 illustrates the general behavior of the mean reattachment length, x_R, vs. the Reynolds number, Re_H, together with the results of Ota et al. [11] and Kottke et al. [17]. In the present experiments, the time-mean reattachment length, x_R, is defined as the position where the forward time fraction (g_p) is 0.5. In Refs. [11, 17], however, x_R was defined as the distance from the separation point to the point of maximum mass transfer. The range of Re_H covered in the present study belongs to the regime in which the flow separates as a laminar flow, undergoes transition to a turbulent flow, and reattaches as a turbulent flow [2]. The reattachment length, x_R, decreases rapidly with Re_H for relatively small Re_H, and x_R reaches a minimum around $Re_H \cong 2000$. As Re_H increases further, x_R increases mildly. As noted, the previous investigations [8, 11, 16-17] established the above

findings, and it has been observed that the dependence of x_R on Re_H weakens at large Re_H, say Re_H >5000. The apparent minor quantitative disparities between the present results and the preceding reports are thought to be associated with different methods to determine x_R, plate lengths, blockage ratios, aspect ratios, and free stream turbulent intensity. The influences of the blockage and of the aspect ratio of the plate were examined by Cherry et al. [2]. For the present experimental setup [blockage 4.84%, aspect ratio 20.0], the preceding data of [2] give $x_R \cong 10$ H as the large-Re_H limit, which is in good agreement with the present experimental results.

The alterations in x_R brought forth by the introduction of pulsation are exemplified in Fig. 3. Here, the data for $A_o = 0$ or $f_p = 0$ represent the cases of non-pulsating flow. It is immediately clear that, for the three pulsation frequencies tested, the mean reattachment length decreases as the pulsation amplitude A_o increases. Furthermore, this trend is more conspicuous for higher pulsation frequencies. Also, for fixed A_o, x_R decreases as f_p increases. In summary, the reattachment length is reduced significantly as a large-amplitude, high-frequency pulsation is added to the free stream. This finding is similar to the results obtained by Parker and Welsh [14] and Hourigan et al. [15] who investigated the effects of transverse perturbation on the flow separation and heat transfer around a blunt plate.

The distribution of pressure on the surface of the plate, expressed in C_P, is displayed in Fig. 4. The data for $A_o = 0$ corresponds to the case of a non-pulsating free stream, and the C_P-data for this case is consistent with the published results [2, 5]. As exhibited in Fig. 4, the location of minimum-C_P moves upstream, as the pulsation amplitude increases for fixed f_p, or as the pulsation frequency f_p increases for fixed A_o. This implies that the separation bubble undergoes a significant shrinkage in size by the introduction of pulsation. Furthermore, the minimum C_P takes a larger negative value as A_o increases. This reflects the fact that the reverse flow intensifies, as the impact of the pulsation becomes noticeable. The overall size of the separation bubble is determined basically from a balance between the entrainment rate from the recirculation zone into the shear layer and the re-injection rate from the reattaching shear layer [1]. The pulsation in the free stream is believed to augment the entrainment rate, which turns up in the

reduction of the height and length of the separation bubble. Similar results were noted as to the effect of free-stream turbulence on the size of the separation bubble [1]. In related studies, similar findings were obtained for the case of local forcing to the flat front face of an axisymmetric circular cylinder [18-19].

Another important observation in Fig. 4 is that, with the introduction of pulsation, the pressure at far downstream location ($x \cong 20H$) does not recover its free-stream value. This pressure loss becomes more pronounced as A_o or f_p increases. The above finding is akin to the effect of free stream turbulence on the separation bubble [1]. This significant non-recovery of pressure at far downstream after the flow reattachment, which is caused by the free stream pulsation, points to the presence of a large-scale vortex. For a pulsating free stream, this large-scale vortex, which sheds from the separation bubble, persists even after the flow has reattached on the surface of the plate. In the case of a non-pulsating free stream, the previous studies indicate that the large-scale vortex shed from the separation bubble weakens through viscous diffusion by its interaction with the wall surface [7]. Consequently, for a non-pulsating flow, a nearly-full recovery of pressure is achieved after the reattachment point [7].

The effect of the amplitude of free stream pulsation, with fixed values of f_p and Re_H (f_p=20 Hz, and Re_H = 1000), on the profiles of the mean longitudinal velocity is elaborated in Fig. 5. The measurement points in the longitudinal direction are made non-dimensional by using the reattachment length x_{R0} for the corresponding non-pulsating flow. For the non-pulsating flow, the maximum negative velocity is seen to be $-0.25U_o$ around x/x_{R0} = 0.6, which compares favorably with the preceding results for high Reynolds numbers [5-6]. As pointed out earlier, the introduction of pulsation causes the size of the separation bubble to shrink, both in length and height. Figure 5 also indicates that the impact of pulsation is comparatively weak in the forward portions of the bubble ($x/x_{R0} \leq 0.4$); however, the influence of pulsation is relatively strong at farther downstream locations. At still further downstream points, the effect of pulsation weakens, and this is attributable to the increasing viscous effects stemming from the bounding wall. Around $x/x_{R0} > 4.0$, the effect of pulsation on the mean velocity profile appears to have diminished.

Figure 6 exhibits the measurements of velocity profiles by means of a split-film probe. In this case, the pulsation frequency is varied for fixed A_o = 0.04 and Re_H = 1000. The longitudinal position x is made dimensionless by using the reattachment length x_R pertinent to each pulsating condition. The lateral position is non-dimensionalized as y/x_{R0}. As stated, as f_p increases, the separation bubble becomes thinner and the reverse-flow intensifies. It is noticeable that, in the forward portion of the plate between the leading-edge separation point and the reattachment point, the reverse flow, in general, weakens measurably due to the viscous effects of the wall. This implies that, by the introduction of pulsation, the point at which the reverse flow becomes zero moves upstream toward the leading-edge. This observation is linked to the behavior of local mass transfer under pulsating conditions, which will be discussed later [see Fig. 11]. Obviously, after the reattachment point is passed, the effect of pulsation on the velocity profiles substantially diminishes.

Figure 7 shows the replotted velocity profiles of Fig. 6 in the separation bubble by using y/y_d and x/x_R. The separation bubbles are seen to collapse nearly into a single separation bubble. This implies that the basic shape of the separation bubble does not change much by the free stream pulsation components. Also, the principal characteristic length scales for the global configuration of the separation bubble are the time mean reattachment length, x_R and the time-mean height of the edge of the separated shear layer, y_d. These observations are consistent with the previous report[5].

The turbulent components of velocity are examined in Figs. 8-10. Ref [5] defines the lateral position y_o at which $\overline{u^2}$ attains a maximum to be the center of the shear layer. This assertion can be verified by cross-comparing the profiles of longitudinal velocity with the distributions of $\overline{u^2}$. For the case of a non-pulsating flow, the value of y_o varies little with x in the region $x/x_{R0}>0.6$, which agrees with the previous findings [5]. Also, for the non-pulsating flow, the maximum value of $\sqrt{\overline{u^2}}/U_o$ for $x/x_{R0}>0.6$ is approximately 0.26, which is in fair agreement with the existing data [5-6]. After the reattachment point is passed, a sharp decline in the longitudinal normal Reynolds stress, or the longitudinal r.m.s. velocity, is discernible. This is attributable to the presence of the bounding wall in the reattached flow, which leads to inhibition of vortex-pairing process

[22-23].

It is notable that the pulsation gives rise to an appreciable increase of u^2, and this is most pronounced for A_o = 0.082 at x/x_{R0} = 0.2 [see Fig. 8(c)]. A plausible physical explanation is that x/x_{R0} = 0.2 corresponds to the location at which the vortex-merging, due to the pulsation component, takes place. It has been ascertained [21] that vortex-pairing increases turbulence intensities in the separated layer; afterward, the turbulence intensity decreases. The gradual attenuation of turbulence intensity is caused by the interaction of the separated shear layer with the bounding wall, and the interaction point is strongly influenced by pulsating components. The present data on $\overline{u^2}$ reveal that, by the introduction of pulsation, the vortex-pairing process is forced to take place in the more forward portion of the plate. This observation runs parallel with the fact that the length of the separation bubble decreases, as A_o increases.

3.2 Mass Transfer Characteristics

The measured mass transfer rate, expressed by the local Sherwood number, Sh, is plotted versus the longitudinal distance x^* ($\equiv x/H$) for varying A_o in Fig. 11. The earlier studies [4, 9-10, 13-15] established that the mass(or heat) transfer coefficient attains a maximum around the reattachment point, and decreases monotonically with x^* after this reattachment point. The overall pattern of the Sh- x^* plots fits the above general description. A closer inspection of the plots of Fig. 11 indicates that, for f_p fixed, as A_o increases, the location of the maximum Sh moves upstream. This is compatible with the observation that the size of the separation bubble is reduced. Also, this trend is corroborative of the distributions of wall static pressure [see Fig. 4] as well as of the mean longitudinal velocity [see Figs. 8-10]. With increasing A_o, the augmentation of Sh within the region of the separation bubble becomes discernible. The enhancement of Sh is more pronounced in the forward portion leading to the reattachment point. After the reattachment point is passed, Sh decreases faster with x^* as A_o increases. Physically, as the pulsation effect increases, the entrainment of the high-energy fluid outside of the separation bubble becomes more vigorous by the action of the intensified re-circulating flow driven by the motion of a large-scale vortex. This causes a substantial augmentation of mass transfer, especially in the vicinity of the reattachment point, which was also

observed in the study of Hourigan et al. [15]. They demonstrated that the large-scale vortex structure plays an important role in the transport of energy in the flow. It was also shown that when a transverse sound field is applied, the maximum Nusselt number increases and the location at which this maximum is found shifts toward the leading edge. The Sh-data of Fig. 11 also suggest that the impact of pulsation is far-reaching, well into the far downstream regions (x/H>20.0 in Fig. 11).

In summary, the overall convective mass transfer rate is found to increase when the free-stream pulsation is imposed. It is worth pointing out that this finding is analogous to the case of heat transfer [14-15].

It is to be mentioned that a local minimum in the Sh-curve is seen in the fore-portion of the plate [e.g, x/H $\cong$ 1.5 in Fig. 11 (a)]. The existence of this local minimum-Sh was also noted in the previous studies for non-pulsating flows [4]. It was thought that this minimum-Sh point corresponds to the location of the secondary separation point [4, 7] at which the surface velocities are very small [see Figs 5 & 6]. The present results illustrate that, as A_o increases, the secondary separation point is shifted upstream, due to the strengthened reverse flow. Figure 11 implies that, for the largest value used in the experiment, A_o = 0.082, this secondary separation point has moved upstream such that it nearly coincides with the leading-edge separation point. The influences of f_p, with the same A_o and Re_H, are evident in Figs 11(a) & 11(b). The changes caused by pulsation are more pronounced for higher f_p, and the reduction in size of the separation bubble is more apparent. Figure 12 exhibits the effect of Re_H. At higher Re_H, the changes in the Sh-curves are less pronounced, since the relative influence of pulsation weakens at much higher Re_H.

4. Conclusion

Laboratory experiments were performed to portray the flow and mass transfer characteristics.

By the introduction of pulsating components into the free stream, principal changes in flow characteristics are visible. The reattachment length is reduced measurably, and the separation bubble shrinks in size. The far-downstream pressure does not recover its free stream value. The influence of pulsation is relatively strong in the rearward portion of the bubble. After the reattachment point is passed, the effect of pulsation on the mean velocity profiles diminishes. Also, the pulsation causes an appreciable augmentation of u^2.

The general pattern of Sh vs. x^* plots indicates that Sh reaches a maximum around the reattachment point. The location of maximum-Sh is shifted upstream as the pulsation amplitude A_o increases. The enhancement of Sh in the separation bubble is noticeable as the pulsation increases. The alterations brought forth to the Sh - x^* curves are more notable for higher f_p. The comparative influence of pulsation weakens at much higher Re_H.

5. Acknowledgments

The authors are grateful to the referees who provided constructive comments and additional references. This work was partially supported by a research grant from the Korea Science & Engineering Foundation (KOSEF).

6. References

1. R. Hillier and N. J. Cherry, The effects of stream turbulence on separation bubbles, J. Wind Eng. and Industrial Aerodynamics, 8, 49-58(1981).
2. N. J. Cherry, R. Hillier and M. E. M. P. Latour, Unsteady measurements in a separated and reattaching flow, J. Fluid Mech., 144, 13-46(1984).
3. P. I. Cooper, J. C. Sheridan and G. J. Flood, The effect of sound on forced convection over a flat plate, Int. J. Heat Fluid flow, 7, 61-68(1986).
4. K. S. Hwang, H. J. Sung and J. M. Hyun, Mass transfer measurements from a blunt-faced flat plate in a uniform flow, Int. J. Heat and Fluid Flow, 17, 179-182(1996).
5. M. Kiya and K. Sasaki, Structure of a turbulent separation bubble, J. Fluid Mech., 137, 83-113(1983).
6. M. Kiya and K. Sasaki, Structure of a large-scale vortices and unsteady reverse flow in the reattaching zone of a turbulent separation bubble, J. Fluid Mech., 154, 463-491(1985).
7. M. Kiya, Separation bubbles, Theoretical Applied Mechanics, 173-191(1989).
8. J. C. Lane and R. I. Loehrke, Leading edge separation from a blunt plate at low Reynolds number, ASME J. Fluids Engineering, 102, 494-496(1980).
9. S. Mori, H. Nakagawa, A. Tanimoto and M. Sakakibara, Heat and mass transfer with boundary layer flow past a flat plate of finite thickness, Int. J. Heat Mass Transfer, 34, 2899-2909(1991).
10. T. Ota and N. Kon, Heat transfer in the separated and reattached flow on a blunt flat plate, ASME J. Heat Transfer, 459-462(1974).
11. T. Ota, Y. Asano and J. Okawa, Reattachment length and transition of the separated flow over blunt flat plates, Bulletin of the JSME, 24, 941-949(1981).
12. T. Ota and M. Narita, Turbulence measurements in a separated and reattached flow over a blunt flat plate, ASME J. Fluids Engineering, 100, 224-228(1978).
13. T. Ota and N. Kon, Turbulent transfer of momentum and heat in a separated and reattached flow over a blunt flat plate, ASME J. Heat Transfer, 102, 749-754(1980).
14. R. Parker and M. C. Welsh, Effects of sound on flow separation from blunt flat plates, Int. J. Heat and Fluid Flow, 4, 113-128(1983).

15. K. Hourigan, L. W. Welch, M. C. Thompson, P. I. Cooper and M. C. Welsh, Augmented forced convection heat transfer in separated flow around a blunt flat plate, Experimental Thermal and Fluid Science, 4, 182-191(1991).
16. K. Sasaki and M. Kiya, Three-dimensional vortex structure in a leading-edge separation bubble at moderate Reynolds number, ASME J. Fluids Engineering, 113, 405-410(1991).
17. V. Kottke, H. Blenke and K. G. Schmidt, Einfluss von anstromprofil und turbulenzintensitat auf die unstromung langsangestromter platten endlicher dicke, Warme- und Stoffubertraung, 10, 159-174(1977).
18. L. W. Sigurdson and A. Roshko, The structure and control of a turbulent reattaching flow, Turbulence Management and Relaminarisation IUTAM Symposium Bangalore, India, Springer-Verlag, 1988.
19. L. W. Sigurdson, The structure and control of a turbulent reattaching flow, J. Fluid Mech., 289, 139-165 (1995).
20. H. J. Sung, K. S. Hwang and J. M. Hyun, Experimental study on mass transfer from a circular cylinder in pulsation flow, Int. J. Heat Mass Transfer, 37, 2203-2210(1994).
21. K. B. Chun and H. J. Sung, Control of turbulent separated flow over a backward-facing step by local forcing, Exp. Fluids, 21, 417-426 (1996).
22. T. R. Troutt, B. Scheelke and T. R. Norman, Organized structures in a .reattaching separated flow field, J. Fluid Mech., 143, 413-427(1984).
23. S. Bhattacharjee, B. Scheelke and T. R. Troutt, Modification of vortex interactions in a reattaching separated flow, AIAA J., 24, 623-629(1986).

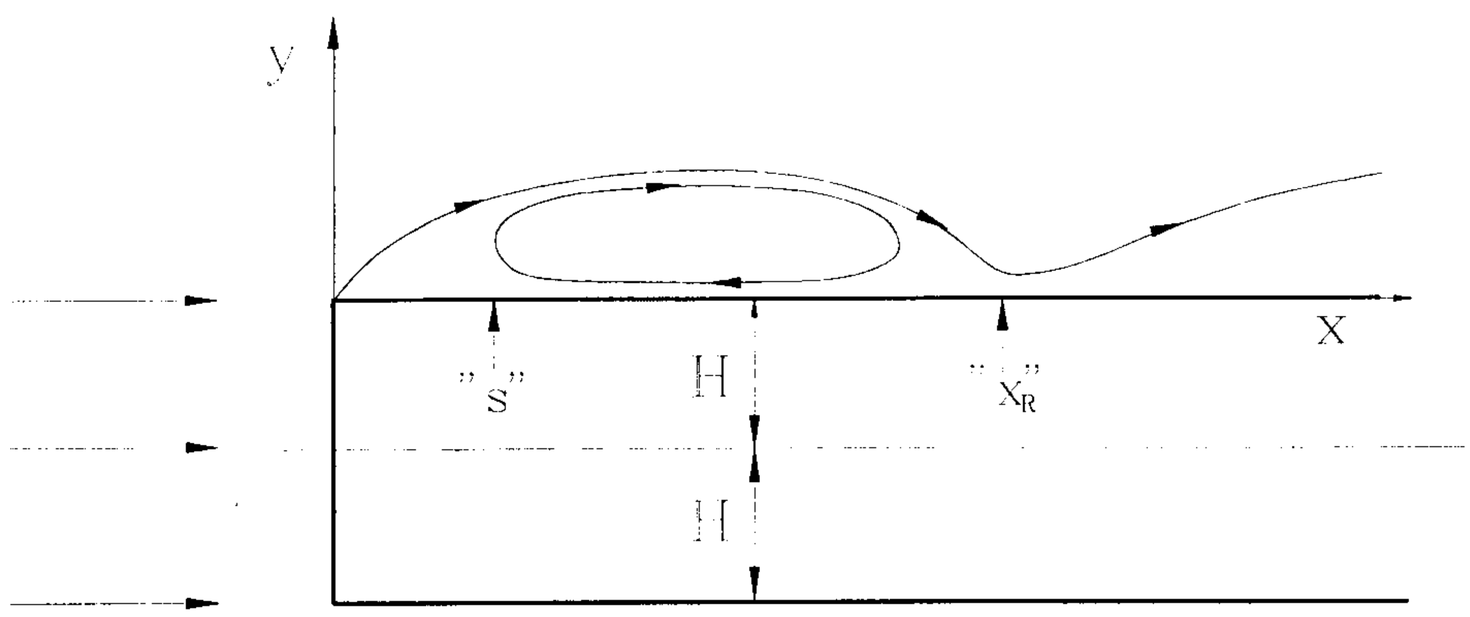

$$U_\infty = U_o \left(1 + A_o \cos 2\pi f_p t\right)$$

Fig. 1 A schema of flow configuration. "s" denotes the secondary separation point and "x_R" the reattachment point.

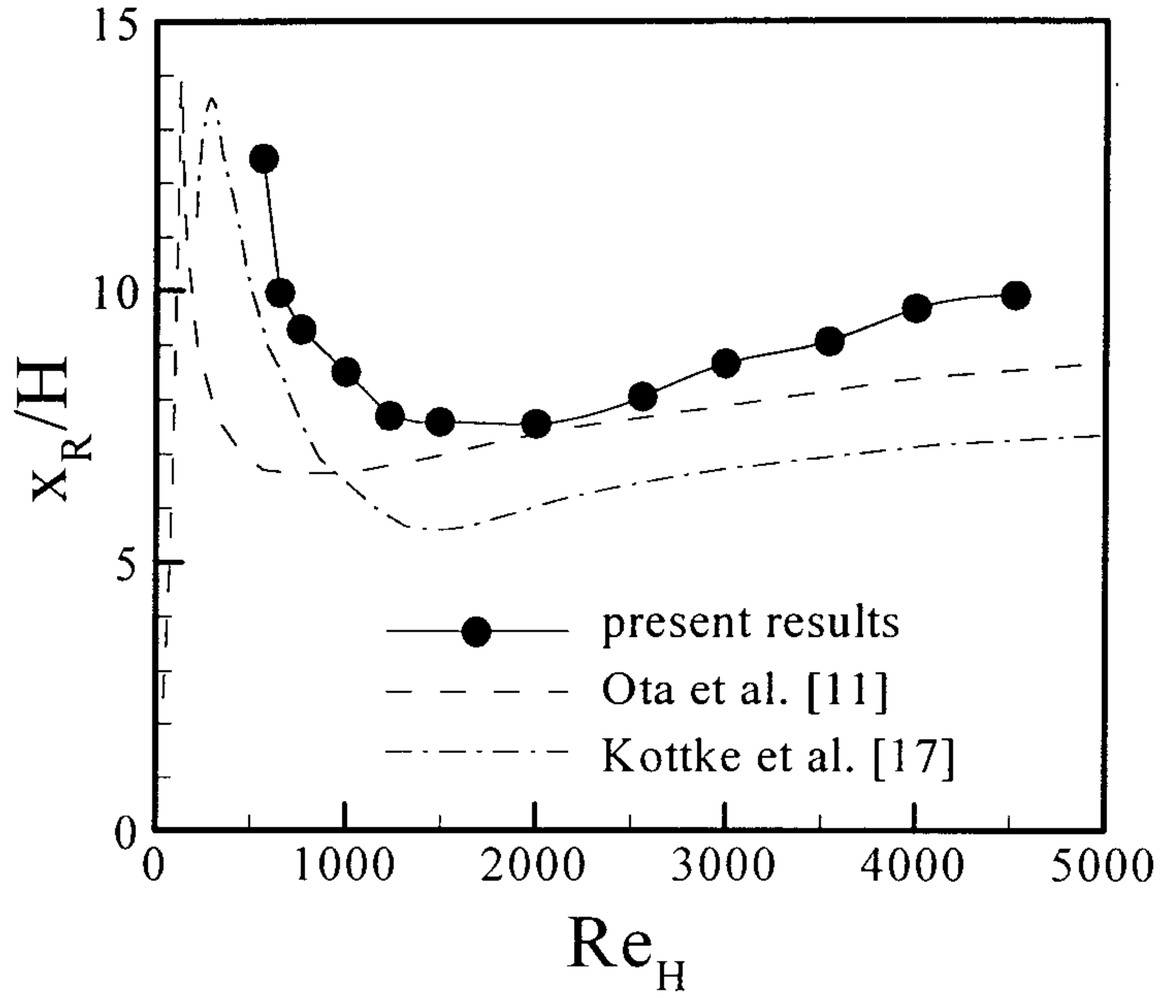

Fig. 2 Time-mean reattachment length x_R vs. Re_H for non-pulsating flows ($A_o = 0$).

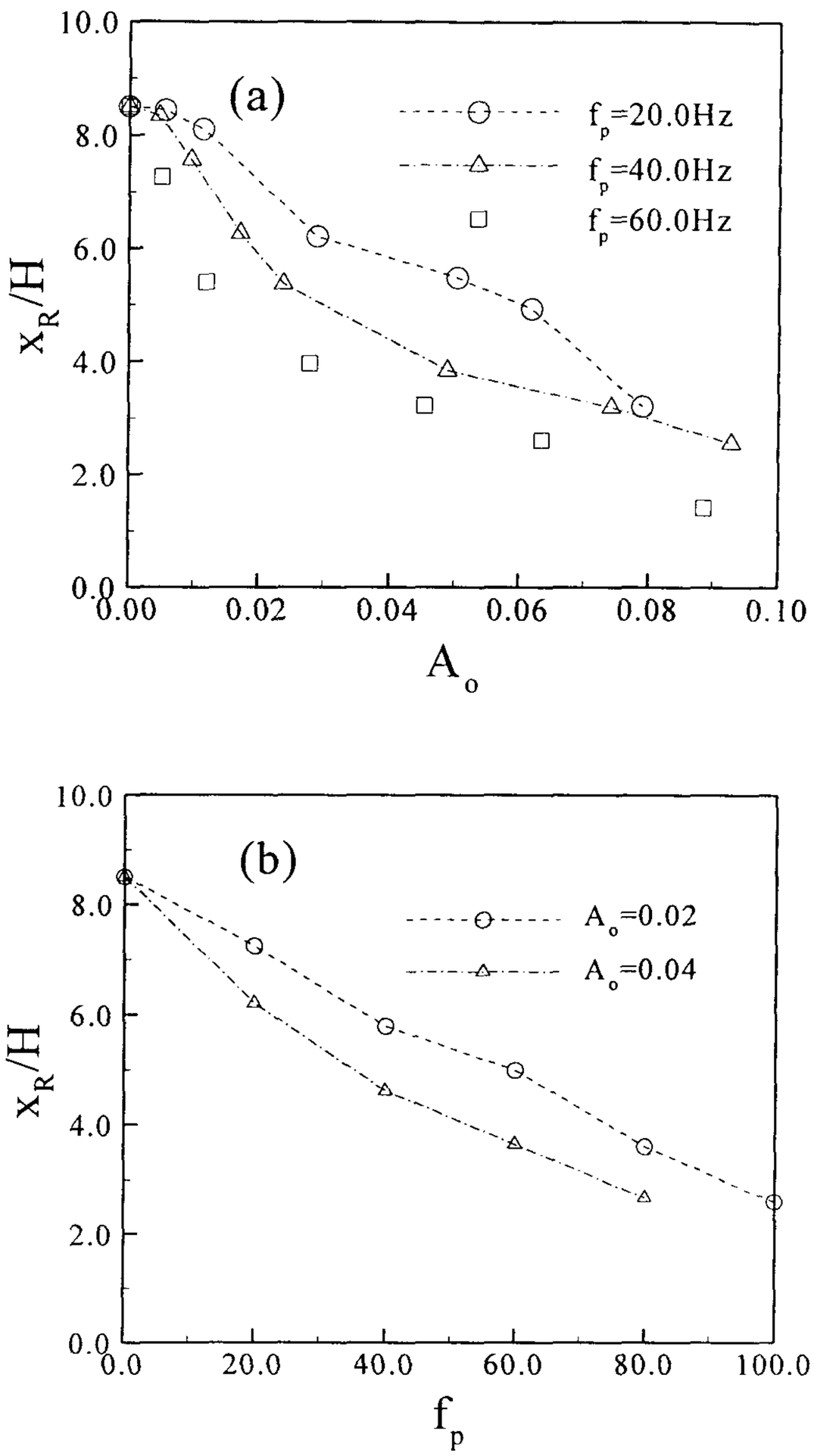

Fig. 3 Variations in time-mean reattachment length x_R for pulsating flows. Re_H = 1000 (a) x_R vs. A_o; (b) x_R vs. f_p.

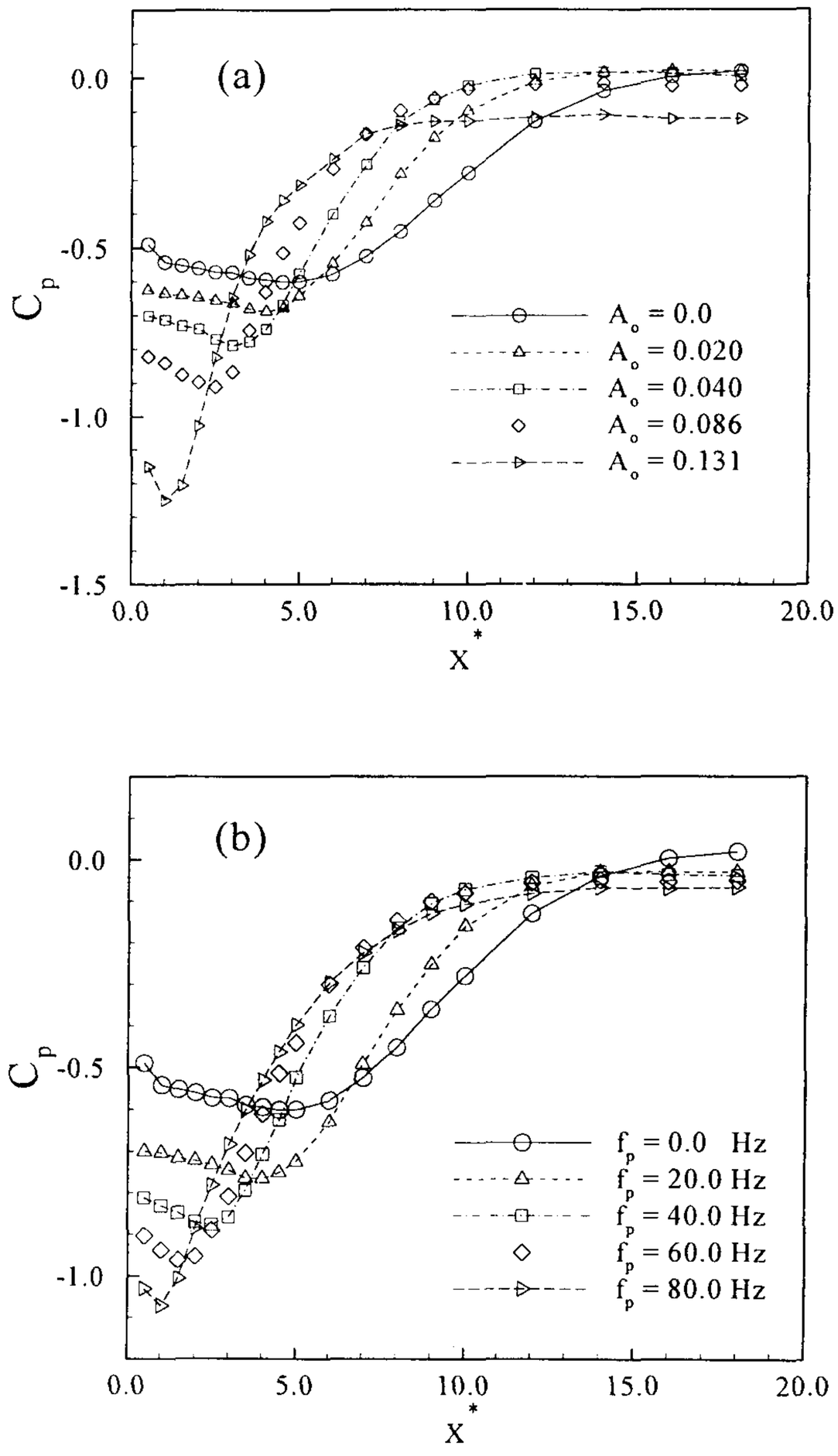

Fig. 4 Stream-wise variations of mean surface pressure coefficient, C_P. Re_H = 2000. (a) Effect of A_o is shown. f_p = 30 Hz. (b) Effect of f_p is shown. A_o = 0.02.

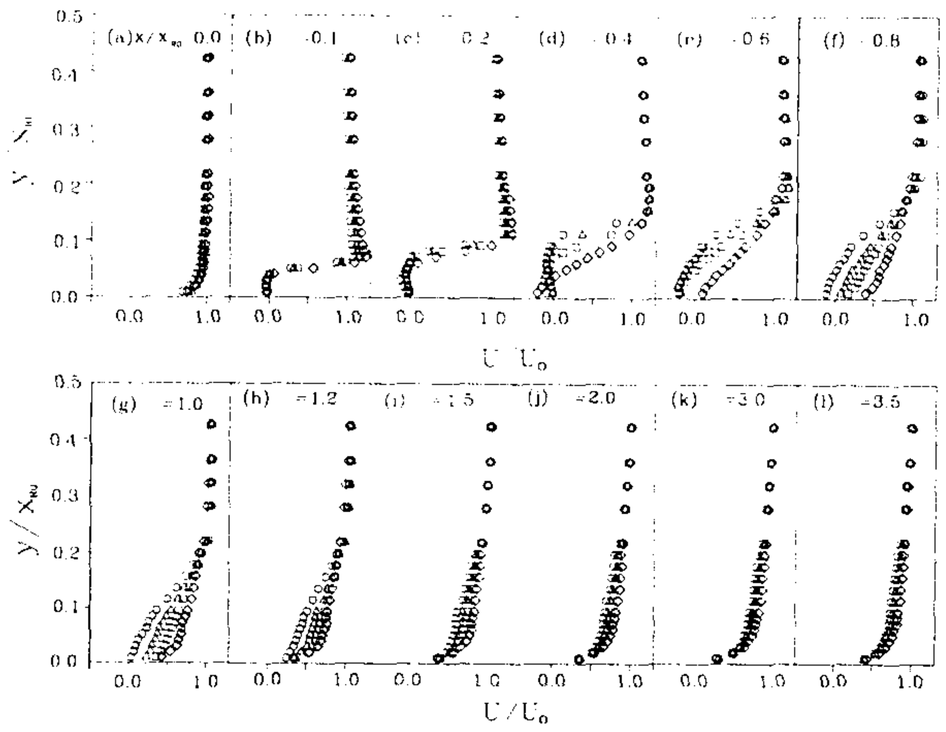

Fig. 5 Stream-wise variations of longitudinal mean velocity U. Re_H = 1000, f_p = 20 Hz. Symbols indicate: ○, A_o = 0(x_R = 8.73H); △, A_o = 0.021 (8.08H); □, A_o = 0.059 (5.58H); ◇, A_o = 0.082 (3.73H).

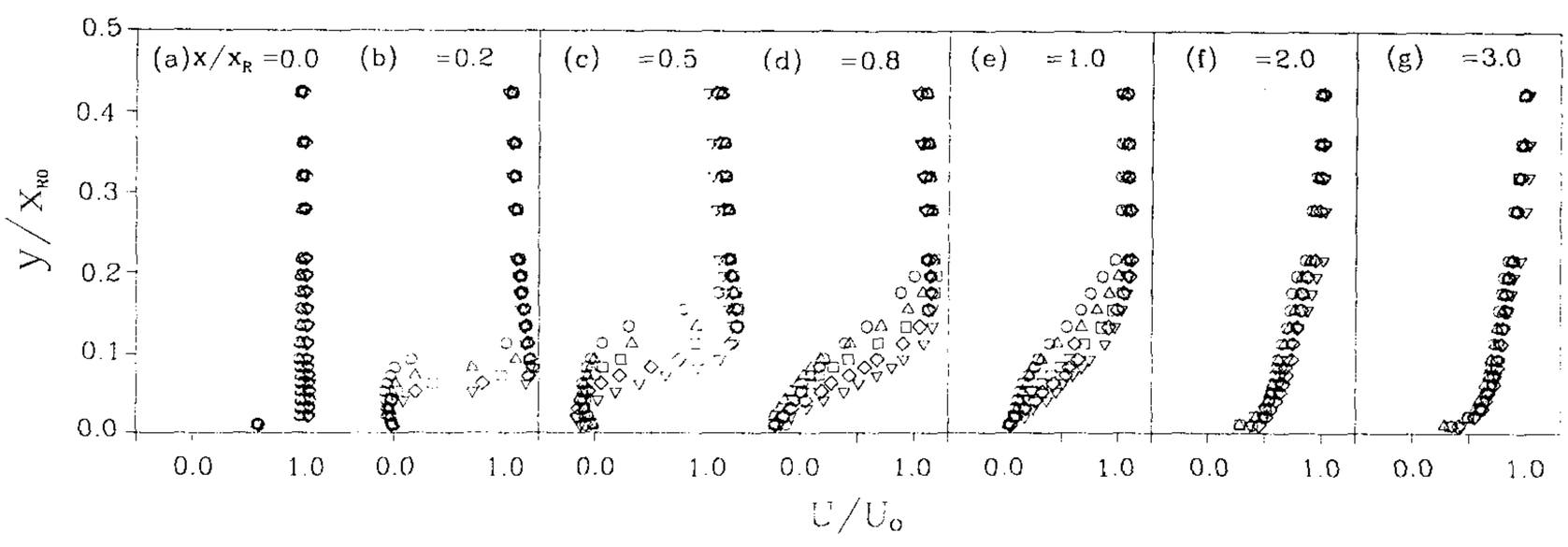

Fig. 6 Effect of f_p on stream-wise variations of longitudinal mean velocity U. Re_H = 1000, A_o = 0.040. Symbols indicate : ○, non-pulsating flow (x_R = 8.73H); △, f_p = 20.0 Hz (6.21H); □, f_p = 40 Hz (4.62H); ◇, f_p = 60 Hz (3.65H); ▽, f_p = 80 Hz (2.69H).

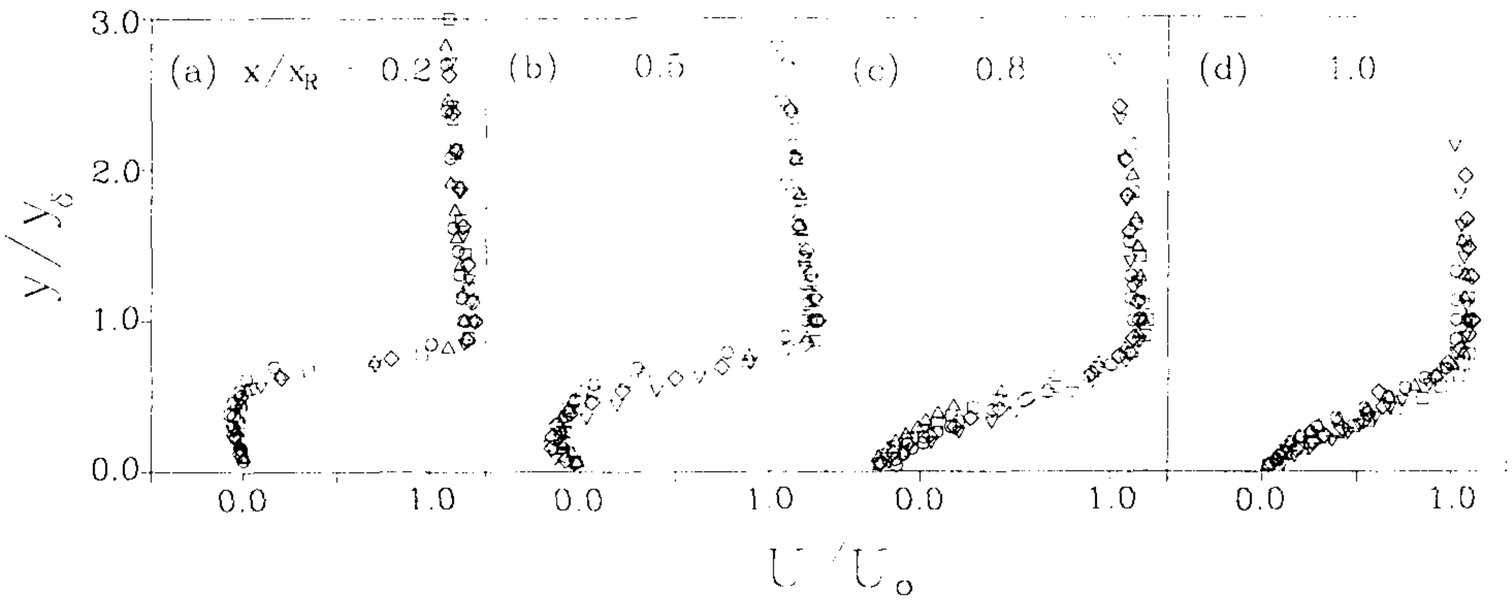

Fig 7 Enlarged plots of U/U_o profiles in the neighborhood of separation bubble. Re_H = 1000, A_o = 0.040. The locations are non-dimensionalized as x/x_R and y/y_d.

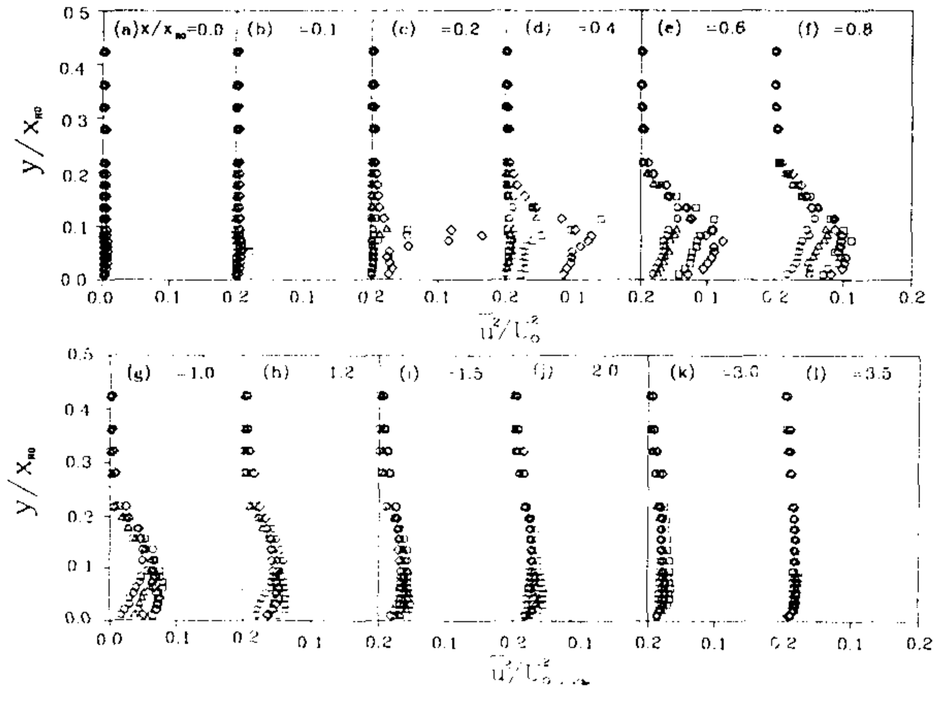

Fig. 8 Stream-wise variations of the longitudinal Reynolds stress u^2/U_o^2 . Re_H = 1000, f_p = 20.0Hz. Symbols indicate: ○, A_o = 0 (x_R = 8.73H); △, A_o = 0.021 (8.08H) ; □, A_o = 0.059 (5.58H) ; ◇, A_o = 0.082 (3.73H).

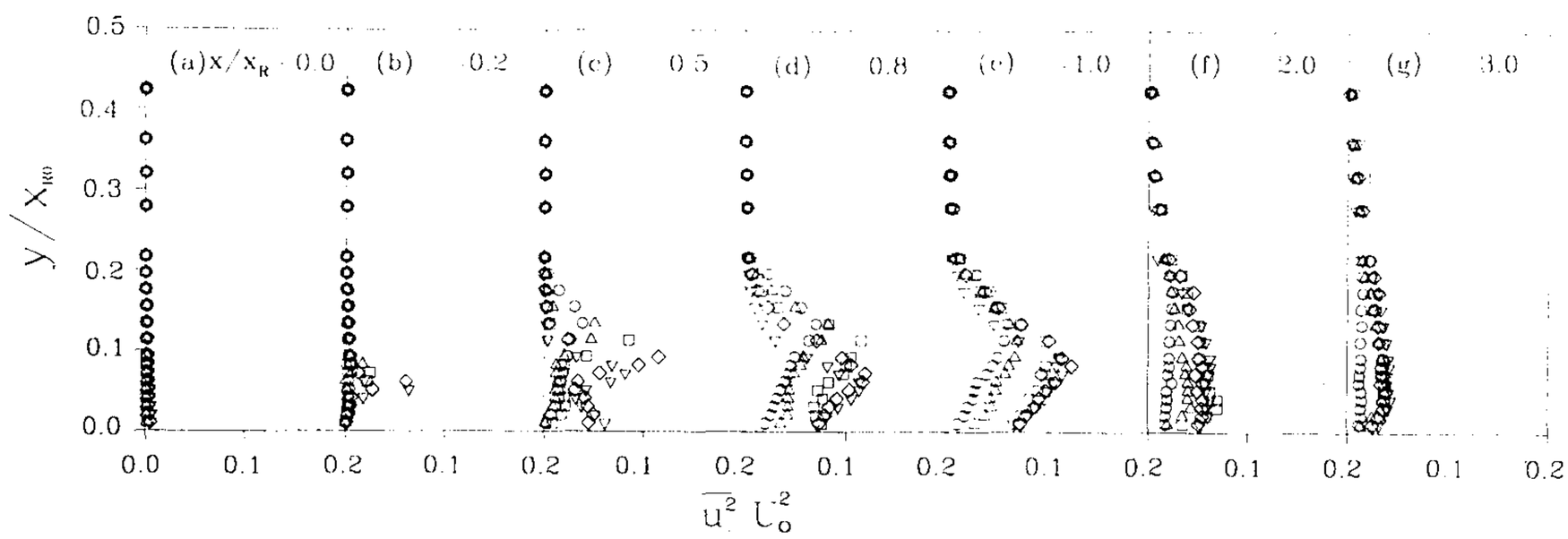

Fig. 9 Stream-wise variations of the longitudinal Reynolds stress u^2/U_o^2. Re_H = 1000, A_o = 0.040. Symbols indicate: ○, f_p = 0.0Hz(x_R = 8.73H) ; △, f_p = 20.0 Hz (6.21H) ; □, f_p = 40 Hz (4.62H) ; ◇, f_p = 60 Hz (3.65H) ; ▽, f_p = 80 Hz (2.69H).

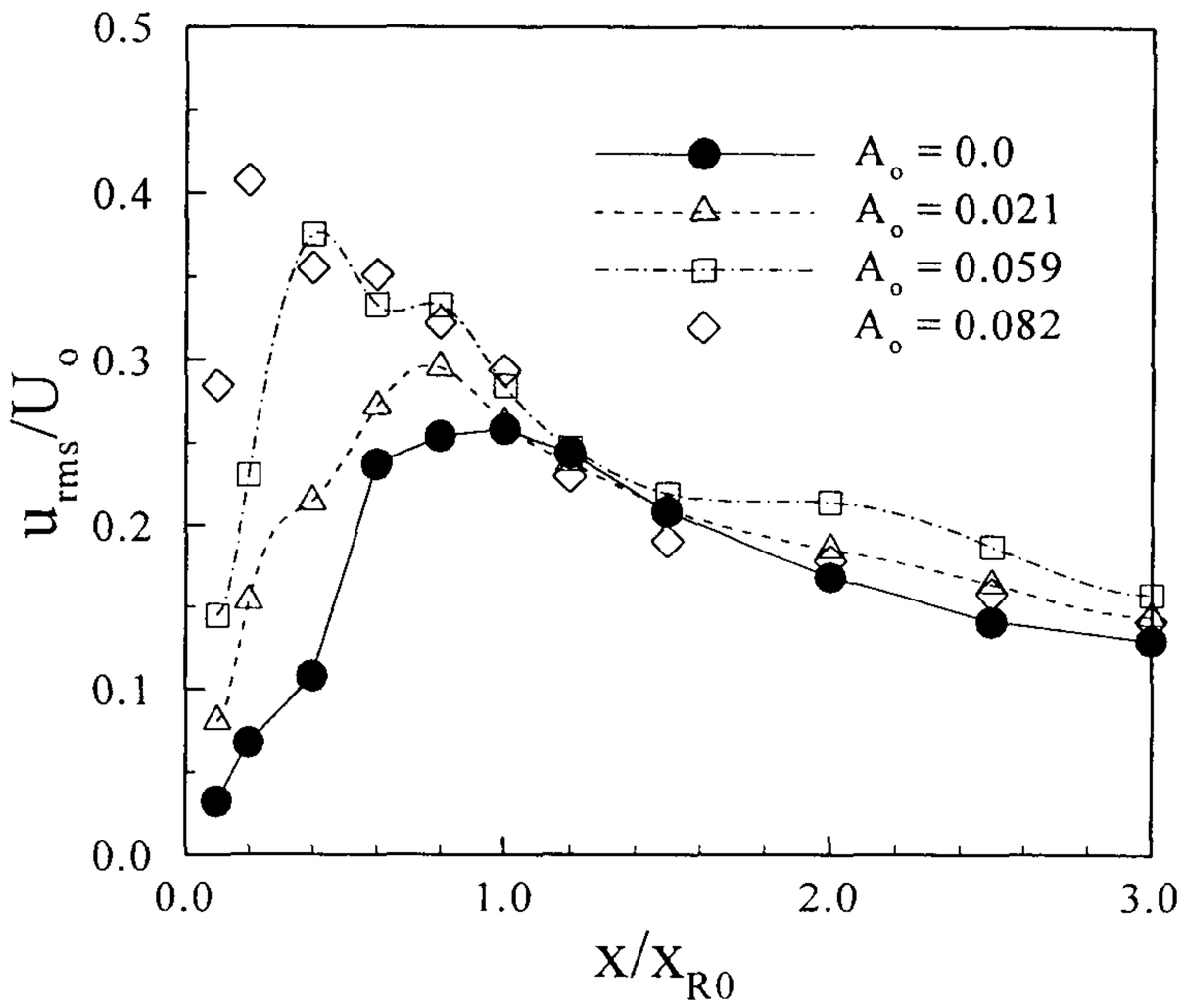

Fig. 10 Stream-wise variations of the maximum longitudinal root-mean-square velocity. Re_H = 1000, f_p = 20.0Hz. Symbols indicate: ○, A_o = 0 (x_R = 8.73H); △, A_o = 0.021 (8.08H) ; □, A_o = 0.059 (5.58H) ; ◇, A_o = 0.082 (3.73H).

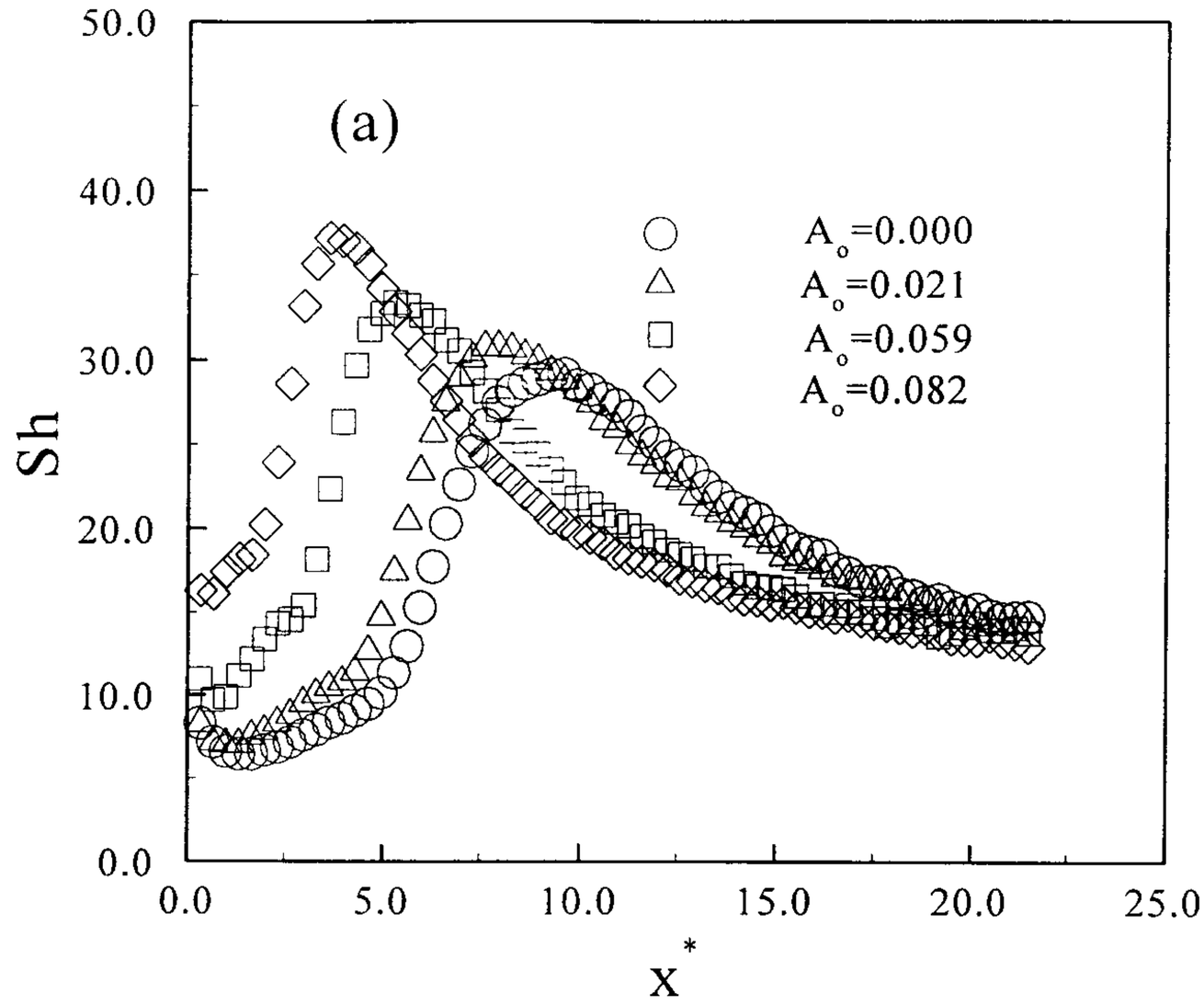

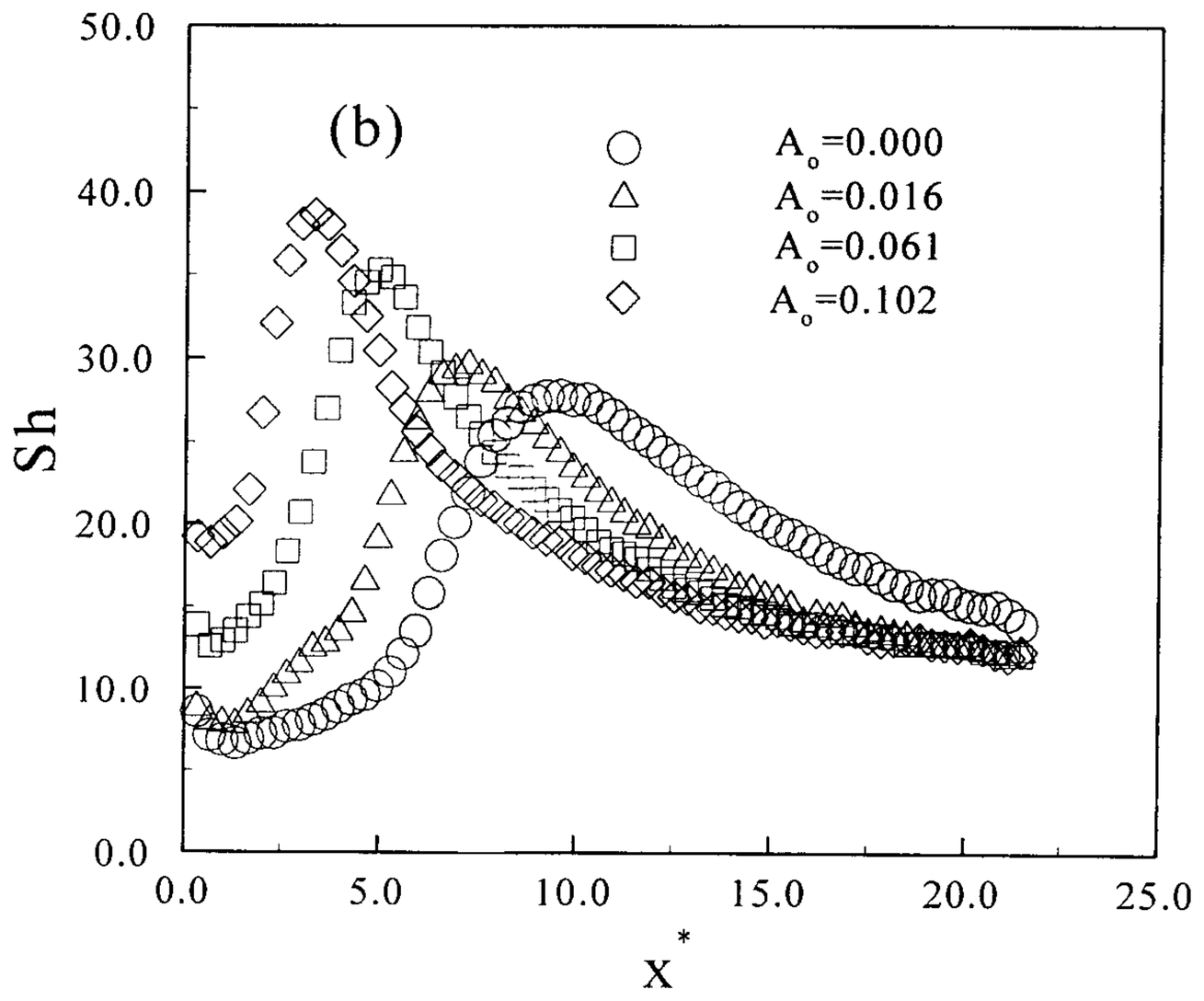

Fig. 11 Stream-wise variations of the Sherwood number Sh. Re_H = 1000. (a) f_p = 20 Hz, (b) f_p = 30 Hz.

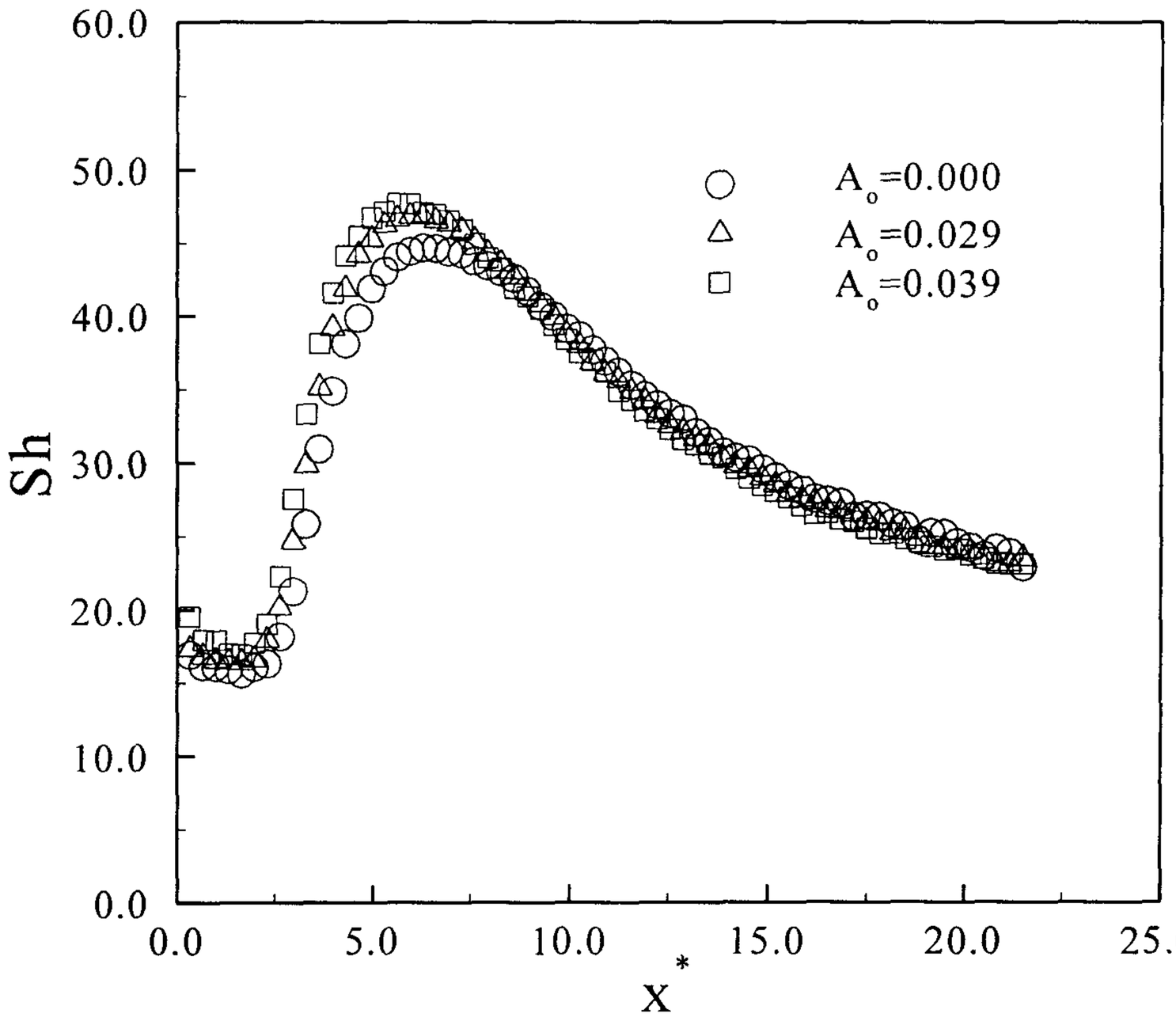

Fig. 12 Stream-wise variations of the Sherwood number Sh. Re_H = 2000, f_p = 20 Hz

제 9 절

TRANSIENT NATURAL CONVECTION IN A CAVITY WITH WALLS OF FINITE THICKNESS

(유한한 두께의 벽을 가지는 용기 내의 과도 자연대류)

NOMENCLATURE

A_f	aspect ratio of fluid region [=H/L]
A_w	aspect ratio of solid wall[=D/L]
C	specific heat at constant pressure
D	thickness of solid wall
g	gravitational acceleration
H	height of cavity
k, k*	thermal conductivity, thermal conductivity ratio[$=k_s/k_f$]
L	length of fluid region
Nu, $\overline{Nu}$	local and average Nusselt numbers
p, P	dimensional, dimensionless pressures[$=pL2/\rho_f\alpha_f^2$]
Pr	Prandtl number[$=\nu_f/\alpha_f$]
Ra	Rayleigh number[$=g\beta L^3(T_H-T_L)/\nu_f\alpha_f$]
Ra*	modified Rayleigh number[$=g\beta L^3\Delta T^*/\nu_f\alpha_f$]
S_c	thermal conductance[$=k^*/A_w$]
T	temperature
t	time
u, v	velocities in x and y directions
U, V	dimensionless velocities in x and y directions[$=uL/\alpha_f$, vL/α_f]
x,y	horizontal and vertical coordinates
X,Y	dimensionless horizontal and vertical coordinates[=x/L,y/L]

Greek Symbols

α, α^*	thermal diffusivity, thermal diffusivity ratio[$=\alpha_s/\alpha_f$]
β	volumetric expansion coefficient of fluid
ρ	density
$(\rho C)^*$	heat capacity ratio[$=(\rho C)_s/(\rho C)_f$]
Ψ	dimensionless stream function
θ	dimensionless temperature[$=(T-T_0)/(T_H-T_L)$]

$\triangle T$	temperature difference[$=(T_H-T_L)$]
$\triangle T^*$	temperature difference between the fluid-solid interfaces at mid-height
t	dimensionless time[$=t\alpha_f/L^2$]
ν	kinematic viscosity

Subscripts

C	cold sidewall
f	refers to the fluid
h	solid-fluid interface of the hot wall
H	hot sidewall
m	vertical centerline of the fluid region
s	refers to the solid
o	reference quantities

요 약 문

사각용기에서의 비정상 자연대류에 관한 수치적인 연구를 수행하였다. 윗벽과 아래벽은 열적으로 단열되었고, 수직의 고체벽은 유한한 두께와 열전도도를 가진다. 초기에 유동이 없이 등온인 상태에서 갑자기 수직벽의 바깥면의 온도를 높이고 낮추어서 유동이 발생한다. 유체부분과 고체부분에 대한 시간에 종속된 Navier-Stokes 식의 수치적인 해를 구하였다. 고체와 유체 사이의 열물성치의 비가 중요한 파라메터가 된다. 열용량비가 증가할수록 유체부분에서의 유동의 발달이 느려진다. 대류 및 전도 시간척도가 추정되었다. 열전도도비와 측벽의 두께의 영향이 묘사되었다. 비정상 열전달에대한 시스템 레일리수의 영향이 분석되었다. 비정상 특성에 대한 1차원 근사열전도모델의 적용가능성을 면밀히 조사하였다.

ABSTRACT

Numerical studies are made of transient natural convection in a square cavity. The top and bottom endwalls are thermally insulated. The vertical solid sidewalls are of finite thickness and of finite thermal conductivity. Flow is driven, from the motionless isothermal initial state, by impulsively increasing (decreasing) the temperature at the outer surface of one (the other) vertical sidewall. Numerical solutions are sought to the time-dependent Navier-Stokes equations for the fluid and the solid regions. The ratios of thermophysical properties between solid and fluid are the significant parameters. As the thermal capacity ratio increases, the development of flow in the fluid region is retarded. The conductive and convective timescales are estimated. The effects of the thermal conductivity ratio and of the thickness of the sidewall are delineated. The effect of the system Rayleigh number on transient heat transport is analyzed. The applicability of the approximate one-dimensional thermal conductance model to the transient features is scrutinized.

1. INTRODUCTION

The most paradigmatic of natural convection in an enclosure is a square cavity with different temperatures specified on the two vertical sidewalls(see, e.g., reviews by Ostrach, 1982 [1]; Hoogendoorn, 1986 [2]; Hyun, 1994 [3]). The benchmark solutions for the steady-state flow and thermal fields for this configuration have been documented for broad ranges of the system Rayleigh number Ra(see, e.g., Davis, 1983 [4]; Le Quere, 1987 [5]) and the Prandtl number Pr. A canonical time-dependent version of the problem was formulated by Patterson and Imberger (1980 [6], hereafter referred to as P&I). They considered the response of an initially motionless, isothermal fluid to impulsive imposition of the two different temperatures at the vertical sidewalls. P&I provided physically insightful and descriptive scenarios for the flow evolutions in the parameter spaces of Ra, Pr and the cavity aspect ratio A_f.

In the above-cited basic models, the horizontal walls are assumed to be thermally-insulated. The vertical sidewalls are taken to be a perfect conductor of zero thickness; the fluid temperature at the inside surface of the wall is instantly equalized to the temperature at the outside surface of the wall. Obviously, this type of sidewall conditions represents a highly idealized version of the practical situations. In fact, some of the notable discrepancies between the experiment(Yewell et al., 1982 [7]) and the predictions by P&I have been attributed to the finite thermal conductance of the sidewalls in realistic experimental setups.

A literature scan reveals that studies on natural convection under more realistic sidewall conditions are not numerous(e.g., Kim & Viskanta, 1984 [8]; Turki & Lauriat, 1990 [9]; Le Breton, 1991 [10]; Chang & Lin, 1994 [11]; Fusegi & Hyun, 1994 [12]). In addition, the majority of these works are concerned with steady situations, and time-dependent features under non-idealized wall conditions do not seem to have been thoroughly dealt with. In the present endeavor, the explicit effects of the solid sidewall of finite thickness on the overall flow evolutions will be delineated by acquiring numerical solutions to the full, unsteady Navier-Stokes equations.

2. MODEL

The flow configuration, together with the coordinates used, is sketched in Fig.1. The key element is the presence of solid sidewalls of thickness D. In line with the basic contentions of P&I, the fluid is initially motionless and in thermal equilibrium with the environment at temperature T_0. At the initial instant, the temperatures at the outside surfaces of the vertical walls are abruptly altered to T_H [$T_0+\triangle T/2$] and TL [$T_0-\triangle T/2$], respectively. The mission is to depict the ensuing transient flow and temperature fields inside the square cavity of width L.

Invoking the Boussinesq-fluid approximation, the governing equations for the fluid region, in properly non-dimensionalized form, read

$$\frac{\partial U}{\partial X}+\frac{\partial V}{\partial Y}=0 \tag{1}$$

$$\frac{\partial U}{\partial \tau}+U\frac{\partial U}{\partial X}+V\frac{\partial U}{\partial Y}=-\frac{\partial P}{\partial X}+\frac{\partial}{\partial X}\left(\mathrm{Pr}\frac{\partial U}{\partial X}\right)+\frac{\partial}{\partial Y}\left(\mathrm{Pr}\frac{\partial U}{\partial Y}\right) \tag{2}$$

$$\frac{\partial V}{\partial \tau}+U\frac{\partial V}{\partial X}+V\frac{\partial V}{\partial Y}=-\frac{\partial P}{\partial Y}+\frac{\partial}{\partial X}\left(\mathrm{Pr}\frac{\partial V}{\partial X}\right)+\frac{\partial}{\partial Y}\left(\mathrm{Pr}\frac{\partial V}{\partial Y}\right)+Ra\cdot\mathrm{Pr}\cdot\theta \tag{3}$$

$$\frac{\partial \theta}{\partial \tau}+U\frac{\partial \theta}{\partial X}+V\frac{\partial \theta}{\partial Y}=\frac{\partial}{\partial X}\left(\frac{\partial \theta}{\partial X}\right)+\frac{\partial}{\partial Y}\left(\frac{\partial \theta}{\partial Y}\right) \tag{4}$$

For the solid region,

$$\frac{\partial}{\partial \tau}\{(\rho C)^*\theta\}=\frac{\partial}{\partial X}\left(k^*\frac{\partial \theta}{\partial X}\right)+\frac{\partial}{\partial Y}\left(k^*\frac{\partial \theta}{\partial Y}\right) \tag{5}$$

In the above, nondimensionalization has been implemented as follows :

(X,Y) = (x,y)/L ; (U,V) = (u,v)/(α_f/L) ; t = tα_f/L^2 ; P = pL^2/$\rho_f\alpha_f^2$; $\theta=\dfrac{T-T_0}{T_H-T_C}$.

The associated initial and boundary conditions can be stated as

$t < 0$, $U = V = \theta = 0$ in the fluid and solid regions, (6)

$t \geq 0$, $U = V = 0$ at $X = 0,\ 1+2A_W,\ Y = 0,\ A_f$, (7)

$\theta = 0.5$ at $X = 0$, (8)

$\theta = -0.5$ at $X = 1+2A_W$, (9)

$$\frac{\partial \theta}{\partial Y} = 0 \qquad \text{at } Y = 0,\ A_f, \tag{10}$$

$$\theta_s = \theta_f\ , \qquad \text{at } X = A_W\ ,\ \ 1+A_W. \tag{11}$$

The relevant dimensionless parameters emerge : $Pr=\nu_f/\alpha_f$, the Prandtl number; $Ra=g\beta L^3(T_H-T_L)/\nu_f\alpha_f$, the system Rayleigh number; $k^*=k_s/k_f$, the conductivity ratio; $\alpha^*=\alpha_s/\alpha_f$, the thermal diffusivity ratio; $(\rho C)^*=(\rho C)_s/(\rho C)_f$, the thermal capacity ratio; $A_f=H/L$, the aspect ratio of fluid region; $A_w=D/L$, the nondimensional thickness of solid wall. Note that Eq.(7) indicates that the entire computational domain consists of the fluid and solid regions to effectively treat the conjugate problem. In the solid region, the viscosity is taken to be a very large value to render the velocity practically zero, i.e., U=V=0 at $X=A_w,\ 1+A_w$.

The above system of equations was solved numerically by using the well-established SIMPLER algorithm(Patankar, 1981 [13]). The specifics of this numerical procedure have been amply documented. In order to obtain higher accuracy, the QUICK Scheme[14] was utilized, and the SIP solver[15] was used to solve the discretized equations. For most calculations, a grid network of [41x41] mesh points was deployed for the fluid region, and the number of grid points for the solid region was varied accordingly. The grid points were concentrated in the vicinities of the solid-fluid interfaces as well as near the horizontal endwalls. A stretched, staggered grid was adopted. At the solid-fluid interfaces, the grid points for vector quantities are located. Also, the faces of control volume for scalar quantities coincide with these interfaces. The harmonic mean of the diffusion coefficients of fluid and solid was used to compute the heat flux at the interface. The time step was determined such that

$$\Delta t \le (10^{-3})\,(\rho C)^* \left[\frac{S_C}{S_C+2}\cdot Ra\cdot \mathrm{Pr}\right]^{-\frac{1}{2}},$$

which indicates that the computational time interval was made proportional to the conduction timescale in the solid. The above equation corresponds to a resolution of 1000 time steps in one period of the Brunt-Vaisala oscillation for the case of a cavity of sidewalls of zero thickness. These considerations are thought to yield sufficient resolution of the principal transient features of the problem in hand. Extensive

benchmark computations as well as grid- and time step- convergence tests were repeated using several different mesh networks. The results were compared against the published data, which included the steady solutions in a cavity with vertical sidewalls of finite thickness(e.g., Turki & Lauriat, 1990 [9]; Kaminski & Prakash, 1986 [16]; House et al., 1990 [17]). Comparisons were also made against the data of P&I and several other cavity flows with extreme parameter values. These exercises verified the robustness and accuracy of the present numerical methodologies.

3. RESULTS AND DISCUSSION

In view of the presence of a large number of parameters, it is helpful to secure data for a standard setup for cross-comparisons. For many typical combinations of solid and fluid in common technological applications, the values of the solid-fluid property ratios encompass broad ranges, e.g., $0.02 \leq k^* \leq 16300$, for wood/mercury to silver/air ; $0.006 \leq \alpha^* \leq 1240$, for wood/air to silver/water; $0.29 \leq (\rho C)^* \leq 3300$, for sand/ water to stainless steel/air. In light of the above data, approximately median values are selected for the standard case, i.e., $k^*=10$, $(\rho C)^*=10$. Furthermore, $A_f=1.0$, and $Pr=0.71$, and $Ra=10^6$, and $A_w=0.2$ are set for the standard configuration. The impact of a pertinent parameter in question is examined by varying that particular individual parameter in the above standard set. The cases that were covered in the present paper are summarized in Table.1.

Descriptions are obtained of the Nusselt number on the inner surface of the hot sidewall, Nu_h and the Nusselt number on the mid-plane, Nu_m, i.e.,

$$Nu_h = -\left(\frac{\partial \theta}{\partial X}\right) \quad \text{at } X=Aw ,$$

$$\overline{Nu_h} = \int_0^1 -\left(\frac{\partial \theta}{\partial X}\right) dY \quad \text{at } X=Aw ,$$

$$Nu_m = \left[-\left(\frac{\partial \theta}{\partial X}\right) + U\theta\right] \quad \text{at } X=Aw+0.5 ,$$

$$\overline{Nu}_m = \int_0^1 \left[-\left(\frac{\partial \theta}{\partial X} \right) + U\theta \right] dY \qquad \text{at X=Aw+0.5 .}$$

The global flow and temperature patterns for the above standard case are displayed in Fig.2(a). For comparison purposes, the corresponding results for the Patterson and Imberger model, in which the sidewalls are of zero thickness and of infinite thermal conductivity, i.e., k^*/A_w, are exhibited in Fig.2(b). Obviously, as shown in Fig.2(a), the process of fluid thermal stratification takes place by combined effects of conduction through the wall and convective activities in the fluid. At the fluid-solid interface, the condition $k_s \left(\frac{\partial T}{\partial x} \right)_s = k_f \left(\frac{\partial T}{\partial x} \right)_f$ is to be satisfied; therefore, the isotherms in the vicinity of the fluid-solid interface are not oriented strictly in the vertical direction. It is discernible that, due to the presence of the finite-thickness sidewalls, the intensity of flow and the strength of stratification are reduced. Also, as anticipated, the transient process in the fluid is retarded owing to the conduction heat transfer in the sidewall.

The prominent transient characteristics of the standard case are elaborated in Fig.3, which illustrate the deviations from the P&I model. The histories of $\overline{Nu}_h$ and $\overline{Nu}_m$ are plotted in Fig.3(a). Evidently, in comparison to the P&I model, the overall heat transfer rate is substantially decreased. Also, the period of early-time oscillations is increased, and the amplitude of these oscillations is reduced. This is attributed to the reduced effective temperature difference within the fluid region. It is also significant that $\overline{Nu}_h$ at $\tau=0$ is zero, which is in line with the realistic situations. Note that, in the case of the P&I model, at the initial instant $\tau=0$, the step-change in temperature is idealized, which gives $Nu_h \rightarrow \infty$ at $\tau=0$. At small times until $\tau \sim 0.04$, Nu_h increases almost linearly with time. This implies that the diffusion time scale over the sidewall is roughly $\tau \sim 0.04$, in which period the heat transfer rate into the fluid grows with time. Similar comparisons are displayed in Fig.3(b) for the maximum vertical velocity V_{max} and for Ψ_{max}.

Changes in the transient process due to the alteration in thermal capacity ratio $(\rho C)^*$ are shown in Fig.4&5. The steady-state features are not affected by the changes in $(\rho C)^*$; only the transient characteristics are influenced by $(\rho C)^*$. As can be inferred from the heat conduction equation for the solid region, Eq.(5), the evolution of the flow field is retarded as $(\rho C)^*$ increases. The time-dependent behavior of Nu_h, Nu_m, V_{max} and Ψ_{max}

is exhibited in Fig.5 for three representative values of (ρC)*. As seen in Fig.5(b), the early-time oscillatory character becomes more distinctive for smaller values of (rC)*. This phenomenon can be explained based on the following physical reasoning. The fact that (ρC)* is small implies that the relative thermal capacity of the solid sidewall is smaller than that of the fluid. Alternatively speaking, a small (ρC)* indicates a large α*. Now, the nondimensional conduction timescale that prevails in the solid region can be derived as:

$$\tau_{cond} \sim \frac{D^2}{\alpha_s}\frac{\alpha_f}{L^2} = \left(\frac{D}{L}\right)^2 / \left(\frac{\alpha_s}{\alpha_f}\right) = \frac{A_w{}^2 \cdot (\rho C)^*}{k^*} \qquad (12)$$

On the other hand, the nondimensional convective timescale for the fluid region for Ra>>1 can be estimated as (e.g. P&I, 1980 [6])

$$\tau_{cond} \sim (Ra^*)^{-\frac{1}{4}} A_f \qquad (13)$$

In the above, Ra* indicates the Rayleigh number based on the actual characteristic temperature difference throughout the fluid system, △T*. Because of the presence of sidewall of finite thickness, △T* is not the same as △T, and △T* should be obtained as part of the solution rather than an externally-specified value. In the present study, △T* was taken to indicate the temperature difference between the fluid-solid interfaces at mid-height, i.e., $\triangle T^* = T[A_w, 0.5] - T[1+A_w, 0.5]$. Consequently, . Clearly, tcond is decreased as (ρC)* becomes small, which indicates that conduction within the solid wall is accomplished over a shorter time. For the parameter values of the present computations, $\tau_{cond} \sim 4\times10^{-3}(\rho C)^*$, $\tau_{conv} \sim 3.4\times10^{-2}$. Thus, the time ts for the system to reach steady-state situations can be asserted to be

$$\tau_s \sim \tau_{cond} + \tau_{conv} \qquad (Ra^* >> 1)$$

The above qualitative assessments are consistent with the results depicted in Figs.4-5. The existence of the oscillatory approach can also be interpreted on similar physical arguments. If τ_{cond} is much smaller than τ_{conv}, a large temperature gradient is developed at the solid-fluid interface over a time duration which is far shorter than the convective time for the fluid. This rapid variation in the boundary condition for the fluid region causes oscillatory behavior(e.g., Davis[4], P&I[6]). In contrast, if $\tau_{cond} > \tau_{conv}$, the response of fluid can be achieved gradually as the conductive heat transfer within the solid

progresses slowly. In the present study, extensive time-step convergence tests were conducted, and the results consistently demonstrated the early-time oscillatory behavior. These validations and the above-stated previous assertions of Davis[4] and P&I[6] on the oscillatory behavior are supportive of the fact that the present oscillations are of physical, rather than numerical, nature.

The impact of $(\rho C)^*$ on the vertical profiles of Nu_h is revealing. As seen in Fig.6, when $(\rho C)^*$ is small, the settlement to the steady state, while undergoing oscillations, takes place over a short period of time. It is also noticeable in the plots of Nu_h in Fig.6(a) that, at small times, relatively large heat transports are seen throughout much of the vertical faces of the wall. As time progresses, owing to the convective activities, cold(hot) fluids occupy the bottom(upper) region of the cavity. Consequently, Nu_h increases(decreases) in the bottom(upper) region. On the other hand, when $(\rho C)^*$ is large, the transitory approach is slow and monotonic. The values of Nuh are very small in the early stage, and Nu_h grows monotonically with time toward the characteristic steady-state, as can be observed in Fig.6(b).

The results obtained by varying the thermal conductivity ratio k* are exhibited in Figs.7-9. As can be seen in Fig.7, a large value of k* implies that the temperature within the entire solid wall region becomes closer to the imposed temperature at the outer surface of the wall. As a result, the fluid region is controlled mainly by convection, and the temperature fields in the fluid develop strong gradients, both in space and time. In the opposite limit of small k*, the solid sidewall acts like an insulator. Obviously, in this case, the convective activities in the fluid are weak, and the vertical isotherms are concentrated near the fluid-solid interfaces.

As remarked earlier, tcond is inversely proportional to k*. Substituting $(\rho C)^*=10.0$, $A_w=0.2$, for the standard set, τ_{cond} becomes

$$\tau_s \sim \frac{0.4}{k^*}$$

Therefore, the time to reach steady state, τ_s, may be estimated as

$$\tau_s \sim \tau_{cond} + \tau_{conv} \sim \frac{0.4}{k^*} + (Ra^*)^{-\frac{1}{4}} \qquad \text{for } Ra^* \gg 1.$$

The above assertion is consistent with the numerical results displayed in Figs.7&8.

Also, the presence of oscillatory approach to steady state, as exemplified in $\overline{Nu_m}$ in Fig.8(b), is anticipated when $\tau_{cond}<\tau_{conv}$, as had been mentioned earlier.

The profile of Nu_h is plotted in Fig.9. When k* is small, the values of Nu_h are generally small, and they grow with time slowly toward the steady state. Since the convective activities are meager, Nu_h is rather uniform in much of the height of the wall. When k* is large, Nu_h approaches rapidly the steady-state, in which Nu_h decreases from the bottom to the top region of the cavity(Davis[4], Le Quere[5]).

Fig.10 illustrates Ψ and θ when A_w=2.0. Obviously, in comparison to the standard case, the flow is weak, and the heat transport is reduced. In order to satisfy the interface condition $\left(\frac{\partial T}{\partial x}\right)_s = \frac{1}{k^*}\left(\frac{\partial T}{\partial x}\right)_f$, a large temperature drop occurs in the solid region. The overall role of Aw is equivalent to 1/k*.

By substituting (ρC)*=10.0, k*=10.0 into Eq.(12), $\tau_{cond} \sim A_w{}^2$, and $\tau_s \sim \tau_{cond} + \tau_{conv} \sim A_w{}^2 + (Ra^*)^{-\frac{1}{4}}$ when Ra*>>1. The time histories shown in Figs.10 and 11 are in support of the above estimation. Also, the presence of oscillatory transitory approach is discernible when $\tau_{cond}<\tau_{conv}$, which is compatible with the results of Fig.11.

The impact of Ra on the global Ψ and θ fields is displayed in Fig.12. As anticipated, as Ra increases, the flow is intensified, and the isotherms in the fluid interior become more horizontally-oriented. For large Ra, and at moderate and large times, the isotherms in the solid walls are not strictly vertical, which stresses the influence of conduction in the solid region.

Time histories of the relevant physical variables are plotted in Fig.13 for varying Ra. For these cases, τ_{cond} is fixed and τ_{conv} decreases as Ra increases. Also, oscillatory transient approach is seen when Ra is large enough such that $\tau_{cond}<\tau_{conv}$, as asserted earlier. The results in Figs.12 and 13 are in qualitative agreement with these observations and with the prior findings[P&I].

4. APPLICABILITY OF THE ONE-DIMENSIONAL THERMAL CONDUCTANCE MODEL

The individual qualitative effects of thermal conductivity ratio (k*) and of wall thickness (A_w) have been scutinized. Therefore, it is useful to combine these two effects into a single parameter; the thermal conductance, S_c, is defined:

$$S_c = \frac{k^*}{A_w} \left[\equiv \frac{k_s}{k_f} \frac{L}{D} \right]$$

In conjunction with the concept of S_c, Walin[18] and several other authors[19-20] attempted to describe the heat flux condition at the fluid-solid interface by using a one-dimensional approximation, i.e.,

$$\left(\frac{\partial T}{\partial x}\right)_f = \frac{k_s}{k_f}\left(\frac{\partial T}{\partial x}\right)_s \cong \frac{k_s}{k_f}\frac{\theta_{out} - \theta_w}{D/L} = S_c \cdot [\theta_{out} - \theta_w]$$

In the above, θ_{out} and θ_w respectively denote the temperatures at the external surface and the fluid-solid interface of the wall. It is emphasized that this approximate one-dimensional thermal conductance model has been shown to be capable of depicting the steady-state global flow patterns with reasonable accuracy. However, this is not the case for the transient state. Fig.14 demonstrates the time-dependent processes with the same S_c but with different make-ups of k* and A_w. Clearly, transient features display marked discrepancies as the combinations of k* and A_w differ. This can also be seen in the considerations of time scales. As in Eq.(12), the transient conductive evolution is determined by $\tau_{cond} \sim A_w^2/k^*$, whereas in the steady limit the flow features are characterized by S_c [$=k^*/A_w$]. This suggests that, in the analysis of transient state, A_w and k* should be treated as separate parameters, rather than in the lumped form of k^*/A_w. It is worth mentioning that, in the limit when S_c is very large, both the transient and steady features can be characterized by the single parameter S_c. Evidently, when S_c is very large, $\tau_{cond} \ll \tau_{conv}$, therefore, the conduction process within the solid region has little influence on the overall fluid convective process.

In summary, the approximate one-dimensional thermal conductance model is useful to depict the steady-state characteristics. However, for the transient process, the individual parameters A_w and k* make separate contributions to the flow features.

5. CONCLUSIONS

The principal parameters are shown to be $(\rho C)^*$, k^*, A_w as well as the nominal system Rayleigh number Ra.

As expected, due to the presence of the sidewall of finite thickness, the fluid flow weakens and the associated heat transport is reduced. The time ts for the system to settle down to the steady state is shown to be a sum of tcond and tconv. The oscillatory transient approach is seen when $\tau_{cond}<\tau_{conv}$.

The steady-state features are not affected by $(\rho C)^*$, although the influence of $(\rho C)^*$ is substantial for the transient process. In general, convection is intensified as $(\rho C)^*$ and A_w decrease. Also, convection becomes vigorous as k^* and Ra increase. The time to reach the steady state is decreased when convective activities are strong.

The approximate one-dimensional thermal conductance model is useful in depicting the major features of steady-state flows. However, in order to describe the transient stages, k^* and A_w should be treated as separate parameters, rather than in the combined lumped form of $S_c=k^*/A_w$.

REFERENCES

1. S. Ostrach, Natural Convection Heat Transfer in Cavities and Cells, Heat Transfer 1982: Proc. 7th. Int. Heat Transfer Conf., Munchen, vol. 1, pp. 365-379, Hemisphere, Washington, D.C., 1982.
2. C. J. Hoogendoorn, Natural Convection in Enclosures, Heat Transfer 1986: Proc. 8th. Int. Heat Transfer Conf., San Francisco, Calif., vol. 1, pp. 111-120, Hemisphere, Washington, D.C., 1986.
3. Jae Min Hyun, Unsteady Buoyant Convection in an Enclosure, Advances in Heat Transfer, vol. 24, pp. 227-320, 1994.
4. G. de Vahl Davis, Natural Convection of Air in a Square cavity: A Bench Mark

Numerical Solution, Int. J. Numer. Methods in Fluids, vol. 3, pp. 249-264. 1983.

5. P. Le Quere, Etude de la Transition a l'Instationnarite des Ecoulements de Convection Naturelle en Cacite Verticale Differentiellement Chauffees par des Methodes Spectrales Chebyshev, Thesis, Universite de Poitiers, France, 1987.
6. J. Patterson and J. Imberger, Unsteady Natural Convection in a Rectangular Cavity, J. Fluid Mech., vol. 100, pp. 65-86, 1980.
7. R. Yewell, D. Poulikakos and A. Bejan, Transient Natural Convection Experiments in Shallow Enclosures, ASME J. Heat Transfer, vol. 104, pp. 533-538, 1982.
8. D. M. Kim and R. Viskanta, Study of the Effects of Wall Conductance on Natural Convection in Differently Oriented Square Cavities, J.Fluid Mech., vol. 144, pp. 153-176, 1984.
9. S. Turki and G. Lauriat, An Examination of Two Numerical Procedure for Natural Convection in Composite Enclosures, Numerical Heat Transfer 1990: AIAA/ASME Thermophysics and Heat Transfer Conf., Seattl, Washington, vol. 130, pp. 107-113, 1990.
10. P. Le Breton, J. P. Caltagirone and E.Arquis, Natural Convection in a Square Cavity with Thin Porous Layers on Its Vertical Walls, ASME J. Heat Transfer, vol. 113, pp. 892-898, 1991.
11. W. J. Chang and H. C. Lin, Wall Heat Conduction Effect on Natural Convection in an Enclosure Filled with a Non-Darcian Porous Medium, Numerical Heat Transfer, Part A, vol. 25, pp. 671-684, 1994.
12. Toru Fusegi and Jae Min Hyun, Laminar and Transitional Natural Convection in an Enclosure with Complex and Realistic Conditions, Int. J. Heat and Fluid Flow, vol. 15, pp. 258-268, 1994.
13. S.V.Patankar, Numerical Heat Transfer and Fluid Flow, Hemisphere/MacGraw-Hill, New York, 1980.
14. B.P.Leonard, A Stable and Accurate Convection Modelling Procedure Based on Quadratic Upstream Interpolation, Computer Methods in Applied Mechanics & Engineering, vol. 19, pp. 59-98, 1979.
15. H.L.Stone, Iterative Solution of Implicit Approximations of Multidimensional

Partial Difference Equations , SIAM J. Numer. Anal., vol. 5, pp. 530-558, 1968.

16. D.A. Kaminski and C. Prakash, Conjugate Natural Convection in a Square Cavity : Effect of Conduction in One of the Vertical Walls, Int. J. Heat Mass Transfer, vol. 29, pp. 1979-1988, 1986.
17. J. M. House, C. Beckermann and T. F. Smith, Effect of a Centered Conducting Body on Natural Convection Heat Transfer in an Enclosure, Numerical Heat Transfer, Part A, vol. 18, pp. 213-225, 1990.
18. G. Walin, Contained Non-homogeneous Flow under Gravity or How to Stratify a Fluid in the Laboratory, J. Fluid Mech., vol. 48, pp. 647-672, 1971.
19. L. Rahm and G. Walin, On Thermal Convection in Stratified Fluids, Geophys. Astrophys. Fluid Dyn, vol. 13, pp. 51-65, 1979.
20. Y. Le Peutrec and G. Lauriat, Effects of the Heat Transfer at the Side Wall on Natural Convection in cavities, ASME J. Heat Transfer , vol. 112, pp. 370-378, 1990.

TABLES

Parameter	Standard case	Computed cases
$(\rho C)^*$	10	0.1 1 100 1000
k^*	10	0.01 0.1 1 100
Ra	10^6	10^4 10^5 10^7 10^8
A_w	0.2	0.01 0.1 0.5 1.0 2.0

Table 1. Parameter values for the standard set and for the computed cases.

FIGURE CAPTIONS

Fig.1. Schematic of flow configuration.

Fig.2. Evolutions of flow(Ψ) and temperature(θ) fields. (a) the standard case; (b) P&I model.

Fig.3. Transient behavior of $\overline{Nu}_h$, V_{max} and Ψ_{max}. Curves A denote the standard case of the present setup, and curves B the P&I model. (a) ———— , $\overline{Nu}_h$; - - - -, $\overline{Nu}_m$, (b) - - - - - - - - , V_{max} ; - - - -, Ψ_{max}.

Fig.4. Evolutions of Ψ and θ-fields. (a) $(\rho C)^*=0.1$, (b) $(\rho C)^*=1000$.

Fig.5. Effect of $(\rho C)^*$ on transient behavior of .

Fig.6. Profiles of Nuh. (a) $(\rho C)^*=0.1$, (b) $(\rho C)^*=1000$.

Fig.7. Evolutions of Ψ and θ-fields. (a) $k^*=0.1$, (b) $k^*=100$.

Fig.8. Effect of k^* on transient behavior of $\overline{Nu}$.

Fig.9. Profiles of Nu_h. (a) $k^*=1.0$, (b) $k^*=100$.

Fig.10. Evolutions of Ψ and θ-fields for $A_w=1.0$.

Fig.11. Effect of A_w on transient behavior of Nu.

Fig.12. Evolutions of Y and q - fields. (a) Ra=104 , (b) Ra=108.

Fig.13. Effect of Ra on transient behavior of $\overline{Nu}$.

Fig.14. Influence of the combinations of k^* and A_w on transient behavior of $\overline{Nu}$. (a) $S_c=0.5$, (b) at $S_c=50.0$, (c) $S_c=500$.

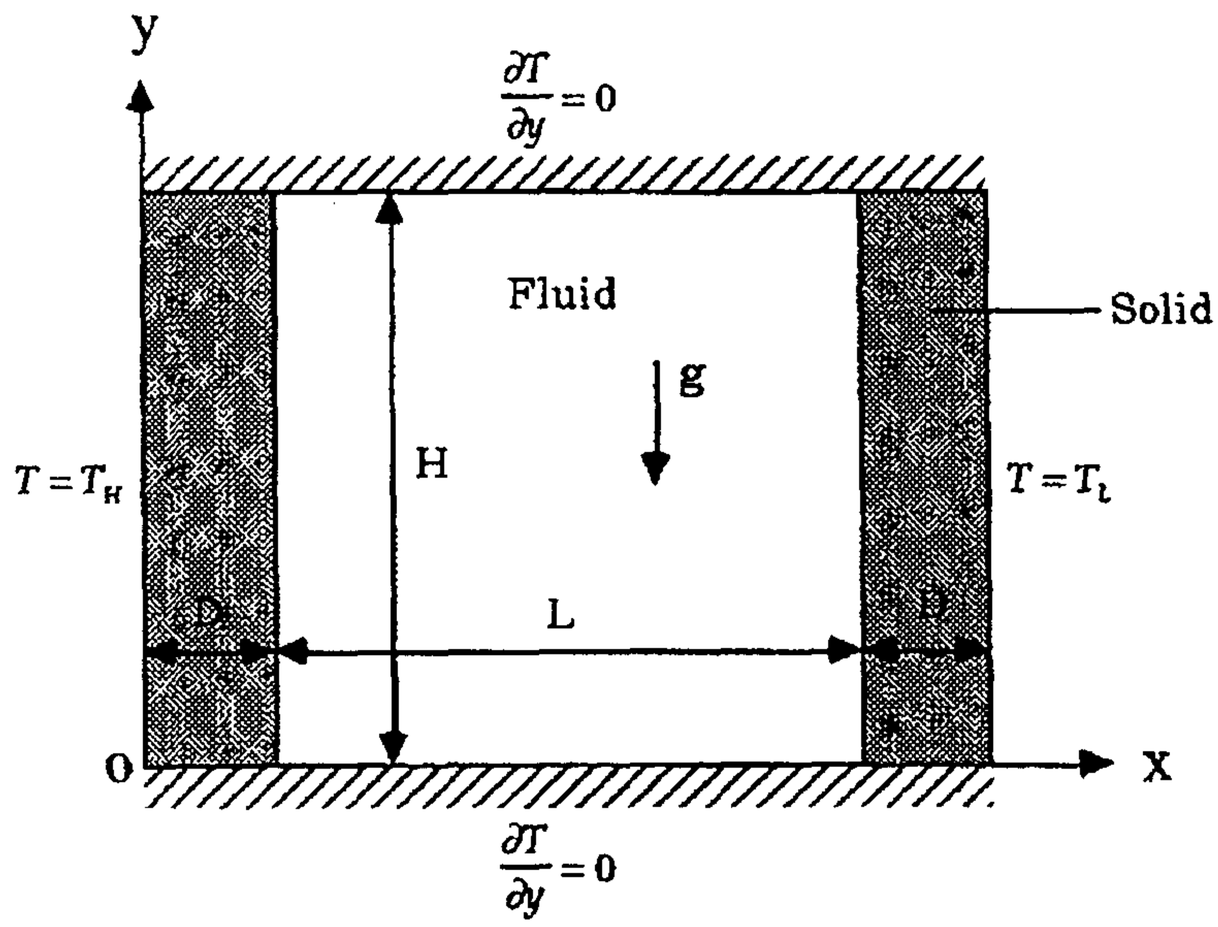

Figure 1. Schematic of flow configuration.

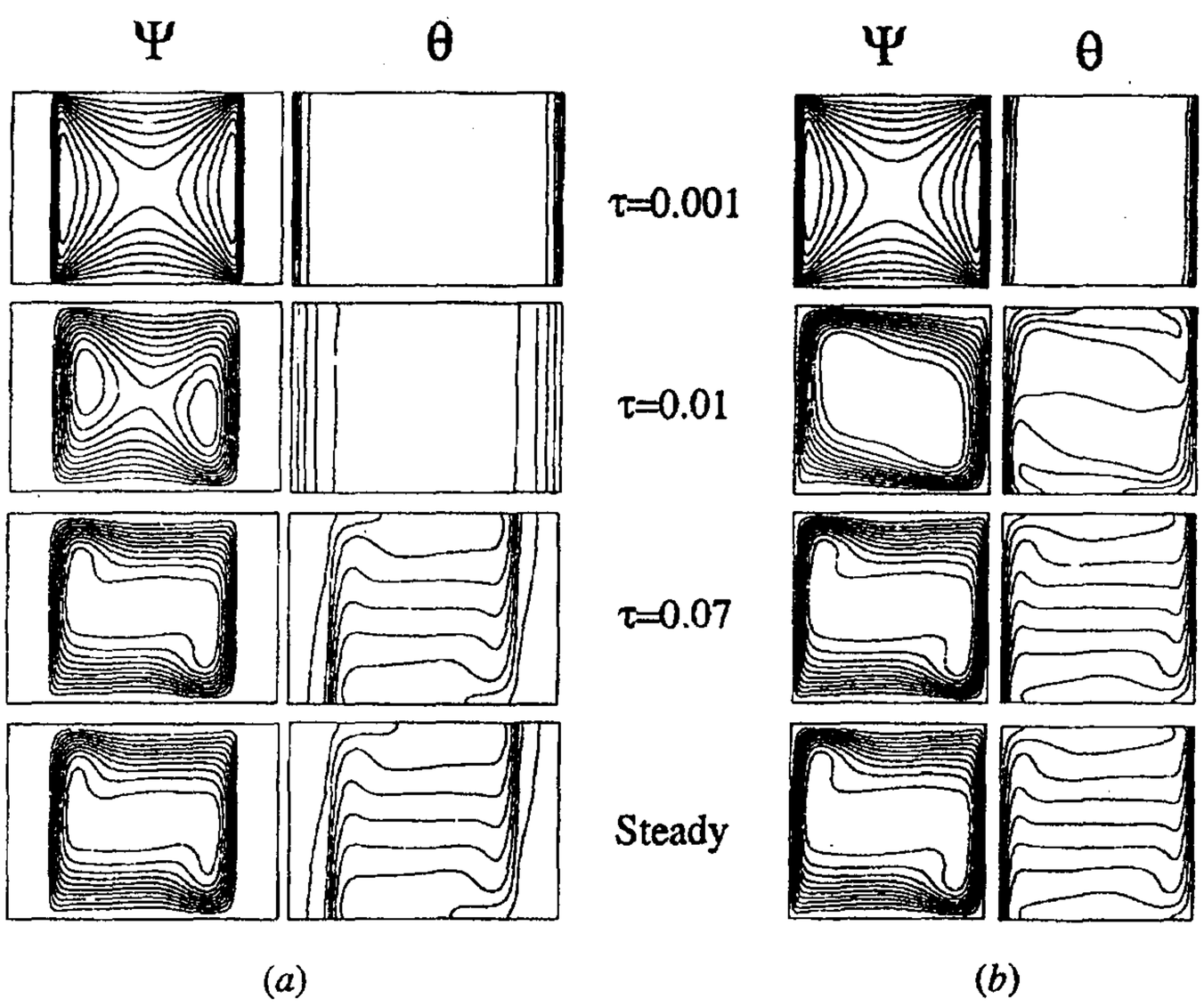

Figure 2. Evolution of flow Ψ and temperature θ fields: (*a*) standard case and (*b*) Patterson and Imberger model.

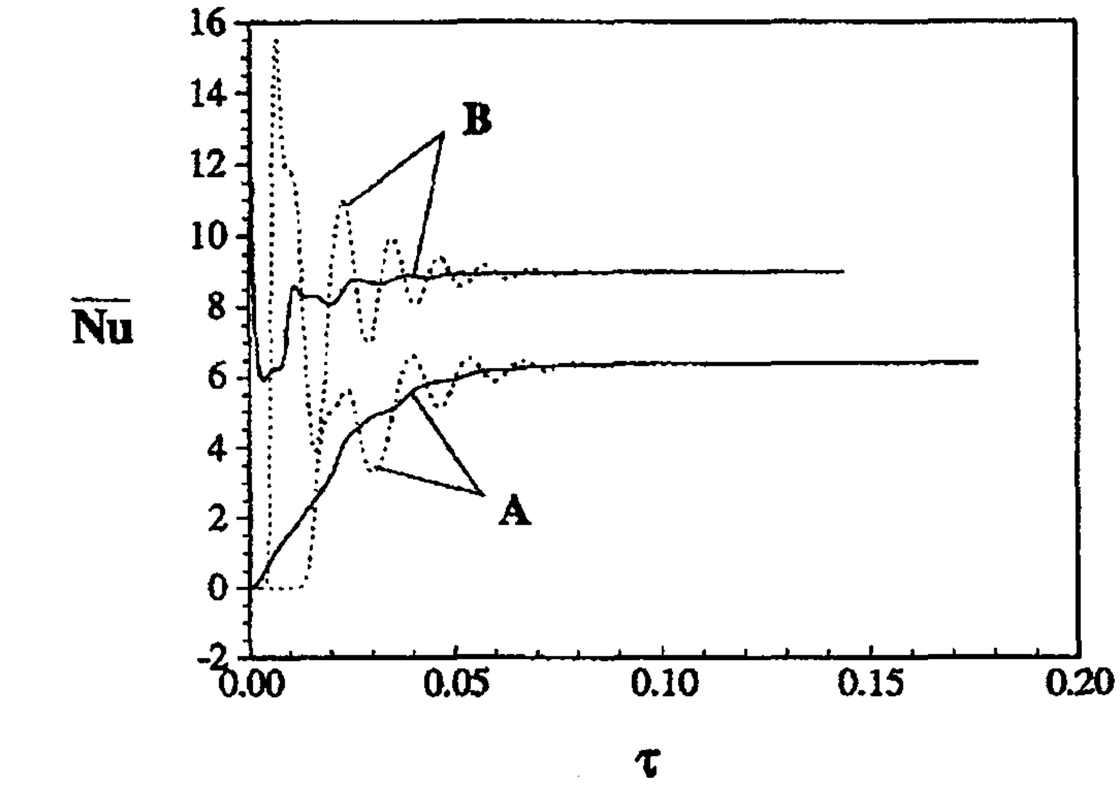

(*a*)

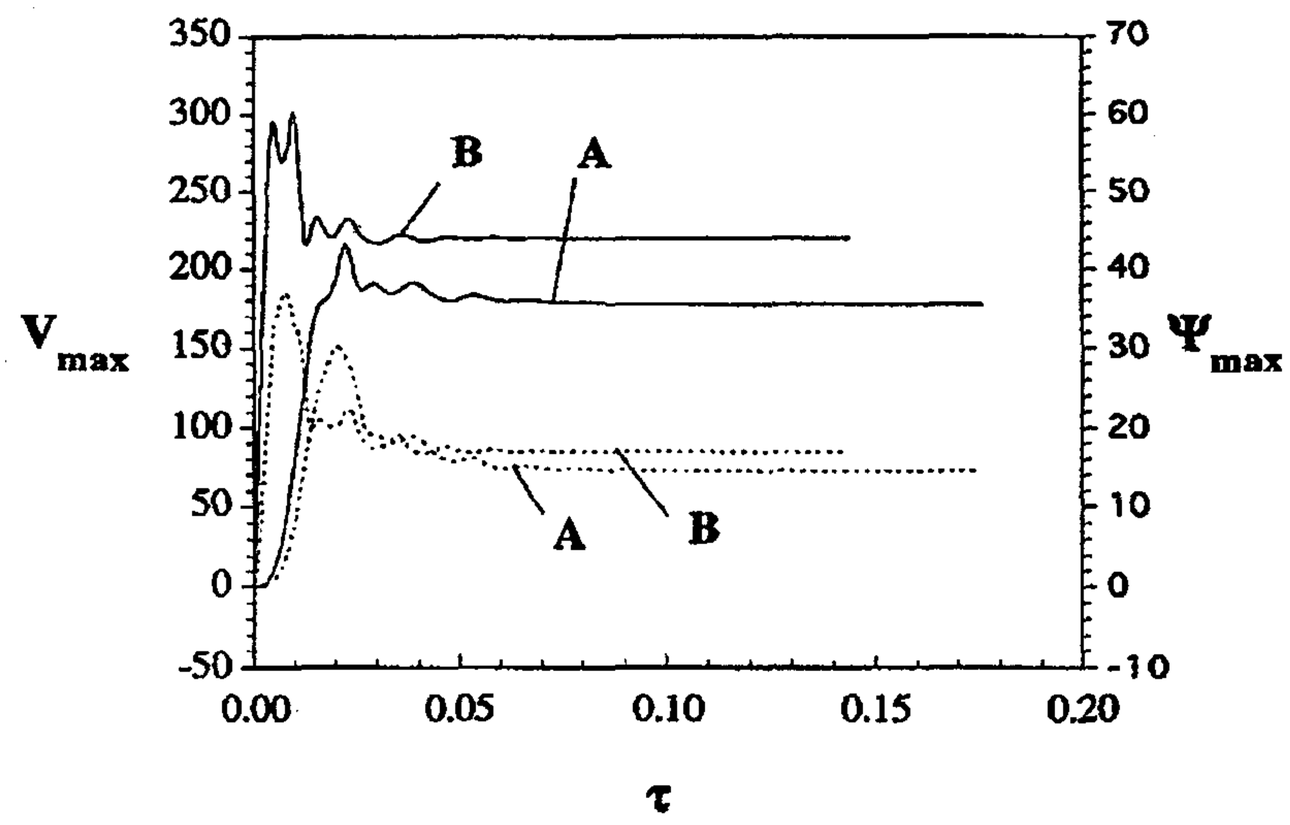

(*b*)

Figure 3. Transient behavior of $\overline{Nu}$, V_{max}, and Ψ_{max}. Curves labeled A denote the standard case of the present setup, and curves labeled B denote the Patterson and Imberger model: (*a*) solid curve, $\overline{Nu_h}$; dashed curve, $\overline{Nu_m}$; (*b*) solid curve, V_{max}; dashed curve, Ψ_{max}.

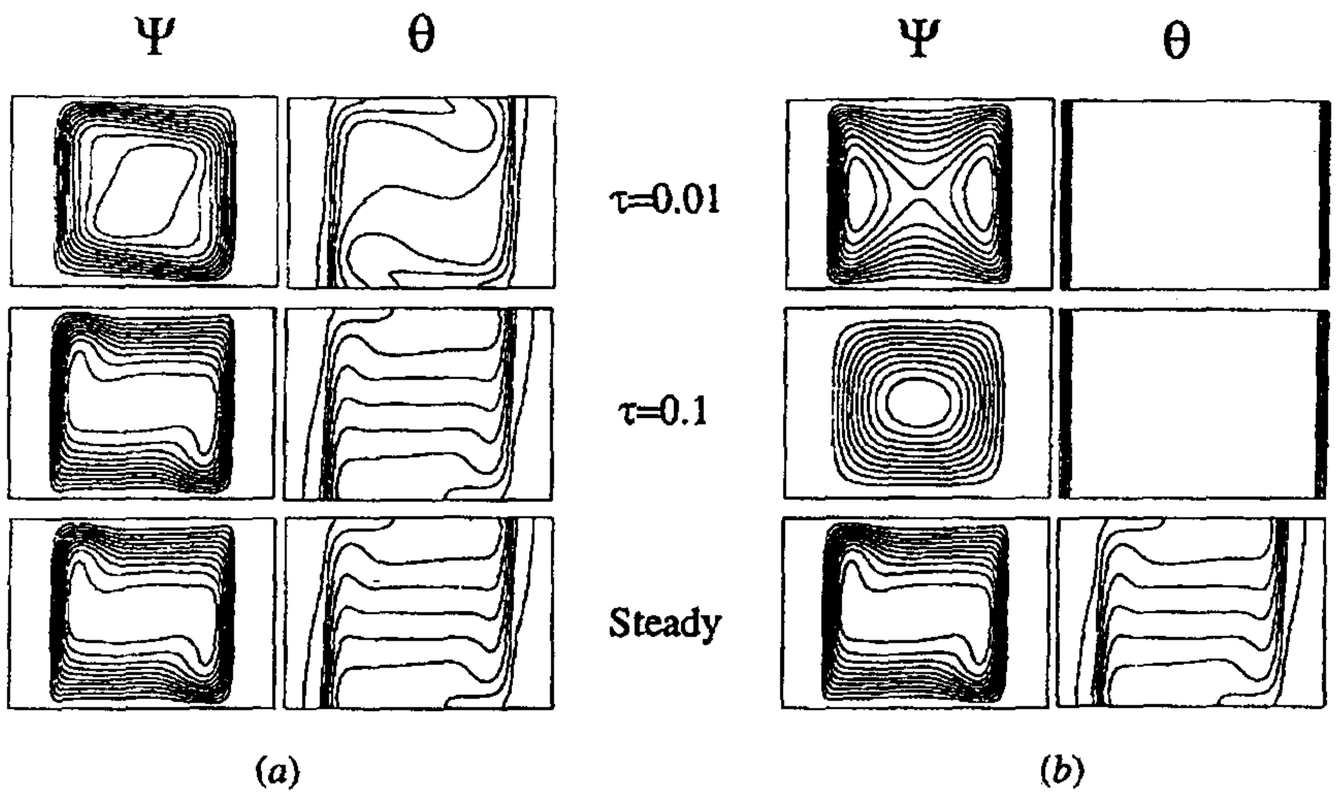

Figure 4. Evolution of Ψ and θ fields for (*a*) $(\rho C)^* = 0.1$ and (*b*) $(\rho C)^* = 1000$.

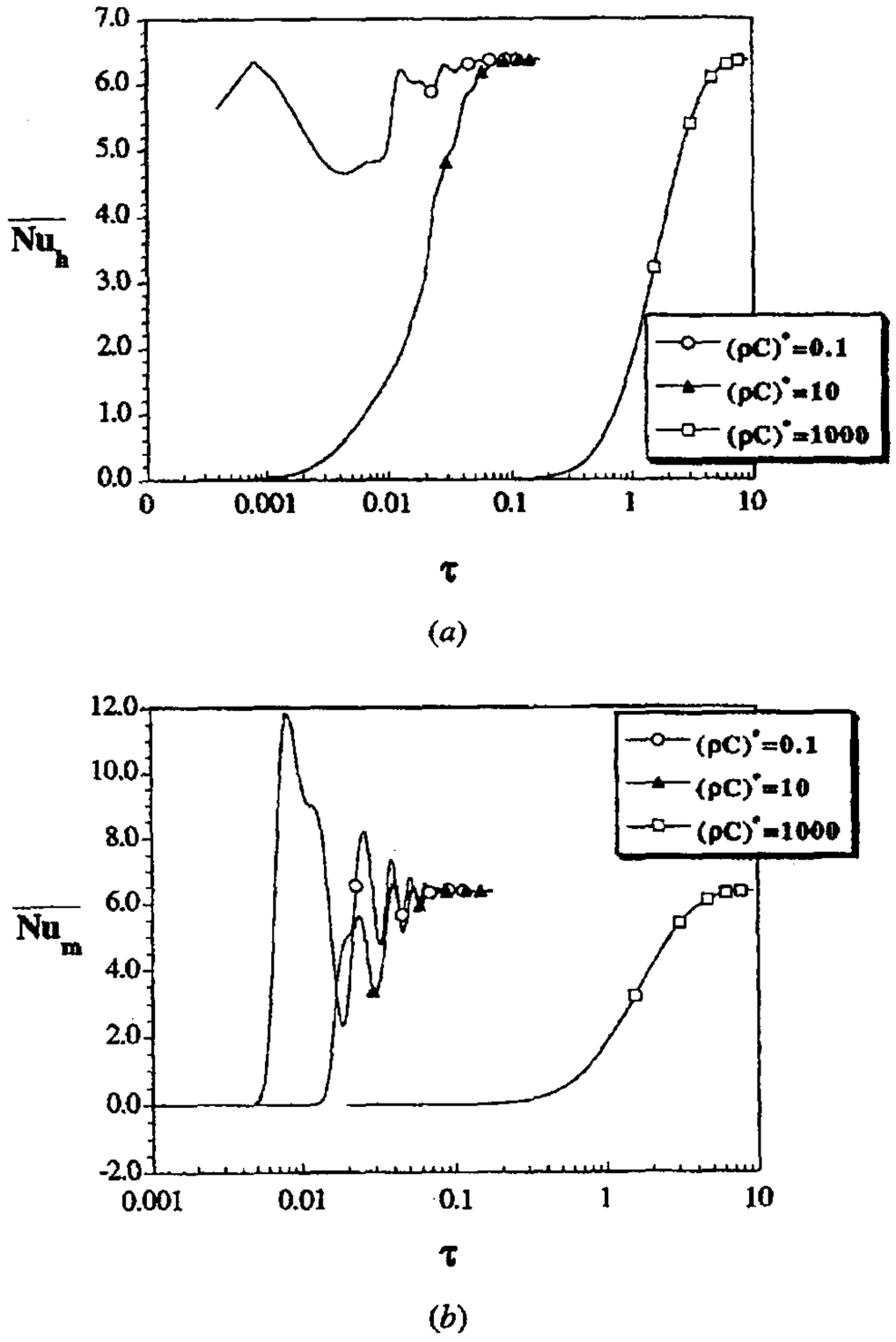

Figure 5. Effect of $(\rho C)^*$ on transient behavior of $\overline{Nu}$.

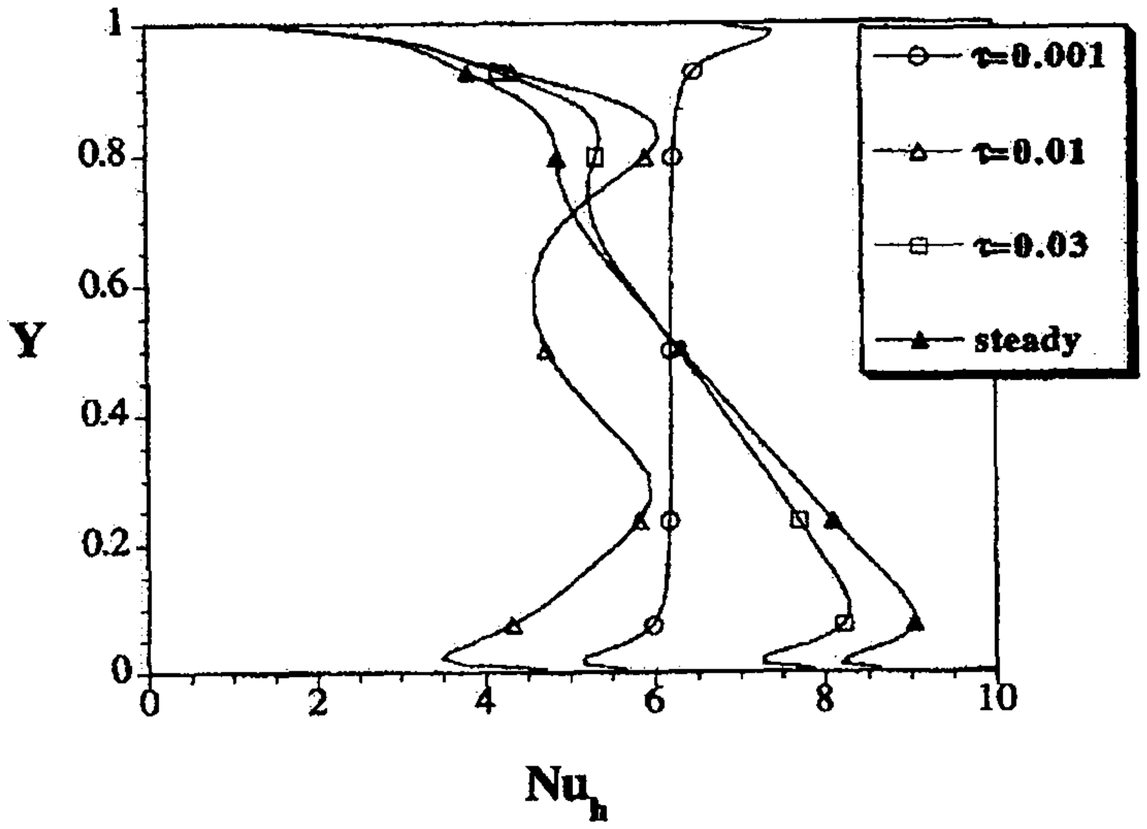

(*a*)

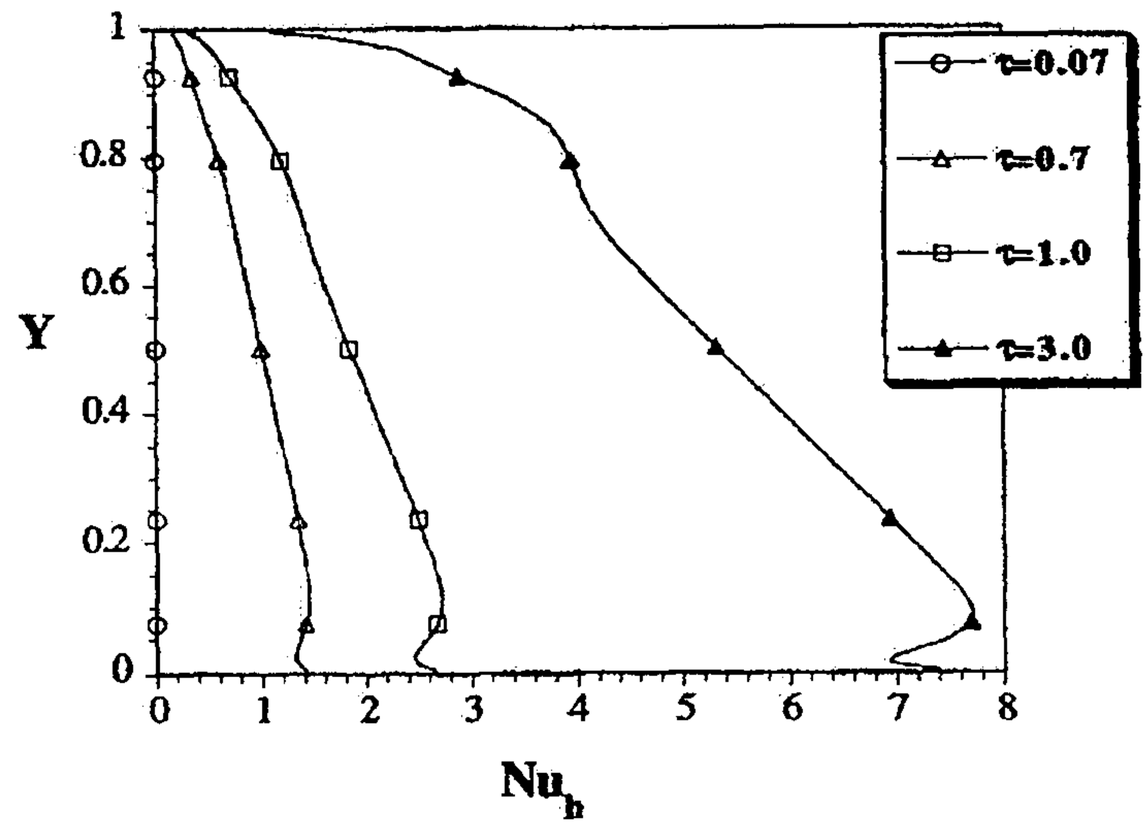

(*b*)

Figure 6. Profiles of $\overline{Nu_h}$ for (*a*) $(\rho C)^* = 0.1$ and (b) $(\rho C)^* = 1000$.

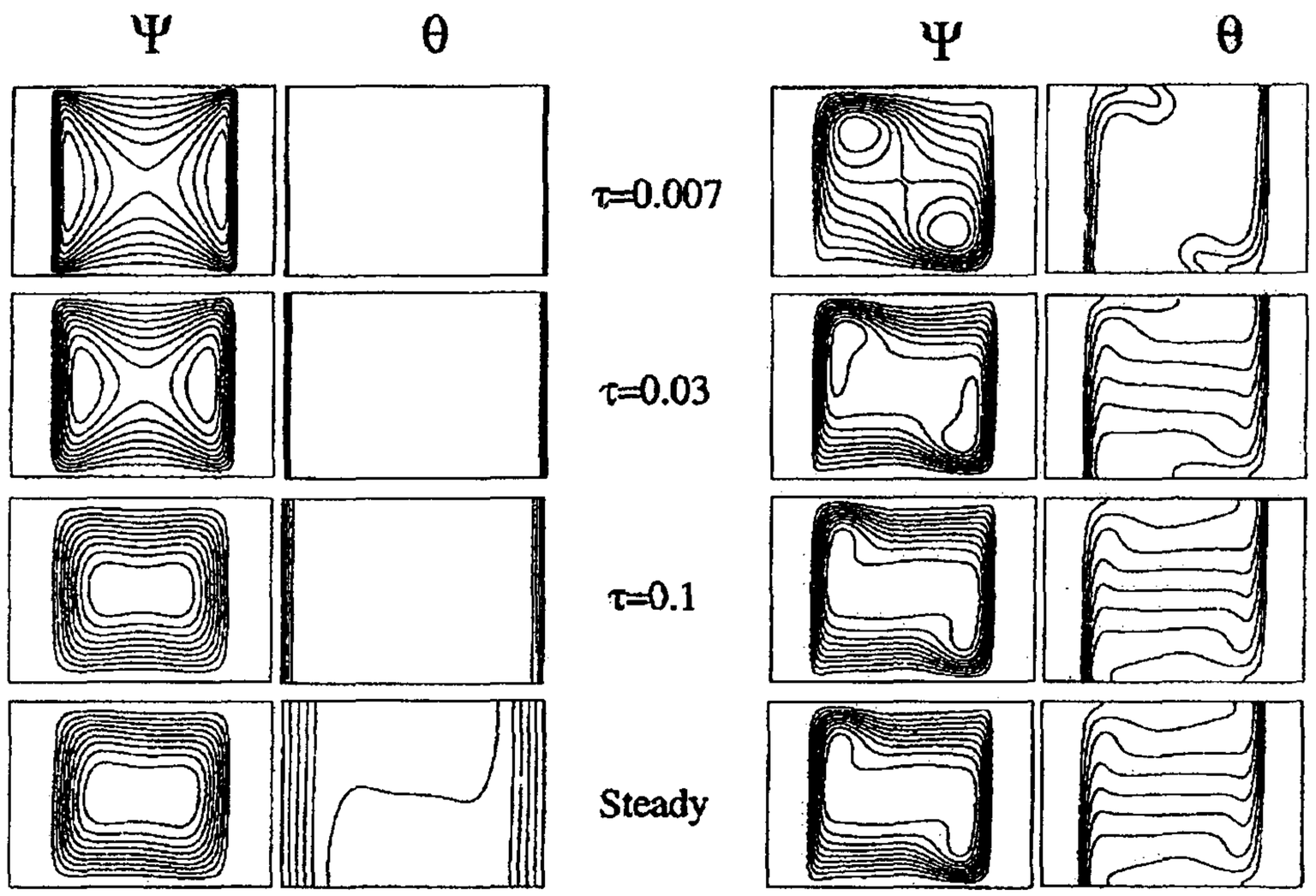

Figure 7. Evolution of Ψ and θ fields for (*a*) $k^* = 0.1$ and (*b*) k^*

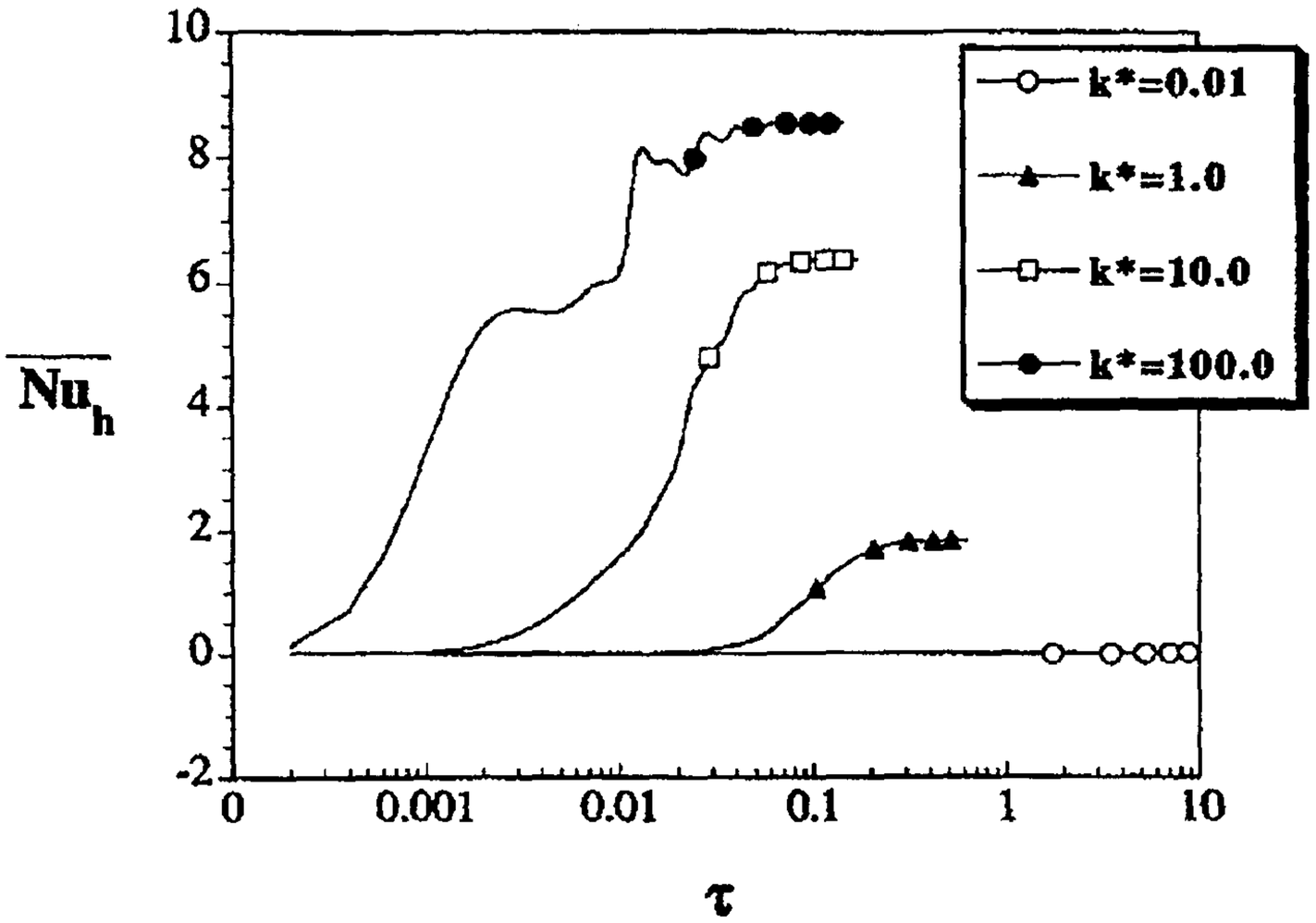

(*a*)

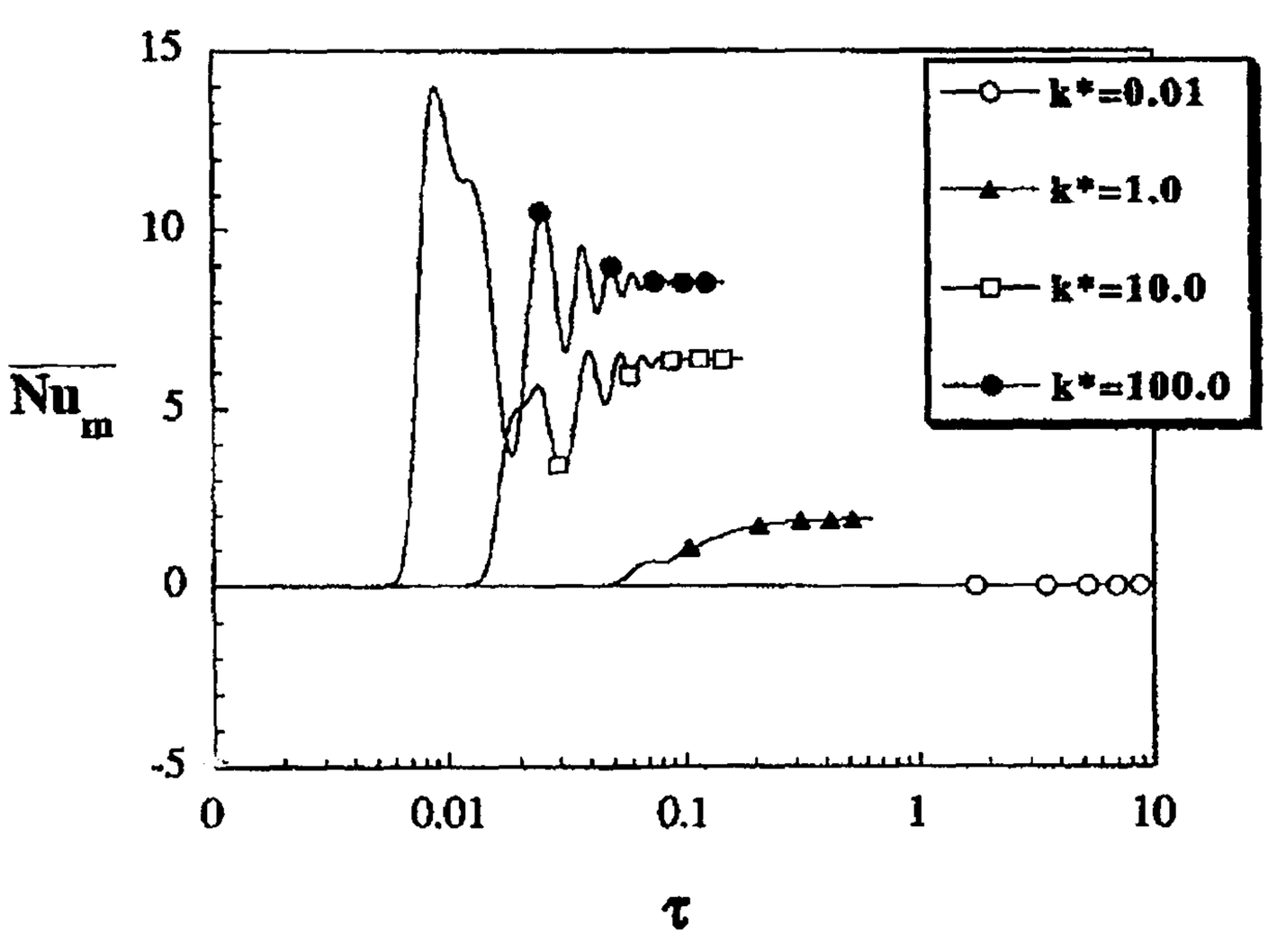

(*b*)

Figure 8. Effect of k^* on transient behavior of $\overline{Nu}$.

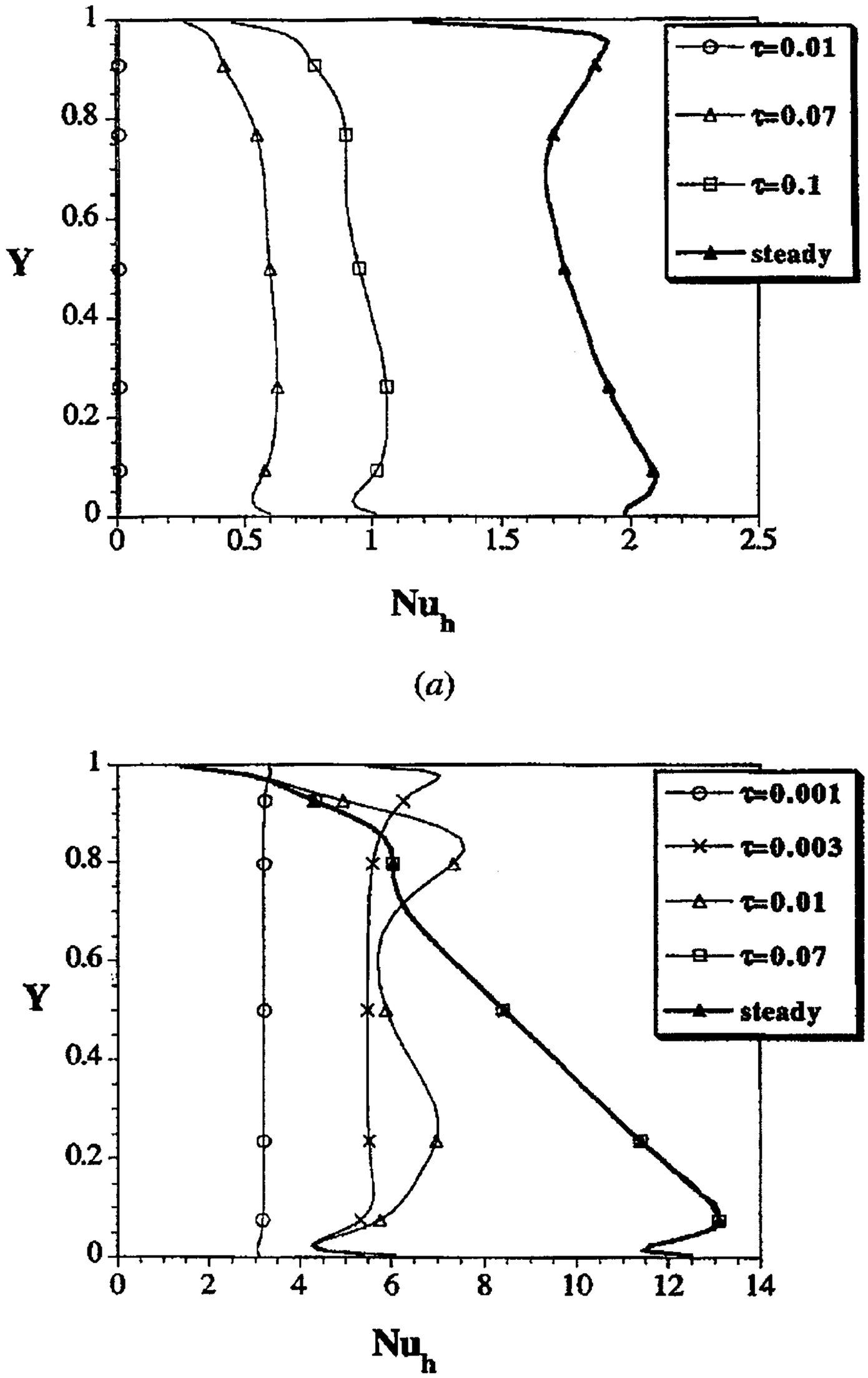

Figure 9. Profiles of Nu_h on (*a*) $k^* = 1.0$ and (*b*) $k^* = 100$.

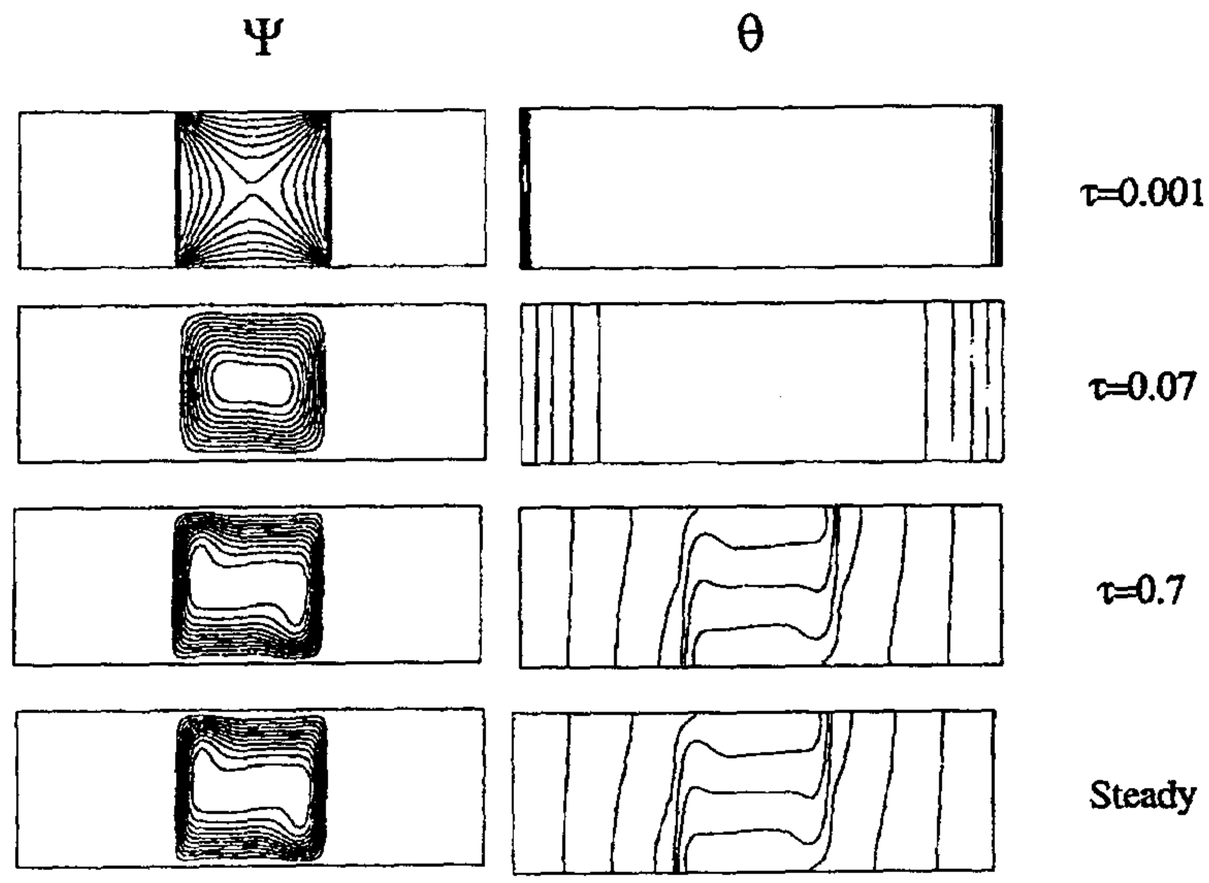

Figure 10. Evolution of Ψ and θ fields for $A_w = 1.0$.

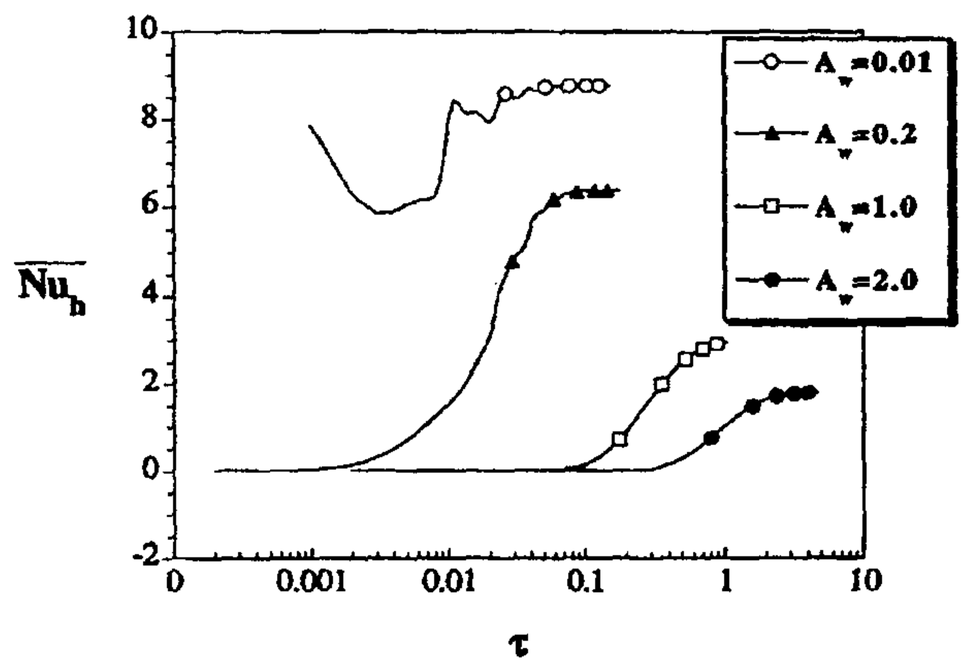

(*a*)

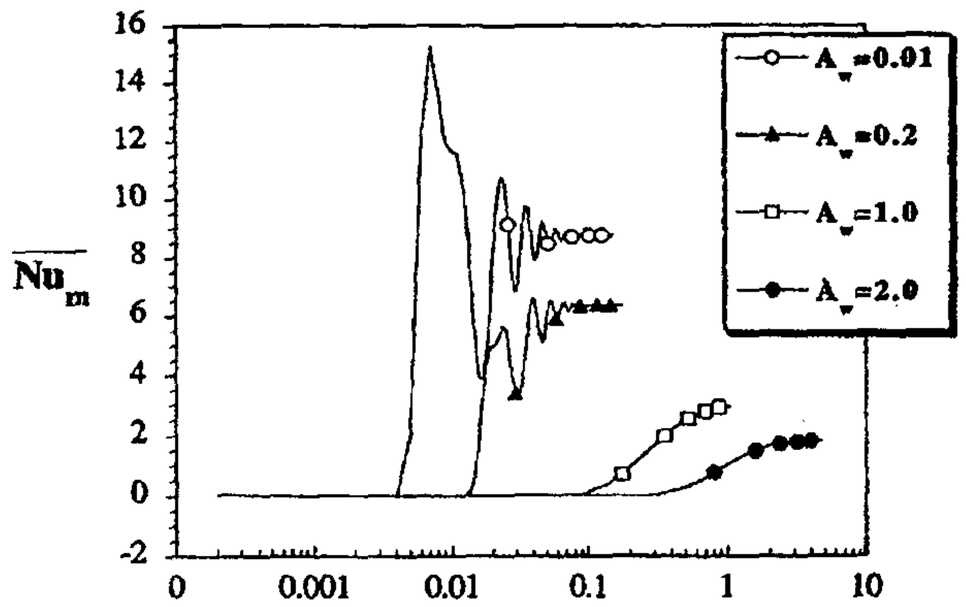

(*b*)

Figure 11. Effect of A_w on transient behavior of $\overline{Nu}$.

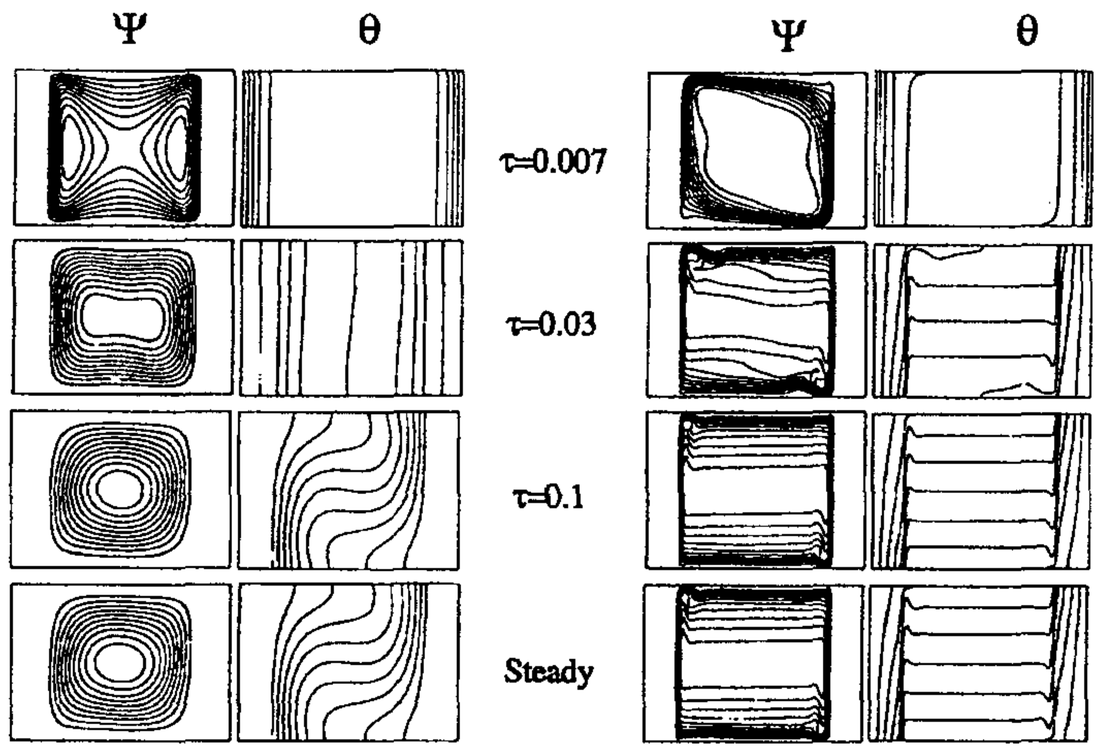

Figure 12. Evolution of Ψ and θ fields for (a) Ra = 10^4 and (b) Ra = 10^8.

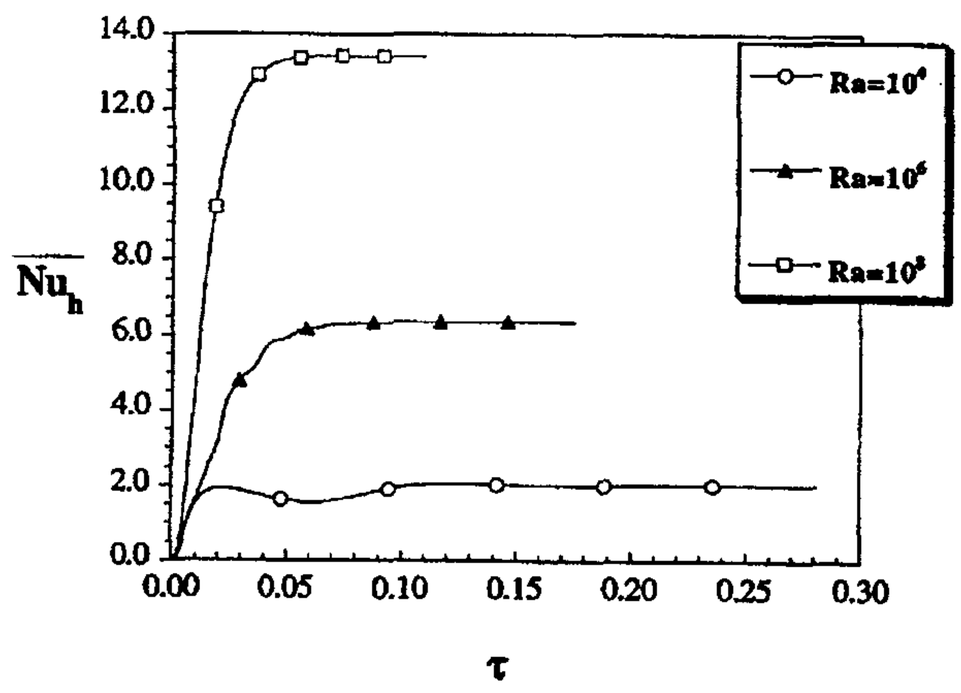

(a)

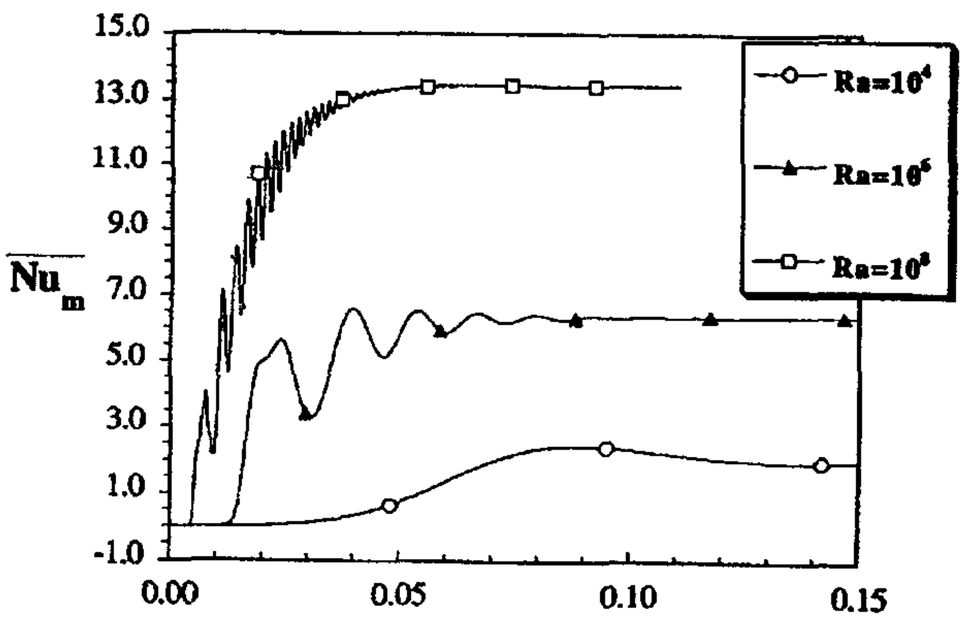

(b)

Figure 13. Effect of Ra on transient behavior of $\overline{Nu}$.

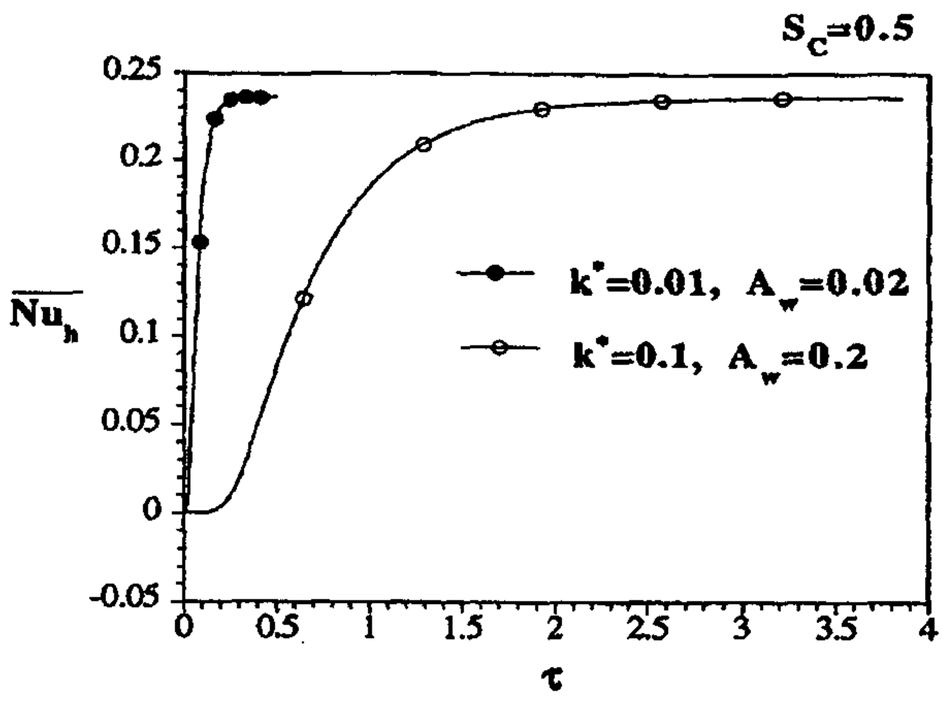

(*a*)

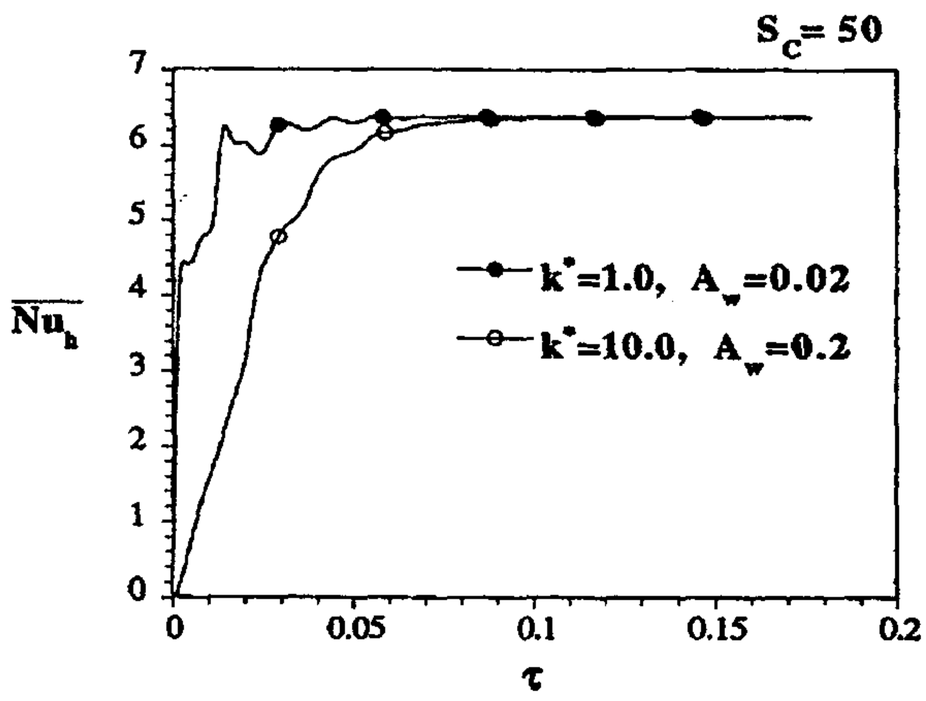

(*b*)

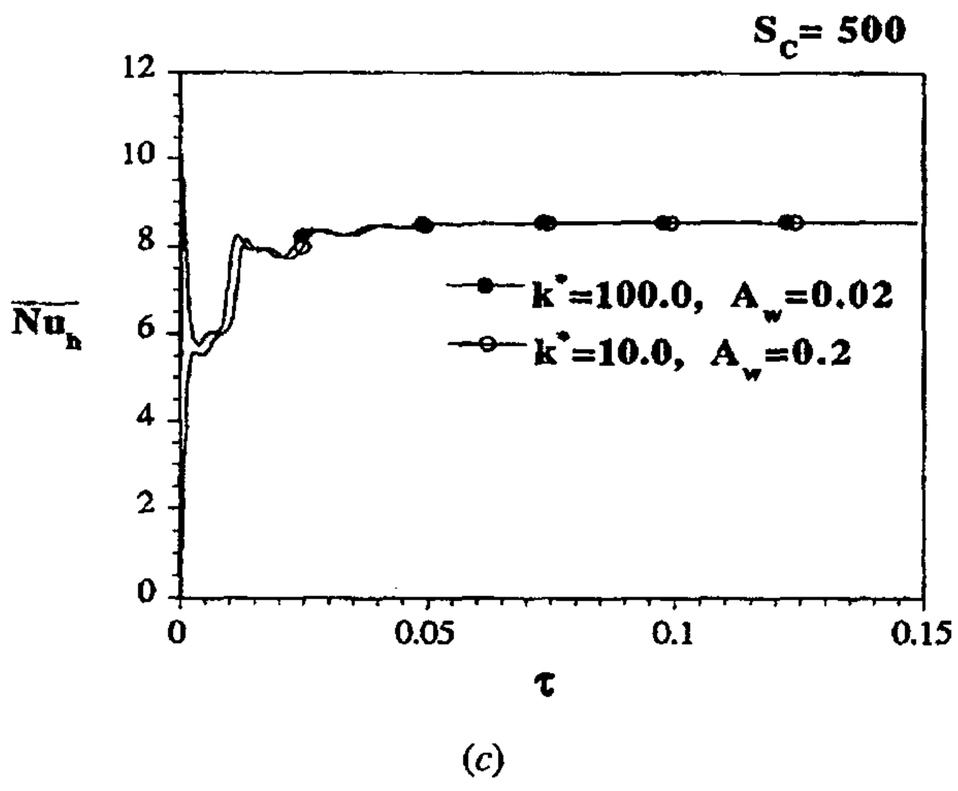

(*c*)

Figure 14. Influence of the combinations of k^* and A_w on transient behavior of $\overline{Nu}$ for (*a*) $S_c = 0.5$, (*b*) $S_c = 50.0$, and (*c*) $S_c = 500$.

제 10 장

Resonant Enhancement of Natural Convection Heat Transfer in a Square Enclosure

(사각용기내의 자연대류열전달의 공진적 증가)

요 약 문

비압축성유체로 채워진 사각밀폐용기 내에서의 자연대류 현상에 대한 수치적인 연구가 수행되었다. 용기의 한쪽 측벽은 차가운 온도로 시간에 따라 일정하게 유지되고 마주보는 가열벽면의 온도는 시간에 따라 정현파적으로 변하는 경계조건을 갖는다. 고정된 레이레이수(10^7)와 프란틀수(0.7)에서 비정상 Navier-Stokes 방정식을 수치적분에 의해 해를 얻었다. 본 연구에서 중요하게 다루워진 인자는 가열벽면에서의 온도의 가진진폭과 가진주파수로 이들의 변화에 대한 유동특성과 열전달특성 특히, 공진현상의 의존성을 깊이 있게 연구하였다. 큰 가진진폭은 시간평균열전달률의 상승을 초래한다는 결과를 얻었고, 또한 공진주파수에서 이 값이 최대가 됨을 밝혔다. 최종적으로 이러한 시간평균열전달률의 공진현상에 대한 메커니즘에 대한 연구가 진행되었다.

ABSTRACT

A numerical investigation is made of natural convection of an incompressible fluid in a square cavity having a constant-temperature cold sidewall and an opposite hot sidewall with sinusoidally-varying temperature. Comprehensive numerical solutions to the Navier-Stokes equations are acquired for a fixed Rayleigh number and a Prandtl number, $Ra=10^7$ and $Pr=0.7$. The amplitude and frequency of the hot wall temperature oscillation are varied. The time-mean heat transfer in the interior as well as the amplifications of fluctuations of instantaneous heat transfer are analyzed. The results disclose that a large-amplitude wall temperature oscillation causes an augmentation of the time-mean heat transfer rate. The maximum gain of the time-mean Nusselt number in the interior occurs at the resonance frequency, at which maximal fluctuations of the Nusselt number are found. The mechanism for resonant enhancement of the time-mean heat transfer is described.

NOMENCLATURE

$A(Nu)$	amplitude of fluctuation of $Nu(t)$, equation (11)
f	dimensional frequency of the hot wall temperature oscillation
g	gravitational acceleration
$G(Nu)$	gain of the time-mean Nusselt number, equation (10)
L	height of the square cavity
N	Brunt- Väisälä frequency, $(\alpha g \Delta T/L)^{1/2}$
$Nu(t)$	instantaneous Nusselt number at a vertical plane, equation (9)
$\overline{Nu}$	cycle-averaged value of $Nu(t)$, equations (8) and (9)
$p,\ p^*$	non-dimensional and dimensional pressures, $p=\dfrac{(p^*+\rho g z^*)L^3}{\rho \nu^2 RaPr}$
Pr	Prandtl number, ν/κ
Ra	Rayleigh number, $Ra=\dfrac{\alpha g \Delta T L^3}{\nu \kappa}$
S	stratification parameter, $S^2=\dfrac{\partial \theta}{\partial y}$
T	dimensional temperature

$t,\ t^*$	non-dimensional and dimensional times, $t = t^*(RaPr)^{1/2}\frac{\kappa}{L^2}$
$u,\ v$	non-dimensional velocities in x and y directions, $(u, v) = (u^*, v^*)(RaPr)^{-1/2}\frac{L}{\kappa}$
$u^*,\ v^*$	velocities in x and y directions
$x,\ y$	non-dimensional horizontal and vertical coordinates, $(x, y) = (x^*, y^*)/L$
$x^*,\ y^*$	horizontal and vertical coordinates

Greek Symbols

α	volumetric expansion coefficient
Δt	time increment for numerical calculations
ΔT	mean temperature difference between the hot and cold sidewalls, $\overline{T_h} - T_c$
$\Delta T_h'$	amplitude of the hot wall temperature oscillation
Δt	time step
Δx	grid spacing
ε	non-dimensional amplitude of the hot wall temperature oscillation, $\Delta T_h'/\Delta T$
κ	thermal diffusivity
ν	kinematic viscosity
θ	non-dimensional temperature, $(T - T_c)/(\overline{T_h} - T_c)$
τ	non-dimensional cycle time, $\tau = 2\pi t/\omega$
ω	non-dimensional frequency, f/N
ψ	non-dimensional stream function, $u = \frac{\partial \psi}{\partial y},\ v = -\frac{\partial \psi}{\partial x}$

Subscripts

c	cold sidewall
h	hot sidewall
i	internal gravity wave oscillation
m	frequency value at which the maximum $G(Nu)$ occurs
r	resonance frequency (at which the maximum $A(Nu)$ occurs)

s	steady state solution for the corresponding case with $\varepsilon=0.0$

Superscript

*	dimensional quantity
$(\bar{})$	cycle-averaged property, equation (9)

1. INTRODUCTION

Natural convection in an enclosure with time-periodic boundary conditions has received much attention in recent years [1-15]. As reviewed by Hyun [16], Fusegi and Hyun [17], and Antohe and Lage [3], the increasing interest is attributable to the relevance of such transient processes in many technological applications. Typical examples are the solar heating varying on a daily basis, and the periodic energizing of electronic devices by the on-and-off heating and/or cooling modes, to name a few.

The main question is how the periodicity of boundary conditions affects the time-dependent flow and associated heat transfer of an enclosed fluid. A practical advantage is that the overall time-averaged heat transfer in the system may be augmented in the case of time-varying boundary conditions as compared with the heat transfer obtained with time-invariant boundary conditions [5-8, 13-15]. Another physically-important aspect of these problems is the possibility of resonance inherent to the system under question [1-7, 12]. Resonance is a phenomenon associated with the eigenmodes of a system, which is essentially independent of the kind of external forcing imposed. If the system is exposed to an external forcing with the correct natural frequency, resonance takes place in which the eigenmodes are excited and amplified.

The numerical work of Lage and Bejan [1] clearly established the presence of resonance in natural convection at high Rayleigh numbers. At one sidewall, a constant temperature was maintained. On the opposite sidewall, a heat flux, which fluctuated in a square-wave fashion, was prescribed. In their problem formulation, resonance was identified by the maximal amplification of fluctuations of the instantaneous Nusselt number at the centerline of the cavity. It was demonstrated numerically that resonance was seen at certain moderate values of frequency. In subsequent papers, Antohe and Lage [3-4] numerically examined the effects of the Prandtl number and the amplitude of the time-varying heating on the convective transport in a cavity.

Parallel efforts were also made on the experimental front. Antohe and Lage [5] conducted precision-controlled experiments for the problem setup of Lage and Bejan [1]. Attention was focused on the influence of periodic heating on the time-mean heat transfer. For a high Rayleigh number based on the average heat flux, the oscillatory heating led to about 20% augmentation of the time-mean heat transfer coefficient in comparison to that obtained by steady heating with the same time-averaged heat flux. The maximum gain of the time-mean heat transfer was seen at a moderate frequency,

which was interpreted to be associated with resonance.

Iwatsu et al. [6] investigated convective motions of an incompressible fluid in a cavity with an externally-imposed vertical temperature difference between the top hot endwall and the bottom cold wall. The aim was to explore the enhancement of vertical heat transfer by applying a mechanical oscillation to the top lid. Obviously, the heat transfer in this stably-stratified fluid system would be purely conductive if the top lid is stationary. Numerical results revealed the existence of resonance at particular frequencies of the top lid oscillation. At resonance frequencies, a substantial augmentation of heat transfer and flow fluctuations was demonstrated.

A canonical configuration for confined natural convection is a sidewall-heated cavity [18-20], in which the horizontal heating is provided by a temperature difference applied between two perfectly-conducting vertical sidewalls. Fu and Shieh [7-8] examined thermal convection which was simultaneously driven by gravity and by the vertical vibration of the cavity. The results disclosed that there exists a resonant convection regime in which the flow and heat transfer interact with the vibration of the gravitational force [7]. For a relatively small Rayleigh number, $Ra=10^4$, the imposed mechanical vibration produced a substantial augmentation of the overall heat transfer rate at the resonance frequency [7-8].

The studies of Antohe and Lage [5], Iwatsu et al. [6] and Fu and Shieh [7] are strongly suggestive of potentially useful applications. They imply that an external oscillation with properly-chosen frequencies will bring forth the resonance of natural convection, which results in an enhancement of the time-averaged heat transfer rate.

A different type of time-varying conditions has also been taken into account. Yang et al. [9] considered a sinusoidally-varying temperature condition on the hot sidewall of a tall rectangular cavity (height:width=3:1). The forcing frequency was fixed and the range of the Rayleigh number was up to 10^6. The effects of frequency and amplitude of sidewall temperature oscillation in a square cavity were examined by Kazmierczak and Chinoda [10], for a fixed Rayleigh number $1.4x10^5$. However, these works did not detect resonance because of the limited ranges of principal parameters covered; in particular, the Rayleigh number was too low. Xia et al. [11] examined the same problem for high Rayleigh numbers. The impacts of the wall temperature oscillation on the flow stability were elucidated, but the frequency was set at a fixed value. The possibility of resonance was not a key issue in these investigations.

Recently, Kwak and Hyun (hereinafter referred to as KH, [12]) performed comprehensive numerical computations for the same problem formulation as adopted by Kazmierczak and Chinoda

[10]. The numerical solutions encompassed a broad range of frequency, and the results clearly illustrated the presence of resonance. The fluctuations of the Nusselt number were substantially amplified by the periodically-varying temperature condition with the proper resonance frequency. The physical mechanism of resonance was delineated by examining the evolutions of detailed flow and temperature fields over a cycle. Quantitative comparisons were conducted for the resonance frequency between the numerical results and the available theoretical predictions. The results show that the flow in this configuration resonates to the internal gravity-wave oscillations.

It is to be noted that, in the studies of KH [12], the amplitude of the temperature oscillation imposed at the sidewall was set to be small. They used the nondimensional amplitude $\varepsilon = 0.1$, which implies that the amplitude of temperature oscillation at the boundary wall was 10% of the mean temperature difference between the two sidewalls. Because of this constraint, the cycle-averaged flow and temperature fields do not deviate much from those of the corresponding non-oscillating case with the same time-mean value. In the present study, the basic analysis of KH [12] is extended to the cases when the amplitude of the temperature oscillation at the boundary wall is finite. The aim is to explore the changes in time-averaged heat transfer rate in the cavity especially when the external thermal forcing is applied at the proper resonance frequency. In order to focus on the effects of amplitude of the external thermal forcing, numerical solutions are obtained for values of ε up to ε=1.0 with *Ra* and *Pr* fixed. A large value of *Ra*, $Ra=10^7$, is chosen. Guided by the earlier studies [5,12], *Pr* is selected to be $O(1)$, which has been known to give rise to pronounced results of resonance. It is shown that, as observed in the prior investigations [5-8], the time-averaged heat transfer in the present configuration is altered appreciably by an application of large-amplitude oscillatory thermal forcings at the boundary.

2. THE NUMERICAL MODEL

Consider a square cavity filled with an incompressible Boussinesq fluid having constant physical properties. The top and bottom horizontal walls are thermally insulated. The left sidewall is kept at a constant temperature T_c. The temperature at the right sidewall, T_h, varies with time as $T_h = \overline{T_h} + \Delta T_h' \sin(ft^*)$, where $\Delta T_h'$ and f are respectively the amplitude and frequency of the hot wall temperature oscillation. The mean temperature difference between the two sidewalls, $\Delta T = \overline{T_h} - T_c$, is positive and constant. The flow configuration is schematically described in

Fig. 1. The time-varying thermal boundary condition at the hot vertical wall is depicted in Fig. 2.

The governing equations are the two-dimensional Navier-Stokes equations for a Boussinesq fluid. These, in nondimensional form, are expressed as

$$\frac{\partial u}{\partial t}+\frac{\partial}{\partial x}(u^2)+\frac{\partial}{\partial y}(uv)=-\frac{\partial p}{\partial x}+\left(\frac{Pr}{Ra}\right)^{1/2}\left(\frac{\partial^2 u}{\partial x^2}+\frac{\partial^2 u}{\partial y^2}\right), \tag{1}$$

$$\frac{\partial v}{\partial t}+\frac{\partial}{\partial x}(uv)+\frac{\partial}{\partial y}(v^2)=-\frac{\partial p}{\partial y}+\theta+\left(\frac{Pr}{Ra}\right)^{1/2}\left(\frac{\partial^2 v}{\partial x^2}+\frac{\partial^2 v}{\partial y^2}\right), \tag{2}$$

$$\frac{\partial \theta}{\partial t}+\frac{\partial}{\partial x}(u\theta)+\frac{\partial}{\partial y}(v\theta)=\left(\frac{1}{PrRa}\right)^{1/2}\left(\frac{\partial^2 \theta}{\partial x^2}+\frac{\partial^2 \theta}{\partial y^2}\right), \tag{3}$$

$$\frac{\partial u}{\partial x}+\frac{\partial v}{\partial y}=0, \tag{4}$$

In the above, non-dimensionalization was effectuated by using L, NL and, $1/N$ as reference scales for length, velocity, time, respectively. Here, N is the Brunt- Väisälä frequency, i.e., $N^2\equiv\alpha g\Delta T/L$. The temperature was non-dimensionalized as $\theta=(T-T_c)/\Delta T$. The relevant dimensionless parameters are the Rayleigh number, $Ra=\alpha g\Delta TL^3/\nu x$; the Prandtl number, $Pr=\nu/x$; the non-dimensional amplitude of thermal forcing, $\varepsilon=\Delta T_h'/\Delta T$; and the non-dimensional frequency, $\omega=f/N$.

The boundary conditions are

$$u=v=\frac{\partial \theta}{\partial y}=0, \qquad \text{at } y=0,1; \tag{5}$$

$$u=v=\theta=0, \qquad \text{at } x=0; \tag{6}$$

$$u=v=0,\ \ \theta=1+\varepsilon\sin(\omega t), \qquad \text{at } x=1. \tag{7}$$

A finite-volume procedure based on the SIMPLER algorithm [21] was employed to solve the system of equations (1)-(4). The numerical accuracy of the present method is $O(\Delta t,\Delta x^2)$, where Δt and Δx are the time step and grid spacing. The present numerical model was verified by reproducing the results of Lage and Bejan [1] and other benchmark configurations. The numerical methodologies were described in detail in KH [12].

For all the computations, a grid with (82×62) mesh points in the $(x\times y)$ domain was used. Grid stretching was performed to resolve thin boundary layers on the solid walls. A small time step, $\Delta t=2\pi/(1024\omega)$, i.e., 1024 time steps per cycle, was used. Extensive convergence

tests were carried out, and the robustness of the present code has been established [12].

In actual computations, a steady state solution was acquired for a corresponding non-oscillating case ($\varepsilon = 0$), which is referred to as the basic state. This solution was used as the initial condition in simulating the cases of time-varying temperature conditions ($\varepsilon \neq 0$). This approach was adopted by previous works [1-4,12], which resulted in saving a considerable amount of computation time.

Numerical computations were conducted for ε=0.1, 0.5, and 1.0 with fixed values of *Ra* and *Pr*, i.e., $Ra=10^7$ and *Pr*=0.7. The frequency of the wall temperature oscillation encompassed the range $0.1 \leq \omega \leq 1.5$. Guided by the earlier study [12], attention was focused to the frequency band near the expected resonance frequency.

Here, it is advantageous to introduce several operators. The mean value $\overline{\phi}$ of an oscillating property $\phi(t)$ over a cycle can be written as

$$\overline{\phi} = \frac{\omega}{2\pi} \int_{t_o}^{t_o + 2\pi/\omega} \phi(t)\ dt\ . \tag{8}$$

The instantaneous Nusselt number, $Nu(t)$, averaged over the vertical plane at $x=a$, is obtained as

$$Nu(t)_{x=a} = \int_0^1 \left[\frac{\partial \theta}{\partial x} - u\theta (RaPr)^{1/2} \right]_{x=a} dy\ . \tag{9}$$

The positive sign of $Nu(t)_{x=a}$ implies that the heat is transported from the right part to the left part relative to the vertical plane $x=a$. In order to assess the impact of the wall temperature oscillation on the heat transfer characteristics, the following definitions are made

$$G(Nu) = \frac{\overline{Nu} - Nu_s}{Nu_s}, \tag{10}$$

$$A(Nu) = \frac{Max\{Nu(t)\} - Min\{Nu(t)\}}{Nu_s}, \text{ for } t_o \leq t \leq t_o + \frac{2\pi}{\omega}. \tag{11}$$

It is recalled that Nu_s denotes the corresponding value of *Nu* in the case of non-oscillating wall temperature ($\varepsilon = 0$), which is $Nu_s [\equiv Nu(t=0)]$ in the present numerical procedure. $G(Nu)$ and $A(Nu)$ represent the gain and the fluctuating amplitude of heat transfer relative to the corresponding non-oscillating value, respectively. The values of $G(Nu)$ and $A(Nu)$ are estimated by using solution during a cycle after the approximate steady periodic state has been reached.

In the present study, that the values of $Nu(t)$ are estimated at the hot wall, at the cold wall, and at the vertical plane (x=0.5). For the basic-state solution ($\varepsilon = 0$), heat balance (difference between the hot and cold wall Nusselt numbers) is satisfied within $O(10^{-6})$. In the case of oscillating

wall temperature, the values of $\overline{Nu}$ estimated at the above three different positions show agreement within 1% relative error.

3. RESULTS AND DISCUSSION

Fig. 3 depicts the temporal behavior of $Nu(t)$ at the vertical mid-plane x=0.5. For all the cases, $Nu(t)$ settles down to a quasi-steady periodic form after several cycles. Fig. 3(a) shows the results for ε=0.1. The fluctuation of $Nu(t)$ at a moderate frequency ($\omega = 0.67$) is far more pronounced in comparison with the cases of small ($\omega = 0.4$) and large ($\omega = 1.0$) frequencies. This points to the presence of resonance. Following the previous arguments of Lage and Bejan [1] and KH [12], the resonance can be identified by maximal amplification of fluctuation of $Nu(t)_{x=0.5}$ at a certain specific frequency (referred to as the resonance frequency ω_r). The results for larger amplitudes ε=0.5, 1.0 are displayed in Figs. 3(b) and 3(c). The qualitative behavior of oscillation of $Nu(t)$ is generally similar to that for ε=0.1. However, quantitative differences are ostensible; the fluctuating amplitude of $Nu(t)$ becomes substantially larger as ε increases from 0.1 to 1.0.

The effects of ε and ω on the fluctuation of $Nu(t)$ at x=0.5 are scrutinized in Fig. 4, in which existence of resonance is discernible. For the three values of ε, the curves of the normalized amplitude $A(Nu)/\varepsilon$ exhibit the sharp resonance peaks. The values of the resonance frequency, ω_r at which the maximum $A(Nu)$ occurs, are listed in Table 1.

An interesting finding in Fig. 4 is that $A(Nu)$ displays a similar parametric dependence on ω. It is noticeable that the $A(Nu)/\varepsilon$ vs. ω curves for the three values of ε exhibit a very similar trend. The results for ε=0.1 and ε=0.5 disclose that the influence of ε on $A(Nu)/\varepsilon$ is found to be insignificant. Put it alternatively, $A(Nu)$ is approximately proportional to ε when ε is small. This is in line with the theoretical prediction of Antohe and Lage [3] that the resonance amplitude of the Nusselt number is a nearly-linear function of the amplitude of the applied heat flux. Small differences are seen when ε is large.

The present results are consistent with the general discussion on the issue of the superposing oscillation on a steady basic flow. In a system without damping, any periodic excitation with the correct natural frequencies of the system would give rise to an oscillation with infinite amplitude. In the presence of damping, the amplification characteristics are controlled mainly by the damping

mechanism of the system. In the present calculations, *Ra* and *Pr* are fixed, i.e, the viscous and diffusive dampings are constrained. If ε is sufficiently small so that the effect of the superimposed oscillations is linear, the resulting amplification is linearly proportional to ε, without affecting f_r. However, when ε becomes large, nonlinear behavior is manifest and it distorts both $A(Nu)$ and f_r. All these behaviors are shown in the present results.

Next, the effect of ε on the time-mean heat transfer rate is described. A careful inspection of Fig. 3(c) discloses that the temporal behavior of $Nu(t)$ at $\omega=0.77$ is almost sinusoidal but not symmetric about the value of Nu_s. This is indicative of the fact that $\overline{Nu}$ deviates from the corresponding value of the non-oscillating case. In order to confirm this assertion, the values of $G(Nu)/\varepsilon$ at x=0.5 are plotted versus ω in Fig. 5. For ε=0.1, $\overline{Nu}$ remains almost unchanged from Nu_s at all frequencies. As remarked by KH [12], the overall time-mean characteristics of natural convection remain substantially unchanged by the sidewall temperature oscillation when the amplitude of forcing is small. However, as ε increases, the effect of ε on $\overline{Nu}$ becomes conspicuous. When ε is appreciable, $G(Nu)$ increases with ε in a nonlinear manner (note that in the ordinate $G(Nu)/\varepsilon$ is plotted). As shown, the time-mean heat transfer rate is augmented measurably when the wall temperature oscillates with a large amplitude. The maximum gain of $\overline{Nu}$ relative to Nu_s is approximately 4.2% (for ε=0.5) and 13.1% (for ε=1.0).

The dependency of $G(Nu)$ on ω is also illustrated in Fig. 5. For small ω, $G(Nu)$ has an almost constant but finite positive value; e.g., $G(Nu)$=0.0866 for ε=1.0 and $\omega=0.1$. When $\omega \ll \omega_r$, the impacts of wall temperature oscillation can penetrate the full cavity [8,10]. In this case, the periodic responses of natural convection can be deduced from a series of steady state solutions, each of which may be computed with a constant hot wall temperature in the range of $1-\varepsilon \leq \theta_h \leq 1+\varepsilon$. When the amplitude of forcing is small, $\varepsilon \ll 1$, the time-dependent flow and heat transfer exhibit oscillatory behavior which is almost symmetric about the basic state solution ($\varepsilon \cong 0$). However, when ε is large, this argument is no longer valid. It is worth noting that the amount of heat transported by natural convection from the hot wall to the cold wall does not vary linearly with the temperature difference between the two sidewalls. Consequently, the fluctuation of $Nu(t)$ is not symmetric about Nu_s. These considerations offer plausible physical explanations for the deviation of $\overline{Nu}$ from Nu_s at small frequencies (see, e.g., Antohe and Lage [5]).

On the other hand, as ω increases beyond ω_r, $G(Nu)$ decreases with ω. As stressed in the previous works [8,10,12], when $\omega \gg 1$, the direct effects of the wall temperature oscillation are confined to the vertical boundary layer on the hot sidewall; the fluid in the interior does not feel the presence of the hot wall temperature oscillation. Thus, the deviation of $\overline{Nu}$ from Nu_s is small. The $G(Nu)$- ω curves in Fig. 5 exhibit a secondary peak at a frequency which is larger than ω_r. Since the presence of a secondary peak is not clearly discernible in the $A(Nu)$- ω curves in Fig. 4, this peak can not be interpreted conclusively as the existence of another distinct frequency of the system. This issue should be examined in detail in the forthcoming investigations.

It is important to note that the maximum gain of time-mean heat transfer occurs at a moderate frequency in a band near the resonance frequency, ω_r. The values of the frequency at which the maximum $G(Nu)$ takes place, ω_m, are listed in Table 1. The present result is supportive of the assertion that the maximal gain of the time-mean heat transfer coefficient, which is observed at a moderate frequency, is interpreted to be a consequence of resonance.

Another effect of large ε can be found in Figs. 3(a) and 3(b); when ε is large, $Nu(t)$ becomes negative at some instant during a cycle. In order to make a physical interpretation of this result, the $A(Nu)$ vs. ω curves for ε=1.0 are shown in Fig. 6 at three representative locations, i.e., at the cold sidewall (x=0.0), at the vertical mid-plane (x=0.5), and at the hot sidewall (x=1.0).

The value of $A(Nu)/2$ at the cold wall is less than unity, and this is smaller than $A(Nu)/2$ at the hot wall and at the vertical mid-plane. Considering that $G(Nu) \sim O(10^{-1})$, heat is always transferred out of the cavity at the cold wall. On the other hand, the value of $A(Nu)/2$ at the hot wall is much greater than unity. Put it alternately, the instantaneous values of $Nu(t)$ can be negative. This again implies that heat is instantaneously transferred either into the cavity or out of the cavity at the hot wall during a cycle. Here, it is useful to follow the descriptions of KH [12]; a cycle can be divided into the cooling ($\theta_h < 1.0$) and heating ($\theta_h > 1.0$) phases at the hot wall *relative* to the mean temperature ($\overline{\theta_h} = 1.0$). The negative value of $Nu(t)$ at the hot wall can occur when the hot wall temperature becomes lower than the fluid temperature in the thermal boundary layer in the cooling phase. When $\varepsilon = 0$, the fluid releases thermal energy fully to the cold wall. However, when $\varepsilon > 0$, there exists another choice in that thermal energy is partially returned to the hot wall in the relative cooling phase. The difference between the Nusselt numbers at the hot and cold walls is indicative of the transient thermal storage capacity of the system (see, e.g., Antohe and Lage

[2]). As illustrated in Fig. 6 as well as in KH [12], $A(Nu)_{x=1}$ increases with ε and ω, i.e., the latter mechanism tends to outweigh the former. In this case, the system has the capacity to store thermal energy in transient states.

It is also discernible that $A(Nu)$ at x=0.5 has a peak value at $\omega = \omega_r$, which is much larger than $A(Nu)$ at the cold wall and at the hot wall. As a result, the Nusselt number at x=0.5, has a negative value of very large absolute magnitude at some time instance, as shown in Fig. 3(c). The fluid in the cavity experiences the heat transport from the left half domain to the right half domain and vice versa periodically during a cycle. However, the occurrence of negative value of $Nu(t)$ in the interior has a different origin; it is of convective nature. The maximal amplification of $Nu(t)$ at x=0.5 is closely associated with maximal fluctuations of the flow at $\omega = \omega_r$. In particular, the negative value of $Nu(t)$ at x=0.5 take places when the clockwise (CW) flow circulations are developed, which will be shown later.

The discussion will now be centered on the resonance cases. In order to acquire a physical insight into resonance, detailed descriptions of the evolutions of flow and temperature fields over a cycle are needed, as displayed in Figs. 7-8.

Fig. 7 depicts the time-dependent flow patterns in the periodic steady state over a cycle for $\varepsilon = 1.0$ and $\omega = 0.77$. The sequential growth and disappearance of the counterclockwise (CCW) and clockwise circulations in a cycle are discernible. The CW and CCW circulations represent the influences of the relative cooling and heating phases, respectively. During the relative heating phase in Fig. 7 ($19 \leq \tau \leq 19.5$), the CCW circulations are intensified with time, and the maximum strength of flow occurs near the time instant at which the relative heating has been fully accomplished. During the relative cooling phase ($19.5 \leq \tau \leq 20$), the reverse process takes place.

Here, it is pointed out that the CW circulations as well as the CCW circulations grow to fill the bulk of the cavity, as shown in Fig. 7(a). It is noted that, for the case of ε=0.1, the CCW circulations dominate in the cavity at all time instants. When ε is small, the fluctuating components of the flow are overshadowed by the global flow driven by the mean temperature difference between the two sidewalls [12]. However, for ε=1.0, the flow fluctuations at the resonance frequency are comparable to the flow sustained by the mean temperature difference between the two sidewalls. Consequently, the wall temperature oscillation with a large amplitude causes a substantial amplification of flow, therefore, the instantaneous flow differs much from the basic state.

Sequential plots showing the evolutions of temperature field over a cycle are depicted in

Fig. 8. It is obvious that the isotherms in the interior exhibit a periodic tilting over a cycle. This temporal behavior of the interior fluid was previously reported by KH [12], although the degree of tilting was smaller due to a small value of ε (ε=0.1) used in [12]. This suggests that the resonance is associated with the internal gravity wave modes. It also reinforces the earlier assertion that the mechanism of resonance is largely independent of the forcing amplitude.

The influences of a large amplitude ($\varepsilon = 1.0$) are exemplified in Fig 8. The regions of $\theta > 1.0$ are seen in the upper part of the cavity at all times throughout a cycle. This implies that the cycle-averaged temperature field deviates much from that for the case of non-oscillating hot-wall temperature ($\varepsilon = 0.0$). Figs. 7 and 8 demonstrate that both the time-mean solutions and the instantaneous solutions are affected much by the wall-temperature oscillation when ε is large.

The time-mean flow patterns and temperature fields are acquired by averaging the time-dependent solutions over a cycle, which are illustrated in Fig. 9. Differences between the time-mean solution for ε=0.1 and the basic state solution (ε=0.0) are hardly discernible. This again supports the assertion of KH [12] that the impacts of wall temperature oscillation of small amplitude on the time-mean solutions are meager. However, for ε=0.5, both the flow and temperature fields display noticeable changes from the basic state. For ε=1.0, the deviations from the basic state are pronounced. In particular, the structure of flow and temperature fields in the interior, rather than in the boundary layers, is significantly changed. This, of course, is the case with a large value of ε. As mentioned before, when ε is large, the time-varying responses of flow and temperature fields in a cycle are no longer symmetric about the basic state. The asymmetric characteristics manifest the differences of the cycle-averaged time-mean solution from the basic state. These lead to the enhancement of the time-mean heat transfer rate.

When ε is large (see Fig. 4 for ε=1.0), the departure of the time-mean temperature field from the basic state provides a plausible explanation for the shift of the resonance frequency toward a larger value. The present results shown in Figs. 4-8 are consistent with the previous finding of KH [12] that the flow resonates with the internal gravity wave oscillations. For the present configuration, Paolucci and Chenoweth [19] estimated the frequency of the internal wave modes. The frequency of the fundamental mode can be expressed, in the present non-dimensionalization scheme, as

$$\omega_i = \frac{S}{\sqrt{2}}, \tag{12}$$

where $S^2 (\equiv \partial\theta/\partial y)$ is a parameter indicating the overall strength of stratification.

KH [12] estimated the stratification factor S of the basic state by using a linear fitting to the vertical temperature distribution at the horizontal mid-width plane of the cavity (x=0.5). The predicted values of ω_i were in good agreement with the numerically-acquired values of ω_r. In this study, S is obtained from the cycle-averaged solutions, rather than the basic state; S is evaluated by using the temperature profile in the range $0.2 \leq y \leq 0.8$ on the vertical plane at x=0.5. This reflects the fact that, when ε is large, the time-mean temperature field differs appreciably from the basic state. The estimated values of S and ω_i are listed in Table 1. It is seen that $\omega_i \approx \omega_r \approx \omega_m$. The slightly larger value of the resonance frequency for ε=1.0 is a consequence of the fact that the time-mean temperature field is more strongly stratified, therefore, the frequency of internal gravity mode has a slightly larger value.

CONCLUSION

Numerical computations have been conducted for natural convection in a sidewall-heated cavity with a time-varying temperature at the hot sidewall, $\theta_h = 1 + \varepsilon \sin(\omega t)$. The effects of amplitude of the wall temperature oscillation on the time-mean heat transfer and the amplifications of fluctuations of the instantaneous heat transfer are investigated.

The amplification characteristics of the fluctuation of the heat transfer in the interior are linearly dependent on ε when ε is small. When ε is large, the time-mean heat transfer is augmented measurably from the corresponding value for the case of the non-oscillating temperature condition (ε=0.0). The maximum gain of the time-mean heat transfer rate is seen at the resonance frequency at which maximal fluctuation of heat transfer takes place. This suggests that the augmentation of time-mean heat transfer is a consequence of resonance.

Although the influences of ε are discernible both in the time-mean and instantaneous flow and temperature fields, the basic mechanism of resonance is largely independent of the amplitude of thermal forcing. The evolutions of flow and temperature fields over a cycle and the theoretical predictions based on the analyses of the cycle-averaged temperature fields indicate that the flow resonates with the internal gravity-wave oscillations.

In this study, attention is limited to the special case of Ra=10^7 and Pr=0.7 to concentrate on the amplitude effect on the time-mean heat transfer. Due to the sensitivity of the natural convection

to inertial effects, the cases with different *Ra* and *Pr* will be of interest. Another restriction is that the present study is performed under the Boussinesq-fluid approximation, which may not be valid in the case of large ε or ΔT. It is also stressed that the non-Boussinesq effects are known to influence the oscillatory modes of the basic-state flow. Subsequent efforts to resolve these issues are being planned for future work.

ACKNOWLEDGEMENTS

Appreciation is extended to the referees who provided constructive comments and suggestions. This work was supported in part by a grant from the Center of Excellence (COE) Program of the Ministry of Education, Science, Sports and Culture, Japan.

REFERENCES

1. J. L. Lage and A. Bejan, The resonance of natural convection in an enclosure heated periodically from the side, *Int. J. Heat Mass transfer*, 1993, **36**, 2027-2038.
2. B. V. Antohe and J. L. Lage, A dynamic thermal insulator: inducing resonance within a fluid saturated porous medium enclosure heated periodically from the side, *Int. J. Heat Mass Transfer*, 1994, **37**, 771-782.
3. B. V. Antohe and J. L. Lage, Amplitude effect on convection induced by time-periodic horizontal heating, *Int. J. Heat Mass Transfer*, 1996, **38**, 1121-1133.
4. B. V. Antohe and J. L. Lage, The Prandtl number effect on the optimum heating frequency of an enclosure filled with fluid or with a saturated porous medium, *Int. J. Heat Mass Transfer*, 1997, **40**, 1313-1323.
5. B. V. Antohe and J. L. Lage, Experimental investigation on pulsating horizontal heating of an enclosure filled with water, *ASME J. Heat Transfer*, 1996, **118**, 889-896.
6. R. Iwatsu, J. M. Hyun and K. Kuwahara, Convection in a differentially-heated square cavity with a torsionally-oscillating lid, *Int. J. Heat Mass Transfer*, 1992, **35**, 1069-1076.
7. W. S. Fu and W. J. Shieh, A study of thermal convection in an enclosure induced simultaneously by gravity and vibration, *Int. J. Heat Mass Transfer*, 1992, **35**, 1695-1710.
8. W. S. Fu and W. J. Shieh, Transient thermal convection in an enclosure induced simultaneously by gravity and vibration, *Int. J. Heat Mass Transfer*, 1993, **36**, 437-452.
9. H. Q. Yang, K. T. Yang, and Q. Xia, Periodic laminar convection in a tall vertical cavity, *Int. J. Heat Mass Transfer*, 1989, **32**, 2199-2207.
10. M. Kazmierczak and Z. Chinoda, Buoyancy-driven flow in an enclosure with time-periodic conditions, *Int. J. Heat Mass Transfer*, 1992, **35**, 1507-1518.
11. Q. Xia, K. T. Yang, and D. Mukutmoni, Effect of imposed wall temperature oscillations on the stability of natural convection in a square enclosure, *ASME J. Heat Transfer*, 1995, **117**, 113-120.
12. H. S. Kwak and J. M. Hyun, Natural convection in an enclosure having a vertical sidewall with time-varying temperature, *J. Fluid Mech.*, 1996, **329**, 65-88.
13. M. Kazmierczak and A. Muley, Steady and transient natural convection experiments in a horizontal porous layer: The effects of a thin top fluid layer and oscillating bottom wall temperature,

Int. J. Heat Fluid Flow, 1994, **15**, 30-41.

14. J. Mantle, M. Kazmierczak, and B. Hiawy, The effect of temperature modulation on natural convection in a horizontal layer heated from below: high Rayleigh number experiments, *ASME J. Heat Transfer*, 1994, **116**, 614-620.
15. J. L. Lage, Convective currents induced by periodic time-dependent density gradient, *Int. J. Heat Fluid Flow*, 1994, **15**, 233-240.
16. J. M. Hyun, Unsteady buoyant convection in an enclosure, *Advances in Heat Transfer*, 1994, **34**, 277-320.
17. T. Fusegi and J. M. Hyun, Laminar and transitional natural convection in an enclosure with complex and realistic conditions, *Int. J. Heat Fluid Flow*, 1994, **15**, 258-268.
18. J. Patterson and J. Imberger, Unsteady natural convection in a rectangular cavity, *J. Fluid Mech.*, 1980, 54, 417-421.
19. S. Paolucci and D. R. Chenoweth, Transition to chaos in a differentially heated vertical cavity, *J. Fluid Mech.*, 1989, **215**, 379-410.
20. Le Quere, Transition to unsteady natural convection in a tall water-filled cavity, *Phys. Fluids A*, 1990, **2**, 503-514.
21. S. V. Patankar, *Numerical Heat Transfer and Fluid Flow*, McGraw-Hill, New York 1980.

Table 1. Summary of the present numerical simulations.

		$\varepsilon=0.0$	$\varepsilon=0.1$	$\varepsilon=0.5$	$\varepsilon=1.0$
maximum amplification	$A(Nu)$	0.0	0.662	3.40	7.29
of fluctuation of $Nu(t)$	ω_r	-	0.67	0.67	0.77
at x=0.5 (Fig. 4)					
maximum gain of $\overline{Nu}$	$G(Nu)$	0.0	0.00213	0.0421	0.131
(Fig. 5)	ω_m	-	0.68	0.65	0.77
estimated values from	S^2	0.880	0.884	0.920	1.17
the cycle-averaged	ω_i	0.66	0.66	0.68	0.76
solutions, (Fig. 9 and					
equation (12))					

FIGURE CAPTIONS

Fig. 1 Schematic diagram of the flow configuration.

Fig. 2 Time-dependent temperature boundary conditions at the vertical sidewalls.

Fig. 3 Time-dependent behavior of the Nusselt number at the vertical mid-plane (x=0.5). (a) ε=0.1; (b) ε=0.5; (c) ε=1.0.

Fig. 4 Effects of ε on the $A(Nu)/\varepsilon$ variation with ω (x=0.5).

Fig. 5 Effects of ε on the $G(Nu)/\varepsilon$ variation with ω (x=0.5).

Fig. 6 Variation of $A(Nu)$ vs. ω at three locations, x=0, x=0.5 and x=1.0. ε=1.0.

Fig. 7 Sequential plots showing the periodic stream functions in a cycle. ε=1.0, $\omega = 0.77$. The time instants, $\tau(=2\pi t/\omega)$, are given in the figures. The contour increments are $\Delta\psi = 0.004$. The dashed lines indicate the negative contour values.

Fig. 8 Same as in Fig. 7 except for contour plots of isotherms. $\Delta\theta = 0.1$. The dashed lines indicate the contour values $\theta \geq 1.0$.

Fig. 9 Contour plots of stream functions (upper frames) and isotherms (lower frames) (a) of the basic-state solution, and (b)-(d) of the cycle-averaged solutions. $\Delta\psi = 0.001$ and $\Delta\theta = 0.1$.

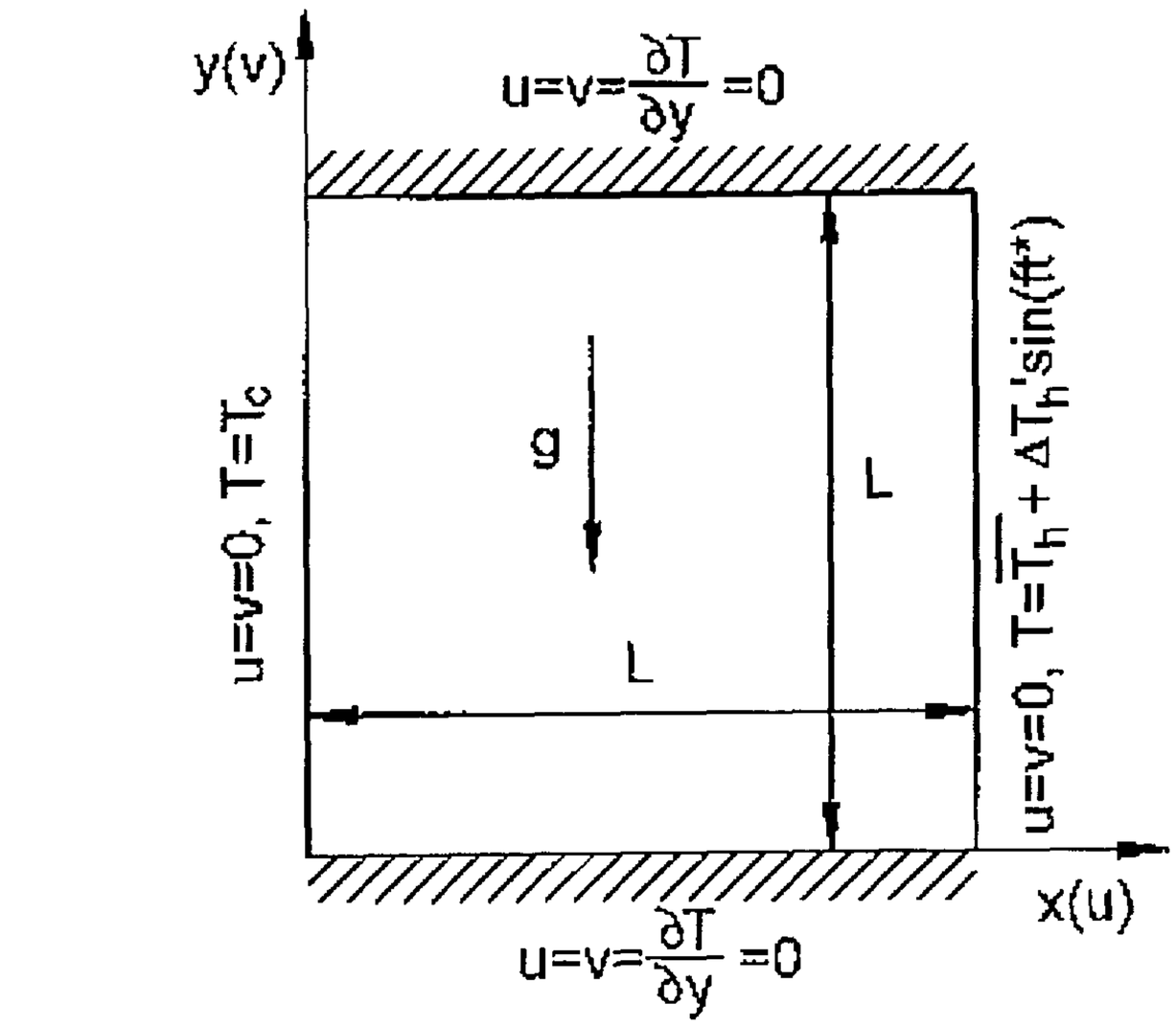

Fig. 1. Schematic diagram of the flow configuration.

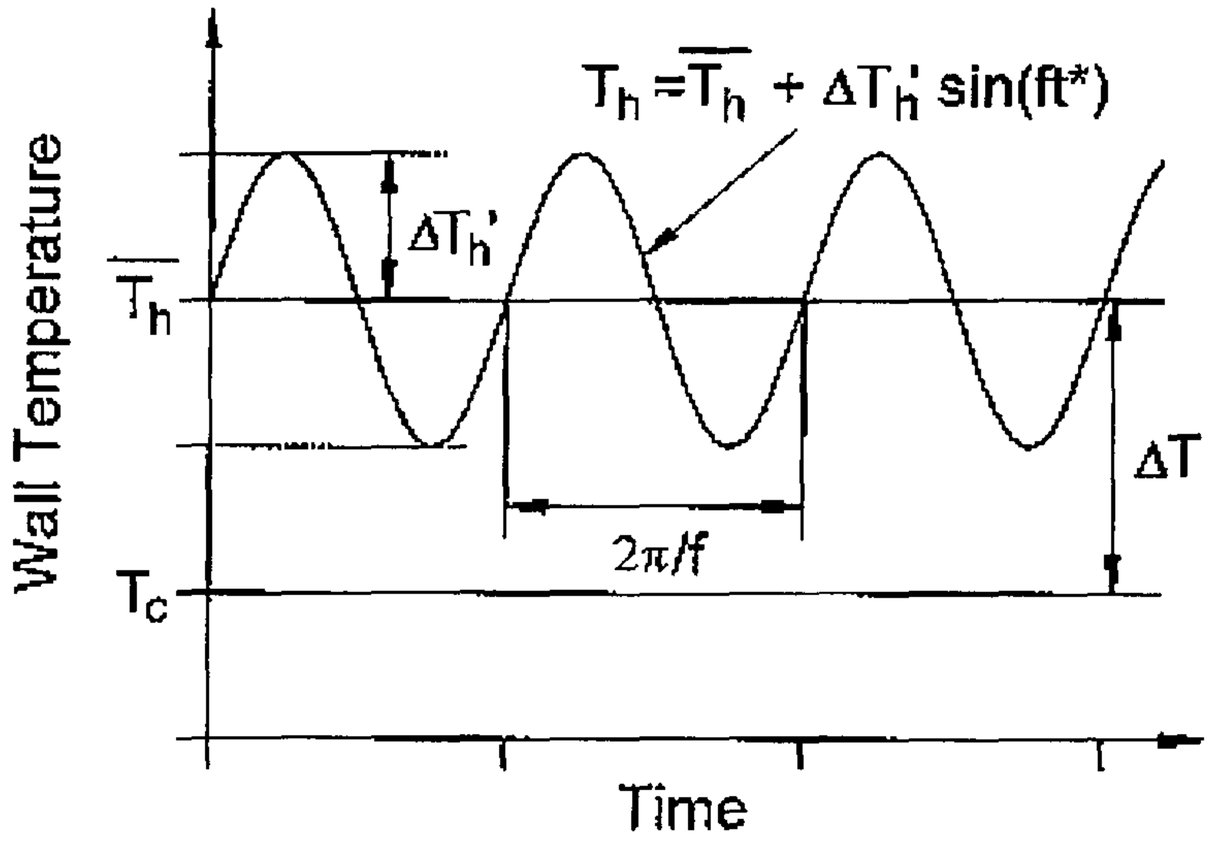

Fig. 2 Time-dependent temperature boundary conditions at the vertical sidewalls

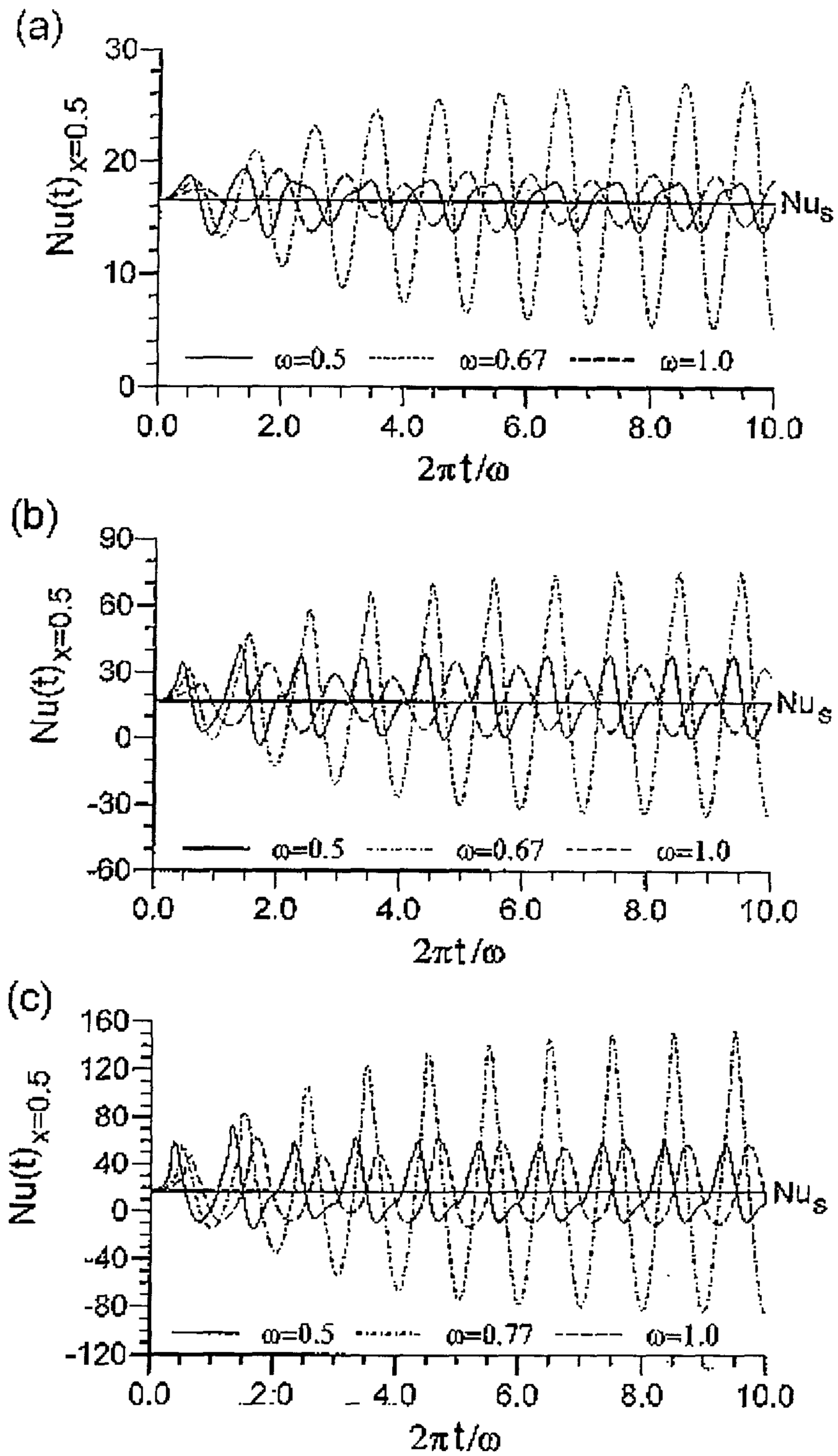

Fig. 3 Time-dependent behavior of the Nusselt number at the vertical mid-plane (x=0.5). (a) ε=0.1; (b) ε=0.5; (c) ε=1.0.

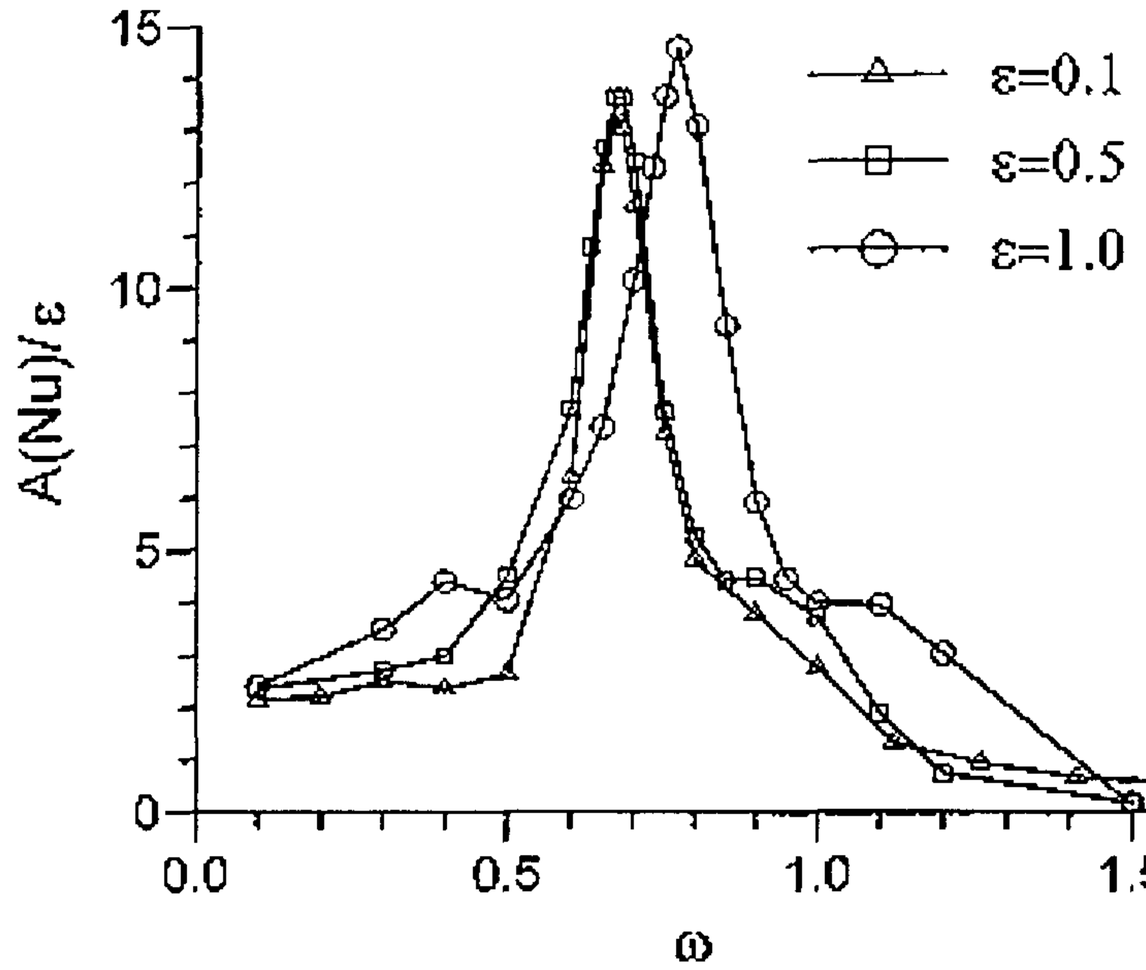

Fig. 4 Effects of ε on the $A(Nu)/\varepsilon$ variation with ω (x=0.5)

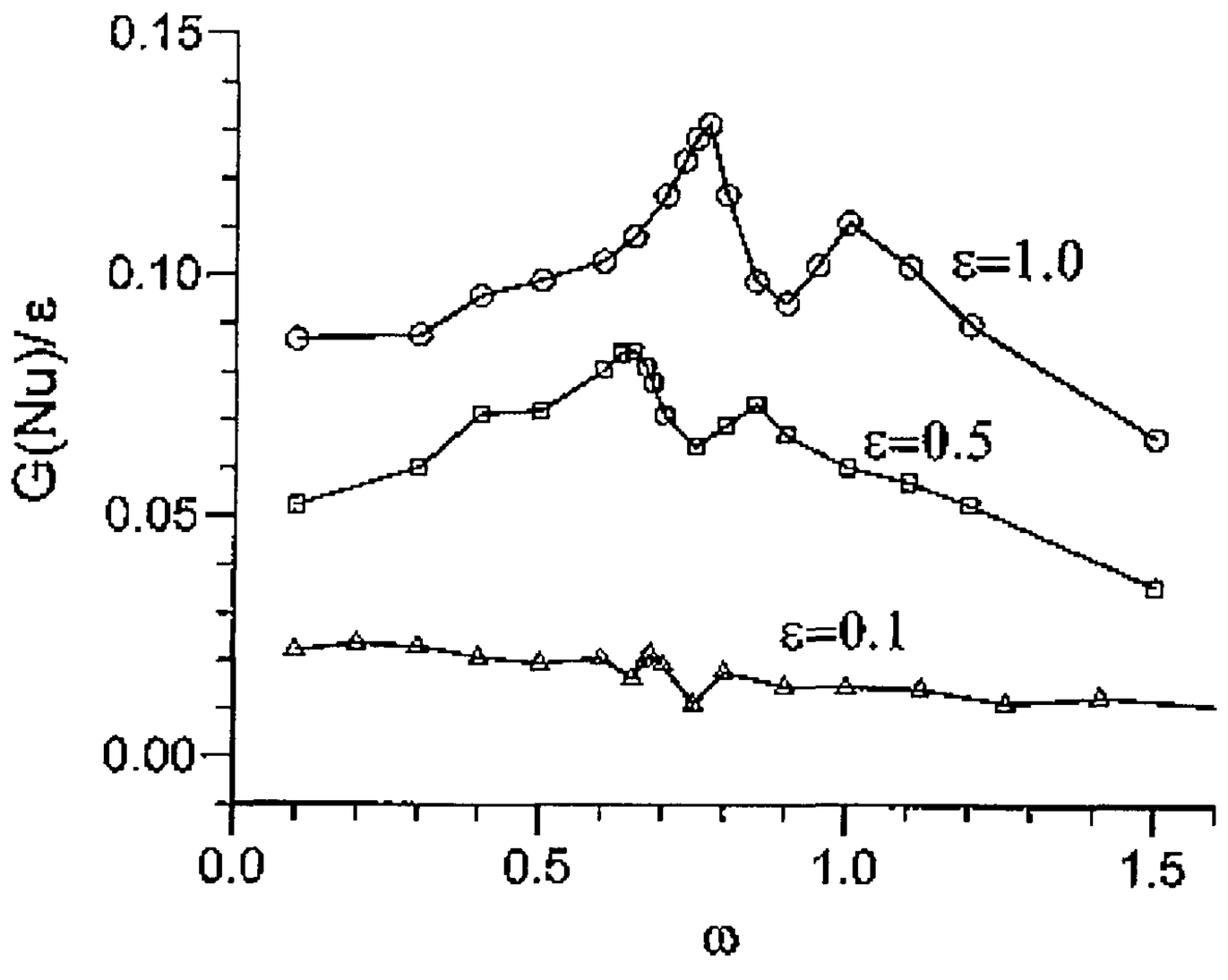

Fig. 5 Effects of ε on the $G(Nu)/\varepsilon$ variation with ω (x=0.5).

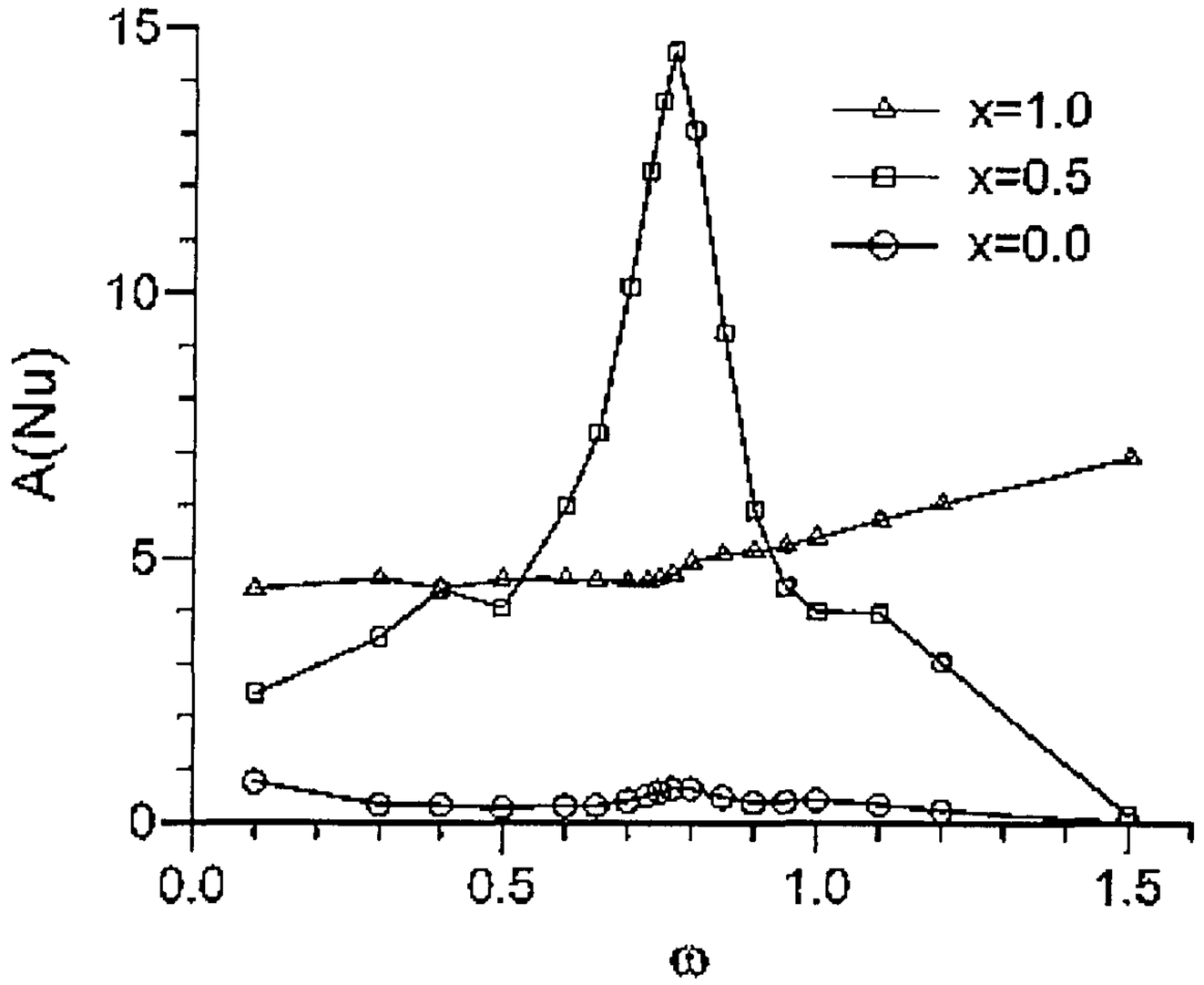

Fig. 6 Variation of $A(Nu)$ vs. ω at three locations, x=0, x=0.5 and x=1.0. ε=1.0.

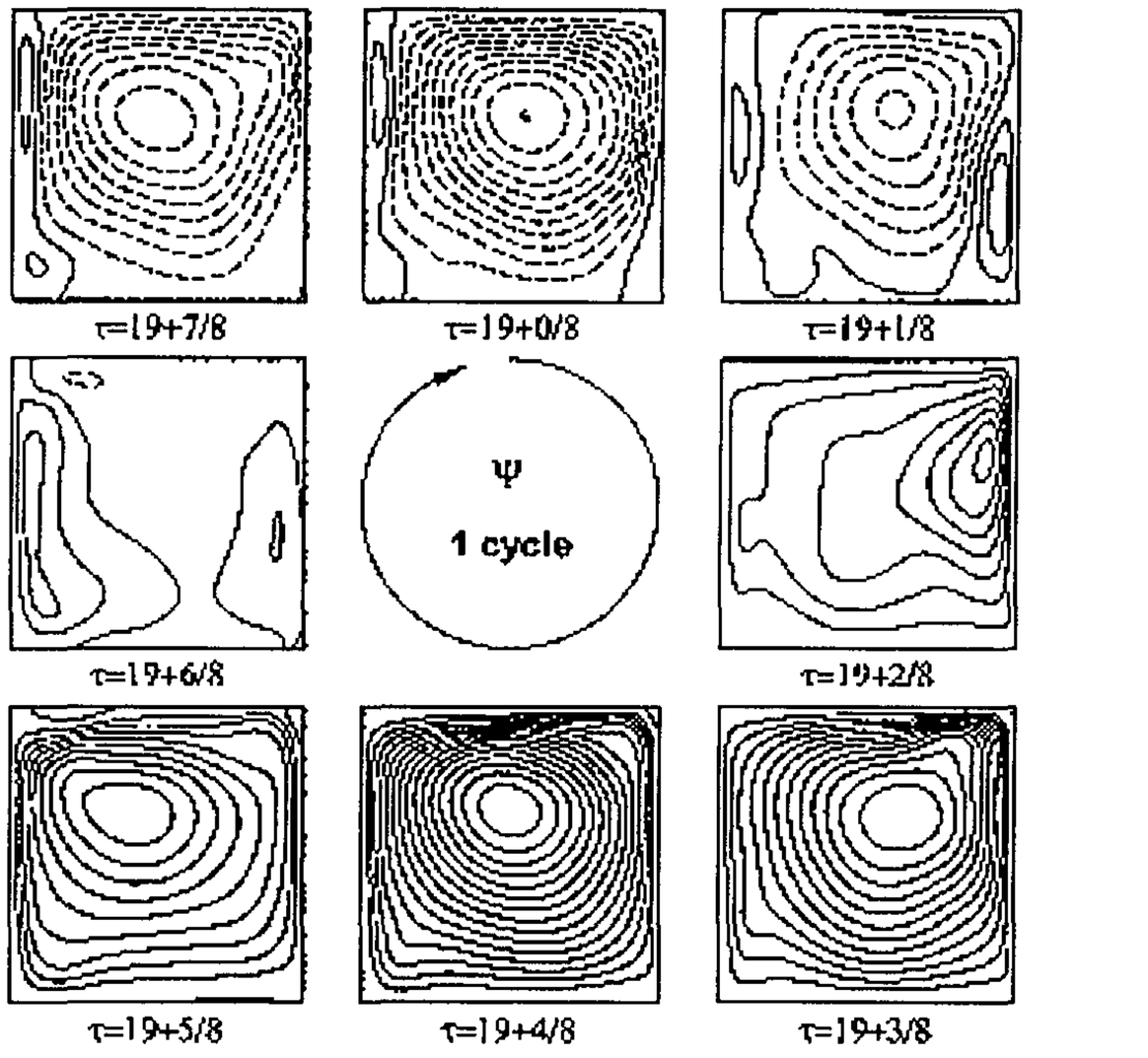

Fig. 7 Sequential plots showing the periodic stream functions in a cycle. ε=1.0, $\omega = 0.77$ The time instants, $\tau(=2\pi t/\omega)$, are given in the figures. The contour increments are $\Delta\psi = 0.004$ The dashed lines indicate the negative contour values.

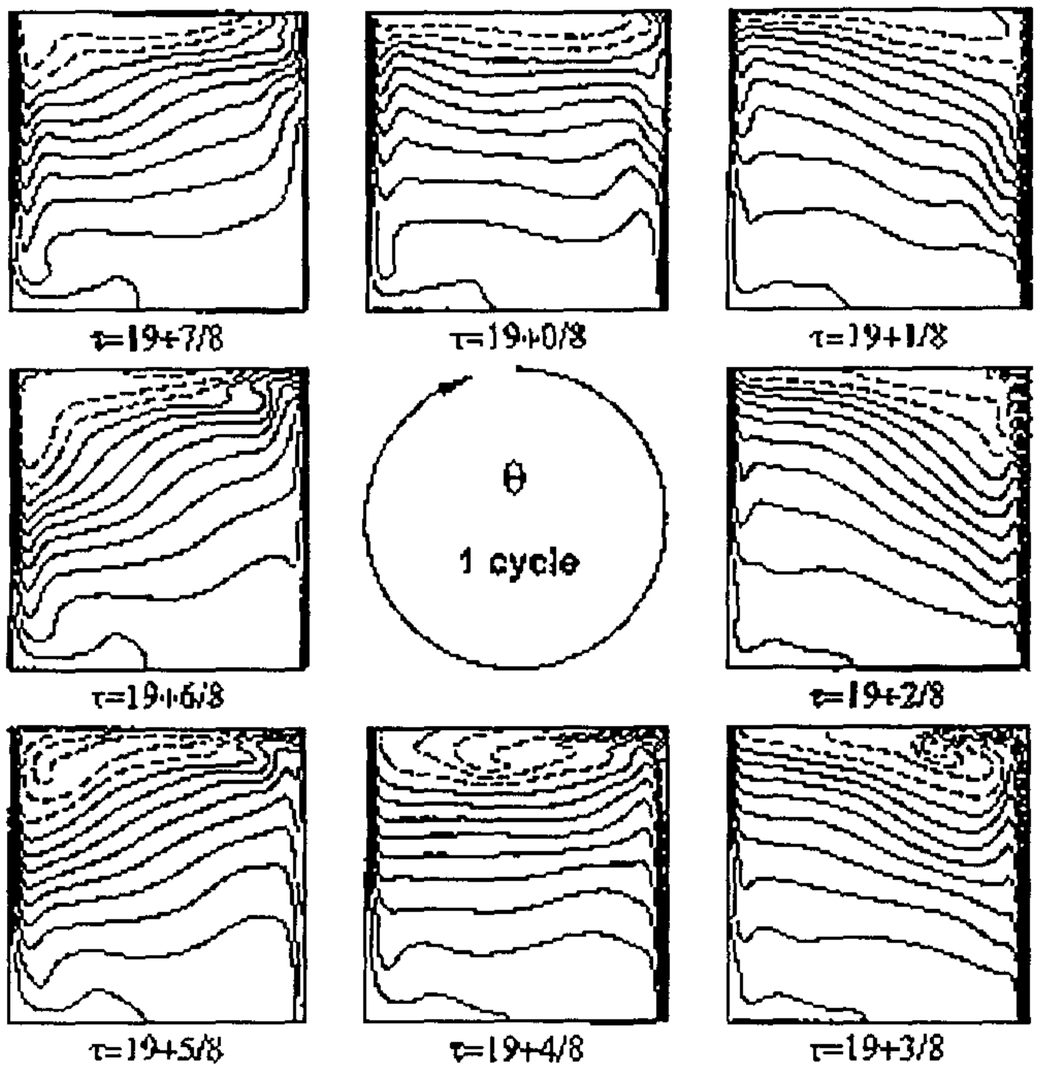

Fig. 8 Same as in Fig. 7 except for contour plots of isotherms. $\Delta\theta = 0.1$. The dashed lines indicate the contour values $\theta \geq 1.0$.

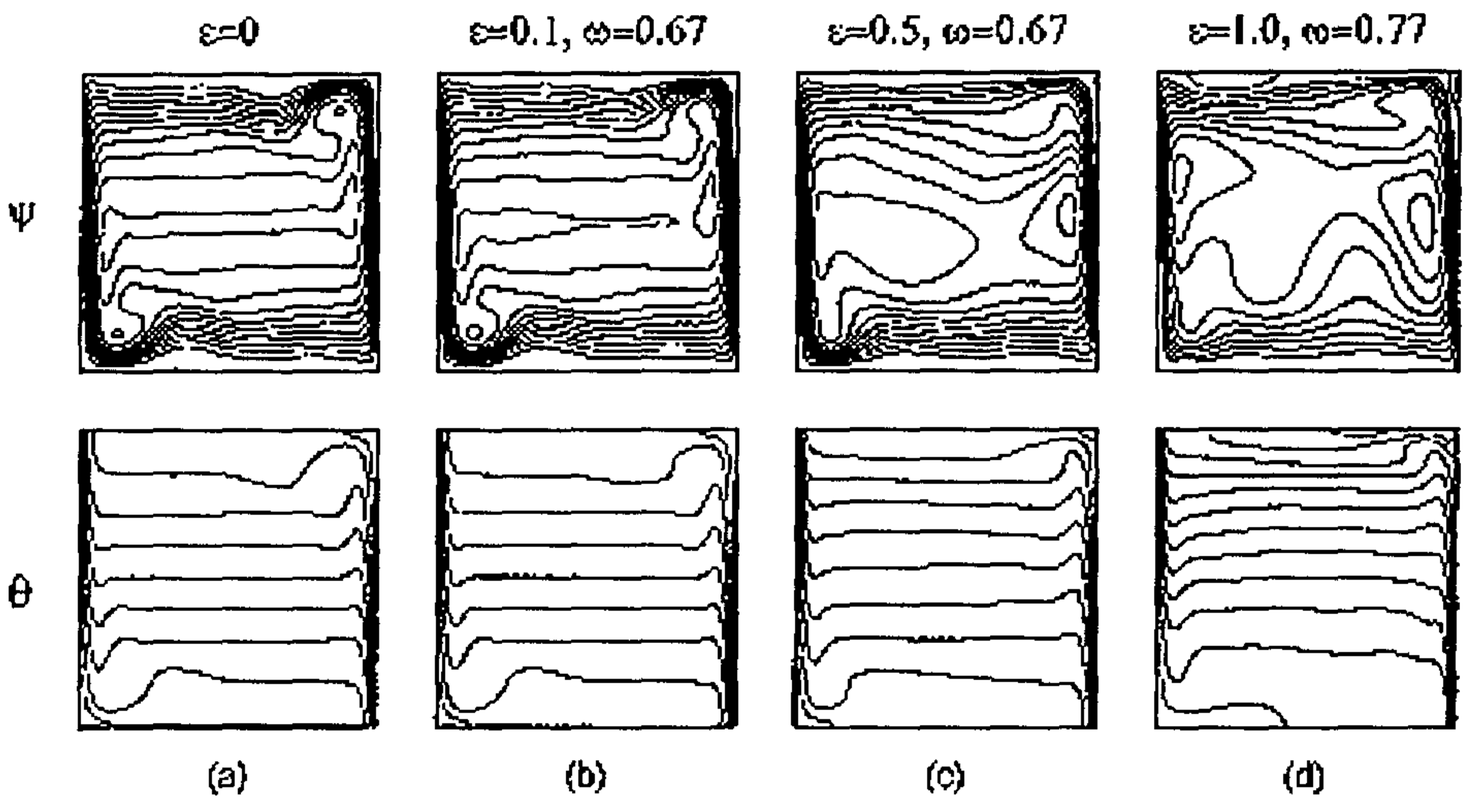

Fig. 9 Contour plots of stream functions (upper frames) and isotherms (lower frames) (a) of the basic-state solution, and (b)-(d) of the cycle-averaged solutions. $\Delta\psi = 0.001$ and $\Delta\theta = 0.1$.

제 11 절

Augmentation of convective heat transfer by a torsionally-oscillating shrouded underlay disk

(비틀림적으로 요동하는 덮개판에 의한 대류열전달의 조정)

요 약 문

수직으로 세워진 원형실린더내에서의 유체유동과 열전달 특성에 대한 조사가 이루어졌다. 중심측에 대하여 $\Omega=\varepsilon\lambda\cos(\lambda t)$의 회전율로 회전하는 위쪽벽에 의해 유동이 발생한다. 위벽의 온도는 아래벽보다 높아서, Brunt-Vaisala진동수가 N인 안정한 성층화를 이룬다. 준정상상태 주기적 유동의 현저한 특성을 예시하는 믿을만한 속도와 온도데이터가 구해졌다. 성층화가 증가함에따라 정상상태의 자오면유동은 위벽에 가까운 좁은 영역에 국한된다. 시스템이 정확히 자연주파수에 가진될 때인 특별한 N/λ값에서 공진이 확인된다. 초보적인 비점성 해석으로 관성중력진도의 모드를 알 수 있고, 본 수치데이터는 비점성해석결과와 잘 일치한다. 자오면 유동의 변동부분과 너셀수의 진폭은 공진조건에서 확연한 극점을 나타낸다. 공진에 대한 물리적인 설명을 제공하기 위하여 변동속도와 온도의 발달상황을 면밀히 조사하였다.

ABSTRACT

An investigation is made of fluid flow and heat transfer characteristics in a vertically-mounted circular cylinder. Motions are generated by the top endwall disk, which oscillates about the central axis with rotation rate $\Omega=\varepsilon\lambda\cos(\lambda t)$ The temperature of the top disk is higher than that of the bottom disk, producing a stable stratification of Brunt-Vaisala frequency N. Numerical solutions are acquired to the time-dependent Navier-Stokes equations. Comprehensive velocity and temperature data are obtained, which illustrate salient features of quasi-steady periodic flows. As the stratification increases, the steady meridional streaming is confined to a narrow region close to the top disk. Resonance is identified at particular values of (N/λ) , when the system is excited at correct natural frequencies. An elementary inviscid analysis indicates the modes of inertial-gravity oscillations, and the present numerical data are in close agreement with the inviscid results. The amplitudes of fluctuating parts of meridional flow and of Nusselt number display distinctive peaks under resonance conditions. Details of evolutions of fluctuating velocities and temperatures are scrutinized to offer physical explanations for resonance.

NOMENCLATURE

A = aspect ratio of the cylinder [$\equiv \frac{H}{R}$]

A( ) = amplitude of the fluctuating component

C_{ke}=kinetic energy coefficient

C_T = torque coefficient

C_p= pressure coefficient

E = Ekman number [$\equiv \frac{\nu}{H^2 \Omega}$]

H = cylindrical container height

J = Bessel function

N= Brunt-Vaisala frequency [$\equiv \left(\frac{\alpha g \triangle T}{H} \right)^{\frac{1}{2}}$]

Nu = Nusselt number

Pr=Prandtl number [$\equiv \frac{\mu / \rho_B}{k/(\rho_B c_p)}$]

R = cylindrical container radius

Re = rotational Reynolds number [$\equiv \frac{R^2 \Omega}{\nu}$]

S = Stokes layer thickness [$\equiv \left(\frac{2\nu}{\lambda} \right)^{\frac{1}{2}}$]

St_λ = stratification number

T = torque on the disk (in Chp.2) or temperature (in Chp.3)

T_B = temperature at the bottom disk

T_T = temperature at the top disk

c_p = specific heat

k = thermal conductivity

(r, ϕ, z) = cylindrical coordinates

(u, v, w) = velocity components

(u_f, w_f) = unsteady fluctuating parts of meridional flows

(u_s, w_s) = steady parts of meridional flows

GREEK SYMBOLS

Ω = mean rotation speed

$e\varepsilon$ = non-dimensional amplitude of oscillation

δ_s = non-dimensional Stokes layer thickness [$\equiv (2\nu/\lambda)^{1/2}/H$]

δ_E = non-dimensional Ekman layer thickness [$\equiv (2\nu/\Omega)^{1/2}/H$]

η_S = axial coordinate scaled by the Stokes layer thickness [$\equiv (H-z)/\ (2\nu/\lambda)^{1/2}$]

η_E = axial coordinate scaled by the Ekman layer thickness [$\equiv (H-z)/\ (2\nu/\Omega)^{1/2}$]

λ = torsional-oscillating frequency

μ = viscosity coefficient

ν = kinematic viscosity

θ = nondimensional temperature [$\equiv \dfrac{T-T_B}{\triangle T}$]

ρ = density

σ_{mn} = eigen-frequency

τ_t = spin-up time [$\equiv E^{-\frac{1}{2}}\ \Omega^{-1}$ for $\varepsilon > O(1)$, ($\equiv E^{-\frac{1}{2}}\ \Omega^{-1}\ \varepsilon^{-1}$ for $\varepsilon < O(1)$)]

Ψ = meridional streamfunction

ξ_{mn} = zeros of the first order Bessel function $J_1(\xi)$

SUBSCRIPTS

s = cycle-averaged component

f = unsteady fluctuating component

m = the number of waves or cells in the radial direction

n = the number of waves or cells in the axial direction

INTRODUCTION

Flow driven by a rotating disk has posed a long-standing fundamental problem. An elementary classical model was conceived by von Karman, which dealt with an infinite disk rotating steadily in an infinite expanse of a homogeneous viscous fluid. Similarity solutions were obtained for the three-component axisymmetric velocity field [see, e.g., Schlichting, 1968]. Flows maintained by a steadily-rotating finite endwall disk lid in a closed circular cylinder, for large rotational Reynolds numbers, have been investigated extensively. These constitute crucial issues in both the basic fluid dynamics research and a multitude of technological applications [e.g., Pao, 1971; Alonso, 1975; Bertela & Gori, 1982; Lang et al., 1994; Lim & Hyun, 1997].

The majority of preceding studies were concerned with the cases when the rotation rate of the disk is constant. Time-dependent flows, which arise when the rotation rate of the disk is time-variant, have not received much attention in the literature. The practical relevance of a temporally-varying rotation of disk can easily be appreciated by noting that the output from the electric motor drive in the laboratory turntable is seldom steady and constant. A canonical flow model can be constructed when the rotation rate of the disk is oscillatory in time. Early theoretical studies of flow induced by torsional oscillations of a disk were reported by Rosenblat [1959] and Benney [1961]. These investigations assumed a small-amplitude torsional oscillation of an infinite plane disk in an unbounded constant-density fluid. By means of a linearized analysis, these works provided qualitative descriptions of the primary flow and identified a second-order meridional flow. In particular, the structure of steady and fluctuating parts of meridional flow was depicted. Lim & Hyun [1997] acquired numerical solutions to the full Navier-Stokes equations for an oscillating shrouded disk in a closed cylinder. The azimuthal and meridional flows when the amplitude of oscillation is finite were examined, and the qualitative patterns of meridional steady streaming were verified by laboratory flow visualizations. These reports supplied baseline information on the axisymmetric flows at large rotational Reynolds numbers when the disk undergoes torsional oscillations.

Analysis of heat (and/or mass) transfer from a rotating disk, in conjunction with the induced flow field, has been performed in several rudimentary configurations [Sparrow & Gregg, 1960; Kreith et al., 1963; Lehmkuhl & Hudson, 1971]. These earlier accounts were concerned with the changes in transport properties in the fluid due to the presence of one or more steadily-rotating disks. Experimental measurements of mass transfer from the steadily-rotating disks were obtained, and heat transfer coefficients were estimated by resorting to the analogy between heat and mass transfers.

The present paper explores the flow and heat transfer properties from a torsionally-oscillating shrouded disk in a vertically-mounted cylinder. Specifically, the oscillating disk, which constitutes the top endwall, is held at a higher temperature than the stationary bottom endwall disk of the cylinder. In essence, the introduction of a vertical temperature contrast $\triangle T$ gives rise to a stable stratification, and the strength of stratification is characterized by the system Brunt-Vaisala frequency N. The case of a homogeneous constant-density fluid corresponds to N=0 [or $\triangle T=0$].

It is proposed here to portray the structures of velocity and temperature fields in the cylinder, both instantaneous and time-averaged. One overriding concern is to describe the augmentations in heat transfer induced by the oscillation of the top endwall disk. Obviously, in the absence of this endwall motion, no fluid flows are generated and the heat transfer will be purely conductive; and the Nusselt number at the endwall disk would be unity. The enhancement of heat transfer, owing to the convective activities in the fluid caused by the top endwall disk, is of primary interest. The present effort to probe into the heat transfer characteristics brings forth a more fundamental question on the existence of resonance in the stratified fluid system. Clearly, there are two major frequencies involved in the problem formulation; i.e., the Brunt-Vaisala frequency, which inherently represents the buoyancy effect in the system, and the frequency of oscillation of the disk, which reflects the externally-controllable system excitation frequency. A rudimentary reasoning points to the possibility of resonance if these two frequencies are related to each other. In a similar, but somewhat different, context, the presence of resonance has been identified in the examples of mixed convection [Iwatsu & Hyun, 1992] and of natural convection with temporally-varying thermal boundary conditions

[Lage & Bejan, 1993; Kwak & Hyun, 1996]. The key contention is that, when the system natural frequency is related to the external forcing frequency, intensification of the amplitudes of time-dependent flow variables is realized. This phenomenon was termed resonance in the present context. Scaling arguments were put forth by Lage and Bejan (1993) to estimate the resonance frequency for the case of a confined natural convection in a square cavity with temporally-oscillating heat fluxes at the sidewall. Numerical results were examined by Kwak & Hyun (1996) to derive the resonance frequency for a confined natural convection in a cavity with an oscillating sidewall temperature. The present endeavor aims to shed further light on the resonance in the case of a mixed convection in a cylinder in which forced convection is provided by the torsional oscillation of the top endwall disk.

Comprehensive numerical solutions to the governing time-dependent Navier-Stokes equations are produced. The wealth of numerical results allows a systematic evaluation of flow intensification and attendant heat transfer augmentations as the amplitude and frequency of the disk oscillation encompass broad ranges. The effects of the overall system rotational Reynolds number and of the strength of imposed vertical temperature difference $\triangle T$ are delineated. Emphasis will be placed on gaining an improved physical understanding of the nature of resonance pertinent to the present mixed convection problem formulation.

The model

Consider a vertically-mounted closed circular cylindrical container (radius R and height H; aspect ratio Ar=H/R), which is completely filled with an incompressible fluid of viscosity coefficient μ, specific heat C_P, and thermal conductivity k. The Boussinesq-fluid approximation is invoked, i.e., $\rho=\rho_B[1-\alpha(T-T_B)]$, where ρ_B and T_B refer to the reference density and temperature at the bottom endwall disk (z=0), respectively, and α the coefficient of thermometric volume expansion. These physical properties of the fluid are taken to be constant. The top endwall disk (z=H) executes a torsional oscillation with angular velocity $\Omega = \varepsilon\lambda\cos(\lambda t)$, and the rest of the solid walls of the cylinder are stationary. The temperatures of the top disk (z=H) and bottom disk (z=0) are respectively T_T and T_B, and , to insure a gravitationally stable temperature contrast, $\Delta T(=T_T-T_B)>0$. The cylindrical sidewall is assumed to be thermally insulated [see Fig.3.1].

It is advantageous here to implement nondimensionalizations in the following fashion:

$$(r',z') = (r, z)/R;\ t' = \lambda t;\ (u', v', w') = (u, v, w)/(\lambda R);$$

$$p' = \frac{P}{\rho_B \lambda^2 R^2};\ \theta = \frac{T - T_B}{\Delta T};$$

$$St_\lambda = \left(\frac{H}{R}\right)^{\frac{1}{2}}\left(\frac{N}{\lambda}\right) = \left(\frac{H}{R}\right)^{\frac{1}{2}}\frac{(\alpha g \Delta T/H)^{\frac{1}{2}}}{\lambda};\ St = \frac{N}{\varepsilon\lambda} = \frac{St_\lambda}{\varepsilon};$$

$$Re_\lambda = \frac{\lambda R^2}{\mu/\rho_B};\ Re = \frac{\varepsilon\lambda R^2}{\mu/\rho_B} = \varepsilon Re_\lambda;\ Pr = \frac{\mu/\rho_B}{k/(\rho_B c_p)};$$

$$Ra = \frac{g\alpha\Delta T R^3}{(\mu/\rho_B)(\kappa/\rho_B c_p)}. \qquad (3.1)$$

In the above, prime denotes the dimensionless quantities, and g the gravity. The principal nondimensional parameters are St_λ, the stratification number; Re, the rotational Reynolds number; and Pr, the Prandtl number and e denotes the dimensionless amplitude of torsional oscillation of the top endwall disk. Furthermore, it can be rewritten that $St_\lambda^2=Ra/(Re_\lambda^2\ Pr)$. Note that St_λ represents basically the ratio between the Brunt-Vaisala frequency pertinent to the system N and the forcing frequency of disk

oscillation λ, and it is modified by the aspect ratio.

The fluid motion is governed by the time-dependent Navier-Stokes equations, which, written in cylindrical polar coordinates (r, φ, z) with corresponding velocity components (u, v, w), read, in nondimensional form [primes are dropped from the dimensionless quantities] :

$$\frac{\partial u}{\partial t} = -\frac{1}{r}\frac{\partial}{\partial r}(ruu) - \frac{\partial}{\partial z}(uw) + \frac{v^2}{r} - \frac{\partial p}{\partial r} + \frac{1}{Re_\lambda}\left[\frac{\partial}{\partial r}\frac{1}{r}\frac{\partial}{\partial r}(ru) + \frac{\partial^2 u}{\partial z^2}\right]$$

(3.2)

$$\frac{\partial v}{\partial t} = -\frac{1}{r}\frac{\partial}{\partial r}(ruv) - \frac{\partial}{\partial z}(vw) + \frac{uv}{r} + \frac{1}{Re_\lambda}\left[\frac{\partial}{\partial r}\frac{1}{r}\frac{\partial}{\partial r}(rv) + \frac{\partial^2 v}{\partial z^2}\right] \tag{3.3}$$

$$\frac{\partial w}{\partial t} = -\frac{1}{r}\frac{\partial}{\partial r}(ruw) - \frac{\partial}{\partial z}(uw) - \frac{\partial p}{\partial z} + \frac{1}{Re_\lambda}\left[\frac{1}{r}\frac{\partial}{\partial r}\left(r\frac{\partial w}{\partial r}\right) + \frac{\partial^2 w}{\partial z^2}\right] + St_\lambda{}^2\theta \tag{3.4}$$

$$\frac{\partial \theta}{\partial t} = -\frac{1}{r}\frac{\partial}{\partial r}(ru\theta) - \frac{\partial}{\partial z}(w\theta) + \frac{1}{Re_\lambda \cdot \mathrm{Pr}}\left[\frac{1}{r}\frac{\partial}{\partial r}\left(r\frac{\partial \theta}{\partial r}\right) + \frac{\partial^2 \theta}{\partial z^2}\right]$$

(3.5)

$$\frac{1}{r}\frac{\partial}{\partial r}(ru) + \frac{\partial w}{\partial z} = 0 \tag{3.6}$$

Computations commence from an initially motionless state with a vertically-linear temperature profile, i.e., $\theta = z/Ar$, which pertains to the conductive heat transfer mode. At time zero, the prescribed torsional oscillation is imposed on the top endwall disk. The main thrust of the problem lies in the large-time, quasi-steady periodic behavior, and the initial transitory approach is not of much interest. In accordance with the problem statement, the boundary conditions are

$$u = v = w = 0, \quad \frac{\partial \theta}{\partial r} = 0 \qquad \text{at} \quad r = 1 \tag{3.7}$$

$$u = v = w = 0, \ \theta = 0 \qquad \text{at} \quad z = 0 \tag{3.8}$$

$$u = w = 0, \ v = \varepsilon\, r \cos t, \ \theta = 1 \qquad \text{at} \quad z = Ar. \tag{3.9}$$

To satisfy numerical stability requirements, the boundary conditions at the central axis are applied at a small, but finite, radius ($r=r_i$) [see Warn-Varnas et al., 1978;

Hyun et al., 1982, 1983]:

$$u=0, \quad \frac{\partial(v/r)}{\partial r}=0, \quad \frac{\partial w}{\partial r}=0, \quad \frac{\partial \theta}{\partial r}=0 \qquad \text{at } r = r_i \ . \qquad (3.10)$$

The above system of equations is solved by utilizing a well-established finite-difference numerical methodology. The numerical procedure adopted is essentially a mark-and-cell type, and it has been validated in a large number of simulations of rotating and stratified flows [e.g., Warn-Varnas et al., 1978; Hyun et al., 1982,1983; Lim & Hyun, 1997]. The specifics of the numerical schemes and algorithms have been amply documented, and they are not reproduced here. The time step Δt was taken to be sufficiently small to insure both numerical stability and resolution of the results. For most computations, after extensive test runs, the mesh network selected was typically (50X60) in the (r-z) meridional plane, and Δt was chosen such that one oscillating cycle consisted of $4096(=2^{12})$ time steps. It was set r_i=0.001, and changes in r_i in the range $0.001 \leq r_i \leq 0.005$ produced no noticeable alterations in the global flow patterns. Comprehensive convergence tests with respect to grid spacing and time interval were carried out, and the outcome was satisfactory [see the quantitative verifications in Lim & Hyun, 1997].

Results and discussion

In most runs, about five to ten oscillation cycles were needed to settle down to the quasi-steady state. Also, it was set Ar=1.0 and Pr=1.0, and interest was focused on the explicit effects of the disk oscillations, which are characterized by ε and Re_λ, and of the influence of imposed vertical stratification, which is represented by St_λ.

It is useful to define the cycle-averaged value, denoted by subscript s, and the time-fluctuating component, shown by subscript f , i.e.,

$$\theta(t) = \theta_s + \theta_f(t)$$

where $\theta_s \equiv \int_t^{t+2\pi} \phi dt$, in which Φ stands for an instantaneous physical variable. Also, $A(\Phi_f)$ represents the amplitude of the fluctuating component Φ_f.

First, the effect of the buoyancy is scrutinized. Fig.3.2 illustrates the global patterns of the steady meridional streaming (u_S,w_S). In the plots, the meridional stream function Ψ_S, which is defined such that $u_s = \frac{1}{r}\frac{\partial \Psi}{\partial z}$, $w_s = -\frac{1}{r}\frac{\partial \Psi}{\partial r}$, is shown. The parameters are ε=2.0, Re=1000. As is apparent in Fig.3.2, the oscillation of the top disk generates steady axial motions toward the top disk at small and moderate radii. In the vicinity of the oscillating disk, the fluid is propelled radially outward. At large radii near the cylindrical sidewall, constrained by the finite geometry, the meridional flow turns away from the oscillating disk and points downward along the vertical sidewall. This completes the overall circulatory path, and this general behavior was corroborated by flow visualizations for a homogeneous fluid [Lim & Hyun, 1997]. The impact of buoyancy reduces, in general, the magnitudes of the meridional velocities, as shown in Fig.3.2. [note the difference in scales for the values of Ψ_S of Fig.3.2] The introduction of stable stratification suppresses vertical motions, therefore, as St increases, the region of appreciable meridional flows tends to be confined to the area closer to the oscillating disk. As seen in Fig.3.2(c), when St is large, the meridional flows in the bulk of the interior, with the exception of a small zone adjacent to the disk, are practically nil.

The plots of the deviation of the time-averaged temperature θ_s from the initial-state vertically-linear profile z/Ar are also illustrated in Fig.3.2 , i.e., $\theta_d = \theta_s - z/Ar$. It is discernible that as stratification increases, the size of the area in which qd is appreciable shrinks, and this zone tends to be concentrated toward the oscillating top disk. Also, the magnitude of θ_d is reduced substantially as St increases. Under complete dominance of conduction, θ_d vanishes. Therefore, as seen in Fig.3.2, the presence of non-vanishing θ_d points to convective activities. As the overall imposed stratification increases[see Fig.3.2(c)], heat transport in much of the interior region, except in a narrow zone close to the top disk, is accomplished by conduction. As displayed earlier, the fluid is pumped from below toward the oscillating disk at small and moderate radii. Therefore, the fluid in the upper part of the cylinder is replaced by the colder fluid

originating from the lower part of the cylinder. In the upper region of the cylinder of large radii near the vertical sidewall, the warm fluid near the top disk is propelled radially outward and it descends. These spatially-varying features of temperature fields are more conspicuous as St increases, and only in the upper part of the cylinder the averaged temperature field deviates from the initial linear temperature distribution. In the middle and bottom portions of the cylinder, the fluid temperature remains virtually unchanged from the conduction-controlled vertically linear profile. In the upper region of the cylinder, convection is dominant. Due to the disk oscillation, the fluid at small and moderate radii is colder than the initial state, and the fluid at large radii is warmer than the initial state. It is important to note that the oscillation of the upper disk brings forth radial temperature gradients in the regions of intense convective activities.

As to the azimuthal flows, much of the descriptive statement of Lim & Hyun(1997) for the case of a homogeneous fluid is qualitatively applicable to the present problem. The azimuthal velocity field is restricted to a region adjacent to the oscillating disk, and the (dimensional) vertical extent of this region is scaled by the thickness of the Stokes layer, $O\,(\nu/\lambda)^{1/2}$, where n stands for the kinematic viscosity. Except in this zone, the azimuthal velocities in much of the cylinder interior are practically zero. This general property of the v-field remains largely unaltered as St increases in the range of the present computations.

One central issue in the discussion of temporally-periodic rotating flows of a stratified fluid is the presence of inertia-gravity wave oscillations. As the classical treatise[e.g.,Greenspan,1968] demonstrated, the restoring forces due to the rotational effect and the gravity give rise to internal oscillations. In the present context, the fluid system is excited by the externally-controllable mechanical oscillation of the upper disk. Therefore, a fundamental consideration leads to the possibility of resonance if the frequency of the disk oscillation and the frequency of the intrinsic internal gravity-inertial oscillation are related. Under resonance conditions, the fluid motions are intensified and the resultant convective heat transfer is enhanced. The notion of resonance in natural convection in a non-rotating confined space, with periodic thermal forcings, has been dealt with recently [e.g., Lage & Bejan, 1993; Kwak & Hyun,1996].

In the case of rotating flows of a homogeneous fluid, resonance phenomenon in connection with the inertial oscillations has been addressed [e.g., Aldredge, 1976]. Iwatsu et al. [1993] identified the resonance conditions by monitoring the augmentation in a square cavity with an oscillating flat lid under an imposed vertical temperature differential.

Consider axisymmetric flows in a cylindrical container, filled with an inviscid, incompressible fluid with a vertically-linear stratification. By assuming a wave-like solution, the eigenfrequency σ_{mn} of this fluid system can be found, by undergoing an elementary analysis [see, e.g., Greenspan, 1968]:

$$\sigma_{mn} = N\left[1+\left(\frac{\xi_m^{\,2}}{n^2\pi^2}Ar^2\right)^{-1}\right]^{-\frac{1}{2}} \tag{3.11}$$

with the corresponding eigenfunction in the form of [in dimensional notation]

$$J_0\left(\xi_m\frac{r}{R}\right)\sin\left(n\pi\frac{z}{H}\right),$$

where J_0 denotes the first-order Bessel function. In the above, m and n are the integer indices denoting the (m,n)th mode in the (radial and axial) directions, N the previously-defined Brunt-Vaisala frequency, ξ_m the mth positive root of the first-order Bessel function. Clearly, σ_{mn} indicates the frequency of modes of inertial-gravity oscillations which are inherent to the rotating and stratified fluid system under present consideration.

As remarked earlier, a key argument is the presence of resonance when the above-cited eigenmodes of the system are excited and amplified if the externally-applied excitation frequency λ matches the correct natural frequency. The impetus of the present study is to establish the resonance phenomenon and to portray the intensification of flow and augmentation of convective heat transport.

It is useful to define the radially-averaged instantaneous Nusselt number at height z:

$$\mathrm{Nu(t)} = \int_{r=0}^{r=1}\left[-\mathrm{Pr}\cdot Re\cdot w\cdot\theta+\frac{\partial\theta}{\partial z}\right]rdr$$

This can further be divided into the cycle-averaged value Nu_s and the time-fluctuating component $Nu_f(t)$, i.e.,

$$Nu_s=\int_t^{t+2\pi} Nu(t)dt,$$

$$Nu_f(t)=Nu(t)-Nu_s.$$

Detection of resonance can be made by inspecting the characteristics of the fluctuating parts of flow variables. Fig.3.3 exhibits the behavior of $A(\Psi_f)$ at selected locations versus St_λ . Obviously, the meridional flows are vigorous in the interior region of the cylinder [note the difference in scales for $A(\Psi_f)$ in Figs.3.3(a), 3.3(b) and 3.3(c)]. Clearly, the dominant mode of inertial-gravity oscillations is the (1,1)mode. This mode corresponds to a disturbance whose radial extent fills the entire cylinder radius (m=1), and a half-wave of this mode fits the whole cylinder height (n=1). The afore-stated inviscid analysis yields σ_{11}=0.773N, the second mode σ_{12}=0.521N, and the third mode σ_{13}=0.377N, etc. Also, since the rotation rate of the top disk, $\Omega(t)$, is sinusoidal with frequency λ, the pertinent frequency for the absolute magnitude of the rotation rate, $|\Omega(t)|$, is 2λ. Notice that the temporal behavior of meridional flows is in response to $|\Omega(t)|$. Therefore, the base-mode resonance is expected when $2\lambda_{re}=\sigma_{11}$, which points to $St_{re}=Ar^{\frac{1}{2}}\left(\frac{N}{\lambda_{re}}\right)=2.59$. In Fig. 3.3, it is evident that the primary peak in $A(\Psi_f)$ is seen at St_λ=2.6, which is in close agreement with the above reasoning based on inviscid analysis. The secondary and tertiary peaks in $A(\Psi_f)$ in Fig.3.3 are found St_λ=3.58 and St_λ=5.26, respectively. These correspond to the second and third modes of excitation, i.e., when $2\lambda=\sigma_{12}$ and $2\lambda=\sigma_{13}$, respectively. The overall results in Fig.3.3 are supportive of the concept of flow intensification under resonance conditions, and the numerical values derivable from the inviscid theory are shown to be reasonably accurate in assessing the resonance frequencies.

Fig.3.4 demonstrates the variations of the kinetic energy of meridional flows. Obviously, the kinetic energy generally decreases with St_λ; as ascertained in Fig.3.2, the overall meridional flows are attenuated as the system stratification is increased. In Fig.3.4, the curves of kinetic energies display local peaks under resonance conditions, which is in line with the assertions of Fig.3.3, i.e., St_λ=2.6, 3.8, and 5.3 for local peaks. These establish that the physical variables peak when the resonance conditions are met. For large values of Re and Ra, the inertial-gravity oscillations based on the inviscid consideration provide valid estimates of the eigenmodes of the system.

The enhancement of heat transport is illustrated in Figs. 3.5 and 3.6. In Fig.3.5, the explicit variation of $A(Nu_f)$ with St_λ is plotted. In the parameter values covered, the base-mode resonance condition, i.e., St_λ=2.6, is largely unaffected as the amplitude of the disk oscillation e varies. In the middle portion of the cylinder, the augmentation of the fluctuating part of heat transfer, $A(Nu_f)$, is most pronounced. The numerical results are reorganized in Fig.3.6 to delineate the effect of St. The resonance points on the St_λ -axis remain virtually unchanged as the overall stratification increases, which is consistent with the foregoing physical arguments.

The details of the temporal variation of the Nu-profile are elaborated in Fig.3.7. The intensification of Nu-profiles under resonance in the middle and bottom regions of the cylinder is in evidence [see Fig.3.7(b)].

In plots displaying the instantaneous flow variables, the fluctuating parts are masked by the dominant steady features. However, in an effort to gain physical insight into the mechanism of resonance, it is useful to examine the details of the time-fluctuating components of flow. The ensuing discussions run closely to the physical pictures advanced by Kwak & Hyun (1996) for natural convection in a cavity with time-oscillating thermal boundary conditions.

The disk rotation can now be divided into four phases, as shown in Fig.3.8. Phases I & III (II & IV) represent deceleration (acceleration) in the absolute magnitude of the rotation rate. It is important to note that the fluctuating part of meridional flow, relative to the steady motion, diminishes (intensifies) in phase I & III (II & IV). Here, it is stressed that the crucial part in the discussion is the temporal behavior of Ψ_f relative to

the steady streaming.

Sequential plots of Ψ_f and $\theta_f[\equiv\theta - z/Ar - \theta_s]$, the fluctuating part of temperature deviation, for the resonance case ($St_{re}=2.6$) are illustrated in Fig.3.9. Note that the temperature field θ_f displayed here represents the deviations relative to the origional, conduction-dominant vertically-linear profile. It should be remembered that the full instantaneous flow field consists of these fluctuating parts and the more prominent steady flows portrayed in Fig.3.2.

First, the flow evolution is scrutinized. At time τ_a , the full domain is occupied by a clockwise (CW) circulation cell, which was developed by the disk acceleration in the previous oscillation cycle. At time τ_b, a weak counterclockwise (CCW) circulation forms near the stationary bottom disk. As the rotation rate of the disk approaches zero (see frames c, d, e), the CCW grows from the bottom and fills most of the cylinder. In phases II, a reverse process takes place. In summary, in an half cycle, the CW and CCW circulating cells are developed and they disappear subsequently.

In an endeavor to identify heat transport under resonance conditions, the movements of the cold spots, relative to the steady temperature field, are traced. In Fig.3.9(a), a cold spot, characterized by negative values of θ_f, is visible in the bottom region of the cylinder. This represents the vertical intrusion of cold disturbances (from the bottom cold disk) which were developed in the acceleration phase ($\tau=\tau_a$) of the previous cycle. These disturbances were transported by the general upwelling motions of the steady streaming. As is discernible in Figs.3.9(b) and 3.9(c), this cold disturbance travels upward in much of the interior region. Only in a zone close to the cylindrical sidewall, hot disturbances are seen. These represent the downwelling near the sidewall, carrying hot fluids which were in contact with the top hot disk. Around $\tau=\tau_d$ and $\tau=\tau_e$, the cold disturbances are broken into two parts. One forms the cold zone in the upper region, adjacent to the top disk; another is found in the sidewall area of the bottom region of the cylinder. The upper cold disturbance weakens and subsequently dies out. The bottom cold zone moves toward the axis and later moves upward as described earlier.

The above pictures provide a clue for the resonant convection. While the cold disturbance is in contact with the top hot disk, heat transfer takes place. This heated

fluid travels downward at large radii due to the steady streaming, and when this hot fluid gets into contact with the bottom cold disk, heat is transferred from the fluid to the bottom disk. Therefore, the key assertion is that, in order to achieve maximum heat transfer, the two events, i.e., (1) the generation and disappearance of cold and hot spots; and (2) the development and diminishing of the CW and CCW circulations, are synchronized. When this is satisfied, resonance is materialized. The frequency of event (1) is characterized by the inertial-gravity oscillation, and event (2) is largely controlled by external excitation of frequency 2λ. As seen in Fig.3.9, when 2λ and σ_{mn} are approximately equalized, flow and heat transfer take place in a broader region of the cylinder and the intensities of these are increased.

The qualitative pictures of temporal behavior of Ψ_f and θ_f under off-resonance conditions are exemplied in Figs.3.10&3.11. In Fig.3.10, $St_\lambda > St_{re}$, which can be interpreted as $\lambda<\lambda_{re}$ if N is unaltered. The external excitation is of low frequency.The period of external forcing is longer than the period of the occurrence and disappearance of hot and cold spots. This mismatch of the two times leads to a lower effective heat transfer rate. As seen, the patterns of fluctuating part of flow produce horizontally-stacked circulation cells, which undercuts vigorous convective activities. This feature was emphasized in Kwak & Hyun (1996). In Fig.3.11, a qualitatively opposite case is demonstrated. For a fixed N, $\lambda>\lambda_{re}$, reflecting the fact that the external excitation is of high frequency. The mismatch of the above-described two times is seen. The velocity patterns produce a vertically-stacked structure, which lessens effective convective heat transport. [see Kwak & Hyun, 1996]

Conclusion

As the overall stratification increases, the steady meridional streaming is concentrated to a narrow region close to the top disk. Inspection of the fluctuating parts of meridional velocity and of the Nusselt nimber leads to the identification of resonance conditions.

The frequencies σ_{mn} of the inertial-gravity oscillations, as obtained by inviscid analysis, provide reasonably accurate descriptions of the system eigenfrequencies. For meridional flows, when excitation frequency 2λ is equal to σ_{mn}, resonance takes place. Substantial enhancements of $A(\Psi_f)$ anf $A(Nu_f)$ are realized under resonance conditions, and this phenomenon is pronounced in the middle portion of the cylinder.

A scrutiny of the flow evolutions is supportive of the above assertion that flow and heat transport are augmented when the resonance condition is satisfied.

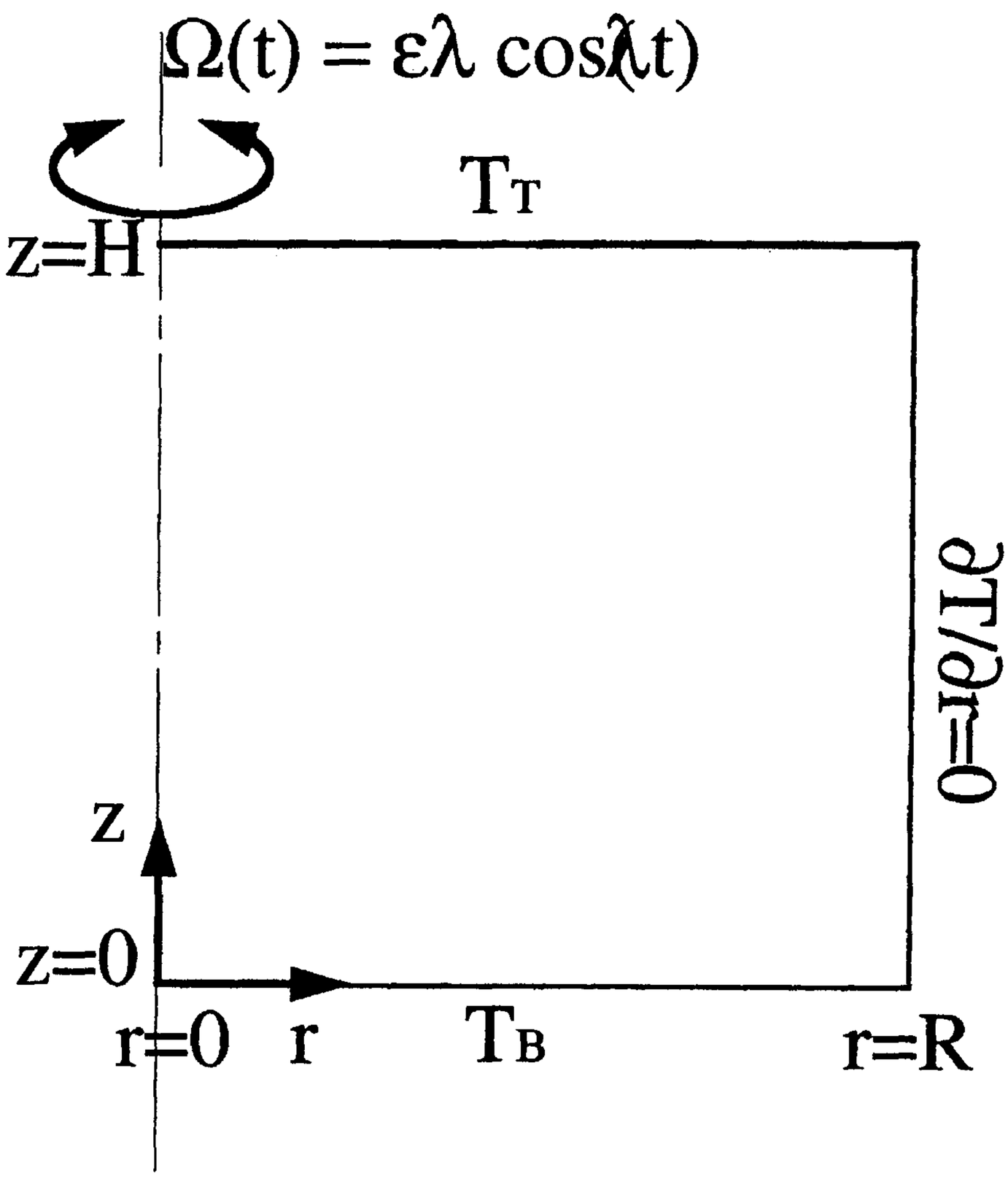

Figure 3.1 Flow configuration.

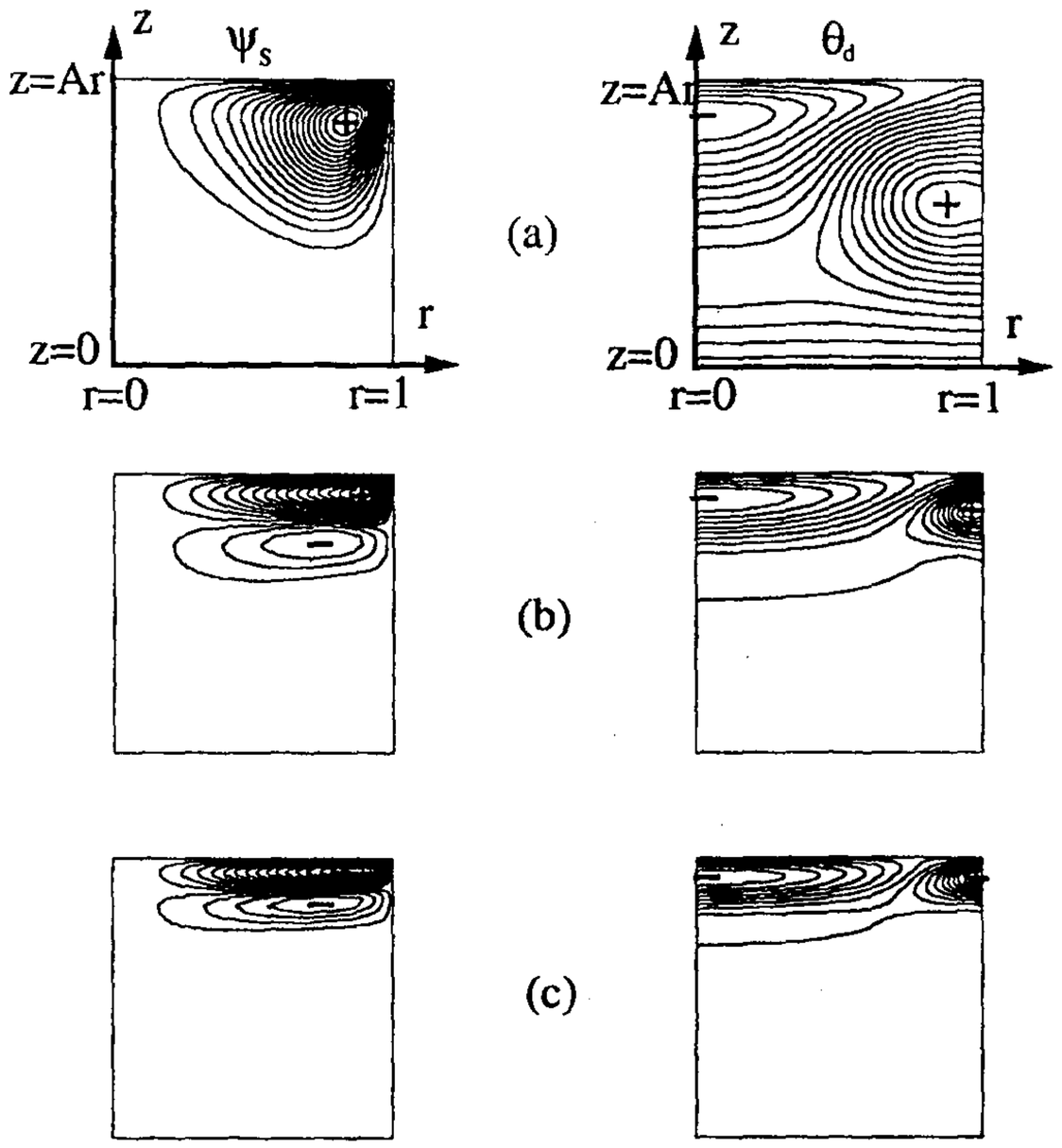

Figure 3.2 Left column shows the stream function Ψ_s, for steady meridional flows (u_s, w_s), scaled by $Re_\lambda^{-1/2}$. Right column shows θ_d, the deviation of steady temperature (θ_s) from the origional linear profile, i.e., $\theta_d \equiv \theta_s - z/Ar$. ε=2.0, Re=1000.

(a) St = 0.1. $\Psi_{max} = 5.702\text{x}10^{-3}$, $\Psi_{min} = -0.187\text{x}10^{-3}$, $\Delta\Psi = 2.94\text{x}10^{-4}$,
$\theta_{max} = 3.285\text{x}10^{-1}$, $\theta_{min} = -1.334\text{x}10^{-1}$, $\Delta\theta = 2.31\text{x}10^{-2}$;

(b) St = 1.3. $\Psi_{max} = 2.033\text{x}10^{-3}$, $\Psi_{min} = -0.443\text{x}10^{-3}$, $\Delta\Psi = 1.24\text{x}10^{-4}$;
$\theta_{max} = 0.665\text{x}10^{-1}$, $\theta_{min} = -0.211\text{x}10^{-1}$, $\Delta\theta = 0.438\text{x}10^{-2}$;

(c) St = 5.0. $\Psi_{max} = 0.724\text{x}10^{-3}$, $\Psi_{min} = -0.211\text{x}10^{-3}$, $\Delta\Psi = 0.468\text{x}10^{-4}$;
$\theta_{max} = 0.137\text{x}10^{-1}$, $\theta_{min} = -0.0811\text{x}10^{-1}$, $\Delta\theta = 0.109\text{x}10^{-4}$.

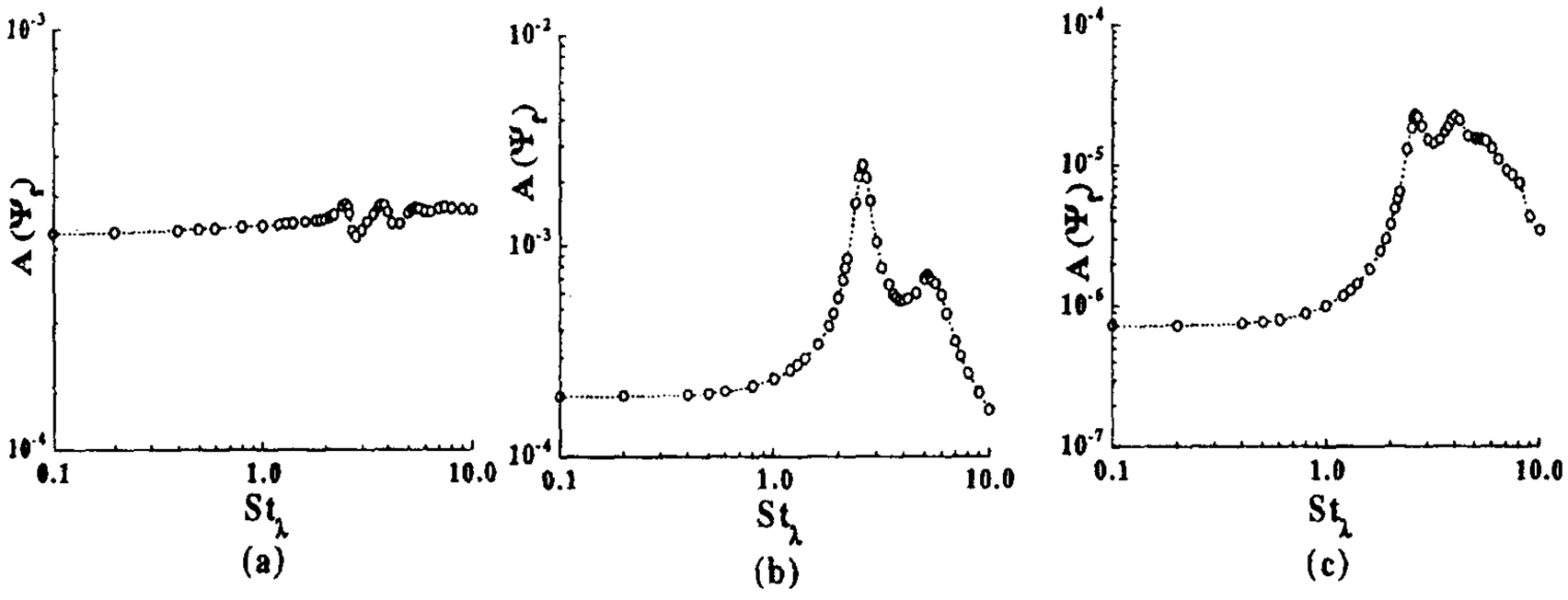

Figure 3.3 Amplitude of the fluctuating part of meridional streaming, $A(\Psi_f)$, vs. St_λ. ε=2.0, Re=1000. The radial location is r=0.5, and vertical locations are: (a) z/Ar=0.98; (b) z/Ar=0.5; (c) z/Ar=0.02.

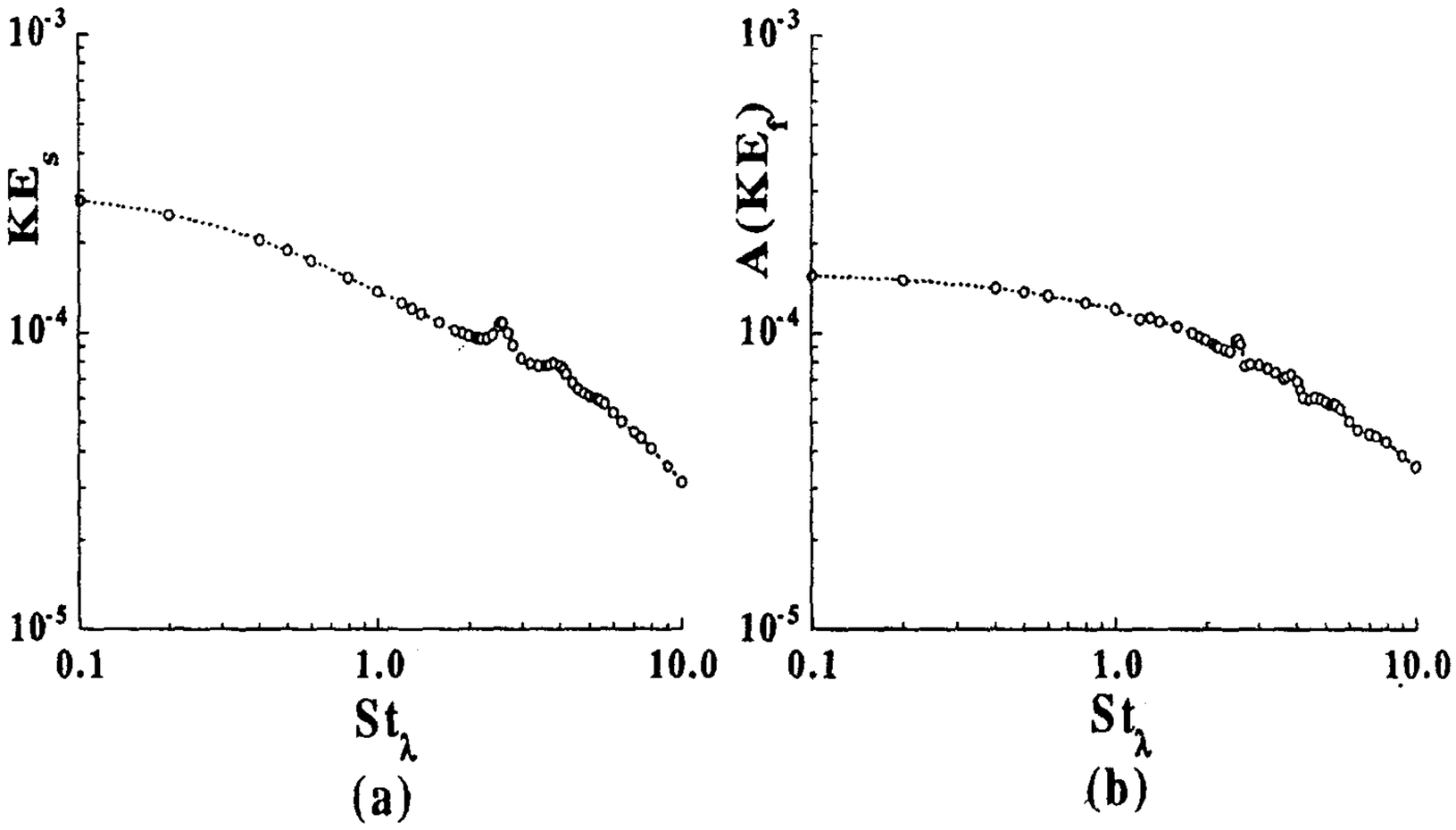

Figure 3.4 Kinetic energies of meridional flow vs. St_λ. (a) steady part; (b) fluctuating part. ε=2.0, Re=1000.

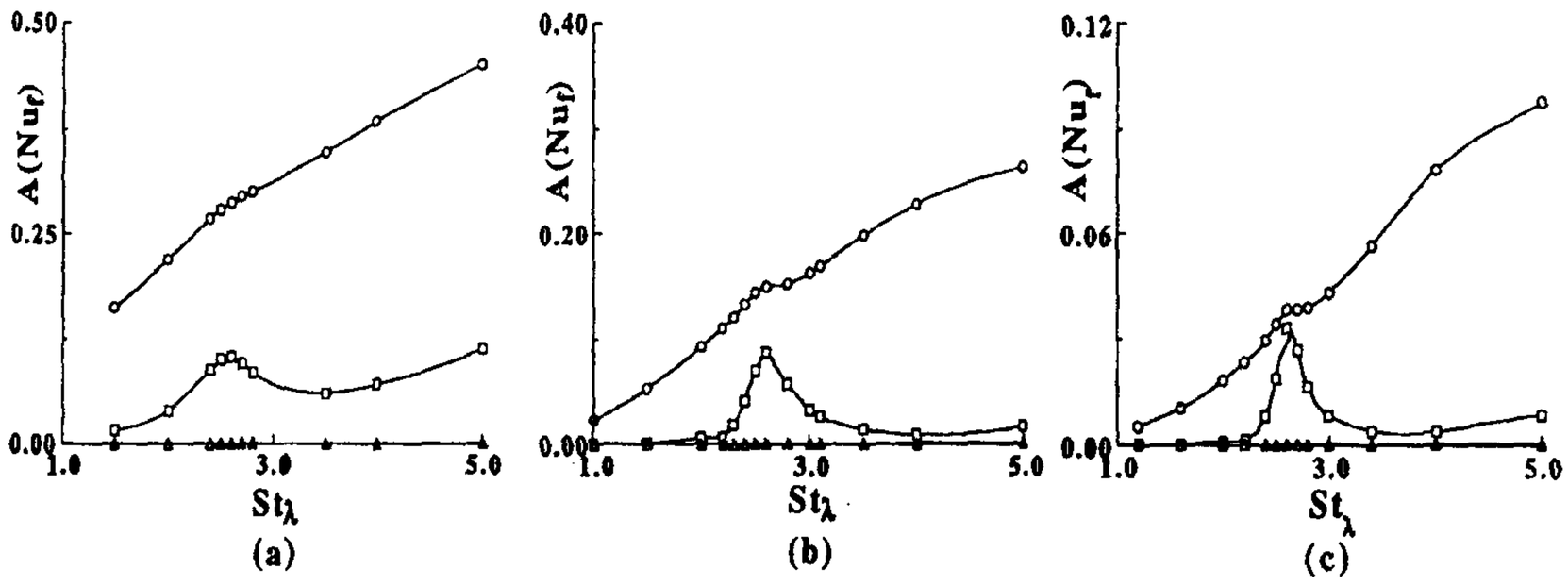

Figure 3.5 Amplitude of fluctuating part of the Nusselt number, $A(Nu_f)$ vs. St_λ. The radial location is r=0.5, and vertical locations are : ○ , z/Ar=0.98; □ , z/Ar=0.5; △ , z/Ar=0.02. Re=1000.

(a) St=0.5; (b) St=1.0; (c) St=2.0.

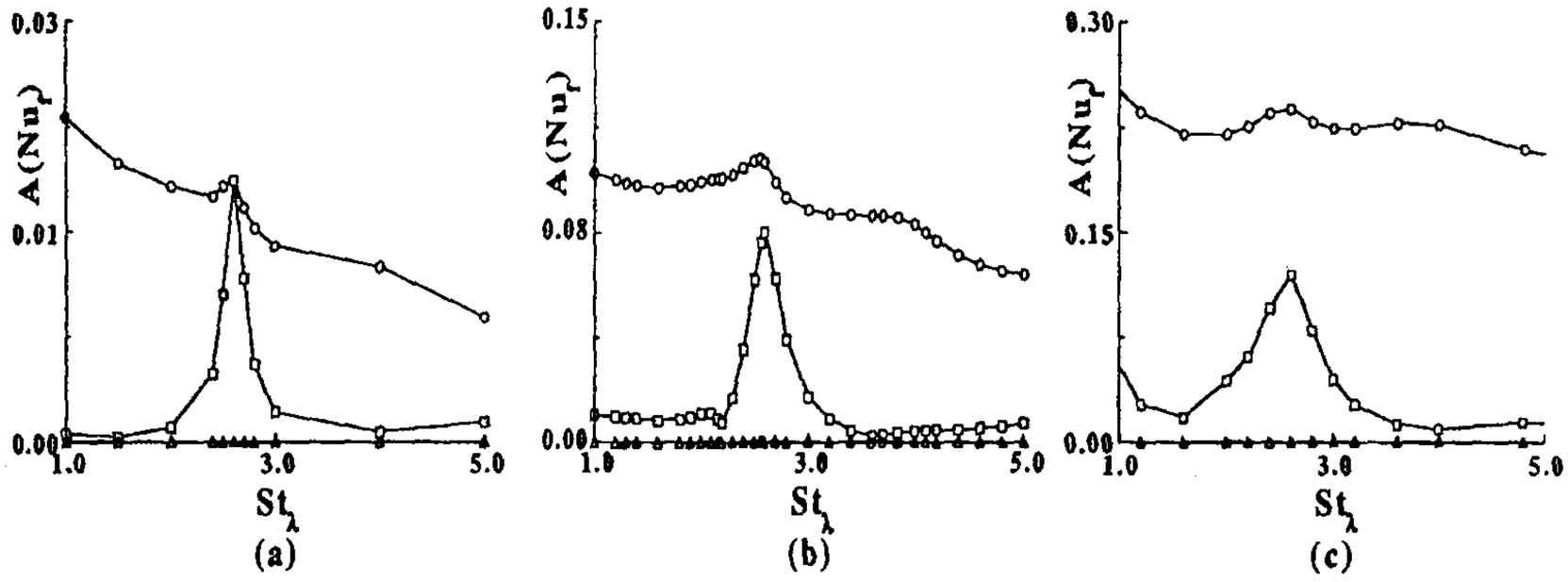

Figure 3.6 Amplitude of fluctuating part of the Nusselt number, $A(Nu_f)$ vs. St_λ. The radial location is r=0.5, and vertical locations are : ○ , z/Ar=0.98; □ , z/Ar=0.5; △ , z/Ar=0.02. Re=1000.

(a) ε=1.0, (b) ε=2.0, (c) ε=4.0.

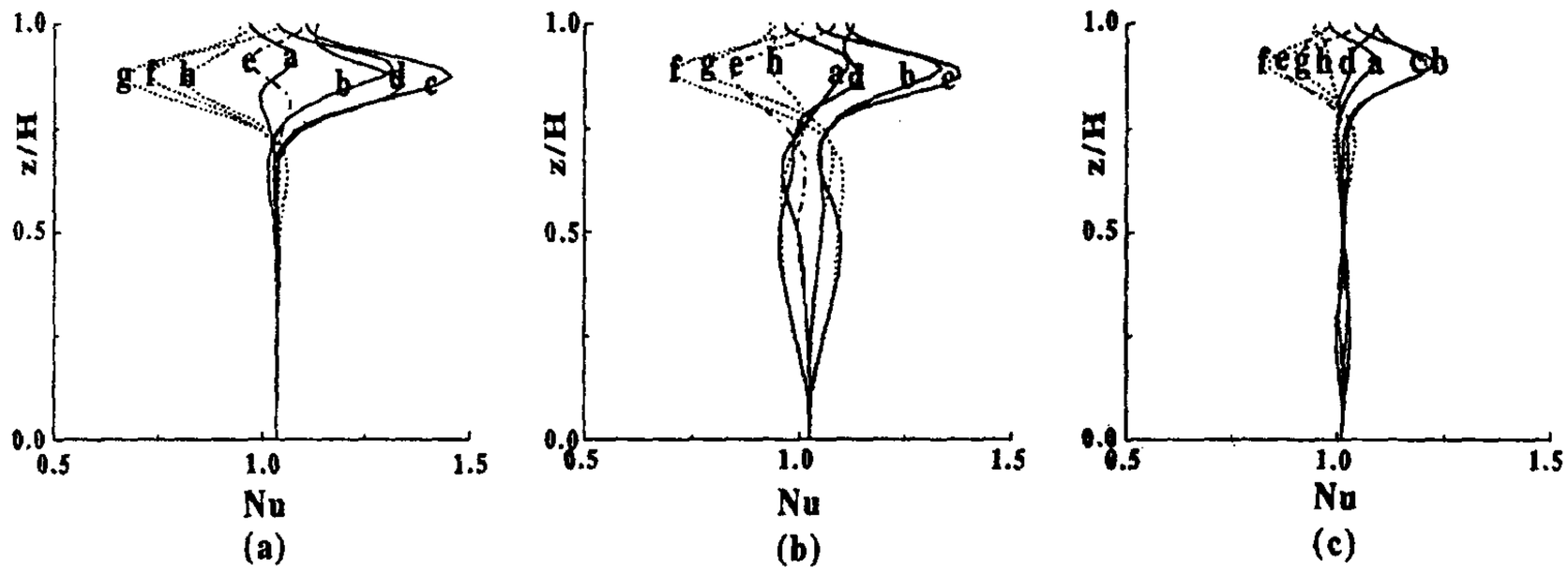

Figure 3.7 Vertical profiles of the Nusselt number Nu, over a half cycle of the top disk oscillation. Conditions are Re=1000, ε=2.0. Times(λt) for the curves are : a, 0; b, π/8; c, π/4; d, 3π/8; e, π/2; f, 5π/8; g, 3π/4; h, 7π/8; i, π.

(a) St_λ=2.0, (b) St_λ=2.6, (c) St_λ=3.0.

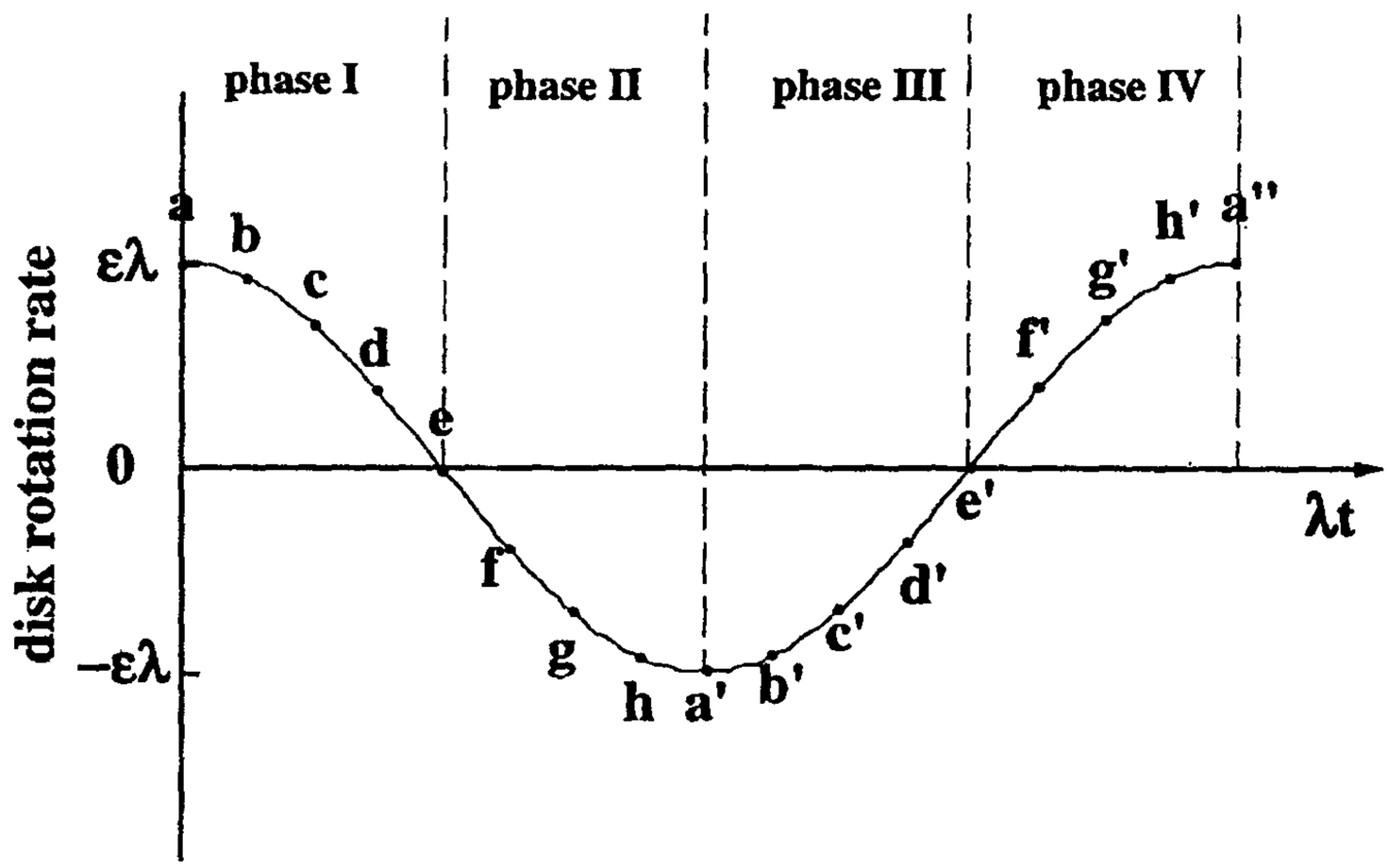

Figure 3.8 Evolution of the angular velocity of the top disk.

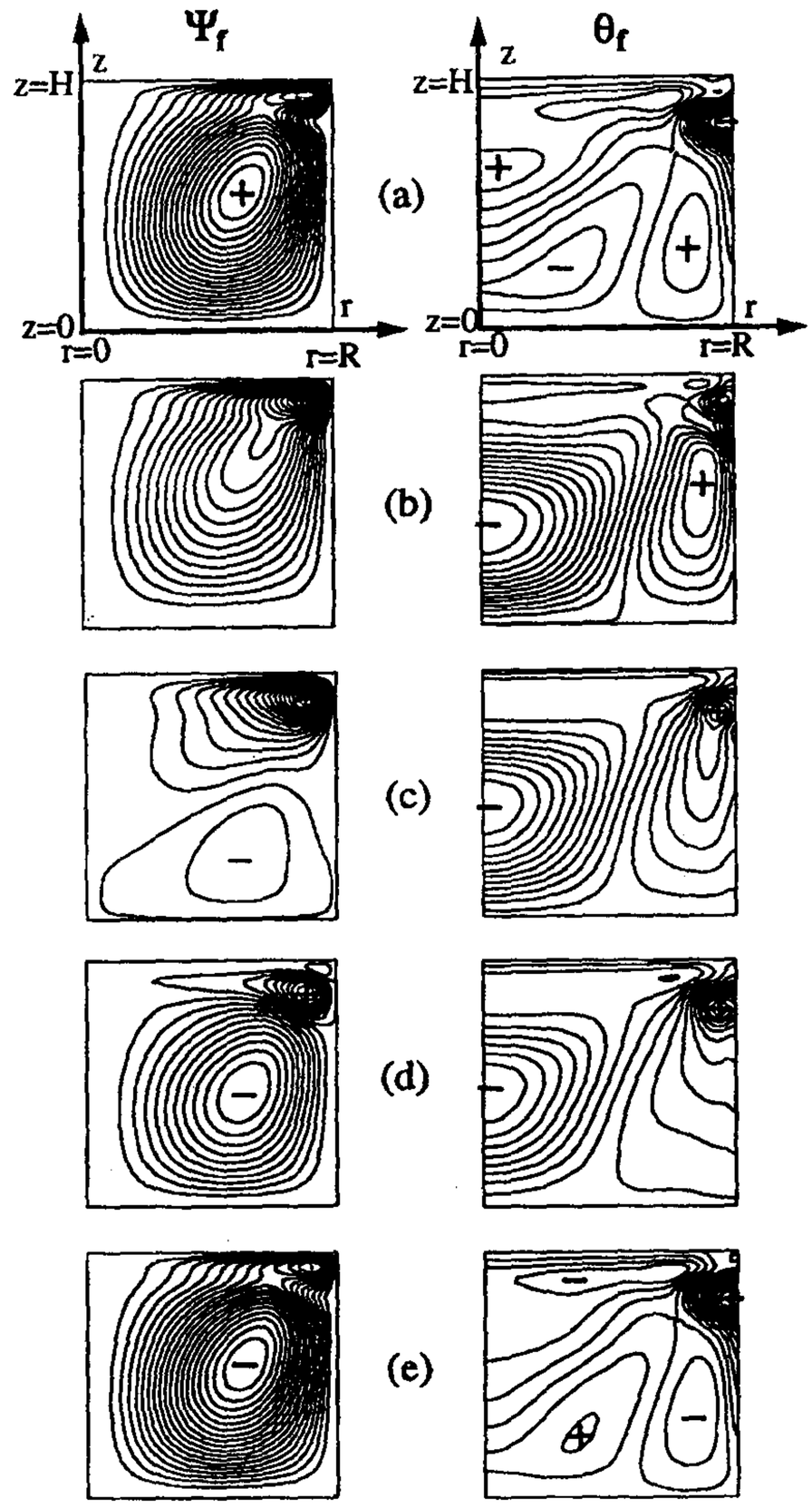

Figure 3.9 Plots of meridional stream function Ψ_f for the fluctuating meridional flow (u_f, w_f), and fluctuating temperature θ_f , under resonance condition, i.e., $St_\lambda=St_{re}=2.6$. Times for the frames are (a) $\lambda t=0$, (b) $\lambda t=\pi/8$, (c) $\lambda t=\pi/4$, (d) $\lambda t=3\pi/8$, (e) $\lambda t=\pi/2$, (f) $\lambda t=5\pi/8$, (g) $\lambda t=3\pi/4$, (h) $\lambda t=7\pi/8$, (i) $\lambda t=\pi$. Re=1000, ε=2.4.

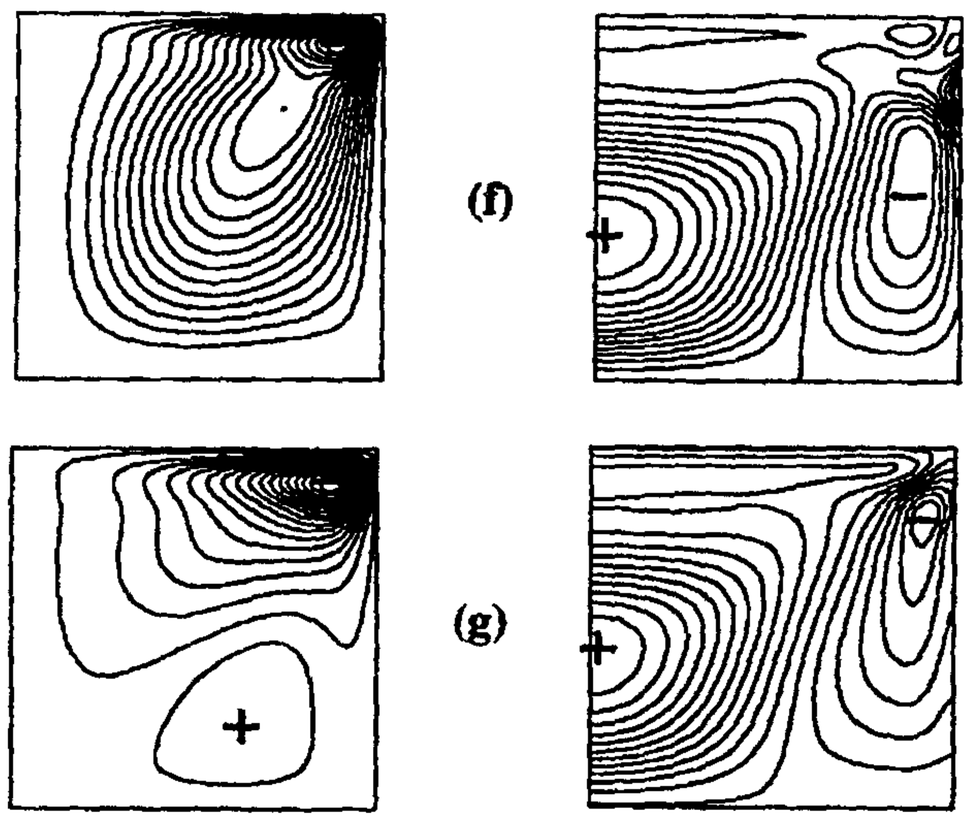

Figure 3.9 (Continued)

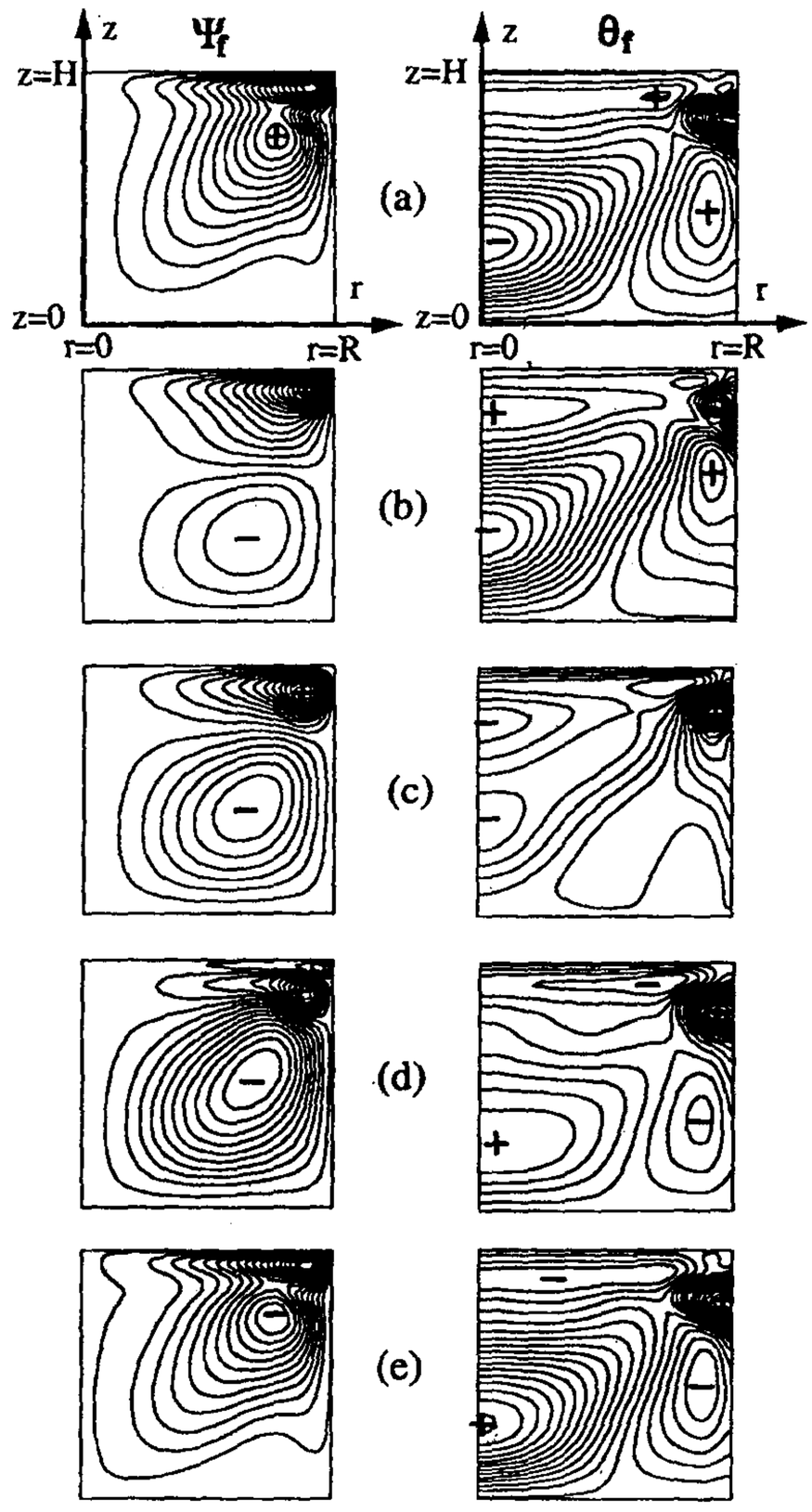

Figure 3.10 Plots of meridional stream function Ψ_f for the fluctuating meridional flow (u_f, w_f), and fluctuating temperature θ_f, under off-resonance condition, i.e., St_λ=3.0. Times for the frames are (a)λt=0, (b)λt=π/8, (c)λt=π/4, (d)λt=3π/8, (e)λt=π/2. Re=1000, ε=2.4.

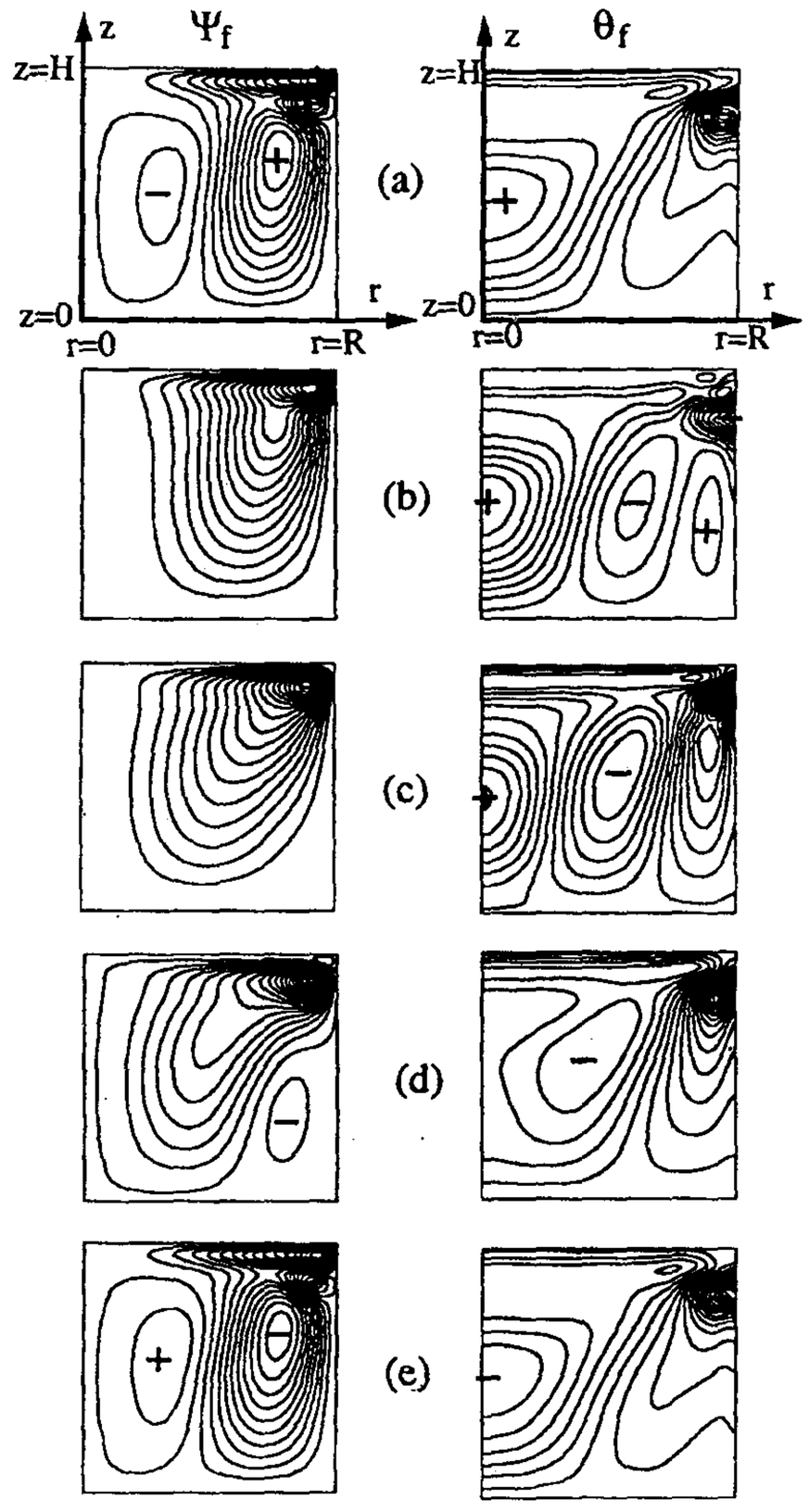

Figure 3.11 Plots of meridional stream function Ψ_f for the fluctuating meridional flow (u_f, w_f), and fluctuating temperature θ_f , under off-resonance condition, i.e., St_λ=2.2. Times for the frames are (a)λt=0, (b)λt=π/8, (c)λt=π/4, (d)λt=3π/8, (e)λt=π/2. Re=1000, ε=2.4.

제 12 절

Axisymmetric inertial oscillation in a rotating cylindrical container

(회전하는 원통 용기내에서의 축대칭 관성진동)

요 약 문

유체로 채워진 회전하는 실린더내의 관성파를 수치적인 방법으로 연구하였다. 실린더는 중심축에 대하여 $\Omega_c = \Omega + \varepsilon\lambda\cos(\lambda t)$의 회전률로 회전한다. 유동장과 압력장을 구하기 위하여 축대칭 지배방정식에 대한 시간진행 유한체적법이 이용되었다. 본 수치 시뮬레이션의 목적은 윗벽과 아래벽 근처에 나타나는 요동하는 에크만-경계층 (Ekman boundary layer)의 펌핑작용에 의한 축대칭의 관성진동을 일으키는 것이다. 공진은 평균회전주파수에 대한 가진주파수의 다양한 비에 대하여 무차원 압력차 (Cp)와 무차원 운동에너지(Cke)의 진폭을 통하여 관찰되었으며, 가시화 되었다.

ABSTRACT

Inertial waves in a fluid-filled rotating cylinder, which oscillates about the central axis with rotation rate $\Omega_c = \Omega + \varepsilon\lambda\cos(\lambda t)$, are studied using a numerical method. A time-marching finite volume method of the axisymmetric governing equations is used to obtain the flows and pressure fields. The object of this numerical simulation is to excite axisymmetric inertial oscillations through the pumping action of the oscillatory Ekman boundary layer near the top and bottom disk. Resonances are detected via the amplitude of non-dimensional pressure difference (Cp) and of non-dimensional kinetic energy (Cke) for various ratios of the excitation to the mean rotation frequency (Ω/λ) and are visualized.

NOMENCLATURE

A = aspect ratio of the cylinder [$\equiv \frac{H}{R}$]

A( ) = amplitude of the fluctuating component

C_{ke}=kinetic energy coefficient

C_T = torque coefficient

C_p= pressure coefficient

E = Ekman number [$\equiv \frac{\nu}{H^2 \Omega}$]

H = cylindrical container height

J = Bessel function

N= Brunt-Vaisala frequency [$\equiv \left(\frac{\alpha g \triangle T}{H} \right)^{\frac{1}{2}}$]

Nu = Nusselt number

Pr=Prandtl number [$\equiv \frac{\mu / \rho_B}{k/(\rho_B c_p)}$]

R = cylindrical container radius

Re = rotational Reynolds number [$\equiv \frac{R^2 \Omega}{\nu}$]

S = Stokes layer thickness [$\equiv \left(\frac{2\nu}{\lambda} \right)^{\frac{1}{2}}$]

St_λ = stratification number

T = torque on the disk (in Chp.2) or temperature (in Chp.3)

T_B = temperature at the bottom disk

T_T = temperature at the top disk

c_p = specific heat

k = thermal conductivity

(r, ϕ, z) = cylindrical coordinates

(u, v, w) = velocity components

(u_f, w_f) = unsteady fluctuating parts of meridional flows

(u_s, w_s) = steady parts of meridional flows

GREEK SYMBOLS

Ω = mean rotation speed

$e\varepsilon$ = non-dimensional amplitude of oscillation

δ_s = non-dimensional Stokes layer thickness [$\equiv (2\nu/\lambda)^{1/2}/H$]

δ_E = non-dimensional Ekman layer thickness [$\equiv (2\nu/\Omega)^{1/2}/H$]

η_S = axial coordinate scaled by the Stokes layer thickness [$\equiv (H-z)/(2\nu/\lambda)^{1/2}$]

η_E = axial coordinate scaled by the Ekman layer thickness [$\equiv (H-z)/(2\nu/\Omega)^{1/2}$]

λ = torsional-oscillating frequency

μ = viscosity coefficient

ν = kinematic viscosity

θ = nondimensional temperature [$\equiv \frac{T-T_B}{\triangle T}$]

ρ = density

σ_{mn} = eigen-frequency

τ_t = spin-up time [$\equiv E^{-\frac{1}{2}}\ \Omega^{-1}$ for $\varepsilon > O(1)$, ($\equiv E^{-\frac{1}{2}}\ \Omega^{-1}\ \varepsilon^{-1}$ for $\varepsilon < O(1)$)]

Ψ = meridional streamfunction

ξ_{mn} = zeros of the first order Bessel function $J_1(\xi)$

SUBSCRIPTS

s = cycle-averaged component

f = unsteady fluctuating component

m = the number of waves or cells in the radial direction

n = the number of waves or cells in the axial direction

INTRODUCTION

When the fluid is in steady-state rigid-body rotation with uniform rotation rate Ω, inertial waves can be excited by applying a disturbance to the rotating fluid. In order for the inertial waves to be generated, many methods are used up to now. Of present concern is the case when the cylinder rotation rate includes a small-amplitude, synusoidally-varying oscillatory component, i.e., $\Omega + \varepsilon\lambda\cos(\lambda t)$.

In this case, a wide ranging , systemically-organized turntable experiment was conducted by Aldridge(1977), using a similar method of measuring perturbation pressure differences. The purpose was to assert the existence of axisymmetric inertial oscillations. The experimental observations were centered on monitory the rapid increase of perturbation pressure difference $\triangle$p over a broad range of the frequency ratio Ω/ω. Clearly, as the externally-specified forcing frequency w approaches the inertial oscillation frequency of the system, a sharp increases in pressure difference $\triangle$p is manifested. The experimental results of Aldredge(1977) demonstrated the the expected increases in $\triangle$p near the resonance frequency. In practical terms knowledge of the values of resonance frequencies is essentially in the design and operation of height-speed rotating fluid machinery. Large increases in perturbation pressure near the resonance conditions could lead to violent system vibrations and severely undermine the performance of fluid-containing high-speed rotating devices [Kim & Hyun, 1997].

As the classical treatise demonstrated [Greenspan,1968], the restoring forces due to Coliolis accreration give rise to inertial oscillations in the rotating fluid. In the present context, the fluid system is excited by the externally-controllable mechanical oscillation of the cylinder. Therefore, fundamental consideration leads to the possibility of resonance if the frequency of the cylinder oscillation and the frequency of the system are related. Under resonance conditions, the fluid motions are amplified.

In inviscid perturbed fluids in rotation, the equations are hyperbolic in the range of frequency ratio, $\Omega/\lambda > 0.5$, giving rise to the oscillations implying the disturbances originating at boundary discontinuity will be transmitted without attenuation through the bulk of the fluid along conical characteristic surfaces inclined at $\sin^{-1}(\lambda/2\Omega)$ to the

rotation axis [McEwan, 1970; Greenspan, 1968]. Wood(1965) estimated the magnitude of the individual modes, establishing that the characteristics from the corners of the cylinder processing at a small angle to the rotation axis, provided they ultimately re-reflected upon themselves, were realized as discontinuities in velocity or in velocity gradient, depending upon the geometry of the reflection. These discontinuities are naturally smoothed out in the presence of viscosity by internal shear layers established along the characteristic surfaces. These were later experimentally observed by McEwan (1970).

Other investigations have been made using numerical solutions of the unsteady Navier-Stokes equations. Heuser at al.(1986), using a linealized axisymmetric equations, obtained the flow & pressure fields which were compared with theoretical predictions. Kim & Hyun (1997) considered the full, time dependent Nivier-Stokes equations. When the entire cylinder undergoes a spin-up process from rest with an impulsively-started rotation rate, numerical solutions were compared with Aldridge┌s experimental data, illustrated the change in eigenfrequency with time, and classical inviscid theory.

In the present paper, numerical solutions to the governing full Navier-Stokes equations will be considered. The comprehensive numerical solutions will have to verify the inertial oscillation frequencies, which had been measured in the experiments [Aldridge, 1977; Greenspan, 1968] and predicted by the inviscid theory [Greenspan, 1968]. A more advantage of the present numerical results lies in the breadth and depth of the available flow data. And, the details of flow over a cycle will be thoroughly analyzed. Emphasis will be placed on obtaining a physical interpretation of the nature of resonance phenomenon.

The numerical model

As shown in Fig.4.1, an incompressible fluid of constant density ρ fills completely a cylindrical container. Computational conditions are that the aspect ratio A(=H/R) is 2, the half angular displacement ε is 3° and the Ekman number E(=ν/H^{2}Ω) is $6.25\times 10^{-6}\leq E\leq 6.25\times 10^{-5}$. The fluid is considered in lower half region of the cylinder. Denoting the velocity components (u,v,w) for rotating cylindrical coordinates (r, ϕ,z), which rotate with angular frequency Ω about the axis, the rotating fluid motion is governed by the axisymmetric, time-dependent, Navier-Stokes equations:

$$\frac{\partial u}{\partial t}=-\frac{1}{r}\frac{\partial}{\partial r}(ruu)-\frac{\partial}{\partial z}(uw)+\frac{v^2}{r}+2\Omega v-\frac{1}{\rho}\frac{\partial p}{\partial r}+\nu\left[\frac{\partial}{\partial r}\frac{1}{r}\frac{\partial}{\partial r}(ru)+\frac{\partial^2 u}{\partial z^2}\right] \tag{4.1}$$

$$\frac{\partial v}{\partial t}=-\frac{1}{r}\frac{\partial}{\partial r}(ruv)-\frac{\partial}{\partial z}(vw)-\frac{uv}{r}-2\Omega u+\nu\left[\frac{\partial}{\partial r}\frac{1}{r}\frac{\partial}{\partial r}(rv)+\frac{\partial^2 v}{\partial z^2}\right] \tag{4.2}$$

$$\frac{\partial w}{\partial t}=-\frac{1}{r}\frac{\partial}{\partial r}(ruw)-\frac{\partial}{\partial z}(uw)-\frac{1}{\rho}\frac{\partial p}{\partial z}+\nu\left[\frac{1}{r}\frac{\partial}{\partial r}\left(r\frac{\partial w}{\partial r}\right)+\frac{\partial^2 w}{\partial z^2}\right] \tag{4.3}$$

$$\frac{1}{r}\frac{\partial}{\partial r}(ru)+\frac{\partial w}{\partial z}=0 \tag{4.4}$$

At the initial state, the fluid is at rigid-body rotation:

$$u = w = v = 0 \qquad \text{at } t = 0. \tag{4.5}$$

All computations were started from an initially solid rotation state, and at time zero a sinusoidal perturbation is imposed on the cylinder. The thrust of the present effort lies in the large-time, quasi-steady, periodic behavior. In accordance with the problem statement, the boundary conditions are

$$u = w = 0,\ v=\varepsilon\lambda R\cos(\lambda t) \qquad \text{at } r = R, \tag{4.6}$$

$$u = w = 0,\ v=\varepsilon\lambda r\cos(\lambda t) \qquad \text{at } z = 0, \tag{4.7}$$

$$\frac{\partial u}{\partial z} = \frac{\partial v}{\partial z} = w = 0 \qquad \text{at } z=H/2. \tag{4.8}$$

The amplitude of the perturbation, $\varepsilon\lambda$ is specified by the half angular displacement, ε, and the perturbation frequency, λ.

The above system of equations is solved by employing a finite-volume method based in the SIMPLER algorithm (Patankar, 1980). The governing equations were descretized on a straggered grid. Spacial differencing schemes of a second-order accuracing were adopted for the equation terms. A central differencing was used for the diffusion terms, and a recently-modified version of the QUICK scheme was utilized for calculating the nonlinear convective terms [Hayase et al., 1992]

For most computations, the mesh network was typically (80X80) in the (r-z) axial half plane, and Δt was chosen such that one oscillating cycle consisted of $4096(=2^{12})$ time steps. The present grid resolution was adequate to delineate the oscillating boundary-layer structure. To resolve these thin boundary layers adjacent to the solid walls, grid stretching was implemented such that at least 5 grid points were located in the oscillating Ekman layer.

Time-dependent solutions were produced by executing a time-marching integration of the governing equations. Guided by the preceding studies on spin-up [Greenspan & Howard, 1963; Wedemeyer, 1964; Lim & Hyun, 1997], the transitory time tt to reach the quasi-steady periodic state is estimated as

$$\tau_t \sim E^{-1/2}\ \Omega^{-1}$$

in which $E(\equiv \frac{\nu}{\Omega H^2})$ is the Ekman number. In the present study, calculations continued up to a time level of nearly τ_t, at which the quasi-steady state was shown to have been established. And, the quasi-steady state was thought to have been established when the nondimensional values of the flow variables differ less than 10^{-5} over the interval of one cycle.

Result and discussion

First, we consider axisymmetric flows in a cylindrical container, filled with a inviscid, incompressible fluid with a mean rotation rate Ω. In this case, the eigen-frequency ratio and eigenfunction of the rotating fluid system are (Greenspan,1968)

$$\frac{\Omega}{\lambda}_{mn} = \frac{1}{2}\left[1+\frac{n^2\pi^2}{\xi^2{}_m Ar^2}\right]^{\frac{1}{2}}, \tag{4.8}$$

$$J_0\left(\xi_{mn}\frac{r}{R}\right)\cos\left(n\pi\frac{z}{H}\right) \tag{4.9}$$

where ξ_{mn} is the mth root of $J_1(\xi_{mn})$. The (m,n) pair is used to denote the axisymmetric inertial oscillations: m is the number of waves or cells in the radial direction while n is the number of waves or cells in the axial direction.

First, it is necessary to establish that the oscillation in the numerical solutions are indeed the inertial oscillations. For this purpose, the above classical solution for the inertial frequencies of an inviscid fluid in a state of rigid-body rotation at Ω provides a reference. At the eigenfrequency ratio specified by Eq.(4.8), in a bravery, numerical calculations are performed. At these theoretical eigenfrequency ratio $(\Omega/\lambda)_{mn}$, the meridional streamings, which correspond to the expected resonant motions at an instant when the cylindrical container experiences its greatest angular deceleration, of the nine modes (m,n), where the number of cells in the radial direction m=1, 2, 3 and the number of cells in the axial direction n=2, 4, 6, shown in Fig.4.2, only lower half region of the cylindrical container, agree well with inviscid prediction. The number of cells of present calculations are comparable to the inviscid fluid theorem. As inviscid predictions, each modes of inertial oscillation has cells in a whole region.

Fig.4.3 denotes time history of the reduced pressure difference at points (r,z)=(0,H/4) and (0,H/2), the total kinetic energy of meridional flow which is defined as:

$$C_{ke} = 4 \int_0^{Ar} \int_0^1 (u^2 + w^2) \cdot r \cdot dr \cdot dz.$$

Near the transitory time τ_t, flows reach the quasi-steady periodic state as shown in Fig.4.3. If the oscillatory Ekman layer on the lower disk and the Stokes layer on the sidewall is excepted, in the interior fluid region, the total kinetic energy will be conserved at the oscillatory steady-state ($>\tau_t$). In the interior fluid region, all azimuthal kinetic energy excepted for boundary layer fluid must be converted to the meridional kinetic energy over half cycle of the oscillatory frequency. Under off-resonance conditions, the meridional kinetic energy is less then resonance condition (see Fig.4.4). Oscillating values of total angular momentum of the fluid cylinder are confined within the oscillatory Ekman layer on the disk and Stokes layer on the sidewall. Because, with exception for viscous boundary layer, the conservation of angular momentum in the interior fluid must be satisfied.

In Fig.4.5, the non-dimensional pressure amplitude $A(C_p)$, which is nomalized by $\varepsilon R^2 \Omega^2$, vs. Ω/λ is plotted at the near resonance condition, i.e., the primary (1,2)mode which has the theoretical eigenfrequency $(\Omega/\lambda)_{1,2}=0.7886$. As close to the anticipated value $(\Omega/\lambda)_{1,2}=0.7886$, a sharp increase in $A(C_p)$ is detected as shown in Fig.4.5(a). These results serves to exemplify the fact that the system triggers inertial oscillations at selected values of Ω/λ.

In the concept of flow intensification under resonance, the kinetic energy of meridional flows, which are represented in non-dimensional form as C_{ke}, will become the evidence of resonance. Fig.4.5(b) shows amplitude of the non-dimensional kinetic energy, $A(C_{ke})$, with frequency ratio Ω/λ. As shown in

Fig.4.5(b), the peak is detected at $\Omega/\lambda \sim 0.789$, that is in close agreement with the previous reasoning based on inviscid analysis.

It is found that the bandwidth of frequency ratios Ω/λ, in which $A(C_p)$ and $A(C_{ke})$ show substantial increases, is very narrow at small Ekman number so that a rapid decay away from the resonance frequency is seen in Fig.4.5. As E increases, the bandwidth is widen that is evidence of viscosity effects.

Relationship between the boundary layer and the interior fluid is very important. These relationship will be explained by inviscid theory. For inviscid perturbed fluids in rotation, governing equations are hyperbolic in the range of frequency ratio, $\Omega/\lambda > 0.5$, as in Eq.(4.8), giving rise to the oscillations implying that disturbances originating at boundary discontinuities will be trans-mitted without attenuation through the bulk of the fluid along conical characteristic surfaces inclined at $\sin^{-1}\left(\frac{\lambda}{2\Omega}\right)$ to the axis :

$$\frac{r}{R} \pm \frac{1}{\sqrt{\left(\frac{2\Omega}{\lambda}\right)^2 - 1}} \frac{z}{H} = \text{constant} \qquad (4.10)$$

which emanate from the top and bottom corners of the cylinder, and across the continuation of these cones by reflected at the side, ends and axis of the cylinder.

Discontinuities may be interpreted in terms of a superposition of stationary internal waves, all having the same frequency but different wave lengths, and with their wave-fronts parallel to the characteristic cones. Discontinuities will, in abscance of modes, be realized as discontinuities in the velocity components and their gradients across the cones [Wood, 1965; Baines, 1967; Greenspan, 1968].

In real viscous fluid, these characteristics are made experimentally visible by the free shear layers along characteristic cones [McEwen, 1970]. Fig.4.6 shows these free shear layer with respect to the perturbation frequency ratio Ω/λ. In Fig.4.6 the instantaneous meridional flows and azimuthal velocities, in which the rigid-body rotating components of azimuthal velocity have been substracted, are chosen at maximum angular velocity and maximum deceleration rate of the cylinder to emphasize the structure of the free shear layers. Fig.4.7 shows the sine of the characteristic angle measured relative to the rotating axis, as a function of disturbance frequency. As Ω/λ increases, the characteristic angle approaches zero.

Before an internal convection flow to be induced by oscillatory Ekman layer entrainment, azimuthal velocities are developed during the time scale $O(\Omega^{-1})$ within Stokes layer. After several periods of the oscillatory rotating cylinder, interior fluid is

affected by oscillatory Ekman pumping mechanism. If when $\frac{2\Omega}{\lambda} \gtrsim 1$, in which inertial oscillations are possible, these oscillations will be developed by oscillatory Ekman pumping mechanism.

Sequential plots of instantaneous meridional streaming Ψ for the (2,1)mode are illustrated in Fig.4.8(A). At time (a), clockwise (CW) circulation cell is occupied in the interior fluid with exception for a small CCW cell on the bottom disk. As the rotation rate of the cylinder decreases, the CCW cell grows from the corner of bottom diak with the fixed angle, which is determined by the oscillation frequency ratio Ω/λ and is confined in the nerrow region, and fills most of the cylinder after a number of reflection [see (c), (d), (e) & (f) of Fig.4.8A]. In phase $\pi<\lambda t<2\pi$, a reverse process takes place.

Fig.4.8(B) shows sequential plots of azimuthal velocities under resonance condition. When the cylinder experiences maximum angular velocity, disturbed azimuthal velocities are divided into two parts: a plus (minus) value at the lower (upper) region. In sequential plots from (d) to (f), from the corner of the bottom disk, angular momentum is transferred to the interior fluid by oscillatory free shear layer. These free shear layer will be to connect two regions between viscous boundary layer and inviscid interior fluid.

Sequential plots of reduced pressure fields are illustrated in Fig.4.8(C). At the time experienced maximum angular velocity of cylinder, almost maximum pressure is detected at (r, z) = (0, Ar/2) over one cycle, it is indicated that the dimensionless pressure difference C_p have same phase with the oscillatory rotating cylinder under resonance condition. While, under off-resonance conditions, these phase difference of C_p will be larger.

Fig.5.9 shows exemplary plots of meridional streaming at critical value of the existence of inertial oscillation and very small disturbance frequency. At high frequency limit, i.e. $\Omega/\lambda=0.5$, meridional flows are confined within near oscillating disk and then interior flows are almost zero. In inviscid rotating fluid analysis, as Ω/λ approaches to 0.5, characteristic angle to the rotation axis approaches to $\pi/2$.

When Ω/λ is 0.5, disturbances originated from the bottom corners of the cylinder can not affect whole interior fluid. When Ω/λ is large value, propagation direction of disturbance is almost vertical. In order for disturbance to propagate to the whole interior region, a number of reflection are necessary. Because of energy loss due to a number of reflection, disturbances decay out after many reflections. Consequently, fluid within moderate range of radii is blinded to the disturbances originated from the bottom (or/and top) corners of the cylinder.

Conclusion

Numerical results of the governing time-dependent Navier-Stokes equations show to the existence of inertial oscillations at selected frequencies Ω/λ.

The presence of peak value of C_p and C_{ke} leads to the identification of the resonance frequency Ω/λ.

Flow visualizations of resonance modes and free shear layers at non-resonance conditions have been obtained based on the numerical data.

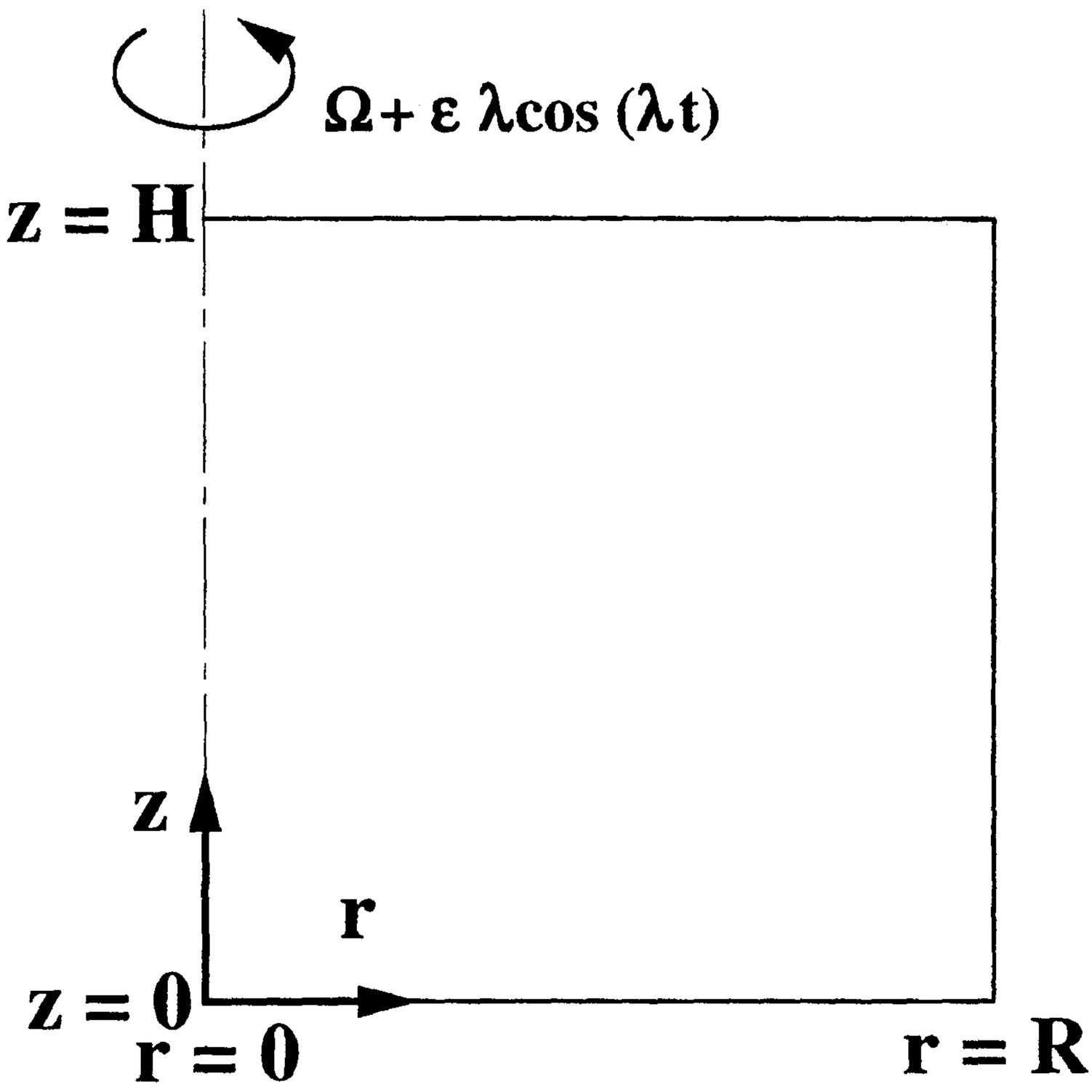

Figure 4.1 Flow geometry and coordinate system.

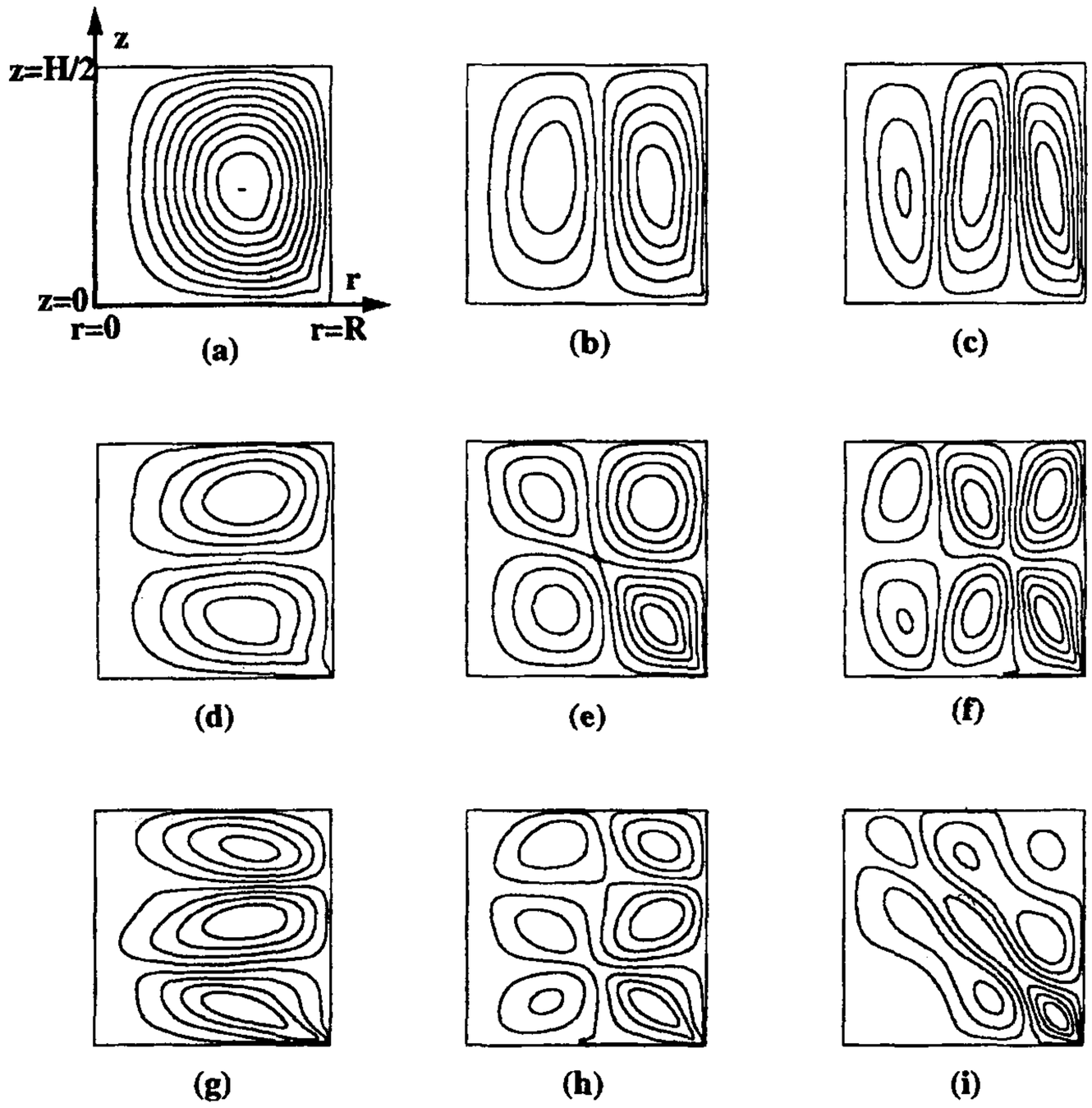

Figure 4.2 Exemplary plots of meridional stream function Ψ at eigen-frequencies given by Eq.(4.8): (a) $(\Omega/\lambda)_{1,2}=0.7886$, (b) $(\Omega/\lambda)_{2,2}=1.223$, (c) $(\Omega/\lambda)_{3,2}=1.695$, (d) $(\Omega/\lambda)_{1,4}=0.586$, (e) $(\Omega/\lambda)_{2,4}=0.749$, (f) $(\Omega/\lambda)_{3,4}=0.952$, (g) $(\Omega/\lambda)_{1,6}=0.540$, (h) $(\Omega/\lambda)_{2,6}=0.623$, (i) $(\Omega/\lambda)_{3,6}=0.736$.

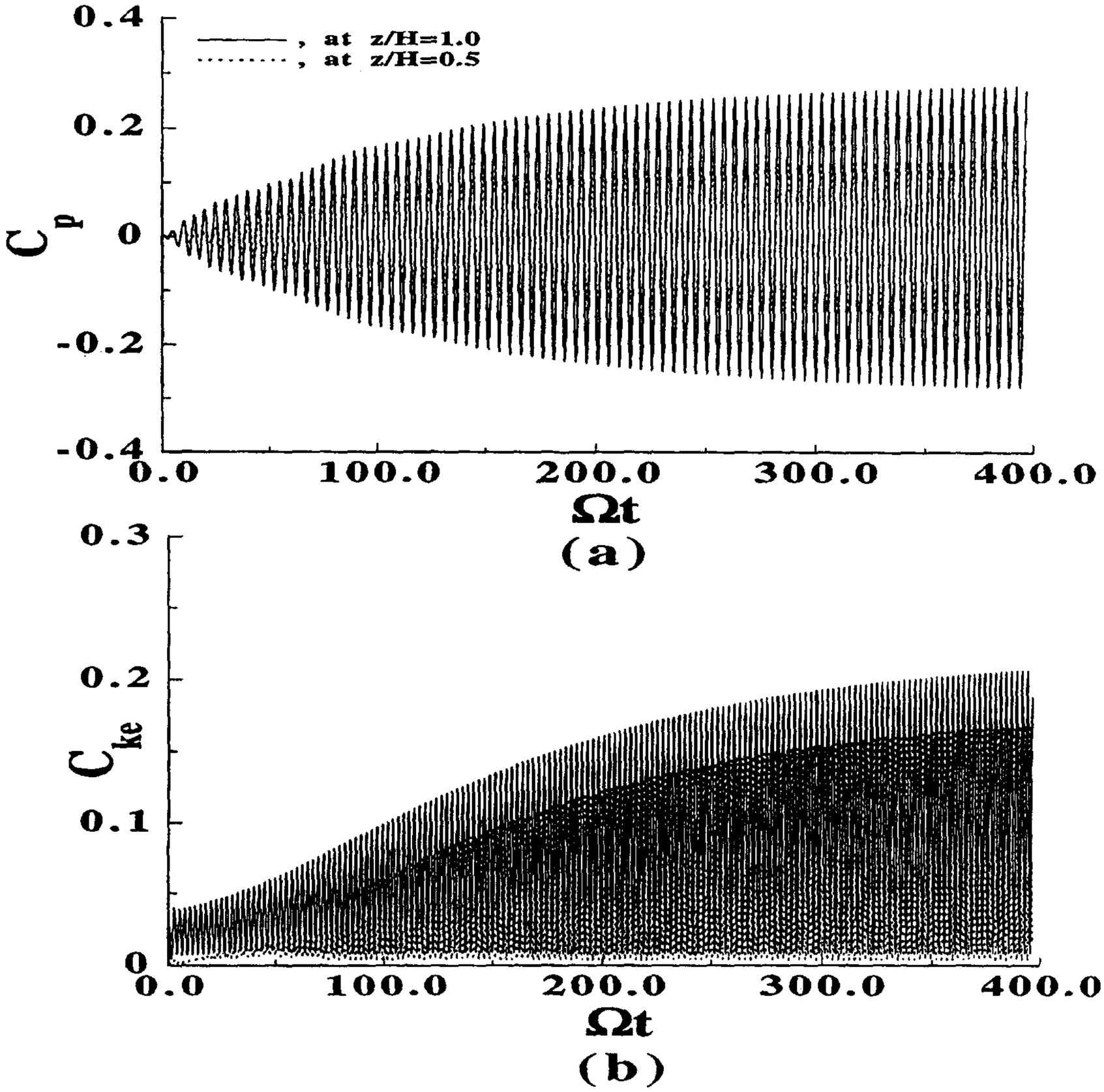

Figure 4.3 Time history of C_p & C_{ke} under resonance condition.

$E = 6.25 \times 10^{-6}$, Ar = 2.0, $\varepsilon = 1^{\circ}$, and $\Omega/\lambda = 0.789$.

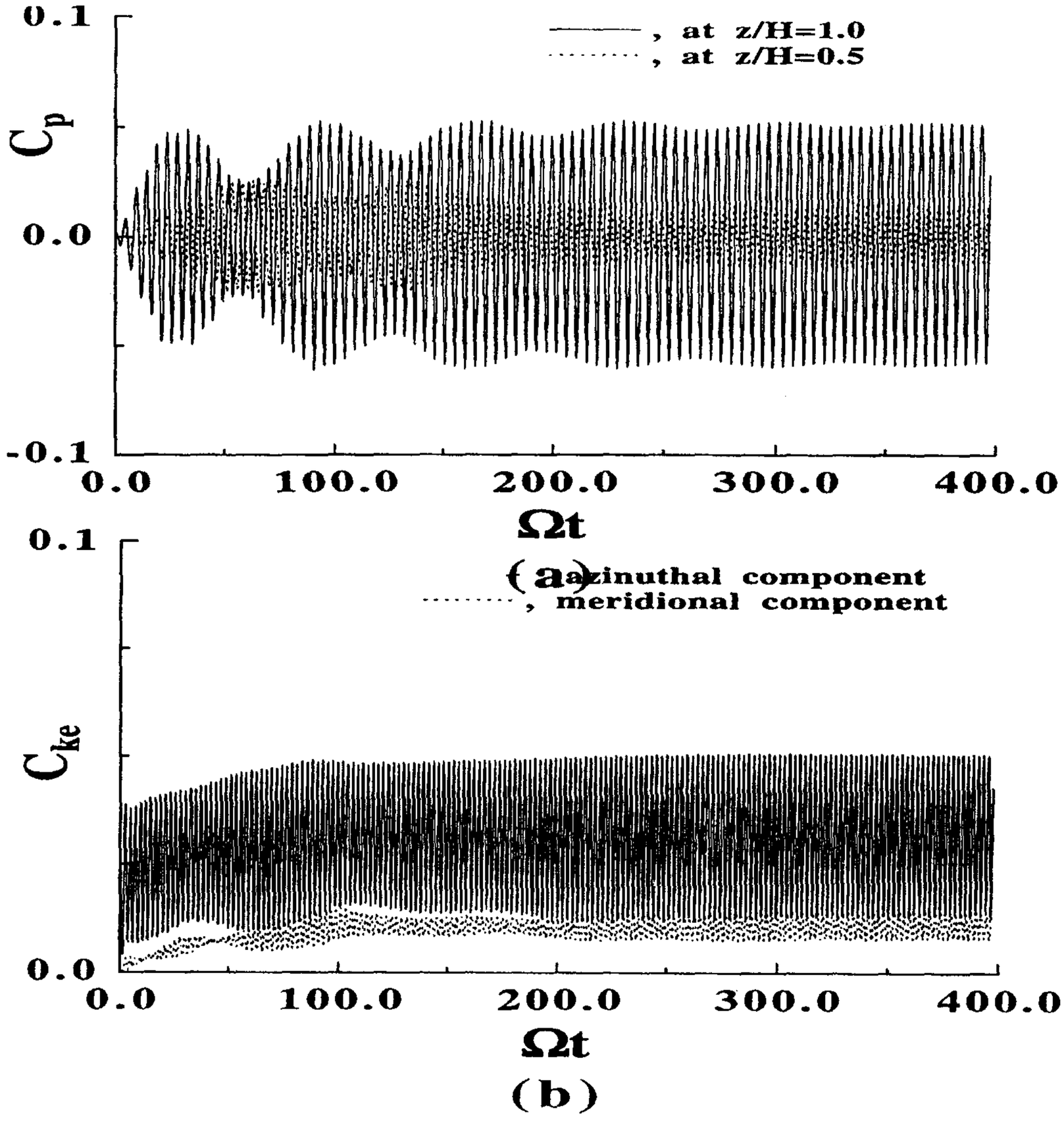

Figure 4.4 Time history of C_p & C_{ke} under off-resonance condition.

$E = 6.25 \times 10^{-6}$, Ar = 2.0, $\varepsilon = 3^{\circ}$ and $\Omega/\lambda = 0.736$

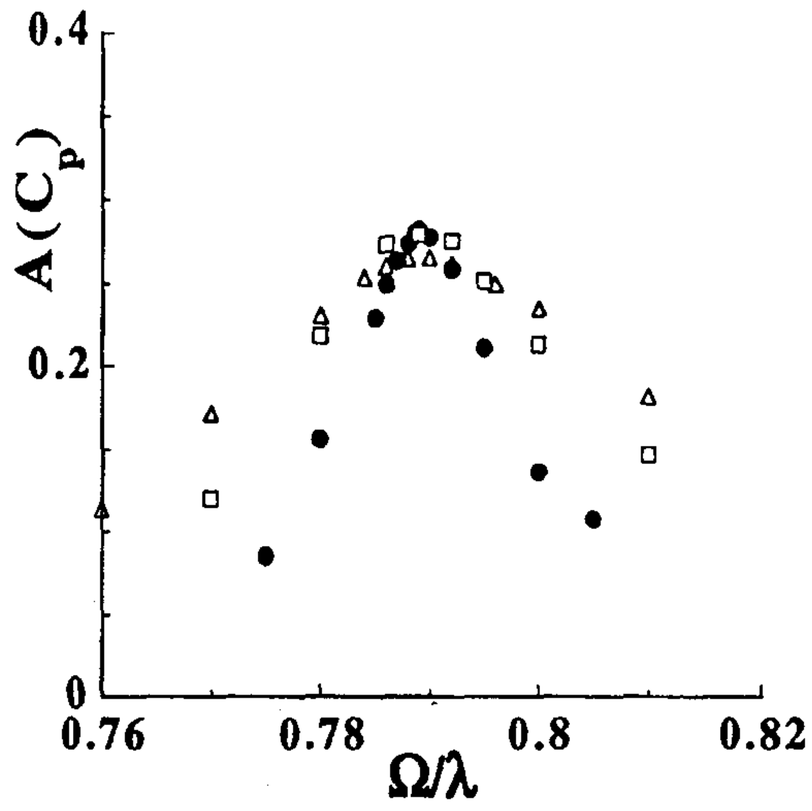

Figure 4.5 Behavior of $A(C_p)$ and $A(C_{ke})$ with Ω/λ at near resonance, i.e., (1,2)mode.

(a) $A(C_p)$ vs. Ω/λ, (b) $A(C_{ke})$ vs. Ω/λ.

○ , $E = 6.25 \times 10^{-6}$; □ , $E = 2.5 \times 10^{-5}$; △ , $E = 6.25 \times 10^{-5}$.

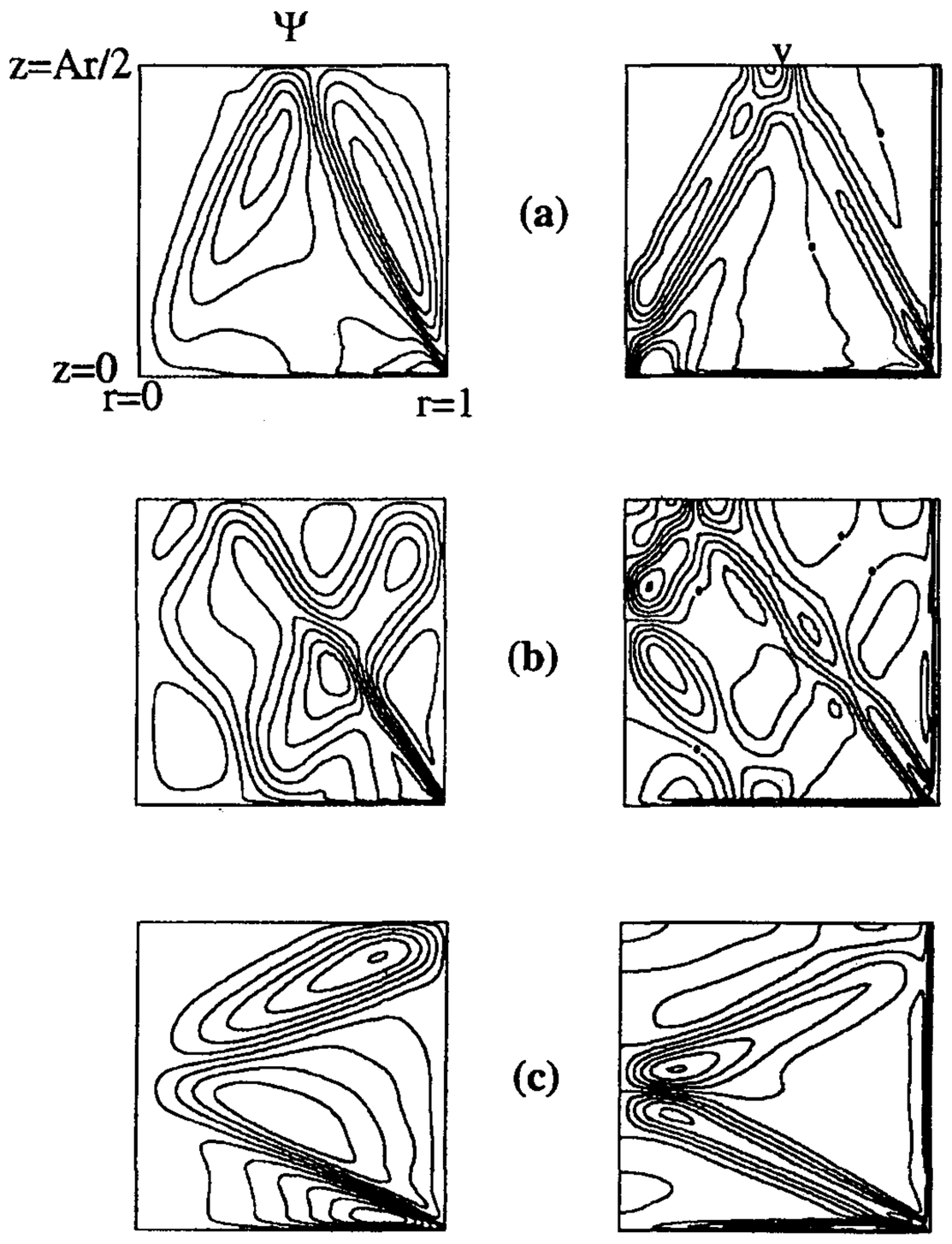

Figure 4.6 Left (right) column shows the meridional stream function, Ψ (the azimuthal velocity, v). (a) $\frac{\Omega}{\lambda}$=1.118, (b) $\frac{\Omega}{\lambda}$=0.902, (c) $\frac{\Omega}{\lambda}$=0.559.

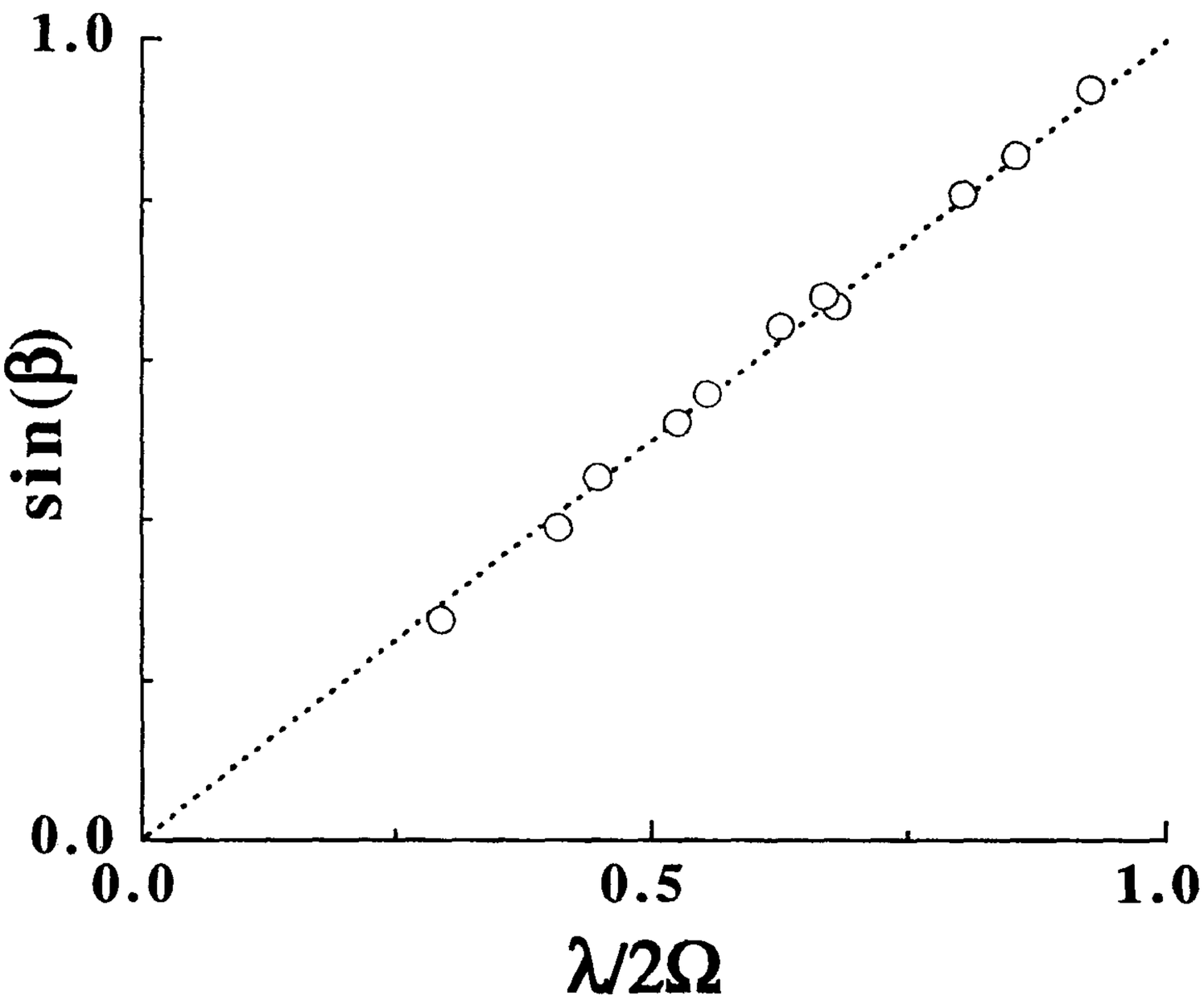

Figure 4.7 Characteristic cone angle β to axis.

——— , theoretical values; O , present results.

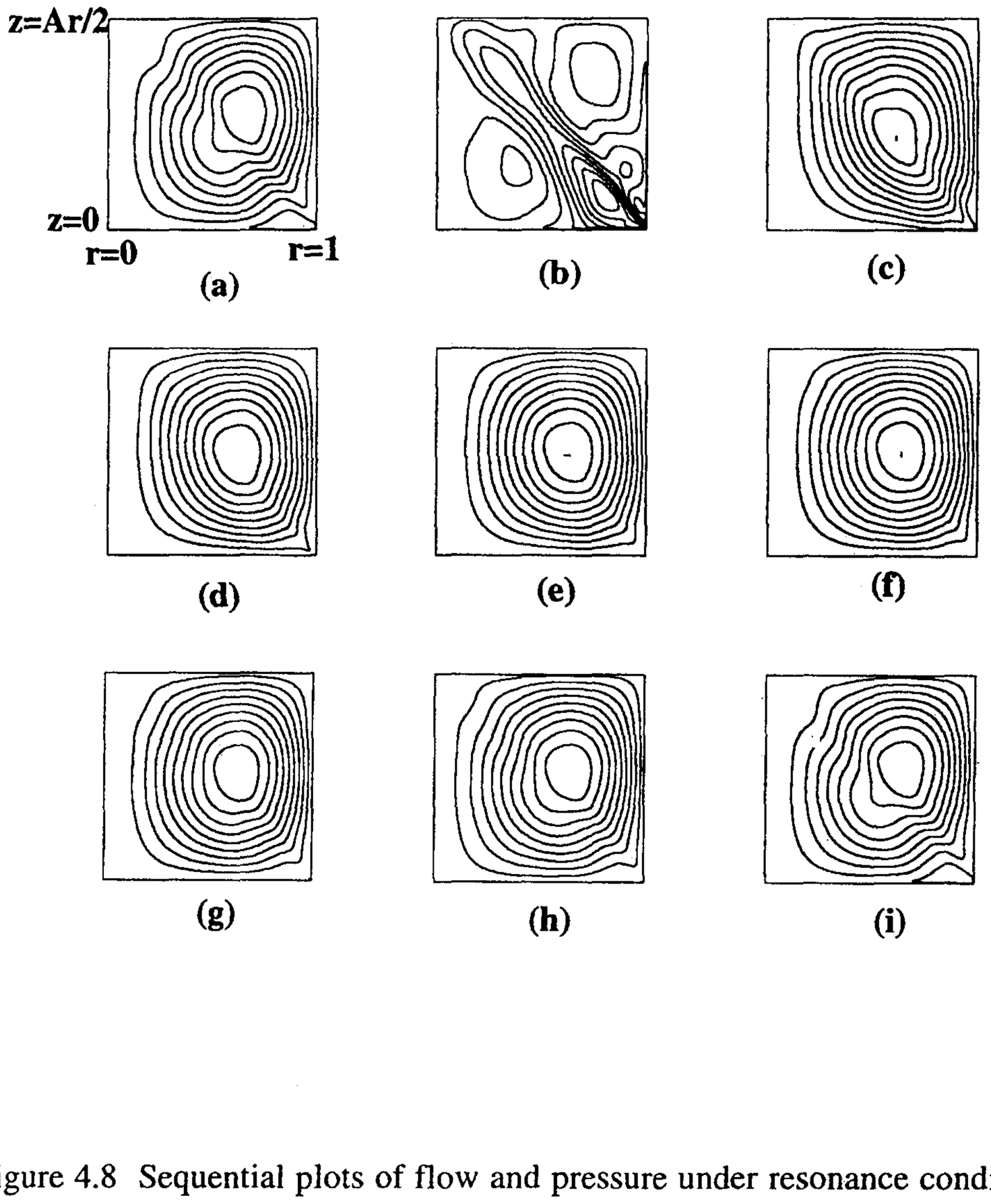

Figure 4.8 Sequential plots of flow and pressure under resonance condition. (A) meridional stream function Ψ, (B) azimuthal velocity v, (C) reduced pressure p.

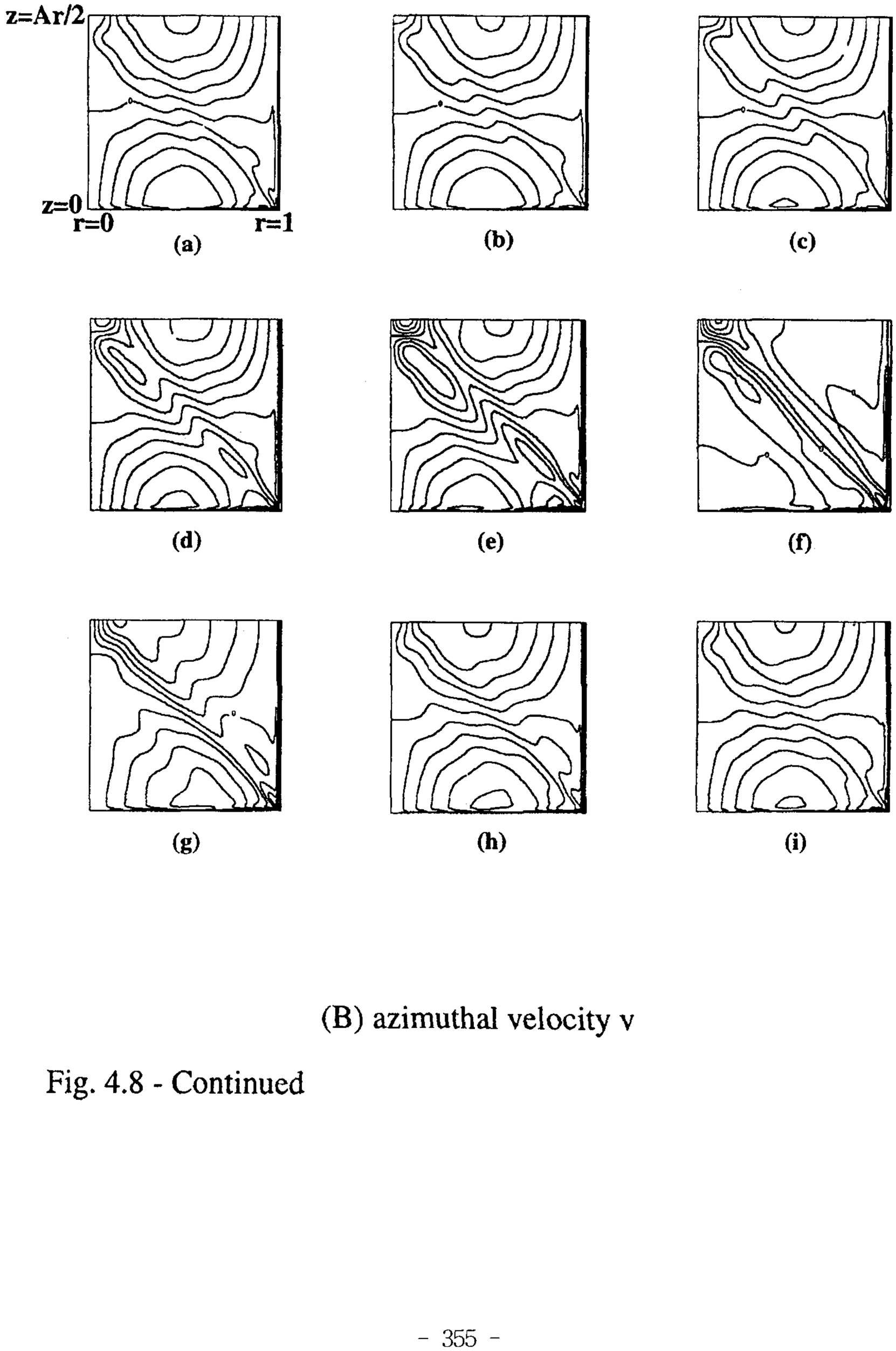

(B) azimuthal velocity v

Fig. 4.8 - Continued

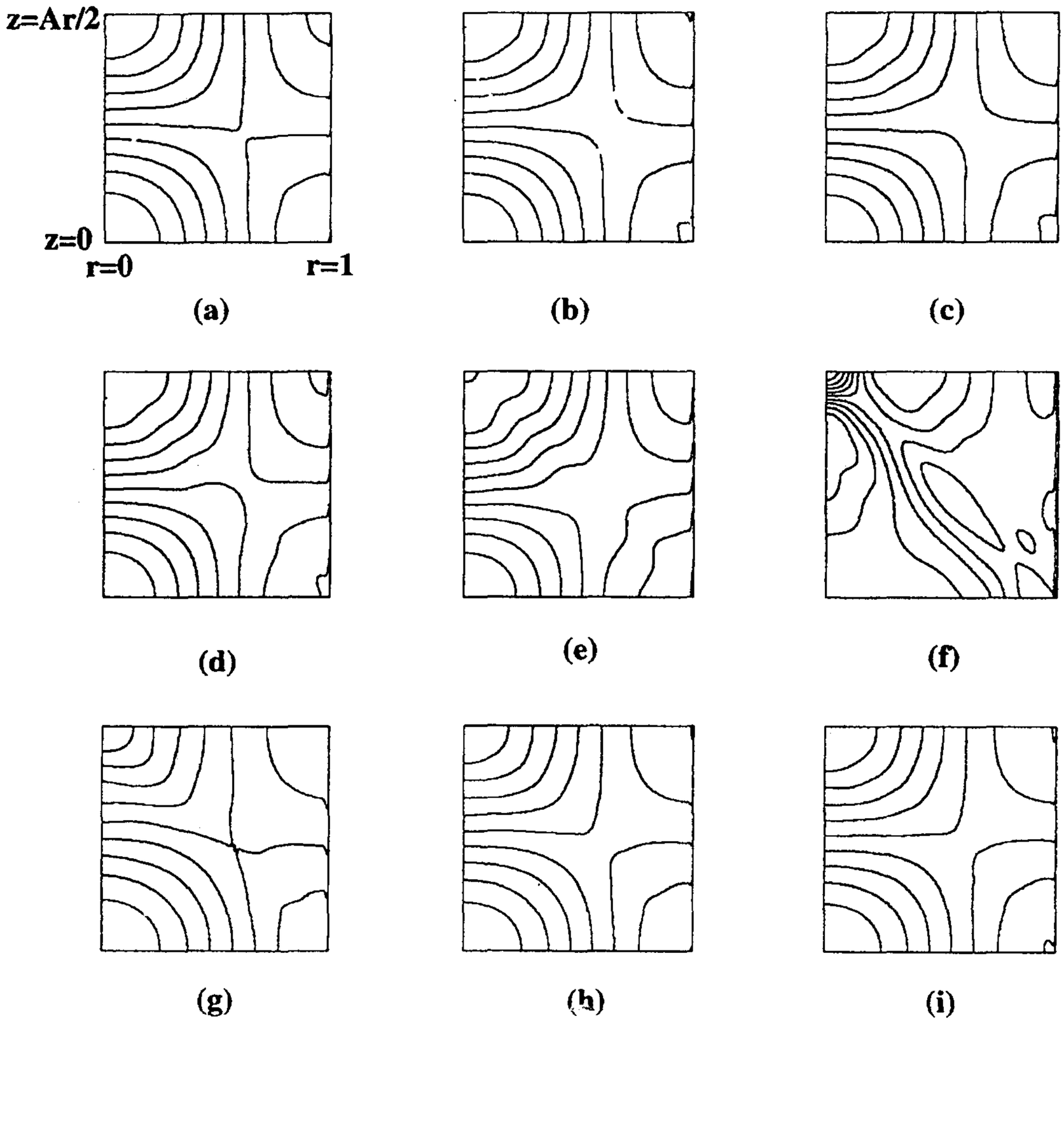

(C) reduced pressure p

Fig. 4.8 - Continued

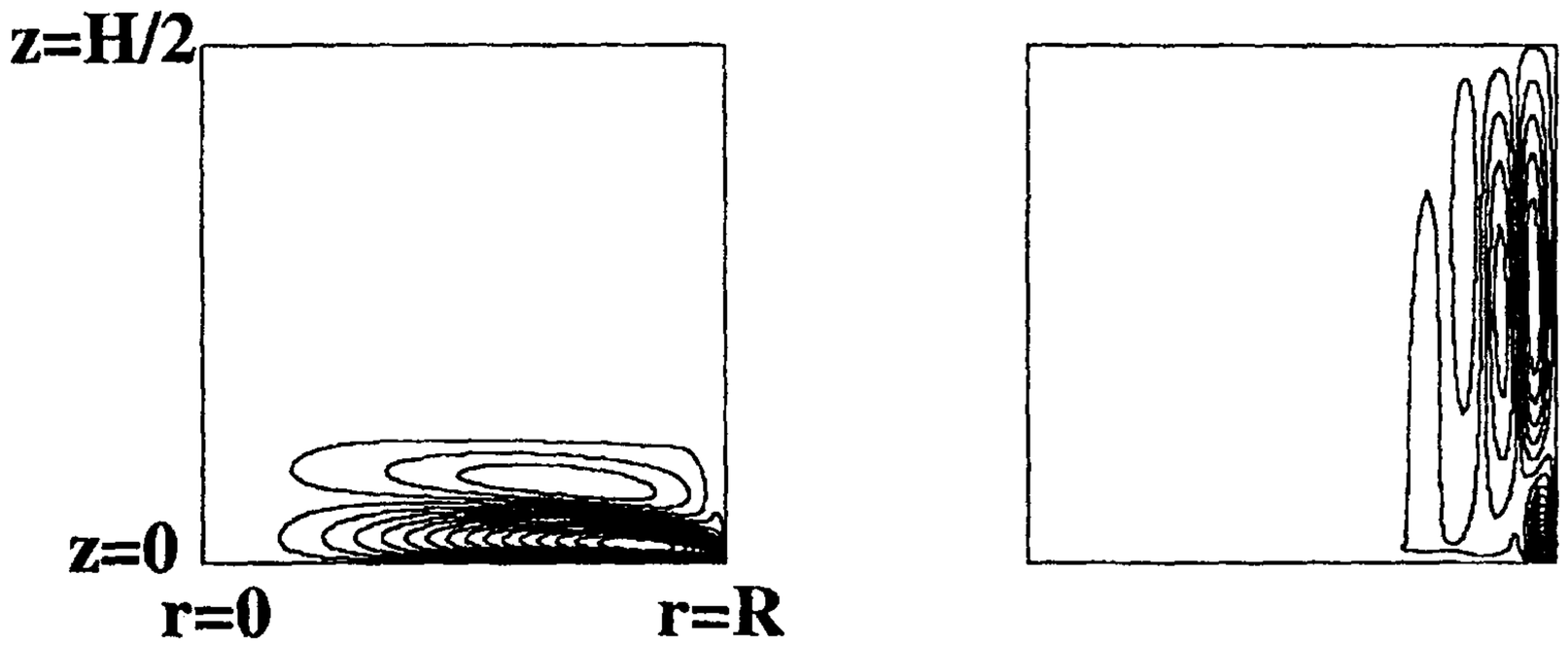

Figure 4.9 Plots of meridional stream function Ψ.
(a) $\frac{\Omega}{\lambda}$=0.5, (b) $\frac{\Omega}{\lambda}$=10.0.

제 13 장

Effect of aspect ratio on mass transfer from a rotating cup

(회전하는 컵으로부터의 물질전달에 관한 세장비의 효과)

요약문

참고문헌[1]의 후속 연구로서는 컵의 안 벽면으로부터의 물질 전달 특성에 대해서 수치적인 연구를 한다. 컵의 형상비(L/R)의 영향, 특히 형상비가 아주 작을 때와 아주 클 때에 대해서 논의하였다. 모든 형상비의 범위에서 컵 안의 유동장과 농도장에 대해서 수치적인 연구를 하였다. 작은 형상비에서(높이가 낮은 컵) 각속도는 밑 판 근처의 얇은 범위에서만 나타내었다. 대류 작용은 일반적으로 미약하였다. 큰 형상비에서(높이가 높은 컵) 내부 유동장은 주로 원통 벽면에 영향을 받는다. 밑 판은 전체 내부 유동에 미치는 영향이 작다. 속도 분포와 농도 구배를 나타내었다. 두 가지 농도조건에 대해서 밑 판에서의 국부 Sherwood 수(Sh)의 영향을 제시하였다. 수치 결과는 이전에 발표된 평균 Sh수에서의 경험식이 형상비의 많은 영역에서 유용한 근사식임을 밝혀주었다.

Abstract

As a sequel to Ref. [1], a numerical study is made of mass transfer characteristics from the interior wall of a rotating cup. The specific effect of the aspect ratio of the cup, L/R, is delineated, especially when L/R is either very small or very large. Over a range of L/R, numerical solutions portray the flow and concentration fields inside the cup. For small L/R (a shallow cup), the angular velocity is conspicuous only in a narrow layer adjacent to the base disk.

Convective activities are generally meager. For large L/R (a deep cup), the interior flow field is governed principally by the cylindrical sidewall. The influence of the base disk on the global interior flow pattern is minor. Profiles of the velocity and concentration distributions are exhibited. The behavior of the local Sherwood number Sh is depicted for two types of concentration conditions at the disk. The numerical results establish that the previously-reported empirical formula for the average Sh provides useful approximations over a broader range of L/R

1. Introduction

Ref. [1] reports on a numerical study of mass transfer characteris cup-like cylindrical vessel, which rotates about its central longitudinal was focused on the enhancement of transfer properties, caused by the rotation inner surface walls of the cup to the surrounding fluid. The numerical solut to the governing Navier-Stokes equations provided detailed data on the local number $\overline{Sh}$ as well as the average Sherwood number . The earlier experiment o by using a naphthalene sublimation technique, gave an empirically-construct for $\overline{Sh}$ as functions of Re and (L/R) in the range up to $Re \gtrsim O(10^3)$. In the Re denotes the rotational Reynolds number of the cup [$\equiv wR^2/\nu$], where w rotation rate of the cup, R the inner radius, and ν the kinematic viscosity L the height of the cup. It was shown that the numerical results of [1] for close agreement with the experimental findings of [2].

In this note, the methodologies of [1] are extended to explore the explicit impact of the aspect ratio (L/R) on the transfer properties. In [2], only values of (L/R) of order unity were considered. It is stressed that the transport characteristics are heavily influenced by the geometrical constraints, and the aspect ratio is a primal factor in determining the container shape. The purpose of this note is to examine the variations of Sh and Sh when (L/R) encompasses a wide range. In particular, extreme values of (L/R) are of special concern. For these cases, the global flow patterns as well as the attendant transfer properties show qualitatively different features. In light of the present numerical results, the validity of the empirical correlation formula of [2], which is based on measurements for (L/R) of O(1), will be assessed in a broader parameter space of Re and (L/R).

2. Results and discussion

The flow configuration, numerical solution procedures, and the tre

boundary conditions have been fully explained in [1], and they will not be reproduced here. In the present computations, a total of six cases of L/R=0.25, 0.5, 1.0, 2.0, 4.0, 6.0, were adopted.

The flow and concentration fields surrounding the cup walls at high exemplified in Figs. 1 and 2. In a similar manner to ref. [1], the angula ($\equiv v/r$) is shown in frame (a), and the meridional stream function Ψ in fr Here, Ψ is defined such that $u=(1/r)(\partial\Psi/\partial z)$ and $w=-(1/r)(\partial\Psi/\partial r)$. concentration field C is displayed in frames (c) and (d) for type A [non-t endwall base] and type B[constant-concentration endwall base], respectively concentration is constant [C=1.0] at the cylindrical wall surface.

Fig. 1[for L/R=0.25] is typical of the results for small aspect r rotating cup is shallow in depth, and the angular velocity in the bulk o interior is uniform in the radial direction. In the axial direction, the ang conspicuous only in a narrow boundary layer adjacent to the endwall base, diminishes rapidly as z increases away from the boundary layer. At large r increases to meet the no-slip condition of the cylindrical sidewall. The behavior of (v/r) and Ψ in much of the central radial locations is akin to that of a rotating flat disk. The fluid is drawn into the cup interior, due to the action of the rotating endwall base, in the central portion; in order to satisfy the mass continuity, the fluid moves toward the opening of the cup in the region close to the cylindrical sidewall. The concentration field for type A indicates that convective activities are minimal in the bulk of the interior, and strong radial gradients of concentration are seen in the close vicinity of the sidewall. For a transferring base[type B], the overall transport process is heavily influenced by conduction, since the global convective transfers are weak.

The flow structure for moderate L/R was extensively discussed in [1] reader is referred to that paper for details. Fig. 2 is illustrative of the L/R. Clearly, the radial dependence of the angular velocity is discernible. T the cup(L) is much larger than the radius of the cup(R); the interior flu

determined primarily by the cylindrical sidewall. In the bulk of the interior, v/r increases radially. In an extremely thin layer adjacent to the endwall base, v/r undergoes very steep changes to accommodate the no-slip condition at the solid wall. The meridional flow displays substantial variations in the radial as well as in the axial directions. As demonstrated in frames (c) & (d), the difference in C-field between type A and type B is relatively small. This is not unexpected in view of the fact that, for a deep cup, the impact of the base on the global flow characteristics is minor. The C-field is determined primarily by the conditions of the cylindrical sidewall. Only in the region very close to the base, the C-field displays appreciable difference between type A and type B. In the bulk of the central interior region, the meridional flow is not vigorous; therefore, the iso-C lines tend to be axially parallel, which implies that the flow is under heavy influence of conductive transport from the cylindrical sidewall. In passing, it is worth mentioning briefly the flow pattern in the exterior region of the cup. The stated objective of this paper is to study the forced convection from the interior surface of the cup; therefore, as remarked earlier, the solutions for the exterior regions are not of direct interest. However, the computed flow patterns in the bottom portions of the exterior regions are suggestive of the Taylor-Couette vortex[see ,e.g., ref. [3]]. This flow pattern is more pronounced when L/R becomes large, as in Fig. 2. The mass transfer from the external surface of the cup is not a subject of the present account; it will be dealt with in subsequent endeavors.

Based on the computed flow data, the variance of local Sherwoodnumber examined in Fig. 3. First, for type A(non-transferring base), Sh_c at the cylindrical sidewall is shown. The mass transfer coefficient Shc over much of the cup height diminishes appreciably as the cylinder aspect ratio increases beyond O(1). Similar behavior is noted for Sh_c for type B(transferring base), although the rate of decrease of Sh_c with L/R is less

pronounced for type B than type A. The Sherwood number Sh_b at the endwall base in the central interior portion demonstrates minor dependence on L/R. The role of the base endwall disk weakens for large L/R, which results in a reduction of Sh_b at large radii.

Finally, summarizing the entire numerical data, the variation of the with L/R is scrutinized in Fig. 4. Comparisons are made between the present n results and the empirically-fitted formula of [2]. Cross-checks of the res that the empirical formula tends to portray the average Sherwood numbe reasonable accuracy. This comparison gives credence to the applicabilit empirical relation over a wider range of L/R than that actually used in the e In Fig. 4(c), for comparison purposes, the numerical data for Sh_b are check the results of an isolated flat disk rotating in its own plane(ref. [4]). Evi a cup, as L/R diminishes, approaches that for a flat disk.

3. Conclusion

When L/R is very small, the flow patterns are qualitatively similar to a rotating flat disk. Convective activities are meager in the bulk of the i non-transferring base endwall disk. For a transferring base, conductio significant role.

When L/R is large, the interior flow is determined chiefly by the cylindrical sidewall. Only in an extremely thin boundary layer on the base disk, velocities undergo rapid changes. Differences in the concentration fields are generally small between the two types of the base conditions.

The local mass transfer coefficient at the cylindrical sidewall, Sh_c very small over much of the cup height when $L/R \gtrsim O(1)$. However, this tenden less pronounced for type B than for type A. Also, as L/R increases, the influence of the base disk weakens, which results in a reduction in Sh_b at the base.

Cross-comparisons with the numerical data establish tha

empirically-obtained formula for Sh is applicable in a broader range of L/R.

Acknowledgments.----- This work was supported in part by a research countract from the Tong Yang Machinery & Engineering Co., Korea.

References

1. W. N. Kim and J. M. Hyun, Mass transfer characteristics for a r cup-like cylinder, Int. J. Heat Mass Transfer (accepted for publication (1995

2. E. M. Sparrow and A. Chaboki, Heat transfer coefficients for a cup-li rotating about its own axis, Int. J. Heat Mass Transfer 25, 1333-1341 (1982).

3. H. Schlichting, Boundary Layer Theory. McGraw-Hill Inc.,(1979).

4. E. M. Sparrow and J. L. Gregg, Heat transfer from a rotating disk to any Prandtl number, ASME J. Heat Transfer 81, 249-251 (1959).

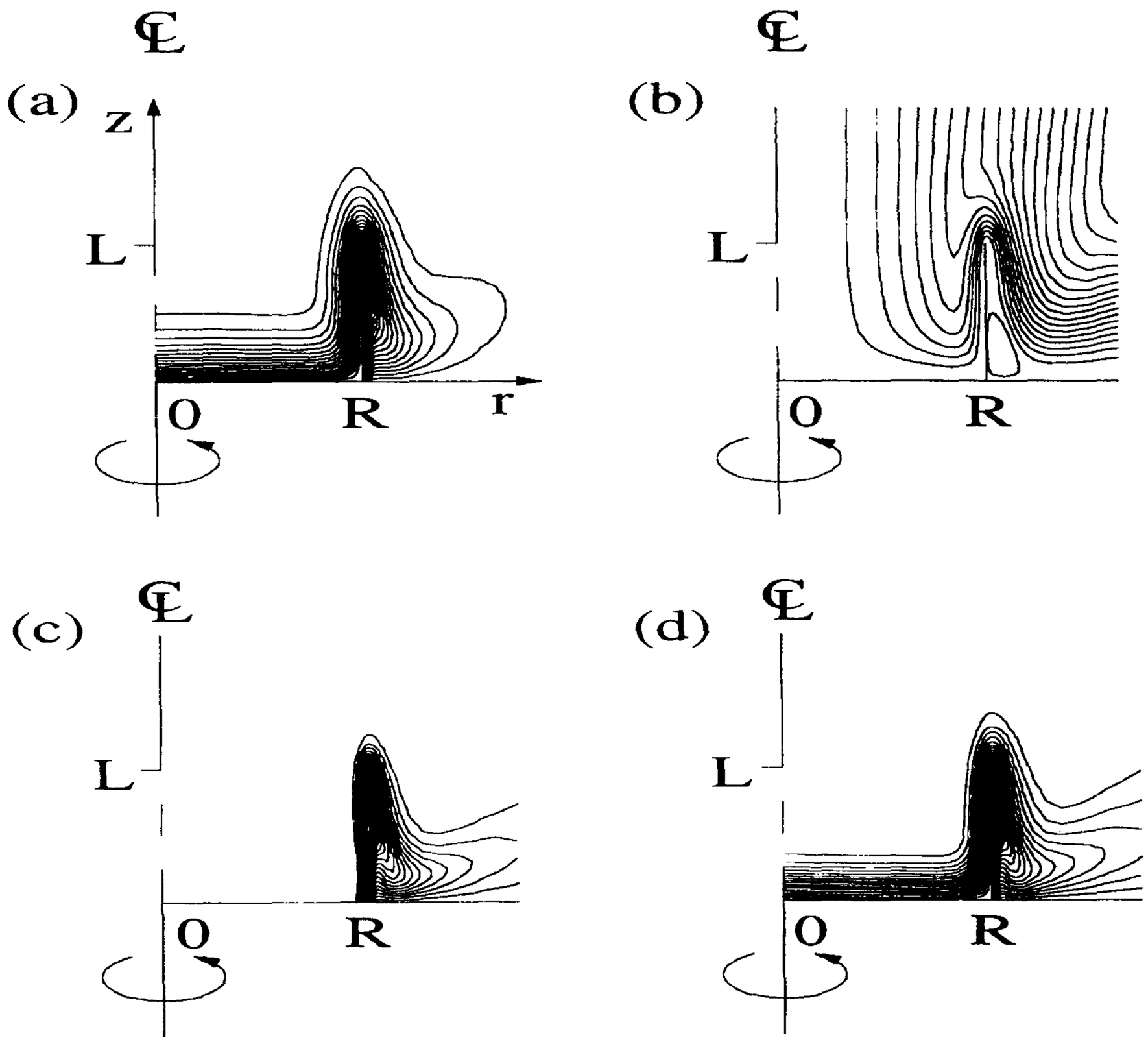

Fig. 1. Depiction of flow field. Re=800, L/R=0.25. The numbe contour is 20.

(a) Angular velocity(v/r) field.

(b) Meridional stream function Ψ, nondimensionalized by R^3u

(c) Concentration(C) field for type A.

(d) Concentration(C) field for type B.

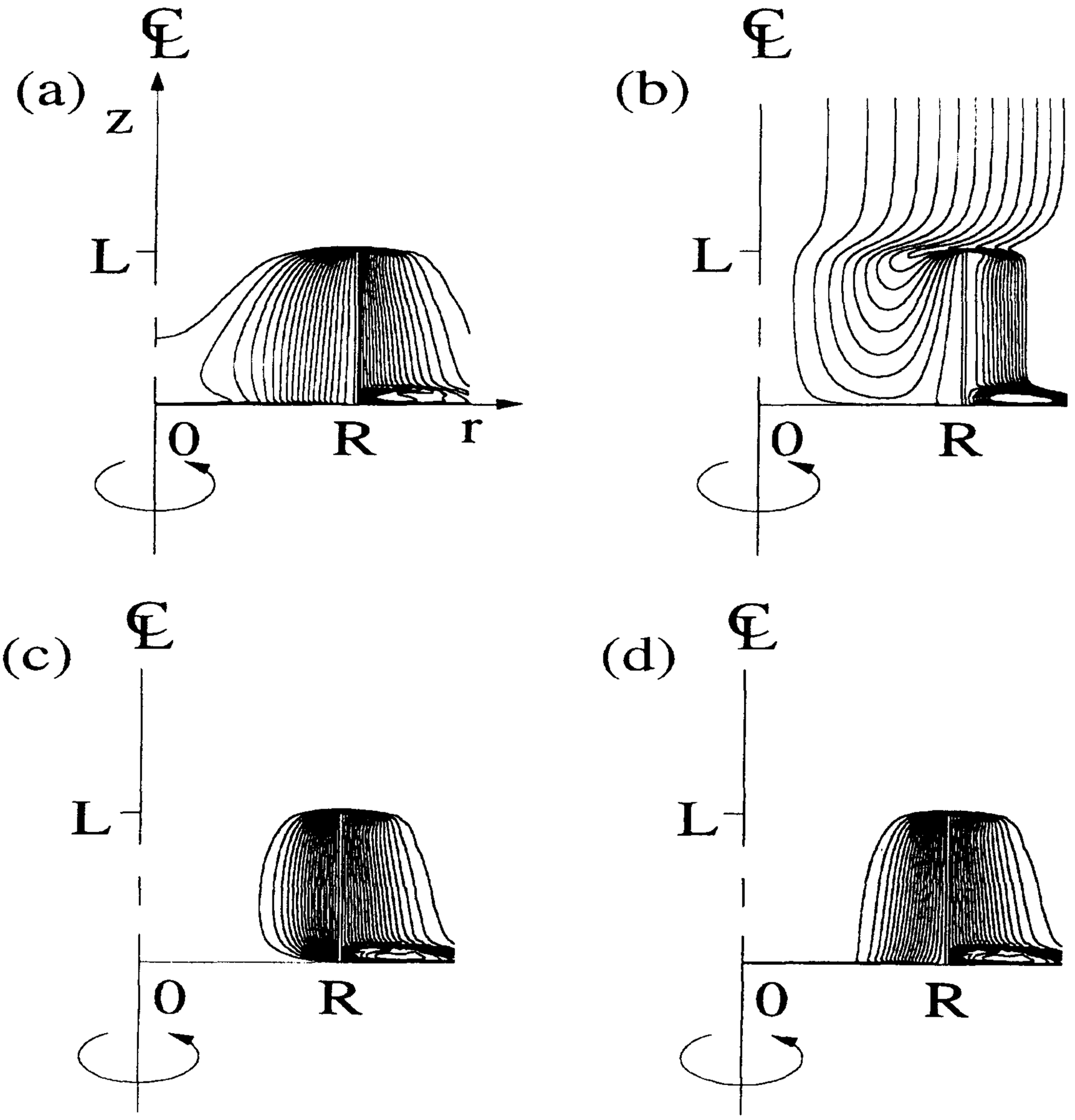

Fig. 2 . The same as in Fig. 1, except for L/R=6.0.

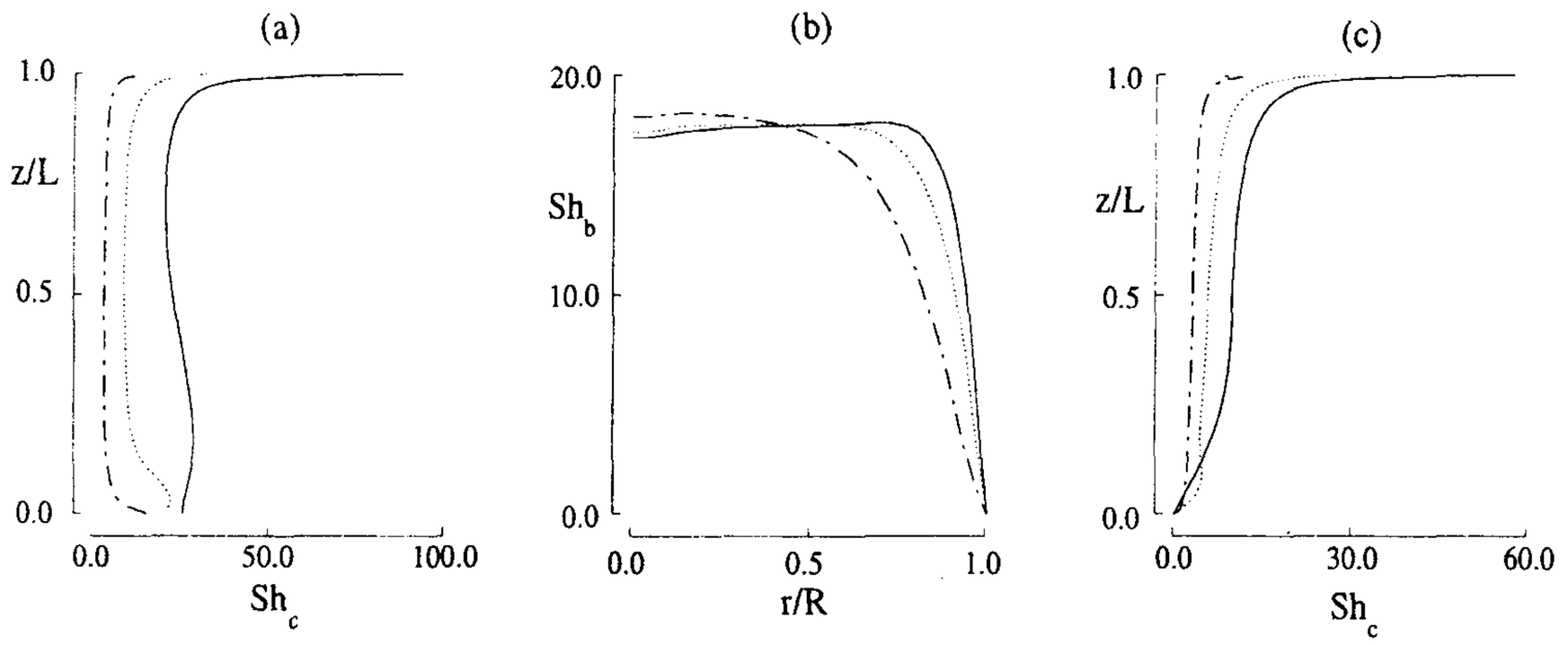

Fig. 3. Distributions of the local Sherwood number. Re=800.

(a) Local Sherwood number Sh_c at the cylindrical sidewall. Type

(b) Local Sherwood number Sh_b at the base disk. Type B.

(c) Local Sherwood number Sh_c at the cylindrical sidewall. Type

_____, L/R=0.25; ....., L/R=1.0; __ . __, L/R=6.0.

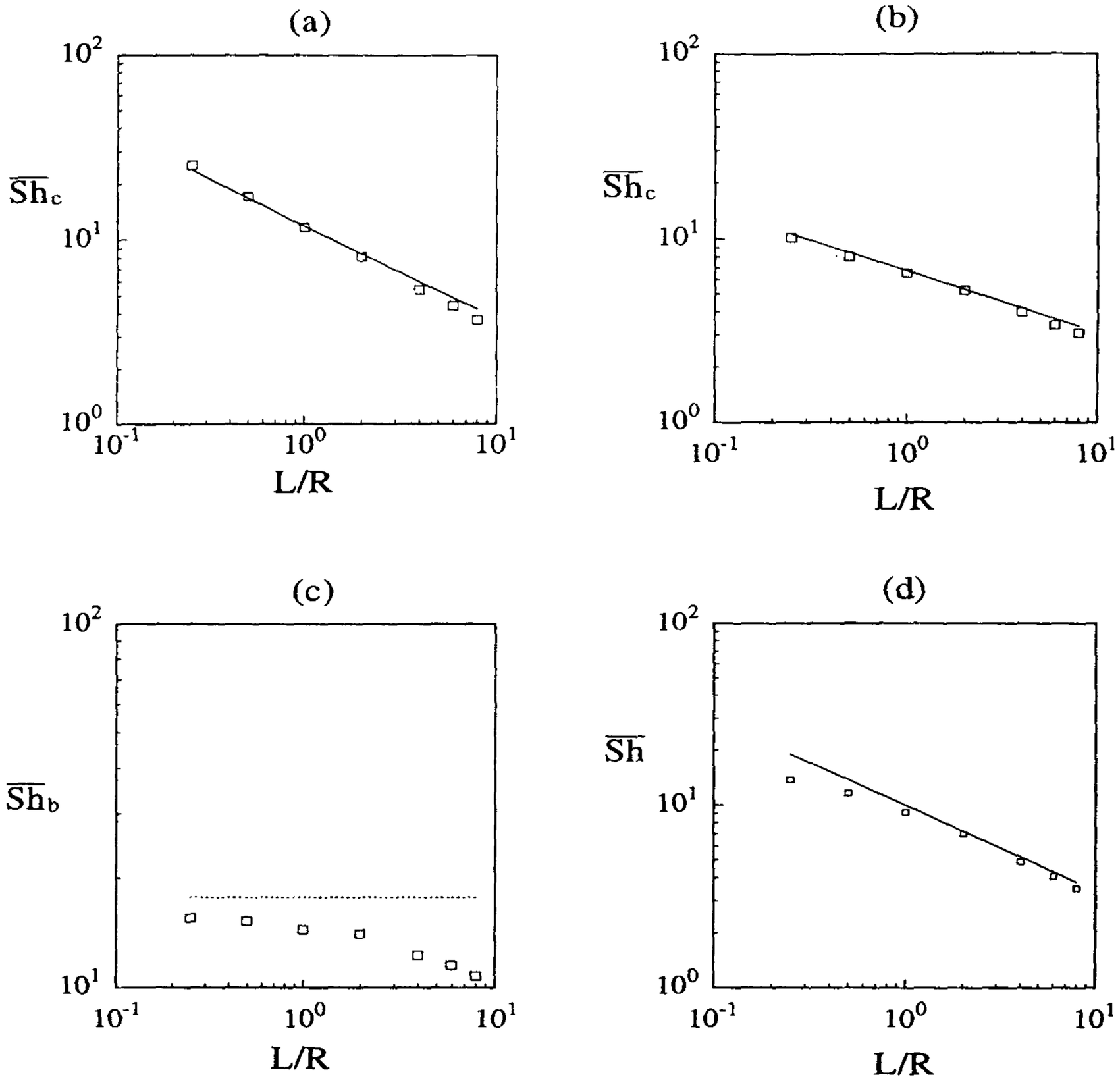

Fig. 4. Averaged Sherwood number $\overline{Sh}$ vs. L/R. Re=800.

(a) $\overline{Sh}_c$ at the cylindrical wall. Type A.

(b) $\overline{Sh}_c$ at the cylindrical wall. Type B.

(c) $\overline{Sh}_b$ at the base disk. Type B.

(d) $\overline{Sh}$ at the entire wall surface. Type B.

_____, experimental results of ref. [2];

□ , present numerical data;

....., result for a rotating disk of ref. [4].

제6장. 공동연구개발 목표 달성도 및 대외 기여도

제1절. 연구개발 목표 달성도

'결정성장에 있어서의 회전유동과 대류현상의 해석'이라는 과제명에 따라 회전유동과 대류현상에 관련한 전반적인 유동 및 열전달의 물리적 특성을 이해하기 위한 연구를 수행하였다. 자연대류현상의 유체유동 및 열전달과 회전유체유동에 대한 KAIST와 일본 Kyushu Univ.연구팀과의 국제공동연구를 효과적으로 수행하였다. KAIST와 Ozoe 연구팀의 상호협력연구를 수행함으로서 실험및 계산능력이 향상되었다. 또한, 연구원들의 훈련을 통한 연구개발의 잠재력이 강화되었다. 첨단 기계전자산업에서 자주발생하는 결정성장문제에 관계된 유동및 열전달 특성에 대한 풍부한 연구자료를 제공하였다. 수치해석에 필요한 계산소프트웨어를 개발 하였고, 실제 회전기계의 성능향상방법과 기법을 제시하였다.

본 연구과제와 관련된 많은 연구 결과를 해외 유명 학술지에 게재하였다. 따라서, 본 연구과제의 목표를 충분히 달성하였다고 판단된다.

제2절. 기대성과 및 대외 기여도

1.기술적 측면

유체역학 및 열전달 분야의 양측연구소의 연구자원과 인력을 조합함으로써 효율적이고 유능한 연구팀을 구성할 수 있으며, 앞으로 유체역학 분야의 수치 모델화 기술과 모형실험의 기술 축적을 가져올 것이다. 이것은 회전유체기계의 제조산업에 직간접의 효과를 이룰 것이다. 유체역학 분야에서 일본과의 상호교류는 KAIST의 연구진에게 첨단의 실험기법과 수치계산기법을 접하는 기회의 제공과 함께 기술정보의 습득의 기회를 제공함으로써 KAIST 연구원들의 연구능력을 증대시켰다. 수치계산과 모형실험에 의해 제공되는 연구자료들은 기술혁신형의 장치와 현대 기계전자산업설비의 설계자와 운전자에게 유용한 기술정보를 제공할 것이다.

2. 경제 산업적 측면

본 연구의 성공적인 수행은 첨단기계전자산업의 회전기계의 설계시, 또는 생산기술상 수반되는 제반 열전달 및 유체유동의 이해에 필요한 유용한 정보를 제공한다. 이와 같은 제반 연구자료가 회전기기의 제작및 생산기술에 활용될 경우 기기의 성능 향상을 이룰 수 있을 뿐 아니라 선진국으로 부터의 기술이전에 소요되는 비용의 절감이 가능하다. 또한, 국내의 설계기술의 축적은 국내산업의 부가가치를 줄 것이다.

본 연구의 결과로 개발된 실험기법및 유체유동해석 프로그램을 각 분야에 적용하여 상용화하면 국내산업계에 사용되고 있는 외국페키지의 대체 효과를 가져와 수입 대체효과를 기대할 수 있다.

3. 기타

본 연구의 수행으로 인한 연구결과는 회전유체기계에 대한 학문적 연구 및 공학적인 측면에서 중요한 의의를 가진다. 특히 결정성장 문제에서 고순도의 결정을 획득하기 위한 기술적 자료를 제공하며 현장 기술자의 운전능력의 신장에 기대되는 바가 크다. 첨단전자산업에서 고순도의 반도체웨이프가 요구되고 있는 실정이며 본 연구의 성공적인 수행으로 이러한 결과를 산업현장에 직접 응용될 수 있을 것이다. 또한 본 연구의 결과들은 국외 유명 논문집에 게재되었으며 한국의 위상을 국외에 알리는 기회가 되었다. 또한 본과제의 수행함으로서 획득된 고급연구인력은 본과제와 관련된 산업분야에서 주도적 역활을 할 것으로 기대된다.

제7장. 공동연구개발결과의 활용계획

첫째, 결정성장문제에서 도가니의 형상, 회전및 열적조건은 결정형성에 영향을 미친다. 본 연구 결과를 도가니의 형상설계 및 고순도의 결정성장을 위한 기술적 자료로 이용한다.

둘째, 회전하는 원통용기내의 유동장은 회전결정성장장치의 간단한 모형을 제시하며, 본 연구에서는 회전속도에 미소한 교반을 주어 실제상황에 근접한 모형실험과 수치계산을 수행하였다. 이에 대한 수치적, 모형실험적 자료들을 회전결정성장장치의 설계및 운전에 기술적 정보로 제공한다.

세째, 본 연구의 수행을 통하여 유동의 전영역에 대하여 동시에 속도를 구하는 PTV(Particle Tracking Velocimetry)을 개발하였다. 이는 Point by point 식의 LDV 속도측정 방법과는 달리 전유동장에 대해 동시 측정을 가능하게 한다. 이러한 실험적 방법은 유체역학분야의 실험효율의 증대를 가져온다.

네째, 터보기계 등의 내부에서 발생하는 열유동의 특성의 이해를 통하여 운전및 설계시 기초적인 자료로 활용한다.

제8장. 참고 문헌

[1] H.P.Greenspan, 1968, The Theory of Rotating Fluids, Camblidge University Press, New York.

[2] D. Metzer & N. Afgan, 1984, Heat & Mess Transfer in Rotating Machinery. Hemispere, New York.

[3] J. M. Hyun et al., 1983, Numerical solutions for spinup from rest in a cylinder, J. Fluid Mech. 127, pp 263-281.

[4] R. J. Ribando et al., 1989, Flow in a partially filled, rotating tapered cylinder, J. Fluid Mech. 203, pp. 541-555.

[5] J. M. Hyun et al., 1982, Numerical solution for the spin-up of a stratified fluid, J. Fluid Mech. 117, pp 71-90.

[6] Y. G. Kim, 1991, Development of digital vector velocimetry method and its application to rotating flows, Ph. D. thesis, Iowa University

[7] J. W. Chew, 1982, Computation of flow and heat transfer in rotating cavities, Ph. D. thesis, Sussex University.

[8] G. E. Heuser et al., 1986, A numerical simuration of inertial waves in a rotating fluid, Computer Method in Applied Mech. and Engs. 57, pp. 207-222.

[10] D. R. Olander, 1978, The gas centrifuge, Scientific American, vol. 239, pp. 27-33.

[11] J. S. Park, 1990, Transient flows of a compressible fluid in a rapidly-rotating cylinder, Ph. D. Thesis, KAIST.

[12] M. A. Shadday, R. J. Ribando & J. J. Kauzlarich, 1983, Flow of an incompressible fluid a partially field, rapidly rotating cylinder with a differentially rotating endcap, J. Fluid Mech. vol. 130, pp. 203-218

[13] M.F.Larrousse, 1987, Transport Phenimena During Spin-Up/Spin-Down in the Bridgman_Stockbarger Technique, PhD thesis.